FLOW CHARACTERISTICS IN SIMULATED ARTERIES AND THEIR RELATIONSHIP TO ATHEROSCLEROSIS

A thesis
submitted for the degree of
Doctor of Philosophy
at the
University of Canterbury
by

Conan J. Fee

Department of Chemical & Process Engineering
University of Canterbury
New Zealand
1989

Dedicated to my father, my family and my friends...
but most of all to Glenda.

The scientist and the artist are both trying to extend our understanding of experience by the use of creative imagination, subjected to critical control. Both are seekers of truth who make indispensible use of intuition.

- B. Magee on Karl Popper.

The person *least* likely to develop atherosclerosis is:

a hypertensive, bicycling, unemployed, hypo-β-lipoproteinic, hypolipaemic, underweight, premenopausal female dwarf living in a crowded room on the island of Crete before 1925, and subsisting on a diet of uncoated cereals, safflower oil,and water.

- A.N. Howard, 1966 International Medical Tribune of Great Britain, June 30.

Acknowledgements

The following people have helped me throughout my work and I wish to express my sincere thanks to you all. Firstly, I thank Dr. John Abrahamson, my supervisor, who was always open to new ideas and provided a constant source of fresh conceptual approaches to the subject of this thesis. What an education and a pleasure it has been to work with you, and to absorb from you, my philosophy of scientific method.

The technical staff of the Department of Chemical & Process Engineering have never failed to provide the solutions to difficult technical problems. I don't think any one of you escaped my hare-brained schemes over the past few years, and certainly your collective efforts and skills are very much appreciated.

I have enjoyed knowing the library staff, past and present, and thank you for your friendliness and the personal approach you give to the library service. We, at the Engineering School, are very fortunate in this respect.

The secretarial staff in the Department of Chemical & Process Engineering have always been friendly and willing to help on a personal level - an advantage of our relatively small department, I think.

Thank you also to the procession of computer "gurus" (fellow students), who unravelled the mysteries of the various computer problems, which surfaced to threaten my sanity from time to time, and to my fellow postgraduate students, in general, for their companionship - it's been fun. Good luck to you all.

I must express my gratitude to the following people who have assisted me by providing equipment throughout the period of my experimental work: Professor I.R. Wood of Civil Engineering (LDA equipment); Professor D.C. Stevenson of Mechanical Engineering (spectrum analyser and microphone equipment); Staff and students of the Zoology Department (movie camera, hydrophone and preamplifier); and all the technical staff of those departments, who facillitated these loans.

I would also like to thank Professor W.E. Stehbens, of the Wellington Clinical School of Medicine, University of Otago, for introducing me to the field of haemodynamics and for providing useful comments in the initial stages of this work.

The Medical Research Council of New Zealand kindly provided personal support in the form of a Postgraduate Scholarship. Equipment grants were provided by the National Heart Foundation of New Zealand and the University of Canterbury.

I also appreciate the help of Lynn Anderson and of Pat Jordan in the printing and the binding of my thesis, respectively.

I have reserved my thanks to two special people until last. Firstly, to my father, thank you for everything over the past few years. How lucky we, your children, are. Lastly, Glenda - you deserve the pride of final mention. Words cannot express all of my gratitude to you, but for all that you have given up, so that I could complete my work, I am truely grateful. A PhD student at full gallop is not the easiest animal to be around at times, I know, and what a task the final run would have been without you and your help.

Abstract

An experimental investigation into the link between haemodynamics and atherosclerosis is reported in this thesis. A model of a C-shaped tortuosity of the cervical portion of the human internal carotid artery (ICA) was constructed from perspex and the flow of water through the model studied by dye visualisation and Laser Doppler Anemometry (LDA), for both steady and pulsatile flow conditions. Dynamic similarity between water flow in the model and blood flow in the artery was scaled by the Reynolds number and the frequencies of unsteady flow components scaled by the Strouhal number.

Dye visualisation results are presented in a series of photographs, which illustrate the flow features in the model at given Reynolds numbers. Several differences from classical Dean-type motions in curved pipes were observed, including axial flow separation, flow asymmetry and an unexpected region of reverse flow, situated at the outer wall of the first bend in the model.

A series of axial isovel contour maps were generated from LDA measurements, for planar slices located throughout the straight sections of the tortuosity. These are presented in the form of cross-sections, normal to the pipe's central axis for steady flow conditions, for a Reynolds number of 1500. The contours show the existence of separation regions, bounded by free shear layers, which are located along the walls downstream of the inner bends. Axial isovel contour maps are also presented for planar slices near the walls of the tube, under pulsatile conditions, for a mean Reynolds number of 1500 and a flow variation of ±50% about the mean. The flow features were qualitatively similar to those seen under steady flow conditions but the intensities of the separated flows were lower during pulsatile flow than during steady flow. The separation regions were observed to move back and forth along the walls of the tube. Steady flow conditions did not allow the quantitative prediction of the locations or magnitudes of pulsatile flow features at the same instantaneous Re. Shear rates at the walls of the tube were estimated from the contours, giving an estimate of the wall shear stresses.

Regions in the model where flow separation was observed, consistently matched reported sites of proliferative atheroma in the tortuous ICA. It is concluded that regions subjected to low mean shear stresses but high fluctuating components of shear stress are associated with the proliferative lesion. Stress fluctuation fatigue of the arterial wall may play a role in initiating the proliferative lesion, by stimulating reparative processes, as suggested by Stehbens (1979). Pressure fluctuations are also

implicated in the etiology of proliferative lesions. Separated shear layers in these regions are thought to be a source of pressure fluctuations, felt at the wall, especially near the reattachment position.

Regions subjected to unidirectional, high shear rates, matched reported sites of atrophic atherosclerotic lesions and sites of calcification in early atheroma. The magnitude of the shear stresses in these regions does not appear to be as important, in relation to atrophic lesions, as the presence of a unidirectional shear stress. Stress fluctuation fatigue was not indicated as the cause of degenerative changes to the wall in these regions.

A modification has been suggested of the unified hypothesis, described by Steinberg (1983), for the initiation and progression of atherosclerosis, allowing for the action of haemodynamic influences, especially in the initial stages of the disease. It has been postulated that haemodynamic factors may act in three ways: by inducing endothelial injury; by causing stress fluctuation fatigue of the blood vessel wall material; and/or by altering the transmural permeability to macromolecules, in particular low density lipoproteins.

The transendothelial transport of macromolecules, in particular Low Density Lipoproteins (LDL's), via pinocytotic vesicles was examined. An exponential factor, allowing for hindered diffusion through the vesicle neck was derived and included into Arminski et al's (1980) equation, describing the permeability of an endothelial cell. The effect of convective perturbations on the observed diffusion coefficient of LDL within the short vesicle neck was found to be negligible. A mechanism for the convective enhancement of vesicular loading is postulated, which depends crucially on the spontaneous curvature of the vesicle wall material. Convective movements through the vesicle neck may overide a geometric equilibrium concentration partitioning effect, which limits the internal vesicle LDL concentration resulting from diffusional loading, to about one third of the plasma concentration. Hence, transendothelial cholesterol transport may be increased by convective loading, in the presence of blood flow disturbances, to 3 times over that resulting from diffusional loading only.

TABLE OF CONTENTS

List of Figures

Appendices Figures

List of Plates

List of Tables

Chapter 1

Introduction

1.1 The Importance of Haemodynamics Study:

Atherosclerosis, the disease of the larger arteries, occurs with varying degrees of severity in the human vascular system. The distribution of the arterial wall lesions of atherosclerosis (atheroma or atheromic plaque) within the arterial tree suggests a strong correlation between the affected areas and the local blood flow conditions. This fact has been noted by many researchers (to name a few: Texon 1957, Rowsell et al 1965, Glagov 1965, Caro et al 1971a, 1971b, Fry 1972, Rodkiewitz 1975, Caro et al 1978, Stehbens 1979, Bharadvaj et al 1982, Mc Millan 1985, Friedman 1986, Caro et al, 1987) and has led to a large body of literature regarding the study of blood flow or haemodynamics.

Cardiovascular diseases are responsible for more than 50% of all deaths in the Western world, with atherosclerosis being the most frequent cause of death (Stehbens 1979). By comparison with other Western countries, NZ and Australia have high rates of cardiovascular diseases. In 1968, the age standardised mortality rates from all cardiovascular diseases were higher in Australia than in NZ. By 1983 the situation had reversed, so that mortality rates from coronary disease and cardiovascular disease were 15% and 12% higher respectively in both sexes in NZ. During the same period, the decline in cardiovascular disease accounted for 90% of the decline in all causes of death in NZ (Beaglehole et al 1986).

Beaglehole and Jackson (1985) regarded changes in the management of patients with symptomatic coronary heart disease between 1968 and 1981 as being of secondary importance to the reduction of the major coronary risk factors in reducing mortality rates in Auckland, NZ. They associated the decline in coronary heart disease mortality rates with a decrease in the consumption of dairy products, a reduction in self-reported cigarette smoking habits, improved control of hypertension and possibly by reductions in blood serum cholesterol levels and an increase in habitual physical activity in the community.However, it cannot be concluded from studies of this type

that cardiovascular diseases are prevented by the reduction or elimination of risk factors. Risk factors have been identified by epidemiological studies, but the identification of causes and the elucidation of the mechanisms of cardiovascular diseases require investigation at a more fundamental level.

The study of haemodynamics in relation to atherosclerosis is important for two reasons. Firstly, some light may be shed on the initiation and progression of the disease. This may be helpful in assessing the relative importance of the risk factors associated with the disease, such as age, sex, diet, smoking habits, etc... Secondly, the causes of the disease may yet be attributable to some modifiable haemodynamic behaviour, allowing the possibility of the prevention or at least the retardation of atheroma.

1.2 The Definition of the Problem:

Thompson (1986) described the characteristic lesion of atherosclerosis as a fibrous plaque which consists of a cap of smooth muscle cells covered by a layer of endothelium and a core containing yellowish lipid (figure 1-1). Up to 25% of the lesion consists of lipid, mainly esterified cholesterol. The cholesterol is derived almost entirely from the blood and not from local synthesis.

The tendency for atheroma to contain large levels of cholesterol led many researchers in the past (not unreasonably) to believe that the blood serum cholesterol level is the major causitive factor of the disease. A rather insidious error, namely that lipid buildup is in itself indicative of atheroma, must be avoided in order to prevent the confused interpretation of experimental results designed to test this hypothesis. Many early studies subject to this error were carried out on animals fed with cholesterol-rich diets. The presence of cholesterol-rich streaks on the arterial walls of these animals, found after excision, was attributed to the effects of atherosclerosis. Hence the affect of dietary cholesterol on the incidence of atherosclerosis "proven" in a rather cyclic fashion. According to Stehbens (personal communication), it is possible that the lipid streaks were manifestations of a fat storage disease and not atheroma at all. Furthermore, it has now long been recognised that lesions resulting from high-cholesterol diets show differences from those occurring spontaneously in man (Duff, 1951).

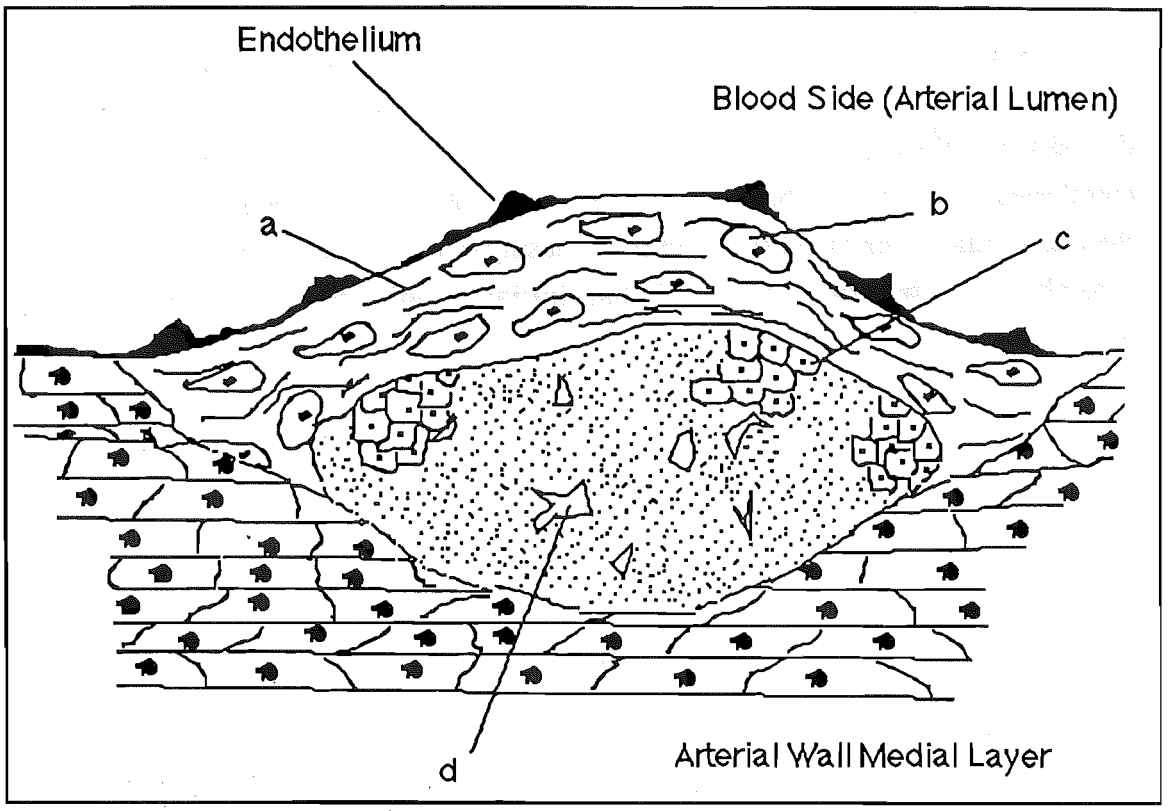

Figure 1.1
The Atherosclerotic Lesion (Thompson 1986)
a) Collagen b) Smooth Muscle Cells c) Foam Cells (containing cholesterol)
d) Extracellular Cholesterol Crystals

In addition to the above description of the atheromic plaque, it has been noted (Miasnikov 1962, Stehbens 1979, Ross 1986) that the affected artery exhibits calcification, proteoglycan accumulation, a loss of elasticity, cracking, stenosis (narrowing of the arterial lumen), aneurysm (ballooning out of the vessel wall) and a diminution of elastic tissue. A proliferation of smooth muscle and foam cells in the intimal layer of the arterial wall occurs and is referred to as intimal thickening.

It may be observed from the above descriptions that the atheromic plaque has a complex structure. One of the problems confounding a clear picture of the initiation and progress of atherosclerosis is that there is still argument over the relative importance of the constituent features of the atheromic plaque.

The 1981 report of the Working Group on Arteriosclerosis of the Nat. Heart, Lung and Blood Institute of the US dept of Health and Human Services describes atherogenesis as follows:

"Atherogenesis is the process that culminates in atherosclerosis. In it's initial stages, the inner layer of an affected artery becomes thickened by deposition of fat,

particularly cholesterol, together with an increase in the number of cells in the innermost layer of the artery. Some arteries, even in the same organ, are affected more than others, possibly because of local differences in blood pressure and flow. As the deposits of fat and cells enlarge, a reaction to their presence sets in and gradually culminates in scarred and thickened plaques. These plaques protrude into the lumen of the artery, hampering blood flow and predisposing to the formation of a blood clot (or thrombus) on the surface.....What initiates early fat deposition or cell multiplication is not clear. A current hypothesis is that injury to the endothelium is the initiating factor".

The outstanding feature of the above description of atherogenesis is the emphasis placed on fat deposition. There is no reference to loss of wall elasticity,diminution of elastic tissue, cracking or calcification and proteoglycan accumulation. There is also scant reference to the position of atherosclerosis - contrary to the actual case, the implication is that whole arteries are affected equally throughout.

Stehbens (1979) proposed an alternative definition of atherogenesis, viewing atherosclerosis as a progressive disease:

"Atherosclerosis may be defined as the degenerative and reparative changes in the blood vessel walls that are the direct consequence of haemodynamically induced fatigue...Lipid accumulation and calcification may be non-specific changes due to the affinity of non-phagotosed cell debris for lipids and calcific deposits respectively. The complications from which man dies, are due to decreased tensile strength, or reparative intimal proliferation which compensates for the increased fragility".

Clearly there is a conflict over the importance of cholesterol in atherogenesis. Whilst the description of the US National Institutes of Health and Human Services points to cholesterol and lipid deposition as the major factor in atherogenesis, Stehbens regards lipid deposition as a complication of lesser importance than haemodynamically-induced fatigue and probably secondary to the initiation of atherosclerosis.

Jellinek and Detre (1986) (while making no mention of haemodynamics) also regard the onset of lipid accumulation to be secondary to intimal proliferation and describe arteriosclerosis (sic) as a proliferative disease of the arterial intima. Despite this, they argue that an altered transmural permeability *precedes* the onset of intimal proliferation, inferring that the transport of material into or out of the arterial wall is crucial as an early feature of atherosclerosis. Their hypothesis is a variation on the earlier lipid filtration hypothesis, which states that atherosclerosis derives from the alteration of the barrier to lipid transport across the arterial wall.

It is by no means clear what effect the lesions themselves have on the progression of atherosclerosis. Stehbens (1986), in his studies of the tortuous internal carotid artery, pointed out two distinct types of lesion, apparently depending on the local haemodynamic forces. A proliferative lesion formed in areas where flow separation or low shear was expected (figure 1-2), whilst a non-proliferative (or atrophic) lesion appeared where the highest blood velocity or highest shear was expected. According to Meyer (1975), in the early stages of atheroma, the proliferative sites are subject to lipid accumulation and the atrophic lesions to calcification. Later, as the disease progresses, the atheroma at each site becomes less distinguishable from the other. Meyer suggests that the progression of the atheroma is different at each site. The site of the atrophic lesion, initially subject to calcification, alters to accumulate lipids in a different way to that in which lipid accumulates initially at the proliferative site and vice versa.

It is therefore important to examine the effects of haemodynamics on the *initial* lesions of atherosclerosis, as the characteristics of the lesions themselves complicate the progression of the disease at later stages. Once the relationship between haemodynamics and early atheroma has been clarified, the progression of the disease can be studied.

The correct mechanisms by which atherosclerosis is initiated and progresses have probably yet to be proposed. Given the distribution of atheroma in the vascular system, the correct mechanism for initiation, at least, is likely to include a haemodynamic influence.

1.3 Scope and Objectives of the Study:

In this thesis, a mechanism is proposed by which local blood flow characteristics may influence the transport of macromolecules (in particular cholesterol) through the endothelial cell layer of the blood vessel wall. This proposal is based on the mechanism of trans-endothelial macromolecular transport via pinocytotic vesicles which has been described by other workers, including Smith 1969, Casley-Smith & Chin 1971, Weinbaum & Caro 1976, Rubin 1977, Arminski et al 1980 and Hiram & Nir 1984. Experimental work is carried out on the hydrodynamic flow through an arterial model in order to assess the likely effects of blood flow on the arterial wall.

It was recently brought to the author's attention that the role of pinocytotic vesicles in the mass transport of macromolecules has been put in doubt by the work of Frokjær-Jensen (1980, 1984) and Bundgaard et al (1983). Their studies, using ultrathin serial sectioning of frog mesenteric capillaries showed that previous

conclusions regarding pinocytotic vesicles were subject to anomalies, caused by the thickness of the sections studied by electron microscopy. Frokjær-Jensen (1984) suggested that his findings were consistent with the view that macromolecular transport may occur through occasional large pores that develop in the endothelia rather than vesicular transport. The proposal of Chapter 3 may be modified to account for this, with little change in the mode of haemodynamic enhancement of the transport rate.

The approach taken was to find an arterial configuration that is prone to atherosclerosis but which possesses a simple flow geometry. The simpler the flow geometry, the more general should be the findings with regard to the relationship between atherosclerosis and haemodynamics.

The cervical portion of the human internal carotid artery fulfills both requirements. In normal subjects, this section of the artery is straight, with no branches or bifurcations. It is also relatively free of atheroma. In about 15% of the population, a redundant length of the artery develops, forming varying degrees of tortuosity, from mild undulations to severe kinking and even coiling (figure 1-2). In these persons, the tortuous section of the artery is prone to a higher incidence of atherosclerosis than in normal subjects (Metz et al 1961, Weibel & Fields 1965, Desai & Toole 1975). Assuming there are no inherent abnormalities in the arterial wall tissues of the tortuosity, the only causitive factor for atherosclerosis is blood flow.

The large variance in the degree of tortuosity made the choice of the model's geometry fairly arbitrary (within certain limits) and this, coupled with the absence of branches and bifurcations made the model attractive for flow studies. Several simplifications from the actual artery were made in the model.

1. The model was rigid-walled.
2. The tube was of constant circular cross-section throughout.
3. The model was symmetric about it's midpoint.
4. The toruosity was confined to one plane.
5. Because blood behaves essentially as a Newtonian fluid at the shear rates typically found in the larger arteries, water was used as the flow medium.
6. Much of the experimentation was carried out under steady flow conditions. This provided a fundamental case for flow analysis. It was thought that most features of pulsatile flow would be evident in steady flow.

7. Pulsatile flow was simplified from the in vivo pulse wave to a sinusoidal-type flow variation.

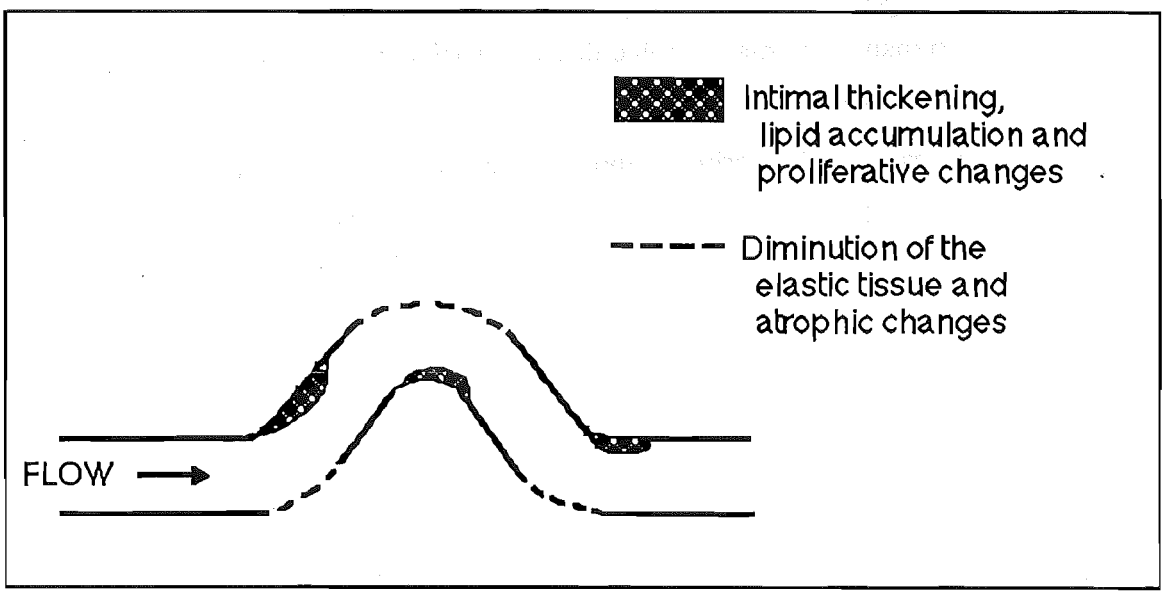

Figure 1.2

Atheromic Sites in the Tortuous Internal Carotid Artery (Stehbens 1987).

While these simplifications undoubtedly made the flow conditions rather artificial, they allowed the study of the flow features that were due to the arterial geometry alone. It was decided that a more realistic model would merely increase the complexity of the study and decrease the generality of the results.

The objectives of the study were:

1. To examine the flow features in the model over a range of Reynolds numbers for both steady and pulsatile flow conditions.
2. To compare the observed flow features with those of related flow geometries and to assess whether any of the theoretical or numerical analyses of related geometries might be useful in predicting the flow features in the present model.
3. To locate the flow features in the model under steady and pulsatile flow conditions for comparison with the known locations of atheroma in vivo.

4. To estimate the likely physical effects of the flow on the walls of the model and from them the effects of blood flow on the walls of the blood vessels.

5. To propose a robust mechanism by which haemodynamics might affect the transport of macromolecules (in particular cholesterol) through the arterial wall.

6. To examine the various hypotheses for the initiation and progression of atherosclerosis in the light of the experimental results.

1.4 Organisation of the Thesis:

In Chapter 2, background information on atherosclerosis and some of the atherogenesis hypotheses is presented. The physiology of the arteries in general and the internal carotid in particular are described. The literature regarding some of the types of flow likely to be encountered in the model is reviewed, with particular emphasis on the flow in curved pipes.

In Chapter 3, the proposed mechanism for the influence of haemodynamics on cholesterol transport is developed. Some of the circumstantial evidence supporting the mechanism is presented.

Experimental methods and apparatus are described in Chapter 4. Experimental results obtained from dye visualisation and laser Doppler anemometry studies for steady and pulsatile flow conditions are presented in Chapter 5, along with an attempt to measure wall pressure fluctuations under steady flow conditions.

A discussion of the results and their relevance to the physiological situation is given in chapter 6. Chapter 7 contains the conclusions of the study and suggestions for further work.

Chapter 2

Physiology and Relevant Fluid Dynamics

2.1 The Tortuous Internal Carotid Artery and the Model:

Flow studies were carried out in an idealised model of the tortuous cervical portion of the human internal carotid artery (ICA). The cervical portion of the ICA is normally straight and has no branches or bifurcations, making it attractive for flow studies. When excessive length develops in the cervical portion of the ICA, varying degrees of flexure occur, ranging from slight undulations through to C-shaped or S-shaped tortuosities, coiling and even kinking, (figure 2-1) in which the angulation is such that some stenosis occurs (Metz et al 1961, Weibel and Fields 1965, Desai and Toole 1975). According to Weibel and Fields, kinking appears to be an acquired syndrome, occurring mostly in older individuals in whom arteriosclerotic disease and the ageing process are important factors in the exaggeration of an already tortuous vessel.

The ICA is prone to a higher than normal incidence of atherosclerotic attack when it exhibits tortuosity, coiling or kinking (Metz et al 1961, Weibel and Fields 1965, Meyer, 1975), suggesting a relationship between the flow characteristics in the blood vessel and atherogenesis. Peterson et al (1960) remarked on the absence of atheroma in the straight (normal) ICA. Ku et al (1985) also noted minimal intimal thickening in the normal ICA under pulsatile conditions and that the flow in the ICA was unidirectional, with no flow disturbances. Samuel (1956) showed considerable evidence of proliferative atheroma in a C-shaped tortuosity of the petrous portion (situated distally to the cervical portion) of the ICA in similar positions to those in the cervical portion indicated by Stehbens (1987), shown in figure 1.2.

Flow enters the internal carotid artery from the common carotid artery via the carotid sinus. The carotid sinus is a short, bulbous section situated at the entrance to the internal carotid (figure 2-1). The contraction in vessel diameter in going from the

sinus to the ICA may stabilise the flow downstream somewhat (McDonald 1974). Acting against this flow stabilising affect is the bifurcation of the common carotid artery into the internal and external carotids just prior to the carotid sinus with the probable associated flow separation at the flow divider and also in the regions of expansion in the sinus. Separation was shown under steady flow conditions by Bharadvaj et al (1982) in a model of the carotid bifurcation and this separation region (with inherent low shear stress at the wall) has been associated with proliferative atheroma (Peterson et al 1960, Heath et al 1972, Zarins et al 1981, Ku et al 1985).

The range of ICA flexure observed in vivo allowed considerable scope in choosing a model for this study. It was decided for the sake of simplicity to use a C-shaped configuration with the tortuosity lying in one plane (the plane of symmetry) and symmetrical about the mid-point of the C-bend. The configuration was chosen to match closely that shown in Fig.1 no. 4 of Stehbens and Fee (1985), as this exhibited the unusual flow features the most readily of all the models in that study. In vivo studies of the C-shaped tortuosity were available (Stehbens 1986, 1987, Greenhill and Stehbens 1985, Meyer 1975), offering the possibility of comparison between in-vivo and in-vitro results.

The geometry of the model (figure 4-1) was rigidly defined with the bends having radii of curvature equal to the tube diameter (20 mm). Straight sections between the three bends were inclined at 70° to the upstream and downstream sections. The length of the straight sections were equal to the tube diameter. This configuration was within the range of geometries found in vivo. The diameter of the tube was 20 mm compared to 8 mm in the ICA. Dynamic similarity was ensured by using the Reynolds number

$$Re = \frac{\rho D u}{\mu}$$

; where ρ is the density of the fluid, D is the vessel diameter, u is the mean velocity based on the volumetric flow rate and μ is the fluid viscosity.

2.2 The Relevance of Hydrodynamics to Haemodynamics:

In contrast to water, blood is not a Newtonian fluid, but a suspension of cells and droplets in a colloid-like solution. Normal human blood contains about 47% (expressed as a haematocrit level of 47) by volume of small, easily deformable

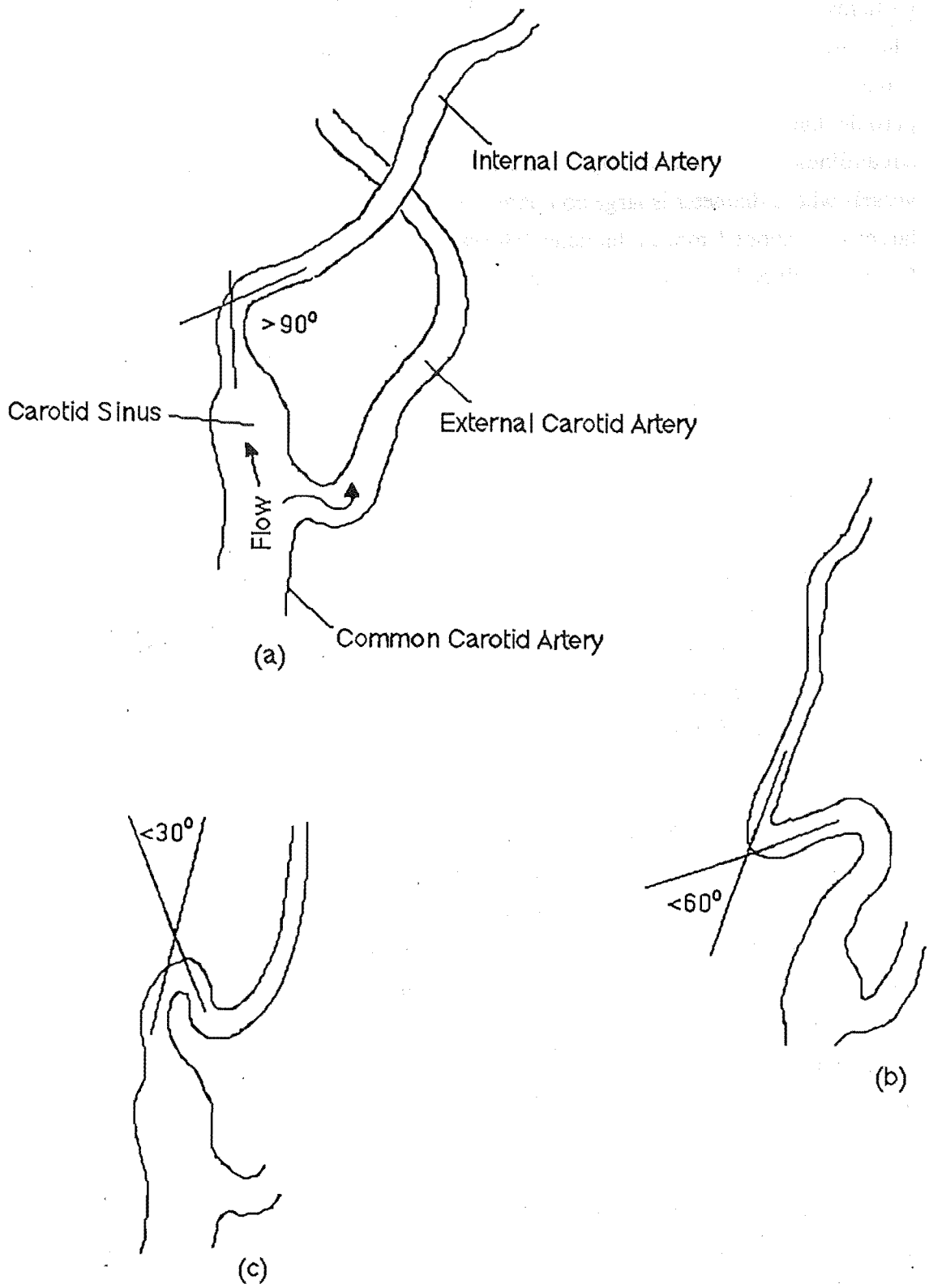

Figure 2.1
Tortuosities of the Internal Carotid Artery (Weibel & Fields 1965)

particles - the red platelets - which comprise about 97% of the particles in the blood. The normal red blood cell is a biconcave disk, with a major diameter of about 8 μm and a thickness of about 2 μm. The Reynolds numbers of these particles (based on the particle diameter) is very small (O[10^{-4}]) and so they may be assumed to follow the streamlines of the flow closely. Blood may be regarded as an homogeneous fluid in vessels whose diameter is large compared to the size of the particles - that is, in vessels larger than about 1 mm in diameter (Hussain 1975, Merrill 1969). Stein and Sabbah (1980) concluded that the presence of red blood cells at a normal haematocrit level did not cause greater disturbances than would be expected in a Newtonian fluid of equal viscosity.

At the shear rates present in the larger arteries (above 100 s^{-1}), blood behaves as a Newtonian fluid, with a viscosity of 3.24 cP at 37°C (Merrill 1969). McDonald (1974) defines blood as having a viscosity of about 0.004 Nsm^{-2}, and a density of about 1005 kg m^{-3}. In the case of arterial flows then, blood rheology (differences from Newtonian behaviour) might be viewed as irrelevant. However, a transition between the Casson (1959) region, in which a certain yield shear stress must be applied before flow begins and the Newtonian region occurrs somewhere in the range 16 - 100 s^{-1}, depending on haematocrit (Hussain 1977). The yield shear stress is very low however, at 0.05 dynes cm^{-2} (Rahn et al 1967). This corresponds to a local blood shear rate of about 15 s^{-1}.

According to Merrill (1969), blood rheology appears to be most relevant to slow flows in which the blood is treated as a continuum and in which the mean shear stress is relatively low. This is exactly the condition likely to be found in areas of flow separation and low stress , which have been most often associated with proliferative atherosclerosis. In his summary, Merrill points out that the relevance of blood rheology to physiological flows is to make the stopping of flows easier, the starting of flows more difficult and slow flows more energy consuming than would be expected if blood were a strictly Newtonian fluid.

It appears that the hydrodynamic features of the flow through the model should give a good indication of the macroscopic haemodynamic features for the same geometry, with dynamic similarity scaled by the Reynolds number. Also blood may be assumed to behave as a Newtonian fluid. In recirculating flows beneath separated shear layers however, the shear rates may be low enough to invalidate the assumption of Newtonian flow behaviour. In such cases, the tendency would be for blood to stagnate more readily than a Newtonian fluid. In pulsatile flow, areas of low shear stress would also tend to resist acceleration more in haemodynamic flow than in the hydrodynamic situation.

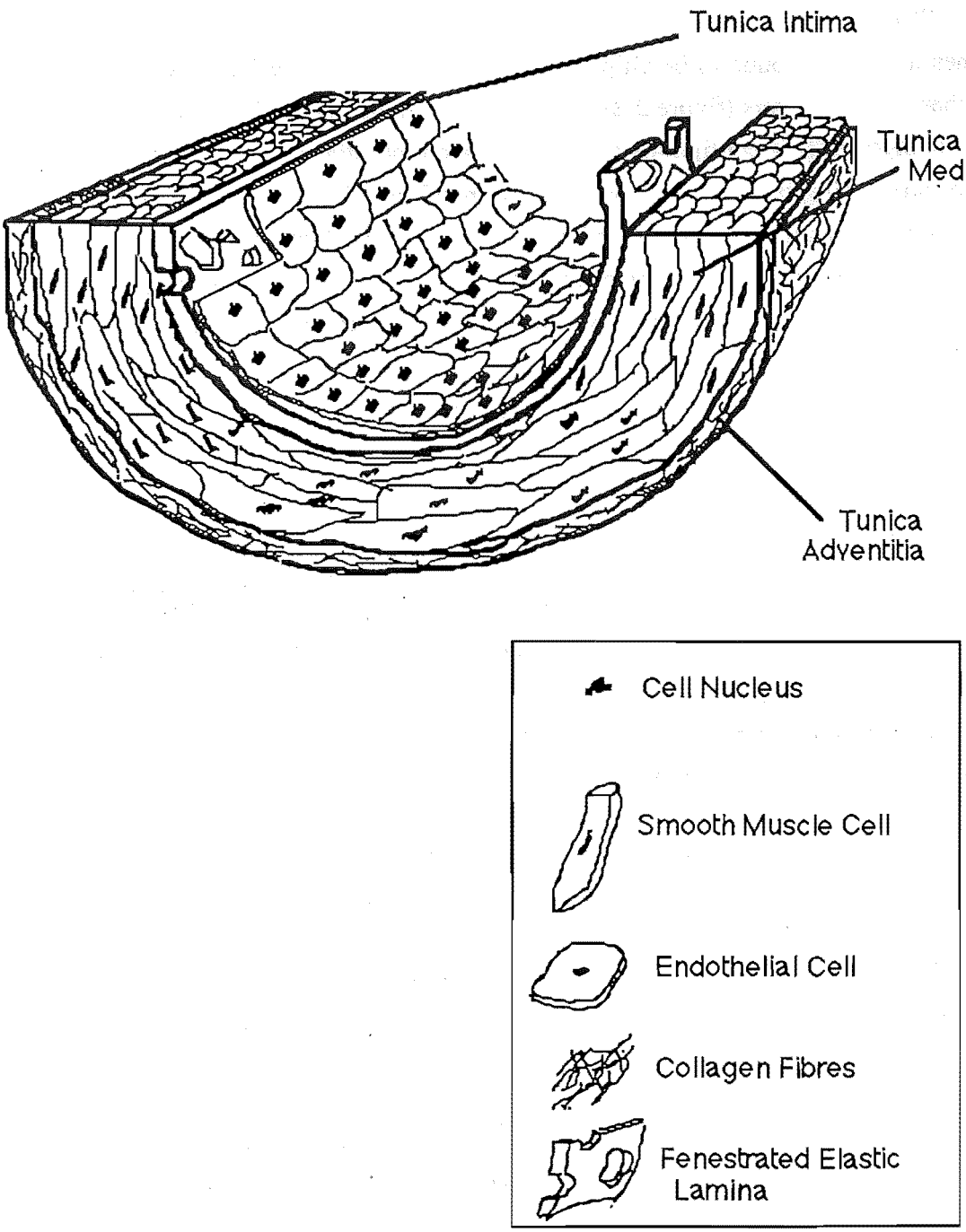

Figure 2.2
Cross-section of the Arterial Wall

2.3 The Arteries and Associated Flow Effects:

The arteries in vivo are normally of circular cross-section, though some branches have been found to be elliptic (Caro et al 1966). The walls are made up of three characteristic layers (figure 2.2). The innermost layer, the tunica intima, consists of two components: a contiguous monolayer of endothelial cells which forms the smooth inner lining of the arterial wall, surrounded by a layer of elastic tissue, the elastic lamina. The intima is surrounded by what is often the thickest component of the wall, the tunica media. This is comprised of smooth muscle cells interspersed with elastic tissue and collagen. The relative amounts of smooth muscle and elastin vary from artery to artery, with a tendency towards a predominance of muscular tissue with increasing distance from the heart. Hence the peripheral arteries of diameter less than about 1 cm (of which the ICA is one) are referred to as "muscular arteries" and those closer to the heart and larger than 1 cm in diameter (including the aorta), are named the "elastic arteries".

Surrounding the media is the outermost layer of the arterial wall - the tunica adventitia. This layer merges with the surrounding tissue at it's outer edges, often without a clear boundary and consists largely of connective tissue (collagen fibres) and some elastin. In the larger arteries the adventitia also contains the vaso vasorum, a network of capillaries which supply nutrients to the outer wall tissue.

Obviously, in contrast to the model, the arterial wall is not rigid. A longitudinal movement of the wall might be expected to be induced by viscous drag as the blood is pumped through the artery. However this has been measured to be only a matter of a few μm at most, and even this may have been caused by longitudinal shortening with vessel dilatation (McDonald 1974), rather than viscous drag. The arteries may then be considered to be restrained or tethered longitudinally.

The radial dilation of the arterial wall has been measured by several workers (McDonald 1974) but with considerable disagreement in result due to the uncertainties in the effect of the measurement methods employed. A reasonable figure appears to be about a ±5% change with respect to the mean radius. Recently, Barth et al (1988) measured the % changes in the common carotid artery by ultrasound and found the changes to range from ±3.16% to ±4.78%. The effect of the wall elasticity on the flow velocity profile within the artery is unimportant as long as the path length of a fluid element is small compared to the wavelength of the pressure pulse driving the flow (Wormersley 1957, Lightfoot 1974, Caro et al 1978). This condition is fulfilled in the larger arteries, where the wavelength is in excess of 3 metres.

The effect on the smaller scale dynamics of a compliant flow boundary such as the endothelium is more difficult to assess. Hansen & Hunston (1974) found that a hydroelastic instability in the form of a wave structure in a purely elastic surface-liquid interface will be set up under a turbulent boudary layer if the quotient

$$\frac{V}{\sqrt{\frac{G}{\rho_L}}}$$

exceeds 1.41, where V is the free-stream velocity of the fluid, G is the shear modulus of the compliant boundary and ρ_L is the density of the liquid. For blood flow, ρ_L = 1005 kg m^{-3} (McDonald 1974). The shear modulus μ of detached endothelial cells cultured from the bovine aorta was measured (Sato et al 1987) by the micro-pipette method, to be in the range 0.07 dyne cm^{-1} to 0.24 dyne cm^{-1} (7 x 10^{-5} Nm^{-1} to 2.4 x 10^{-4} Nm^{-1}), depending on the method of detachment. Trypsin-detached cells had elastic shear moduli at the lower end of the range, possibly due to the digestion of native membrane proteins by the trypsin. Mechanically detached cells had shear moduli in the range 0.14 - 0.24 dyne cm^{-1} (1.4 - 2.4 x 10^{-4} Nm^{-1}). For the purposes of this calculation, μ is taken to be 0.20 dyne cm^{-1} (2 x 10^{-4} Nm^{-1}). In Sato et al's experiments, μ was calculated from measurements of the aspirated length drawn into a pipette with a radius of about 3μm. Dividing μ by the radius should give an area elastic shear modulus required for the quotient of Hansen & Hunston. The result is G = 670 dyne cm^{-2} (67 N m^{-2}). Then

$$V \geq 1.41 \sqrt{\frac{G}{\rho_L}}$$

for the instability to occur in the endothelial cell layer. Substituting in the above values for the endothelial cell and blood, an instability will not be set up unless the blood velocity is greater than 36 cm s^{-1}. The blood velocity may exceed this value during systole, but for the most part would be less than the critical value.

Benjamin (1960) examined the effect of a flexible boundary on hydrodynamic stability. He found that a stabilising effect of the boundary on the flow was possible, but that it depended strongly on a balance between the relative wave speeds in the boundary material and the fluid, the compliancy of the boundary and the viscous damping of the wall, which, suprisingly, has a de-stabilising effect. Unfortunately, the

mechanical properties of the endothelial cell layer are not well enough characterised at the present time to take advantage of Benjamin's analysis (and the later study of Landahl 1961) in predicting the likely effect of the endothelial cell layer on the stability of the blood flow.

Gad-el-Hak et al (1984) showed that compliant surfaces interacted only with turbulent boundary flows and not with a laminar boundary layer, despite free stream speeds in the latter of over twice the corresponding velocity for the turbulent case. The blood flow in the ICA is likely to be laminar for the most part, but secondary flows may cause turbulent spots at various sites, in which Hansen & Hunston's quotient might be applicable.

It is concluded that the flow in arteries may, to a first approximation, be likened to that in rigid pipes. The macroscopic flow features exhibited in the rigid-walled model are likely to reflect those in the corresponding tortuous artery for the same flow conditions, despite the compliance of the arterial wall. Some flow stabilisation may occur in vivo due to the effect of the compliant endothelial layer, but the effect of this on the macroscopic flow features , such as the positions of flow separation, magnitudes of shear stress, etc would be small.

2.4 Atherogenesis:

The gross lesion of atherosclerosis is described in section 1.2 of this thesis.

A vast body of literature concerning the pathogenesis of atherosclerosis exists (as even a brief perusal of the journals pertaining to the vascular system will show) and it is beyond the scope of this thesis to attempt a review. However, a brief description of some of the more common atherogenesis theories is provided here as an introduction to the subject. For a more comprehensive treatment, the reader is directed to the works of Texon (1960), Fry (1973), Stehbens (1979), Brown & Goldstein (1984), Jellinek & Detre (1986), Thompson (1986), Ross (1986) and Steinberg (1987).

2.4.1 Metabolic Theories:

The metabolic theories of atherogenesis focus on reduced enzyme activity as their key features. Wilens (1951) showed that areas susceptible to atheroma demonstrate intimal thickening before lipid deposition. This has also been noted by Jellinek & Detre (1986) and others. Adams et al (1969) found a strong correlation

between intimal thickening and a loss of enzyme activity and suggested that intimal thickening reduces the flux of O_2 to medial enzyme sites, thereby reducing enzyme activity. A relation between hypoxia (reduced oxygen tension) and intracellular lipid deposition was pointed out by Dixon (1961) and Kjeldsen et al (1968) demonstrated this with cholesterol-fed rabbits.

2.4.2 The Filtration Theories:

The filtration theories hold that lipid accumulation occurs because of a mechanical barrier to the passage of fatty materials across the arterial wall. One premise of this, however, is that the internal elastic membrane is the most significant barrier to filtration of large molelcules from the blood to the tissue. This is not likely to be the case due to the fenestrated nature of the elastic lamina. It has been shown (Karnovsky 1967, Fry 1972, Siflinger et al 1975, Caro 1978) that the endothelial cell layer in fact provides the rate-limiting step in the transfer of macromolecules into the arterial wall.

2.4.3 The Response to Injury Theory:

First proposed by Virchow (1856), this hypothesis postulated that injury occurs specifically to the endothelial cells lining the artery (French 1966, Ross and Glomsett 1973, 1976). The injury may result from several sources and may upset a balance between the normal process of cell death and renewal and lead to intimal thickening. Once cholesterol influx exceeds efflux and catabolism, the lesion formation may progress towards irreversibility and the clinical disease then develops.

Ross (1981) described a modified version of the response to injury hypothesis in that an altered transmural permeability occurs by injurious events (caused by mechanical forces, chemical agents, toxins, immunological injury, viruses, etc...) affecting the endothelial layer, which controls the permeability to a large extent. The endothelial injury might result in endothelial cell separation, desquamation, or an altered trans-endothelial permeability. Once this has occurred, the changes may lead to platelet adhesion and thrombosis and the adhesion of blood monocytes, which might then migrate into the tissue. The interactions amongst substances derived from platelets and monocytes as well as from plasma, such as lipoproteins or hormones, may stimulate the migration of smooth mouscle cells from the media into the intimal layer and initiate the proliferation of these cells.

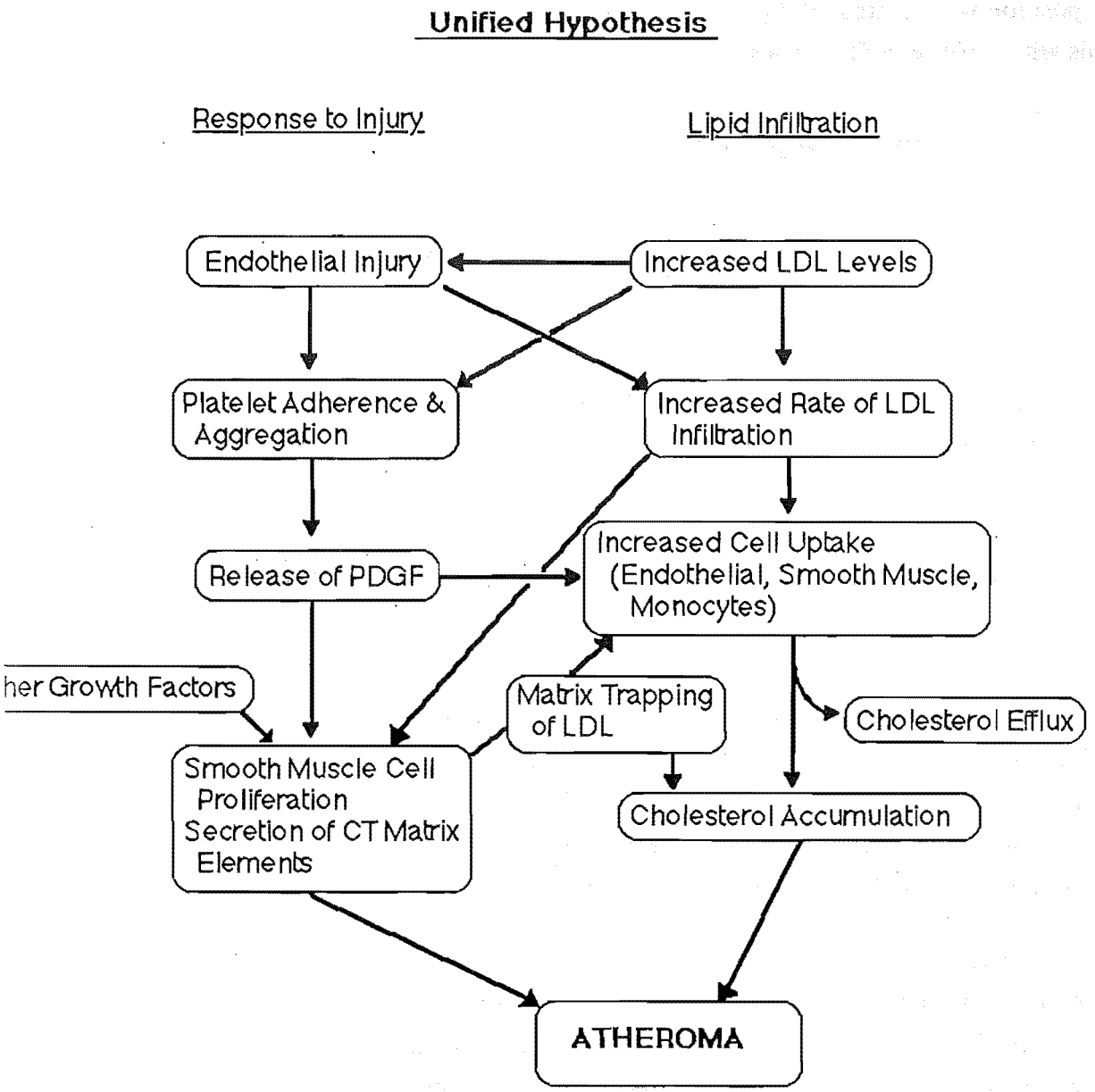

Figure 2.3
The "Unified Hypothesis" of Atherogenesis (Steinberg 1983)

2.4.4 The Lipid Theory:

The lipid hypothesis holds that lipid (usually meaning cholesterol bound up in Low Density Lipoprotein, LDL) is a sufficient cause for atheroma. Steinberg (1983) cites the occurrence of galloping atherosclerosis in subjects suffering from familial hypercholesterolemia as proof that LDL can be a sufficient cause of atherosclerosis. He holds that, in terms of risk factors, the 10-year-old child with homozygous familial hypercholesterolemia has only one such risk factor, since it does not smoke and does not suffer from hypertension, obesity or diabetes mellitus. At the risk of anticipating a later section, I should point out that Steinberg completely ignored haemodynamics in his argument. LDL could just as well be described as an accelerating factor rather than a causitive factor by his own arguments.

The lipid hypothesis interacts with several stages of the response to injury hypothesis. LDL may be the initial injurious factor and endothelial cell injury immediately increases LDL infiltration to the wall tissue (Carew et al 1983). Platelet aggregation (Insel et al 1978) and smooth muscle cell growth (Fischer-Dzoga et al 1976) may be stimulated by LDL. Platelet-Derived-Growth-Factor (PDGF) increases the expression of LDL receptors on smooth muscle cells and thus increases their uptake of lipid (Ross & Klebanoff 1971). These and other factors suggest a strong interaction between the hypotheses, to the extent that they could be combined into one more comprehensive "Unified Hypothesis" as in figure 2.3 (Steinberg 1983).

2.4.5 The Haemodynamic Theory:

The haemodynamic concept of atherosclerosis considers the laws of fluid dynamics as the primary factor in the etiology of atherosclerosis, accounting for the localisation of atherosclerosis as well as the progressive pathologic changes at specific areas of predilection (Texon 1960). In addition to "the laws of fluid dynamics", Texon also stated that a biologic factor must also be considered, namely the local reparitive reaction of the wall of the vessel, especially the intima:

> *"Differences in the biologic* response to injury *and differences in the tissue or fabric structure may determine the nature and degree of atherosclerotic change. The effects of other factors such as age, sex, race, diet, nutritional status, lipid metabolism, drugs, hormones, associated disease, hypertension and stress require re-evaluation as secondary factors. It is suggested that these factors may merely modifiy the primary haemodynamic mechanism."*

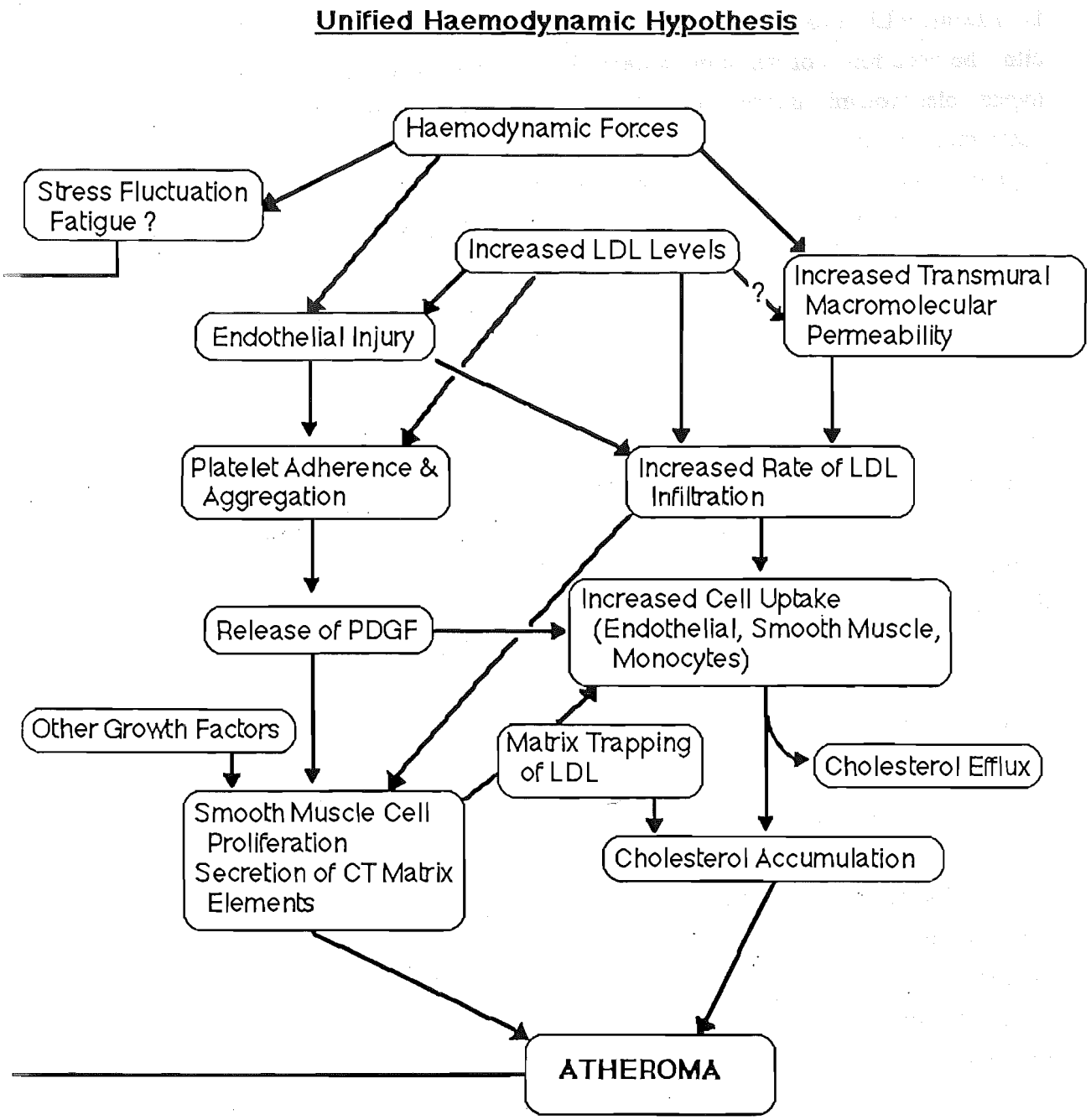

Figure 2.4

The Unified Haemodynamics Hypothesis

2.4.6 Comments:

Each of the above theories has it's own strengths and weaknesses, but none offers the complete answer to the question of the etiology of atherosclerosis. The major common weakness of the metabolic, filtration, response to injury and lipid hypotheses is that none of them allows for the focal nature of atheroma - a fundamental feature of atherosclerosis. The haemodynamic hypothesis is the only one to account for this, and is indeed based upon the locality of atheromic predilection itself.

In fact, a combination of the haemodynamic hypothesis and the unified hypothesis of Steinberg is the strongest of all those proposed to date, as it may account for all of the pathologic changes inherent in atheroma.

There is nothing to suggest that the progression of the disease does not follow the scheme(s) laid out in the unified hypothesis - the haemodynamic theory does not prohibit this possibility. It does, however, provide for the initial step in atherogenesis, filling the gap of both the lipid and the response to injury hypotheses. Haemodynamic factors may effect an endothelial injury and/or an altered trans-endothelial macromolecular permeability. A more complete unified hypothesis is illustrated in figure 2.4. In this "Unified Haemodynamic Hypothesis", two steps are labelled with question marks. It has yet to be shown that increased LDL levels can affect the transmural permeability of an artery, though possibly the release of a vesicle (see Chapter 3) from the endothelial cell wall may be triggered by the passage of an LDL molecule through the stalk and hence pinocytotic vesicular transport across the endothelium accelerated. This is not a necessary condition for the initiation of atherosclerosis under the proposed scheme of figure 2.4. Secondly, the stress fluctuation fatigue of the wall suggested by Stehbens (1979) has not been demonstrated to date, though this view depends very much on the definition of the term "fatigue". For instance, enhanced vesicular transport might be considered to consitute fatigue. The inclusion of haemodynamically-induced fatigue in the scheme of figure 2.4 is justified on the grounds that no distinction is made here between the atrophic and proliferative lesions of atheroma. If this distinction were made, this step might more properly be included with those factors involved in the etiology of atrophic atheroma than those of the proliferative lesion considered here.

It is with the haemodynamically-altered trans-endothelial macromolecular permeability that this thesis is concerned.

2.5 Relevant Fluid Dynamics:

2.5.1 Introduction:

In this section some of the flow features relevant to the experimental model used in this study are reviewed. The emphasis is on providing a basis for discussing the flow field likely to be encountered experimentally, rather than on predicting, in a quantitative fashion, the occurrence or form of any particular flow features. This section is not intended to provide the reader with an exhaustive review of all the phenomena related to physiological flows, but only those aspects of fluid dynamics relevant to the experimental work in this study. The physiological significance of any particular flow feature is a subject for discussion, where appropriate, in the light of experimental results.

In section 2.5.2.1 the steady fully-developed laminar flow in curved pipes is reviewed. Two important flow parameters are introduced: the curvature ratio, δ, which is a measure of the abruptness of the bend, and the Dean number K, which is a type of Reynolds number incorporating the curvature ratio. The flow features are described for a range of curvature ratios, $0.01 < \delta < 0.66$, and the Dean number, $85 < K < 5000$. The experimental model used in this study has a relatively high curvature ratio $\delta = 0.5$, and experiments were carried out at low to moderate Dean numbers, $100 < K < 1700$.

Steady flow in the entry region of curved pipes exhibits different flow behaviour from the fully-developed case and is described in section 2.5.2.2. Flow development is shown to depend strongly on the entrance flow conditions, and the analysis of Smith (1976) with Poiseuille flow upstream of the bend is of particular relevance, showing a region of upstream influence prior to the bend. Other phenomena, such as separation and a cross-over point of the maximum wall shear from the inner to the outer bend walls, are also predicted and shown experimentally by various authors. Flow through the bends constituting the experimental model in this study will undoubtedly exhibit entrance flow behaviour.

The steady fully-developed and entry flow cases are extended to pulsatile flow in curved pipes in sections 2.5.3.1 and 2.5.3.2. Pulsatile flow with a non-zero mean (as opposed to purely oscillatory flow) exhibits a flow pattern arising from a balance between the steady and unsteady components of flow. The degree of pulsatility is expressed by the Womersley parameter, α. Increasing α from zero leads to departures from the steady flow pattern, including flow reversal, separation, a shift in the maximum axial velocity position across the tube and increased vortical motions. In

man at rest, the values of the Womersley parameter for the aorta and carotid arteries are about 92 and 18 respectively, based on a heart rate of 1.2 Hz, an aorta diameter of 2.5 cm, and a carotid diameter of 0.5 cm.

Two experimental investigations of steady and pulsatile flow through pipes of varying curvature are mentioned briefly in section 2.5.4. The tubes used in both of these studies have very small curvature ratios, and so are of only moderate relevance to this work.

In section 2.5.5, some aspects of separated shear layers are reviewed in order to point out the possibilities regarding their form, interactions with flow boundaries and nearby flow phenomena such as vortices, and their transient behaviour. Because of the complexity of three-dimensional flow separation in general, and the flow patterns in the three consecutive bends of high curvature ratio in the experimental model, no attempt is made to predict the quantitative characteristics of the separated flow expected experimentally.

2.5.2 Steady Flow:

2.5.2.1 Flow in Curved Pipes:

The laminar flow of Newtonian fluids in smooth straight pipes is well understood, largely through the 19th century work of Hagen (1839), Pouseuille (1840, 1841) and Reynolds (1883). However, the introduction of axial curvature results in a more complex flow dependent on a balance of inertial, viscous and centifugal forces, first noted by researchers in the early 20th century. A shift of the maximum axial velocity towards the outer wall of a curved pipe was observed by Williams et al (1902), and Eustice (1910, 1911) showed the existence of secondary flow by injecting ink into water flowing in a curved pipe.

Dean in his theoretical treatment (1927, 1928) contributed a major advance in the understanding of the laminar flow in curved pipes by recognising the dependence of the flow on both the pipe radius to axial curvature ratio δ, and the Reynolds number, and combining these parameters into a dimensionless number now known as the Dean number (White 1929). Many variations of the Dean number have been employed by researchers since that time, confusing the comparison between studies, and an appeal by Berger, Talbot and Yao (1983) for a universally accepted Dean

number is answered in this thesis by the use of the form described by them as the simplest :

$$K = 2\delta^{1/2} Re = \left(\frac{a}{R}\right)^{1/2} \frac{(2aU)}{\nu}$$

; where U is the mean axial velocity, ν the kinematic viscosity, a the pipe radius, R the axial curvature taken along the centreline and δ the curvature ratio equal to a/R.

However, useful as it is, it is not sufficient to decribe all curved pipe flows using the Dean number alone. Although the dependence of flow in general on δ is much smaller than that on K, an investigation of the effect of δ independent of Re yields some suprising results. For instance, Berger. Talbot and Yao (1983) note that the flow resistance for a strongly curved pipe, $\delta = 0.5$, is less than that of a loosely coiled pipe, $\delta = 0.01$, when $K > 85$. Lin (1972) indicated that a significant δ effect can appear when δ is as small as 0.07. Conversely, Austin and Seader (1973) remark that the effect of δ is largely accounted for in the Dean number, but their results are for $\delta \leq 0.2$, and extrapolation to larger δ is not admissable. Most numerical studies assume a very small value of δ (ie: $\delta \ll 1$). The tortuosities of the internal carotid artery may have high curvature ratios and the model used in the present study has $\delta = 0.5$.

Dean's (1927-28) solution of fully developed laminar flow in a toroidally curved pipe with low K (≤ 96 by the definition given above) and δ, amounted to a perturbation of ordinary Poiseuille flow, with calculation of the influence of inertial terms by successive approximations (Berger, Talbot & Yao 1983). Figure 2.5 shows the resultant axial and secondary streamlines. As observed by Williams et al (1902), the position of the maximum axial velocity is shifted towards the outer wall of the tube. The secondary flow according to Dean (1927,1928), takes the form of two counter-rotating vortices, axisymmetric about the plane of symmetry. The resultant streamlines consist of two counter-rotating helices, in good qualitative agreement with the experimental observations of Eustice (1910). The centres of the two secondary vortices are placed very near $\alpha = \pm \pi/2$ (see figure 2.5).

Dean's solution was valid for Dean numbers < 96. The upper limit of laminar flow is a Reynolds number of about 5830, or K = 5000, according to Taylor (1929) who carried out flow visualisation experiments to test White's (1929) conjecture that a critical Re exists for curved pipes as it does for straight pipes. Collins and Dennis (1975) solved the fully developed flow field for $96 \leq K \leq 5000$ and, from their calculations, showed some interesting features at the higher Dean numbers. As K is increased, two new boundary layers become evident. The maximum axial velocity is

increased and approaches closer to the outer wall, giving rise to an axial flow boundary layer along the outer wall. At the same time, the centres of the secondary vortices are forced both further from the plane of symmetry and back towards the inner wall, due to a secondary flow boundary layer about the pipe circumference. The vortices are skewed by an adjustment to the pressure gradient set up by the boundary layers (Berger et al 1983). The flow visualisation experiments of Akiyama et al (1983) show the secondary streamlines at K = 666 and δ = 0.11 very well, alongside numerical results.

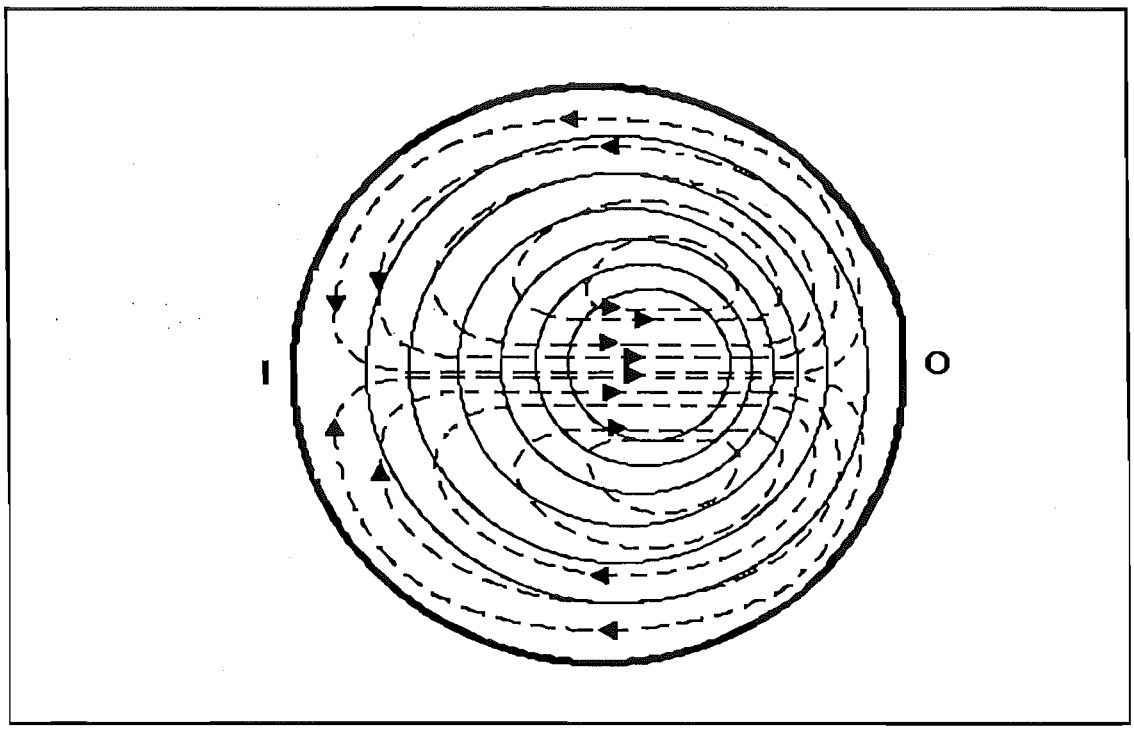

Figure 2.5
Axial (———) and Secondary (----------) Flow Contours in Fully-Developed Deans Flow Through a Curved Pipe at Small Dean Number. (I = Inner Side, O = Outer Side.)

Greenspan (1973), in a numerical analysis for 96 < K < 5000, noted oscillations in the axial streamlines near the tube axis for K = 5000, and explained these as possibly the onset of turbulence. Collins and Dennis (1975) did not find these oscillations for K = 5000 and cast some doubt on the comparative accuracy of Greenspan's forward and backward difference method of calculation. Mislayah (1980) showed secondary vortex oscillations for K = 171, which should give rise to axial

velocity oscillations. At such a low Dean number (and $\delta = 0.09$) one would not expect turbulence, but rather unsteadiness.

The change in position of the secondary vortices seems to depend on the Dean number, a fact pointed out by Greenspan (1973) in his solutions over the range $96 \leq K \leq 5000$, but not mentioned by Collins and Dennis, despite similar results. Greenspan noted that for $K < 500$, the core of the secondary vortices move towards the outer side of the pipe, in agreement with earlier observations. For $K > 500$, the movement is in the opposite direction, towards the inner side. Austin and Seader (1973) show this trend by numerical analysis for $K > 800$, and the numerical results of Tuesdale and Adler (1970) show it to be the case for $K > 200$. This point seems to have been overlooked by Berger, Talbot and Yao in their review (1983).

The positions of the secondary vortices appears to be quite important, particularly in view of the existence of a 4-vortex family of solutions shown by Dennis and Ng (1982) and independently by Nandakumar and Masliyah (1982), in accordance with the bifurcation theory of Benjamin (1978 a,b FCP 480). In the 4-vortex solutions, the axial flow maximum splits into two maxima, axisymmetric with repect to the plane of symmetry near the outer wall, with a saddle-type minimum between them (figure 2.6).

The rest of the axial flow field is similar to that of the 2-vortex solutions (see figure 2.5). The secondary flow contains the usual pair of counter-rotating vortices, but they are closer to the inner wall, and in addition, there is another pair of counter-rotating vortices. These are also axisymmetric, but are closer to the outer wall, and of opposite vorticity to the corresponding vortex of the first pair. From Nandakumar and Masliyah's (1982) calculations, the second vortex pair appears to be of higher vorticity than the first, and the cross-sectional area of the second vortex pair does not change much with the Dean number, unlike the first pair.

It is interesting to note, that the 4-vortex solutions are obtainable, as suggested by Benjamin (1978), if the bifurcation point is approached by relaxing the flow slowly from the upper side, by decreasing the Dean number (either numerically or experimentally). This suggests that the 4-vortex solution becomes a possibility in periodic flow, during the deceleration part of the phase, at certain critical Dean numbers and (large) flow periods.

Masliyah (1979), shows 4-vortex solutions, both numerically and experimentally, for curved ducts of semicircular cross-section, with the flat face on the outer edge of the curve. An interesting feature of the flow calculated by Masliyah for the 2-vortex solutions, is the existence of two distinct, though small, axial velocity

maxima near the outer wall where, in a pipe of circular cross-section only one occurs. These maxima become more distinct with a saddle-type minimum between them on the plane of symmetry for the 4-vortex solutions.

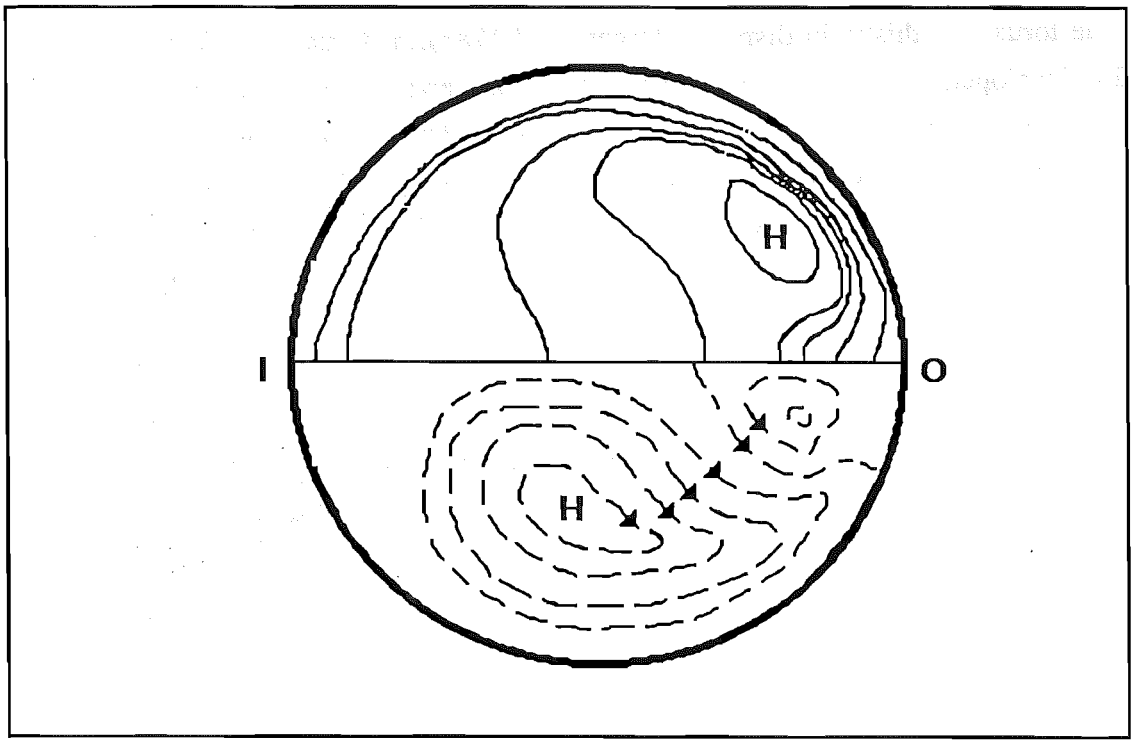

Figure 2.6

Axial (top semicircle) and Secondary (bottom semicircle) Flows for the 4-Vortex Solutions to Flow in a Curved Pipe.

Cheng et al (1983) show by flow visualisation, the 4-vortex secondary flow, described as "centrifugal instability", for both semicircular and fully circular curved pipes. The 4-vortex secondary flow is shown in the circular pipes at $K = 976$ for $\delta = 0.448$, and at $K = 674$ for $\delta = 0.1010$. The latter is lower than the bifurcation point $K = 956$ found numerically by Dennis and Ng (1982). The second vortex pair appears to move away from the outer wall with increasing Dean number, while the position of the first pair remains constant. Dual solutions have also been observed in curved tubes of rectangular cross-section, for example in the studies of Winters (1987) and Soh (1988).

The secondary boundary layer (about the pipe circumference) adjusts to an increasing centrifugal force with increasing K, by thinning near the outer wall, where the boundary layer acts as a sink, and thickening near the inner wall, where it acts as a source for the outwardly-directed secondary flow through the central core. The latter

may take on a jet-like structure at high Dean numbers, then termed the "re-entrant jet" (Adler, 1934).

Adler (1934), Barua (1963), and Yao and Berger (1975) suggest secondary flow separation at the inner bend, resulting from the collision at the inner wall of the two secondary flow boundary layers which develop about the upper and lower walls of the torus, but this is in dispute (Berger et al 1983).In Barua's (1963) model for fully-developed flow, separation occurred about 27° away from the inner bend. Yao and Berger (1975) are in reasonable agreement with Barua for their analysis of entry flow, with separation occuring about 30° from the inner bend for K = 894. Soh and Berger (1984) show no separation for fully developed flow, even though separation does occur during entry flow in their model. This is explained by an argument based on inertia, whereby the fluid moving about the secondary boundary layer has "enough room" between the velocity maximum and $\alpha = 180°$ to slow down to rest when the flow is developed (figure 2.5), since the positions of V_{max} move outward and away from $\alpha = 180°$ as flow develops downstream. On the contrary, in entry flow, the velocity maximum occurs close to the inner wall (figure 2.7), and separation occurs as a result of "overshoot" past the stagnation point into the re-entrant jet. The centres of the secondary vortices move towards the inner wall with increasing Dean number and so the possibility of secondary flow separation at high Dean number arises, going by Soh & Berger's argument.

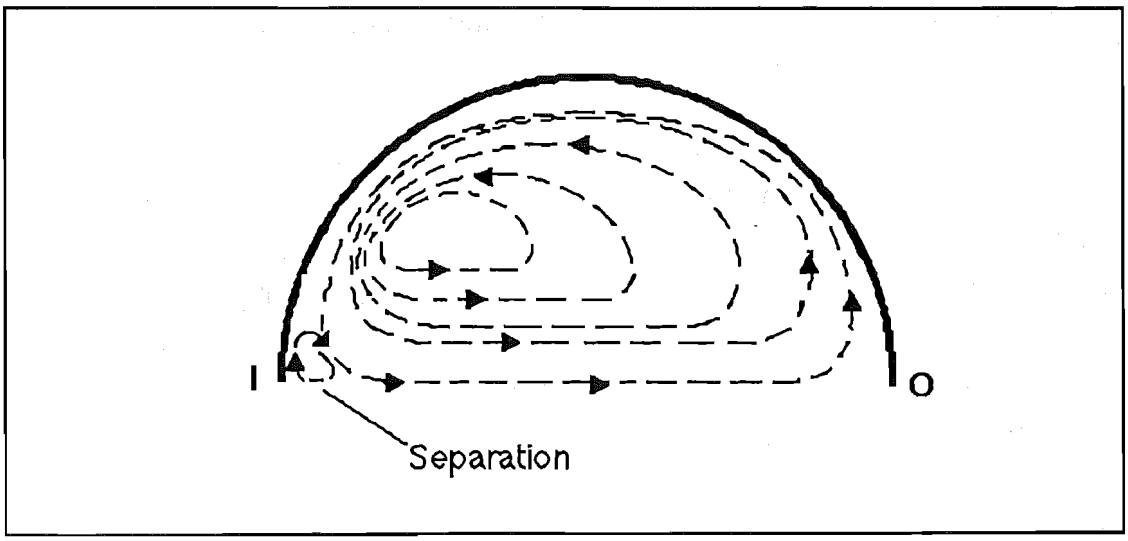

Figure 2.7

Secondary Streamlines Near the Entrance to a Curved Pipe. Note that the centre of the vortex is closer to the inner side (I) than in figure 2.5, hence flow separation occurs.

In a treatment of laminar flow in a square duct of strong curvature, Humphrey et al (1977) found, both numerically and experimentally, a small recirculation region on the outer wall, near the side walls, indicating separation there.

The tendency for the secondary boundary layer to thin near the outer wall with increasing centrifugal force due to increased Dean number may provide a condition conducive to the formation of Görtler vortices in the secondary boundary layer, although this has not been mentioned in the literature, to the author's knowledge. Görtler vortices may form in counter-rotating pairs orientated in a streamwise direction along a concave wall (figure 2.8) when the Görtler number, G_{δ} is greater than 15.8 (Schweizer and Scriven, 1983), with

$$G_{\delta} = \left(\frac{d_1}{R}\right)^{1/2} \frac{(Ud_1)}{\nu}$$

where d_1 is the boundary layer thickness, and U_o is the mainstream velocity, in this case, the resultant of primary and secondary velocities outside the boundary layer (figure 2.7). In effect, the Görtler vortices represent a similar kind of centrifugal instability to Dean-type motion. G_o is a type of Dean number with the boundary layer thickness, d_1, providing the equivalent length scale to the radius of the tube, a, in the expression for K. When fully-developed flow is present in the tube upstream of the bend, the boundary layer extends out to the centre of the tube, so that $d_1 = a$. In the case where the secondary boundary layer of Dean-type motion is able to grow to a significant size with respect to the radius of the tube and the secondary velocity becomes appreciable, the Görtler instability may arise, with the vortices aligned about the wall. If Görtler vortices form in the secondary boundary layer, they could either be entrained in the re-entrant jet-like outwardly-directed flow, or interact with an axial separation layer, should one occur. If secondary flow separation occurred, the Görtler vortices would destabilise the resultant free shear layer. In the present study, G_{δ} in the secondary flow will exceed 15.8 if the thickness of the boundary layer exceeds 10% of the tube radius of 10mm and the secondary flow velocity exceeds 50% of the axial mean velocity of 8 cms^{-1} for a Reynolds number of 1500.

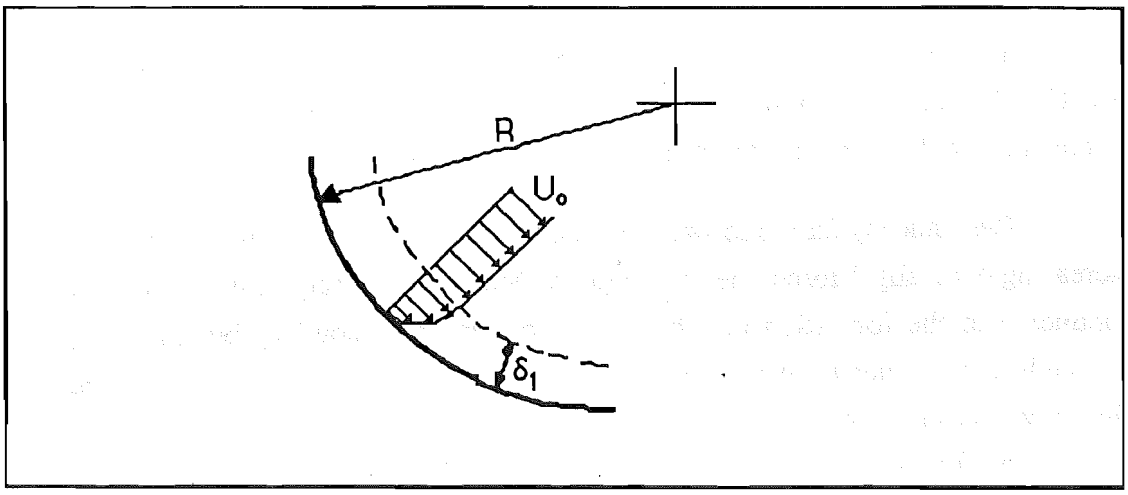

Figure 2.8

Flow About a Concave Wall Which May Cause the Görtler Instability .

2.5.2.2 Entry Flow:

As in a straight pipe, the flow in a curved pipe requires some axial distance to become fully developed and exhibits different flow phenomena from that of fully developed flow during flow development.

The entry length (l_c) for a curved pipe is less than that for a straight pipe (l_s). This is explained (Singh 1974) by the enhanced mass transfer and convective mixing that occurs in a curved pipe due to secondary flows. Yao and Berger (1975) predict the entry length in a curved pipe to be $l_c = e_1 a(2Re)^{1/2}\delta^{-1/4}$ for large Dean numbers, where e_1 is only weakly dependent on δ, thus leading to the ratio $l_c/l_s \ll 1$. More realistically, for K = 894, and δ = 0.05, the entry length was about half that of a corresponding straight pipe.

Pedley (1980) calculated the term $Re^{1/2}\delta^{-1/4}$ for the flow conditions used by Olson (1971) and by Agrawal et al (1978), and found in each case, a close match between that term and the experimental observations of the closest approach of fully developed flow to the entrance.

Olson and Snyder (1983) used pulsed probe anemometry to study the growth of swirl in curved pipes, with δ = 0.215 and 0.063 at moderate Dean numbers, and suggested a length scale for flow development of $(aR)^{1/2}$. The introduction of a probe shaft (up to 3% of the tube cross-section) into an elliptical flow field may have affected their results, since the flow at any one point in the tube depends on the flow at all the other points in the tube. However, Yao & Berger (1988) demonstrated that $(aR)^{1/2}$ was the proper length scale for flow development.

The axial lengths of the curves used in the present study were only 1.4 to 2.8 x 10^{-3} times the entry length of a straight pipe for the flow rates studied, so that the flow would almost certainly not be approaching the fully-developed state.

Singh (1974) studied flow development numerically, using entry conditions of uniform pressure and uniform velocity across the tube cross-section. He described the flow as being divided into two parts - i) an inviscid core in which the centrifugal force due to the curved motion of the main body of the fluid along the pipe is balanced by the pressure gradient directed towards the centre of curvature and ii), a thin boundary layer in which the viscous forces are balanced by the inertia forces. The secondary flow due to curvature effects in the region close to entry was obtained by perturbing the solution for developing flow in a straight tube. Initially, two singularities occurred in the solution, an origin in the centre of the tube at which the streamline converged, and a stagnation point which represented the point between inwardly and outwardly directed flow along the plane of symmetry. The stagnation point moved from the origin along the plane of symmetry to the outer wall as the flow proceeded downstream, and existed until crossflow from the inner to the outer wall occurred at an axial distance of about 1 radius from the entrance.

Singh also found a cross-over point at which the site of maximum shear changes from the inner wall to the outer wall, where it is found for fully developed flow, and explained it as follows. Initially the fluid experiences less resistance along the outer wall than in a straight tube because of the reduced external flow (with respect to the boundary layer, which is initially small) and a longer wall length, and conversely along the inner wall. Downstream, the secondary flow has grown sufficiently for the fluid near the inner wall to experience a lower resistance due to the thickened stagnation-like boundary layer, which acts as a source for the central cross-flow, and for the fluid along the outer wall to experience an increased resistance due to the reduced displacement caused by the boundary layer being thinned as fluid is drawn away circumferentially ie: where the boundary layer acts as a sink for the central cross-flow. The position of the cross-over point was not dependent on Re or δ, but on the entry condition. For a uniform pressure entry condition, the cross-over point occurred 1.9 radii from the entrance, whilst for a uniform velocity entry condition, the cross-over point occurred at about half this distance, 0.95 radii.

An important point is that the development of flow depends largely on the entry conditions. As Soh and Berger (1984) point out, it is not strictly possible to give entry conditions because the elliptical nature of the flow means that the entry conditions depend on downstream features, and disturbances propagate upstream. Smith (1976) claimed the secondary flow in Singh's (1974) solution was due only to the inlet profile

and that curvature played little part in the solution. He assumed a more realistic inlet condition of Poiseuille flow entering a curved pipe from a straight section, with no slip at the upstream walls, therefore attributing any distortion of the incoming flow solely to the introduction of curvature.

Smith found that the three dimensional boundary layer provoked by the shift of the maximum axial velocity towards the outer wall actually adjusts upstream of the bend. This is due to an upstream response between the axial and circumferential pressure forces and the swirling boundary layer in the virtual absence of any core displacement in the upstream straight pipe. Upstream of the bend, the pressure rises within the boundary layer at the outside wall and falls near the inner wall, causing a positive circumferential slip velocity. With a decrease in axial skin friction at the outer wall and a smaller pressure gradient, fluid moves towards the inner wall, and the resultant acccumulation of fluid near the inner wall (since there is little leakage of circumferential flow to the core) induces an increased skin friction there, reinforcing the pressure gradient and hence, the whole process.

Like Singh (1974), Smith found that the maximum shear occurs at the inner wall, but downstream, when the outward centrifuging of the core eventually overrides the upstream response, a cross-over point is established whereafter the maximum shear occurs at the outer wall. This cross-over point was situated 1.51 radii downstream of the beginning of curvature. Significantly, as well as being independent of Re and δ, Smith found the cross-over point to be independent of the oncoming shear stress, and so independent of the initial profile.

Choi et al (1979) measured wall shear stresses for $139 < K < 2868$, by the electrochemical limiting current method, and found the cross-over point to be 1.9 radii from the entrance, more in agreement with Singh than with Smith. However, contrary to both predictions, the cross-over point seemed to move upstream with increasing K. Yao & Berger (1988) found that the cross-over point for axial wall shear was purely a geometric property, with it's location being a strong function of a/R. Talbot & Wong (1982) studied the wall shear stress by an electrochemical method and found good agreement with Stewartson et al (1980), with a point of minimum wall shear occurring at a predicted separation point. A complex vortex motion was also indicated downstream of this point, though it's shape was too complex for elucidation.

Yao and Berger (1974) considered the entry flow for an inlet condition of uniform velocity, but did not describe the development of flow profiles in detail, other than for a growth of the boundary layer thickness. Growth of the boundary layer

(about the tube circumference) was associated with separation. Separation at the inner wall was also found by Yao & Berger (1988).

Agrawal et al (1978) carried out an experimental investigation of the entry flow in curved pipes with curvature ratios of $^1/_{20}$ and $^1/_7$ and at moderate Dean numbers using a laser Doppler anemometer. The entry condition was for a uniform velocity profile achieved by entering the pipe from a large reservoir, through a bell-shaped inlet. They observed the formation, immediately downstream of the entrance, of a vortex-type velocity distribution in the irrotational, inviscid core and the development, for the highest Dean numbers (< 680) of two pronounced axial velocity maxima near the inner wall, which decreased in strength and moved away from the plane of symmetry as the flow proceeded downstream. These latter, they linked with an imbedded vortex pair. In qualitative agreement with Yao and Berger (1974), separation of the circumferential boundary layer on the inner wall was also indicated. As mentioned above, separation in the developing region along the inner wall was also predicted by Soh and Berger (1984).

A cone-shaped contour of low axial velocity in the centre of the tube cross-section was clearly shown by the experiments of Akiyama et al (1983), and this was in agreement with the experiments of Austin (1971), and the theoretical predictions of Patankar et al (1974) and Akiyama et al (1983), using a fully developed Poiseuille flow as the entry condition. Soh and Berger (1984) solved the flow development for a uniform velocity entry condition ($108 < K < 681$, $\delta = {}^1/_7$ and $^1/_{20}$) and demonstrated double peaked axial velocity profiles, corresponding to a "doubling back" of the axial isovels (figure 2.9). This phenomenon appears to be the same as the cone-shaped local axial velocity minimum of Akiyama et al (1983). Soh and Berger (1984) point to the similar observations of Austin (1971) for entrance flow with a parabolic velocity entry condition, those of Austin and Seader (1973) for fully developed, large-K flow, and the experimental observations of Agrawal et al (1978).

A further finding of Soh and Berger (1984) is that the intensity of the secondary flow in the entry region is affected most by δ, while the shape of the secondary flow is influenced most by Re, with the secondary flow taking on the characteristics of boundary flow behaviour with increasing Re.

Choi et al (1979) suggested a vortex structure in the entry region consisting of several vortex pairs, in contrast to the single pair for fully developed flow (the 4-vortex solutions not having been found at that stage), due to their finding, experimentally, of a valley in the shear stress distribution in the region of the middle of the bend, bounded on either side by peaks of wall shear.

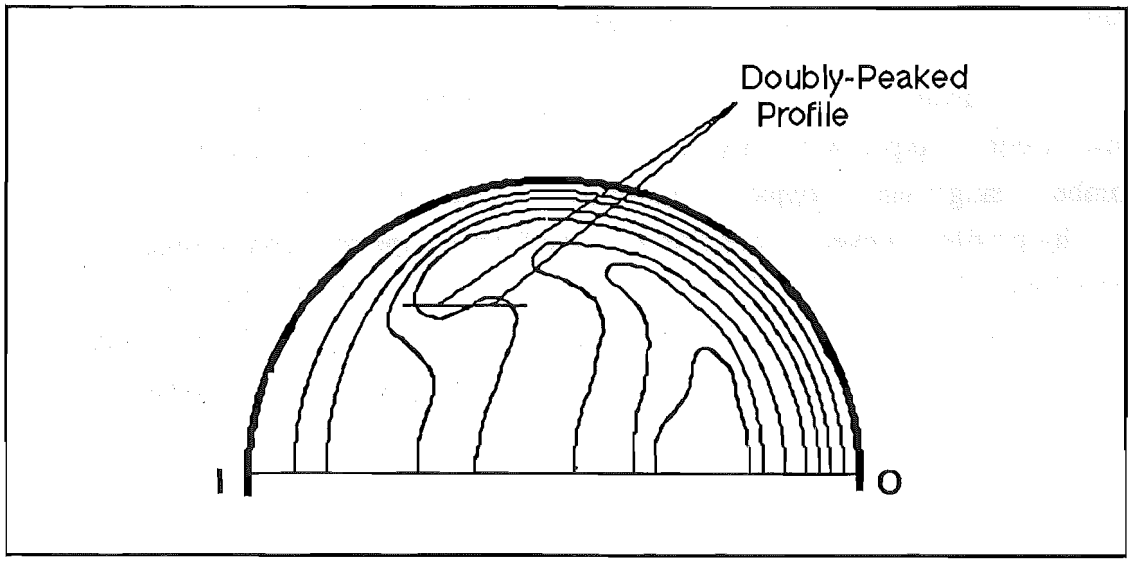

Figure 2.9
Doubly-Peaked Axial Velocity Profile in a Curved Tube.

2.5.3 Pulsatile Flow:

2.5.3.1 Curved Pipes:

The treatment of pulsatile flow in curved pipes has met with considerably less success than that of the corresponding steady flow. However, some first order features such as the position of maximum axial flow and the secondary flow field trends with changing mean velocity and pulsation frequency and amplitude have been elucidated.

Lyne (1971) studied purely oscillatory flow (ie: with zero mean velocity) in a curved pipe with small δ. He found the flow to depend on three parameters:

$$\varepsilon^2 = \frac{\overline{W}^2}{Ra\omega^2}, \quad R_s = \frac{\overline{W}^2}{R\omega}\frac{a}{\nu}, \quad \beta^2 = \frac{2\nu}{\omega a^2} = \frac{2\varepsilon^2}{R_s}$$

The parameter ε^2 is the ratio of the square of the axial particle displacement amplitude to the product of the pipe radius of curvature and the radius of the pipe. R_S is the Reynolds number of the secondary flow, and β^2 is a parameter representing the ratio of the Stokes layer thickness to the pipe radius. W is a typical velocity along the

pipe, and ω is the pulsation frequency. When β is small, viscous effects are confined to a thin (Stokes) layer near the wall, with the central core flow being inviscid.

For small β, and both small and large values of R_S, Lyne predicted the flow to consist of boundary layer regions about the circumference and along the plane of symmetry, without separation. For $\alpha \leq 12.9$ (where α is a measure of the degree of departure from steady flow, called the Womersley parameter in the blood flow literature, $\alpha = a(\omega/\nu)^{1/2}$), the flow was the same as that of the 2-vortex steady flow in a curved tube. For $\alpha > 12.9$, the flow along the plane of symmetry was from the outer bend to the inner bend, contrary to the case for fully developed steady flow. The reason given was that the "centrifuging" generates motion which is entirely confined to the Stokes layer, with the motion being towards the inner side of the pipe near the wall, and towards the outer side of the pipe near the outside of the Stokes layer. This movement towards the outer side in turn generates a rotational component in the core, such that movement is towards the inner wall along the plane of symmetry (see figure 2.10). This 4-vortex solution differs from that of the steady case (Dennis and Ng, 1982). As β increases, the solution tends towards the solution for steady flow.

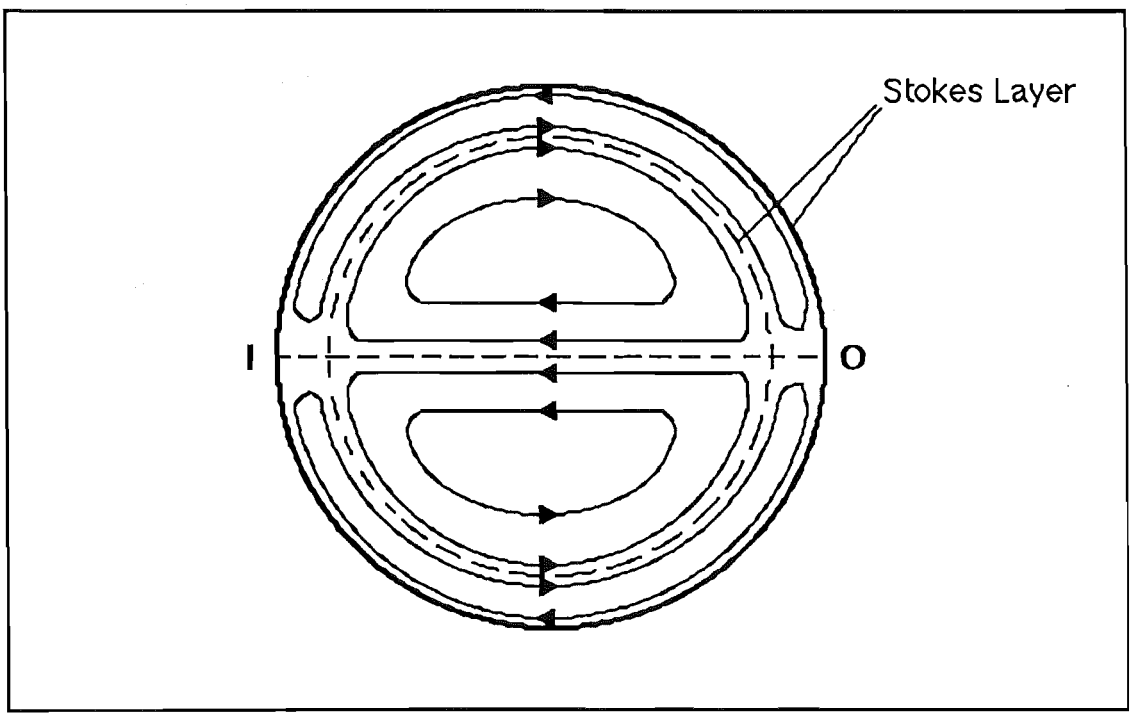

Figure 2.10
Streamlines for small β Showing Centrifugal Effects Confined to the Stokes Layer (Lynne 1971).

Lyne used dye injection to study the flow with parameter values of $\delta = 0.075$, $\varepsilon = 0.18$, $R_s = 24$, $\beta = 0.05$, and observed the predicted interior flow towards the inner wall and circumferential flow towards the outer wall. The flow pattern in the Stokes layer was not observed, probably due to the layer being very small. Bertelsen (1975) and Munsen (1975,1976) both verified Lyne's predictions experimentally, including the β-value for transition from the 2-vortex to the 4-vortex secondary flow. For blood flow through the internal carotid artery and the pulsatile hydrodynamic flow through the model used in the present study, β is approximately 0.28 and 0.25 respectively. From Bertelsen's results, it appears that Lyne-type motion will not occur for $\beta^{-1} \leq 8.7$, so it is not likely to occur in the present experiments, or the internal carotid artery tortuosity in vivo. The above analysis is for a pulsatile flow with a zero mean flow.

The introduction of a non-zero mean velocity complicates the flow, with the resultant flow pattern arising from a balance between the steady and the unsteady components. Smith (1975) studied flow through pipes of arbitrary (though symmetrical) cross-section, driven by a pulsatile pressure variation:

$$\frac{\delta p^*}{\delta(R\theta)} = -\left[\rho^* \omega \overline{W} \cos\omega t + G\right]$$

; where G is the constant, steady component of the pulsating pressure gradient. He used β and R_s to describe the flow, along with a third parameter:

$$D = Ga^3\delta^{1/2}/\rho^*\nu^2$$

; where D is an alternative Dean number, related to that given previously for steady flow ($K = 2Re\, d^{1/2}$) by

$$K = 2\rho^*\nu WD/Ga^2$$

Smith examined the nature of the motion when one of the parameters D and β takes on a large or small value. Whilst the flow pattern for $\beta \ll 1$ and $D \ll 1$ was the same as that found by Lyne (1971), the pattern for $\beta \ll 1$ and $D \gg 1$ showed outward motion of the fluid along the plane of symmetry, similar to that of steady flow, despite the Stokes layer maintaining the centrifuging pattern established in purely oscillatory flow. In the latter case, the strongly oscillatory down-pipe velocity itself induces a negligable centrifugal force in the core, allowing the relatively weak steady flow to dominate, causing outward secondary flow along the plane of symmetry. At the same time, the oscillatory component has considerable centrifugal effect on the Stokes wall layer, promoting the slip velocity, and provoking some inward secondary core motion

at the outside of the Stokes layer. The reversal of secondary flow from outward centrifuging, or Dean-type motion, to inward, or Lyne-type motion, was also observed by Hamakiotes & Berger (1988) above a critical mean Re of 300, with a/R = $1/7$. Axial flow reversal was seen near the walls during a portion of the cycle. When flow reversal occurred, the maximum shear stress occurred at the inner bend. A complex secondary flow vortex structure was also observed. This axial flow reversal is quite likely to occur in the present study, as the curvature ratio is a/R = $1/2$.

Mullin and Greated (1980b) examined the change in secondary flow patterns as α is increased from zero, and showed that the 2-vortex solution of steady flow exists up until $\alpha = 10$, when a stagnation region in the centre of the tube develops into two counter-rotating vortices of opposite vorticity to the original pair. This second pair of vortices initially occupy only a small region in the centre of the tube, but this grows with increasing α, so that the situation portrayed by Lyne (1971) is reached only gradually with increasing α, as the centrifugally generated secondary flow is confined to regions near the wall.

The peak axial velocity is shifted towards the outer wall by secondary flow in the quasi-steady limits of the solution, as in truly steady flow, but the peak is shifted towards the inner wall at large α. Although this shift in the maximum axial velocity appears to match the direction of flow along the plane of symmetry, Mullin and Greated (1980b) found the maximum axial velocity near the inner wall despite the outward centrifuging of the flow along the plane of symmetry.

Lin and Tarbell (1980) presented numerical and experimental results for pulsatile flow in a curved tube, with moderate α-values, below those required to achieve the 4-vortex solution. They observed distinct maxima in pressure drop at certain α-values, leading to the conclusion that there was some "resonant" interaction between the secondary and axial flows. They surmised that when the axial velocity fluctuations were close in frequency to a characteristic frequency corresponding roughly to the circulation time of the secondary motion about the tube, the secondary motion was "excited" giving rise to pressure drop and outer wall shear maxima.

2.5.3.2 Entry Flow:

Singh et al (1978) extended an earlier solution for steady flow in a curved pipe (Singh, 1974) to pulsatile flow. Their analysis predicts that the maximum axial velocity will initially be located near the inner wall, and will shift towards the outer wall downstream, due to the thickening of the secondary boundary layer near the inner wall and thinning near the outer wall. A consequent cross-over of the maximum shear from the inner to the outer wall was also predicted, as well as reversed flow near the

inner wall during the deceleration phase of the cycle, due to the greater response of the slower moving particles there to the adverse pressure gradient.

In a study related to the fully developed case (Mullin and Greated, 1980b), Mullin and Greated (1980a) examined the pulsatile entry flow in a curved pipe for low (quasi-steady) and moderate α. The axial velocity maximum was initially located near the inner wall, but shifted outward downstream, in accordance with Singh et al (1978). For the 0 and $^1/_6\pi$ phase positions, considerable upstream influence was observed (as was the case for steady flow in the solution of Smith, 1975). This upsteam influence was observed to be less severe further into the flow phase, as the effects of secondary flow became more apparent, with a corresponding shift of the maximum axial velocity towards the outer wall. The conclusion was drawn that in the early part of the flow cycle, the secondary flow build-up occurs at a slower rate than the primary flow, so the maximum axial velocity occurs at the inner bend. Further into the flow cycle, the secondary flow has more influence on the axial flow, and the maximum is shifted towards the outer wall.

For both small (α = 0.99) and moderate (α = 4.36) α, flow was fully developed by 90° into the bend.

Chandran and Yearwood (1981) carried out an experimental investigation of pulsatile entrance flow in a tube of circular cross-section (δ = 0.1) with a good approximation to a physiological flow variation. Four interesting features were presented. 1.) The presence of reversed flow along the inner wall during deceleration 2.) The flow did not appear to be fully developed 97° from the entrance 3.) The peak axial velocity moved from the inner wall to the outer wall and back to the inner wall again 4.) Trapped vortical motions were observed at the inner wall of the tube in the downstream region during the acceleration phase.

Talbot and Gong (1983) conducted two experiments, one in a pipe with δ = 1/20 and with α = 8.0, and the other in a pipe with $\delta = ^1/_7$ and α = 12.5. The flow in the first pipe was found to be quasi-steady, and with secondary motions essentially the same in character as low Dean number steady entry flow. In the second experiment, separation of the axial flow appeared at the inner bend during deceleration, starting downstream and propogating upstream towards the pipe entrance. Helical motions imbedded within the Dean circulation were also observed, and during certain portions of the cycle, the secondary motions within the central core took on a jet-like structure.

2.5.4 Varying Curvature:

Muraka, Miyake and Inaba (1976) analysed the steady, laminar flow through once-, twice-, and periodically-curved pipes with small δ. At very small Reynolds numbers, the position of the maximum axial velocity was shifted towards the inner side, and at large Reynolds numbers, towards the outer side. In the latter case, the adaption of flow followed the change in the mean flow direction with a phase lag.

Inaba and Murata (1978) analysed the pulsatile flow through a sinusoidally varying pipe (defined by $y = a.\sin(kx)$; where a is the pipe radius, x is the distance along the pipe axis, y is the amplitude of the deviation of the pipe from a straight line, and k is the wave number of the pipe) with small δ. For the purely oscillatory case, the axial velocity maximum occurred at the inner wall with no phase lag. For the case with non-zero mean, the flow in a pipe, with the wave number of the pipe not small, depended on the steady flow at low values of the Womersley parameter, α, and on the pulsatile component at higher values of α. In a pipe with small wave number, again the flow depended on the steady component for low α, but became more like the purely oscillatory case at higher values of the Womersley parameter.

Kitoh (1987) analysed the flow through bends with swirling flow at entry, including that through triply-connected 90° bends. Deans flow resulted in the first bend, while swirling motion occurred in the 2 downstream bends due to the effect of the bend on the axial shear component set up in the bends immediately upstream. The resultant axial velocity isovels in the second bend were illustrated, showing a distorted form compared to the classical Dean solutions, whereby a large asymmetric stagnation zone occurred near the inner wall. This appeared to correspond to the thickened boundary layer source for secondary flow, distorted by swirl.

2.5.5 Flow Separation:

Boundary layer separation is a well known phenomenon associated with sudden changes in surface geometry. The relatively high curvature ratio ($\delta = 0.5$) of the bends in the model used in this study means that separation is highly likely, particularly in light of the previously-mentioned literature for curved pipes with lower δ, both for steady flow (Barua 1963, Yao and Berger 1988, Soh and Berger 1984) and for pulsatile flow (Singh 1978, Chandran and Yearwood 1981, Talbot and Gong 1983). Separation is also a feature of flow in 90° bends of rectangular section (Humphrey et al 1977, Amano 1984, Amano 1985).

The free shear layer resulting from a flow separation is likely to contain pressure, velocity and consequently local shear fluctuations which could be felt at the wall at the points of separation and of reattachment Also, the separation bubble itself, though, in general, a vortex that is slower moving than the shear layer or the main flow, constitutes an area in which the wall could experience flow conditions different from those in other areas.

The subject areas of flow separation and shear layer behaviour are of considerable depth in themselves, and despite progress, little is understood of the mechanisms involved even for the two-dimensional cases. The behaviour of three-dimensional separation and shear layers, as in the case of curved pipe flow, is particularly complicated and even less well understood. This, coupled with the scant knowledge of high d, curved pipe flow and the complicating factors of multiple bends and unsteady flow, precludes any serious attempt to predict the flow patterns in the model used in this study. However, some of the features exhibited by free shear layers are of relevance, and should be introduced here in order to facillitate the discussion of results in Chapter 6.

There are many configurations which give rise to flow separation, each allowing different conditions to affect the resultant shear layer, including the reattachment region, should one occur. The behaviour of the shear layer may be determined by an upstream influence due to the type of surface impingement, as well as by the flow conditions surrounding the layer (Rockwell and Naudascher 1979, Rockwell 1983) and by the presence of adjacent resonators (cavities) and reflectors, the fluid properties, and even the degree of three-dimensionality (Rockwell 1983).

Of concern here is the three-dimensional shear layer resulting from boundary layer separation in a bend of high curvature, bounded by a recirculation zone (the "separation bubble") and impinging on a relatively plane surface (as opposed to an edge). Fluid elastic properties and the effects of reflectors/resonators are not considered, although these may be of some significance in-vivo due to the rheological properties of blood and the elastic walls bounding the flow, through which noise and the pressure pulse is propogated. The free shear layer arising from separation of the flow around a pipe of high curvature has not been studied, to the author's knowledge, probably because of it's three-dimensional nature.

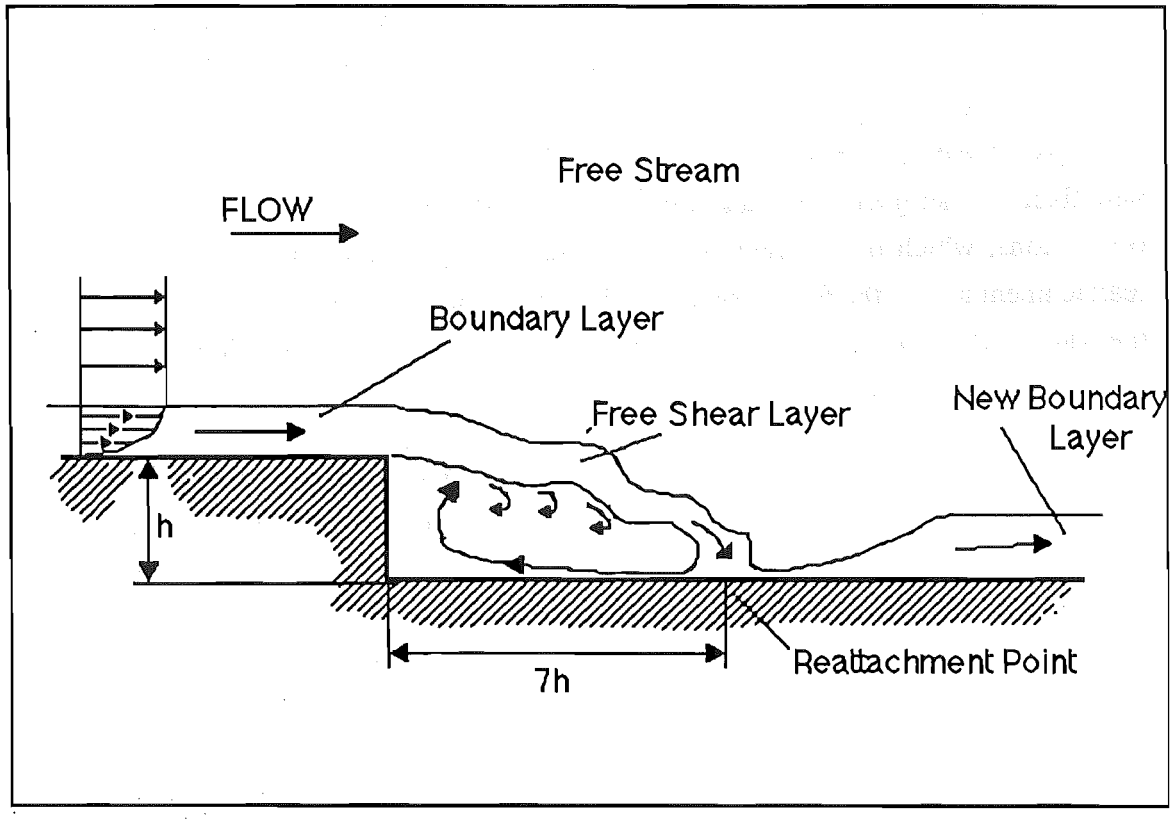

Figure 2.11
Flow Separation Over a Backward-Facing Step.

The flow over a backward-facing step has some analogous features, and these will be described in an attempt to provide a qualitative view of the separated flow behaviour in a curved pipe. However, it should be stressed that there are major differences between the two cases, and the analogy should be approached with caution, particularly when considering qualitative comparisons. Most importantly, the flow over a backward-facing step is largely two dimensional, and has no secondary flows which might affect the downstream progression and even reattachment of the shear layer. Furthermore, the step itself constitutes an area of flow expansion not found in a curved pipe.

Figure 2.11 shows a schematic representation of the flow over a backward-facing step. Flow is largely two-dimensional (disregarding edge effects) in the plane normal to the mean flow. Separation of the laminar boundary layer occurs at the trailing edge of the step. The resultant free shear layer has the form of a mixing layer (as opposed to a jet) and reattaches at a mean downstream position related to the step height and the flow velocty. In the case of pulsating axial flow, there is a large variation in the position of reattachment (Lebouche & Martin 1976, and Mullin et al 1980), especially if the separation edge is not sharp.

Morkovin & Paranjape (1971) postulated that the back and forth motion of the flow deattachment point allows the transformation from irrotational pressure to rotational vorticity perturbations. In the case of pulsatile flow and a rounded separation point (as is the case in vivo and in the model of the present study), the separation point will likely be subject to a back and forth motion, giving rise to free shear layer oscillations, which in turn may lead to a fluctuating velocity effect on the wall at reattachment and/or the formation of vortices which may then come into contact with the walls of the tube. It is these unsteady vortical motions that may be involved in the etiology of athersclerosis.

Lebouche and Martin (1976) found the gross pulsatile flow characteristics in a duct with enlargements on both sides depended on a reduced frequency parameter $F^* = Fh/U$; where F is the frequency of pulsation, h is the step height, and U, the mean velocity. When $F^* < 0.07$, the recirculation vortex was shed and convected downstream. The results of Mullin et al (1980) were in agreement with this prediction.

For most oscillations of the free shear layer to be self-sustaining, a chain of results must occur (Rockwell 1983): impingement of organised vorticity fluctuations upon the surface at reattachment (ie: leading edge interaction); resultant upstream influence (interpreted as upstream pressure waves in liquid flows); conversion of disturbances incident upon the region of the shear layer in the vicinity of the separation edge to velocity fluctuations within the shear layer (ie: trailing edge interaction); and amplification of the fluctuations in the streamwise direction.

Importantly, the first of these conditions is not strictly necessary, and the downstream unsteadiness of a non-impinging shear layer may also act as a region of leading edge interaction (Rockwell, 1983), attributed, in mixing layers, to vortex formation and pairing Dimotakis & Brown 1976, and Rockwell & Knisely 1979). In the case of a curved pipe, some vortices are expected to be present already and the interaction of these with each other in adjacent flow, or with those formed in the mixing layer may cause unsteadiness and hence leading-edge interaction. Again, vortex interaction in the three-dimensional case is complex (Saffman & Baker 1979) and an analysis is beyond the scope of this thesis.

In the case of water flow, the length between separation and reattachment is very small in comparison with the acoustic wavelength and so the source and upstream propogation of perturbations may be treated as purely hydrodynamic, rather than radiative (Rockwell & Naudascher, 1979). Consequently, the sensitive region of the shear layer near the separation edge experiences pressure fluctuations of the order of ρu^2, where u is the local velocity fluctuation (Rockwell, 1983).

The shear layer after separation over a backward-facing step is bounded on one side by a recirculation zone, and on the other by the main flow. For shear layers bounded by a recirculation zone, oscillations may be due to two different mechanisms (Rockwell 1983): classical hydrodynamic instability or a different low-frequency mechanism. In the first case, oscillations are driven by the inherent hydrodynamic instability of the shear layer itself, and have Strouhal numbers ($S_L = fL/U$) in the range 0.5 - 2.5 (Rockwell & Naudascher 1979). If the convective velocity, Uc, of the instability is crudely taken as $U_c = 0.5$, then the ratio of impingement length (L) to the wavelength of the instability (l) take the values $1 < L/l < 5$.

In some geometries, including the backward-facing step and the model in this study, there seems to be persistent (though, in general less coherent) oscillations at Strouhal numbers $SL << 1$. Although the mechanism for these oscillations has not been conclusively demonstrated, it has been hypothesised (Eaton & Johnson 1980, and Naudascher & Rockwell 1978) to be due to an imbalance between the flow entrained by the shear layer and that returned to the recirculation vortex at reattachment. Although it should be possible to combine the conservation of mass in the recirculation zone with the momentum equatons to determine characteristice response times, leading to the most probable oscillation frequency, this may be overshadowed by the compexities of coherent structure/surface interactions at impingement, as well as three-dimensional effects that could alone be a source of low-frequency contributions (Rockwell 1983).

Troutt, Scheelke and Norman (1984) used hot wire anemometry to study the span-wise structures in a two-dimensional, reattaching separated flow downstream of a backward-facing step. Their results supported the existence of large-scale vortices in both the separated and reattached regions of flow, with the flow retaining coherent structures far downstream of reattachment. Bhattacharjee et al (1986) were able to inflict considerable modification of vortex interactions in a reattaching separated flow, by forcing certain controlling frequencies with an acoustic source. A significant decrease in reattachment length was accompanied by changes in the turbulence energy and Reynolds stress levels in the forced flows compared with the unforced flows.

A gentle oscillation of the shear layer at low frequencies prior to separation from a backward-facing step has been shown to control the coherent structures in both laminar and turbulent reattaching shear layers (Roos and Kegelman, 1986).

The flexible nature of an arterial wall may allow it to promote certain frequencies of oscillations in a separated shear layer over others, by way of the

transmission of vibration or sound from the wall and surrounding tissue to the regions of separation and/or reattachment.

Chapter 3

An Hypothesis for the Haemodynamically-Altered Transmural Macromolecular Permeability of the Arterial Endothelium: Proposal and Appraisal of a Theory.

3.1 Introduction:

In the Unified Haemodynamic Hypothesis outlined in Chapter 2, it was proposed that haemodynamics could initiate atherosclerosis by three mechanisms: stress fluctuation fatigue; damage to the endothelium; or by altering the endothelial permeability to macromolecules such as Low Density Lipoproteins (LDL's).

LDL-receptors on the surface of cultured endothelium are saturated at serum LDL concentrations as low as 5 μg/ml (Reckless et al 1978). For quiescent, confluent endothelium (ie: an intact, undisturbed endothelial layer), receptor-independent pinocytosis may be the dominant form of LDL internalisation (Stemerman et al 1984), since the endothelium is exposed to LDL concentrations of more than 800 μg/ml in vivo (Reckless et al 1978). A hypothesis will now be proposed to explain how haemodynamic forces might alter the transmural permeability of the arterial wall to macromolecules if these are transported by hindered diffusion. The hypothesis is based on the theory that macromolecular transport into the arterial wall is rate-limited by the endothelial layer and occurs via pinocytotic vesicular transport.

I am deeply indebted to Dr. John Abrahamson for the many hours of conceptual thinking and discussions that have been indespensible in the development of the following work. His imaginative approach to the subject of vesicular transport has provided a supply of ideas for examination that are by no means exhausted by this thesis.

3.2 Macromolecular Transport across the Arterial Endothelium:

The transport of macromolecules from the blood to the surrounding tissue is

apparently rate-limited by the endothelial layer lining the inner arterial wall (Weinbaum 1979, Arminski et al 1980). This layer consists of flat, spindle-shaped cells about 15 μm long and 0.3 μm thick, which overlap at the ends to form a continuous monolayer of cells with inter-cellular clefts of width 10 to 20 nm (Weinbaum & Caro 1976). These clefts will not allow the passage of molecules larger than about 4 nm in diameter (Casley-Smith & Chin 1971, Stein & Stein 1973), so that macromolecules such as cholesterol and LDL must be transported through the cells themselves.

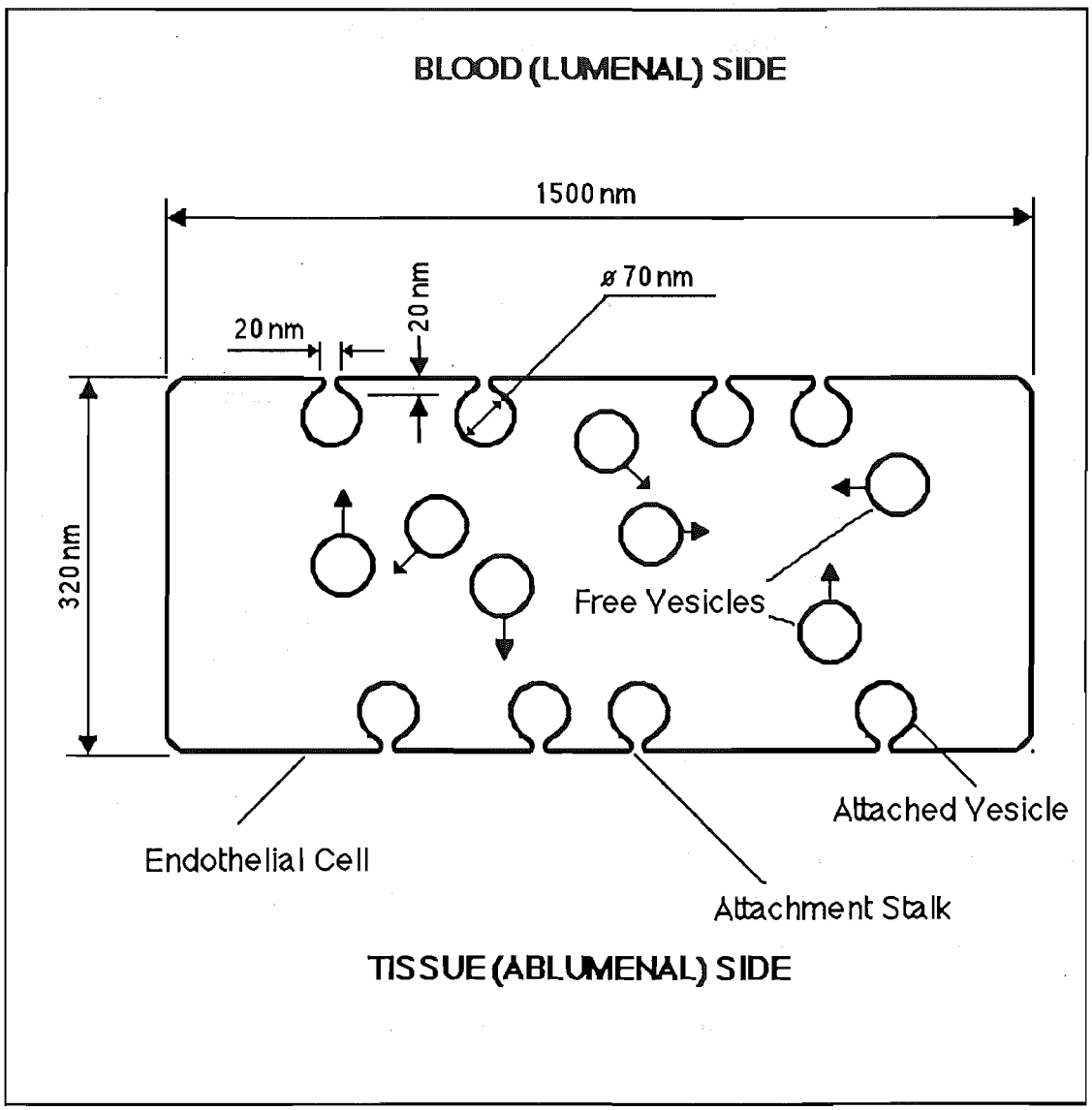

Figure 3.1
The Vesicular Structure of the Endothelial Cell.
Vesicles Are Believed to Perform a "Shuttle Service" from One Side of the Cell to the Other.

Transport of macromolecules is assumed here to be via pinocytotic vesicles as

shown diagramatically (after Weinbaum & Caro 1976) in figure 3.1. The pinocytotic vesicles are approximately spherical with an average internal diameter of about 70 nm. The vesicles exist within the cell in constant numbers and are able to diffuse back and forth across the cell by Brownian motion (Casley-Smith 1969, Caro et al 1976) and attach to the cell wall via a quasi-steady stalk with an internal diameter and length of about 20 nm. This stalk connects the vesicle interior to the cell exterior. After a time, the vesicle stalk detaches from the cell wall and the neck is sealed so that the vesicle interior is kept separate from the cell contents. Any difference in the concentration of a molecular species between the lumenal and ablumenal sides of the cell results in a net transfer, due to vesicular diffusion, of that species across the cell in the direction of the concentration gradient. The loading of the vesicle was estimated by Tomlin (1969), using simple diffusion considerations, to occur quickly (within 10^{-2} seconds) in the absence of molecular sieving effects, compared to the time that the vesicle is attached to the cell wall. In that case, the vesicle contents would reach a concentration equilibrium with the extracellular environment before detachment occurred.

Macromolecular transport across the endothelial layer has been shown (Newman & Zilversmit 1966, Siflinger et al 1974), by the failure of metabolic poison to influence the transport rate, to be largely a passive process. In our context, this means that the driving forces for the migration of free vesicles and the detachment of attached vesicles derive from mechanical rather than metabolic factors. Loudon et al (1979) cited the measured Poisson distribution of labelled ferritin molecules in frog mesenteric capillary vesicles as evidence that the loading process was determined by random movements of the ferritin molecules, ie: by their diffusion.

The rate-limiting step in vesicular transport has been argued (Tomlin 1969, Rubin 1976) to be the vesicular attachment/detachment process, described by the average time between the acts of attachment and detachment from the cell wall. Treating this process as a reversible reaction characterised by a rate constant, Rubin derived an expression for the permeability of a single endothelial cell in terms of the individual mass transport coefficients for each process involved in vesicular transport in series (attachment, detachment, vesicle loading and diffusion across the cell). Using parameters obtained by experiment, he found that the characteristic vesicle diffusion velocity was four times greater than the characteristic velocity of the attachment/detachment process and hence, vesicular transport was rate-limited by the attachment/detachment process. (The detachment process is actually not the exact reverse of attachment (Arminski et al 1980), but this finding does not change the identification of the rate-limiting step.)

Chien et al (1982) measured the ratio of attached to free vesicles by the

extracellular marker ruthenium red and calculated the ratio of vesicle attachment time to the time of diffusion across the cell. They found that the time duration over which the vesicle is attached to the plasma membrane is more than 6 times longer than the diffusion time. In qualitative agreement with Rubin, this indicates that the rate-limiting step in vesicular transport is the vesicle attachment time. Accepting the above arguments, any increase in the transport rate must be due to a decreased attachment time. (See however, later the argument in this chapter concerning the expected LDL concentration within the vesicles.)

A current theory (Rubin 1976, Weinbaum 1979, Arminski et al 1979) is that the vesicle detachment process is brought about by random thermal forces, resulting in the rupture of the vesicle-cell wall stalk. The mean experimental time for this has been reported to be from 10 to 30 seconds (Rubin 1976). However, it is clear that random thermal forces alone cannot account for localised regions in the arteries with greater uptake rates than the bulk of the arterial system. Reported local increases in permeability can be of the order of 100% (Bell et al 1975), requiring a local temperature increase of about 300 K if one relies solely on thermal effects and uses Rubin's model. Clearly, local temperatures of over 600 K are not possible in the arterial system. It follows that there must be another factor which gives rise to a regional variation in vesicular transport and that, given our assumption of the transport being via vesicles, it seems likely that this factor affects the vesicle attachment time.

Both temperature (Caro 1973) and exposure to alcohol (Siflinger et al 1974) increase endothelial permeability to albumin. Both of these factors will have an affect on the physical characteristics of the lipid bilayer constituting the cell and vesicle membranes and, more importantly, the vesicle-cell wall stalk. The detachment process will depend crucially on the physical characteristics of the stalk material. For instance, an increase in the fluidity of the stalk may make it more succeptible to mechanical damage induced by local fluid perturbations.

Experiments have shown that the rate of macromolecular transport across the endothelial layer is sensitive to temperature (Siflinger et al 1975) and a variety of mechanical factors such as the level of shear stress (Caro 1974, Davies et al 1984), pressure oscillations and stretching the arterial wall in an oscillatory fashion (Chien et al 1978, Arminski 1980).

3.3 The Role of Pinocytotic Vesicles in Macromolecular Transport:

It has recently been brought to the author's attention that the role of

pinocytotic vesicles in the mass transport of macromolecules has been questioned by the work of Frokjær-Jensen (1980, 1984) and Bungaard (1983). Their work, using ultrathin serial sectioning of frog mesenteric capillaries, showed that previous conclusions regarding the ultrastructure of the endothelium may have been subject to errors, caused by the thickness of the sections studied by electron microscopy. Very few of the vesicles labelled as "free" in the previous studies were indeed found to be so by ultrathin sectioning. Bungaard concluded that most of the structures previously termed "endothelial vesicles" were in fact invaginations of the cell wall and suggested that they instead be termed "endothelial invaginations". Frokjær-Jensen (1979) concluded that many vesicles group together as clusters that are ultimately continuous with the extracellular space (figure 3.2) and that the low number of free vesicles within the endothelium indicates that the main function of the vesicular system relates to functions other than transport.

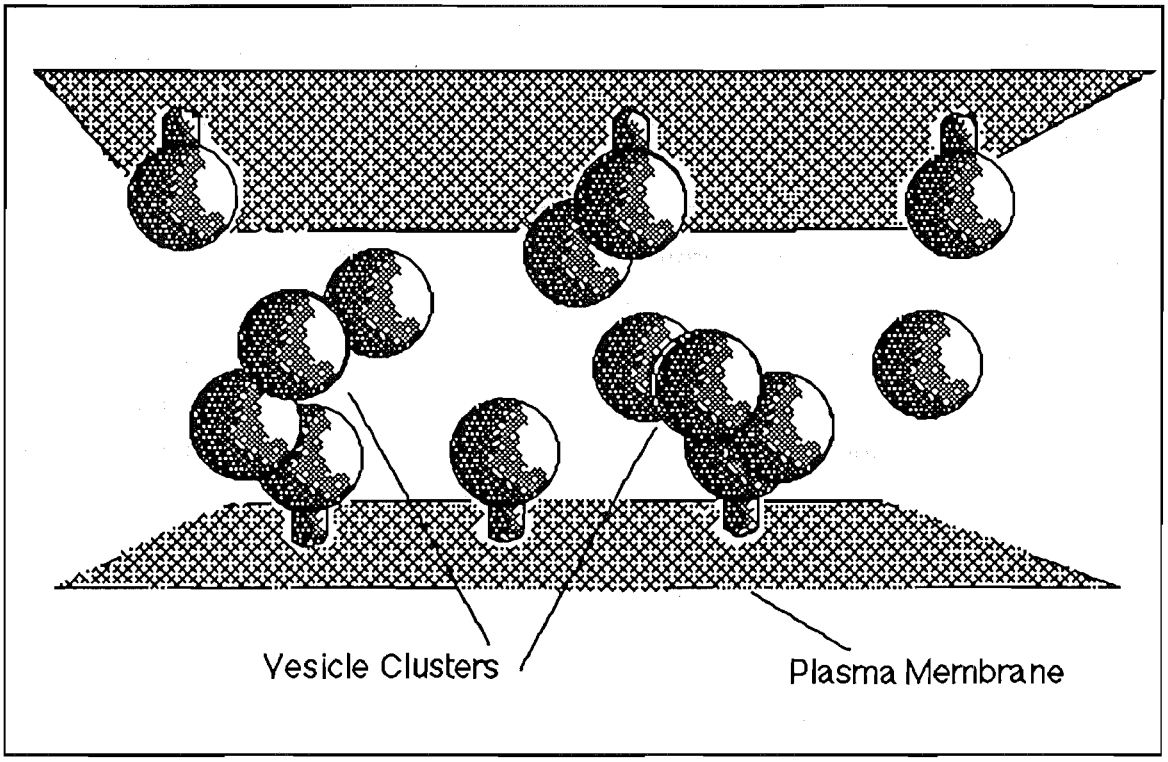

Figure 3.2
The Clustered Vesicle Model of Frokjær-Jensen (1979).

The counting of free vesicles in sections from samples of tissue that have been fixed prior to vesicle marking, does not allow for any transient effects on the vesicle detachment process which may occur in vivo. The standard practice, employed by the above workers for the preparation of sections for the study of the endothelial ultrastrucure, was to fix the endothelial sample after the animal's death and before

vesicular marking. This, of course means that the blood is at rest for some time before fixation, so that the endothelium and the vesicular system is in a static condition at fixation, which may be different from the in vivo condition. Given that the diffusion time across the cells is quite short, it is possible that some number of vesicles which may normally be free in vivo, diffuse to the wall before fixation and attach to the plasma membrane or group together in the clusters (figure 3.2) noted by Frokjær-Jensen (1979). Shea & Raskova (1983) have also identified the use of "slow" fixation techniques as possibly leading to erroneous conclusions regarding the in vivo endothelial ultrastructure.

If the detachment process of vesicles is enhanced by some transient mechanism(s) in vivo, such as external fluid (blood) motions, then static conditions before and during fixation would lead to an under-estimate of the in vivo number of free vesicles by electron microscopy. Clough & Michel (1980) measured the uptake by frog mesenteric capillaries of labelled ferritin molecules introduced before rapid fixation with osmic acid and found that only 5 to 10% of apparently free vesicles were attached to the lumenal plasma membrane. This finding is in contrast to the results of Bungaard et al (1979), who claimed a value of 50%, from experiments where vesicle marking was carried out after a slow fixation with paraformaldehyde-glutaraldehyde.

The possibility of a higher in vivo detachment rate over that present under static conditions suggests a corollary: that localised differences in the vesicular detachment rate between various regions of the arteries might occur due to differences in the prevalent physical environments. In relation to haemodynamics, it would be useful to determine whether any ultrastructural variations in endothelial ultrastructure (for example variations in the ratio of free to attached vesicles) occurs between endothelial cells subjected to different levels of static and oscillatory shear stresses or transendothelial pressure gradients. This has not been done.

Chien et al (1982) carried out experiments to determine the ratio of free to attached vesicles using ruthenium red as an extracellular marker. Their samples were also fixed before marking, exposing their technique for measuring the number of free vesicles in vivo to criticism by the arguments outlined above. Ruthenium red only penetrates those vesicles open to the extracellular spaces and therefore gives a measure of the ratio of the apparently free vesicles identified by electron microscopy (some of which may be attached to the plasma membrane in a plane other than that being observed) to those actually free. They found that only a quarter of apparently free vesicles were actually free but interpreted the consequence of the high number of attached vesicles differently from Frokjær-Jensen. They considered that large molecules may be limited in their transport rate, by their slow loading into the vesicles

(molecular sieving through the vesicle necks). They postulated that the greater the percentage of vesicles attached to the plasma membrane, the greater is the potential for vesicle loading, since the dynamic tracer studies of Loudon et al (1979) indicated that vesicle loading for ferritin may in fact be the rate-limiting step in the pinocytotic vesicular transport process.

Frokjær-Jensen (1984) suggested that his findings were consistent with the view that macromolecular transport occurs through occasional large pores that develop in the endothelia. The following analysis for hindered diffusion applies to this case of large pores as well, with some modifications.

3.4 A Theory for the Convective Enhancement of Diffusional Vesicle Loading:

3.4.1 The Equilibrium Partition Coefficient:

The assumption, in Rubin's theory for vesicular transport, that the vesicle loading process occurs very quickly is based on the estimates of Tomlin (1969) for loading of the vesicles by simple diffusion, in the absence of molecular sieving. However, a major carrier of cholesterol in the blood is LDL, which is also implicated in atherogenesis (Brown & Goldstein 1984). LDL has an average diameter of 22 nm, slightly larger than the average vesicle neck diameter of 20 nm. Diffusive loading of this species in vivo would be subject to significant hindrance. Casley-Smith & Chin (1971) observed molecular sieving effects for the passage of ferritin through the vesicle neck, where the ferritin used had a diameter of only 11 to 12 nm (just over half that of LDL). Loudon et al (1979) studied the labelling of perfused frog mesenteric capillaries by ferritin with a molecular diameter calculated to be about 6 nm, based on an assumed molecular weight and also noted significant hindrance effects.

Considering diffusional loading, the equilibrium concentration of a large molecule, such as LDL, inside the vesicle cavity is related to the exterior bulk concentration by an equilibrium partition coefficient for the vesicle, K_{pv}. This partition coefficient takes into account the limited space which the centre of a particle may randomly occupy within the cavity due to purely geometric considerations, assuming rigid, spherical molecules and rigid walls. The equilibrium concentration may be expressed as:

$$C_{bvo} = K_{pv} C_{bo} \qquad (3\text{-}1)$$

; where C_{bvo} is the interior vesicle concentration and C_{bo} the extracellular bulk concentration.

In Truskey et al (1981) the equilibrium partition coefficient for a hard sphere is related to the ratio, λ^*, of the sphere's radius to the half-dimension of the cavity, by

$$K_{pv} = \left(1 - \lambda^*\right)^n \qquad (3\text{-}2)$$

; where n = 1,2 or 3 for cavities having the shape of a slit, cylinder or sphere respectively. (The definition of λ^* from Colton et al (1975) is misquoted in Truskey et al as being the ratio of the sphere diameter to the half-dimension of the cavity.) If the average LDL radius is taken to be 11 nm and the vesicle interior radius 35 nm, then $k_{pv} = 0.32$. Therefore, the equilibrium concentration of LDL inside the vesicle cavity will be only 0.32 times the bulk concentration, even with no resistance to diffusion into the vesicle's interior due to the neck.

Loudon et al (1979) found that the final concentration of labelled ferritin particles measured within frog mesenteric capillary vesicles was only a third to a quarter of the expected equilibrium concentration calculated from equations equivalent to 3-1 and 3-2. They concluded that either the available volume for a ferritin molecule inside a lumenal vesicle is three to four times less than that calculated using the equilibrium partition coefficient, or that ferritin in lumenal vesicles does not have time to equilibrate with the ferritin concentration in the perfusate. Again following Tomlin (1969), Loudon and his co-workers calculated that the simple diffusional loading of the ferritin molecules would be 99% complete within 10 msec and concluded that there exists a barrier to diffusion in the vesicle. Two known structures were suggested as possibly being responsible for the barrier: the diaphragm, consisting of degraded vesicle wall remnants seen across the vesicle neck shortly after attachment (Clementi & Palade 1969, Arminski et al 1980) and a glycoprotein cellular coating, whose existence was postulated by Luft (1965, 1966).

In the absence of convective transport, the diffusion of the LDL through the vesicle attachment stalk (vesicle neck) will be subject to a similar geometric partitioning effect within the pore, with a partition coefficient K_{pn} for a cylindrical pore:

$$K_{pn} = (1 - \lambda)^{n} \qquad (3\text{-}3)$$

;where n = 2, and λ is a reflection coefficient equal to the ratio of the sphere radius to the pore radius for a pore which is larger than the sphere. λ is equal to 1.0 if the radius of the pore is less than or equal to that of the sphere. Since both the LDL particle diameter and the vesicle neck are subject to a normal distribution about the mean size, λ will have a spread of values with a maximum of 1.0 and decreasing with a distribution shape of half a normal distribution curve. The vesicle neck has been shown (Chien 1982) to dilate with increased pressure, suggesting that systolic pressure will increase the vesicle neck diameter, allowing the passage of particles during systole which may not be able to pass through the neck during diastole.

3.4.2 Macromolecular Flux Across the Endothelium:

Truskey et al (1981) defined the rate of vesicular transport, assuming this occurred by diffusion only and allowing for the equilibrium partitioning effect, as the flux J_s:

$$J_s = K_E K_{pv} \left(C_p - \frac{C_f}{\varepsilon_\phi} \right) \qquad (3\text{-}3)$$

; where K_E is the apparent mass transfer coefficient for vesicular transport across the intimal endothelium; C_p the concentration of macromolecules in the plasma; C_f is the concentration of freely available macromolecules in the solute within the arterial wall; and ε_ϕ the volume fraction of total tissue to which solute is accessible. They state that $K_{pv}K_E$ is equivalent to $\emptyset_R V$ in Weinbaum & Caro's (1976) expression:

$$\sigma = \emptyset_R V \left(L / D_m \right) \qquad (3\text{-}4)$$

; where σ is a dimensionless number characterising the vesicular transport, V is the internal volume of the vesicles, D_m is the macromolecule diffusion coefficient in the interstitial fluid within the arterial wall, L is the thickness of the arterial wall, used to non-dimensionalise distance coordinates and $\emptyset_R$ is the vesicle number flux in either direction described by:

$$\varnothing_R = {}^{N_f}\!/_{2t_D} \qquad (3\text{-}5)$$

; where N_f is the density of free vesicles per unit area of endothelial surface and t_D is the vesicle diffusion time across the cell. Therefore, according to Truskey et al, Weinbaum & Caro's expression (equation 3-4) accounts for the equilibrium partitioning effect on the vesicular internal macromolecular concentration. According to Arminski et al (1980), molecular sieving can be accounted for by multiplying the right hand side of the following equation for macromolecular flux, J:

$$J = \varnothing_R V\left[C_p - C(o)\right] \qquad (3\text{-}6)$$

by an exponential factor:

$$\exp(-{}^{t_f}\!/_{t_a}) \qquad (3\text{-}7)$$

which describes a diffusion barrier with a characteristic passage time t_f at the mouth of a vesicle with an attachment time t_a. C_p and C(o) are dimensional macromolecule concentrations at the lumenal and interstitial surfaces of the cell respectively. Equation 3-6 also takes into account the equilibrium partitioning effect on the internal vesicle macromolecule concentration.

3.4.3 Convection through the Vesicle Attachment Stalk:

Local blood flow disturbances may cause pressure fluctuations at the lumenal side of the endothelial cell. For instance, temporal fluctuations in the position of the reattachment point of a separated shear layer may subject adjacent areas of the artery wall to high and low flow velocities alternately, leading to static pressure fluctuations there. Wall pressure differences of up to twice the maximum kinetic head may result between adjacent areas that are exposed to different local flow conditions. If the fluctuations are fast, equilibration of pressure between areas, and hence across the endothelial cell may not take place. If the pressure drops across the endothelial cell are mainly applied across the lumenally and ablumenally-attached vesicles, the result would be fluctuating pressure gradients along the length of the stalks (figure 3.3). The basis of this postulate is the assumption that the endothelial cell itself is incompressible and is supported by the porous material behind. The interstitial space behind the cells, then allows the communication of pressure swings by fluid movements in a circumferential direction about the arterial wall, as shown in figure 3.4. It is further

assumed that the large pressure swings from the systolic pulse are too slow to lead to transendothelial pressure gradients. The systolic pressure pulse would also be applied equally about the arterial wall circumference. Pressure gradients between adjacent regions of the wall would not be set up in this case, as the pressure would be equally applied about the circumference of the interstitial space. The effect of convection, as a perturbation of the diffusional movement of macromolecules into the vesicle, due to a pressure gradient along the length of the vesicle attachment stalk, can be accounted for as described in the remainder of section 3.4.3 and in section 3.4.4:

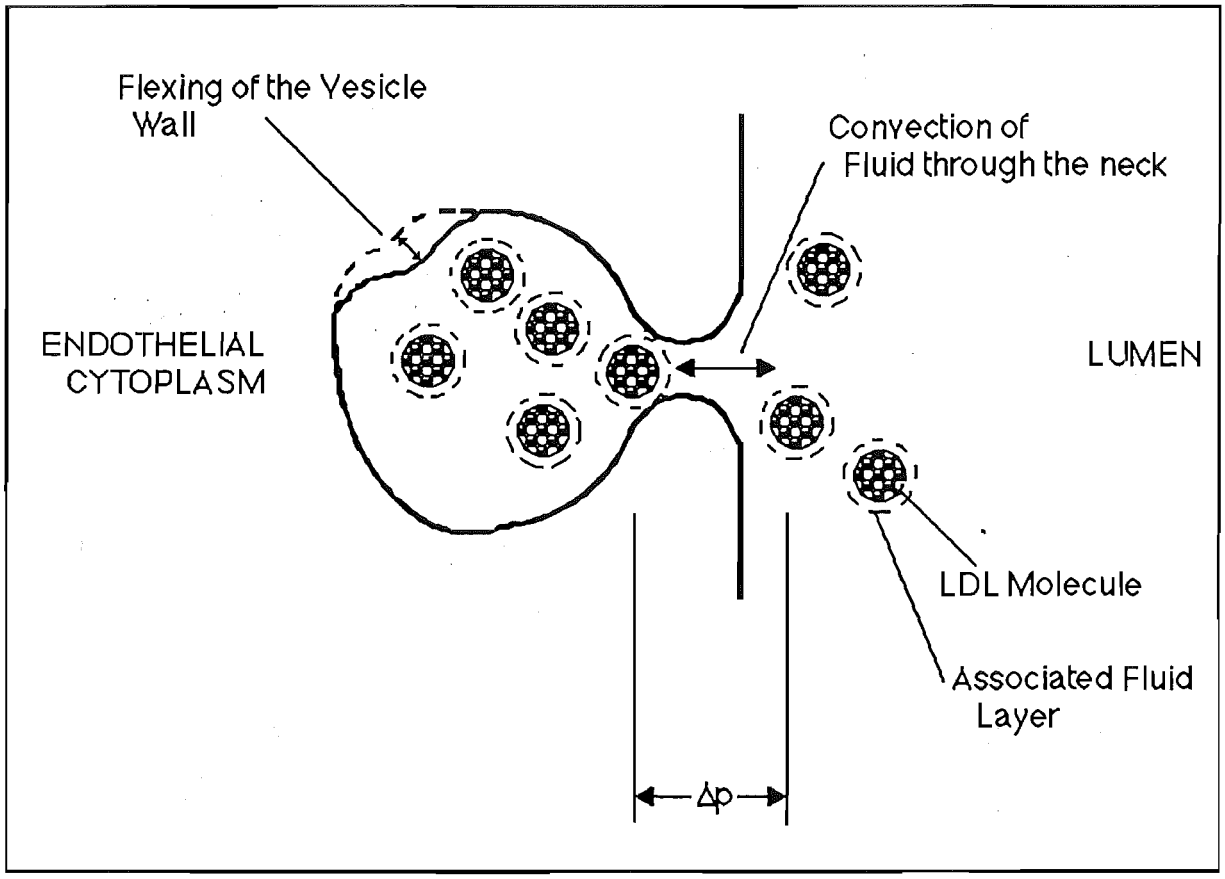

Figure 3.3
Convection Through the Vesicle Neck Caused by Pressure Difference Δp'.

The steady state permeability of an endothelial cell has been expressed as (Arminski et al 1980):

$$P = \frac{J}{C_p - C(o)} \qquad (3\text{-}8)$$

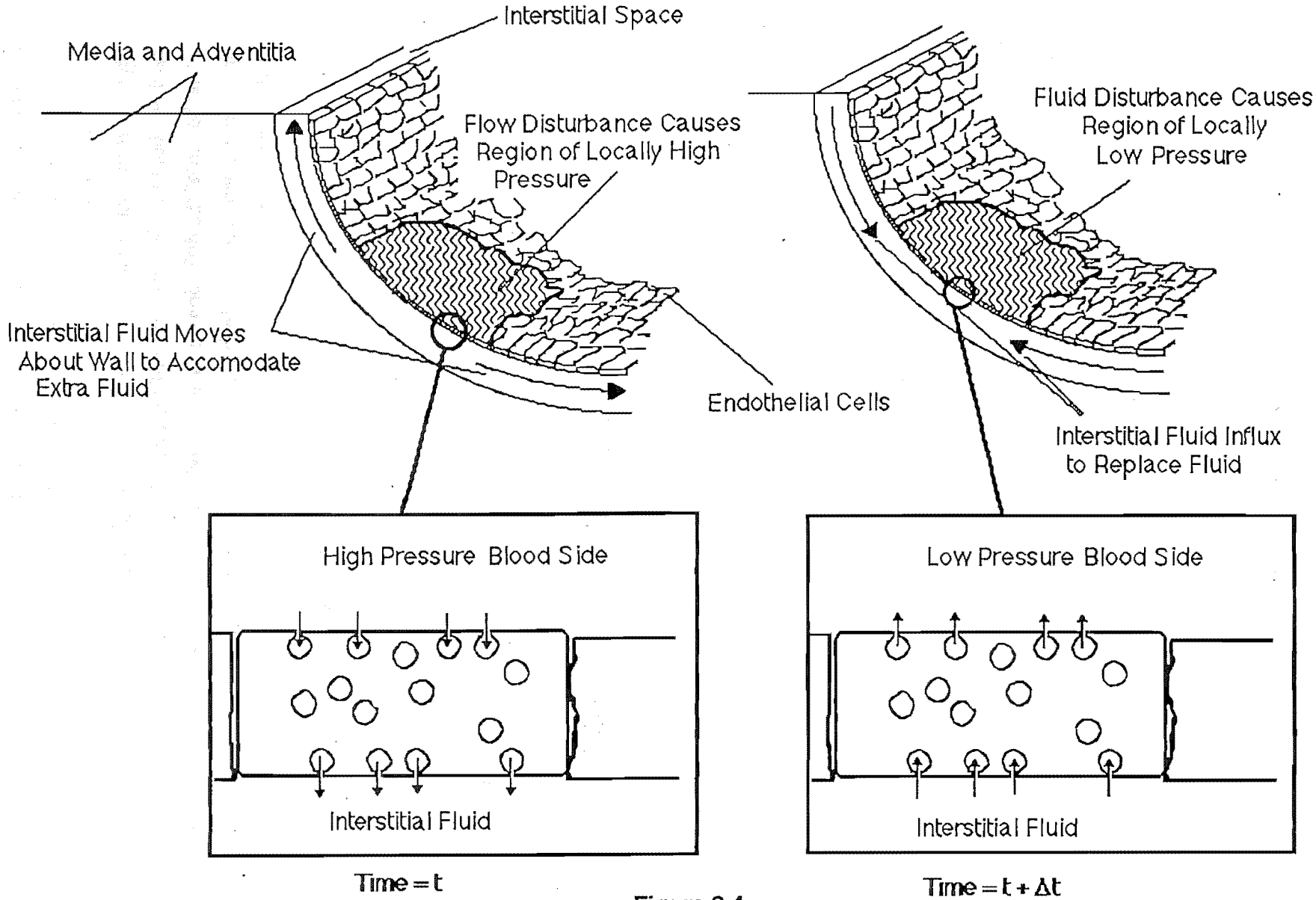

Figure 3.4

Interaction of the Vesicles and the Interstitial

; where J is the net macromolecular flux across the endothelium due to vesicular transport described in equation 3-6.

Since t_f in equation 3-7 is a characteristic passage time, it can be related to the diffusivity of the macromolecule through the vesicle neck. The diffusion of a hard sphere through a long cylindrical pore, disregarding ionic interactions, is scaled by the Peclet number (Malone et al 1978):

$$Pe = \frac{\bar{u}_p l}{D_p} \qquad (3\text{-}9)$$

; where l is the length of the pore, $\overline{u}_p$ is the average velocity of the particle through the pore and D_p is the diffusivity of the particle. The Peclet number Pe of the particle within the pore can be estimated from the Peclet number of the fluid in the pore Pe_∞ by multiplying the latter by a factor F, which is a function of λ so that

$$Pe = Pe_\infty F(\lambda) \qquad \text{; where}$$

$$Pe_\infty = \frac{\bar{u} l}{D_\infty} \qquad (3\text{-}10)$$

; where D_∞ is the bulk diffusivity

and

$$F(\lambda) = \frac{\left[(1 + 2\lambda - \lambda^2)(1 - \lambda)^2 - 3.9\lambda^2 + o(\lambda^2)\right]}{\left[1 + (9/8)\lambda \ln\lambda - 1.54\lambda + o(\lambda)\right]}$$

The velocity $\overline{u}$ of the fluid within the pore can be calculated from the pressure difference $\Delta p'$ through the pore (Dagan et al 1982). In our application we, for the moment, assume no resistance to an internal volume change in the vesicle. The greatest resistance to a change of the vesicle shape at this high curvature, is likely to be due to the bending resistance and thus, for the moment, we assume a zero membrane bending resistance in the following, obtaining the maximum convective effect on diffusion. The effect of the bending stiffness of the lipid bilayer making up the vesicle wall, and the spontaneous curvature of the material, will be considered later in this chapter.

The pressure drop is related to the flow through the pore by (Dagan et al 1982):

$$\Delta p' = \Pi(L) \frac{Q'\mu}{a^3} \qquad (3\text{-}11)$$

; where p' and Q' are dimensional pressure and volumetric flow variables, μ is the dynamic viscosity and a is the pore radius. $\Pi(L)$ is a function of the aspect ratio L and is approximately

$$\Pi(L) = {}^{16L}\!/_{\pi} + 3$$

L is the length to diameter ratio of the pore. For the vesicle neck, L = 1.0 and the exact value of $\Pi(L)$ is 8.06 (Dagan et al 1982). Since the average velocity of the fluid moving through the pore is

$$\bar{u} = \frac{Q'}{\pi a^2}$$

then, substituting this into equation 3-11 and rearranging:

$$\bar{u} = \frac{a \Delta p'}{\Pi(L) \pi \mu} \qquad (3\text{-}12)$$

Substituting equation 3-12 into 3-10 we obtain

$$Pe_\infty = \frac{a \Delta p' l}{\Pi(L) \pi \mu D_\infty} \qquad (3\text{-}13)$$

; where l = 2aL. Equation 3-13 then becomes

$$Pe = \frac{F(\lambda) 2 a^2 \Delta p' L}{\Pi(L) \pi \mu D_\infty} \qquad (3\text{-}14)$$

3.4.4 The Effect of Convective Perturbations on Hindered Diffusion Through an Endothelial Cell:

The effect of fluid convection on the diffusion coefficient along the pore is (Malone & Anderson 1978):

$$D_{obs} = K_{pn} D_{\infty} \left\langle \frac{Pe}{1 - \exp(-Pe)} \right\rangle \qquad (3\text{-}15)$$

The exponential term in the average (angular brackets) can be approximated by a series so that the time of passage t_D is

$$t_D = \frac{l^2}{D_{obs}}$$

$$= \frac{l^2}{K_{pn} D_{\infty} \left[1 + \frac{\langle Pe \rangle}{2} + \frac{\langle Pe^2 \rangle}{12} - \frac{\langle Pe^4 \rangle}{720} + O(\langle Pe^6 \rangle) \right]} \qquad (3\text{-}16)$$

Terms in angular brackets indicate the average values of fluctuating components. Clearly, even if the average of fluctuations is zero, terms with powers of 2 or greater will be non-zero. Hence D_{obs} is always higher than D (where $D = K_{pn} D_{\infty}$) in the presence of fluctuating convective effects (Malone et al 1978).

By putting $t_D = t_f$ in Arminski et al's (1980) expression, we obtain an expression for a diffusion barrier at the vesicle entrance which is dependent on the pressure swing Δp, with a characteristic time of passage through the neck:

$$t_f = \frac{4 a^2 L^2}{D \left[1 + \frac{\langle Pe \rangle}{2} + \frac{\langle Pe^2 \rangle}{12} - \frac{\langle Pe^4 \rangle}{720} + O(\langle Pe^6 \rangle) \right]} \qquad (3\text{-}17)$$

; where

$$\langle Pe \rangle = \frac{2\,F(\lambda)\,a^2 L}{\Pi(L)\,\mu\,\pi\,D_\infty}\langle \Delta p' \rangle$$

$$= \Psi(\lambda)\langle \Delta p' \rangle \quad ; \text{where } \Psi(\lambda) = \frac{2\,F(\lambda)\,a^2 L}{\Pi(L)\,\mu\,\pi\,D_\infty}$$

The factor for the time of diffusion can be inserted into equation 3-6 to give:

$$J = \exp\left(-t_f/t_a\right) \varnothing_R V\left[C_p - C(o)\right].$$

Following Arminski et al's (1980) derivation of the overall permeability of an endothelial cell and including the factor for molecular sieving (equation 3-7), allowing for the effect of convective mixing perturbations on the observed diffusion coefficient:

$$P = \exp\left(-t_f/t_a\right) \frac{\Phi\,V\,\xi(y)}{\xi\,(1-\xi)} \qquad (3\text{-}18)$$

; where Φ is the vesicle release rate, which can be expressed in terms of the number density of attached vesicles N_a and the average attachment time of a vesicle t_a as $\Phi = N_a/t_a$. ξ describes the variation in fluid resistance for the perpindicular motion of a spherical particle between the plasmalemmas, and is related to a vesicle-plasma membrane hydrodynamic interaction parameter, by a transformation of coordinates, so as to provide the proper asymptotic behaviour (Arminski 1980).

The permeability of an endothelial cell is finally:

$$P = \exp\left(-t_f/t_a\right) \frac{N\,V\,k_1^d}{2}\left(\frac{\xi(y)}{\xi\,(1-\xi)}\right)\left[\frac{1}{1+\frac{l^2 N_f^* k_1^d}{2\,D_0}}\right] \qquad (3\text{-}19)$$

; where

$$\left(\frac{\xi}{\xi\,(1-\xi)}\right)$$

is the probability that an attached vesicle will be released and

$$\left(\frac{l^2 k_1^d}{2\,D_0}\right)$$

is the ratio of attachment to diffusion times. N_f^* is the dimensionless form of N_f.

3.5 Magnitude of Convective Effects:

3.5.1 The Diffusional Loading Process:

The hypothesis proposed is that the local diffusion of macromolecules into the vesicles of the endothelial layer is affected by small pressure perturbations inherent in nearby disturbed flow (such as that at the reattaching area of a reattaching shear layer).

An evaluation of the sensitivity of the exponential factor in equation 3-19 to the pressure drop through the vesicle attachment stalk will indicate the magnitude of the effect of local pressure fluctuations on the rate of diffusion of LDL into a vesicle. The exponential factor of equation 3-7 which accounts for hindered diffusion through the vesicle neck is only significantly less than 1.0 if the ratio of t_f to t_a is greater than about 0.1. Since t_a is in the region 5 to 30s, t_f begins to influence the rate for values larger than 0.5 to 3 s, or from equation 3-17, when the the term a^2L^2/D is larger than about 0.5 to 3 s. The vesicle stalk is very short (so that a^2L^2 is $O[10^{-16}]$) and since D_∞ for lipoprotein has been measured to be about 2.7×10^{-11} m^2s^{-1} (Wakeham et al 1976), K_p must be of the order of 10^{-5} for diffusional hindrance to significantly limit the overall permeability. Therefore the exponential factor in equation 3-7 will be significantly less than 1.0 only if the internal radius of the vesicle neck is close to the radius of LDL, say $0.995 \leq \lambda < 1.0$. Since the average diameter of LDL is 2 nm larger than the average diameter of the vesicle neck and the latter is able to dilate with increased pressure, there should exist a fraction of LDL molecules and vesicle necks which will give such a value of λ. LDL molecules which are larger than the vesicle necks will not diffuse into the vesicles, whilst the fraction of LDL molecules and necks

whose radius ratios, λ, are less than 0.995 probably provide a basal trans-endothelial LDL transport rate.

The factor $\Psi(\lambda)$ is of the order 10^{-4} and is only weakly dependent on λ. Therefore Pe is small and has little effect on D until $\Delta p'$ is of the order of 10^3 Pa.

The trans-endothelial transport of macromolecules through "occasional large pores" (Frokjær-Jensen 1984) would probably be subject to hindered diffusion, so that the analysis in section 3.4 would apply. The length of the pores in this case would be at least the thickness of the endothelial layer, giving a larger aspect ratio than that of the vesicle attachment stalk. The hindrance effect would therefore be much larger than that through the vesicle neck, being significant even for particles whose diameter is only a small fraction of the pore diameter.

3.5.2 The Convective Loading Process:

3.5.2.1 Description of Convective Loading:

The above analysis considers the convective mixing effect only as a perturbation on diffusion through the vesicle neck, as is appropriate for a long neck. If the convection through the neck is high enough however (as for a short neck), the LDL and some surrounding fluid will be actively swept, as one body, through the vesicle neck, into the vesicle cavity. The concentration of LDL within these spaces is then no longer a function of the equilibrium partition coefficients.

In the case of a long pore, the package of fluid containing the LDL molecule will be convected back and forth within the pore, adding to the diffusive velocity of the molecule. In the case of a short pore like the vesicle neck, the LDL molecule is able to escape, by diffusion, from the confines of the convected fluid package, once the fluid enters the vesicle cavity. The LDL molecule will therefore not necessarily be contained within the package of fluid which is swept out on the reverse pressure swing. The partitioning effect is lower within the vesicle cavity than in the attachment stalk, so that the LDL molecule, once it has been convected past the narrow opening of the neck, is more likely to diffuse randomly about the cavity than to diffuse out again. Also, any randomness in the location of the wall area where the vesicle buckles, as it allows fluid to enter and leave the cavity, will have a mixing effect, over time, on the vesicle's interior fluid.

3.5.2.2 Resistance to Convection Due to Vesicle Wall Bending Stiffness:

The bending stiffness of the vesicle lipid bilayer wall material is likely to oppose a volume change in the vesicle, causing a resistance to the convective flow into and out of the vesicle cavity. The ease of deformation of the vesicle wall depends crucially on the spontaneous curvature of the wall material, the shape of the vesicle and the pressure difference between the interior and exterior of the cavity. The bending stiffness is lower for an imperfect sphere, than for a perfect sphere, so that any deformations in the spherical vesicle shape, will have the effect of lowering the resistance to convective flow through the vesicle neck caused by the bending stiffness.

For a vesicle with a surface area S, an equivalent sphere radius R_o may be defined by $S = 4\pi R_o^2$. The maximal volume of the vesicle, at a constant surface area S, is $V_o = (4\pi/3)R_o^2$. When the volume V is reduced below V_o, the vesicle becomes easily deformable and can assume a variety of shapes depending on S, V and c_o, the spontaneous curvature of the bilayer wall material (Deuling & Helfrich 1976). The shape of the vesicle possessing the minimal elastic curvature energy, depends on the pressure difference ΔP between the interior and the exterior of the cell, which may arise from a variety of factors, such as osmotic pressures. $\Delta P = p_e - p_i$; where p_e is the exterior pressure and p_i is that of the interior. In particular, the critical value ΔP_c is the pressure difference at which the sphere is in neutral equilibrium:

$$\Delta P_c = (2k_c/R_o^3)(6 - c_o R_o)$$

; where k_c is an elastic constant of the order of 10^{-19} Nm (Servuss et al 1976). In the case of a stomatocyte (where an invagination of the near-spherical vesicle is present), when ΔP is a small fraction of ΔP_c and the spontaneous curvature, c_o, is zero, large changes in V/V_o may occur with small differences in $\Delta P/\Delta P_c$ (Deuling & Helfrich 1976). In this case, a 500 Pa change in ΔP could result in a 6% volume change in the vesicle. The spontaneous curvature of the endothelial vesicle is a crucial variable in determining the ease of deformability and will need to be measured in future work. Vesicles are rarely observed to be perfect spheres, so that stretching of the membrane (which is difficult) would not be required for this volume change.

3.5.2.3 Quantifying Convective Loading:

Assuming a normal serum LDL concentration of 1200 µg/ml (Truskey et al (1981) and a molecular weight for LDL of 2×10^6 (Conn & Stumpf 1976), the volume

of fluid associated with each LDL molecule is calculated to be 2.77 x 10^{-21} m^3. Allowing a change in vesicular volume of 6% of the mean vesicle volume (which is 1.8 x 10^{-22} m^3) per pressure fluctuation cycle, then on average, one could expect an LDL molecule to be convected into the vesicular cavity once every 250 cycles. $\Pi(L)$ = 7.24 for a vesicle with a neck diameter equal to the 24 nm (large enough for a 22 nm diameter LDL molecule to be easily convected through), so that from equation 3-11, the ratio of volumetric flow to the pressure drop along it's length is $Q'/\Delta p'$ = 6.36 x 10^{-23} $m^3 s^{-1} Pa^{-1}$. For a sinusiodal pressure fluctuation, with a frequency of, say, 50 Hz, an appreciable fraction of the maximum pressure drop will exist for about 5 ms per half cycle and two such half cycles are required to sweep a package of fluid into the vesicle and out again. To gain a volumetric flowrate of 1.8 x 10^{-23} m^3 per cycle, the maximum $\Delta p'$ would need to be 56 Pa between the lumen and the vesicle interior. The kinetic head ($^1/_2 \rho u^2$) in the carotid artery could be up to 500 Pa based on a peak flow of 100 cm s^{-1}, offering pressure differences between adjacent wall regions of up to 1 kPa. The total pressure difference is split between the vesicles attached to the lumenal surface and those attached at the ablumenal surface.

There would therefore be a significant convective effect on the loading of LDL, even if the bending stiffness of the vesicle wall opposed the volume change within the vesicle and thereby decreased the flow through the neck by as much as 18 times that calculated from equation 3-11, for a fluctuation frequency of 50 Hz. By the above analysis, it can be seen that decreasing the frequency of the fluctuation will increase the time per cycle that the $\Delta p'$ is near it's maximum value, effectively increasing the available pressure drop for driving the flow through the vesicle neck.

3.5.3 Convective Loading vs Diffusional Loading:

Since the vesicle interior volume is very close to the volume consisting of an individual LDL molecule and it's associated fluid in the plasma, the presence of an LDL molecule inside a vesicle represents a similar LDL concentration to the plasma concentration. As the mean vesicle attachment time has been reported (above) to be in the range 6 to 30 seconds, one LDL molecule could be expected to enter a vesicle subjected to the convective loading process, at a pressure fluctuation frequency of 50 Hz, before detachment. This rate is sufficient to allow the vesicle interior to reach an internal LDL concentration equal to the plasma concentration, before detachment. The vesicles thus subjected to convective loading in the presence of local fluid disturbances, would therefore possess approximately three times the number of LDL molecules expected within a diffusionally-loaded vesicle (assuming the diffusional loading is fast enough), which is limited by the equilibrium partitioning effect. The

increase in LDL transport by convective loading then, is not due to an increase in the rate of vesicular transport across the cell, but on the equilibrium LDL concentration within the vesicles.

Equation 3-6 (Arminski et al 1980) describes the macromolecular flux in terms of the concentration gradient between the lumenal and interstitial spaces, allowing for the equilibrium partitioning effect (Truskey et al 1981). This is appropriate for long trans-endothelial pores. However, if convective effects enhance the vesicle loading in the manner suggested above, for short pores, equation 3-6 will underestimate the transport rate in cells subject to convective disturbances.

If the glycoprotein coating postulated by Luft (1966) exists and hinders diffusion in the manner that Michel (1980) suggests, convection through the vesicle neck may enhance vesicle loading by breaking away the coating from the neck, or increasing the observed diffusion coefficient for hindered diffusion through the coating. The same process might also decrease hindrance that is caused by remnants of the dissolved vesicle wall material that has been observed in the vesicle neck after attachment to the plasma membrane.

The effect of this convective loading of the vesicle in areas of local fluid perturbations would be to increase the transport rate over those areas where no such convective effects occur. In the latter areas, the concentration of LDL in both the vesicle neck and interior space would be limited by magnitudes described by equilibrium partition coefficients.. Equation 3-19 accounts only for diffusional loading and therefore applies only in the case where small or negligable convective effects occur.

In the above discussion, no treatment of the effect of mechanical enhancement of the detachment process for vesicles has been attempted.

3.6 Summary:

The transport of macromolecules across the arterial endothelium by pinocytotic vesicles has been described. In particular, the internalisation of LDL molecules, associated with atherogenesis, from the blood stream is thought to occur mainly by this process, given that LDL receptors on the endothelial cell surface have been reported to be saturated at blood serum LDL levels far below those found in vivo. For purely diffusional loading of vesicles, the vesicle interior concentration of macromolecules is related to the exterior (plasma) concentration by an equilibrium

partition coefficient. For the LDL molecule, this internal concentration is only 32% of the plasma LDL concentration.

Recent studies of endothelial ultrastructure, by ultrathin sectioning, cast some doubt upon the role of pinocytotic vesicles in transendothelial macromolecular tranport. However, the fixation techniques used in the preparation of endothelial cell samples could cause a change from the in vivo ultrastructure of the endothelial cells, leading to an under-estimate of the in vivo ratio of dettached to attached vesicles. Furthermore, the possibility of transient effects in vivo that enhance vesicular detachment over that seen under static conditions, also suggests the possibility that localised differences in vesicular transport exist throughout the arterial system. This may provide a causative link between localised haemodynamic forces and an altered transmural permeability. An altered transmural permeability has been suggested by some workers (for instance Steinberg 1983) to be an atherogenic change to the blood vessel wall.

A theory has been developed, which incorporates the effect of molecular sieving on the diffusional loading of LDL molecules into the vesicles. The time of passage of an LDL molecule through the vesicle neck has been related to an observed diffusion coefficient, D_{obs}, which is lowered from the bulk diffusion coefficient by a geometric partitioning effect in the vesicle neck. D_{obs} has been shown to be enhanced by fluctuating convection, even when the average of the fluctuations is zero. Local blood flow disturbances are postulated to be the source of fluctuating pressure differences between adjacent wall areas, of up to 1 kPa, which may give rise to fluctuating convection through the vesicle attachment stalks and enhance D_{obs}.

Because of the shortness of the vesicle attachment stalk, the molecular sieving effect was found to be significant only when the radius of the diffusing particle (LDL) is greater than about 0.995 times the radius of the vesicle attachment stalk. Since the average diameter of LDL is 10% larger than the average vesicle stalk diameter, a significant fraction of those LDL molecules able to pass through the stalk might fulfill this requirement. The effect of low pressure differences through the attachment stalk on the observed diffusion coefficient was found to be negligable. At higher pressure drops, the convective effect is too large to be considered as merely a perturbation to the diffusion process.

A far greater effect on the loading of vesicles is offered by the possibility of a convective sweeping effect through the attachment stalk. The volume change of the vesicle, required for this process to occur, will be opposed, to some extent, by the bending stiffness of the vesicle wall. The bending stiffness depends crucially on the spontaneous curvature of the wall material, the shape of the vesicle and the pressure

difference ΔP between the interior and exterior of the vesicle. Thus, the spontaneous curvature of the vesicle wall has been identified as a critical property which needs to be determined.

Assuming that the vesicle wall material has a spontaneous curvature of zero and that ΔP is a small fraction of the critical value for a perfectly spherical vesicle, a 6% change in the internal volume of the vesicle could be expected to result from a 500 Pa change in ΔP. At normal plasma LDL concentrations, the fluid associated with this volume change, convected back and forth through the vesicle neck, will contain one LDL molecule approximately once every 250 pressure cycles. The volume of an individual vesicle is close to the volume of each LDL molecule and it's associated fluid in the plasma and therefore this process brings the vesicle interior to an equilibrium concentration equal to the exterior (plasma) LDL concentration. At a pressure fluctuation frequency of 50 Hz, this interior concentration would be reached, on average, before detachment of the vesicle from the plasma membrane occurred.

The convective vesicle loading process is independent of the geometric partitioning effect, which relies on diffusion to be accomplished. Since the equilibrium partition coefficient limits the internal vesicle LDL concentration to 32% of the plasma concentration, the convective loading process could result in a vesicle interior LDL concentration of more than 3 times that expected by diffusional loading. An increased trans-endothelial LDL transport rate, resulting from convective loading of the vesicles, would be due to an increase in the equilibrium LDL concentration within the vesicles, over that which occurs by the diffusional loading process alone.

Chapter 4

Experimental Methods and Apparatus

4.1 The Model:

The model was chosen to simulate an abnormal feature of the cervical portion of the human internal carotid artery, namely a C-shaped distortion, following the nomenclature of Weibel and Fields (1965). Due to the large variation in severity of the tortuosities in vivo, the choice of exact geometry for the model was quite arbitrary. The geometry of the model falls within the range of shapes found in human subjects and the dimensions are shown in figure 4.1.

Perspex was chosen as the construction material, as initial trials and previous experience (Stehbens and Fee, 1985, Stehbens, Fee and Stehbens, 1987) demonstrated that curved tubes could not be manufactured free of cross-sectional distortion in glass without the use of expensive forming equipment. Furthermore the use of perspex reduced difficulties associated with introducing probes into the flow through the walls of the model.

The model was manufactured following the examples of other workers (for example Agrawal Talbot and Gong (1978), Olsen and Snyder (1983), Chandran and Yearwood (1981)) by milling semicircular channels in two perspex blocks using the computer controlled milling machine in the Mechanical Engineering Department at the University of Canterbury. The two halves were highly polished, positioned by pins and joined by screws (Plate 4.1). This resulted in a tube of constant circular cross-section (20 mm) with carefully controlled radii of curvature (equal to the tube diameter) at the bends. The tube could be taken apart for cleaning and fitting probes.

End-pieces (figure 4.1) were constructed to taper slowly from the 22 mm diameter rigid PVC pipe used upstream and downstream to the 20 mm diameter model without discontinuities. These were initially manufactured from brass, but were later replaced by perspex after the inner surfaces were found to be roughened by corrosion.

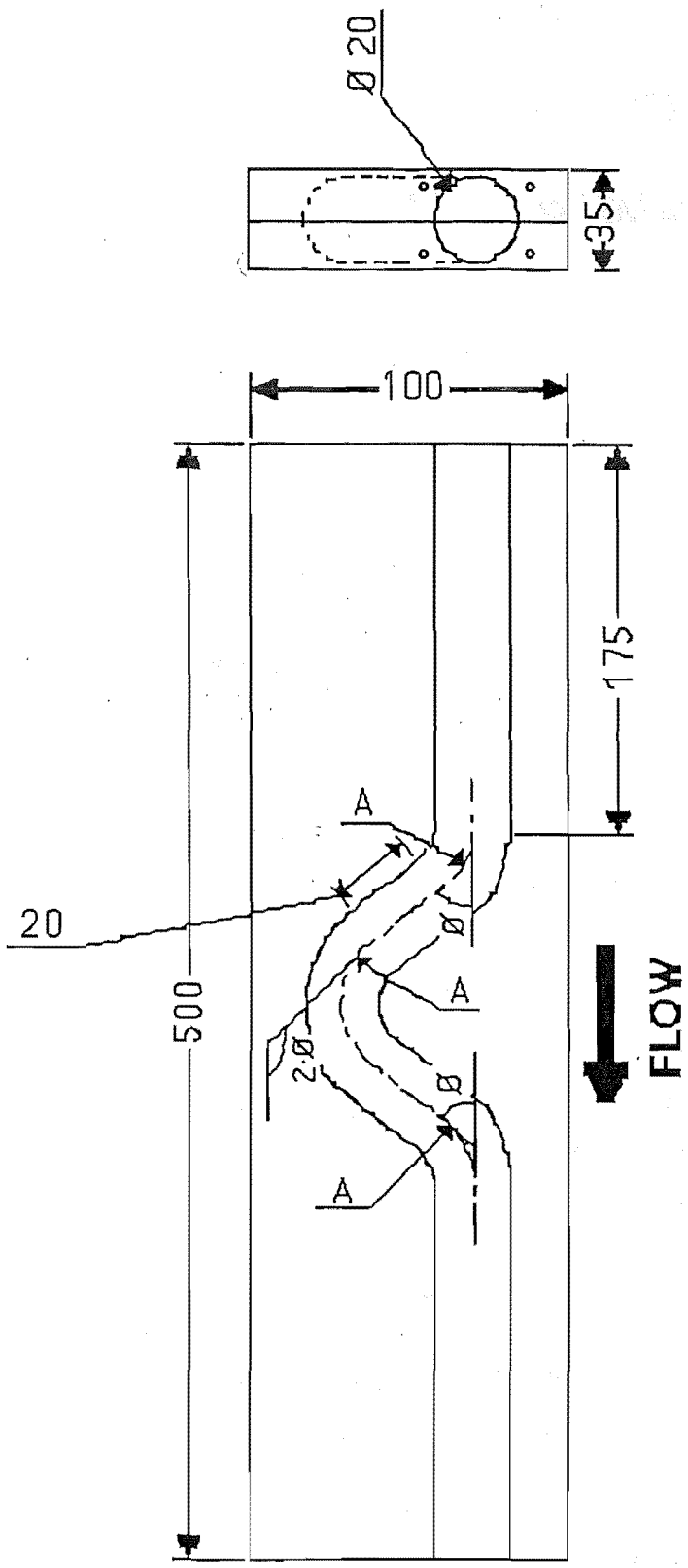

The Model

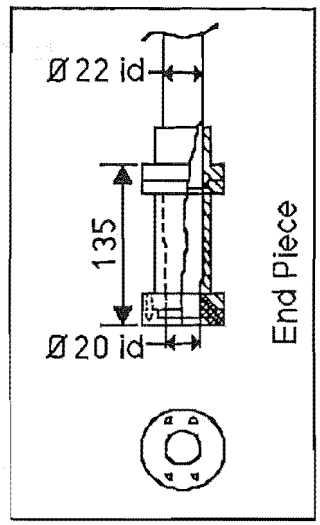

Material: Perspex
Dimensions in mm
Not to Scale
A = ℄ radius 20 mm
Ø = 70°

Figure 4.1
Dimensions of the Model of the Tortuous Cervical Internal Carotid Artery.

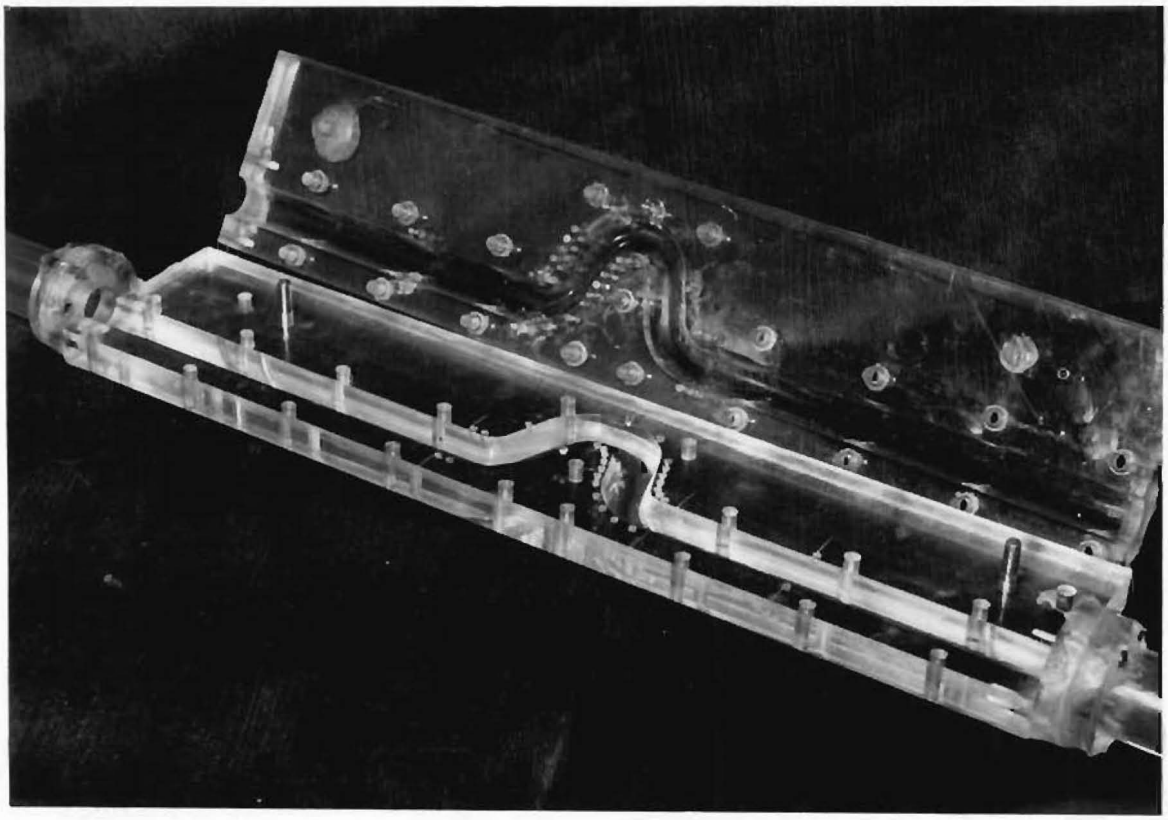

Plate 4.1

The Model of the Tortuous Cervical Internal Carotid Artery.

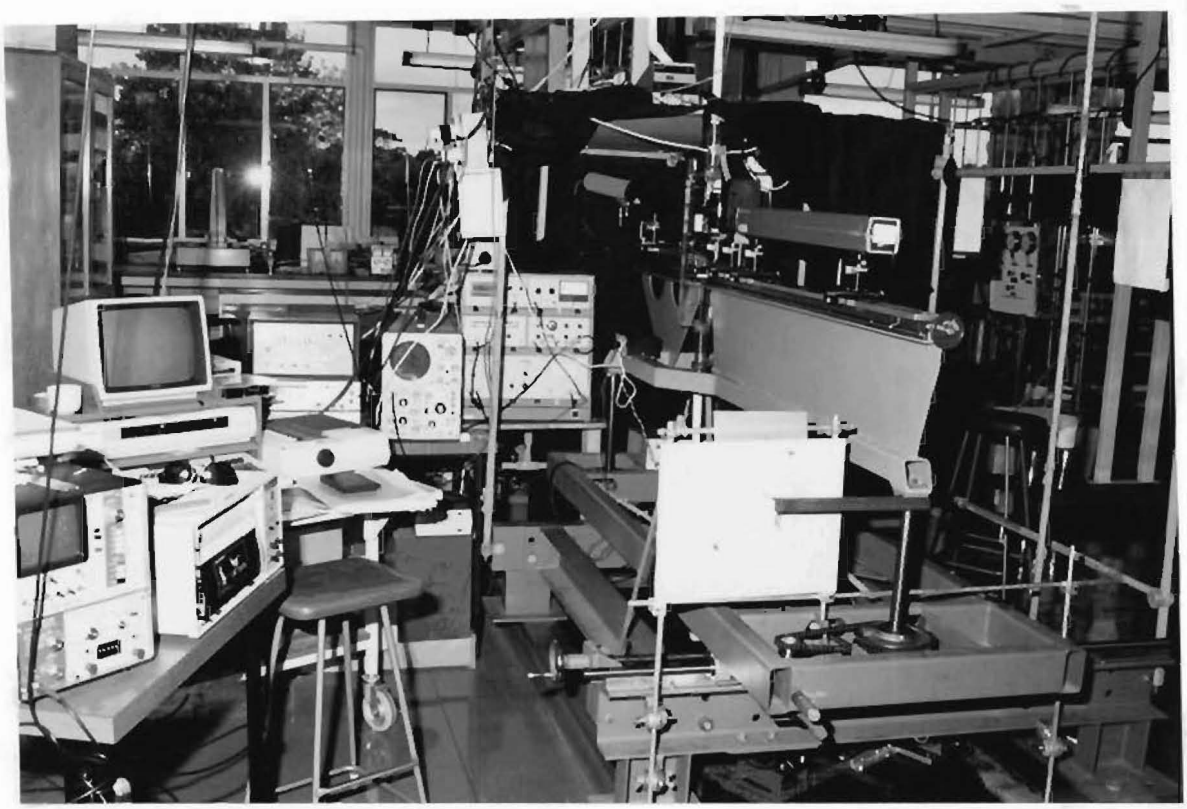

Plate 4.1a

The Experimental Apparatus, Showing the Traversing Table, the LDA and the Data Collection Equipment

The end-pieces were joined to the model by screws, using RTV sealant to prevent small leakages.

4.2: The Flow System:

4.2.1: Steady Flow:

The flow system used is shown in figure 4.2 and is described below.

The model was supported free of vibration over a drain tray. A steady flow was provided via a syphon from a constant head tank on the floor above the model, allowing a straight, smooth rigid entrance length of greater than 150 tube diameters (3.0 m) prior to entering the upstream end-piece of the model. A straight exit length of 40 tube diameters (0.8 m) was provided downstream of the model before flow was deviated to pass through other fittings, such as a rotameter and valves.

The header tank was replenished from the mains supply and water exited to the drain tray from the model outlet and the header tank overflow. A weir was used to maintain the constant height of water in the header tank.

The mean flow rate was measured by a metric size 10 rotameter with a stainless steel float (calibration chart in Appendix L) situated downstream of the model, and the flowrate was controlled by a PVC cock downstream of the rotameter. The rotameter leg served the extra purpose of preventing air from travelling upstream from the flow outlet.

The syphon was filled without entrapping air-bubbles from a mains water supply situated at the lowest point in the system. A three way cock allowed the mains supply pipe to be flushed of air and dirt and the system to be both filled and drained from that point. One way check valves as shown in figure 4.2 allowed air to be flushed from the highest point in the system whilst filling without the loss of water from the syphon leg.

The length of pipe at the highest point in the system acted as an air trap to prevent the entrainment of residual air bubbles in the flow, and ensured sufficient head to allow the lower of the two check valves to operate without leaking. The flowrate of the feed-water supplied to the header tank was controlled by a gate valve and switched on and off by a solenoid valve operated from the same floor as the model.

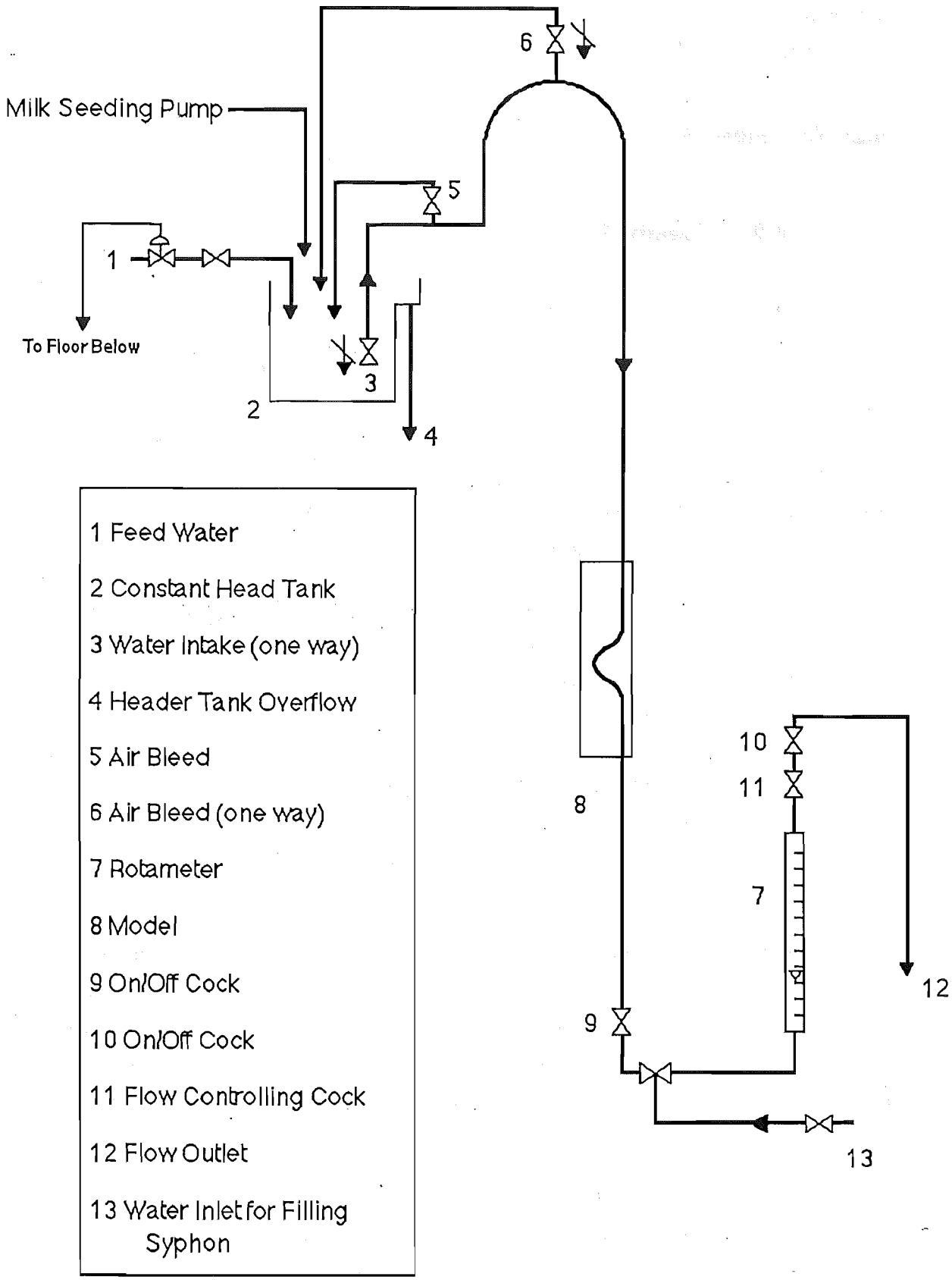

Figure 4.2

The Flow System Used for Steady Flow Experiments.

The water temperature was measured at the header tank to an accuracy of ± 0.5 °C by a copper-constantine thermocouple. The temperature varied by less than 0.5 °C between the header tank and the flow outlet.

4.2.2: Pulsatile Flow:

During initial trials with pulsatile flow conditions, problems were encountered with small air bubbles being entrained in the flow and eventually becoming entrapped in the model itself. The source of these bubbles was traced to dissolved air coming out of solution during residence in the header tank. The siphon leg of the system was removed, but the bubbles still occurred. The problem was solved by pulling the header tank feed water through a valve with a peristaltic pump. This caused a sudden pressure drop and the air came out of solution to be removed from a trap by a water pump before entering the header tank (figure 4.3).

The arrangement shown in figure 4.3 is the final one resulting from several changes made throughout the experimental work, but the entrance and exit legs were kept constant despite changes to the rest of the system.

Pulsatile flow was achieved following the example of other workers (Sobey, 1985, Lin and Tarbell, 1980) by introducing a pulsatile component into a positive steady flow with a piston pump.

A DCL Metering pump was found to have a sinusoidal ram action when operated at full stroke ie: with the vernier stroke length adjustment screw fully withdrawn.

A Kopp Variator gear set was placed between the 1.5 hp motor and the pump and with the use of pulleys, this provided continuous variation of the pump speed from 0.025 cycles per second up to 2 cycles per second.

It was found that the amplitude of flow fluctuation introduced by the pump was a function of the difference between the upstream and downstream flow resistances. The flow resistance downstream of the pump was too high to achieve the desired amplitude at suitably low Reynolds numbers with the system as used for the steady flow experiments. Consequently, the resistance on the downstream side was lowered by removing the rotameter and replacing the 1/2 inch pipe section with 1 inch pipe (while still retaining the air trap section), and incorporating a 1 inch PVC cock.

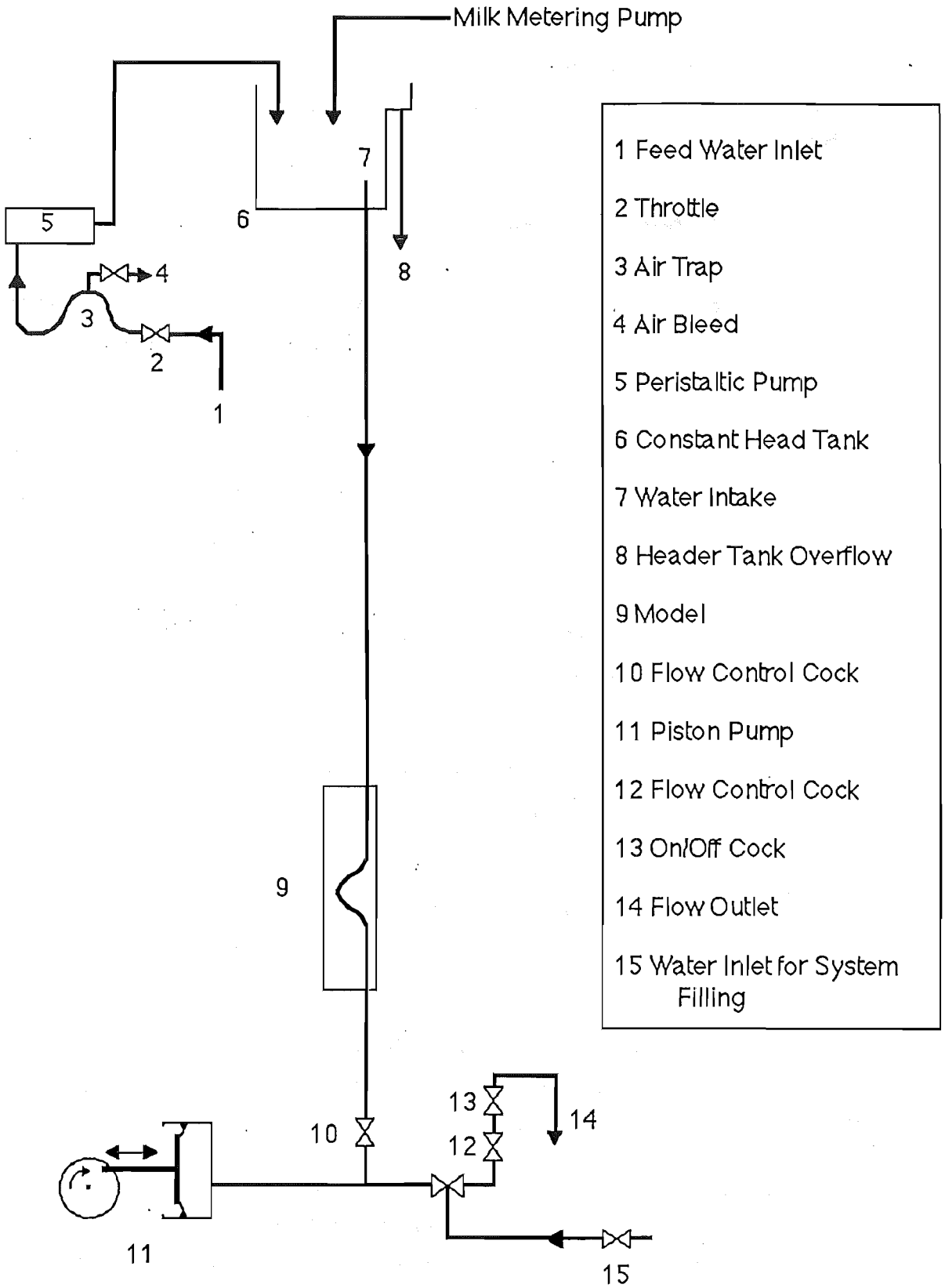

Figure 4.3
The Flow System Used for Pulsatile Flow Experiments.

The rotameter was removed. Flowrates were then measured with the LDA on the centreline of the tube, 8 diameters upstream of the proximal bend.

The amplitude of flow fluctuation could be set by adjusting the valves upstream and downstream of the pump. The pump produced a sinusoidal pressure variation below the model, proportional to the speed of the piston ram, but the shape of the centreline velocity vs time curve was not purely sinusoidal (figure 4.4).

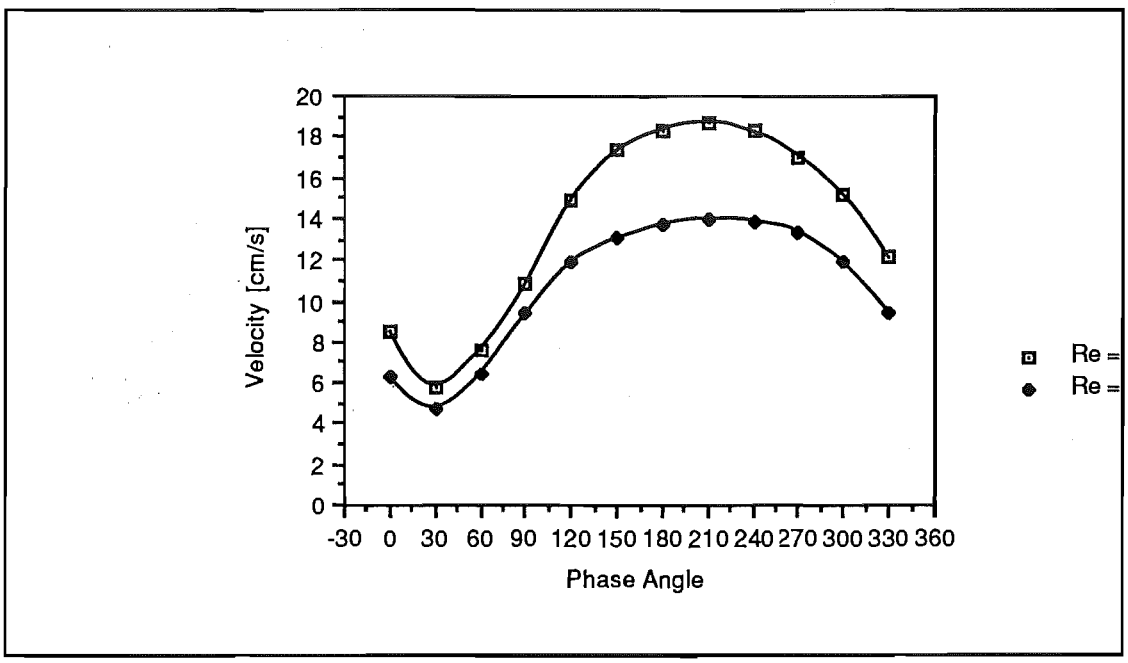

Figure 4.4

Centreline Pulsatile Velocity 8 Diameters Upstream of the Proximal Bend, For Re_{mean} = 1500 & Re_{mean} = 1000

The mean flowrate was lower with the pump operating than during steady-flow conditions, for a given valve setting. The resistance in parts of the circuits changed from Δp proportional to Q with the pump off to Δp proportional to Q^2 with the pump operating. Therefore there was a tendency for the flow to resist deceleration and assist acceleration in the portion of the flow cycle when the velocity was lower than the mean flowrate under steady conditions. This imbalance would be avoided only if the pump did not alter the overall mean flowrate from that of the steady flow condition.

The shaft of the cam driving the pump ram was extended and fitted with a graduated disc which could be rotated relative to the shaft and fixed in position by a locking ring. Together with a pointer located at a fixed position on the shaft, this arrangement was calibrated relative to the ram position. A photocell trigger was

operated through a pinhole in the disc (figure 4.5) and used to trigger electronic measuring equipment, dye injection and motor-drive of a camera at any desired phase angle. The period of the cycle was measured to a resolution of better than 0.1 % by sampling the photocell trigger signal throughout the cycle at a rate of 100 Hz. The length of the cycle could then be determined from the number of samples between high trigger signals.

The period of the pulsatile flow was scaled to match that in the human internal carotid artery by the Strouhal number

$$Str = \frac{f D}{U}$$

; where f is the frequency of the pulse in hertz, D is a characteristic length, chosen in this case to be the diameter of the vessel and U is a characteristic velocity - in this case the average velocity was based on the time-averaged flowrate and diameter of the vessel.

Dynamic similarity was achieved using the Reynolds number

$$Re = \frac{D U}{\nu}$$

; where ν is the dynamic viscosity of the fluid.

Since for dynamic similarity we require that $Re_c = Re_m$, then

$$\frac{L_c U_c}{\nu_c} = \frac{L_m U_m}{\nu_m} \qquad (4.2 - 1)$$

Subscripts c and m stand for carotid and model respectively. For pulsatile similarity we require that $Str_c = Str_m$ so that

$$\frac{f_c L_c}{U_c} = \frac{f_m L_m}{U_m} \qquad (4.2 - 2)$$

combining 4.2 - 1 and 4.2 - 2

$$\frac{f_m}{f_c} = \left(\frac{L_c}{L_m}\right)^2 \left(\frac{\nu_m}{\nu_c}\right) \qquad (4.2 - 3)$$

It can be easily shown that the same result is obtained using the Wormesley parameter α (Wormesley 1957) as a scaling factor, where

$$\alpha = R\sqrt{\frac{n}{\nu}}$$

; where R is the radius of the tube and n is the frequency of pulsation. The Wormesley parameter is dimensionless and is often used to describe physiological pulsatile flow conditions.

The following values of the variables were used to scale the flow:

D_c = 8 mm (from Pedley, 1981)

D_m = 20 mm

$\nu_m = \nu_{water} = 1.058 \times 10^{-6}\ m^2\ s^{-1}$ at 18 °C

$\nu_c = 3.8 \times 10^{-6}\ m^2\ s^{-1}$ for whole blood at 37 °C

With a mean Reynolds number of 1500, this resulted in a pulsation frequency in the model of 0.05 times that of the pulse rate in vivo. The corresponding frequency in the model for a mean Reynolds number of 1000 was 0.03 times the in vivo rate. For convenience, the in vivo rate was taken to be 1.0 Hz.

4.3 Flow Visualisation:

Flow visualisation was carried out by dye injection, although some time was spent initially on H_2-bubble visualisation before that method was abandoned. It is worthwhile to comment on the reasons for discontinuing the H_2-bubble method, as the method is not inherently poor, but merely inappropriate in this study. These comments are in Appendix D.

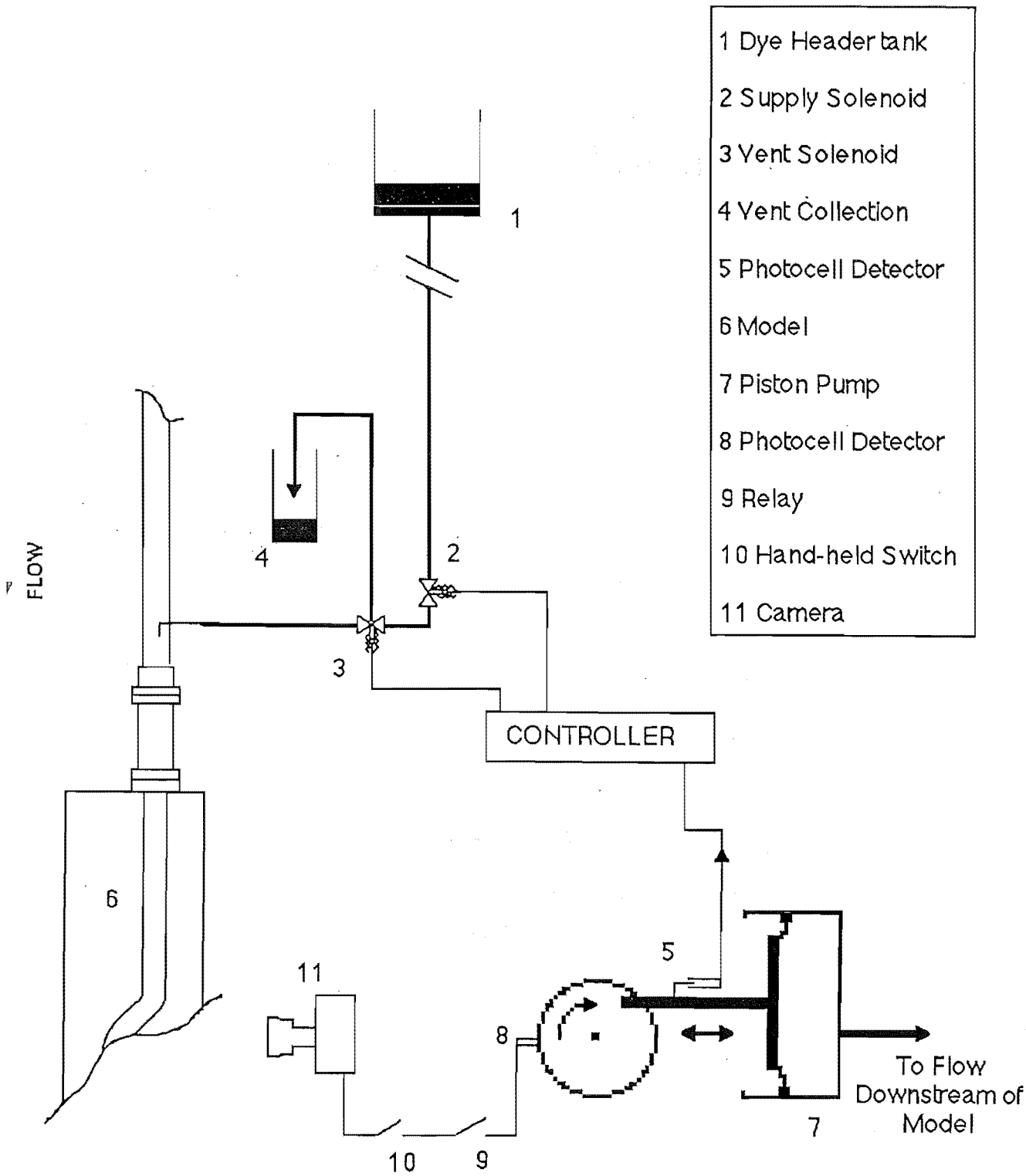

Figure 4.5
The Dye-Injection Apparatus.

4.3.1 Dye Injection Visualisation

Methylene blue dye at a concentration of approximately 3% (kg/l) was used for flow visualisation. The dye was gravity-fed, with the flowrate controlled by a clamp on rubber tubing and switched on and off by a small solenoid valve. A sharp cut-off on switching off the dye supply was obtained by using a second solenoid valve which vented to a small collection bottle at atmospheric pressure between the dye supply valve and the injection point (figure 4.5). Since the pressure at the injection point was above atmospheric pressure, opening the vent valve briefly upon closing the supply valve caused a small backflow from the injection point. This prevented the otherwise gradual trailing-off of the dye stream, thereby providing a sharp cut-off.

An advantage of a sharp dye cut-off was found during the pulsatile flow visualisation. The mean flow variation caused a disturbance in the dyestream at the injection point during low parts of the flow cycle. A photocell apparatus on the ram of the pump (in addition to the photocell mentioned in section 4.2.3) could be used to trigger a timing device to operate the supply and vent solenoid valves. With appropriate delays in the valve timing, clean pulses of dye with variable length could be introduced at any point in the flow cycle with a minimum of dyestream disturbance.

Dye was introduced to the flow via 24 gauge hypodermic tubing at least 45 mm upstream of the model endpiece (350 mm or 700 hypodermic tube diameters upstream of the first bend). The needle passed through a small hole in the wall and was sealed by a silcon-rubber septum.The needle was bent at right angles after entering the flow to provide a length aligned with the axial flow of about 25 mm before the dye injection point. The dye stream could be positioned at any point in the cross-section of the tube upstream of the model by adjusting the distance that the needle protruded into the tube and rotating the needle from side to side.

The dye patterns were photographed with black and white film, using a Nikon FE2 camera with a 55 mm lens, zoom and motor-drive. A yellow filter was used to enhance the contrast of the blue dye against the white background. In the case of pulsatile flow, the camera could be operated remotely at any point in the phase, via a relay triggered by the photocell arrangement on the DCL metering pump. A hand-held switch was connected in series to the photocell trigger so that the camera was triggered at the desired phase angle, but only when the hand-held switch was closed (figure 4.5).

The model was initially backlit through a frosted glass screen to provide a bright, diffuse light. However, this method of illumination was replaced by a flash unit triggered by the camera after it was found that convection within the model occurred due to the heat generated by continuous lighting.

A Bolex 16 mm movie camera was used to capture unsteady details of flow. A timing device was constructed by fixing a graduated disk to a small a.c. motor with a known, constant period of revolution. This was placed in the field of view, giving a measure of the time between frames once the film was developed.

4.4 Laser Doppler Anemometry:

Velocities were measured with a DISA Laser Doppler Anemometer (LDA).

The principles of Laser Doppler Anemometry are well documented (Bates (1977)) and need only a brief description here. The derivation of the equations used to calculate the fluid velocity in the measurement volume is given in Appendix A. A particularly good reference is that of Durst, Melling and Whitelaw (1976).

In differential-mode Laser Doppler Anemometry, two coherent beams of light (obtained by splitting a laser beam) are brought together to form a measurement volume at their intersection at the point in the fluid where the velocity is to be measured (figure 4.6). If the path lengths of each beam from the point of beam splitting do not differ greatly, an interference pattern will be set up at their point of intersection. The light is detected by scattering from small particles moving within the fluid. The velocity of the particles is assumed to match the local fluid velocity. The frequency of the observed interference pattern undergoes a Doppler shift because of the velocity, relative to the observer, of the particles within the measurement volume. This frequency is proportional to the velocity of the particle and, by inference, the fluid velocity within the measurement volume. A photomultiplier observes the light scattered from the measurement volume and emits an alternating current proportional to the velocity of the particle. This frequency is then determined by a frequency tracking unit and the analogue voltage output of the unit is linearly proportional to the input frequency and hence to the particle velocity.

In this study, a DISA Type 55L LDA was operated in the differential Doppler mode with forward scattering, using a Spectra-Physics model 124A 15 mW He-Ne laser with a wavelength (in air) of λ = 632.8 nm (see figure 4.6). A Bragg cell was fitted to the optical unit to enable the measurement of low velocities and the flow direction to be determined.

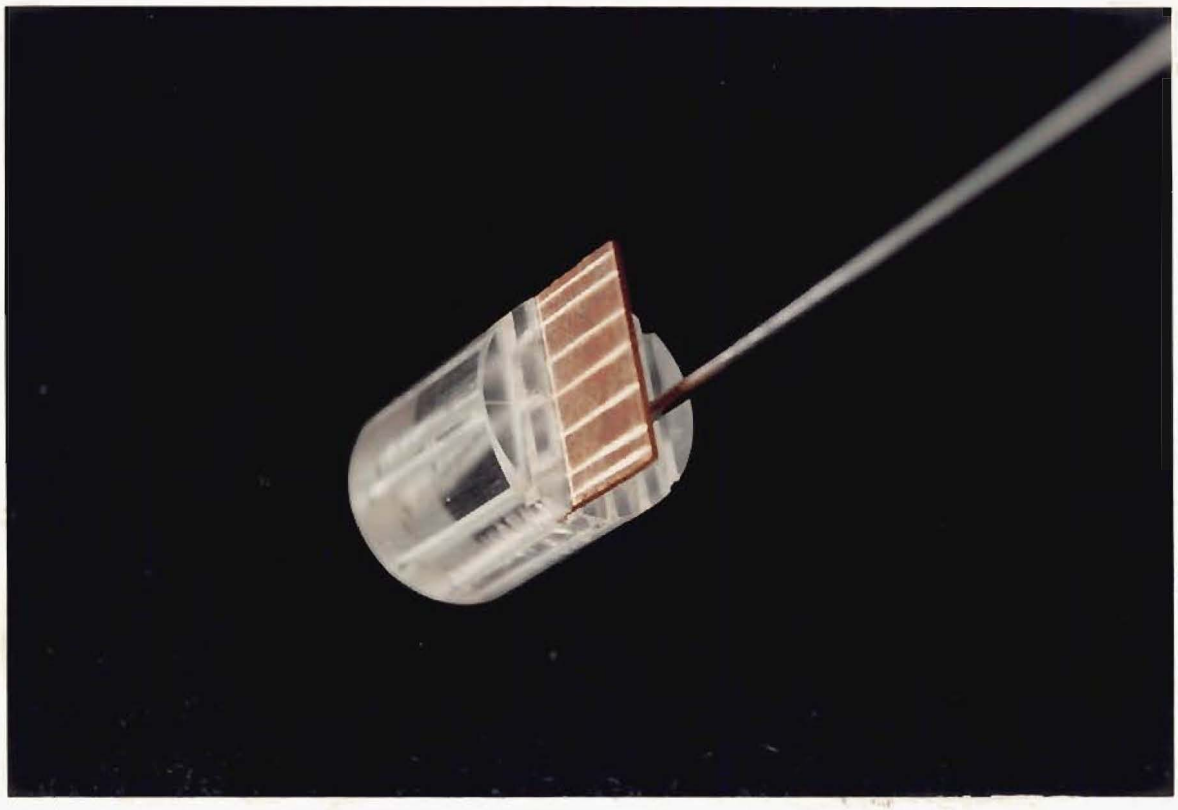

Plate 4.2
The Probe Used to Determine the LDA
Measurement Volume Position

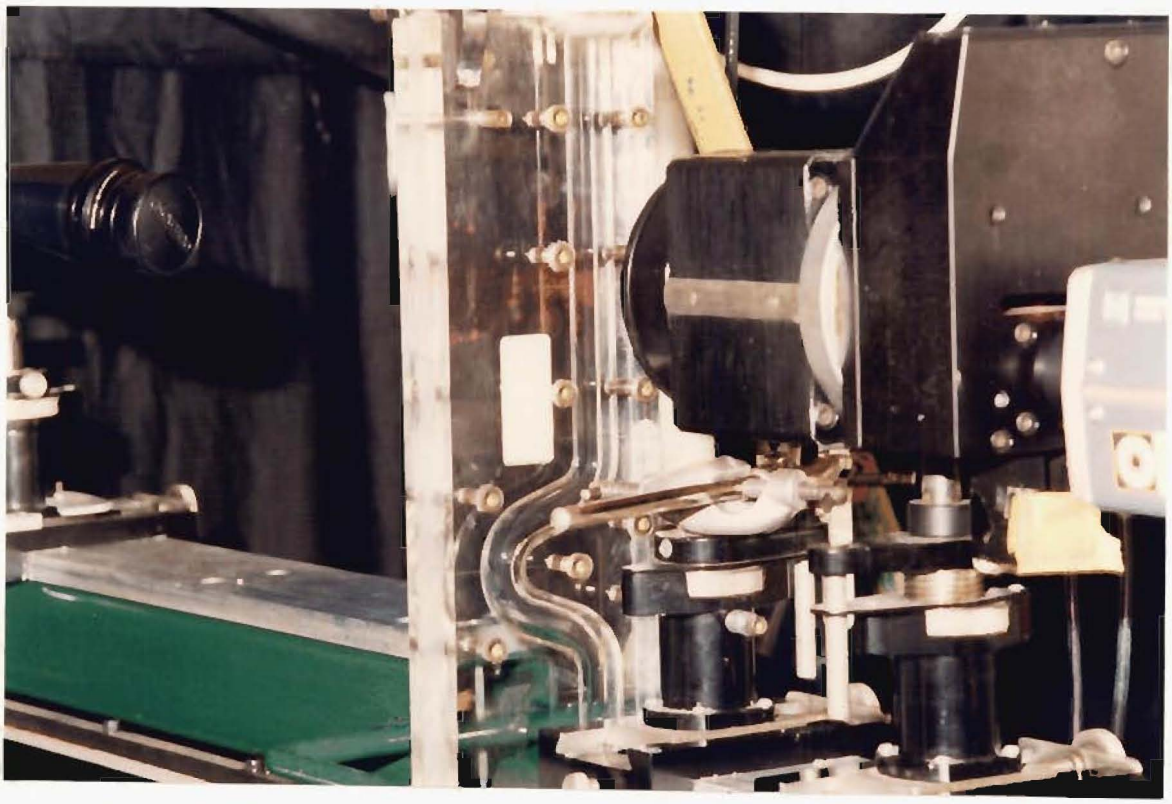

Plate 4.3
The Intersection of the LDA Laser Beams in the Model

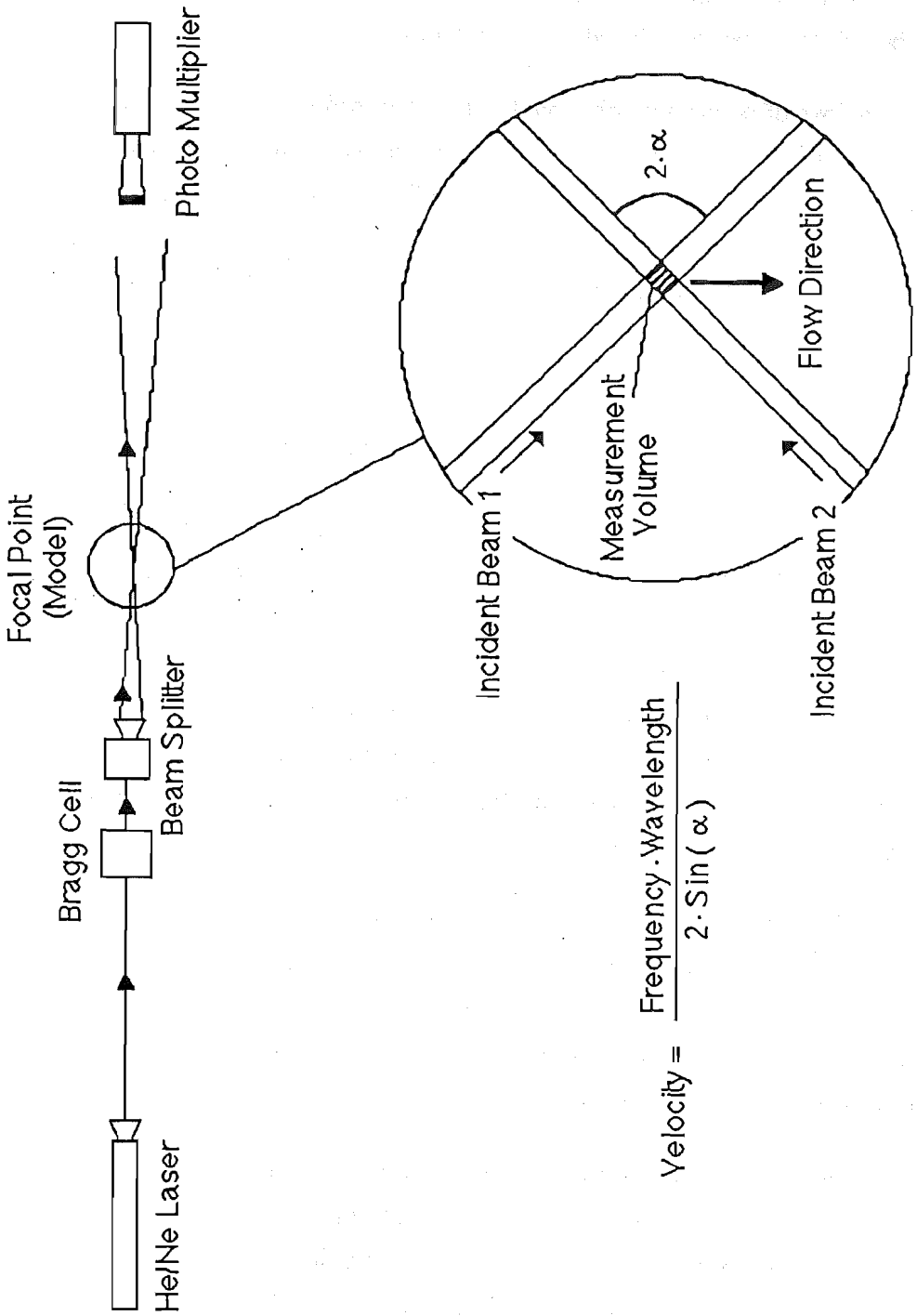

Figure 4.6

The Measurement Volume, Formed by the Intersection of the Two Laser Beams of a Laser Doppler Anemometer.

An optical bench on which the laser, optical unit (including Bragg cell) and photomultiplier were mounted was screwed to a traversing table manufactured by the Mechanical Engineering Department, University of Canterbury (Seeto, 1987) which was modified in this department to provide traversing in three-directions. The position of the beams could be reproduced to within half a beam diameter or 0.3 mm.

A loss of power was observed with the introduction of the Bragg cell and so the water was seeded with milk to improve the strength of the scattered light as reported by Durst et al (1976). Continuous seeding was achieved by adding pre-diluted milk to the header tank feed stream with a DCL metering pump. The water was not recirculated so that problems with milk fouling were kept to a minimum and the model was cleaned regularly.

The position of beam intersection at each measurement point in the model had to be determined. A cylindrical plug was fashioned from perspex to fit snugly into the proximal stem of the model. Slots were milled across the top face of the plug, normal to the plane of beam intersection and rigid wafers inserted with known front-face position (Plate 4.2). Vertical lines were scored at known locations on the front-face of each wafer. By means of position indicators on the traversing table, a map of the measurement volume was devised, related to a datum at the front face of the model. The map of measurement positions was valid in all straight sections of the tube as long as the front face of the model was kept normal to the plane of beam intersection in both the vertical and horizontal directions. The beam intersection position was referred to the datum after each vertical traverse of the laser.

Measurements were restricted to straight sections of the tube and for axial velocity measurements the beams converged in a plane parallel to the axis of the tube (figure 4.7 and Plate 4.3). Therefore, assuming that the both inner and outer surfaces of the model were free of distortion, the beam intersection angle remained constant for both axial and transverse movement.

The beam intersection angle in air was found by measuring the beam separation at various distances from the optical unit. At a distance of 1.0 m, with an accuracy of ± 1.0 mm, the beam intersection angle, θ, could be estimated to an accuracy of about 0.5%. It can be easily shown that the beam intersection in water is not dependent on the refractive index of the perspex, provided that the interfaces between the air, perspex and water are planar and parallel. This condition is met for axial velocity measurements as the beams intersect in a plane which is parallel to the tube's axis as sketched in figure 4.7.

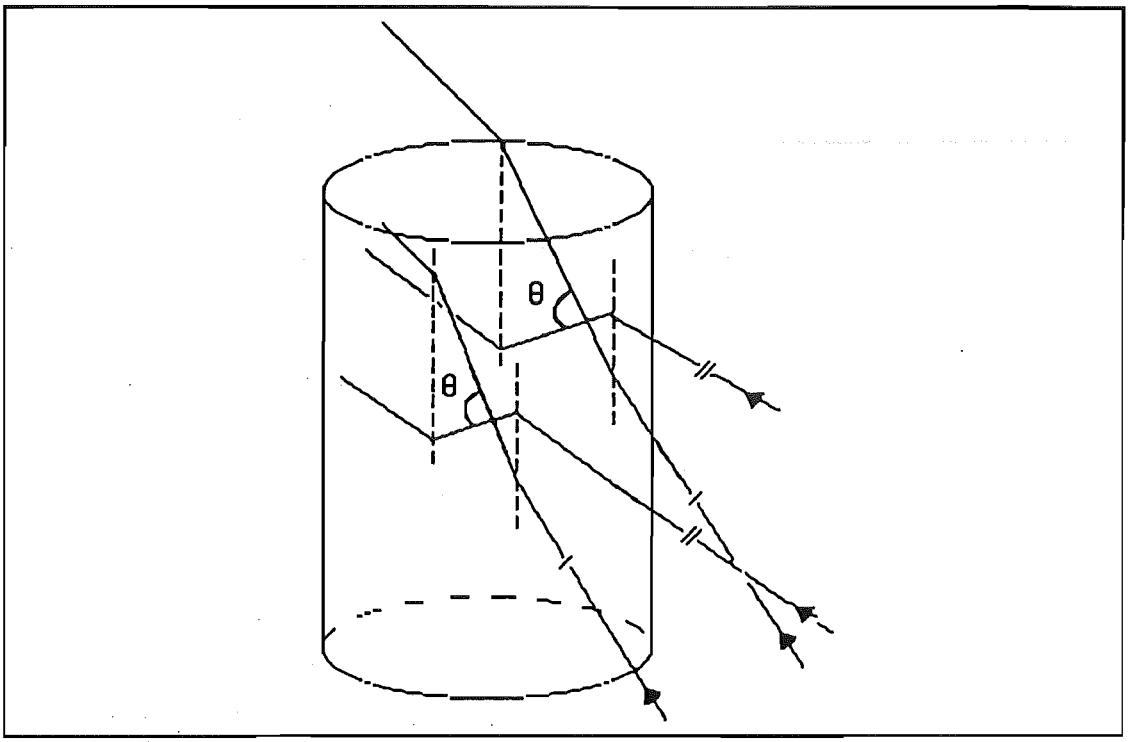

Figure 4.7
The Beam Intersection Angle is Independent of the
Measurement Volume Position For Axial Velocity Measurements.

Referring to figure 4.8, by Snell's law of refraction:

$$\frac{\sin \alpha_a}{\sin \alpha_p} = \frac{n_p}{n_a}$$

; where α is the angle between the incident light beam and the normal to the interface between mediums of refractive index n. The subscripts a, p and w refer to air, perspex and water respectively. Since

$$\sin \alpha_p = \frac{n_w}{n_p} . \sin \alpha_w$$

then

$$\frac{\sin \alpha_a}{\sin \alpha_w} = \frac{n_w}{n_a}$$

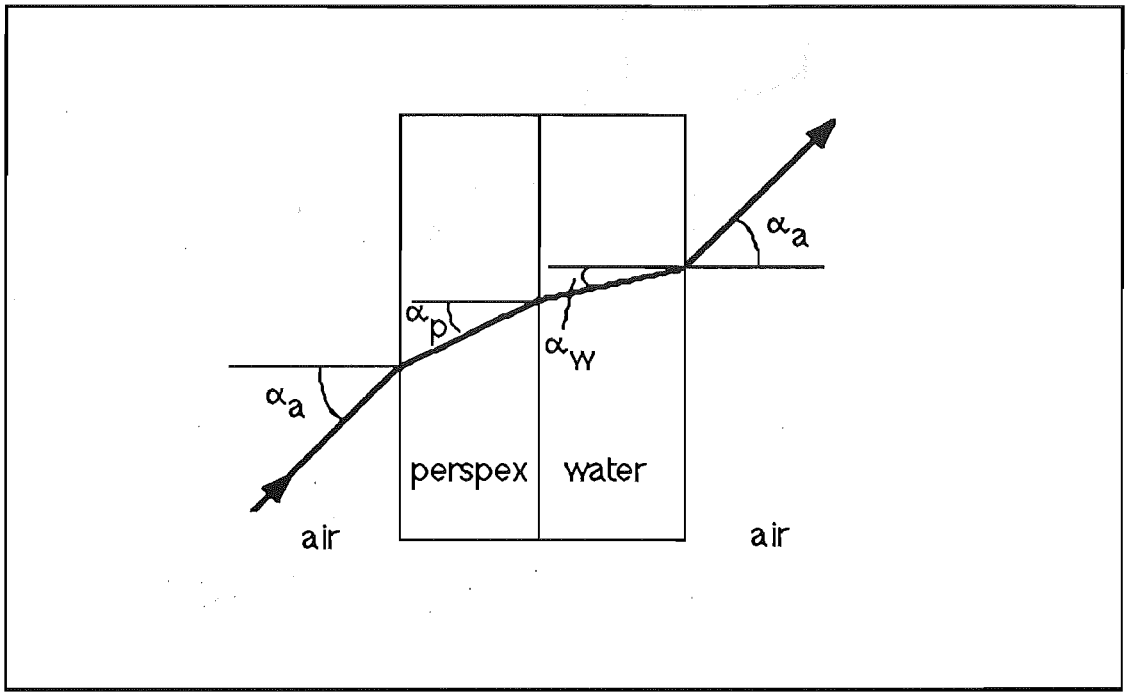

FIGURE 4.8

Refraction of light passing through three media with different refractive indices.

The velocity of the particle moving through the measurement volume is related to the Doppler frequency emitted by the photo-multiplier by:

$$V = \frac{f_D \cdot \lambda}{2\sin\left(\theta/2\right)}$$

; where V is the velocity, f_D is the Doppler frequency, λ is the wavelength of the incident light and θ is the beam intersection angle (figure 4.6). The derivation of the formula is given in Appendix A. $\lambda = 474.7 \times 10^{-9}$ nm. θ was measured to be 22.10° in air and calculated to be 16.68° in water with a refractive index of 1.330. The beam intersection angle varied with each measurement position during radial velocity

measurements and the calculation of this is given in Appendix B.

The frequency tracking unit was internally calibrated, and was checked by measuring the output voltages with known input frequencies (Appendix K). The output voltage was found to be linearly proportional to the input frequency in all frequency range settings. The calibration graphs are included in Appendix K. For a frequency range of 500 kHz:

$$f_D = \frac{\text{Voltage} - 0.1354}{0.0212} \text{ kHz}$$

The frequency imposed by the Bragg cell was measured to be 75.6887 kHz. This corresponded to a null velocity and was subtracted from the measured output hence the subtractive constant in the above expression was cancelled out in the computation of velocity from the output voltage of the frequency tracking unit.

4.5 Data Collection:

The signal from the photomultiplier was fed to both a DISA type 55L20 frequency tracking unit and to one input of a Fairchild dual trace oscilloscope. The oscilloscope provided a qualitative measure of the quality of the Doppler signal entering the frequency tracking unit. A Doppler burst, generated when the light scattered by a particle moving through the measuring volume is detected by the photo-multiplier, has the form shown in figure 4.9. As long as bursts of this shape were seen frequently on the oscilloscope screen, the signal entering the frequency tracker was deemed to be acceptable. When the bursts became infrequent or of low amplitude, the signal was deemed unacceptable.

Although this appears to be a rather subjective decision, usually this condition was also indicated by a high drop-out detection rate and a low signal level in the frequency tracking unit. The frequency tracker output was fed five ways simultaneously to the second input of the dual trace oscilloscope, through a filter unit to a DISA type 55D31 digital voltmeter, an DISA type 55D35 RMS voltmeter, a Nicolet model 444 Mini-Ubiquitous spectrum analyser and to an analogue to digital (A/D) convertor. A Hewlet - Packard analogue x-y plotter was connected to the spectrum analyser.

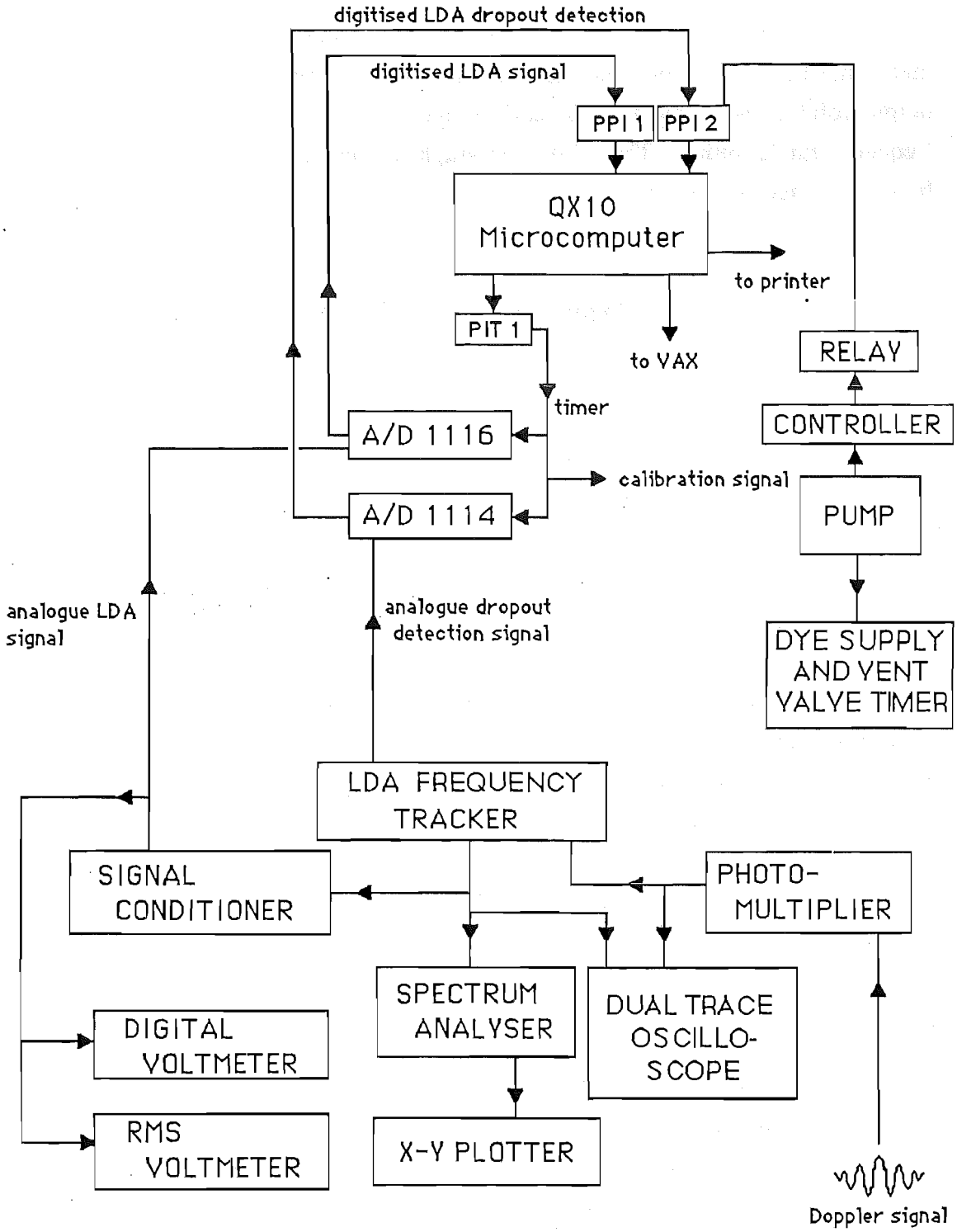

Figure 4.9

The Data Collecting Apparatus for Laser Doppler Anemometry.

For steady flowrates, the digital voltmeter was adequate for measuring the voltage output of the frequency tracker, since the velocities at most measurement positions were constant. Where fluctuating velocities occurred, a Fast Fourier Transform (FFT) was computed by the spectrum analyser. The time-constant of the voltmeter was adjusted until a steady value was obtained at all positions, thereby providing a measure of the average velocity at each point. Data was recorded manually and was input to data files on the departmental Digital Vax 11/730 computer for later computation (see Appendix H for programme listings).

A Serial Parallel Interface (SPI) unit was available to take voltage readings from the the LDA at any desired sample rate up to 300 Hz. This was used to check the time-variance of the LDA signal at a fixed measurement position and the sensitivity of the LDA signal to the position of the pinhole in the receiving optics of the photo-multiplier with respect to the observed measurement volume. These two checks were made because non-reproducible flow profiles were measured upstream of the proximal bend where no flow disturbances were observed or expected.

A check on the LDA output at a fixed measurement position and photo-multiplier observation position showed that the signal did not vary with time but that the output was highly dependent on the position of the photo-multiplier observation pinhole with respect to the apparent beam intersection position. Differences of up to 30% in the LDA output were obtained with successive re-positioning of the photo-multiplier pinhole on a fixed measurement volume position (without moving the laser or optics) and flowrate. Several methods of consistently positioning the observation pinhole on a fixed measurement volume were tried, but with little improvement in reproducibility. The solution to the problem was to shorten the focal length of the beam focusing lens, thereby increasing the beam intersection angle (in air) from 14.06° to 22.21°. This provided a more clearly-defined measurement volume position, allowing a more consistent pinhole positioning. After this change, successive measurements at a fixed measurement position and flowrate were repeatable to within 2%.

A limitation of the SPI unit was that the maximum sampling rate was 300 Hz, limiting the maximum frequency available for Fourier analysis to 150 Hz (by the Nquist sampling theory). More seriously, the SPI required interaction with the VAX between samples and the demand on the VAX by other users resulted in irregular sampling intervals, rendering the data unsuitable for Fourier analysis.

An A/D converter was used to digitise the output of the frequency tracker at a sampling frequency of 20 kHz. The digital output of the A/D converter was linearly

related to the analogue voltage input from the frequency tracker by:

$$\text{Voltage} = 0.0096 \,.\, [\text{A/D}] - 0.0177 \text{ V}$$

An Epsom QX10 computer was programmed in Turbo-Pascal and Z80 machine code to take samples of the digitised LDA output signal from the A/D converter via a Peripheral Parallel Interface (PPI) board. The Turbo-Pascal routines were written by the author while the machine code, used in the sampling loop to provide the fastest available sampling rate, was kindly written by Pat Jannsen (a fellow Ph.D. student). Alterations to the machine code were later made by the author to allow the sampling of an additional input to the PPI board from a second A/D convertor. The total number of samples could be varied, as could the sample rate, which was controlled by a divided-down 0.5 MHz nominal clock chip. The actual frequency of the Peripheral Interval Timer (PIT) chip was measured using a Hewlet - Packard frequency counter and was found to be 498603 Hz. Data was stored on floppy disc for subsequent uploading to the VAX.

The potential data set from the LDA during pulsatile flow experiments was too large for practical data storage. Therefore some pre-storage processing of the raw data was required. The photocell on the pump was used to trigger LDA output sampling at a set phase angle of the flow cycle. A timing diagram of the sampling is shown in figure 4.10.

The use of a rubber pulley belt connecting the Kopp variator to the pump driving motor introduced the possibility of slip occurring, which would lengthen the cycle. The trigger signal was also sampled and used to detect the length of each cycle. Data sets were discarded if the length of a cycle varied by more than 0.5% from the set cycle length.

The sampling programme (NEWAVE.PAS, Appendix H) required at least two complete cycles of acceptable length or the measurement was repeated. The sampling frequency was 100 Hz, giving 2000 and 3000 samples per cycle for mean Reynolds numbers of 1500 and 1000 respectively. The sampling programme detected the beginning and end of each cycle from the trigger signal and was then able to compute an overall average velocity and standard deviation and 12 equispaced, phase-dependent average velocities (and their respective standard deviations) at each measurement position.

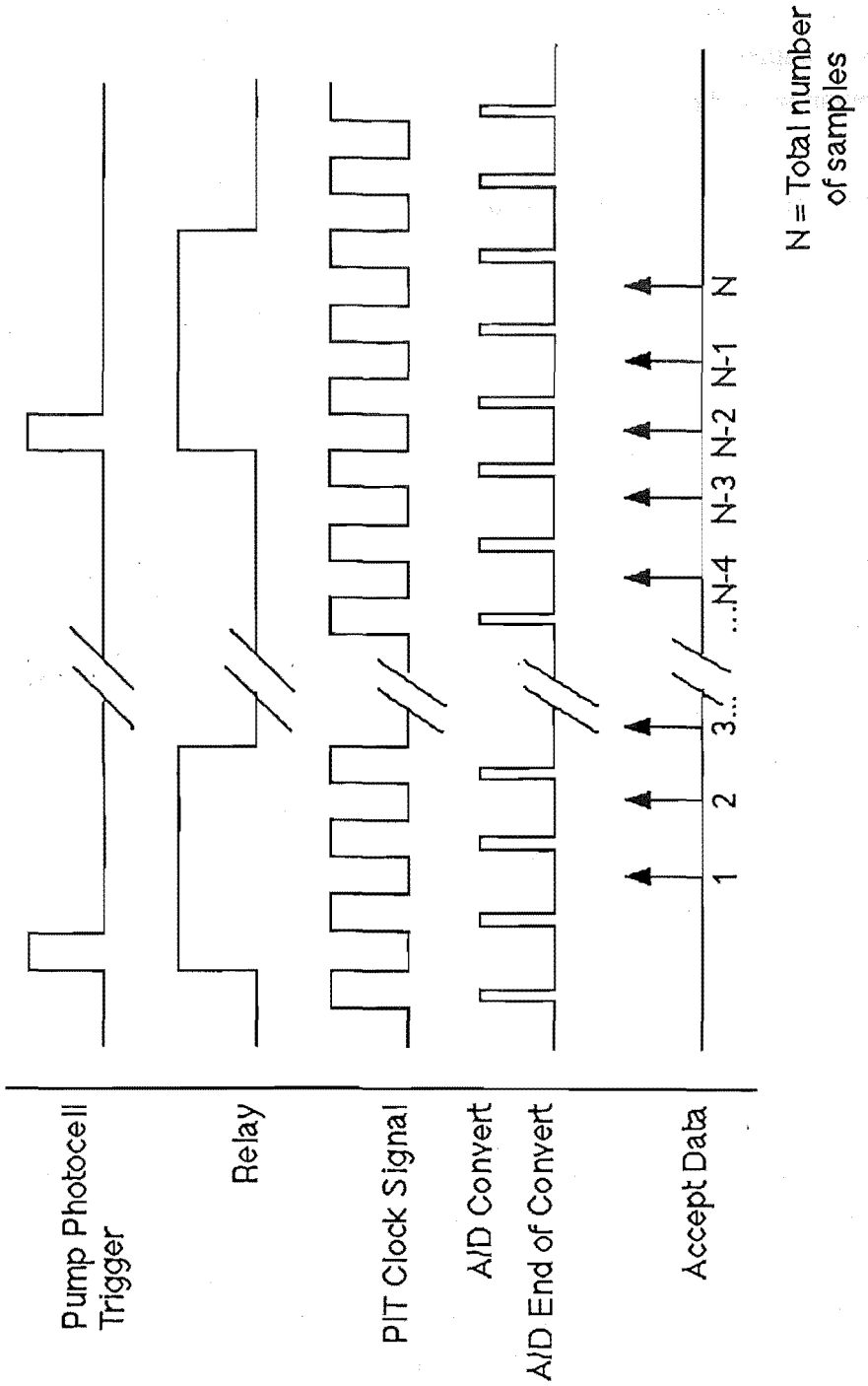

Figure 4.10
Timing Diagram for the Data Collection.

A value from the RMS voltmeter was entered manually at the end of sampling. The computed values were then printed out and stored on floppy disc.

A second program (FFT.PAS, Appendix H) could be run to store 4096 consecutive samples of the digitised LDA output at any frequency up to 2 kHz for later FFT computation on the VAX.

4.6 Wall Pressure Measurements:

A Brüel & Kjær type 8103 hydrophone was used to measure the pressure fluctuations at the wall of the model at the positions shown in figure 4.13. A Brüel & Kjær type 5140 charge-conditioning pre-amplifier was used to amplify the output signal of the hydrophone. The ampilified signal was then fed into the Nicolet model 444 spectrum analyser.

The hydrophone was sealed into a water-tight chamber (Plate 4.4) and joined to the pressure ports as shown in figure 4.14 and Plate 4.5. The pressure port was 0.4 mm in diameter, allowing the measurement of pressure fluctuations with frequencies of up to about 250 Hz (Clark, 1977). The hydrophone probe and port essentially formed a Helmholtz resonator, with a calculated resonant frequency of about 2.7 kHz when water-filled (Appendix F). This frequency was high enough so that resonance did not affect the pressure fluctuations below 250 Hz. The calibration of the the probe was carried out in air[1] and was limited to a maximum incident frequency of about 200 Hz, due to the Helmholtz resonant frequency being lowered by the greater compliance of air over water (Appendix F).

Only one port was in use at a time. To minimise flow disturbances from the ports whilst they were not in use, the probe access holes were plugged (figure 4.15). This was achieved very easily and efficiently in each case by inserting a length of flexible PVC tubing into the probe access hole and pushing a length of brass welding rod into the tubing. The welding rod both sealed the port against water leakage by tightening the fit of the PVC tubing and removed the Helmholtz resonator cavity from the port. When this was done only the 0.4 mm diameter by 1.0 mm long port was open to the flow at the wall. A small amount of silicon grease allowed the plugs to be fitted and removed easily, without disrupting the flow between experiments.

---

[1] The manufacturers (Brüel & Kjær (1978)) state that the sensitivity of the hydrophone is the same in air as in water up to a frequency of 4000 Hz.

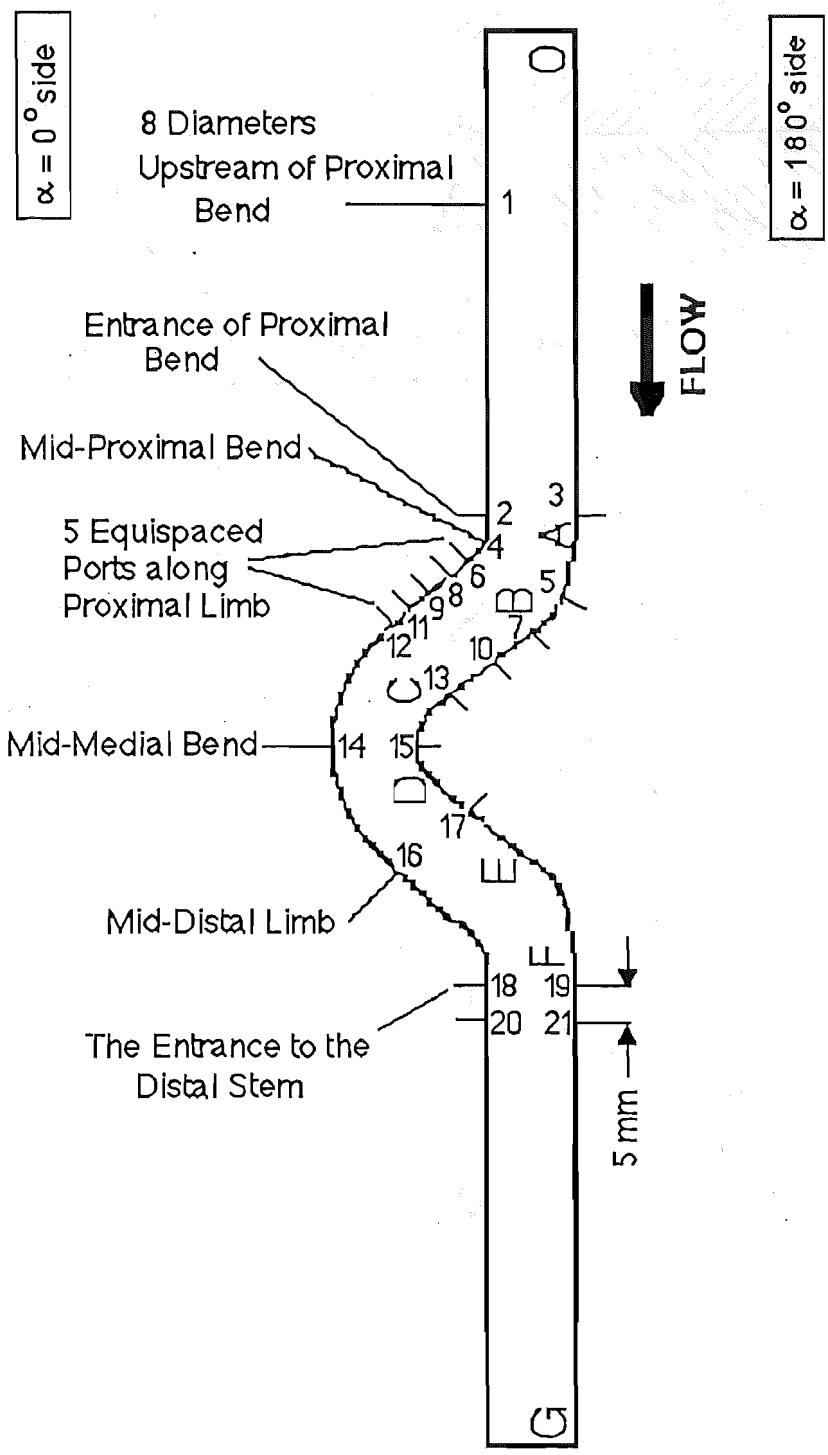

Figure 4.11
Pressure Port Locations for
Wall Pressure Fluctuation Measurements.

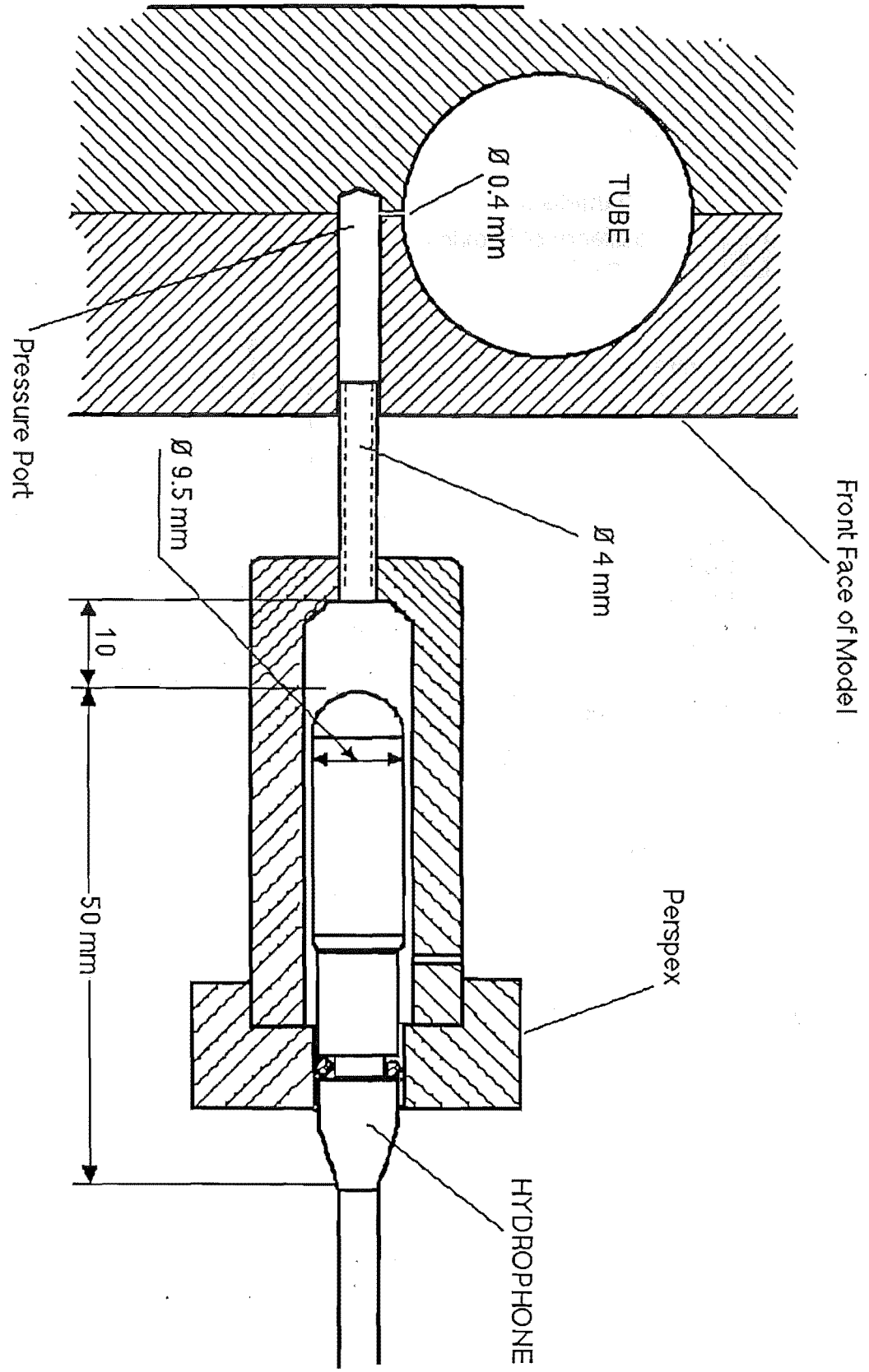

Figure 4.12
The Hydrophone Probe and Port Dimensions.

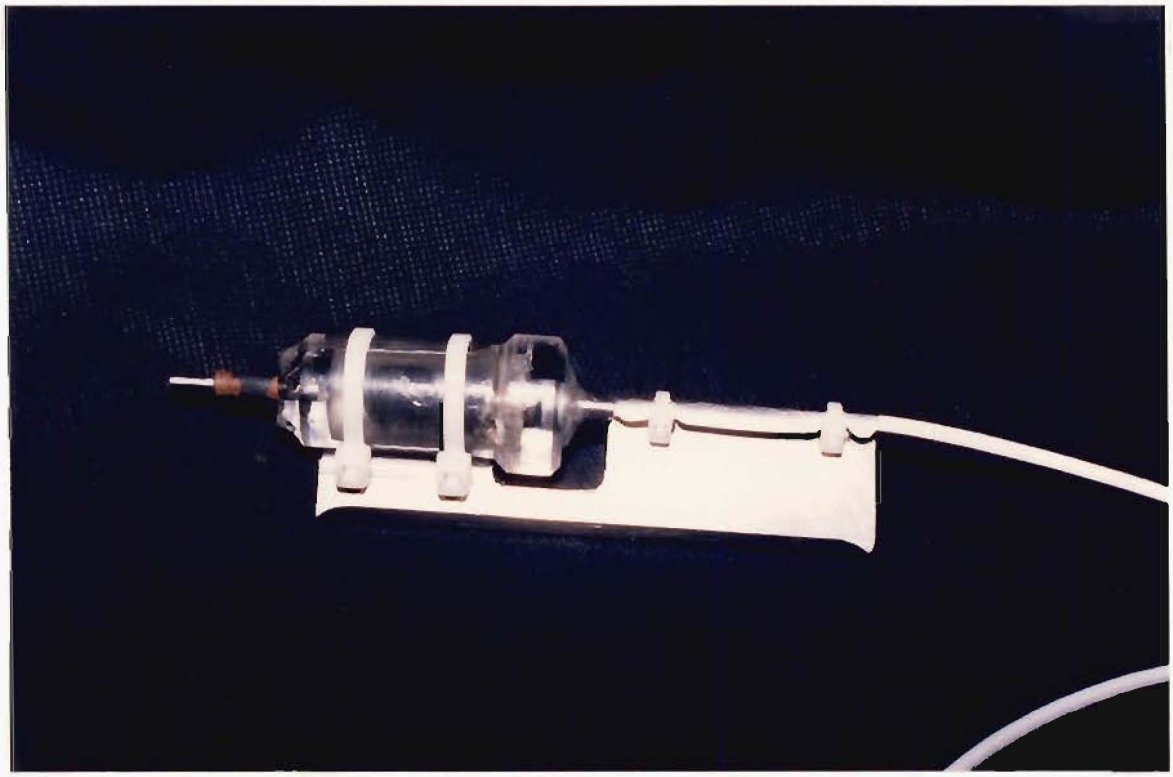

Plate 4.4
The Hydrophone Probe

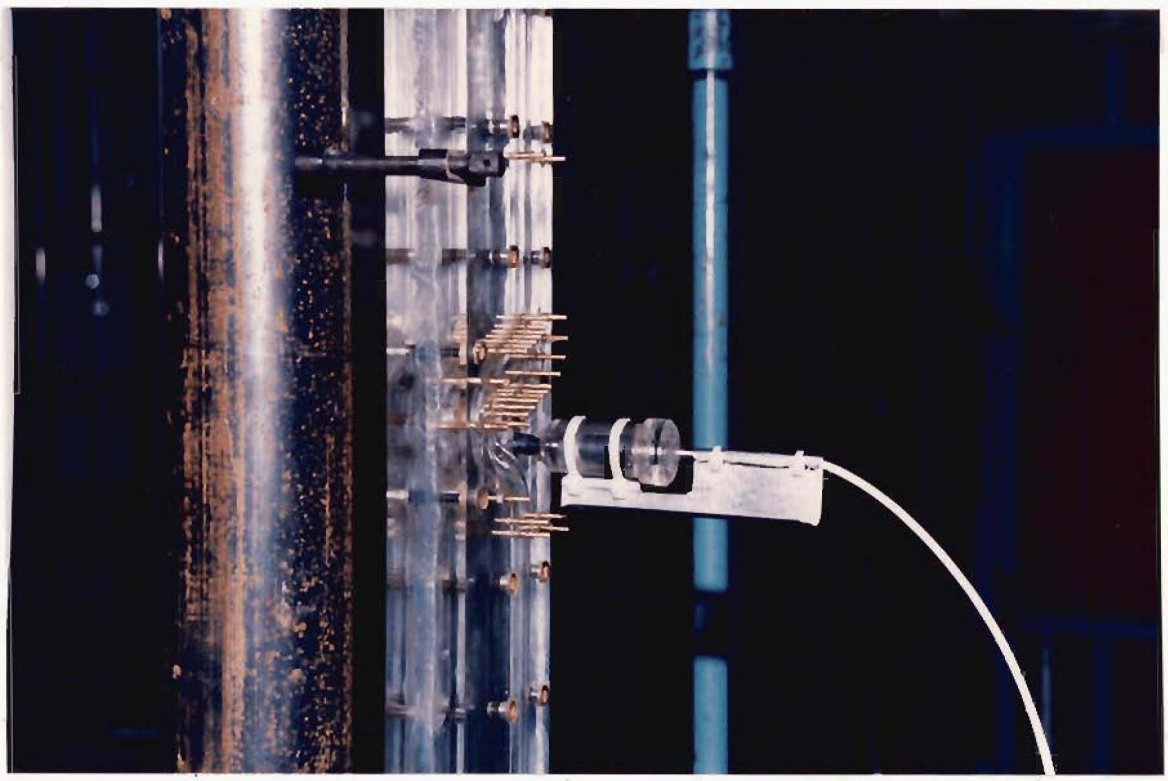

Plate 4.5
The Hydrophone Probe in Position

It was found, during initial experiments, that the probe was extremely sensitive to vibrations of the flow apparatus itself. The hydrophone output was swamped by signals caused by tapping the side of any part of the flow structure and even by a person moving on the floor above or traffic on the road outside the building. The manner in which these disturbances caused a large hydrophone output signal was not obvious but it was thought that pressure fluctuations caused by vibration were transported to the probe from the entrance and exit areas of the flow system. Several modifications were made to the flow system to minimise flow disturbances at the entrance and exit areas and to minimise vibrations of the apparatus (figure 4.14).

The entrance length, model and outlet were removed from the original support frame and securely mounted along a 6 inch mild steel tube, which was itself supported by rubber engine mounts. A 60 kg weight was suspended from the tube in order to increase the inertia of the structure and lower it's natural frequency of vibration. The flow intake was connected to the header tank by a piece of flexible tubing, packed with poly-ethylene beads and the header tank was supported separately from the rest of the flow system. The flexible connection was fitted in order to reduce the effect of structural vibration on the flow system and the poly-ethylene bead packing was used to damp out the pressure fluctuations from surface waves in the header tank.

All valves and cocks were removed from the system and the flowrate through the model was controlled at the flow outlet by flexible tubing packed with poly-ethylene beads. Four packed tubes with different lengths provided the four flowrates studied. The exit length was packed with straws (with the diameter of the straws equal to about one-fifth of the tube diameter) to prevent the upstream propogation of pressure fluctuations from the flow outlet. The end of the flowrate-controlling tubes at the outlet were placed in a constant-head tank to further reduce exit disturbances.

In this way, the signal from the hydrophone probe caused by structural vibrations was lowered 100-fold. However, although the output signal was now of the correct order of magnitude expected from flow-induced pressure fluctuations, it was not immediately obvious whether the reduction of external disturbances was sufficient to allow flow-related pressure fluctuations to be measured. Changes in the frequency spectra were observed with different flowrates, but it was unclear whether these were caused by flow-dependent pressure fluctuations at the wall or flow related overall structural vibrations.

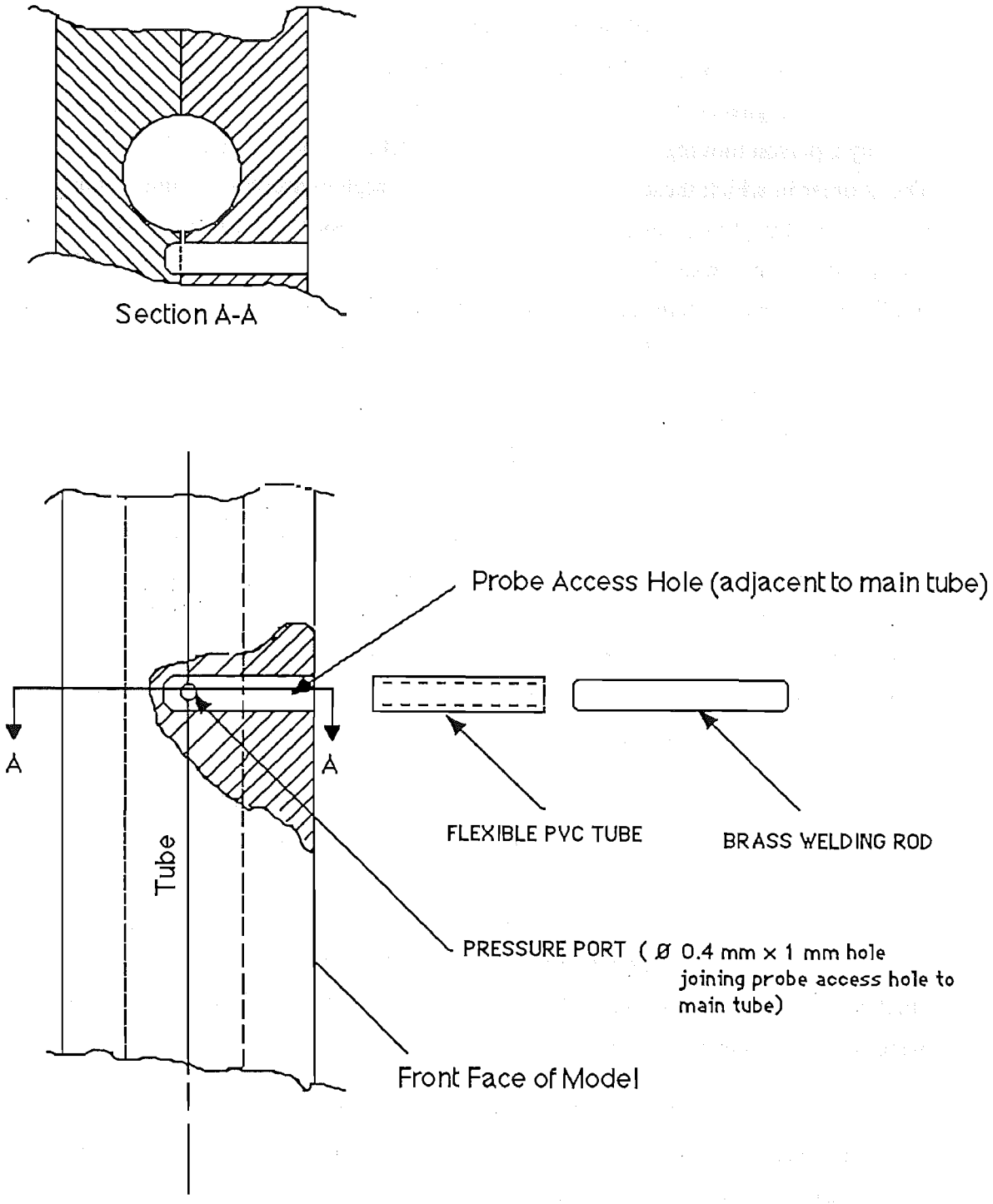

Figure 4.13
The Sealing Method for Ports Not in Use.

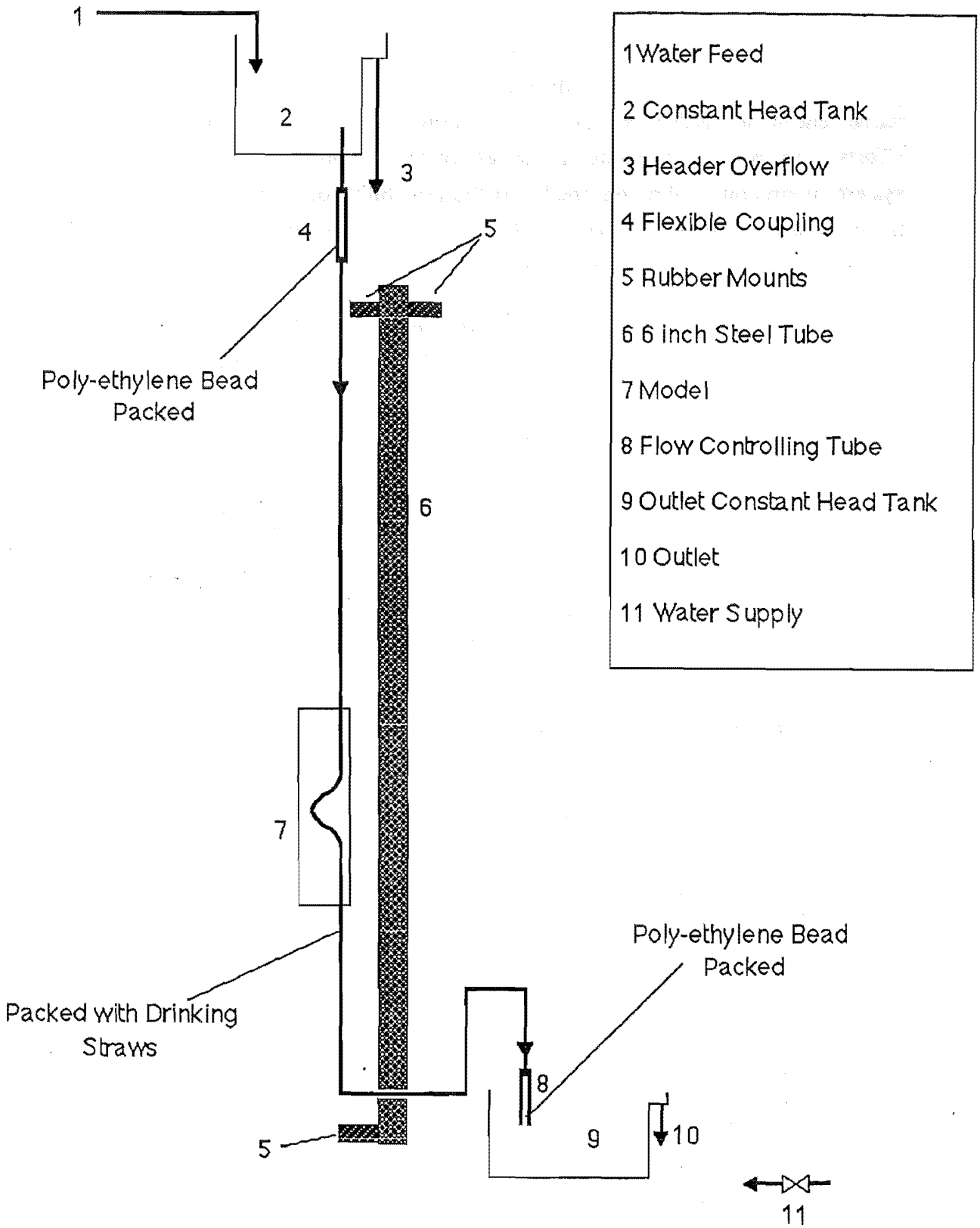

Figure 4.14
The Flow System for Wall Pressure Fluctuation Experiments.

No further improvement could be gained without a major re-design of the flow system and the measuring device. Time did not allow further experimental refinement and it was decided that limited experiments should proceed, with no further efforts to improve the apparatus regardless of the outcome. The sensitivity of the system to structural vibration precluded the possibility of studying wall pressure fluctuations under pulsatile flow conditions because of the vibrations that would be induced by the pump used to create pulsatile flow.

Tests on the effect of the incident frequency on the sensitivity of the probe (Appendix E) showed a 3.43 dB fall off in sensitivity between 24.5 Hz and 196.25 Hz relative to a reference microphone with a flat response curve. The highest frequency examined experimentally was 200 Hz. Repetitions at 175 Hz showed a repeatability of better than 9%, and other points repeated at different frequencies were within this value as well (Appendix E).

The probe exhibited a weak dependance on the incident sound intensity level. At 175 Hz, a decrease in sensitivity of less than 1 dB between a SPL of 1.5 Pa and 12 Pa relative to the reference microphone was observed.

4.7 Experimental Procedures:

4.7.1 Dye Visualisation:

4.7.1.1 Steady Flow:

1. The feed water was switched on and water allowed to flow through the model until the temperature of the water reached a steadystate. This normally took about half an hour.
2. The system was purged of any air bubbles by backflushing from the lowest point in the system.
3. A flowrate was set by the downstream cock and measured by the rotameter.
4. The flowrate and water temperature were recorded.
5. The dye flow was switched on, the dye flowrate adjusted to give a steady streamline and the needle position adjusted to give the desired dyestream position.

6. Photos were taken of the appropriate dye patterns.

7. The rotameter reading and water temperature were checked.

4.7.1.2 Pulsatile Flow:

1. As described above, the feedwater was allowed to reach a steady-state temperature and the system was flushed of air bubbles.

2. The pump was switched on and the period of oscillation set with the programme NEWAVE.PAS as outlined in the LDA procedure below. The pump was allowed to run for at least three cycles before measurements were taken.

3. Flowrate was set by LDA, as outlined below in the LDA procedure, using the centreline velocity 8 diameters upstream of the proximal bend as the set position. The sampling programme was run to measure the mean velocity and amplitude of fluctuation. The pulsatile flow conditions were set to be the same as those studied in the LDA experimental work for a mean Reynolds number of 1500.

4. Two sets of photographs were taken. The first set comprised taking photos at a constant phase angle during two consecutive flow cycles. The photocell pinhole on the pump was positioned at the desired phase angle and photos were taken at the set phase angle by closing the hand-held remote camera trigger. The phase angle was changed and the procedure repeated.

5. The second set of photographs were obtained by using a slotted disk in conjunction with the photocell trigger. The slots were located at 30° phase intervals. Again, the hand-held switch was closed and the camera operated at each of the phase angles set by the photocell trigger and slotted disk. This was repeated for two consecutive cycles.

7. The Bolex movie camera was fully wound and focused on the dyestream.

8. The timing device was switched on and lit from the front by a small spotlight.

9. The backlighting was switched on and the filming carried out. Backlighting time was kept to a minimum to prevent heating of the model. A few minutes were allowed between shots to allow heat to dissipate.

4.7.2 Laser Doppler Anemometry:

4.7.2.1 Steady Flow:

1. All equipment was turned on and left for at least one hour to reach a steady operating temperature.
2. The Bragg cells were set to a frequency of 75 kHz and the optical unit adjusted to give the maximum diffraction.
3. The undiffracted parts of the beam were blocked off with a piece of cardboard to prevent confusion of the beams in the model.
4. The beam intersection positions were referred to a datum at the front face of the model and then positioned at the desired measurement position in the model.
5. The milk metering pump was switched on and time allowed for the scattered light intensity to maximise.
6. The photo-multiplier pinhole was focused on the apparent measurement volume and the shutter opened.
7. The supply current to the photo-multiplier was increased gradually until a sufficiently high input signal was indicated.
8. The tracking frequency of the frequency tracking unit was adjusted manually until the maximum signal amplitude and the minimum signal dropout were observed.
9. The frequency tracking unit was switched from manual to automatic mode, after which it tracked the incoming Doppler frequency.
10. After setting the flowrate, the rotameter and water temperature readings were recorded manually.
12. The frequency tracker output was read from the DISA digital voltmeter and recorded manually.
13. The system was flushed with clean water and an anti-microbial solution for half an hour at the end of each day's experiments to prevent fouling with milk deposits.
14. The inner and outer surfaces of the model were cleanedwith soap and a lint-free cloth regularly to ensure a clear optical path for the laser beams.

4.7.2.2 Pulsatile Flow:

1. All procedures were the same as those above for steady flow conditions, except for the setting of the flow conditions and the data collection.

2. The pump was switched on and the period of the cycle set by the Kopp variator. The period was measured by stopwatch and adjustments made to the Kopp variator until the period was close to the desired period. Finally, the period was measured by the number of samples taken at a sample rate of 100 Hz between consecutive photocell trigger "high" signals.

3. The LDA as positioned to measure the axial velocity on the tube's centreline, 8 diameters upstream of the proximal bend.

4. The sampling programme, NEWAVE.PAS was used to find the mean velocity and amplitude of fluctuation. The cocks upstream and downstream of the pump were adjusted and the measurement repeated until the desired flow conditions were met by trial and error. The shape of the velocity variation with time was monitored on the spectrum analyser and kept as close as possible to a sinusoid.

5. The pump was allowed to run for at least three consecutive cycles before measurements were taken by the QX10 computer with NEWAVE.PAS. Measurements were triggered at a constant phase angle by the photocell on the pump.

6. The sampling programme rejected the measurements if the period of more than one of the three cycles measured varied by more than 0.5% of the set period. If this occurred, the measurements were repeated. The signal dropout rate and the spectrum analyser velocity traces were monitored continuously. If the LDA appeared to lose track, the measurement run was aborted and the programme re-run.

7. An rms voltage reading from the DISA RMS Voltmeter was entered to the computer manually at the end of each measurement run.

8. The programme FFT.PAS allowed the storage of 8000 consecutive velocity samples.

4.7.3 Wall Pressure Fluctuations:

1. All equipment was switched on for at least one hour before measurements

were made.

2. The feed water was allowed to reach a steady temperature.

3. The flowrate was set by fitting one of four different lengths of poly-ethylene bead-packed tubes to the flow outlet.

4. Flowrate was measured several times during pressure measurements, by weighing a sample of outlet water collected over a known time. The water temperature and flowrate were recorded manually.

5. The hydrophone probe was inserted into the first measurement port, 8 diameters upstream of the proximal bend. A Fast Fourier Transform (FFT) was averaged from 64 x 1024 samples using the Nicolet spectrum analyser. The FFT was stored.

6. The probe was inserted into each port in turn and the FFT of the hydrophone output computed from an average of 64 x 1024 samples. The resultant FFT was compared to the stored upstream FFT by both subtraction and by division.

7. The two comparative spectral traces were plotted on the Hewlet-Packard x-y plotter and the frequency and amplitude of the significant peaks recorded manually (the output of the spectrum analyser did not include this information).

8. The pressure fluctuation measurements were carried out at night to ensure the minimum disturbance by vibration of the flow structure.

9. Frequent checks were made on the upstream FFT to ensure that no changes had occurred during measurements. If changes had occurred, measurements were repeated.

Chapter 5

Results

5.1 Introduction:

Flow in the model was studied by dye visualisation and Laser Doppler Anemometry (LDA) under both steady and pulsatile flow conditions. In addition, a hydrophone probe was used to measure the pressure fluctuations along the walls of the model under steady flow conditions only. Experimental methods and apparatus were described in Chapter 4. Results of the dye visualisation experiments are presented in section 5.2. Descriptions of the observed flow phenomena at various Reynolds numbers are given and illustrated with black and white photographs and diagrams.

Axial velocity LDA results are presented mainly in the form of isovel contour plots in sections 5.3 and 5.4. Some transverse velocity measurements are also presented. In section 5.3 steady flow results are given for axial velocities measured over cross-sections of the flow at a Reynolds number of 1500. The object of these measurements was to identify the type of flow predominant in various parts of the model.

Results of pulsatile flow measurements are given in section 5.4. The object of the pulsatile flow measurements was to pinpoint the positions of flow disturbances with respect to the walls of the model. Isovel contours of axial velocities averaged over several complete flow cycles and of time-dependent velocities are presented for LDA measurements near the walls of the tube. The contours are in planar slices, normal to the model's plane of symmetry and aligned parallel to the axis of the tube. Three such isovel contour plots were also made for steady flow conditions at one site in the model, allowing a comparison of steady flow and pulsatile flow phenomena at the same site.

In section 5.5, results of wall pressure fluctuation measurements are given for four steady flowrates in the form of frequency spectra, calculated by the Fast Fourier Transform (FFT). The spectrum of the fluctuations measured at a point upstream of the

first bend in the model is given for each flowrate. The spectra at all other positions were divided by the upstream spectra at the same flowrate and are therefore presented relative to the corresponding upstream spectrum.

5.2 Dye Visualisation:

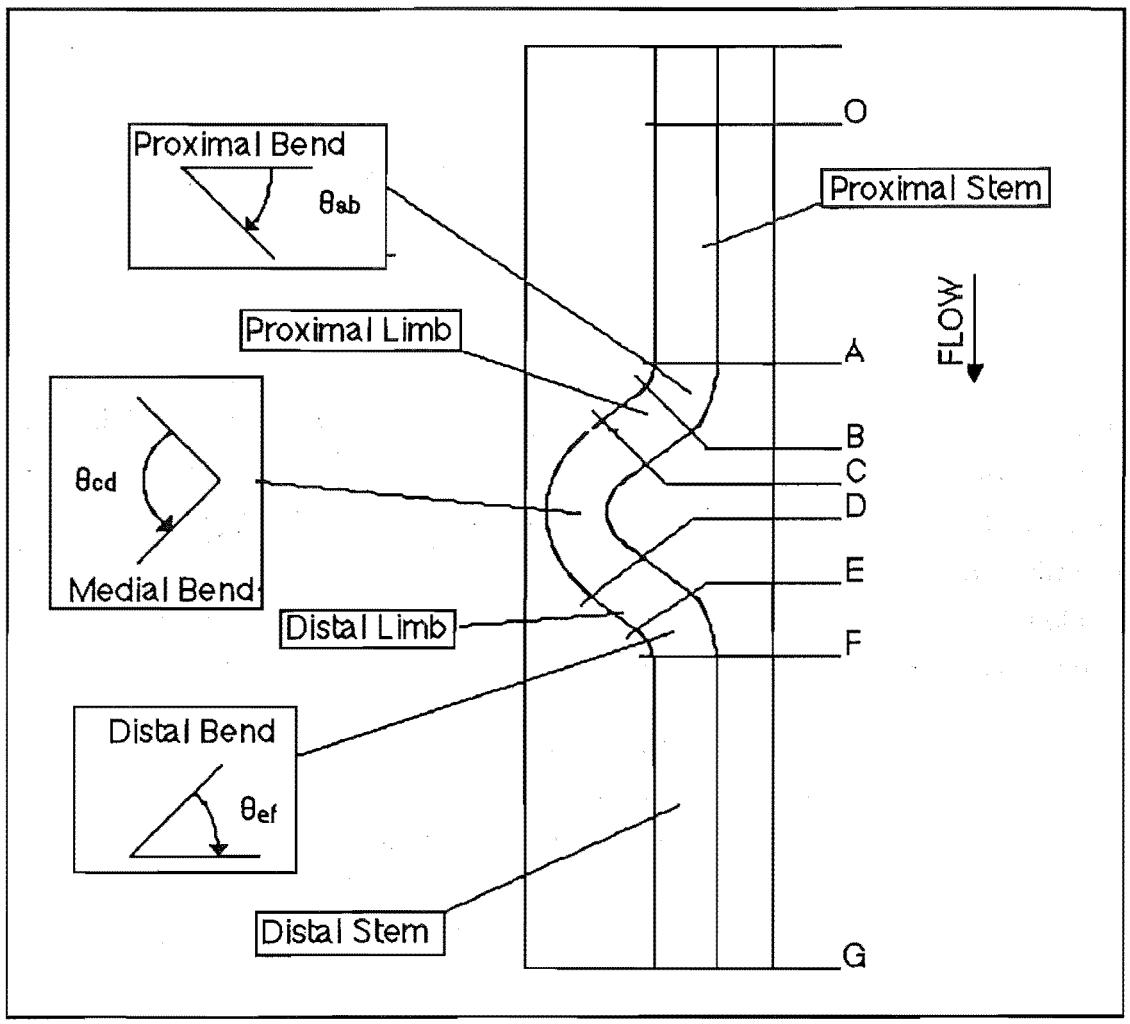

$0° \leq \theta_{ab} \leq 70°$

$0° \leq \theta_{cd} \leq 140°$

$0° \leq \theta_{ef} \leq 70°$

Figure 5.1
Nomenclature

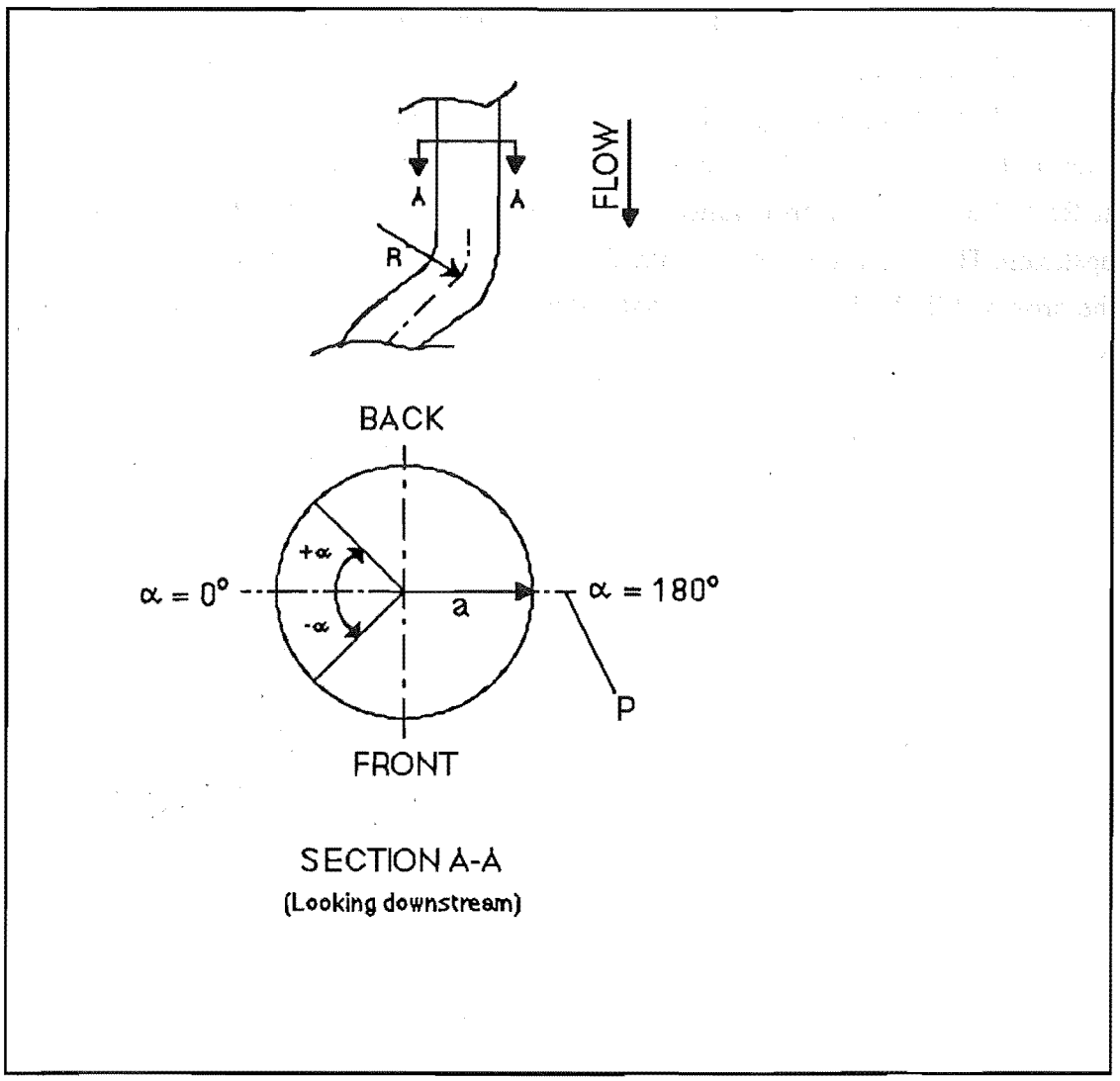

Figure 5.2
Nomenclature

5.2.1 Steady flow:

5.2.1.1 General Flow Features:

Flow in the model was dominated by secondary flow. This occurred in the distal stem, FG (figure 5.1), at low Reynolds numbers, but progressed rapidly to upstream positions with increased flowrate. Flow in the distal stem was asymmetric with respect to plane of symmetry, P even at the lowest Reynolds numbers studied (Re = 100). Again, as with most flow features in the model, asymmetry was observed further upstream with increased flowrates.

The first occurrence of unsteadiness in the flow was observed downstream of the distal bend at a Reynolds number of 463. This took the form of regular waves as

shown in Plate 5.17 at Re = 746. At Re > 500, wavering of the dyestream could be observed in the medial bend,CD. The dye was well mixed upon reaching the distal stem at Re > 1000, making it difficult to determine whether or not true turbulence existed. Localised areas of intermittent turbulence possibly occurred in the distal limb at Re > 1500, though observation was again made difficult by mixing of the dye upstream. The major areas of unsteady flow occurred near regions of separated flow in the proximal limb, distal limb and distal stem, just downstream of the corresponding bends.

5.2.1.2 Specific Flow Features:

Flow in the proximal stem, OA (figure 5.1), was laminar, with a parabolic streamwise velocity profile and no apparent radial or circumferential velocity components, for all flows up to the highest Reynolds number studied (Re = 2434), until just upstream of A where some circumferential flow was observed in a layer near the wall at all flowrates. The parabolic profile is shown in Plate 5.1, with the dye just entering the proximal bend, AB. In OA, flow appeared to be symmetrical with respect to the model's plane of symmetry, P (figure 5.2), though refractive effects made viewing this aspect difficult. The peak axial flow appeared to be located slightly towards the inner wall of the proximal bend from the central axis of the tube when viewed from the front (Plate 5.1).

Flow near the wall of OA began to move circumferentially about each semicircle[1] in a layer of thickness of less than about 0.5 mm, from $\alpha = 180°$ to the region bounded by $-5° < \alpha < +5°$ at a position 0.35 diameters upstream of A (independent of Re), as shown in figure 5.3 and Plates 5.2 and 5.3.

This circumferential flow was maximal at $\alpha = 180°$, decreasing towards the opposite side so that no circumferential flow was evident between $\alpha = -5°$ and $\alpha = +5°$. The circumferential flow in OA at $\alpha = 180°$ began at an axial position defined as the upstream limit of backflow (figure 5.4). A backflow was positioned along $\alpha = 180°$ for a short distance downstream from this point, extending as far as a second axial position, defined as the downstream limit of backflow (figure 5.4). The upstream limit of backflow is shown in Plates 5.1 and 5.2.

---

[1]The hemicircles are defined as the two halves of the tube divided by the plane of symmetry, P.

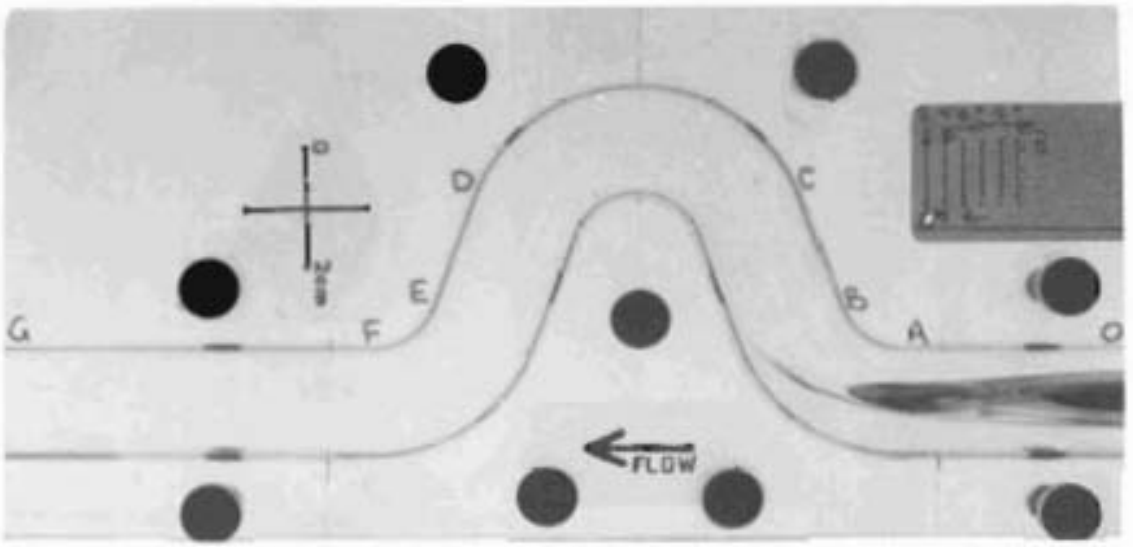

Plate 5.1: Laminar Flow in the Proximal Stem, Re = 373.

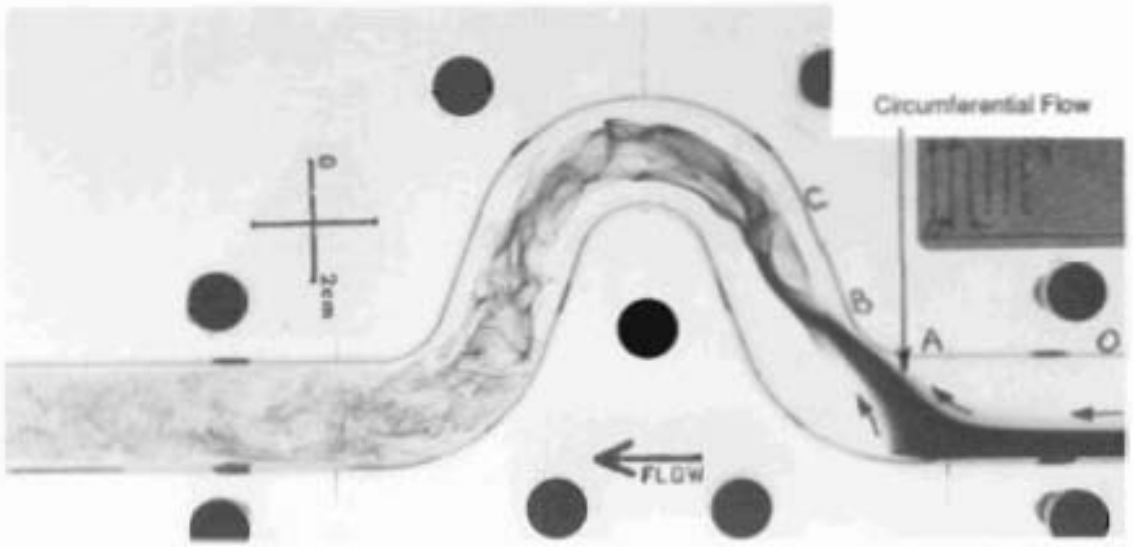

Plate 5.2: Circumferential Flow in the Proximal Stem, Re = 1114.

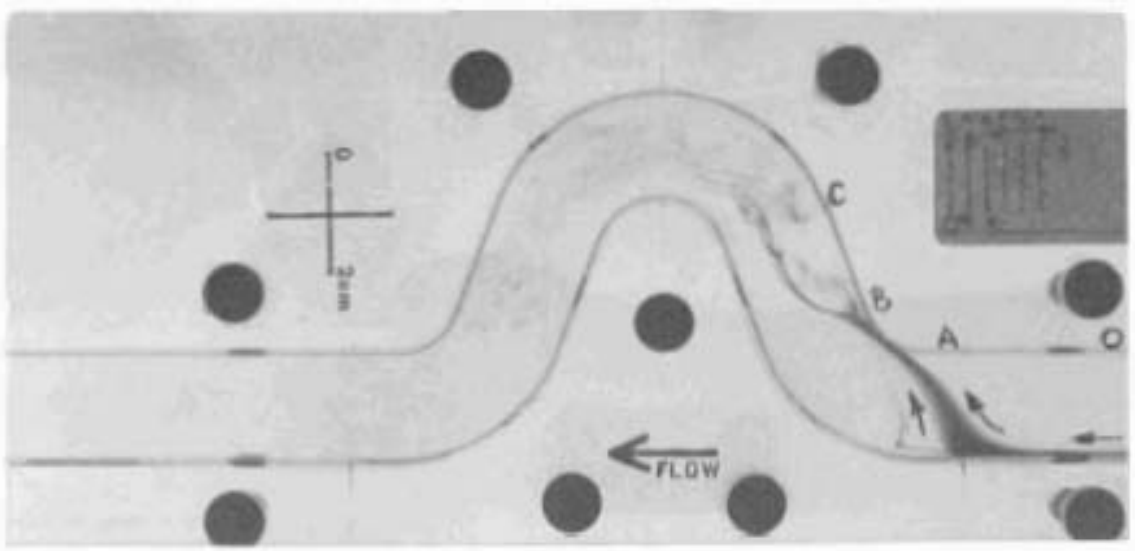

Plate 5.3: Circumferential Flow in the Proximal Stem, Re = 2176.

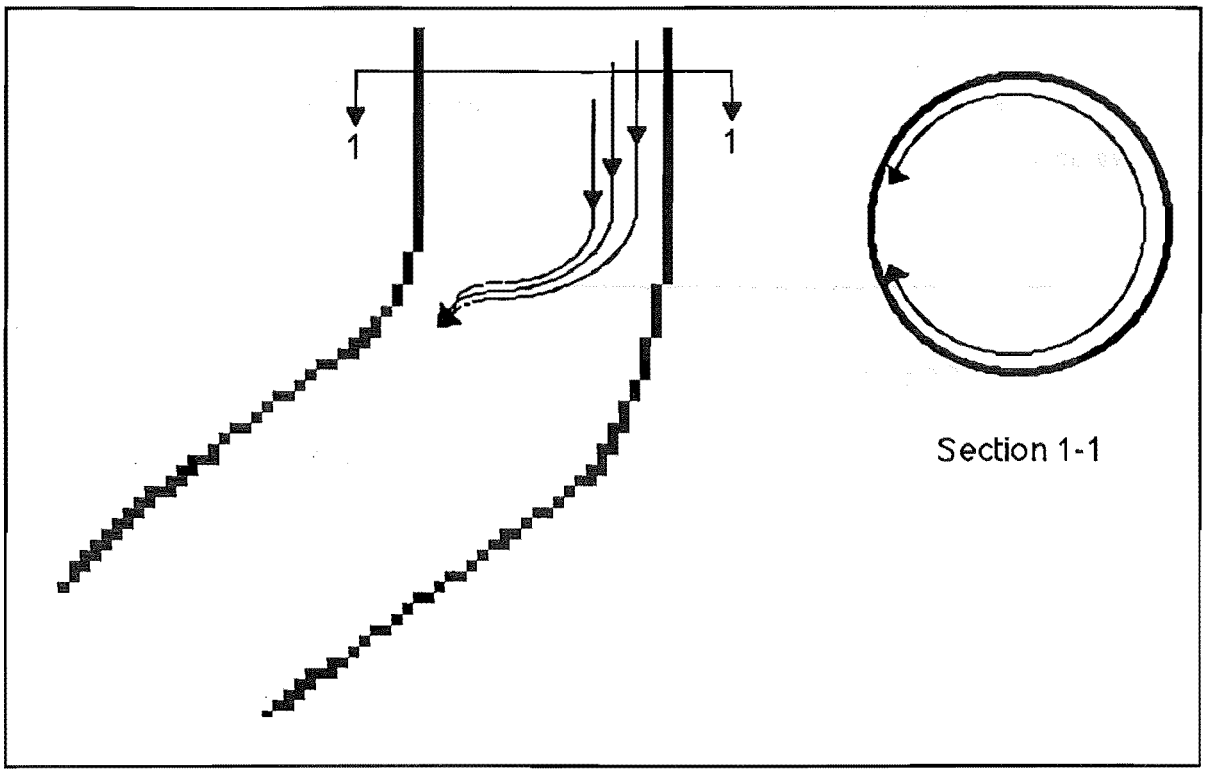

Figure 5.3
Circumferential wall flow at the proximal bend entrance

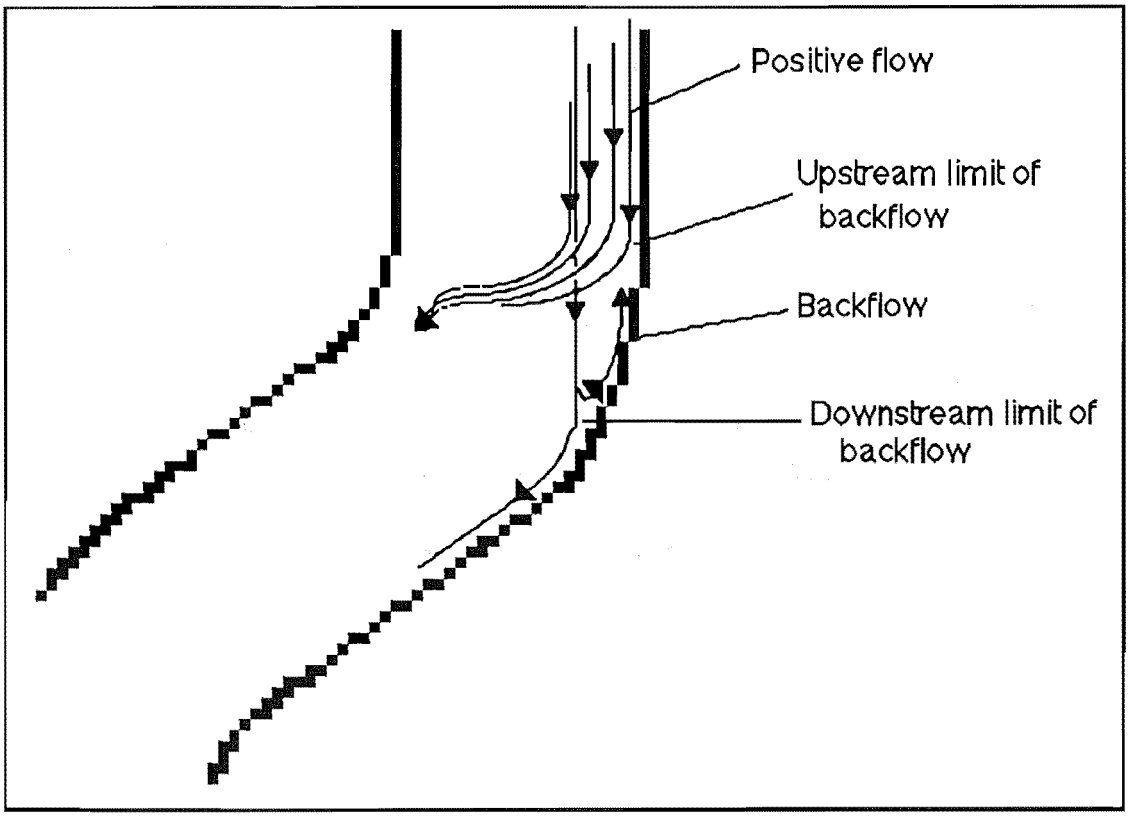

Figure 5.4
Limits of backflow at outer proximal bend wall

The position of the upstream limit of backflow (ie: the changeover point from positive to negative axial flow) relative to A (the bend entrance), depended on the flowrate for Re below 1500, but was constant within experimental error above this value, as shown in figure 5.5.

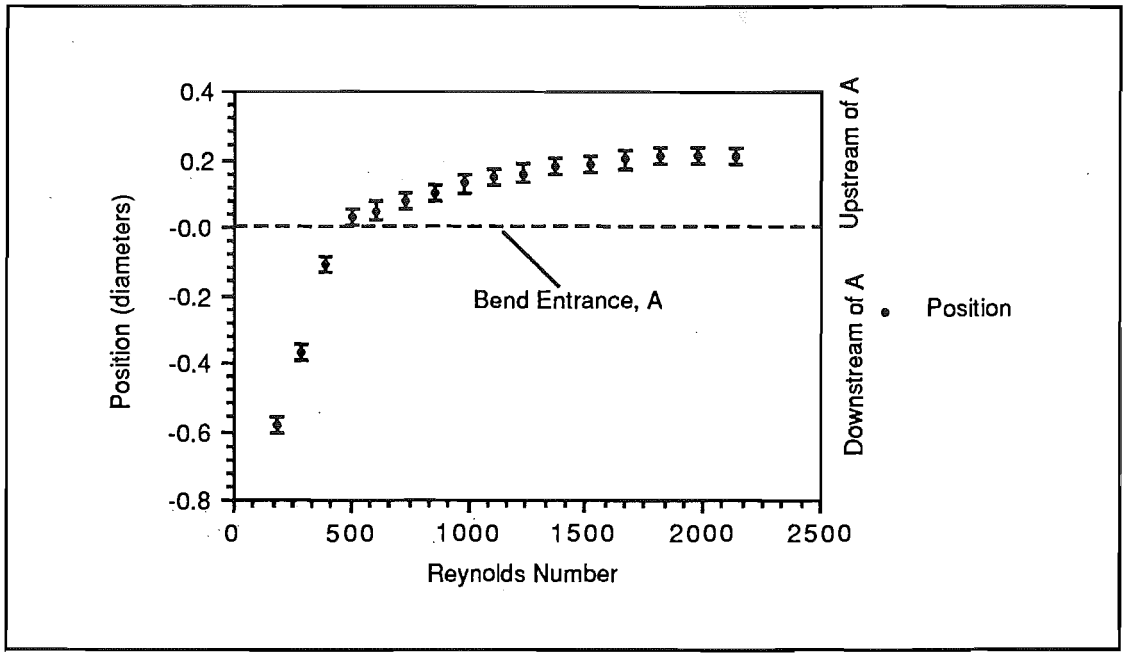

Figure 5.5
Upstream extent of Proximal Bend Backflow
(measured along wall from bend entrance, A)

Flow in the proximal bend AB was smooth and laminar up to a Reynolds number of about 2000 despite significant secondary flow.

Near-wall flow entering the proximal bend within the limits $-5° < \alpha < +5°$ of OA continued through the bend with no circumferential component of velocity, and separated from the wall after entry, as shown in Plate 5.6.

Wall flow in the bend AB, except for the backflow near $\alpha = 180°$ and the separated flow near $\alpha = 0°$, originated in the core flow of the proximal stem, OA. This wall flow was directed circumferentially in each hemicircle from $\alpha = 180°$ towards $\alpha = 0°$ (Plate 5.7).

Dye entering the proximal bend outside the backflow region, in a narrow layer (approx. 2 mm) centred on P, continued through the bend with no velocity component normal to P (Plates 5.8 and 5.9). A radial velocity component parallel to P was directed from $\alpha = 0°$ to $\alpha = 180°$. The backflow region at $\alpha = 180°$, mentioned above,

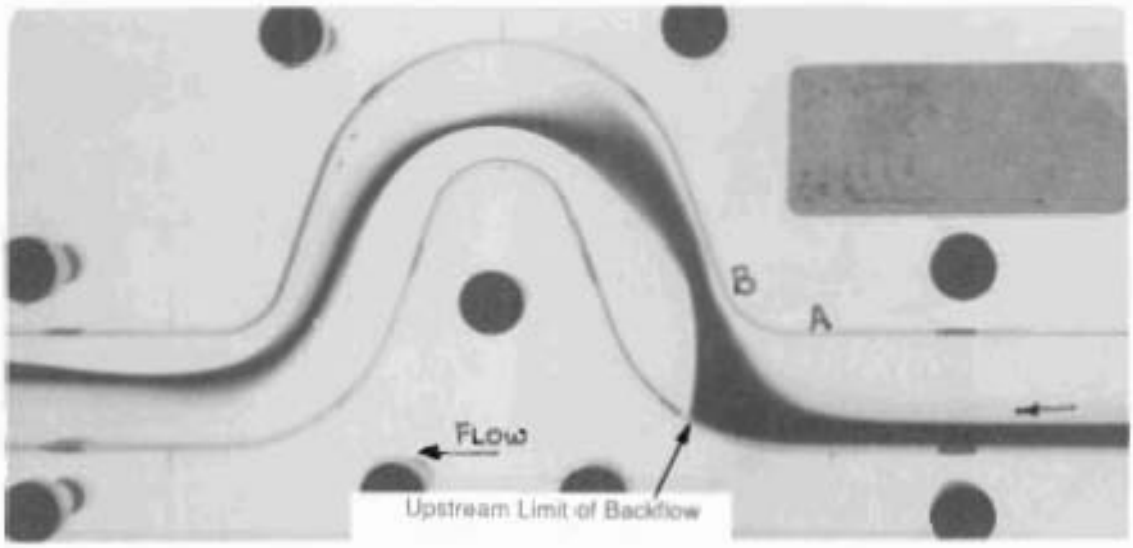

Plate 5.4: Circumferential Flow at Re = 185.

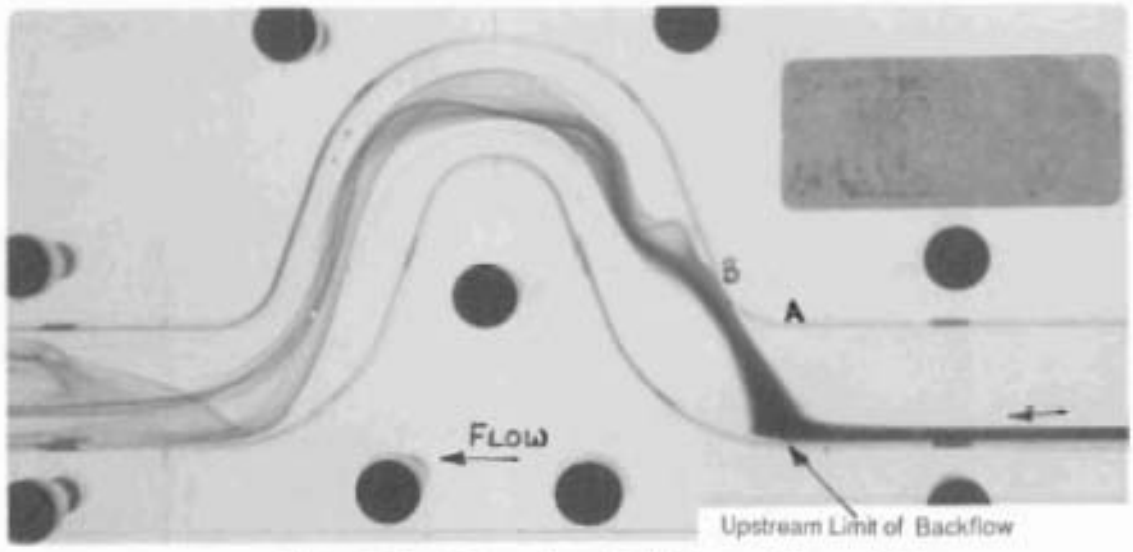

Plate 5.5: Circumferential Flow at Re = 733.

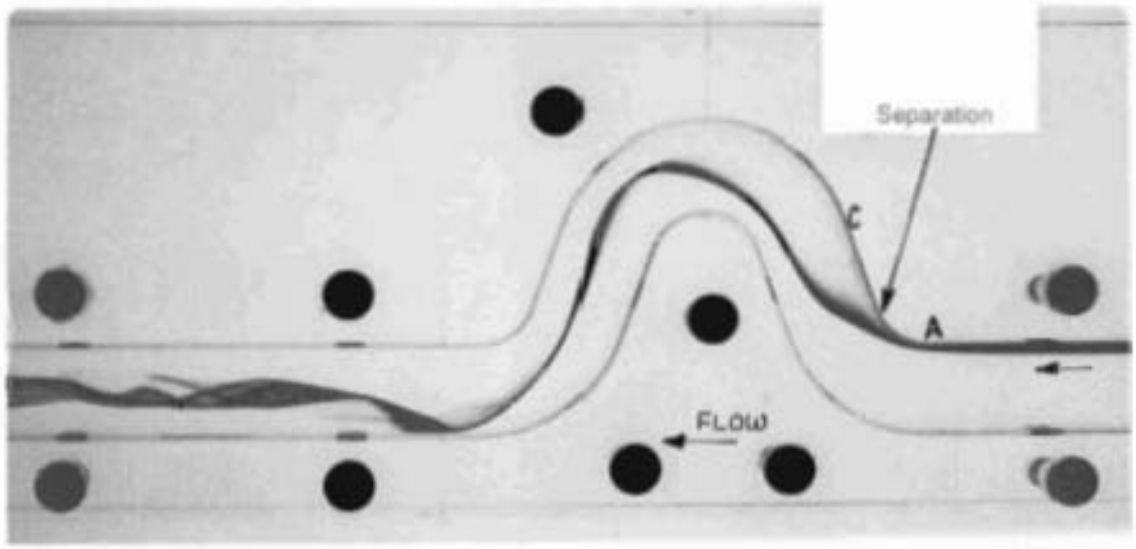

Plate 5.6: Separation at the inner Proximal Bend, Re = 300.

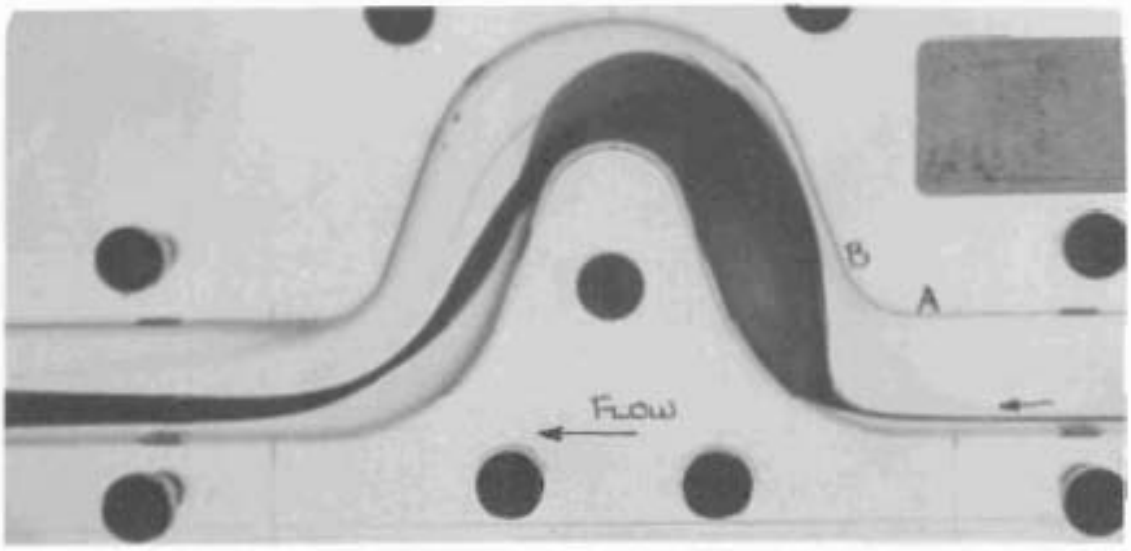

Plate 5.7: Wall Flow in the Proximal Bend, with the Dye Entering in a Compact Stream, 1mm in Diameter, Re = 185.

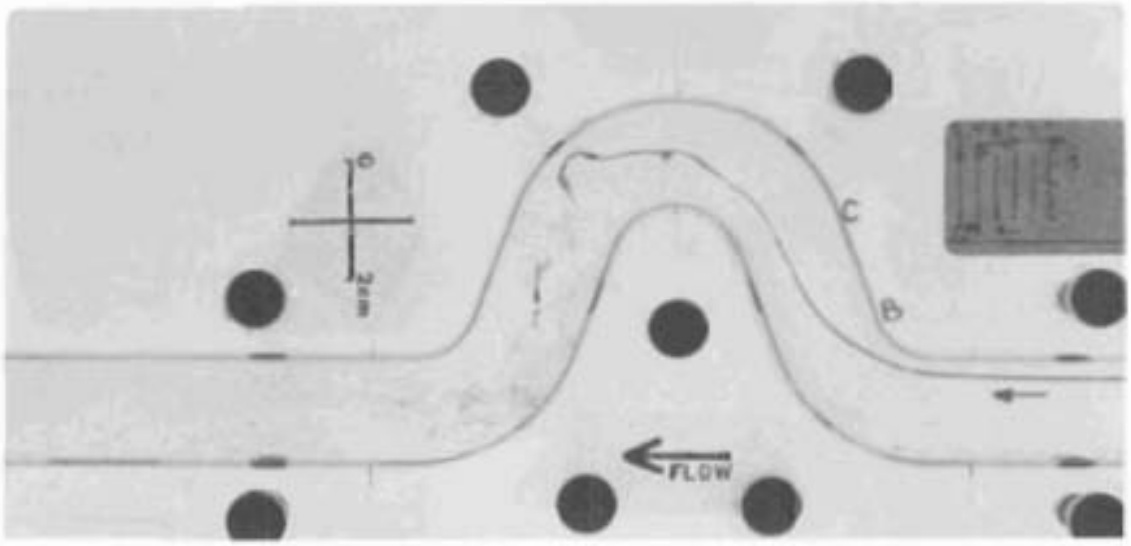

Plate 5.8: Undeviated Flow in the Proximal Limb BC, Re = 2221.

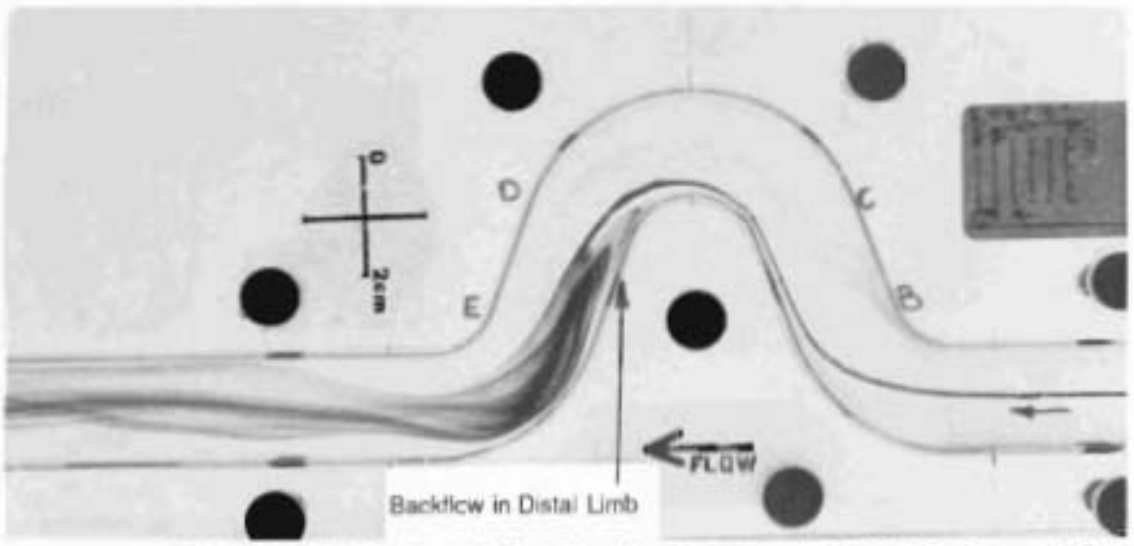

Plate 5.9: Undeviated Flow in the Proximal Limb BC, Re = 554. Note Also, the Backflow in the Distal Limb DE.

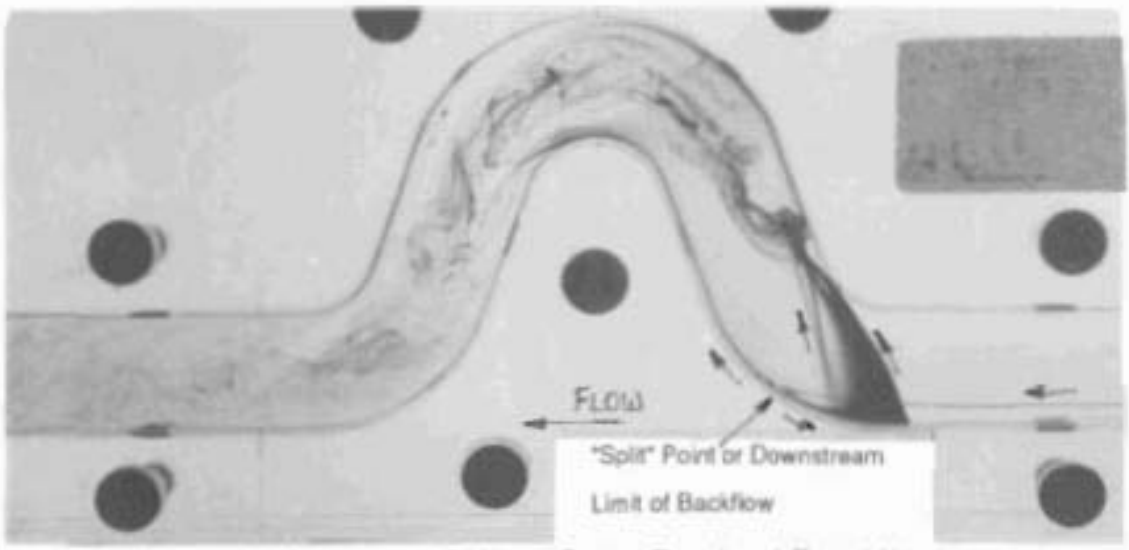

Plate 5.10: Dyestream Split at Outer Proximal Bend Wall, Re = 1662. (Some dye moves upstream to the circumferential flow region, while some moves downstream along BC at $\alpha = 180°$.)

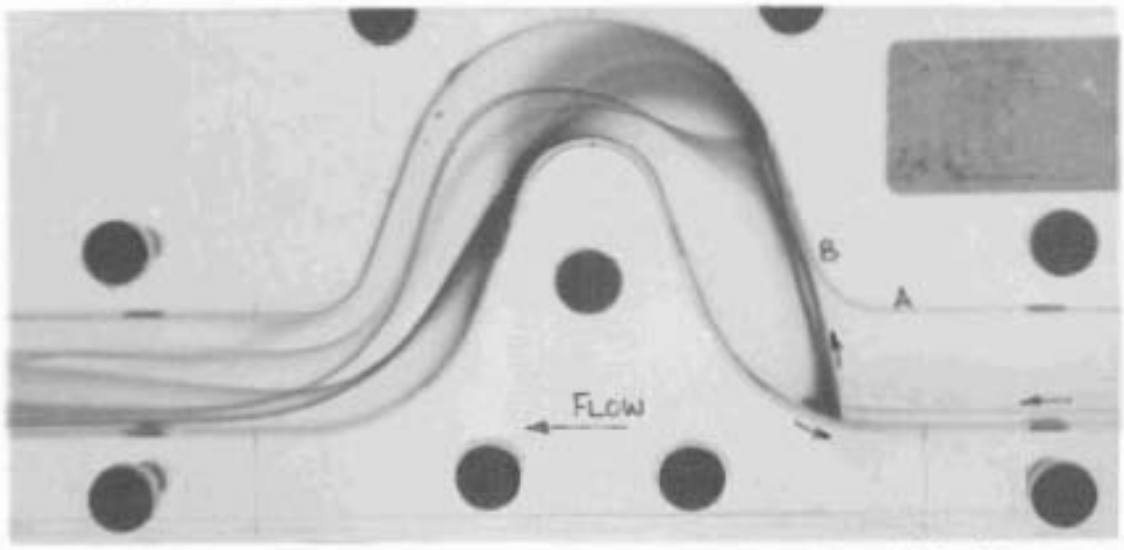

Plate 5.11: Backflow at $\alpha = 180°$ in the Proximal Bend AB, Re = 289.

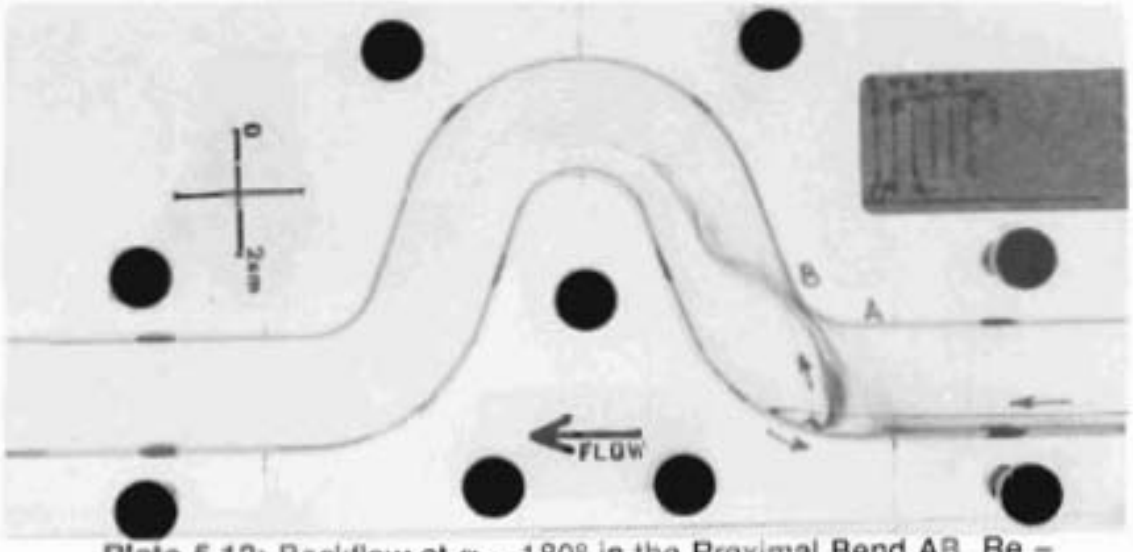

Plate 5.12: Backflow at $\alpha = 180°$ in the Proximal Bend AB, Re = 1114.

extended into the proximal bend to an axial position defined as the downstream limit of backflow (figure 5.4). This position was dependent on Re below 1500 and was constant at about 0.7 diameters downstream of A (the bend entrance) at Re above 1500 (figure 5.6).

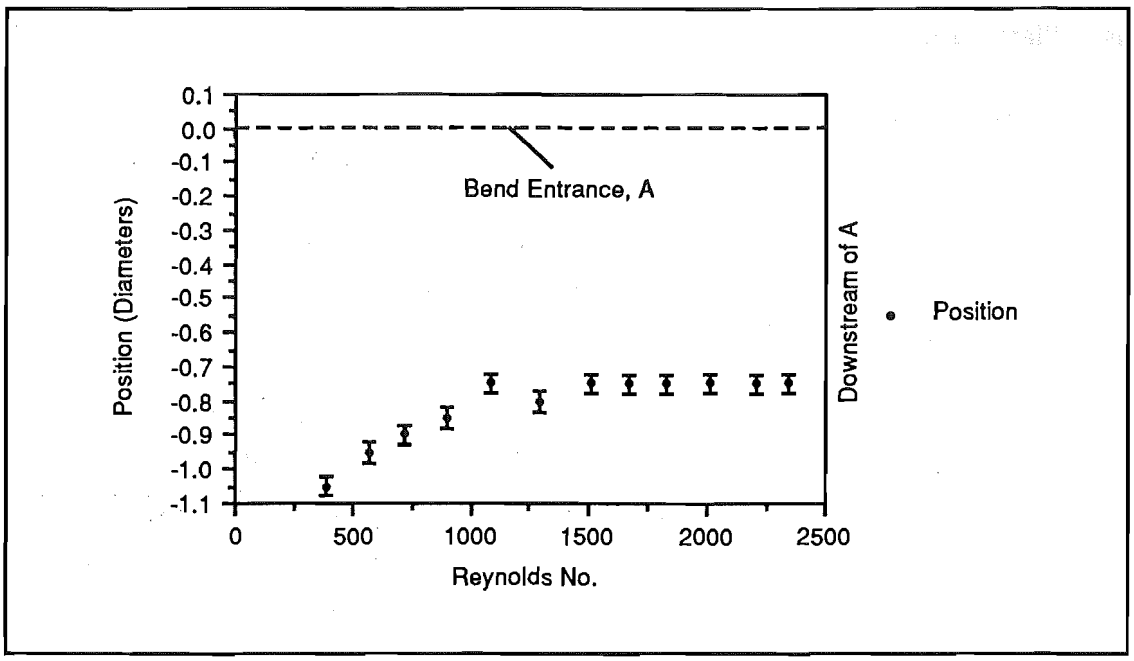

Figure 5.6
Downstream Extent of Proximal Bend Backflow
(measured along wall from bend entrance, A)

A stream of dye entering the proximal bend from just outside the wall flow layer at $\alpha = 180°$ in OA could be positioned such that it would strike the outer proximal bend wall at the downstream limit of the backflow region, resulting in the streamline being split with some dye moving streamwise down and the rest moving upwards along the outer wall (Plate 5.10).

Dye streams near this position but further from the wall in OA were directed in a streamwise direction (Plate 5.9), whilst those closer to the wall were directed upstream along the outer proximal bend wall (Plates 5.11, 5.12 and 5.13) up to the upstream limit. This feature was a part of the upstream effect in OA described above.

At Re less than 600, flow further from the walls exhibited little circumferential movement. At higher flowrates a counter-rotating vortex-pair, one in each semicircle, became evident, extending, at low flowrates, from near B to about mid-BC (Plate 5.14). The upstream end progressed upstream as flowrate increased.

At Re > 1800, the vortices from each hemicircle in the tube joined up about the wall at α = 180°, so that a single,continuous vortex was formed with it's axis aligned circumferentially about the wall. The form of this vortex could be described as a vortex-ring, broken between α = -5° and α = +5°.

Above the original vortex-pair a second vortex-pair was observed aligned parallel to the first, of lower vorticity, smaller radius and similar direction of rotation, as in Plate 5.15.

Whilst the first vortex-pair extended through AB and BC, the secondary vortex-pair appeared to contribute to a vortex structure in AB near α = 0°, θ = 40°.

Axial flow between the vortices and the wall at α = 180° was negative, and both vortices in each hemicircle were surrounded by an envelope of fluid flowing upstream near the wall and downstream between the vortices and mid-tube.

The positions of the two vortices fluctuated in a streamwise direction along the wall over a distance of about 1-2 mm and at a frequency of about 1.3 Hz, in a region within 0.5 diameters downstream of the bend entrance. Associated with this fluctuation was an intermittent transfer, or "jump", of fluid between the vortices and between the vortices and the envelope of fluid surrounding them, as shown in Plate 5.16.

The fluid closer to the centre of the tube streamed towards the outer proximal bend wall and straight through the bend and BC with little circumferential displacement, by-passing the vortical structures in the proximal bend and BC completely, as shown in Plate 5.17.

Overall flow in BC consisted of three distinct parts: a streamwise portion; a helical portion and a vortical structure. The upstream origins (in OA) of the fluid contributing to each of these portions is shown in figure 5.7.

The streamwise portion of flow was directed in a layer spanning and parallel to P (ie: with no vortical component) and in a streamwise direction, such that fluid moved directly through BC, with slight deviation towards α = 180° only within the plane of symmetry, as shown in Plate 5.17. This part of the flow was contained in the half of BC closest to α = 180° and originated in OA along the plane of symmetry, outside the circumferential wall flow (figure 5.7), ie: that flow which was not deviated in the proximal bend AB. Flow was almost parallel to the BC central axis, with a slight angle towards α = 180° as it progressed downstream.

Flow reaching the wall in the straight BC region at α = 180° was likewise

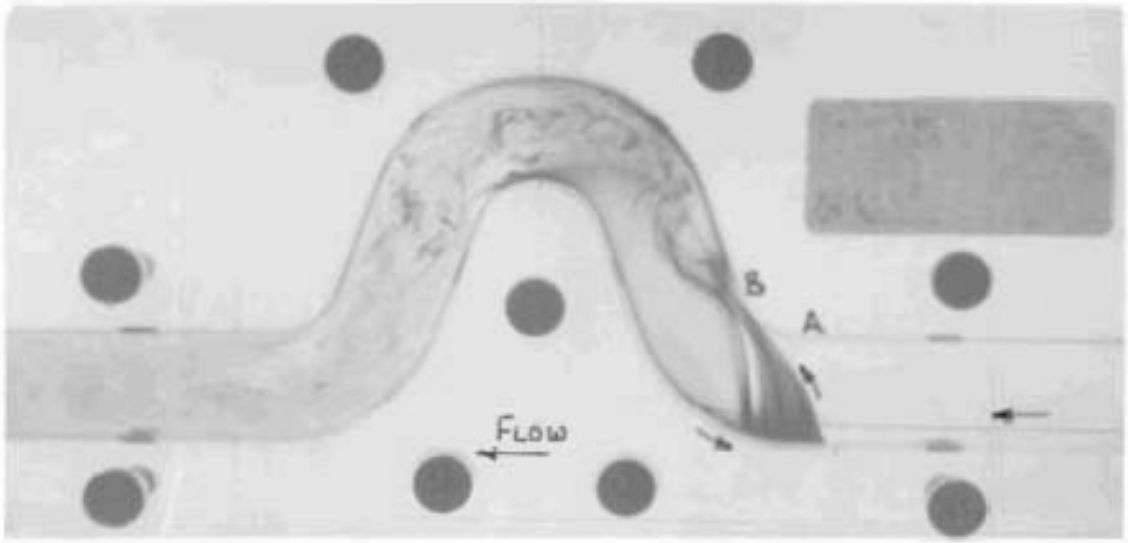

Plate 5.13: Backflow at $\alpha = 180°$ in the Proximal Bend AB, Re = 1971.

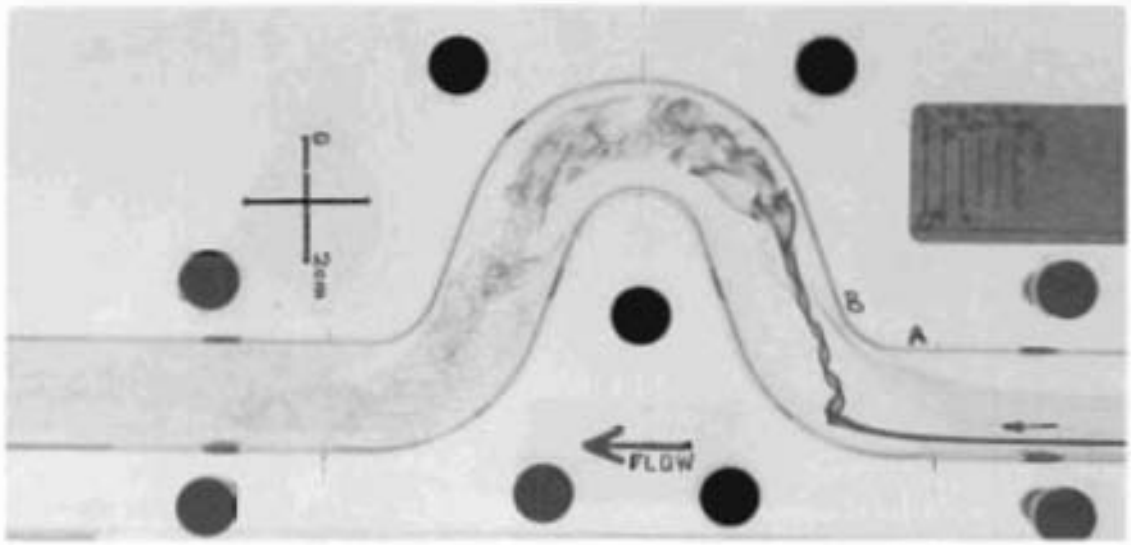

Plate 5.14: Vortex in the Front Hemicircle Proximal Bend and Limb, Re = 1632.

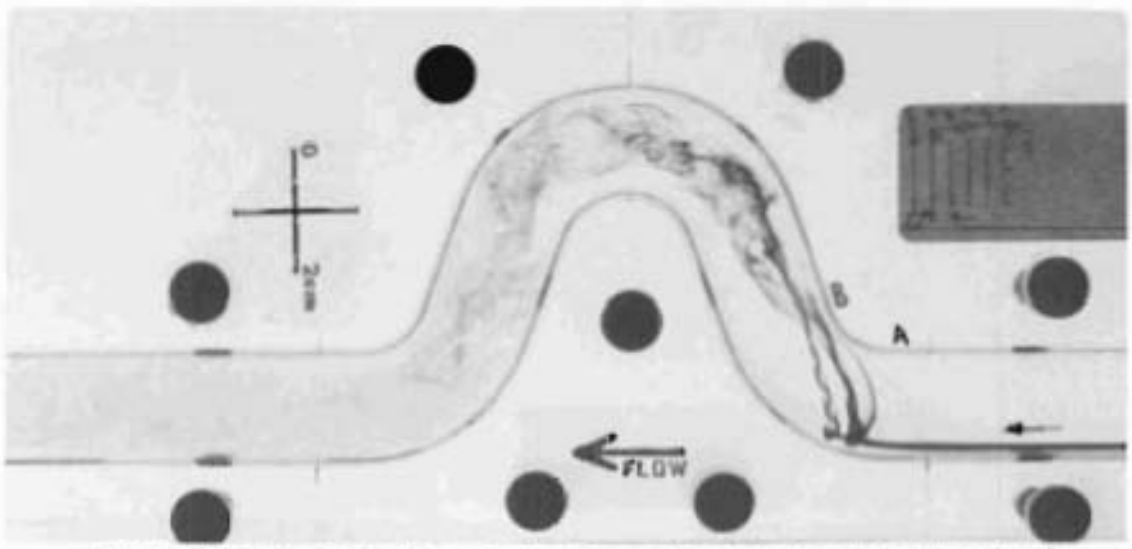

Plate 5.15: Twin Vortices in the Front Hemicircle of the Proximal Bend, Re = 2434.

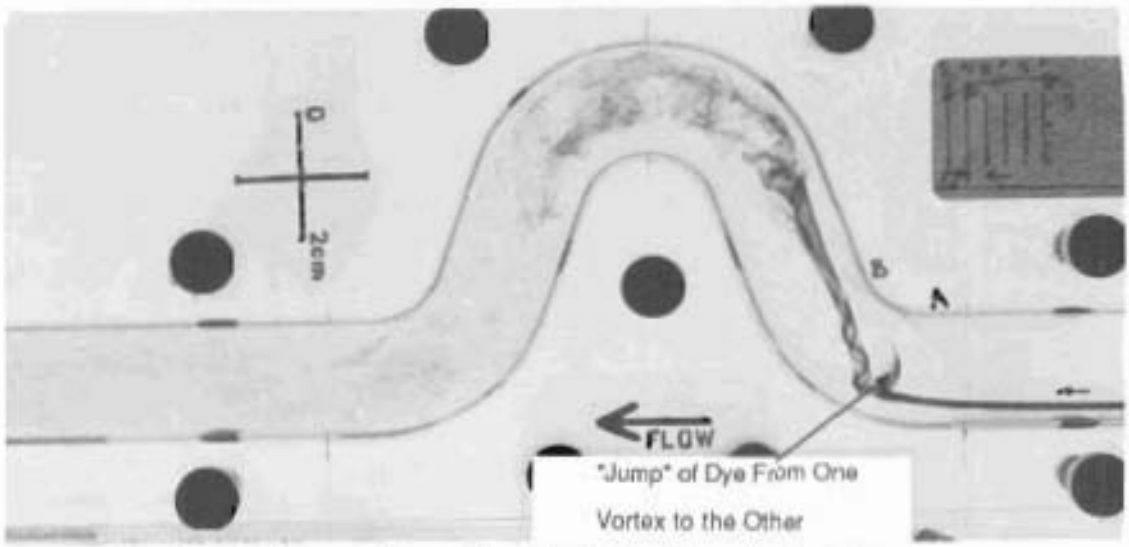

Plate 5.16: Interaction of the Twin Vortices in the Front Hemicircle of the Proximal Bend, Re = 1434. (Note the packet of dye just beginning to "jump" from one vortex to the other.)

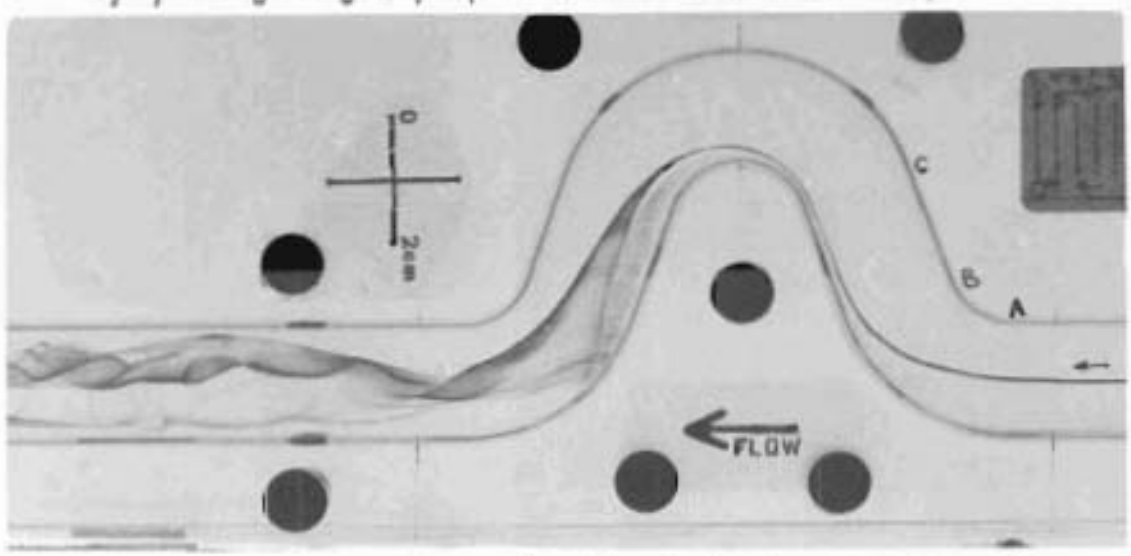

Plate 5.17: Steady, Streamwise Flow in the Proximal Limb, Re = 746.

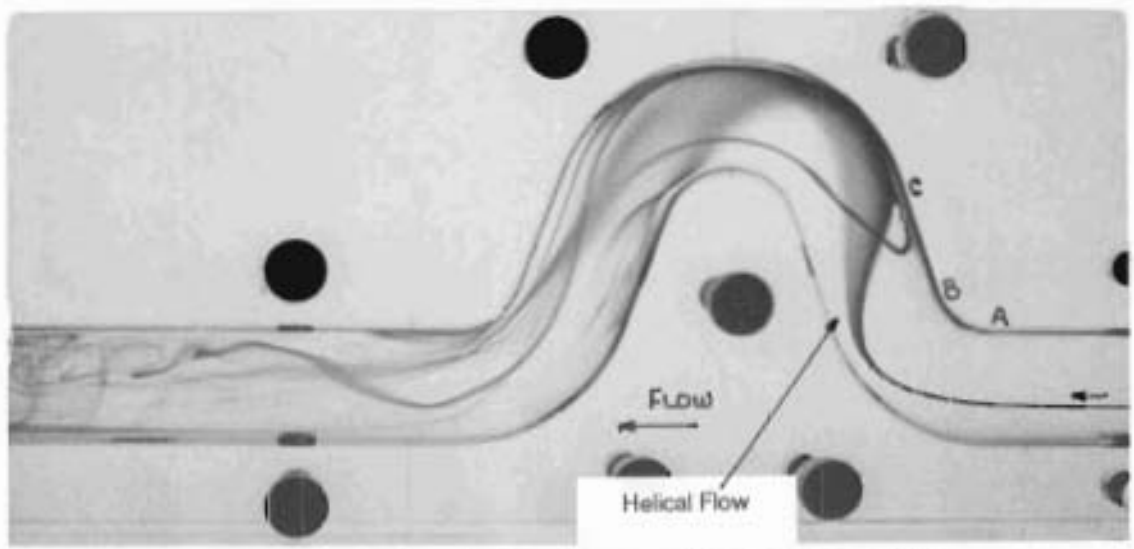

Plate 5.18: Helical Flow in the Proximal Limb, Re = 737.

undeviated in a circumferential direction. The flow was steady up to the highest flowrates observed (see Plate 5.17).

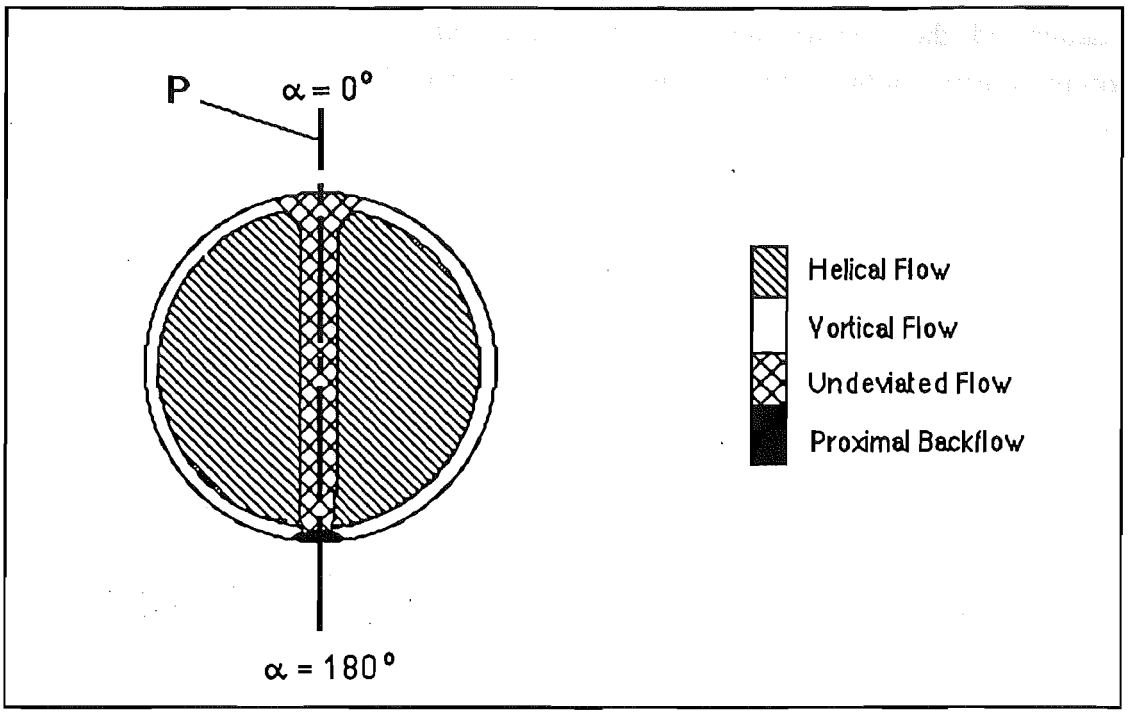

Figure 5.7
Origins of fluid from OA contributing to structures in BC
(cross-section of OA upstream of A)

The second constituent of flow was the helical portion, consisting of circumferential wall flow with a large streamwise component, such that it moved along BC helically in a streamwise direction, as shown in Plate 5.18.

This flow originated in the portion of OA in each half of the tube between P and the wall flow layer. This flow occupied all of the region in BC not taken up by either the stream moving directly through the plane of symmetry or the vortical structure seen in Plate 5.23.

As flowrate was increased, the radius of the helical flow decreased and the axes moved further from the wall, such that the fluid closest to the wall was dominated by the first-mentioned streamwise velocity component.

Flow was steady up to high flowrates except at the downstream end of BC, where the dye stream wavered back and forth across the tube a few millimetres at a

frequency of about 1.25 Hz (see Plate 5.19a-l). As flowrate increased, the position of unsteadiness occurred further upstream, closer to the vortical structure situated in BC at $\alpha = 0°$ (see Plate 5.20).

At the higher flowrates, although the helical nature of the flow was maintained, the flow was unsteady and intermittent movement of the dye stream occurred between the different structures in BC and AB. These are shown in Plate 5.21a-c.

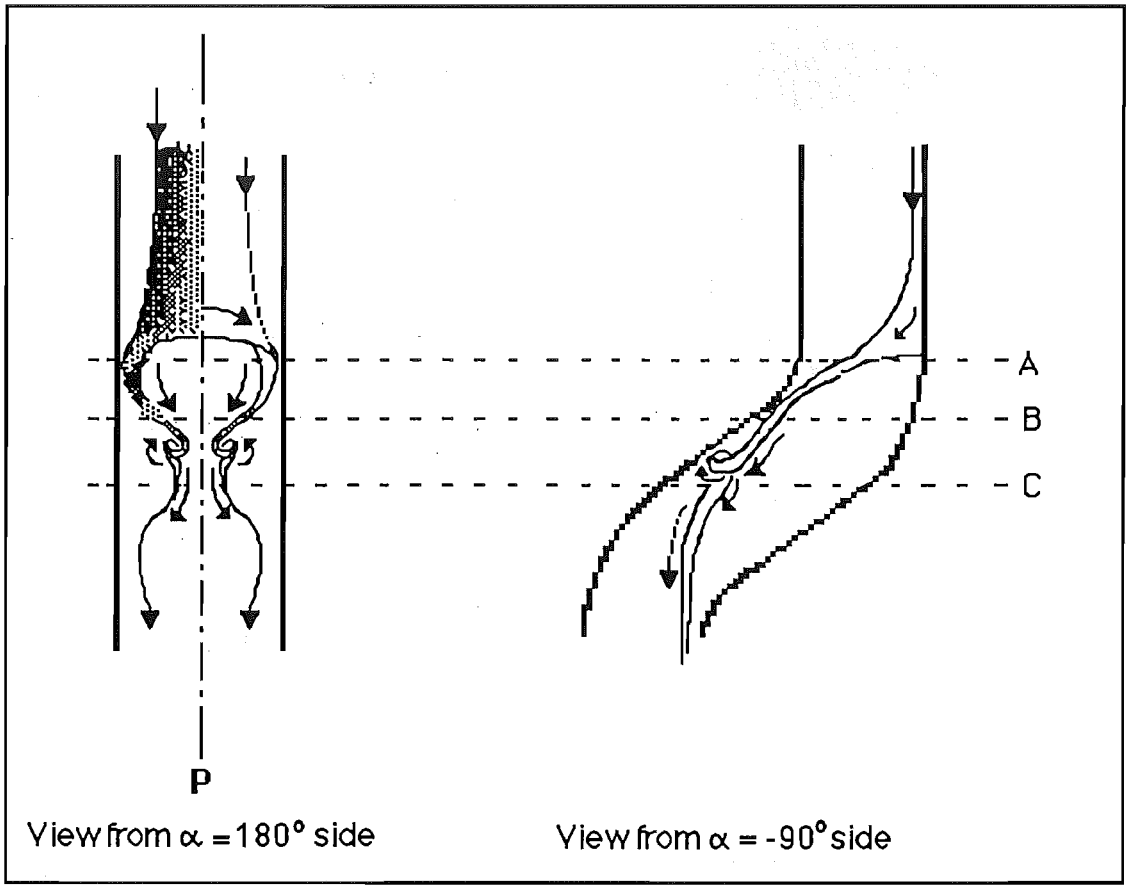

Figure 5.8

Simple vortical structure in BC at low Re, showing dye entering from along the wall near $\alpha = 180°$ in OA.

The third constituent of the overall flow in the section BC was a vortical structure situated close to the wall between $\alpha = +25°$ and $\alpha = -25°$, shown in Plates 5.21a-c, Plate 5.22 and figures 5.8 and 5.9. The structure was relatively simple at low flowrates, consisting of twin vortices approximately symmetrical about P (figure 5.8), fed from both the circumferential wall flow in OA and AB and backflow from the helical portion of the flow in BC where the two vortices met at $\alpha = 0°$ (Plate 5.23). The vortical structure drained downstream into the medial bend CD, with the axis of each constituent vortex following a similar streamline to the streamwise portion of flow

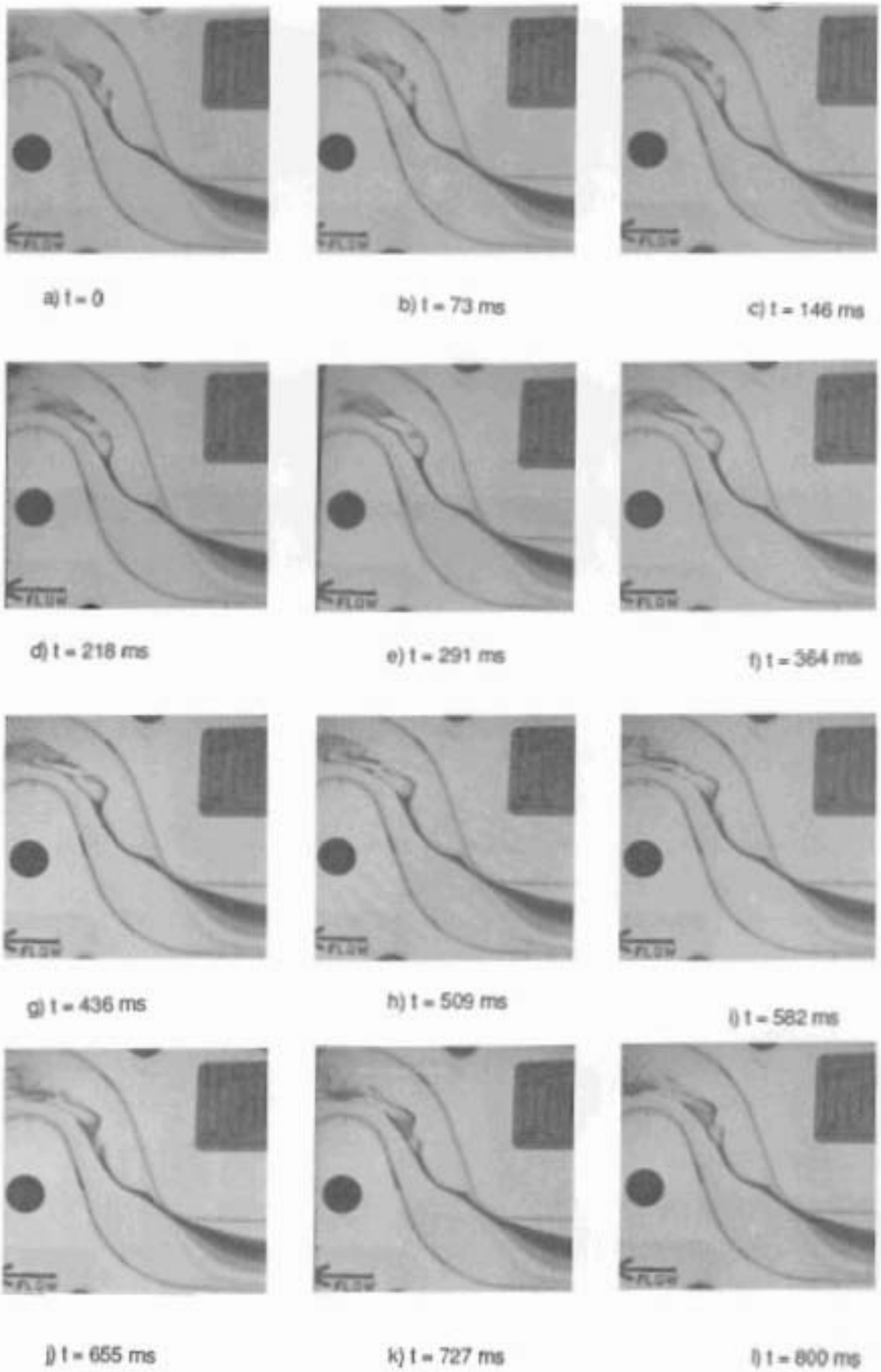

Plate 5.19a-l: Wavering of the Dyestream in the Proximal Limb, Re = 1444. (Note that wavering occurs only in the downstream half of BC. Also, as shown by the similarities of plates (a) and (l), the period of wavering is 0.8 seconds.Exposure time 1/250th seconds.)

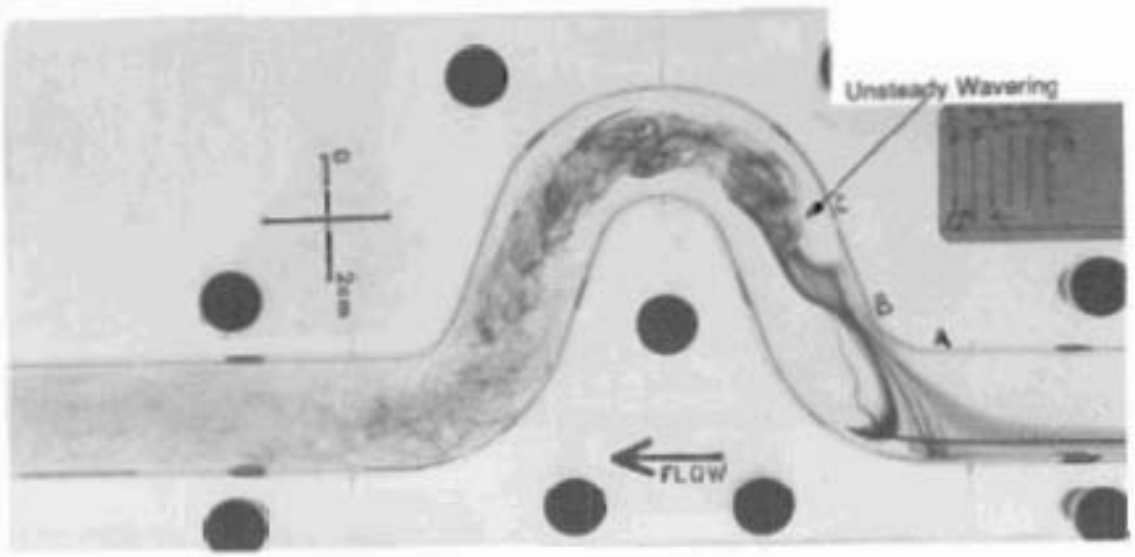

Plate 5.20: Wavering in the Proximal Limb, Re = 1191.

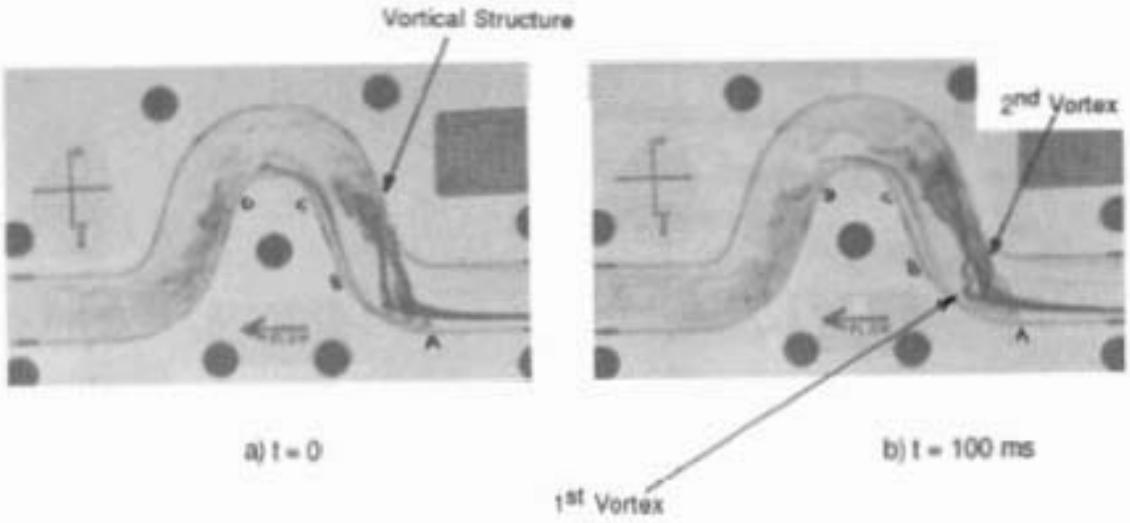

Plate 5.21a-c: Interaction Between the Structures in the Proximal Bend and Proximal Limb, Re = 1926.

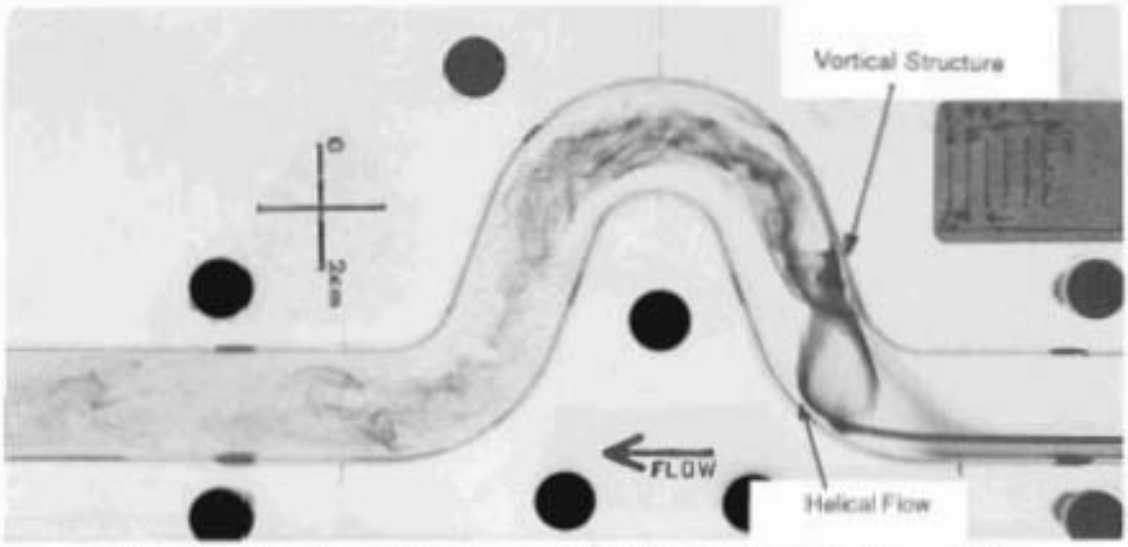

Plate 5.22: Vortical Structure in the Proximal Limb, Re = 1444. (Note also the helical flow about the rear wall of the proximal bend, feeding the structure.)

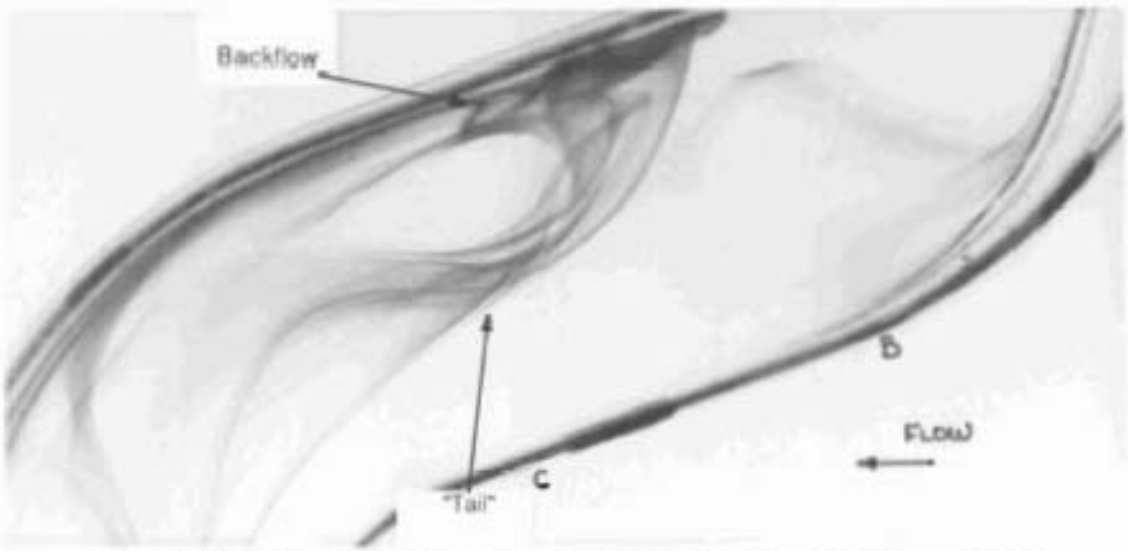

Plate 5.23: Close-up of the Vortical Structure in BC, Re = 1068. (Note the stagnant nature of the flow, evidenced by the presence of dye even though none is seen upstream. Also not the backflow near the wall, evidenced by parabolic bands of dye.)

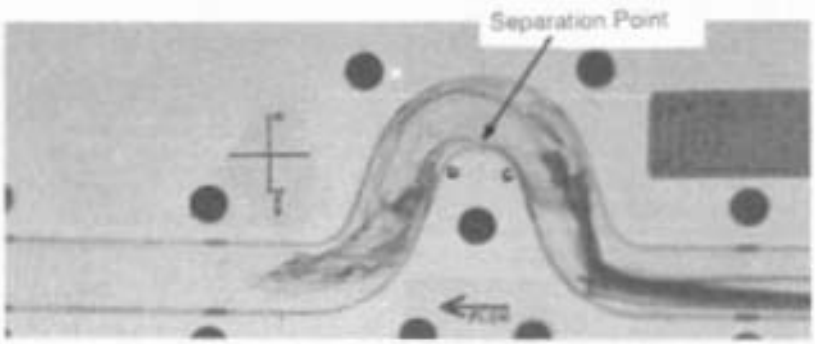

Plate 5.24: Separation at the Inner Apex of the Medial Bend. Re = 1132.

along P.

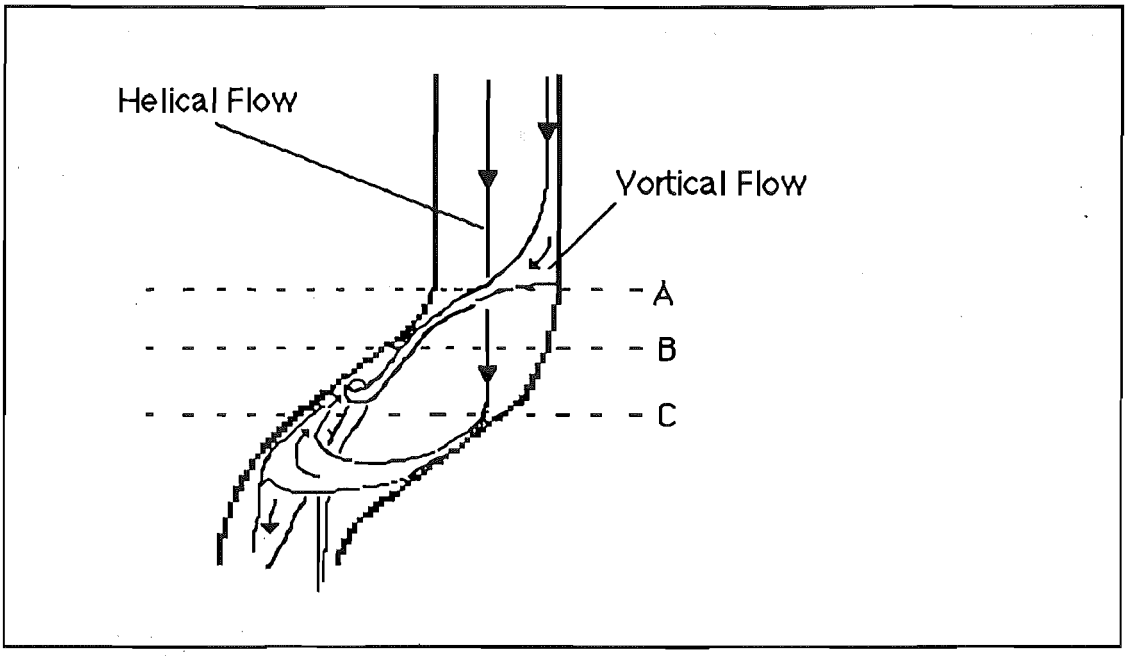

Figure 5.9
Dye from helical portion feeding
vortical structure in BC at low Re

Between the twin vortices and the wall at $\alpha = 0°$, there was a region of backflow which was slow-moving at low flowrates (Plate 5.23). At higher flowrates the whole structure became more complex and assymmetric very quickly, and was difficult to educe because of refractive effects and upstream distortions to the dye streamlines.

The tails of the vortices wavered back and forth in the same manner as the helical flow in BC (Plates 5.19a-l). Again, the position of wavering occurred at the downstream end of BC at low Reynolds no.s and occurred further upstream with higher flowrates. Similarly, the heads of the vortices were situated closer to B with higher flowrates (Plates 5.15a-c).

Flow in the medial bend, CD, was dominated by secondary flow. Note the reversal of geometry here, so that the inner bend occurs at $\alpha = 180°$, while the outer bend occurs at $\alpha = 0°$ (figure 5.1).

At the inner side ($\alpha = 180°$), a layer of fluid originating upstream in the layer of fluid centred on P moved through the bend without circumferential displacement. This layer separated from the inner wall, forming a separation bubble between it and

the wall. Separation occurred downstream of the apex ($\theta > 70°$) at low Re, but by Re = 914 the separation point was at the apex (see figure 5.10 and Plate 5.24).

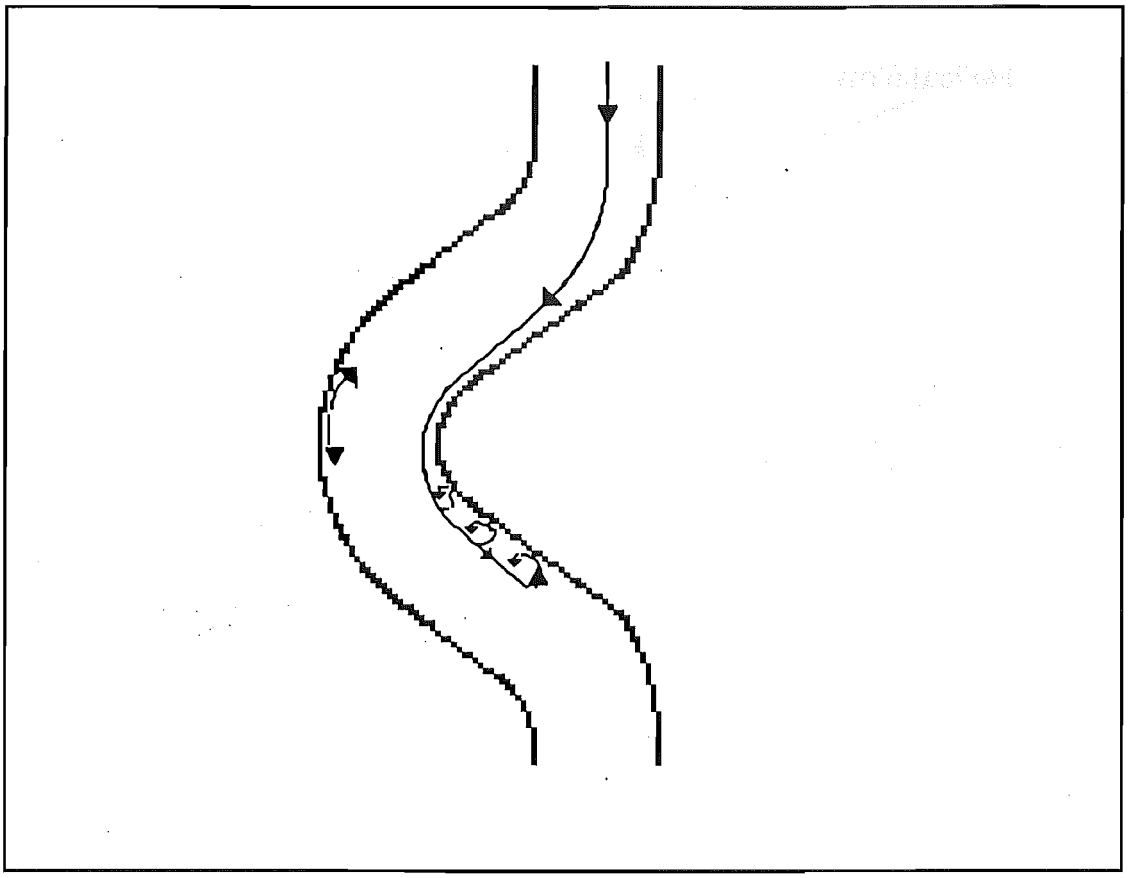

Figure 5.10
Separation in the medial bend

At low flowrates, backflow in the separation bubble was slow-moving and steady (see Plate 5.9), but this became fast and disturbed by Re = 1080. Fluid was entrained into the separation bubble from the separated shear layer such that vortices were formed and shed downstream (Plates 5.26 and 5.29a-i).

Flow in the medial bend was steady up to Re = 700, at which point a slight wavering of the shear layer near $\alpha = 180°$ became evident near D, as shown in Plates 5.27 and 5.28.

The unsteadiness progressed upstream rapidly with flowrate, and at Re = 1000, the wavering had become more marked and was observed at C (the entrance of the bend) as in Plate 5.16. At an Re of 1190 the frequency of wavering here was about

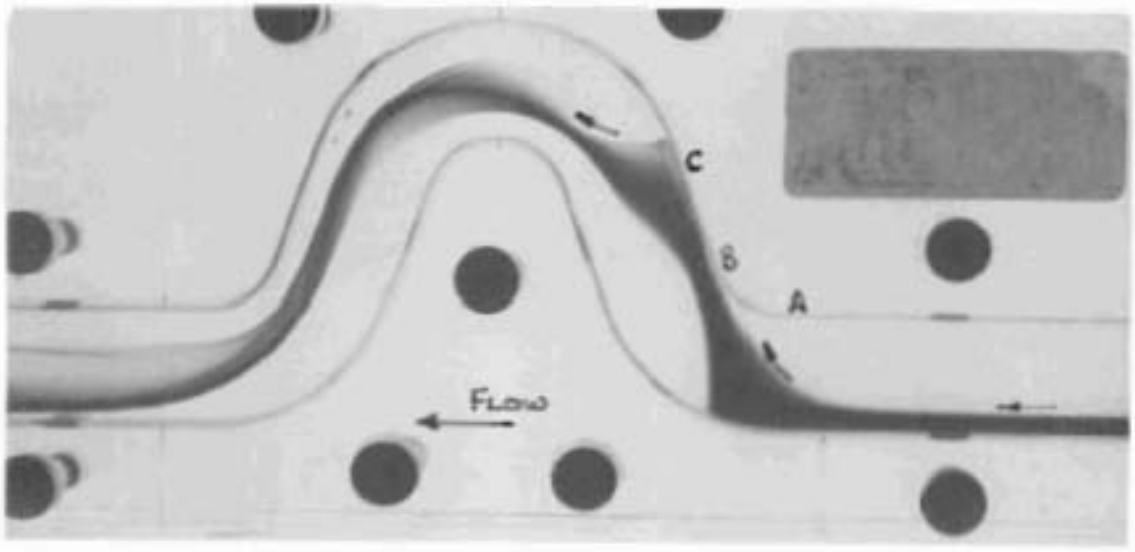

(a)

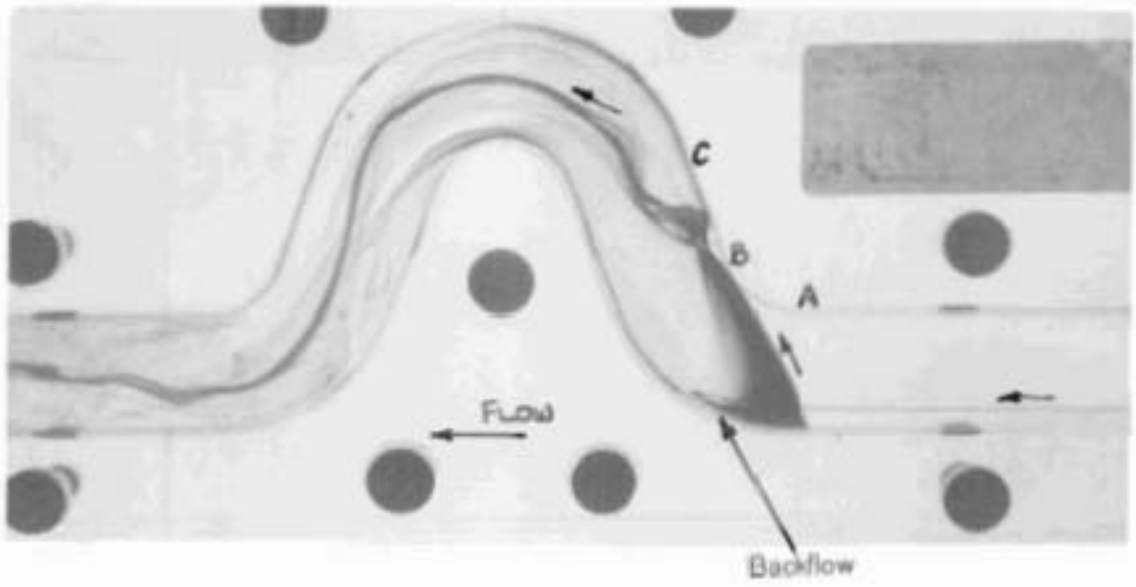

(b)

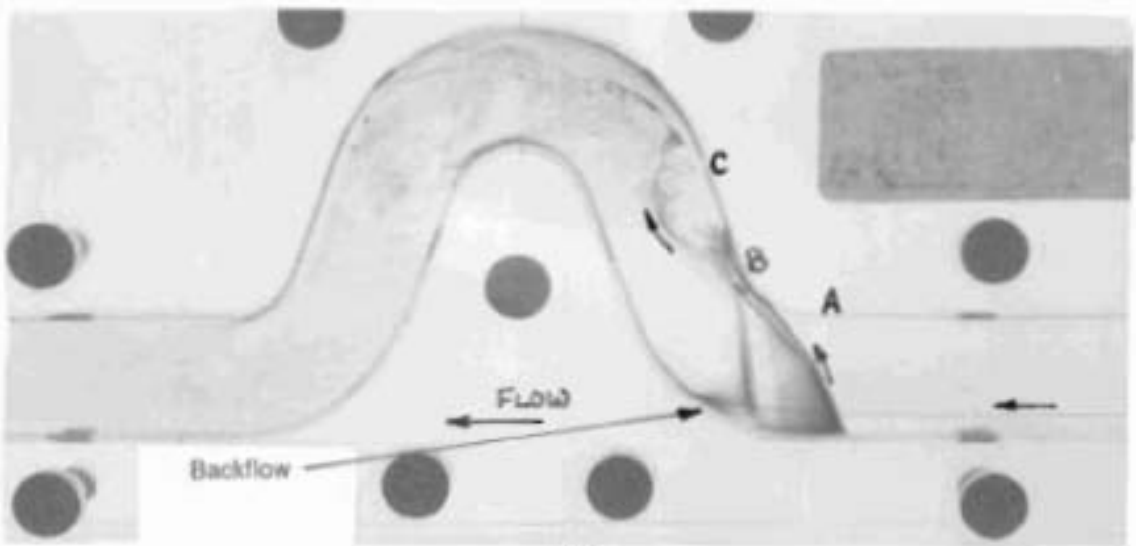

(c)

Plate 5.25a-c: Change in the Positicn of the Vortical Structure with Reynolds Number: (a) Re = 288 (b) Re = 978 (c) Re = 2080.

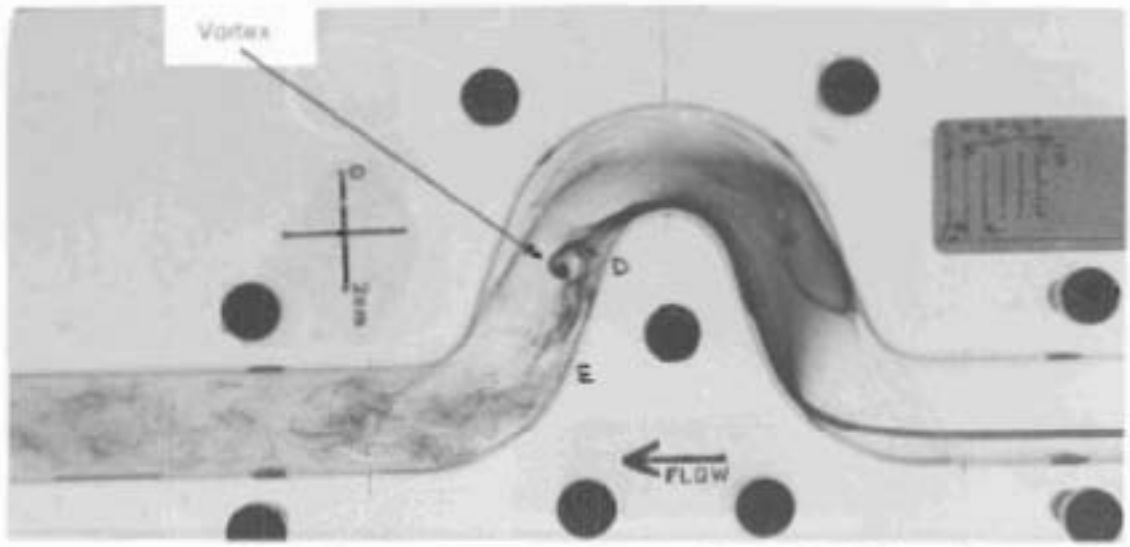

Plate 5.26: A Vortex Forming from the Separated Shear Layer ir the Distal Limb DE, Re = 1202.

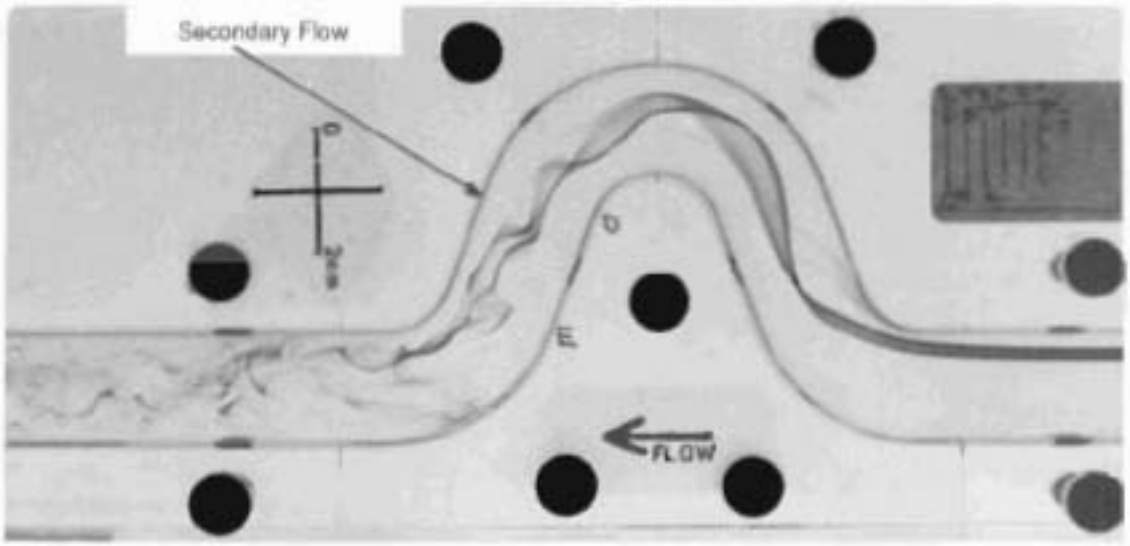

Plate 5.27: Secondary Flow in the Distal Limb, Re = 746.

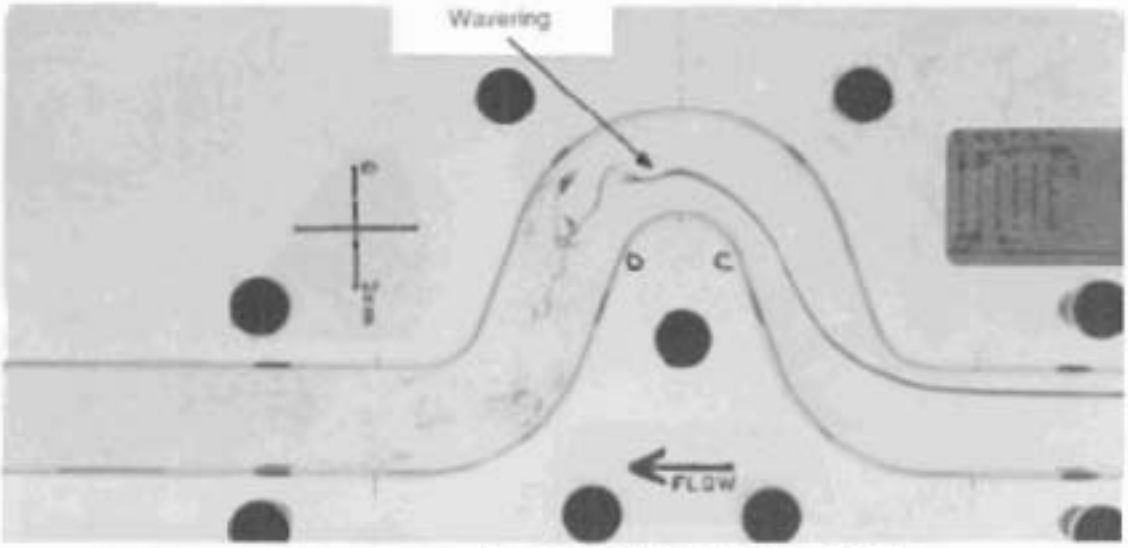

Plate 5.28: Wavering in the Medial Bend, Re = 2004.

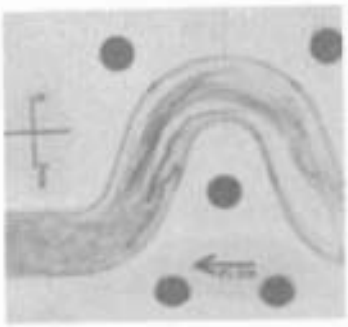

a) t = 0

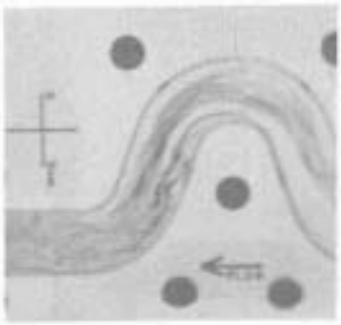

b) t = 38 ms

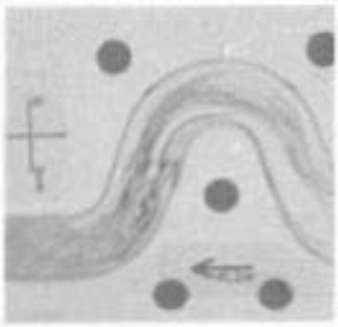

c) t = 75 ms

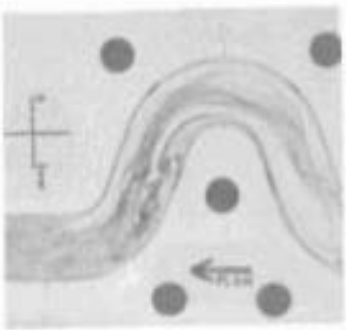

d) t = 113 ms

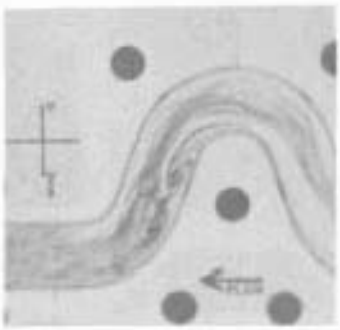

e) t = 150 ms

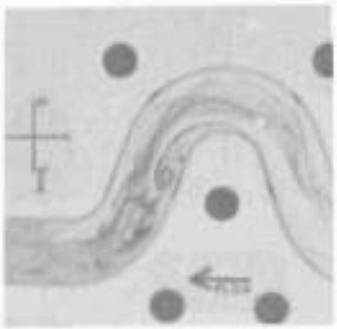

f) t = 188 ms

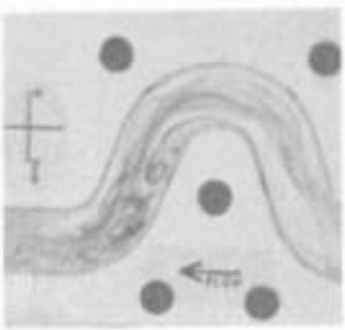

g) t = 225 ms

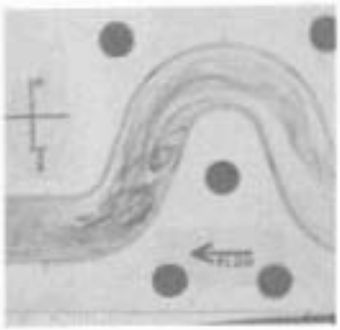

h) t = 263 ms

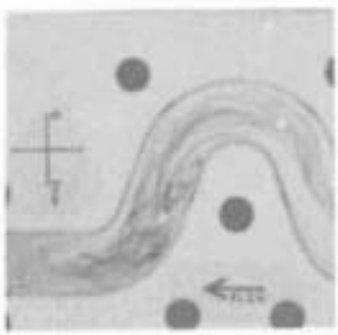

i) t = 300 ms

Plate 5.29a-i: Formation and Dissolution of a Vortex in the Distal Limb, Re = 1132.

2.67 Hz.The wavering motion appeared to be coupled to the formation of vortices from the shear layer.

At Re > 1500, flow was too unsteady for the flow pattern to be satisfactorily observed.

Backflow in the medial bend was observed in the separation bubble at the inner bend wall and (unexpectedly) at the entrance of the mid-bend, C, at the outer side. The latter backflow was slight and indistinct and was part of a stagnant vortex-shaped structure (Plate 5.30).

Downstream of D, the flow pattern was difficult to educe because of upstream distortion of the dye-streams.

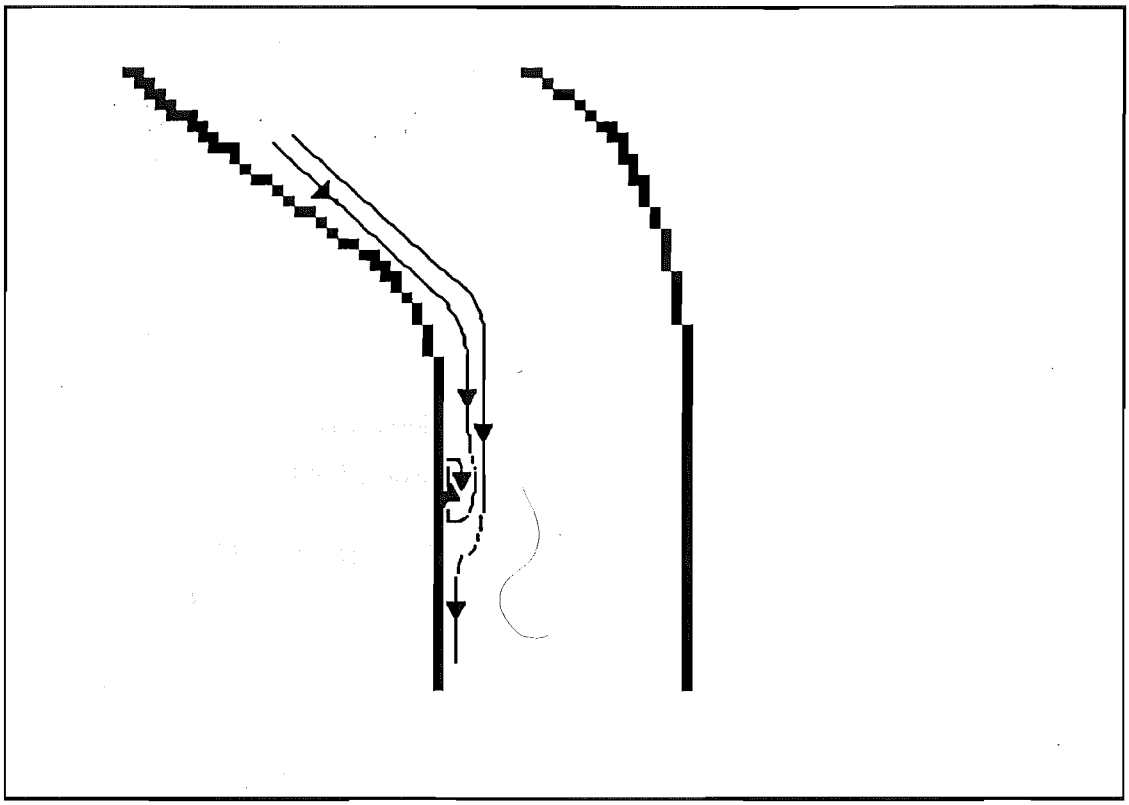

Figure 5.11
Separation in the distal bend

The backflow region initiated at the inner medial bend extended downstream along the wall of the straight section DE at $\alpha = 180°$ as far as the mid-distal bend at Re = 385, but the extent of the region decreased with increased flowrate. Entrainment of

the shear layer at the higher flowrates eventually made it difficult to educe the structures of flow downstream. The backflow region was asymmetric.

Another separation region was observed in the distal stem near the wall at $\alpha =$ 0°, downstream of F as in Plates 5.31, 5.32a-c and figure 5.11. This backflow was slow-moving at low flowrates and occupied a thin layer aligned with P (ie: normal to the wall), extending out about 0.25 diameters towards the centre of the tube.

The separation length decreased and the region became confined closer to the wall at higher flowrates, while the backflow became more disturbed. At Re = 420, the backflow region extended from F to about 0.9 diameters downstream, while at Re = 1092 it had shortened to a region extending from 0.10 diameters upstream of F to 0.6 diameters downstream.

This region was the least stable of all the separation regions and became indistinct at the higher flowrates.

5.2.1.3 Uniform Velocity Entrance Conditions:

A brief study was made of the flow under conditions of uniform entrance velocity, obtained by inserting a bundle of straws (with diameter 13% of the tube diameter) into the tube just upstream of the proximal bend.

The main difference between this flow and that with a fully-developed laminar entrance profile appeared in the proximal half of the model. Circumferential flow was not observed in the proximal stem, OA and was considerably decreased in the proximal bend AB and proximal limb BC. Backflow was not observed in the proximal bend.

Separation occurred at the inner proximal bend (Plate 5.33) and backflow along the $\alpha = 180°$ azimuth of the proximal limb was observed (Plate 5.34).

The most significant difference between the uniform velocity condition and the Poiseiulle entrance condition was the lack of the imbedded vortex structure in the proximal limb of the former condition. The backflow region in the proximal limb was therefore much simpler (Plate 5.34).

Flow appeared to be steady for a greater distance through the tube (Plate 5.35).

Backflow was observed at the $\alpha = 180°$ azimuth of the distal limb DE and the $\alpha = 0°$ azimuth of the distal stem FG (Plate 5.33).

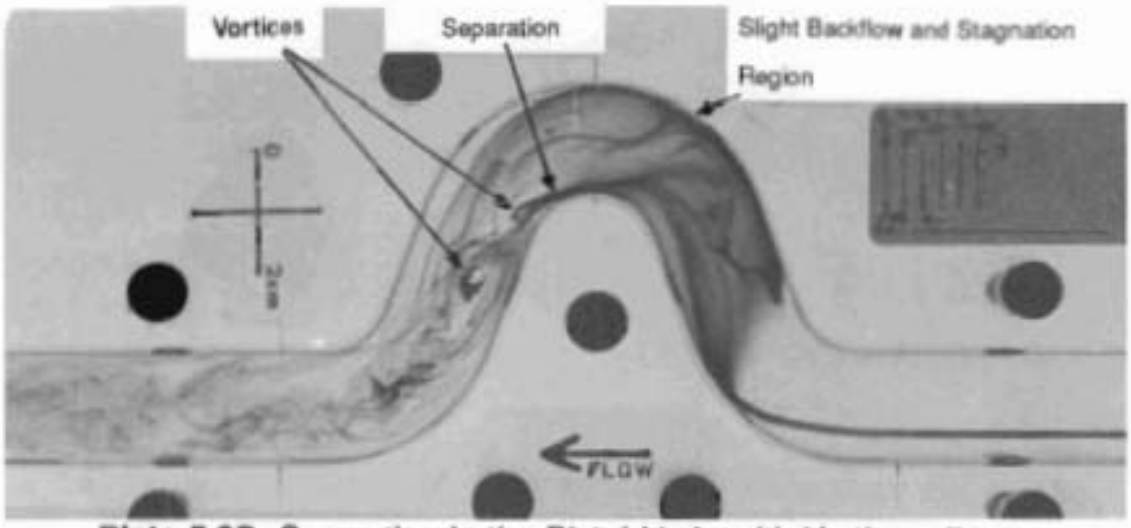

Plate 5.30: Separation in the Distal Limb, with Vortices, Re = 1151.
(Note also, the structure at the outer medial bend wall, with "tail" draining into the middle of the medial bend. Slight backflow was observed here intermittently.)

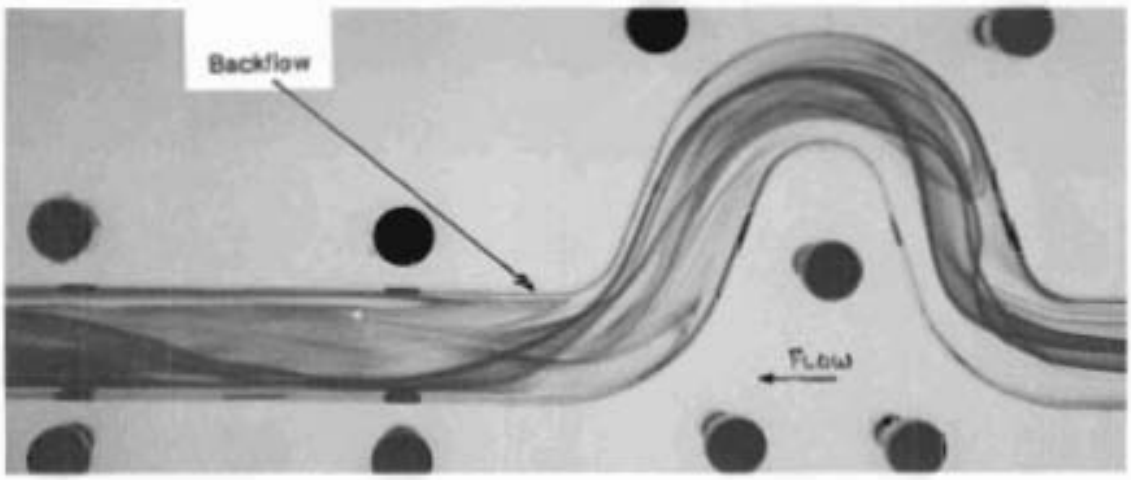

Plate 5.31: Backflow at $\alpha = 0°$ in the Distal Stem FG, Re = 459.

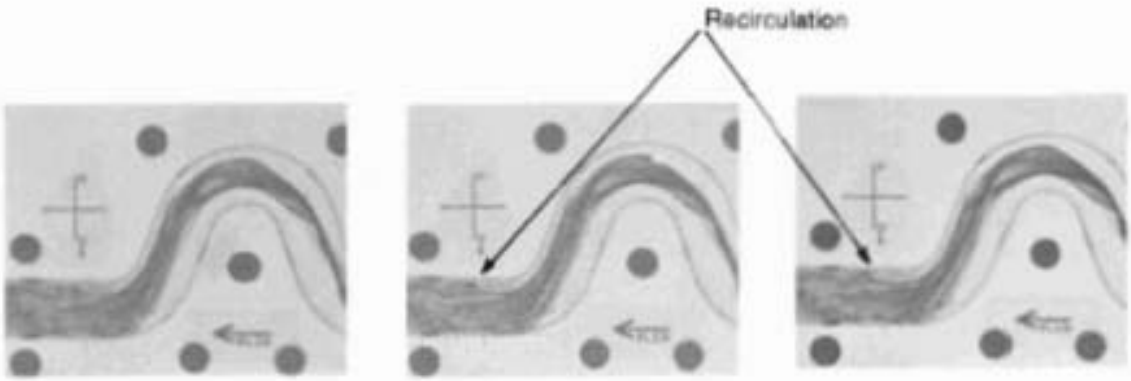

a) t = 0 b) t = 50 ms c) t = 100 ms

Plate 5.32a-c: Recirculation in the Distal Stem, Re = 1132:
(a) time t = 0 (b) t = 50 msec (c) t = 100 msec.

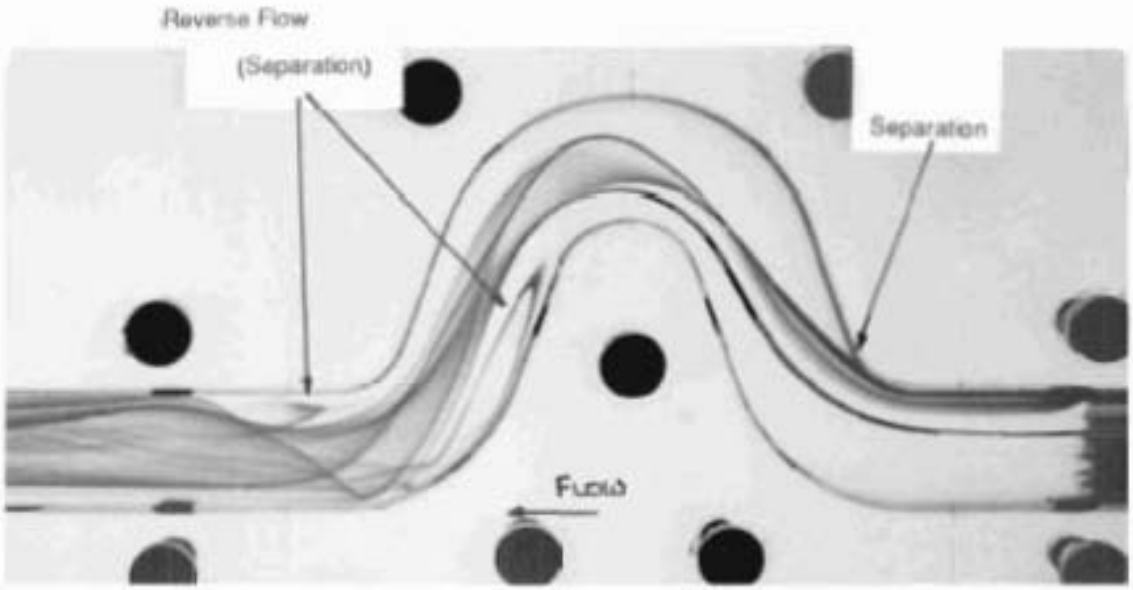

Plate 5.33: Uniform Velocity Entrance Condition, Re = 463.

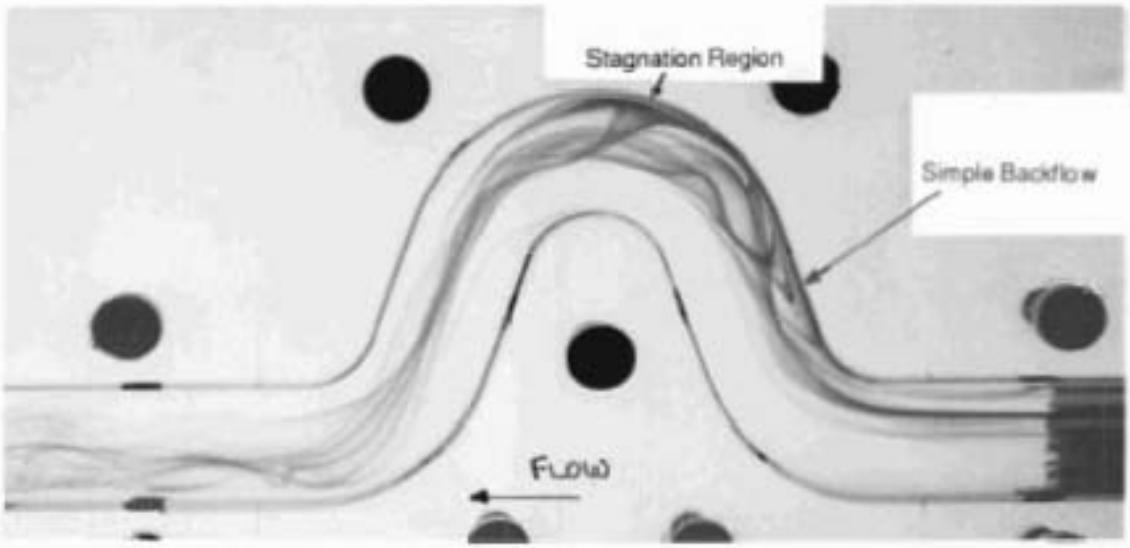

Plate 5.34: Uniform Velocity Entrance Condition, Re = 756.

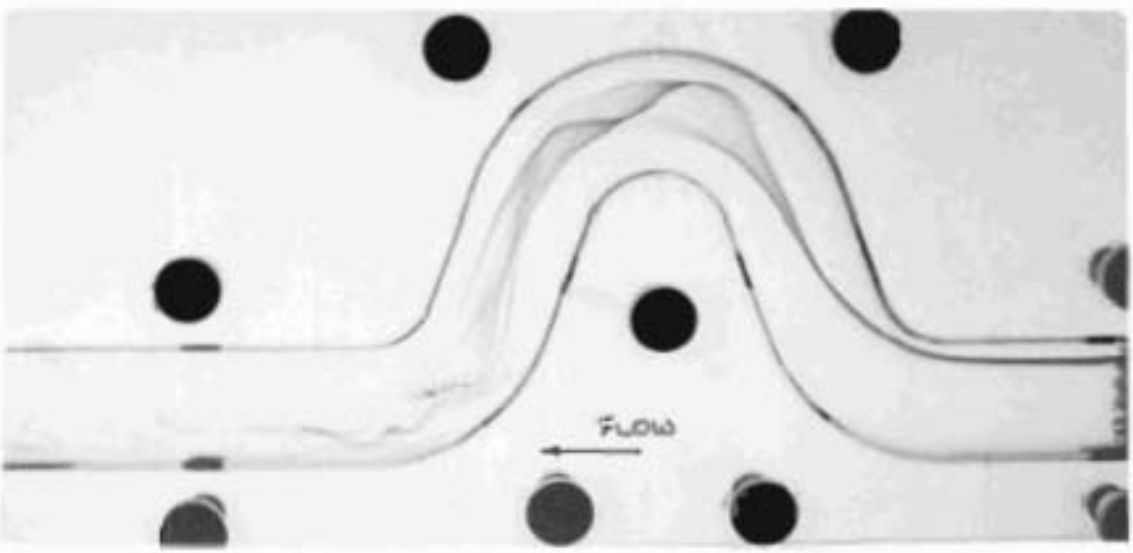

Plate 5.35: Uniform Velocity Entrance Condition, Re = 1023.

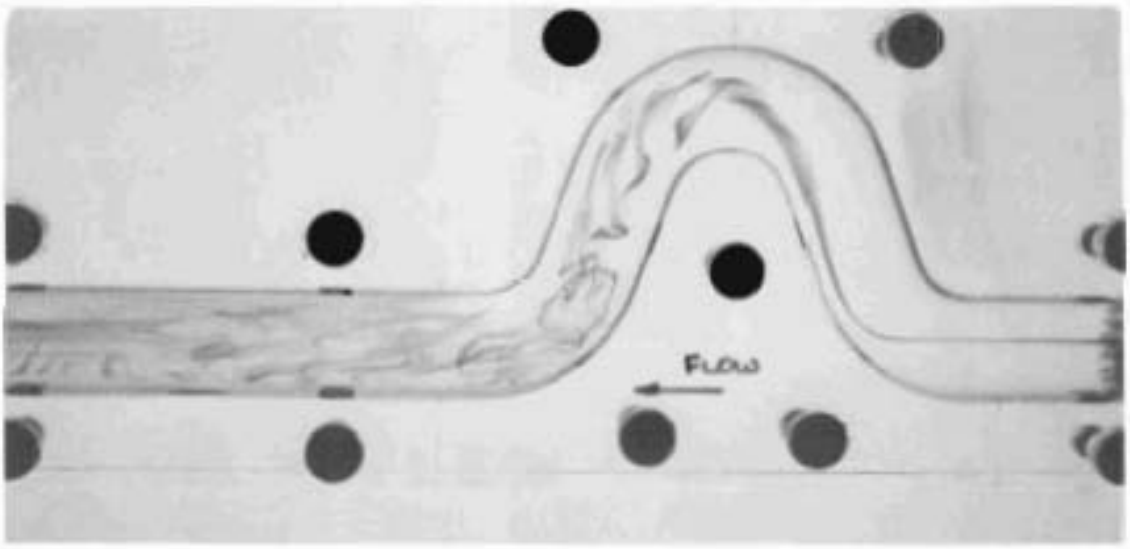

Plate 5.36: Jet Entrance Condition, Re_{tube} = 102, Re_{jet} = 816.

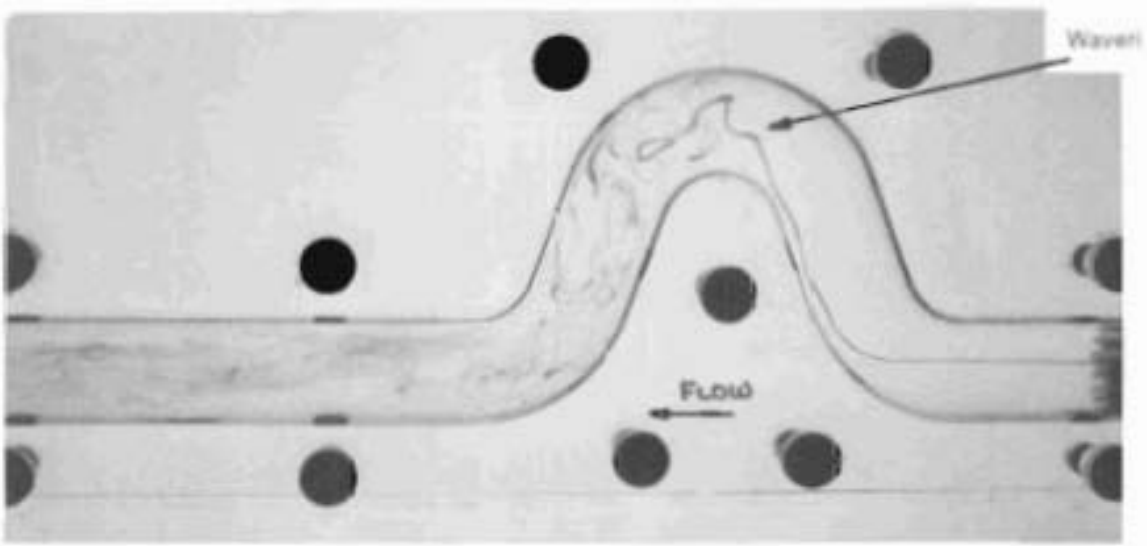

Plate 5.37: Jet Entrance Condition, Re_{tube} = 330, Re_{jet} = 2640.

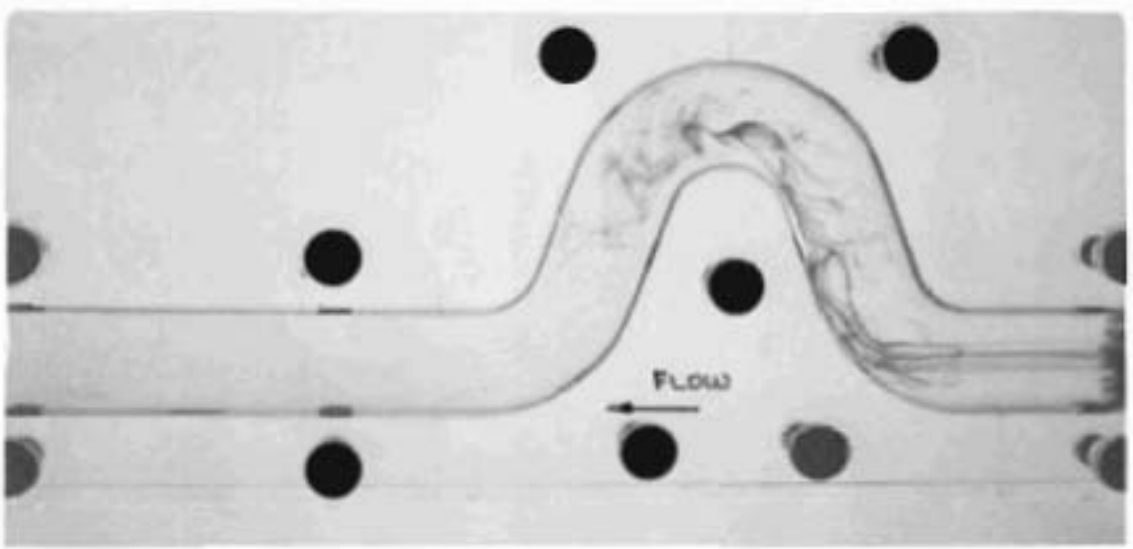

Plate 5.38: Jet Entrance Condition, Re_{tube} = 470, Re_{jet} = 3760.

A slight stagnation region at the outer medial bend wall ($\alpha = 0°$, $\theta_{cd} = 60°$) was observed at Re = 756 (Plate 5.34) similar to that seen under Poiseiulle entrance conditions in Plate 5.30.

5.2.1.4 Jet Entrance Conditions:

A brief study of flow resulting from a jet entrance condition was made (where the jet was formed by blocking all but the central straw in a bundle of straws inserted into the tube as above).

Flow appeared to be dominated by the characteristics of the jet, rather than the geometry of the model. Flow became unsteady at the mid-medial bend at a tube Re of only 100 (Plate 5.36).

Slight wavering was seen in the proximal limb at Re = 330 (Plate 5.37). At Re above this, the flow became quite unsteady by the mid-proximal bend in the expected manner of an unsteady jet (Plate 5.38).

Turbulence appeared in the proximal bend and limb by Re = 769 (Plate 5.39).

5.2.2 Pulsatile Flow:

Photographs of the flow were taken at phase-angle intervals of $\Delta\Psi = 30°$, for a pulsatile flow with a period of 21.5 seconds (scaled by the Strouhal number from the pulse of 1.2 Hz in an average human male). The Reynolds number was set to a mean of 1500, with a flow variation amplitude of about 50% (ie: $750 \leq Re \leq 2250$). The position of the dyestream was limited to near the $\alpha = 180°$ azimuth of the tube, because disturbances were caused by the mean flow variation at the injection point in other parts of the tube. These flow disturbances gave rise to blobs of dye that travelled dowstream from the injection point. In still photographs of the flow, these could be mistaken for departures from streamline, laminar flow. Therefore, the flow visualisation was limited, in pulsatile flow, to the positions shown in Plates 5.40 on.?

The pairs of photographs in Plates 5.40a-d were taken from two consecutive flow cycles for one set phase angle in each case. A comparison of the pairs of plates for each set phase angle shows that the flow was qualitatively repeatable, except in those places where unsteady wavering of the dyestream (or local turbulence) occurred.

In Plates 5.40 e and f, several ring-like vortices can be seen about the entrance to the proximal bend. These vortices appeared to be shed downstream along the wall in the entrance region of the proximal bend at the highest flowrates. These appeared to be

generated from the upstream limit of the proximal bend backflow, described in section 5.2.1.1 and shown in figures 5.4 and 5.5.

A series of photographs was taken at consecutive 30° phase-angle intervals throughout one cycle (Plate 5.41a-m). Plate 5.41m is at an equivalent phase angle to 5.41a, but in the subsequent cycle. As in steady flow, the vortical structure at the α = 0° azimuth of the proximal limb was positioned closer to the proximal bend with increased instantaneous flowrate. It appeared to be lost at the initial acceleration stage of the flow cycle (Plate 5.40d), but was fully re-established 60° later in the phase(Plate 5.40f). Unsteadiness began at the distal end of the model and propogated rapidly upstream with increasing flowrate. The flow appears, in the photographs, to become steady from the upstream end of the model under deceleration, but the mixing of the dyestream during the previous phase angles confuses this observation. The mixed dye seen downstream of steady flow in the model (as in Plate 5.40b) could be the convected remnants of dye mixed by unsteadiness at a previous phase angle upstream.

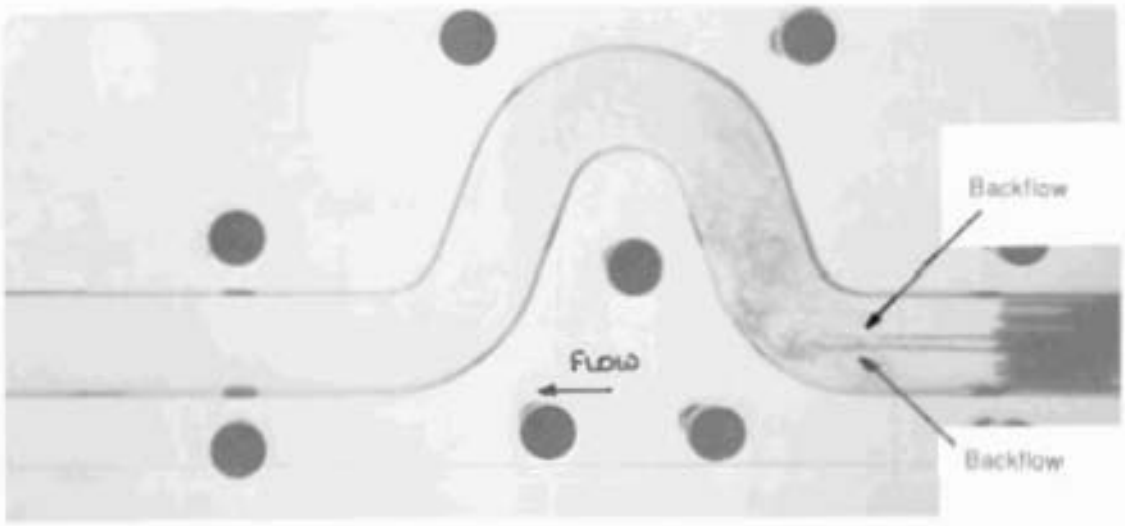

Plate 5.39: Jet Entrance Condition, Re_{tube} = 769, Re_{jet} = 6000.

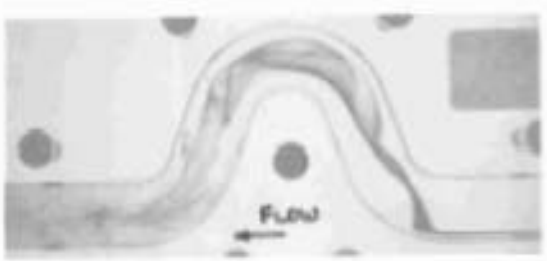

(a) Ψ_1, cycle 1

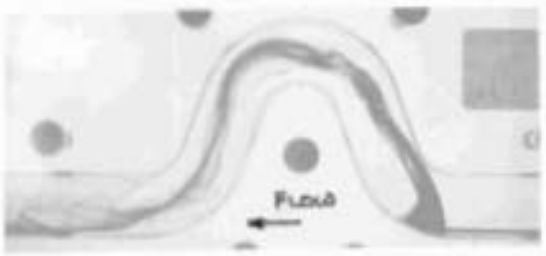

(b) Ψ_2, cycle 1

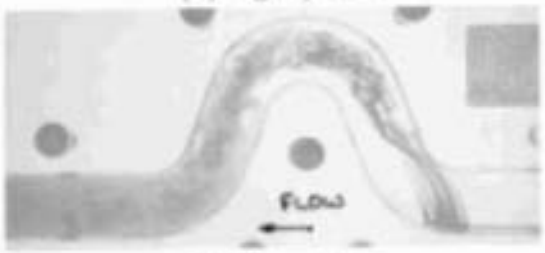

(c) Ψ_3, cycle 1

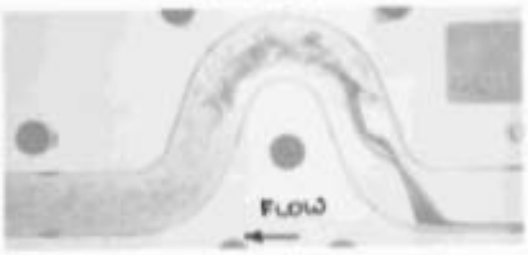

(d) Ψ_4, cycle 1

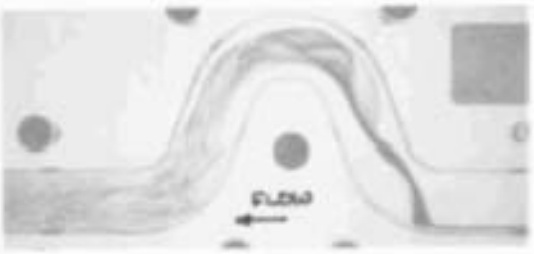

(e) Ψ_1, cycle 2

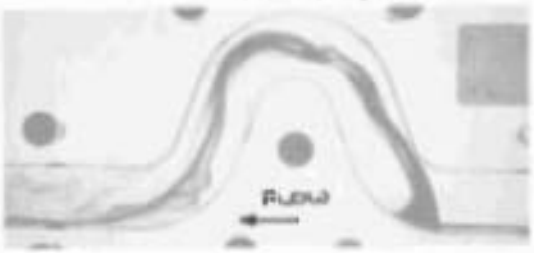

(f) Ψ_2, cycle 2

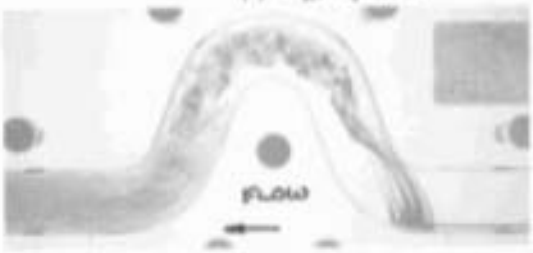

(g) Ψ_3, cycle 2

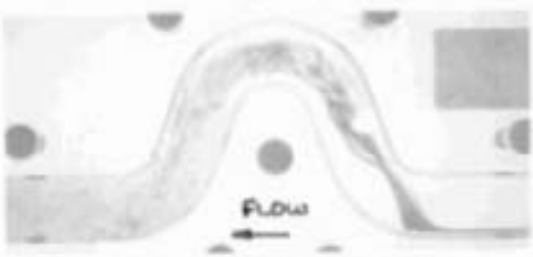

(h) Ψ_4, cycle 2

Plate 5.40a-h: Repeatability of Pulsatile Flow, Re_{mean} = 1500, Flow Amplitude = 50% of Mean: (a) Ψ_1, cycle 1 (b) Ψ_2, cycle 1 (c) Ψ_3, cycle 1 (d) Ψ_4, cycle 1 (e) Ψ_1, cycle 2 (f) Ψ_2, cycle 2 (g) Ψ_3, cycle 2 (h) Ψ_4, cycle 2.

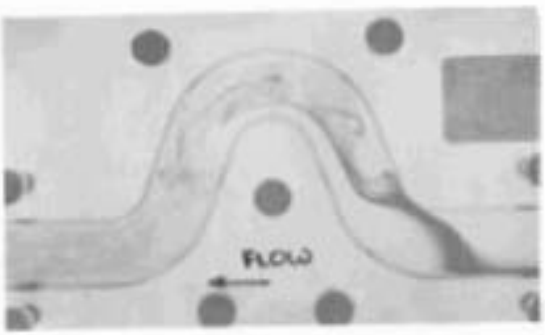

a)Ψ = 0°

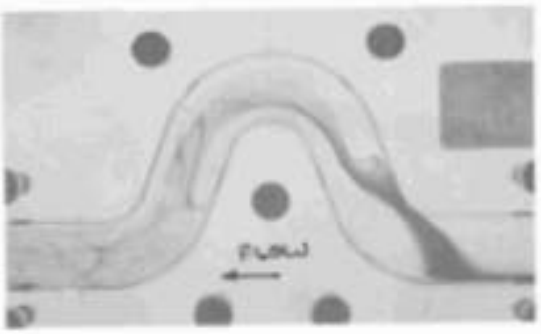

b)Ψ = 30°

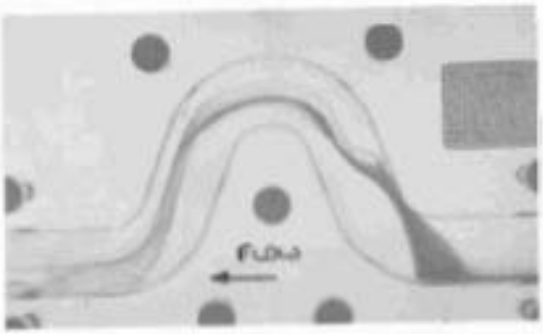

c)Ψ = 60°

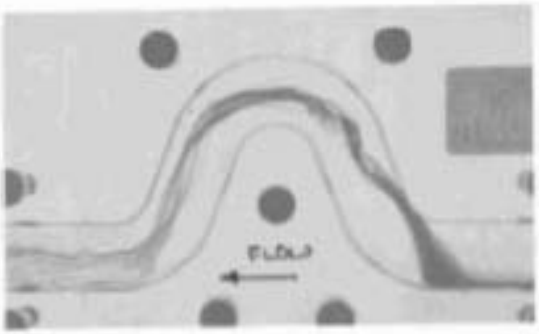

d)Ψ = 90°

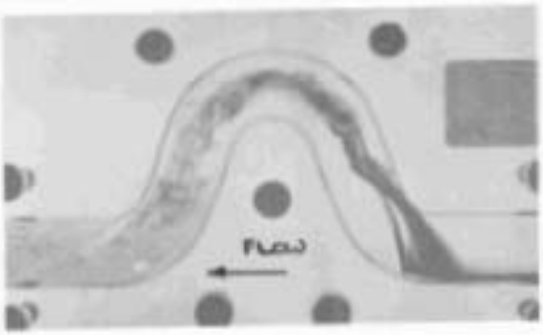

e)Ψ = 120°

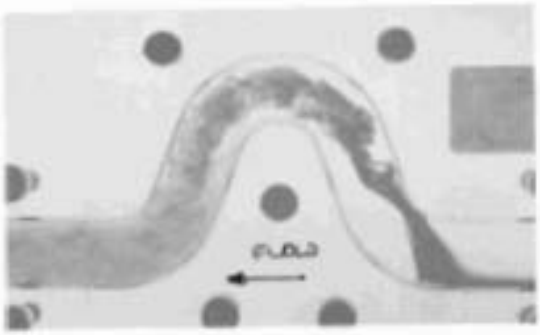

f)Ψ = 150°

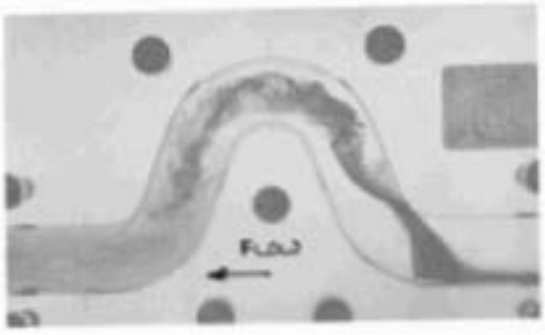

g)Ψ = 180°

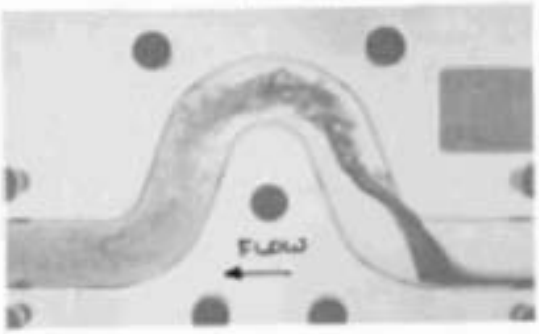

h)Ψ = 210°

Plate 5.41a-m: Pulsatile Flow over One Cycle at Phase Angle Intervals of 30°, Re_{mean} = 1500, Flow Amplitude = 50% of Mean: (a) Ψ = 0° (b) Ψ = 30° (c) Ψ = 60° (d) Ψ = 90° (e) Ψ = 120° (f) Ψ = 150° (g) Ψ = 1800° (h) Ψ = 210° (i) Ψ = 240° (j) Ψ = 270° (k) Ψ = 300° (l) Ψ = 330° (m) Ψ = 360° (or 0° of the next cycle). (continued overleaf...)

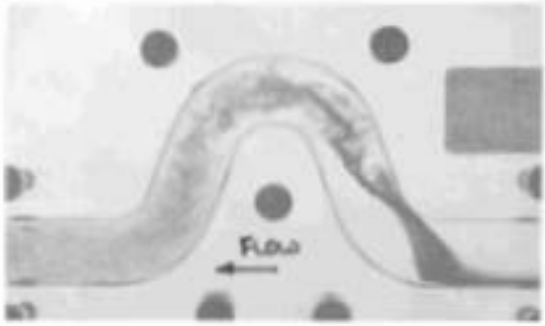

i) $\Psi = 240°$

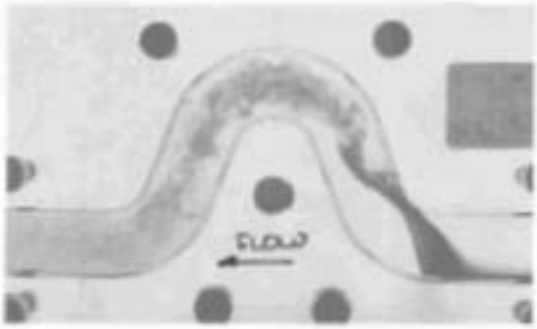

j) $\Psi = 270°$

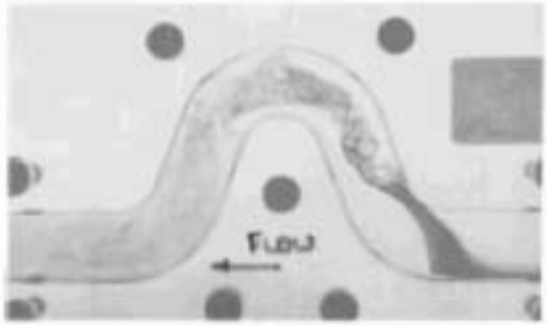

k) $\Psi = 300°$

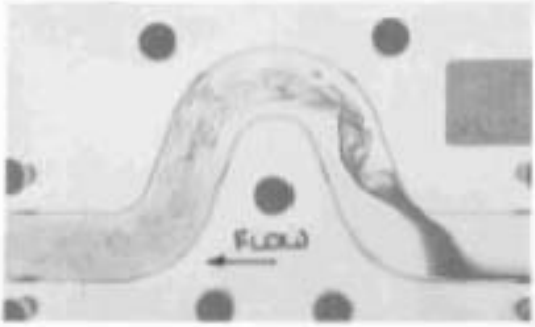

l) $\Psi = 330°$

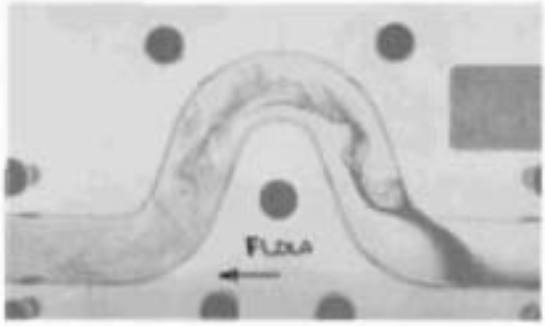

m) $\Psi = 360°$

Plate 5.41 a-m (cont...): Pulsatile Flow over One Cycle at Phase Angle Intervals of 30°, Re_{mean} = 1500, Flow Amplitude = 50% of Mean:

5.3 Laser Doppler Anemometry Results - Steady Flow:

5.3.1 Axial Velocity Plots:

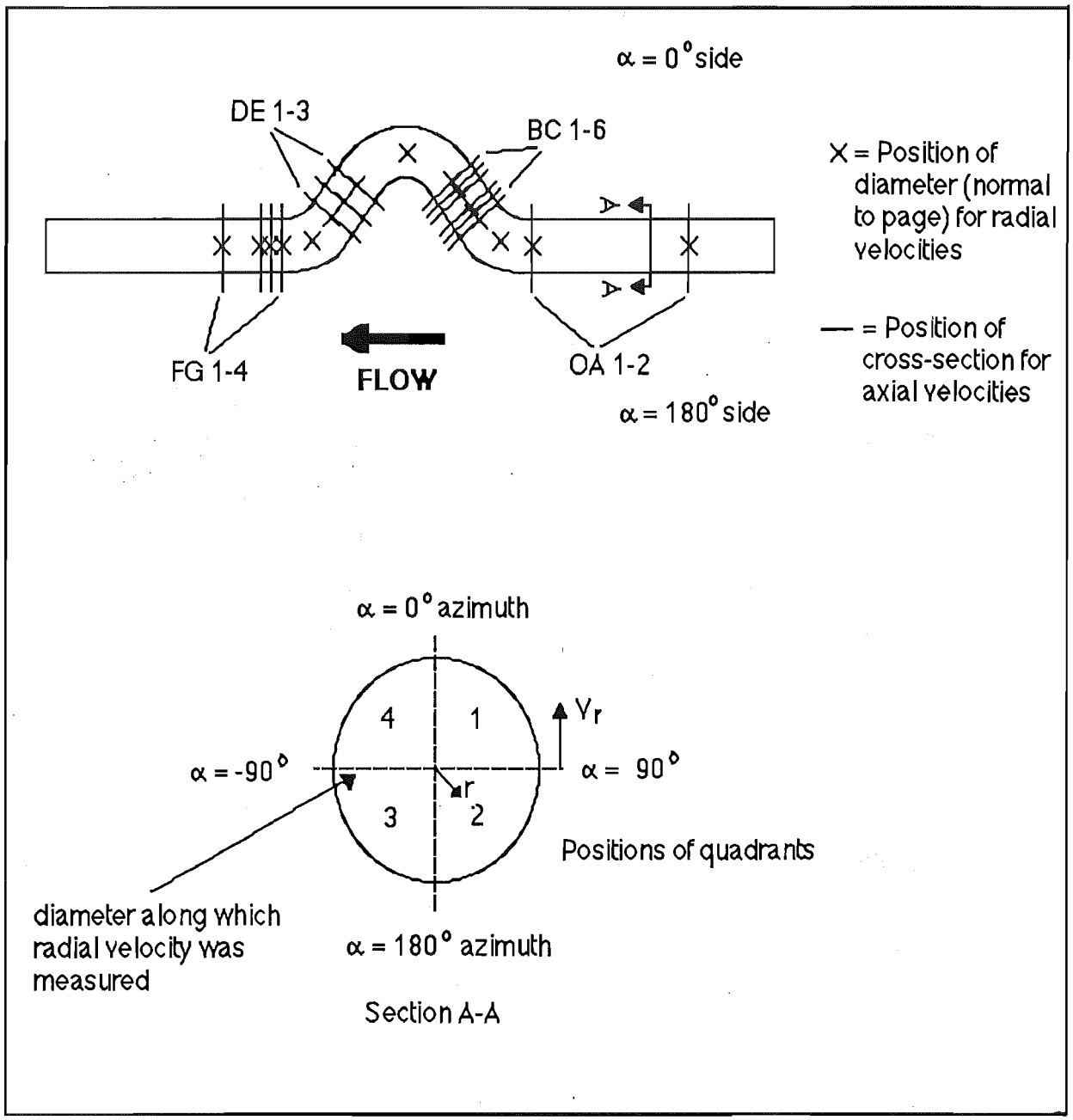

Figure 5.12
Nomenclature

5.3.1.1 Upstream Flow

The following axial velocity contour plots were generated using the U.S.A. National Centre for Atmospheric Research (NCAR) subroutine CONRAN.FOR, in

general from measurements made by LDA at Re = 1500 ± 20. As a check on this programme, data was calculated from the equation for Poiseiulle laminar flow (Equation 5-1) in a straight pipe and used to generate the isovels shown in figure 5.13:

$$\frac{u}{V} = 2\left(1 - \frac{r'^2}{r_w^2}\right) \qquad (5\text{-}1)$$

; where r_w = pipe radius (20 mm); V = mean velocity (8 cm s^{-1}); and u = velocity (in cm s^{-1}).at radius r' (mm).

The result is the expected series of concentric rings centred on the pipe's central axis, corresponding to a parabolic flow profile when viewed from an upstream position on the pipe's central axis. Some of the outer contours in all of the contour plots are incomplete at the α = +90°, -90° and 180° sides of the plots. This was due to the coordinates used to draw the plots, rather than the contour-generating routine. It can be seen that completion of the plots by extrapolation would not influence the shape of the isovels.

In figure 5.14, the triangulation used by CONRAN.FOR is shown. The best contours are obtained when the lines between data points form isoceles triangles. Data points are located at the intersection points of the lines. The measured data used to generate the first experimental isovel contours are plotted in their measurement positions in figure 5.15 to give an indication of the smoothing carried out by the contour plotting routine.

Figure 5.15 shows the measured isovel contours of a cross-section of the flow situated 8 diameters upstream of the entrance to the proximal bend, A. The contours show two differences from the ideal Poiseiulle contours of figure 5.13. Firstly, the maximum velocity was shifted from the centre of the tube to a position in the 1st quadrant (figure 5.15(A)). ie: the flow was asymmetric, with skewed contours.

Secondly, the maximum velocity in the tube was only 13.1 cm s^{-1}, compared with the 16 cm s^{-1} expected (twice the mean velocity of 8 cm s^{-1}).

The contours in figure 5.16 represent the axial isovels 0.15 diameters upstream of A, the proximal bend entrance. As in the upstream contour (figure 4), the maximum velocity was shifted off the central axis towards the inner wall of the bend (A). This feature was more pronounced at this position than upstream. A region of high velocity gradient (high shear) existed about the inner wall (B).

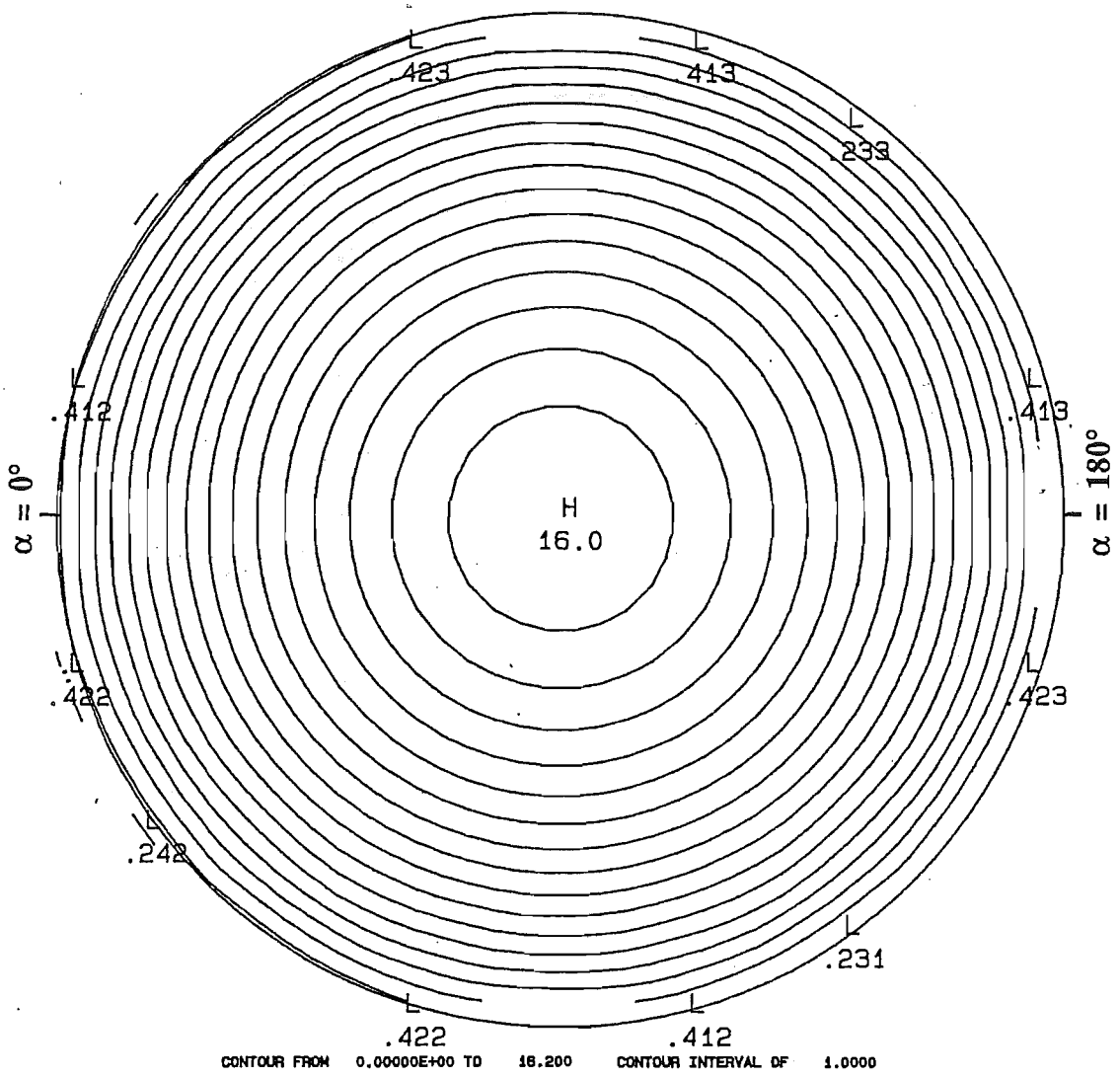

Figure 5.13: Ideal Poiseuille Flow Axial Isovels, Re = 1500.

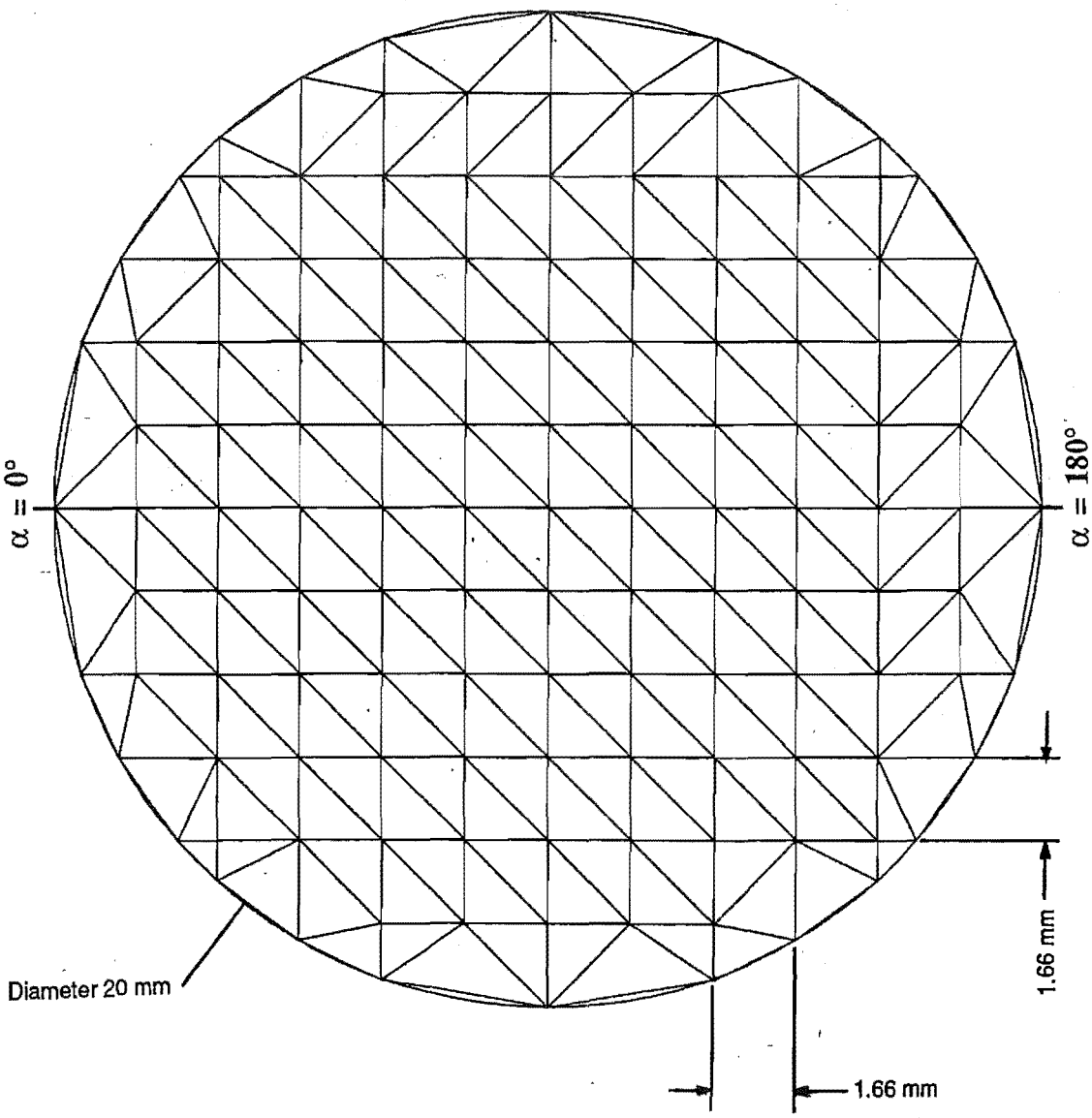

Figure 5.14
Triangulation used by the Contour Plotting Routine.

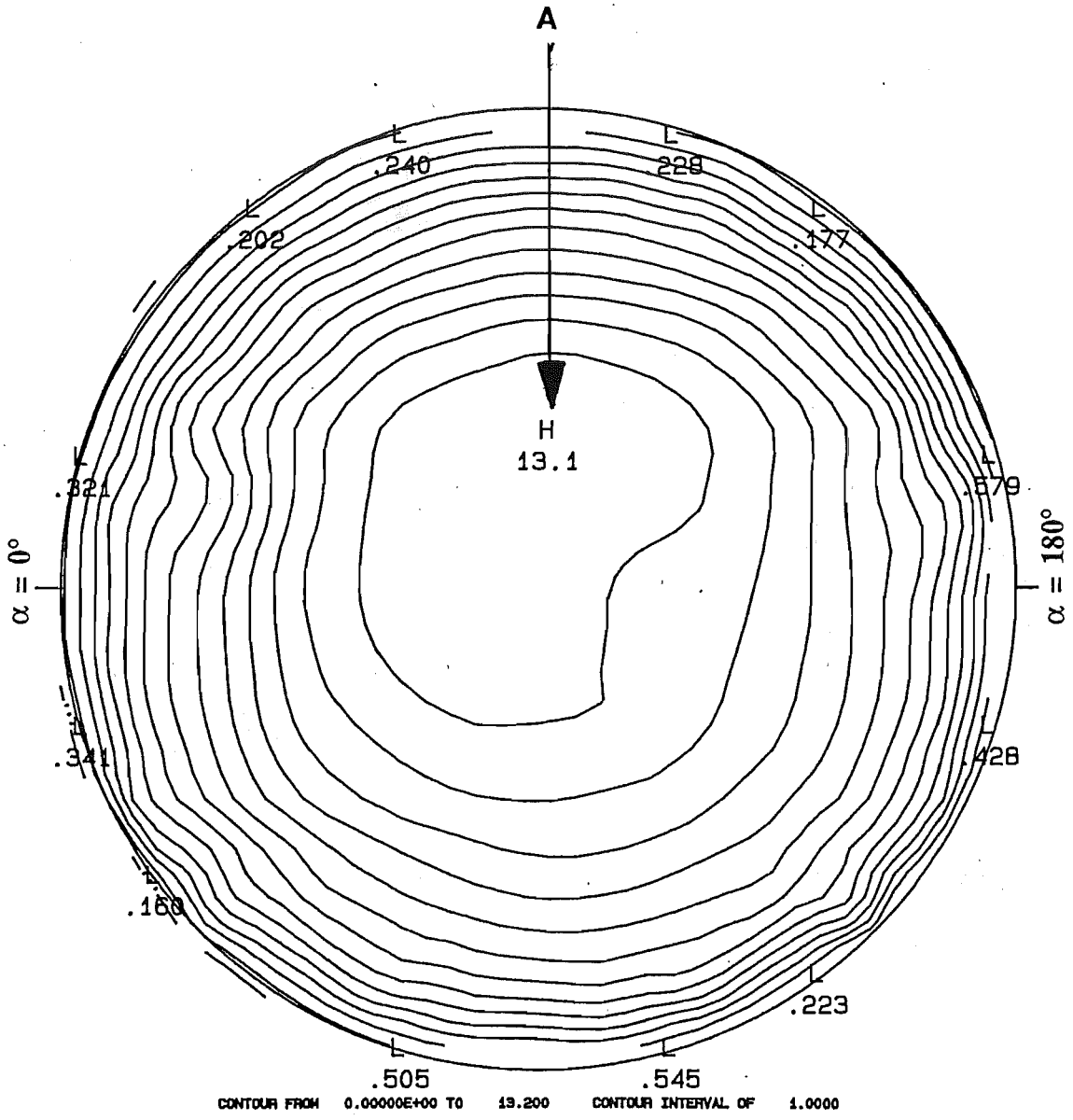

Figure 5.15

OA1, 8 Diameters Upstream of A, Proximal Stem, Re = 1500.

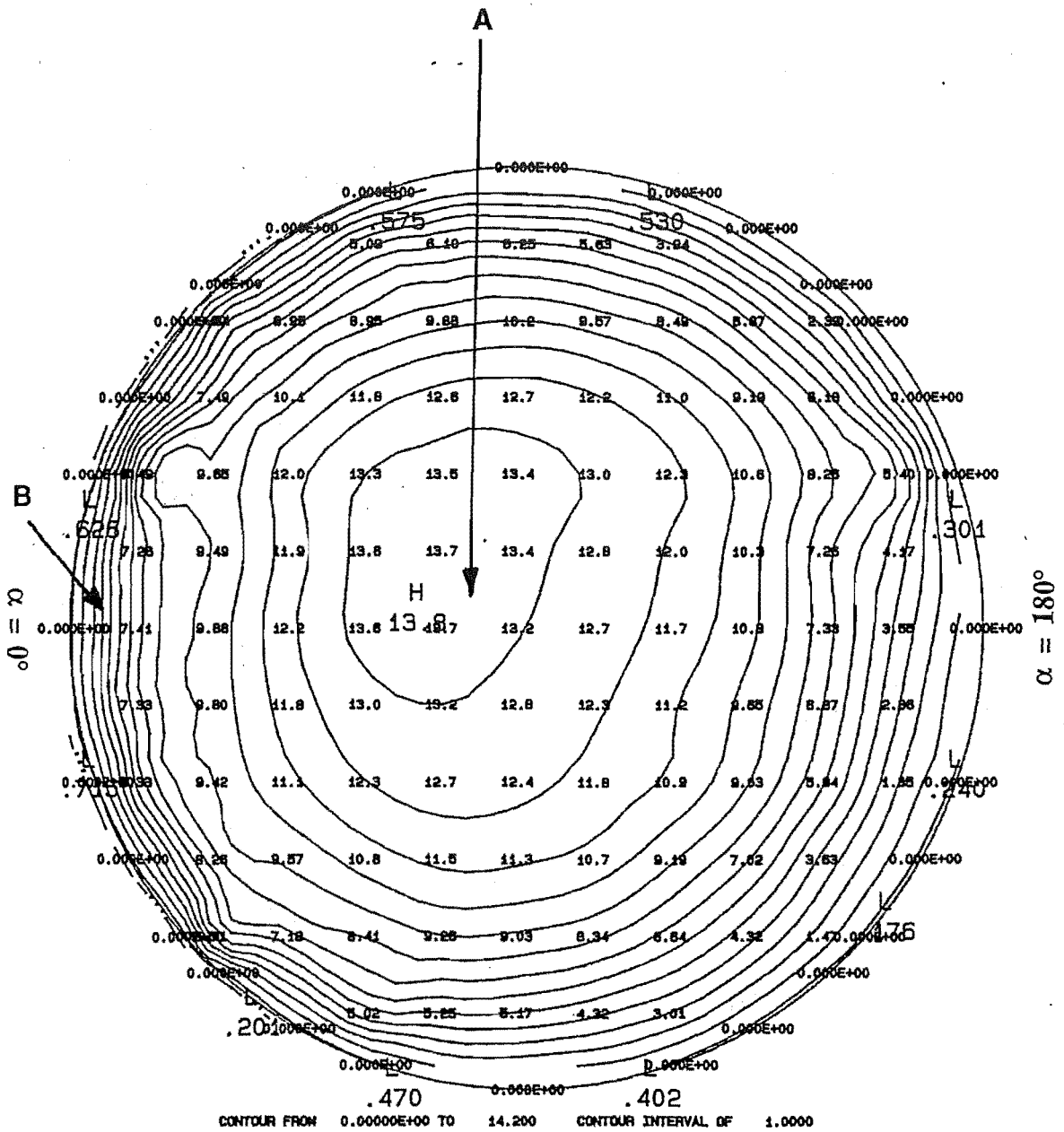

Figure 5.16: OA2, Proximal Stem, Re = 1500.

Three kinks occurred in the contours: two near the $\alpha = 0°$ azimuth and one near the $\alpha = 180°$ azimuth.

5.3.1.2 The Proximal Limb:

The contours taken near the exit of the proximal bend (0.15 diameters downstream of the exit of the proximal bend) shows (figure 5.17) several prominent features. Firstly the contours were asymmetric. Velocity highs on opposite sides of the plane of symmetry, P, located in quadrants 1 (A) & 4 (B and C) occurred at $\alpha = +70°$, $r = 0.36$ and $\alpha = -70°$, $r = 0.29$[1]. In the 4th quadrant, two distinct highs occurred, separated by a shear layer. The second high was positioned at $\alpha = -32°$, $r = 0.32$.

Only one high occurred in the 1st quadrant, closer to the wall, though the shape of the isovel contours at $\alpha = +42°$, $r = 0.32$ (ie: between it and the backflow region) suggests a similar (though weaker) structure (at D) to that in the 4th quadrant.

A steep velocity gradient (E) occurred around the $\alpha = 180°$ azimuth wall extending continuously between positions adjacent to the two highs (ie: form $\alpha = -55°$ to $\alpha = +62°$. A backflow region (F) existed at the $\alpha = 0°$ azimuth wall, between $\alpha = -3°$ and $\alpha = +24°$. The backflow region was asymmetric, with most of it lying in the 1st quadrant, extending 3-4 mm (0.15 - 0.2 diam) towards the middle of the tube. The region extended in a flattened layer about the wall towards the front of the tube.

The maximum velocity lay closest to the $\alpha = 180°$ azimuth wall. Between the separation region and the maximum velocity (where the contours were quite flat) there was a shear region consisting of a large central region (G) with contour lines normal to P, and a "valley" (H) with isovels parallel to P. The shape of the central feature (G) was similar to a basin. This shear layer appeared to be continuous with the high velocity gradient shear layer, which lay about the wall between $\alpha = -55°$ and $\alpha = +62°$, as mentioned above. The high at $\alpha = -32°$, $r = 0.32$ and the "phantom" high at $\alpha = +42$, $r = 0.32$ appeared to separate this shear layer from that bounding the backflow region. The structure of G and H constituted a free shear layer, separating the forward and reverse flows in this cross-section. Unlike a wall shear layer, or boundary layer, a free shear layer is not bounded and is prone to inherent unsteadiness.

Note that the maximum velocity was only about 11.5 - 12.5 cm s^{-1}, but was widely distributed over the tube cross-section.

---

[1] where r is non-dimensionalised by the tube diameter.

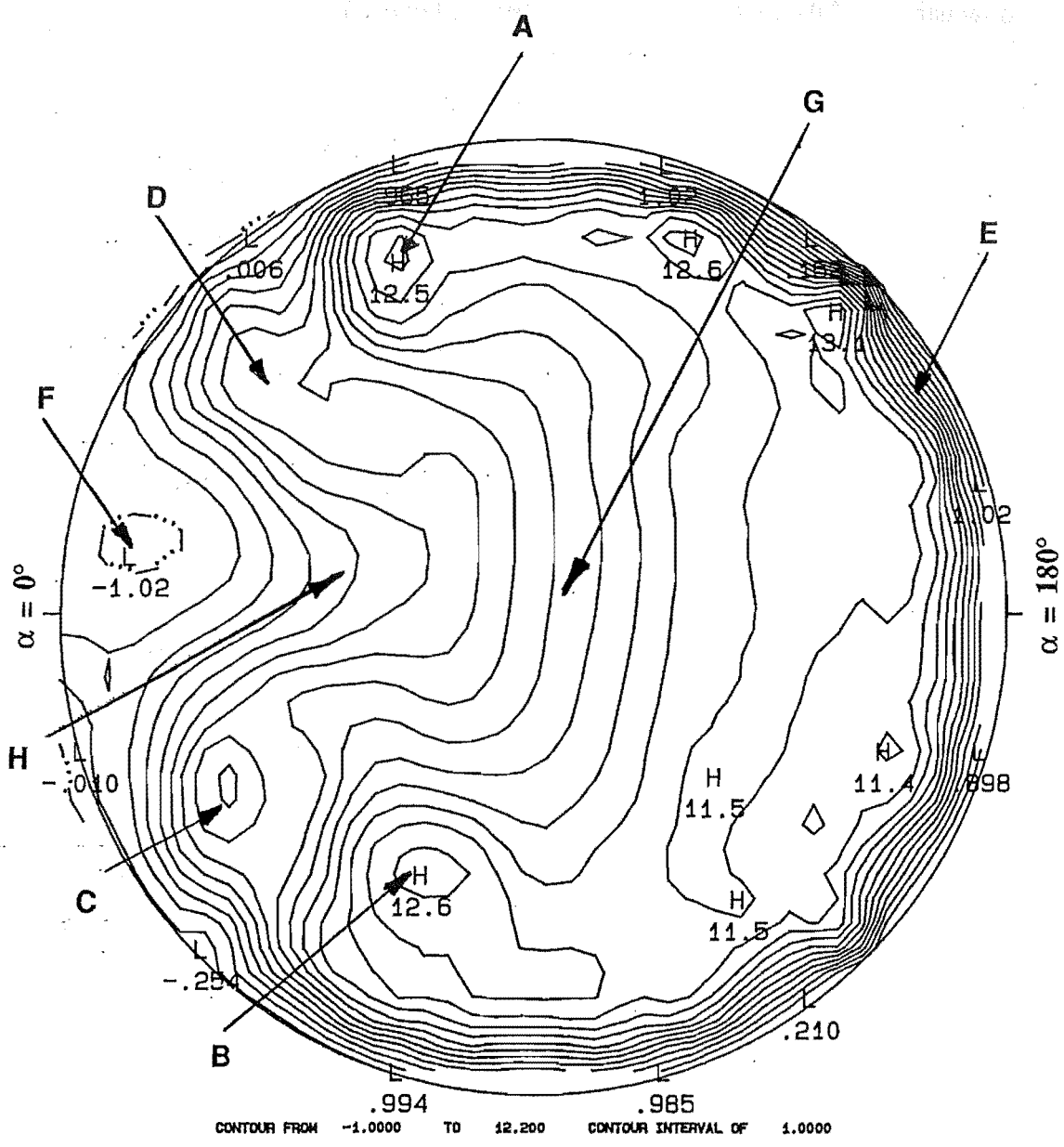

Figure 5.17

BC1, Proximal Limb, Re = 1500.

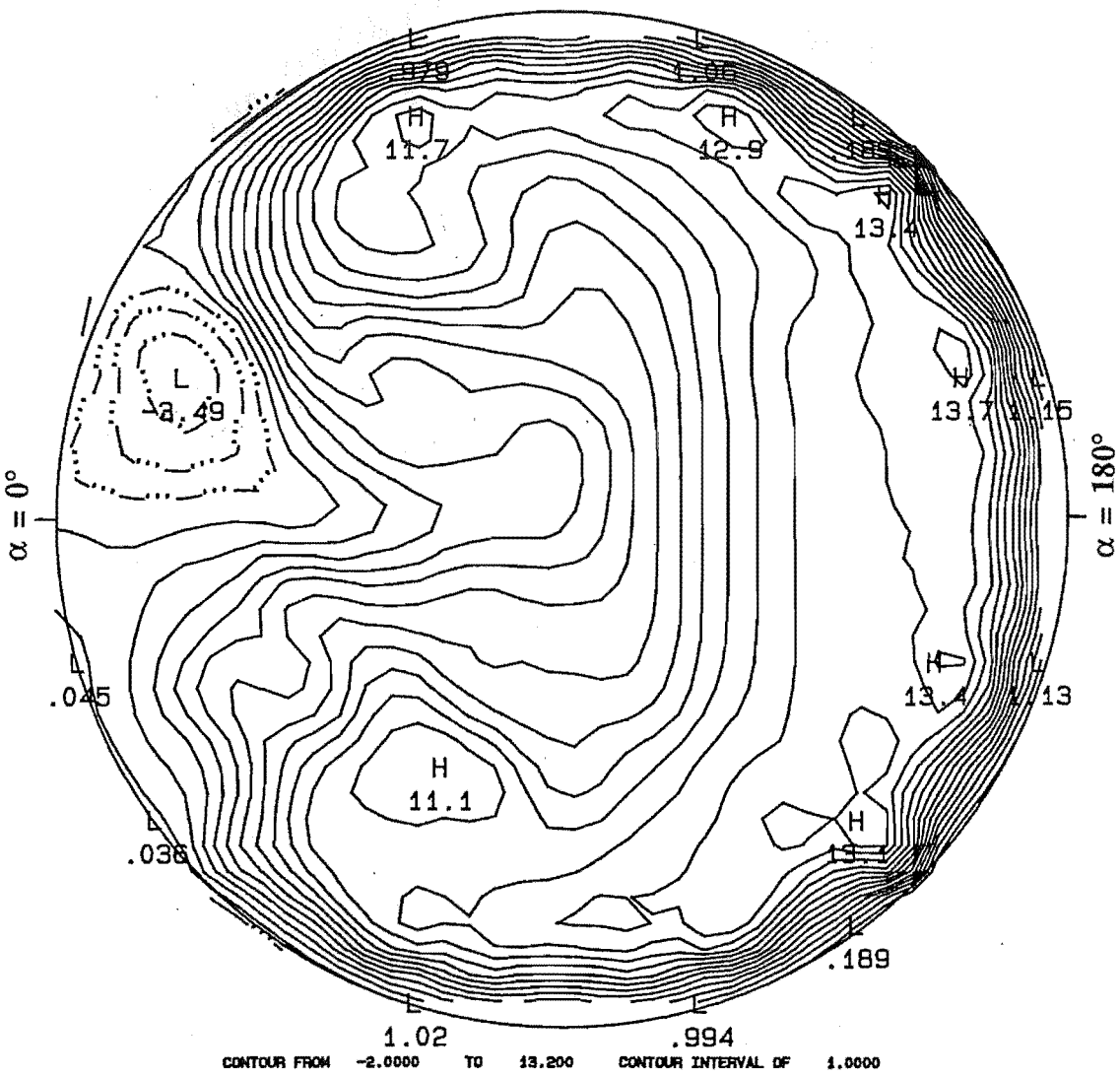

Figure 5.18

BC2, Proximal Limb, Re = 1500.

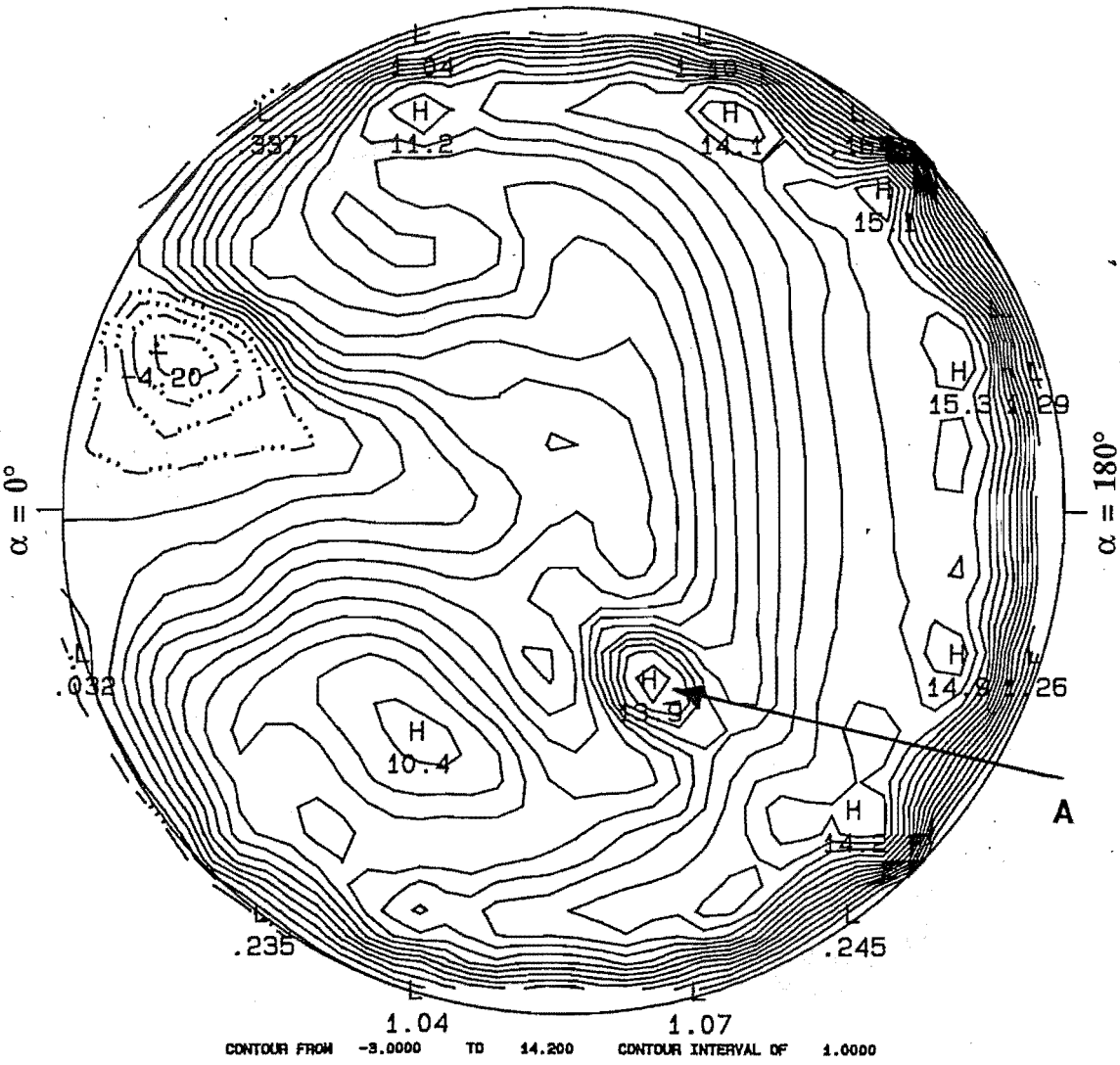

Figure 5.19
BC3, Proximal Limb, Re = 1500

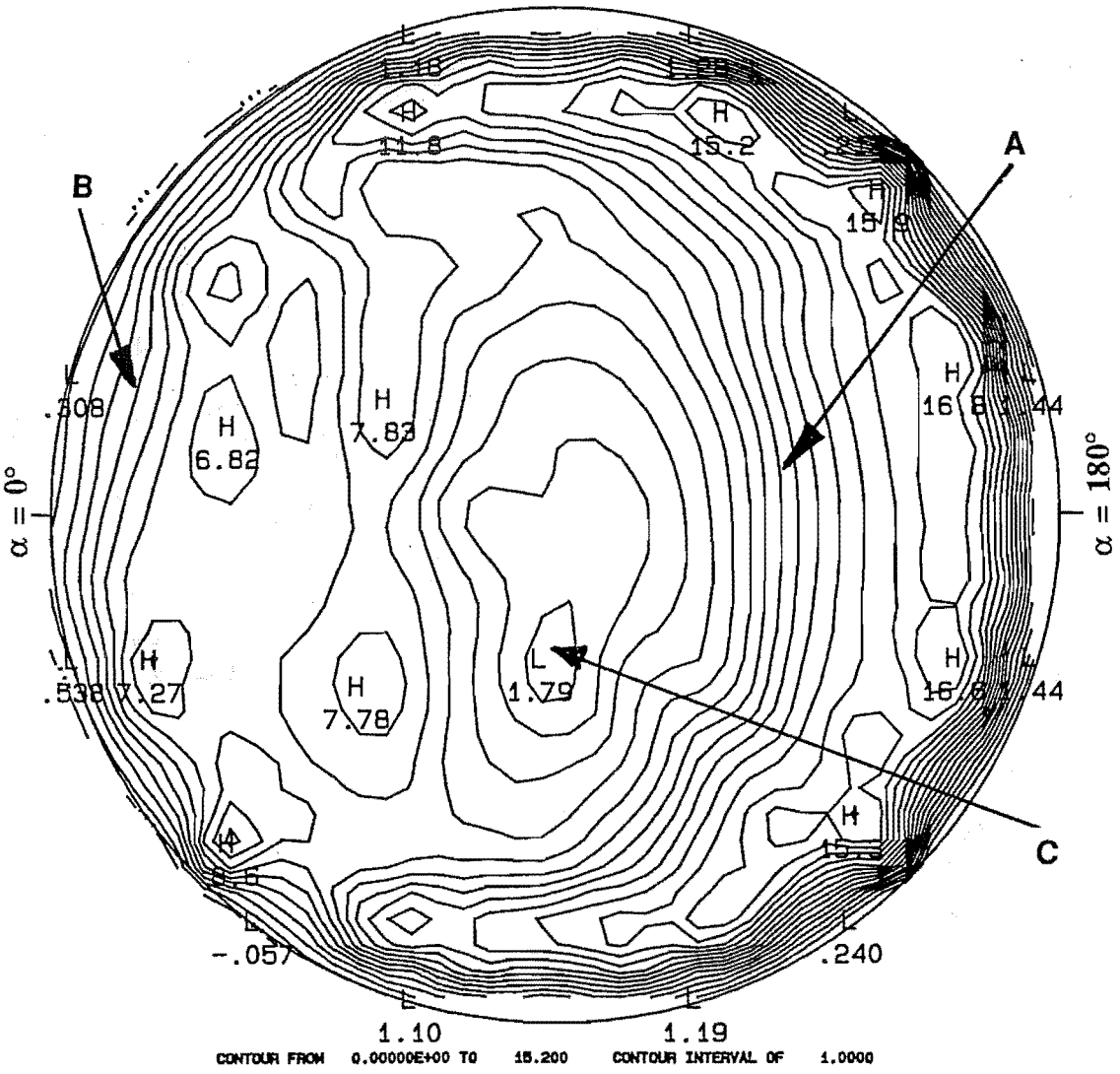

Figure 5.20

BC4, Proximal Limb, Re = 1500.

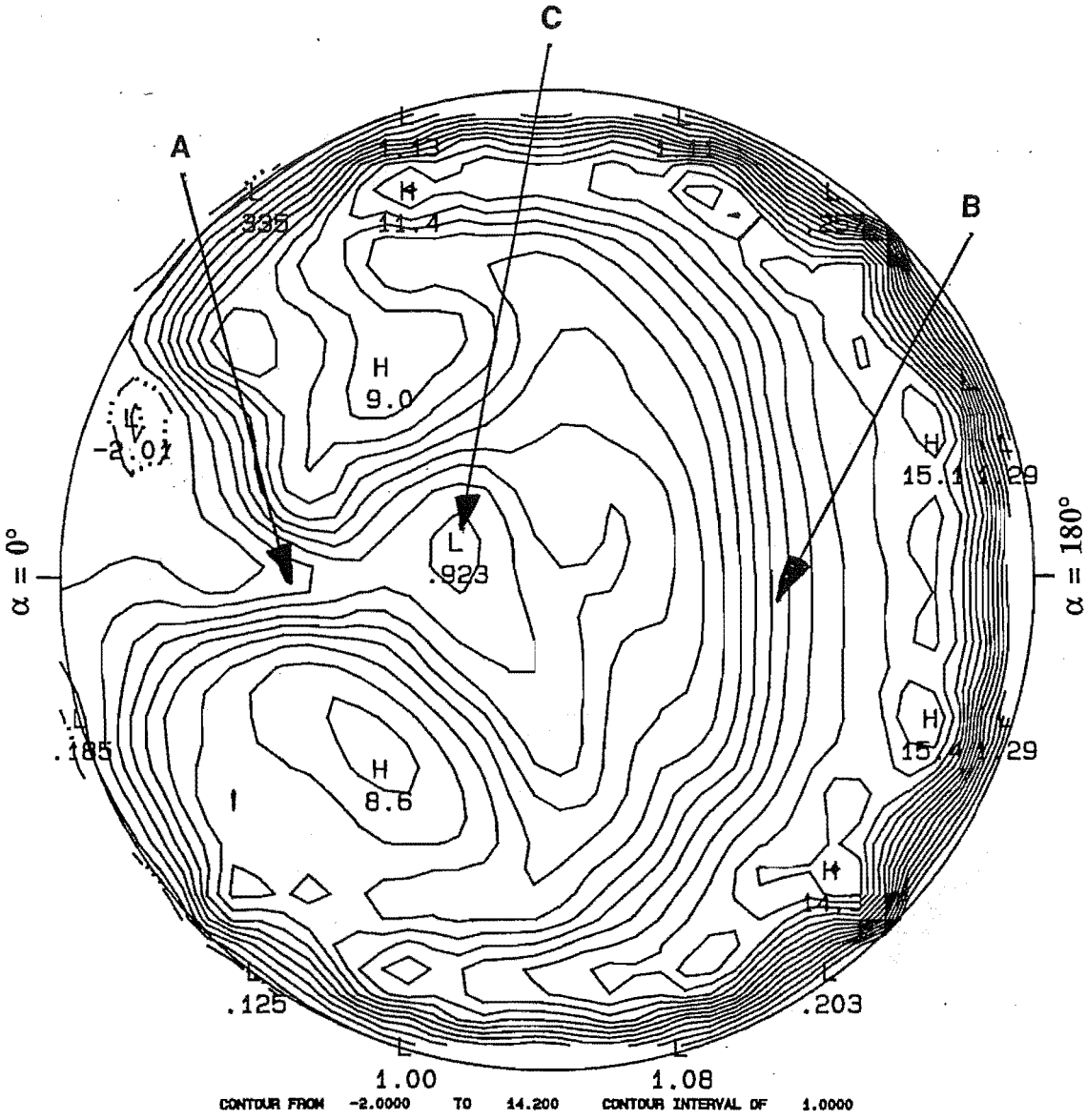

Figure 5.21

BC5, Proximal Limb, Re = 1500.

The separation region was larger at the next contour position, 0.17 diameters downstream (BC2, figure 5.18), extending 0.25 diameters into the middle of the tube near P and spanning between $\alpha = 0°$ and $\alpha = +50°$ at the wall. It was even more markedly asymmetric, being wholly contained in the 1st quadrant. Whilst the contours in other parts of the tube appear to be more symmetric, the high in the 4th quadrant was 10% higher than it's counterpart in the 1st quadrant and the flows in the 2nd quadrant were generally higher than those in the 3rd quadrant. Not withstanding this, the high velocity gradient about the $\alpha = 180°$ azimuth was fairly symmetric wrt P. The highs in the 1st and 4th quadrants were located at $\alpha = +73°$, r = 0.38 and $\alpha = -65°$, r = 0.26. The maximum velocity was more concentrated near the $\alpha = 180°$ azimuth than in the contour plot immediately upstream.

In the third proximal limb contour plot (BC3, figure 5.19), the backflow velocity was greater still (about one third of the maximum velocity in the proximal stem), but the region remained about the same size and shape as in BC2.

The highs in the 1st and 4th quadrants were less intense than those upstream and were situated at $\alpha = 57°$, r = 0.34 and $\alpha = -56°$, r = 0.25. The shear layer near the $\alpha = 180°$ azimuth had increased in intensity so that the maximum velocity was 15.3 cm s^{-1}. The feature was still asymmetric.

The separation region spanned between $\alpha = 0°$ and $\alpha = +36°$. The velocity gradient of the shear layer between the separation region and the position of maximum velocity had increased in intensity, as shown by the closeness of the isovels.

A high in the 3rd quadrant (A) was apparently due to one high velocity measurement and so may be erroneous.

Figure 5.20 shows the axial isovels taken at the 4th proximal limb position, 0.233 diameters downstream of BC3. Note that there was no backflow region present.

The basin-like shear layer still existed (A) with a low between it and the $\alpha = 0°$ azimuth, but the "valley" was no longer present. The basin was closer to the $\alpha = 180°$ azimuth and still straddled P, with velocity gradient parallel to P. A weak boundary layer (B) occurred in place of the backflow region. A very thin backflow region in the contour near the $\alpha = 0°$ azimuth was an extrapolation of the contour-generating subroutine, rather than an actual LDA-measured reverse velocity. The maximum velocity along the 2nd hemicircle wall had increased to 16.8 cm s^{-1}.

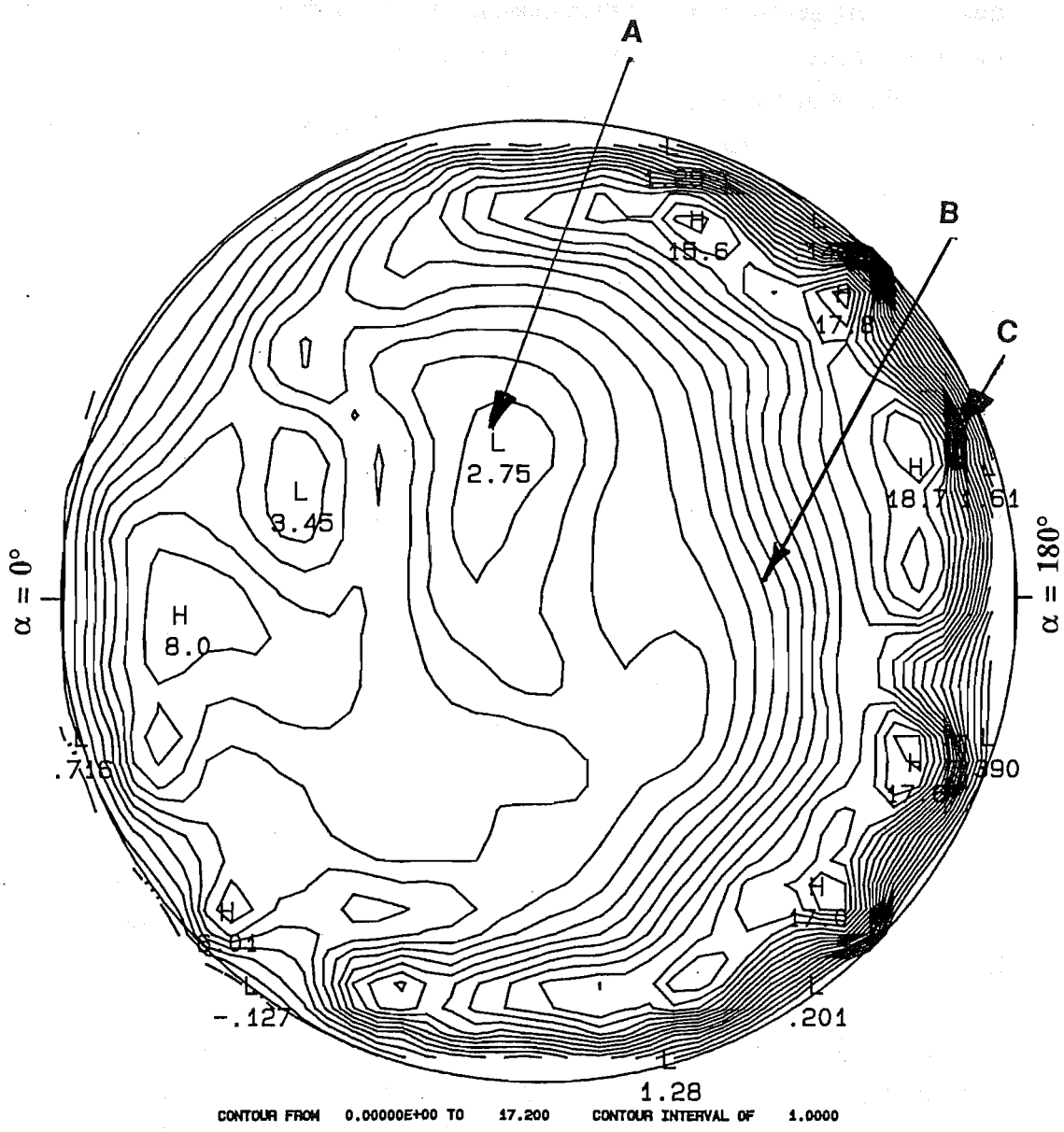

Figure 5.22

BC6, Proximal Limb, Re = 1500.

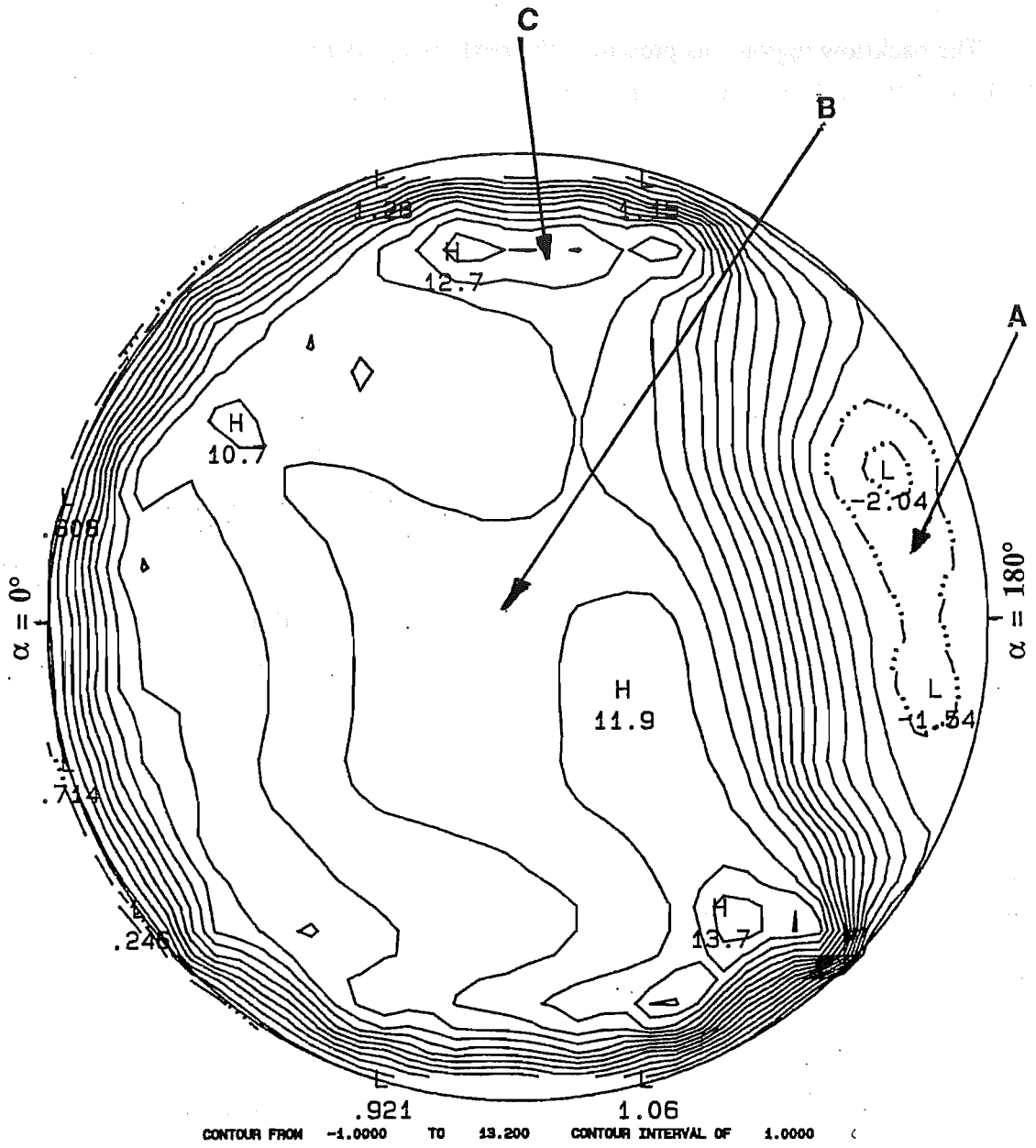

Figure 5.23

De1, Distal Limb, Re = 1500.

The highs in the 1st and 4th quadrants had decreased markedly in intensity. These were located at α = +41°, r = 0.25 and α = -39°, r = 0.24. A low intensity low (C) was located at α = -90°, r = 0.13. This low appeared to be a result of a dilation of the "valley" which appeared in upstream isovel contours, that progressed throughout the proximal.

The backflow region was present in the next (5th) proximal limb contour plot (BC5, figure 5.21), 0.117 diameters downstream of BC4. It was situated between α = 0° and α = +34° and extended about 0.24 diameters in towards the centre of the tube.

A second basin and valley (A) occurred here too, separate from the one seen upstream (B).

The low near the centre of the tube was still present at α = 0°, r = 0.06, between the new separation region and the "top" of the original basin-like shear layer (C). The highs in the 1st and 4th quadrants were clearly defined once more, situated at α = +62°, r = 0.25 and α = -49°, r = 0.24. The maximum at the RHS wall was of slightly lower magnitude than that in the previous plot.

In the final (6th) contour plot of the proximal limb (BC6, figure 5.22), 0.15 diameters upstream of the entrance of the medial bend C, the two highs of the 1st and 4th quadrants were no longer discernable and nor was the backflow region. The central low of the two upstream positions appeared at α = +90°, r = 0.15 (A).

A high occurred near the α = 0° azimuth on P, near to where the separation region had occurred upstream. The central region of the 4th quadrant was of fairly uniform velocity.

A continuous shear layer was observed about the α = 0° azimuth between α = -62° and α = +68°.

The "top" of the original basin was still present (B) and had continued it's movement towards the α = 180° azimuth wall apparent throughout the proximal limb. It appeared to be continuous with the shear layer about the 180° azimuth. The high velocity gradient along the α = 180° azimuth wall was still intact (C) though it was thickened at α = 180°, with the highest velocity of all the positions at 18.7 cm s^{-1}. A shear (boundary) layer had developed about the α = 0° azimuth.

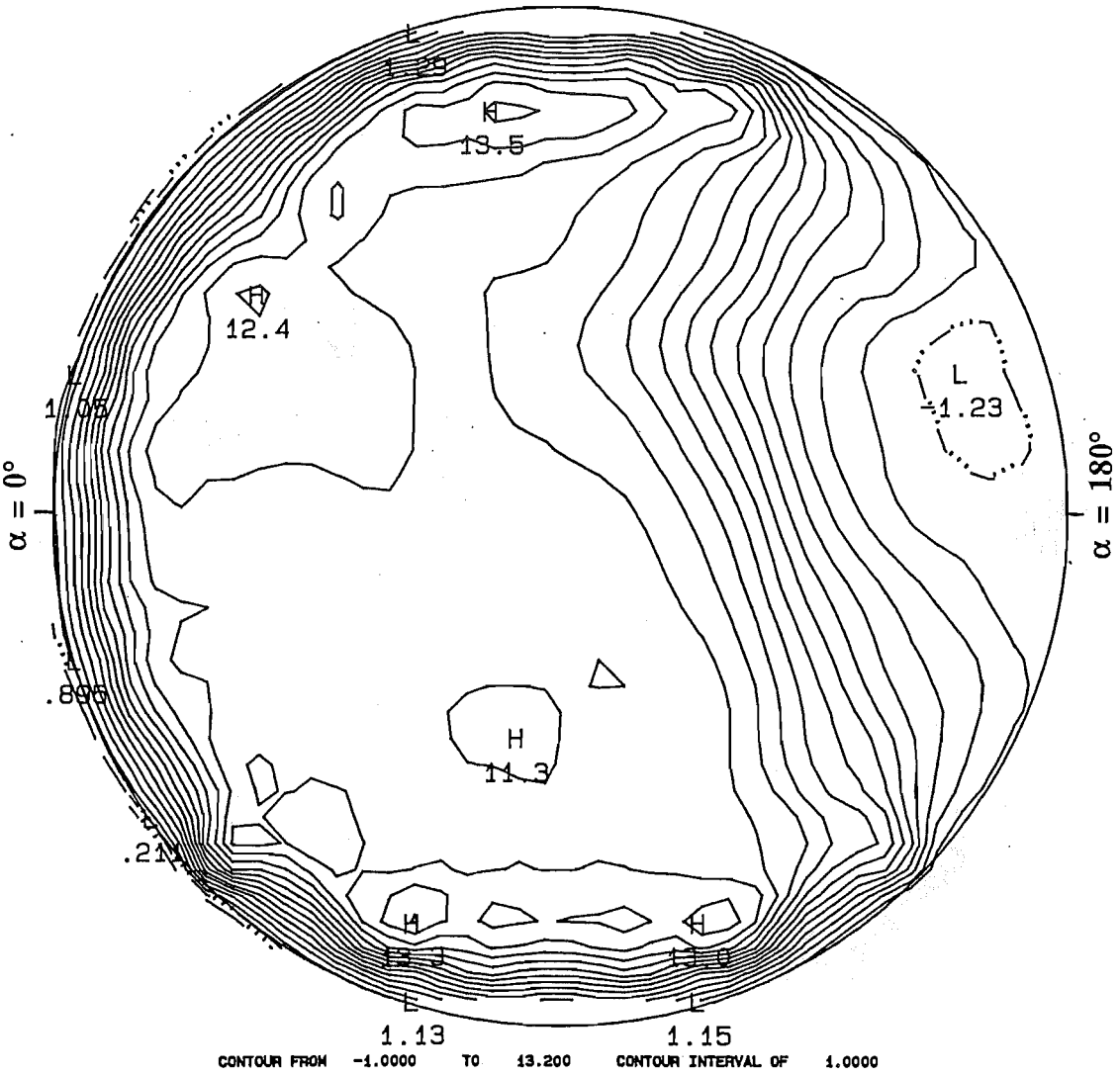

Figure 5.24

DE2, Distal Limb, Re = 1500.

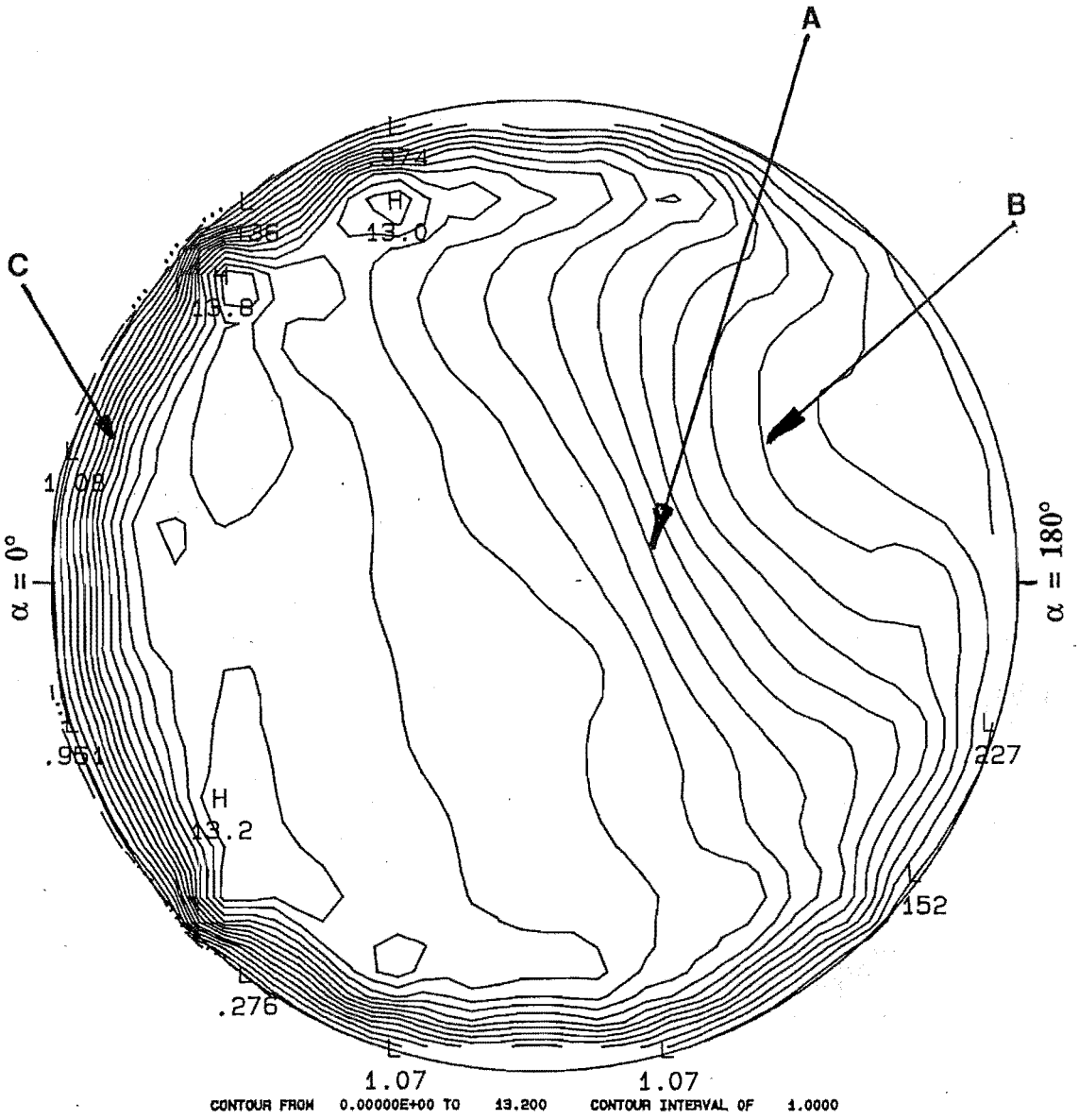

Figure 5.25

DE3, Distal Limb, Re = 1500.

5.3.1.3 The Distal Limb:

A contour positioned at the entrance of the distal limb (0.15 diameters downstream of the exit of the medial bend) showed (figure 5.23) some different characteristics from that just downstream of the proximal bend (figure 5.17).

A backflow occurred at the α = 180° azimuth wall (A), but it was more symmetrically distributed with respect to P than in the proximal limb, though it was still not entirely symmetrical. Rather than extending in towards the centre of the tube in a basin shape, the separated shear layer was rather flat, spanning α = -161° to α = +140° and lay at an angle of 15° to P, just bounding the separation region.

The flow in the centre of the tube (B) was relatively high and of uniform velocity. The velocity gradient near the α = 0° azimuth wall was not as great as it's counterpart near the α = 180° azimuth wall in the proximal limb, but was greater than that in the far upstream proximal stem.

Highs were present in the 2nd (C) and 3rd (D) quadrants, but there was only a slight velocity gradient between them and the flow in the middle of the tube.The highs were closer to the walls than those in the proximal limb, so that the velocity gradients were most marked between the highs and the walls.

The intensity of the shear layer decreased along the distal limb and expanded. The angle of the shear layer to P increased to 35° (figure 5.25, (A)) and the contours of the shear layer became more rounded closer to the α = 180° azimuth (figure 5.25 (B)). The intensity of the backflow decreased along the distal limb until, at the end of the limb it was no longer observed (though it occurred by extrapolation by the contour-generating routine - figures 5.24 & 5.25).

Simultaneously with the increased volume of the tube occupied by the shear layer, (in general slower than the maximum velocity) the two highs of the 2nd and 3rd quadrants moved about the wall to positions at α = +90° and α = -90° respectively by mid-limb (figure 5.24), and into quadrants 1 & 4 by the end of the limb (figure 5.25). Accompanying this, the velocity gradient along the α = 0° azimuth increased, and the maximum velocity (excepting the two highs) shifted closer to the α = 0° azimuth wall. The velocity gradient about the wall, centred at α = 0°, extended from α = -140° to α = +118° along the entire distal limb (Figure 5.25, (C)).

The contours became less symmetric with increasing downstream distance.

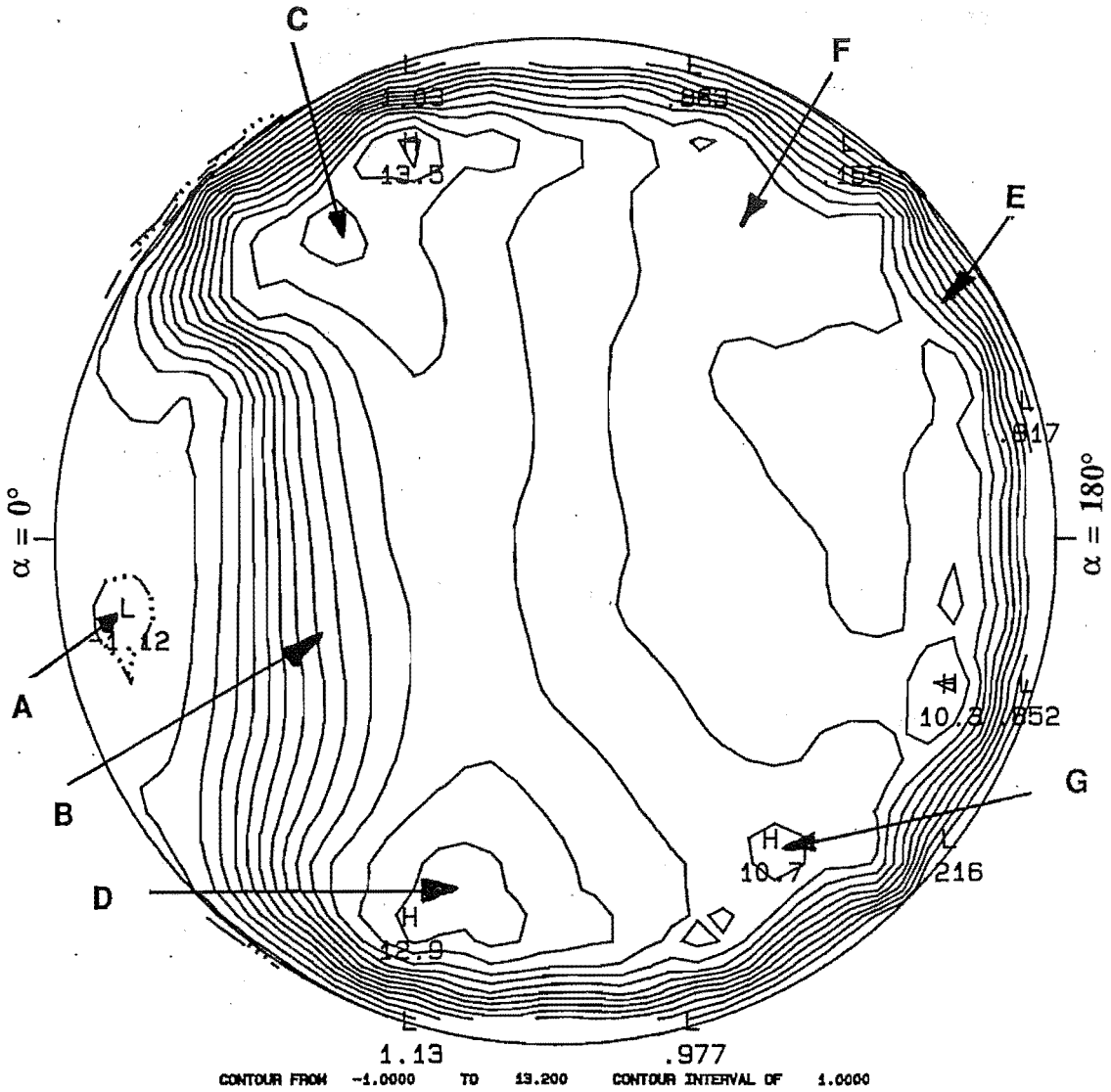

Figure 5.26

FG1, Distal Stem, Re = 1500.

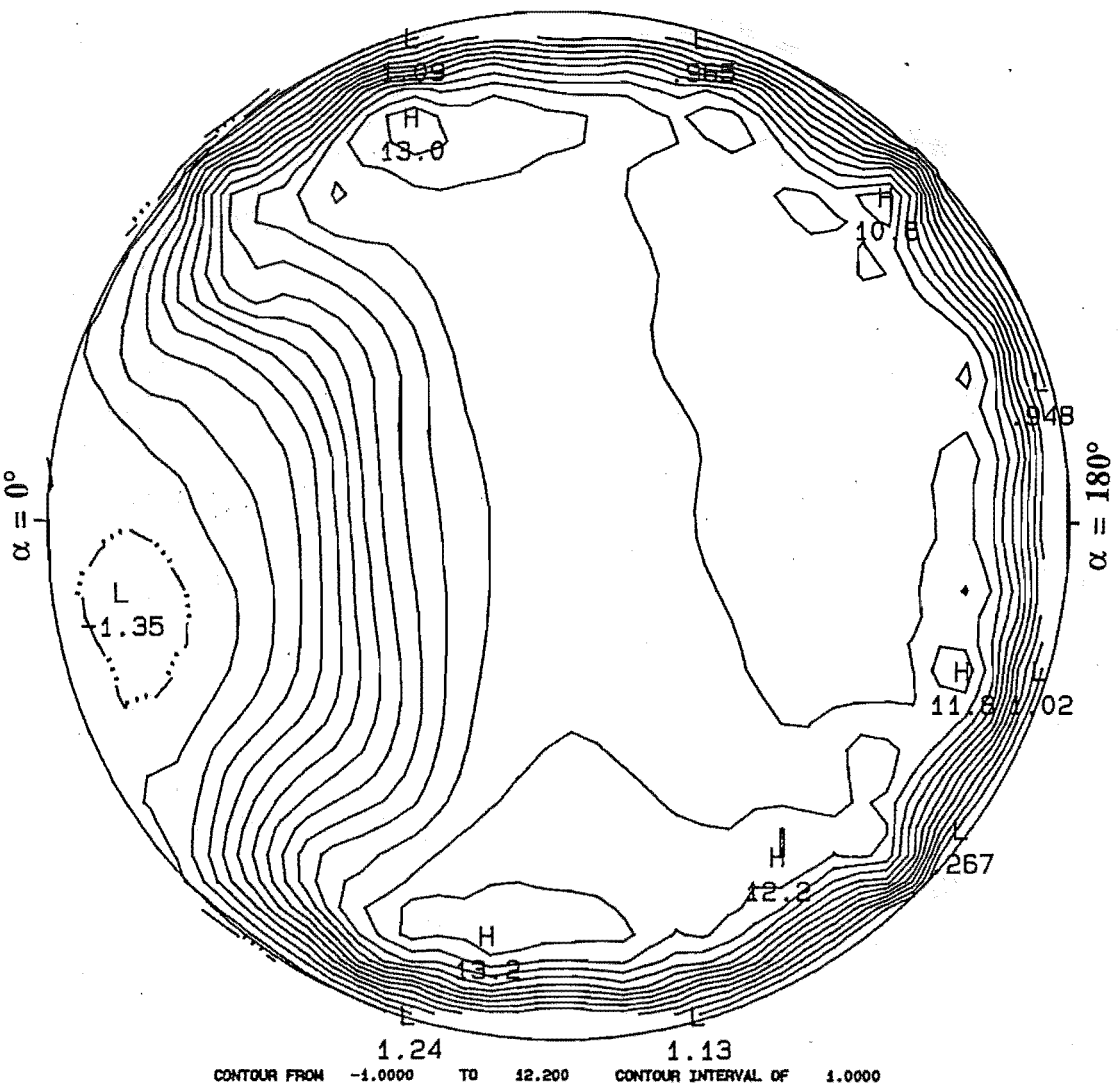

Figure 5.27

FG2, Distal Stem, Re = 1500.

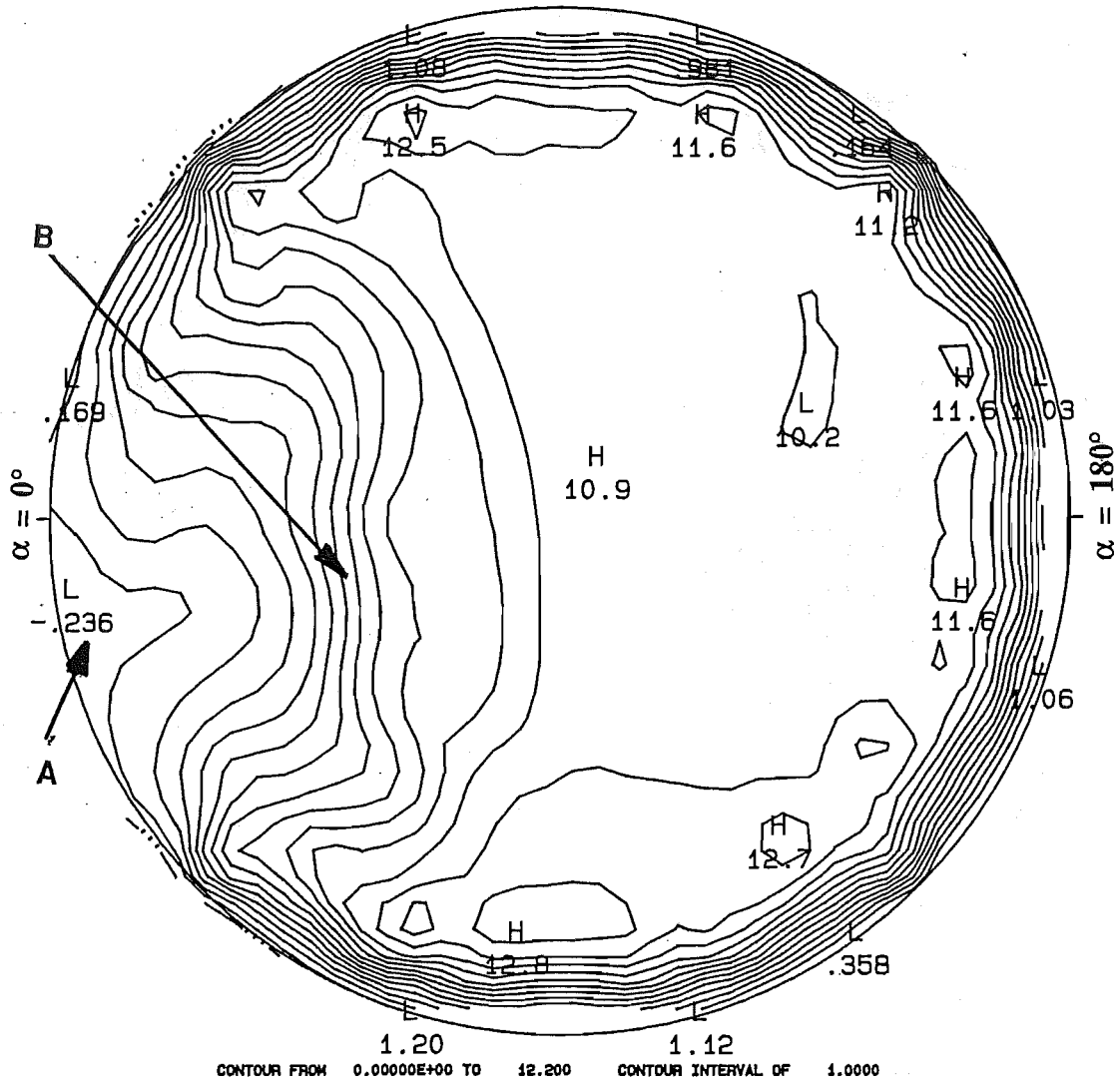

Figure 5.28

FG3, Distal Stem, Re = 1500.

5.3.1.4 The Distal Stem:

Downstream of the distal bend (figures 5.26-5.29) a further separation zone was evident in the contours at the $\alpha = 0°$ azimuth, extending to about 0.5 diameters downstream of the bend (A).

In the contour 0.15 diameters downstream of the bend (FG1, figure 5.26), the backflow was slow-moving and fairly evenly distributed across P at the 1st hemicircle wall. This straddled P between $\alpha = -31°$ $\alpha = +21°$ and extended 0.15 diameters out from the wall at $\alpha = 0°$.

A separated shear layer bounded the separation zone (B) and was flat, normal to P.

Two low intensity highs lay in quadrants 1 & 4 at $\alpha = +60°$, r = 0.40 and $\alpha = -72°$, r = 0.36., near the wall and just outside the shear layer(C and D). These were joined by a region of high flow with velocity gradient normal to P.

The flow in the 2nd and 3rd quadrants was fairly evenly distributed, with flattish contours, except for a high velocity gradient (E) about the wall from $\alpha = +60°$ to $\alpha = -72°$ through $\alpha = 180°$. This extended downstream, so that at the final cross-section (FG4), the high velocity gradient surrounded the entire tube wall. There were also low intensity highs in the 2nd and 3rd quadrants in similar positions to those in the distal limb (F and G).

The contours were intensified 0.28 diameters downstream (FG2, figure 5.27), so that the backflow region had a higher velocity, as had the four highs. The backflow region extended 0.21 diameters into the tube, but was confined to the same circumferential limits as upstream in FG1. The shear layer had broadened and moved away from the $\alpha = 0°$ azimuth, so that the average flow in the 2nd and 3rd quadrants was higher than previously.

The highs in the 1st and 4th quadrants had moved about the wall to $\alpha = +90°$ and $\alpha = -90°$ respectively, whilst the highs in the 3rd and 4th quadrants remained in the same positions.

The axial velocity gradient along the $\alpha = 180°$ azimuth wall intensified with the downstream position.

In the 3rd contour position a further, 0.28 diameters downstream (figure 5.28), the backflow region had almost disappeared. It was situated at the wall in the 4th quadrant (A) and was quite slow. The shear layer became less ordered (B). Other

trends were similar to those shown in position FG2 (figure 5.27) over position FG1 (figure 5.26).

A 4th plot was made 1.5 diameters downstream of the distal bend (figure 5.29). This shows that the backflow region had completely disappeared, as had the free shear layer. A boundary layer surrounded the entire tube cross-section.

The velocity gradient was still higher at the $\alpha = 180°$ azimuth than at the opposite side, and the higher isovels occurred in a semi-circular crescent (A) aligned with the $\alpha = 180°$ azimuth.

The discrete phenomena in the tortuosity and the entrance of the distal stem had gone, signifying the expected return to normal Pouiseulle flow downstream.

5.3.2 Shear Rates:

The shear rates near the wall at $\alpha = 0°$ and $\alpha = 180°$ were plotted in figure 5.30 for each contour plot measurement position. The shear rate for ideal Poiseiulle flow with Re = 1500 was also plotted.

At the contour position OA1, the shear rates were similar to those for ideal Poiseiulle flow, but at OA2, the shear rate had decreased at $\alpha = 180°$ and increased at $\alpha = 0°$.

The shear rates along the walls subject separation regions were close to zero and often negative. The two points bc4 and bc6 in figure 5.30, at $\alpha = 0°$ in the proximal limb where shear rates were higher than those nearby, corresponded to positions where reverse flow was not present in the contour plots (BC4 and BC6).

In all cases, shear rates were highest on the walls opposite separation regions. The highest shear rates overall were seen at $\alpha = 180°$ in the proximal limb, BC.

At the final contour plot measurement position of the distal stem (FG4), the shear rates can be seen to be approaching the ideal Poiseiulle flow shear rates (points fg15 and fg16 on figure 5.30).

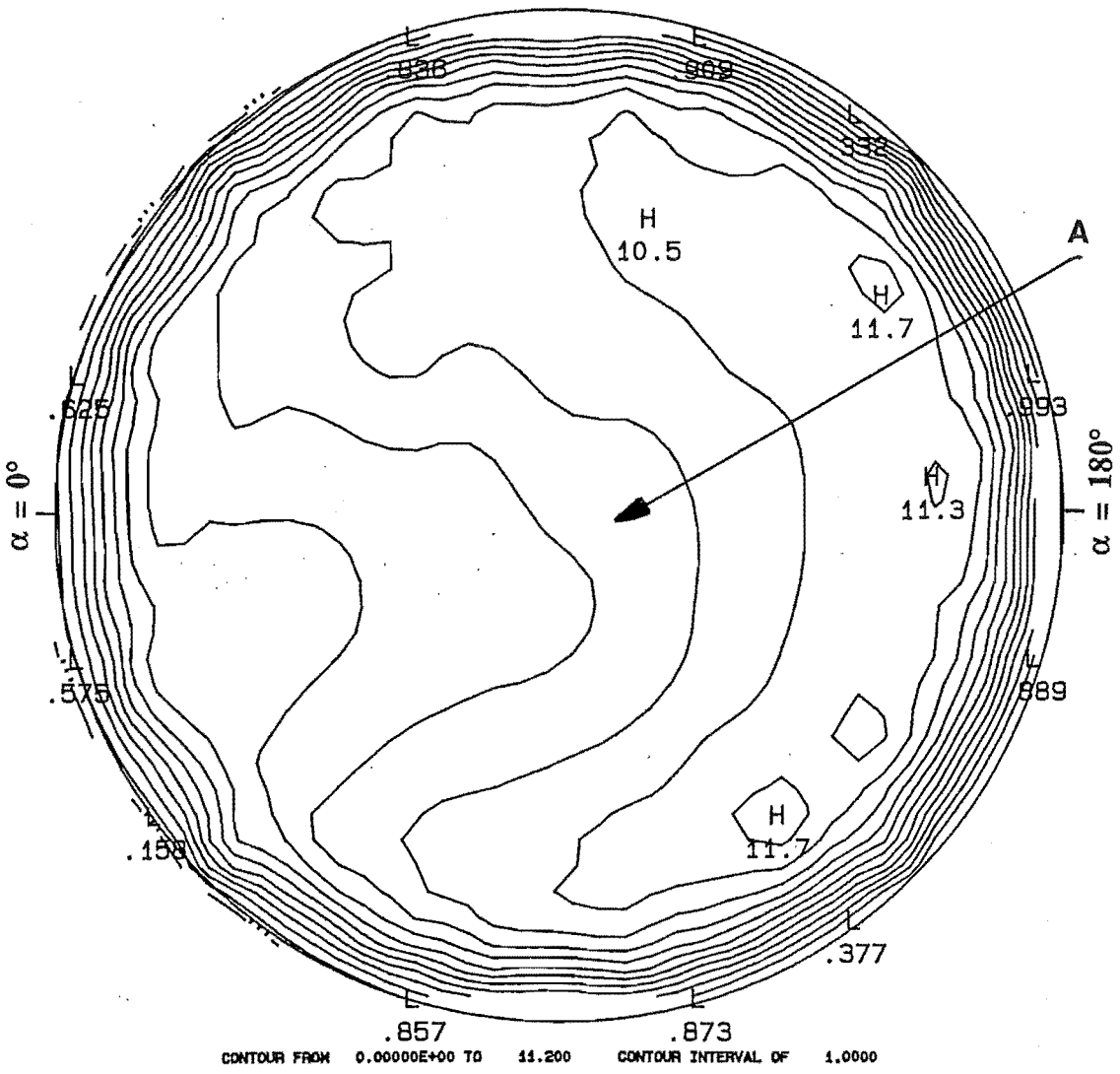

Figure 5.29

FG4, Distal Stem, Re = 1500.

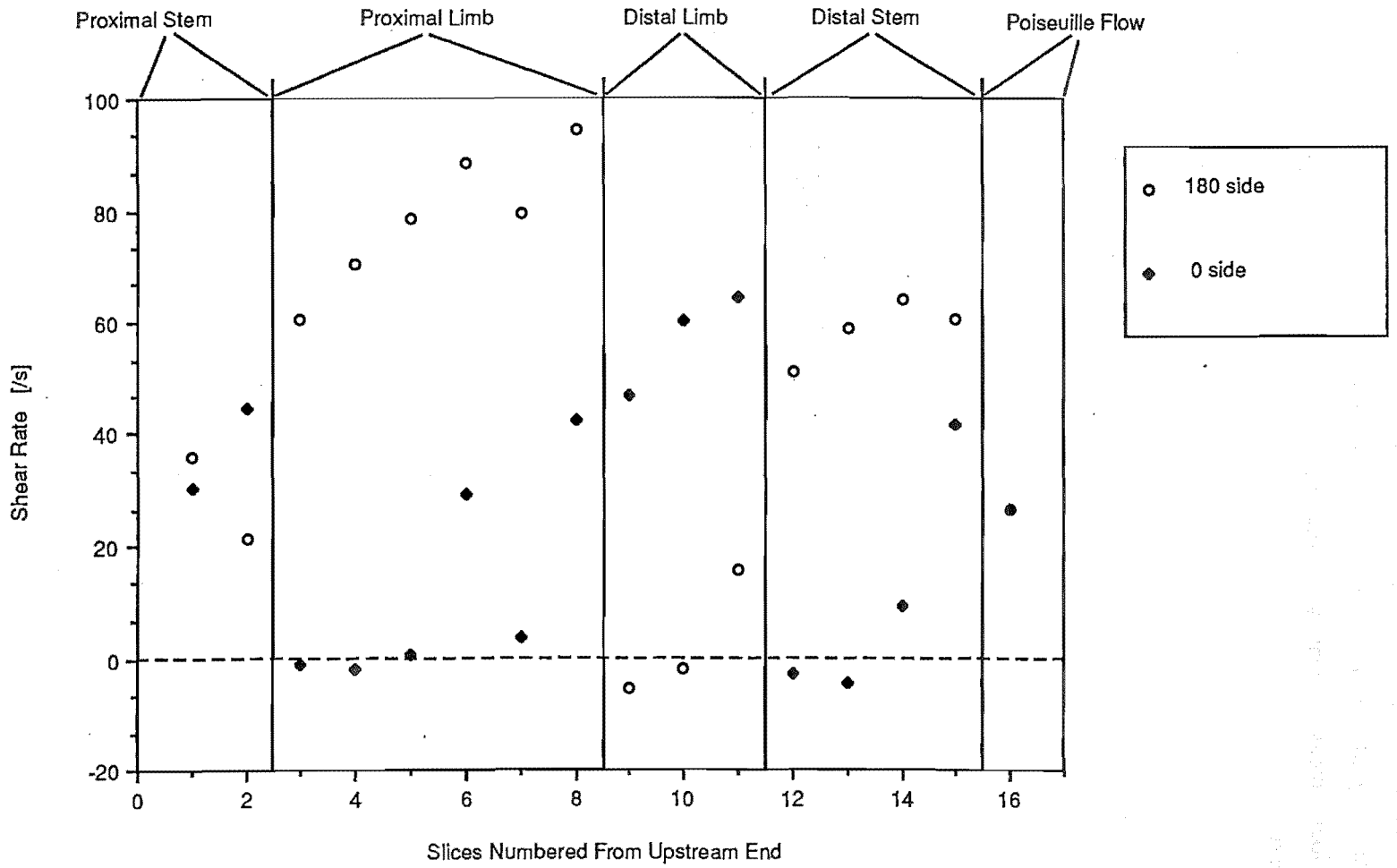

Figure 5.30: Shear Rates Along the $\alpha = 0°$ and $\alpha = 180°$ Walls of the Model at the Isovel Contour Cross-Sections of Section 5.3.1, Re = 1500.

5.3.3 Radial Velocity Plots:

Radial velocity measurements were made along the diameter through $\alpha = -90°$ and $\alpha = +90°$ (figure 5.12), at the same positions as the axial velocity cross-sections (figure 5.13). Radial velocity measurements were also made along the same diameter at the mid-point of each bend.

At OA1, 8 diameters upstream of the proximal bend (figure 5.31), V_r was small, but negative in the centre of the tube, decreasing to zero closer to the walls. (V_r was defined in figure 5.13 as positive towards the $\alpha = 0°$ azimuth.)

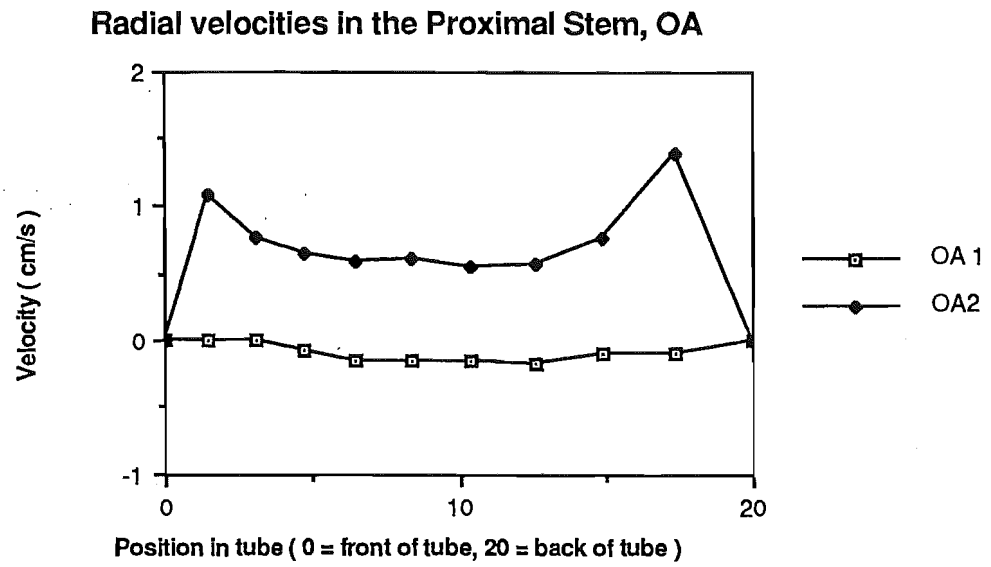

Figure 5.31

At OA2 (figure 5.31), just upstream of the proximal bend entrance A, the flow was positive at all points, with V_r increasing towards the walls. V_r was higher nearer the back wall than the front.

In the proximal bend the profile of OA2 was exaggerated (figure 5.32), so that V_r in the centre of the tube was negative. The positive velocity near the front of the tube was double the magnitude of the negative flow in the centre.

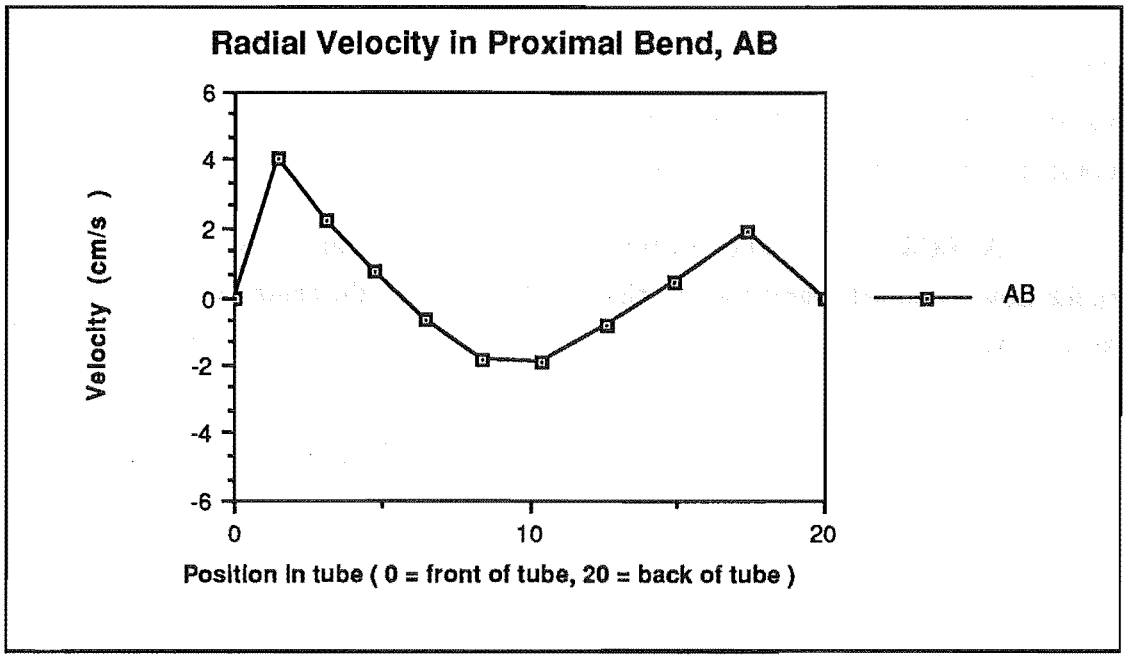

Figure 5.32

At BC1, just downstream of the proximal bend, a similar profile was seen (figure 5.33), but the negative central flow towards $\alpha = 180°$ was 2 to 3 times greater than the positive flow near the walls.

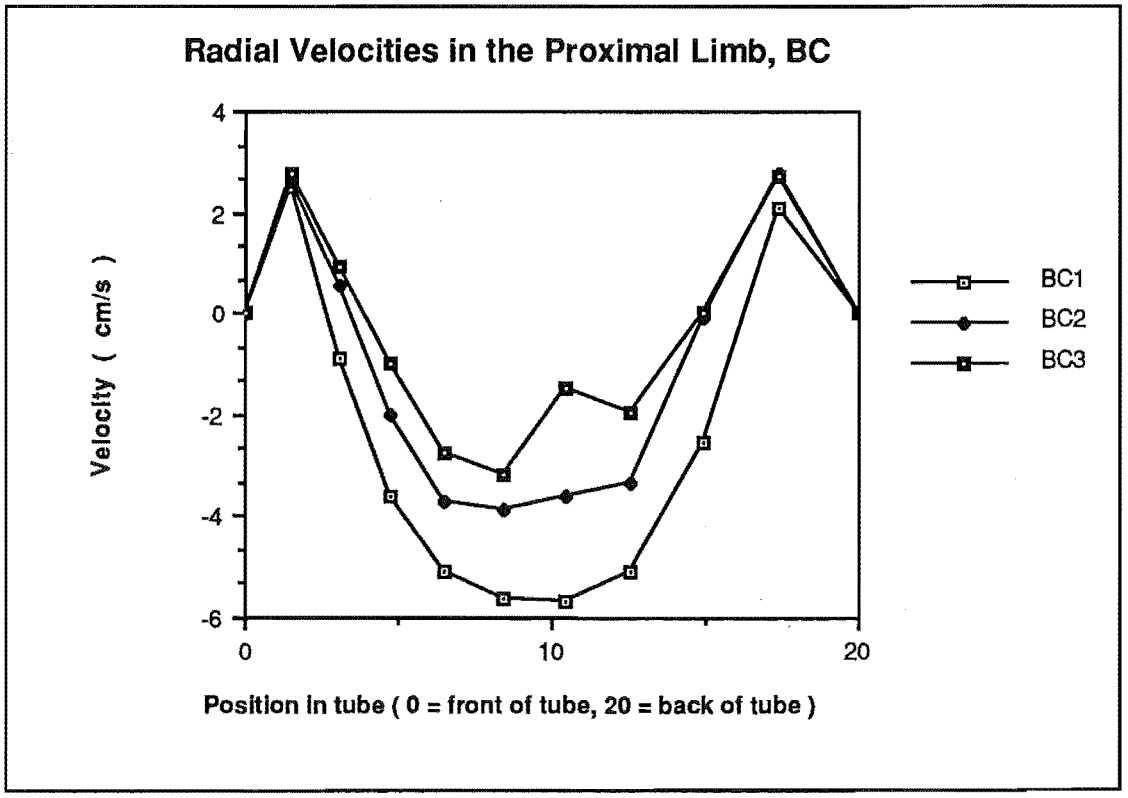

Figure 5.33

The magnitude of the negative central flow had decreased by BC2 (figure 5.33) and by BC3, a kink occurred near the centre of the tube, where the radial velocity was much lower than expected. The positive velocity near the walls remained constant in the upstream half of the proximal limb, BC1 to BC3.

At BC4, the central cross-flow had all but disappeared, though the positive radial flow remained near the walls (figure 5.34). At BC5, the central flow reappeared as an asymmetric kink near the centre of the tube (figure 5.34). This feature was magnified near the exit of the proximal limb at BC6 (figure 5.34).

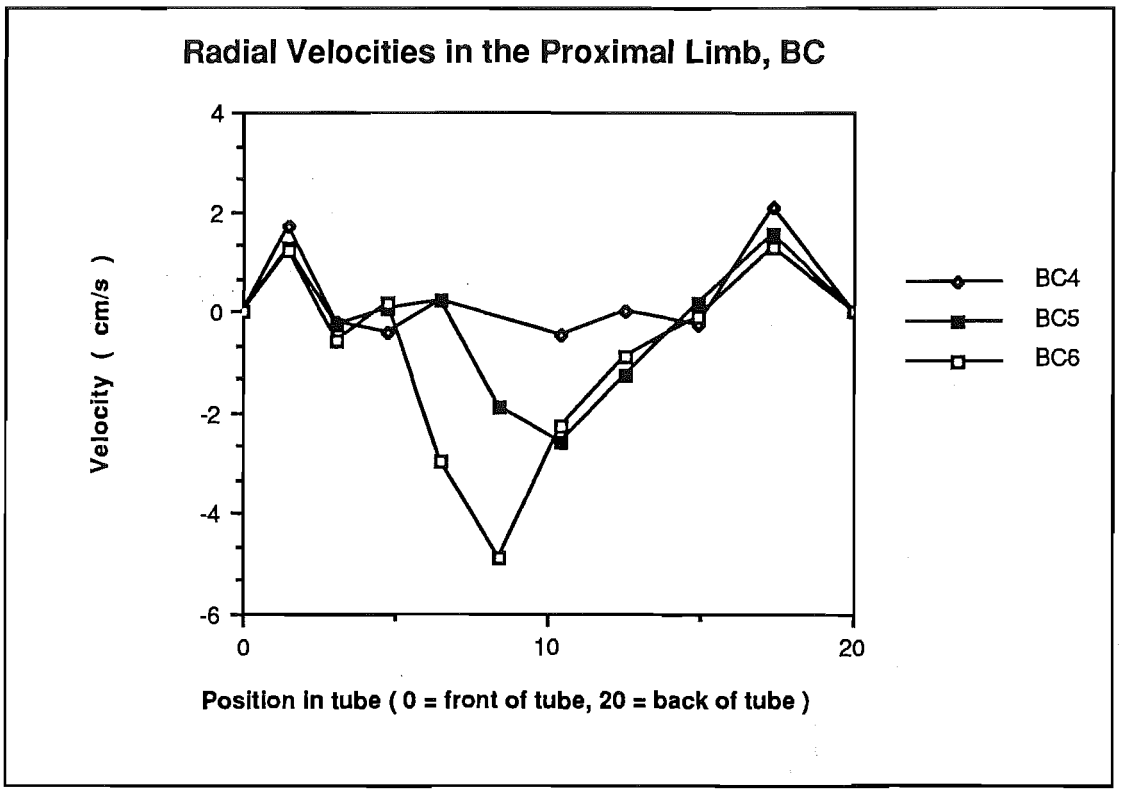

Figure 5.34

The positive flow near the walls decreased slightly throughout the downstream half of the proximal limb, BC4 to BC6 (figures 5.33 and 5.34), but was still present at the final measurement position, BC6 (figure 5.34).

In the medial bend (figure 5.35), the flow was similar to that in the proximal bend (Figure 5.31) except that the central cross-flow (directed towards the outer wall of the bend, $\alpha = 0°$) was more uniform.

(Note that the apparent asymmetry of this profile is not significant, when considering the biased measurement positions.)

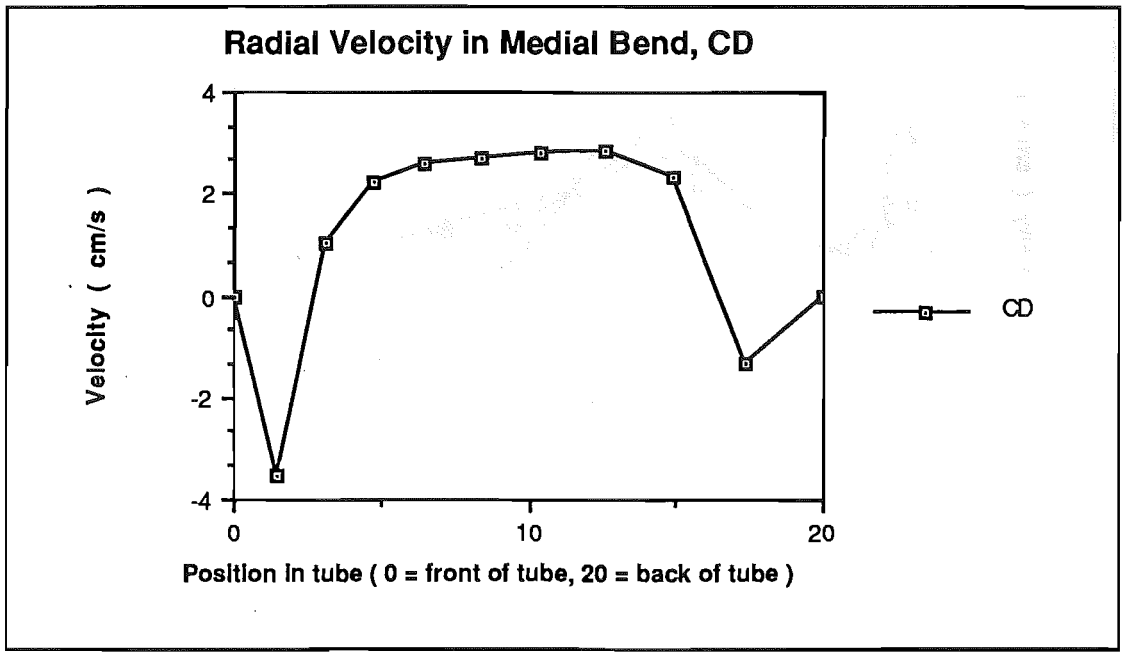

Figure 5.35

In the distal limb (figure 5.36), the central cross-flow was confined to a narrow layer near to the centre of the tube, while the negative flow occupied a broad band between this layer and the walls. The magnitude of V_r decreased rapidly along the distal limb DE, at first (DE2 in figure 5.36) but then increased slightly (DE3, figure 5.36).

Radial flow in the distal bend appeared to be negative at all points in the tube except near the front wall (figure 5.37). However, it is possible that similar flow occurred near the back wall, but that it was missed due to the larger distance between the wall and the rear-most measurement point than the corresponding distance at the front of the tube.

The radial velocities in the distal stem FG, are shown in figure 5.38. The flow near the exit of the distal bend (FG1) was apparently all negatively directed. This cross-flow died out downstream in FG2 and FG3 (figure 5.38) until, 1.5 diameters downstream of the distal bend F, the radial flow had vanished entirely (FG4, figure 5.38).

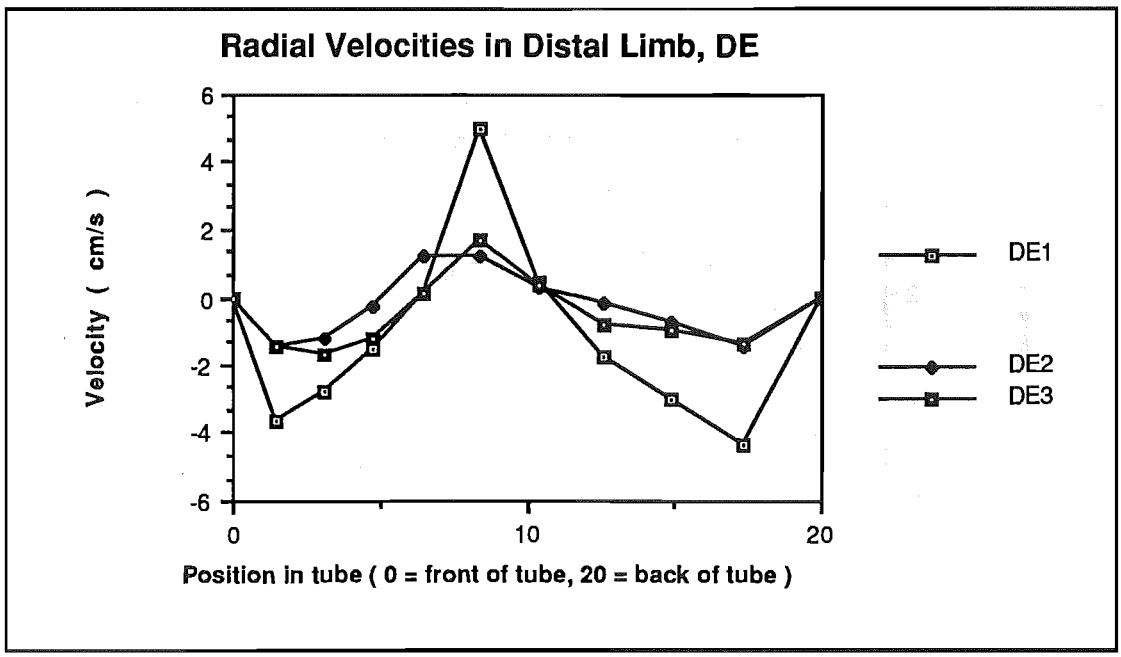

Figure 5.36

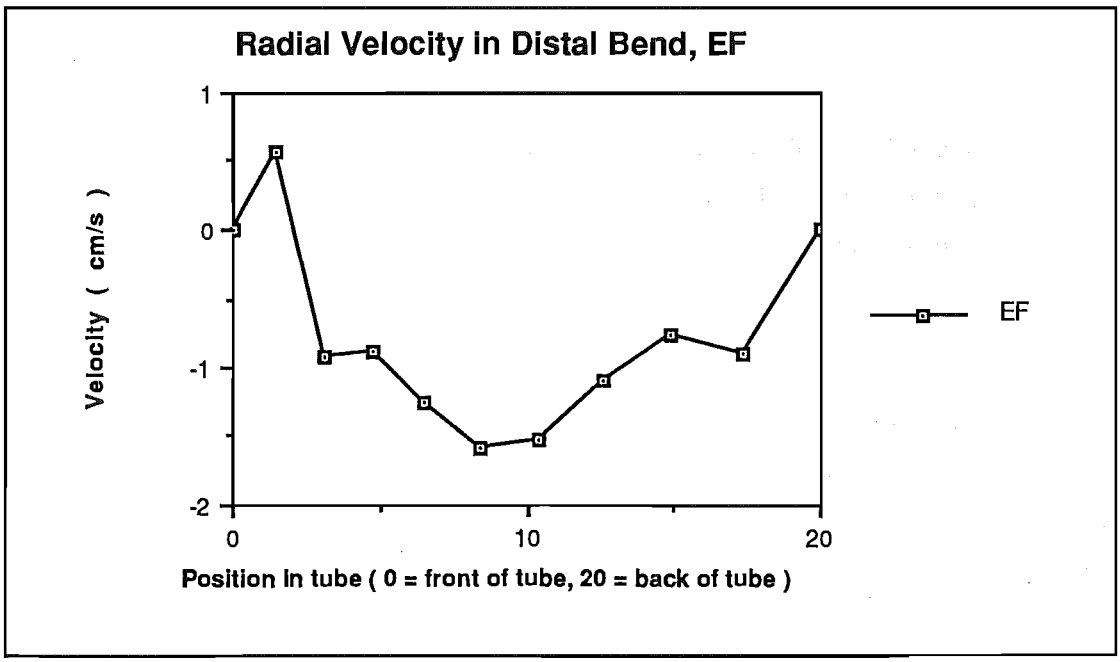

Figure 5.37

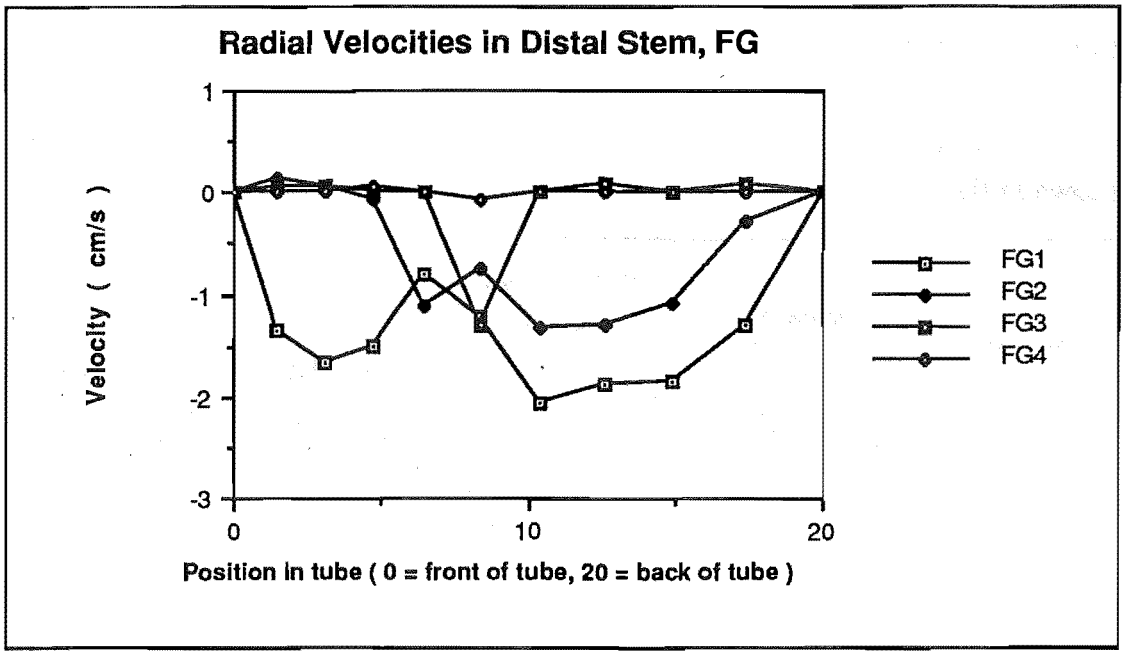
Radial Velocities in Distal Stem, FG
Velocity (cm/s)
1
0
-1
-2
-3
0
10
20
Position in tube (0 = front of tube, 20 = back of tube)
FG1
FG2
FG3
FG4

Figure 5.38

5.4 Laser Doppler Anemometry Results - Pulsatile Flow:

Axial velocities were measured by laser Doppler anemometry at the positions shown in figure 5.39.

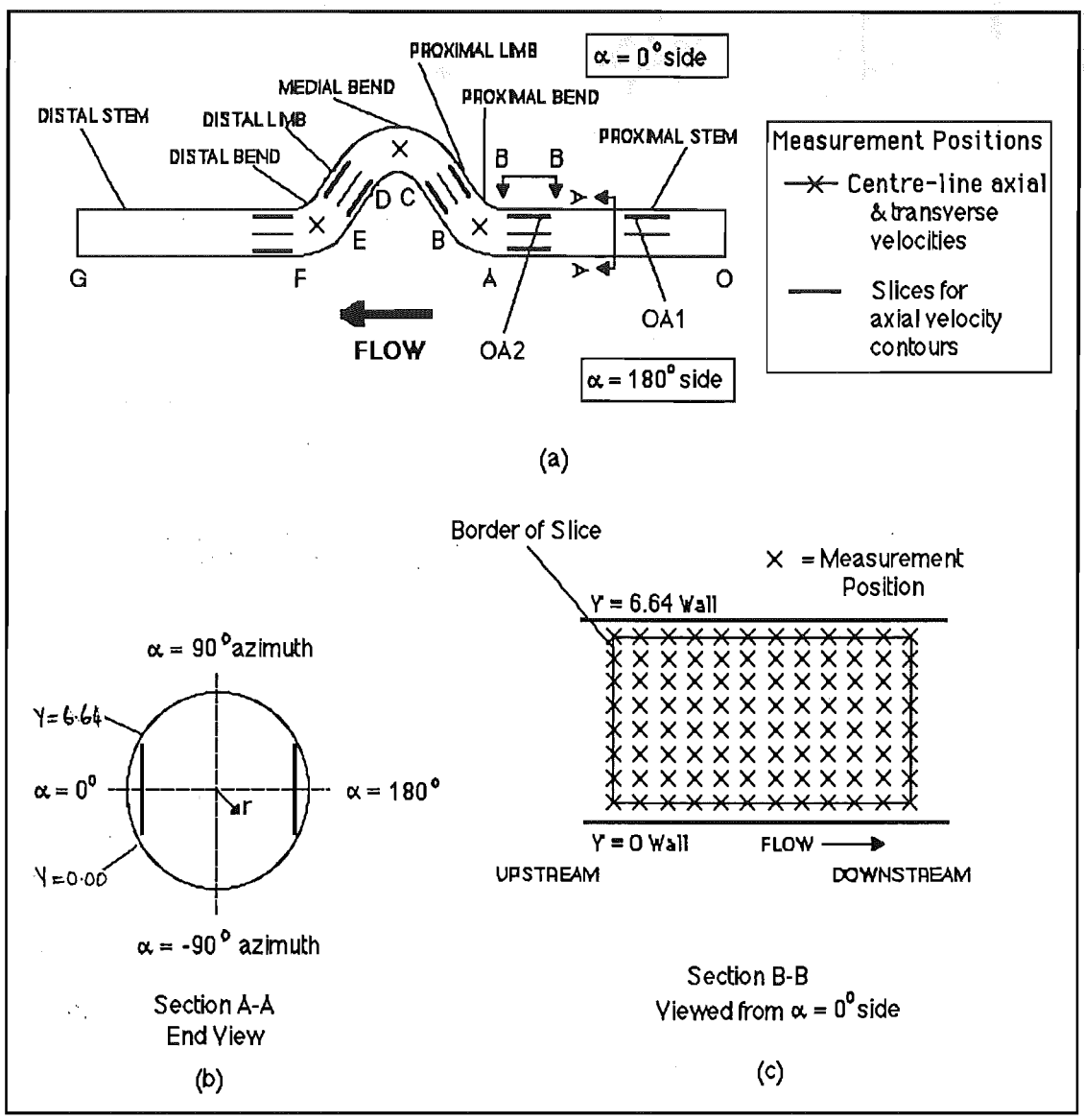

Figure 5.39
Nomenclature
(a) Measurement Positions in Tube (b) Cross-Section Showing End View of Slice (c) Measurement Positions on Slice

Each of the contour positions shown in figure 5.39 corresponds to a planar "slice" through the flow parallel to the tube's central axis and normal to the model's plane of symmetry, P. The slices were positioned as closely as possible to either the $\alpha = 0°$ azimuth or the $\alpha = 180°$ azimuth (figure 5.39(b)), without touching the walls and still allowing the LDA measurement volume to be positioned properly (see

experimental methods section, Chapter 4).

During sampling, the pulse was broken into 12 equal intervals corresponding to phase angle intervals of 30°. The average velocity at each phase angle, Ψ, as well as the overall average velocity was recorded for each measurement position in each slice. Axial velocity isovel contours were generated from these data.

The time-dependent velocities on the centreline of the tube upstream of the proximal bend are shown in figure 5.40 (see chapter 4 for repeatability) for Re_{mean} = 1000 and Re_{mean} = 1500 with a variation of approximately ±50% over the mean centreline velocity in each case. The period of the cycle for Re_{mean} = 1500 was 20 seconds, scaled by the Strouhal number to match the dynamics of a pulse of 1.2 Hz of the average human male. With similar scaling, the corresponding period for Re_{mean} = 1000 was 30 seconds. (See experimental methods section, Chapter 4.)

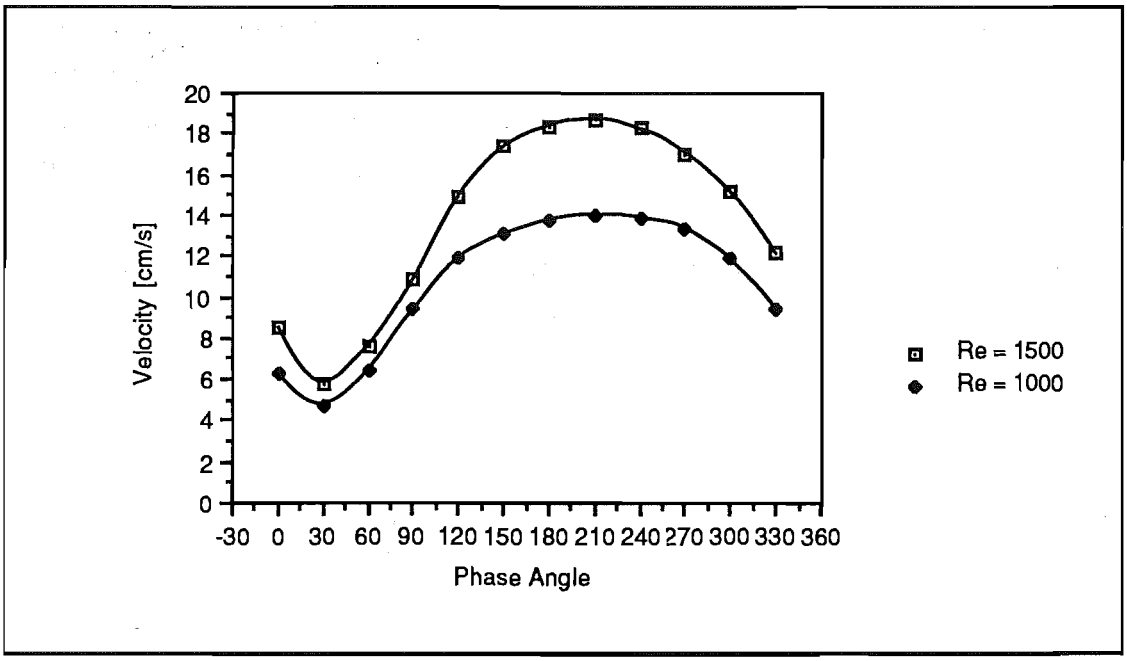

Figure 5.40
Centreline Velocities Far Upstream of the Proximal Bend
Over Pulse Cycle, Re_{mean} = 1500 & Re_{mean} = 1000

Contour plots of the isovels over each "slice" were generated (figure 5.41). Velocity was specified as zero at the walls to fulfill the no-slip condition.

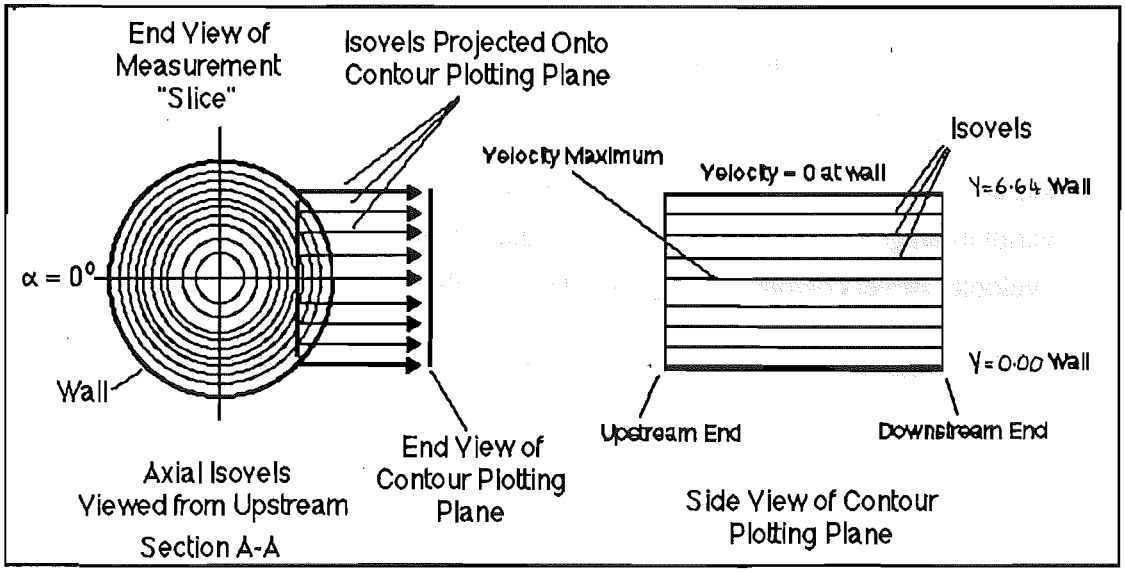

Figure 5.41

Mapping of Velocity Measurements Onto Contour Plane and Ideal Poiseiulle Isovel Contours

The triangulation used by the contours plotting routine, CONRAN.FOR in each slice is shown in figure 5.42 for the slice positioned along the $\alpha = 0°$ azimuth of the proximal limb, BC. Axial velocity measurements were made at the intersection points of the lines shown. The best contours are obtained from this routine when the lines form isoceles triangles. The distances between successive measurement points were measured from a datum defined along one wall (Y = 0.00) and non-dimensionalised in both directions by the distance between successive points in the Y-direction, 1.66 mm. The width of all slices was 11.04 mm from wall to wall, corresponding to Y = 0.00 at one wall and 6.64 at the opposite wall when non-dimensionalised. Measurement points were separated by 2.0 mm in the X (streamwise) direction, or X = 1.20 when non-dimensionalised (see figure 5.42).

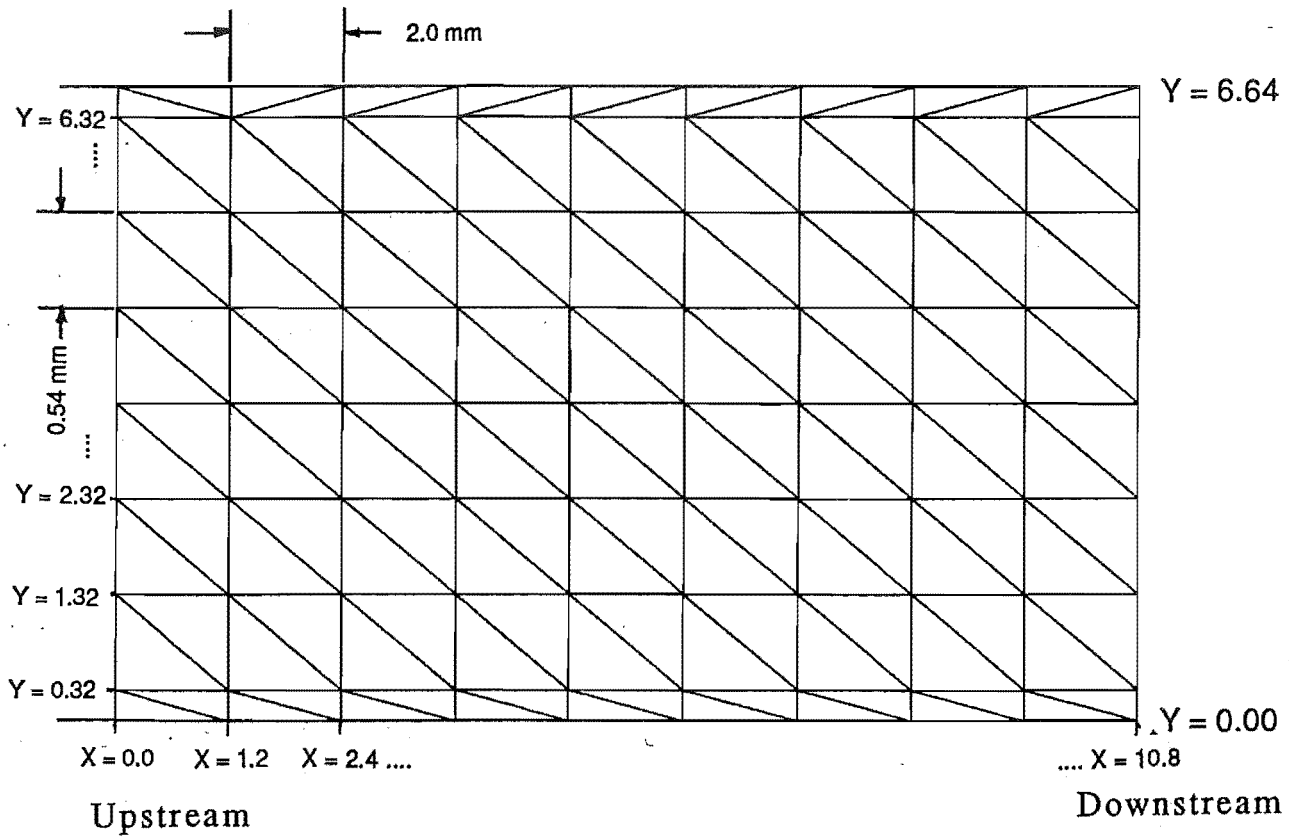

Figure 5.42
Triangulation used by the Contour Plotting Routine.

5.4.1 General Flow Characteristics:

In steady, Poiseiulle, laminar flow through a straight pipe, the isovels should be equispaced and parallel to the pipe's central axis, with the maximum velocity lying along the centreline of the slice (figure 5.41).

The contour plots for pulsatile flow fell into three groups, each with particular flow characteristics. With one exception, included in group 2, the location of the measurement slices in these groups of characteristics consistently matched certain geometric features within the model :

Group 1. In the straight section upstream of the proximal bend ie: in OA.

Group 2. Downstream of a bend, along the wall which formed the inner (greater curved) wall of the bend. This group also included a position along the $\alpha = 180°$ azimuth, just upstream of the proximal bend ie: along the wall that was continuous with the outer (lesser curved) wall of the proximal bend.

Group 3. Downstream of a bend, along the wall which formed the outer wall of the bend.

The general characteristics of each group are summarised in Table 5.1.

5.4.2 Pulsatile Flow Average Velocities:

In the following contour plots, broken contour lines indicate velocities of zero or less. Asterisks on the contour plots indicate positions where negative flow was observed at some time during the cycle. Data values are plotted at their measurement positions in figure 5.43 to give an indication of the amount of smoothing inherent in the contour-generating routine.

5.4.2.1 Group 1:

The contours along the $\alpha = 0°$ azimuth upstream of the proximal bend OA1, (figure 5.43) show that the velocity gradients were moderate and normal to the walls. The average velocity was highest near the mid-region of the slice, though not truely along the centreline. Average flow was positive at all points in the slice, though negative flow occurred at all points at some phase angle.

The slice along the $\alpha = 0°$ azimuth just upstream of the proximal bend, OA2, (figure 5.44) showed some slight differences from that in figure 5.43.

The velocity gradient along the entire Y = 6.64 wall had increased slightly (A), while that along the Y = 0.00 wall had increased only at the downstream end of the slice (B). A positive streamwise velocity gradient occurred along the middle of the slice. An area of low velocity gradient (C) along the Y = 0.00 wall is examined more closely in section 5.4.6.

No other significant discontinuities were observed in these contour plots. Note that flow rarely became negative in this slice, similar to the characteristic of the group 3 contours.

	GROUP		
	1	**2**	**3**
Backflow in Average Axial Velocity?	No.	Yes.	No.
Backflow Anywhere in Cycle?	Yes. Present some of the time in most positions.	Yes. Present all of the time, not in all positions.	No.
Velocity Gradients	Moderate. Very low in half of the cycle.	Low throughout cycle.	High throughout cycle.
Velocity Amplitudes	Moderate.	Low.	High.
Relative Position of Velocity Maximum and Minimum	Always in phase with proximal centreline flow.	Significant area 180° out of phase with proximal centreline flow.	Always in phase with proximal centreline flow.

Table 5.1
Flow Characteristics of Contours by Groups.

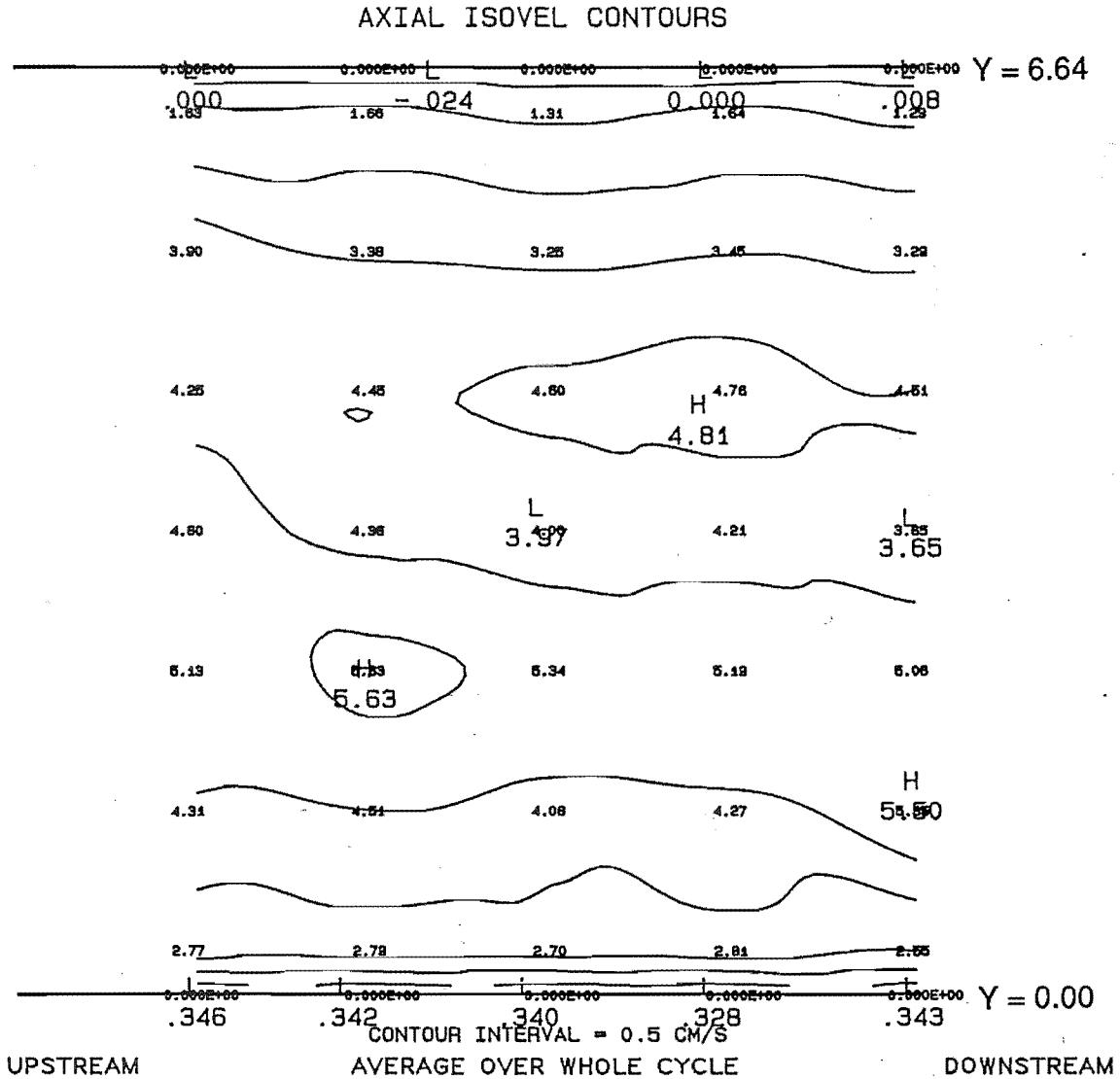

Figure 5.43: Along the $\alpha = 0°$ azimuth of the proximal stem, OA1. $Re_{mean} = 1500$.

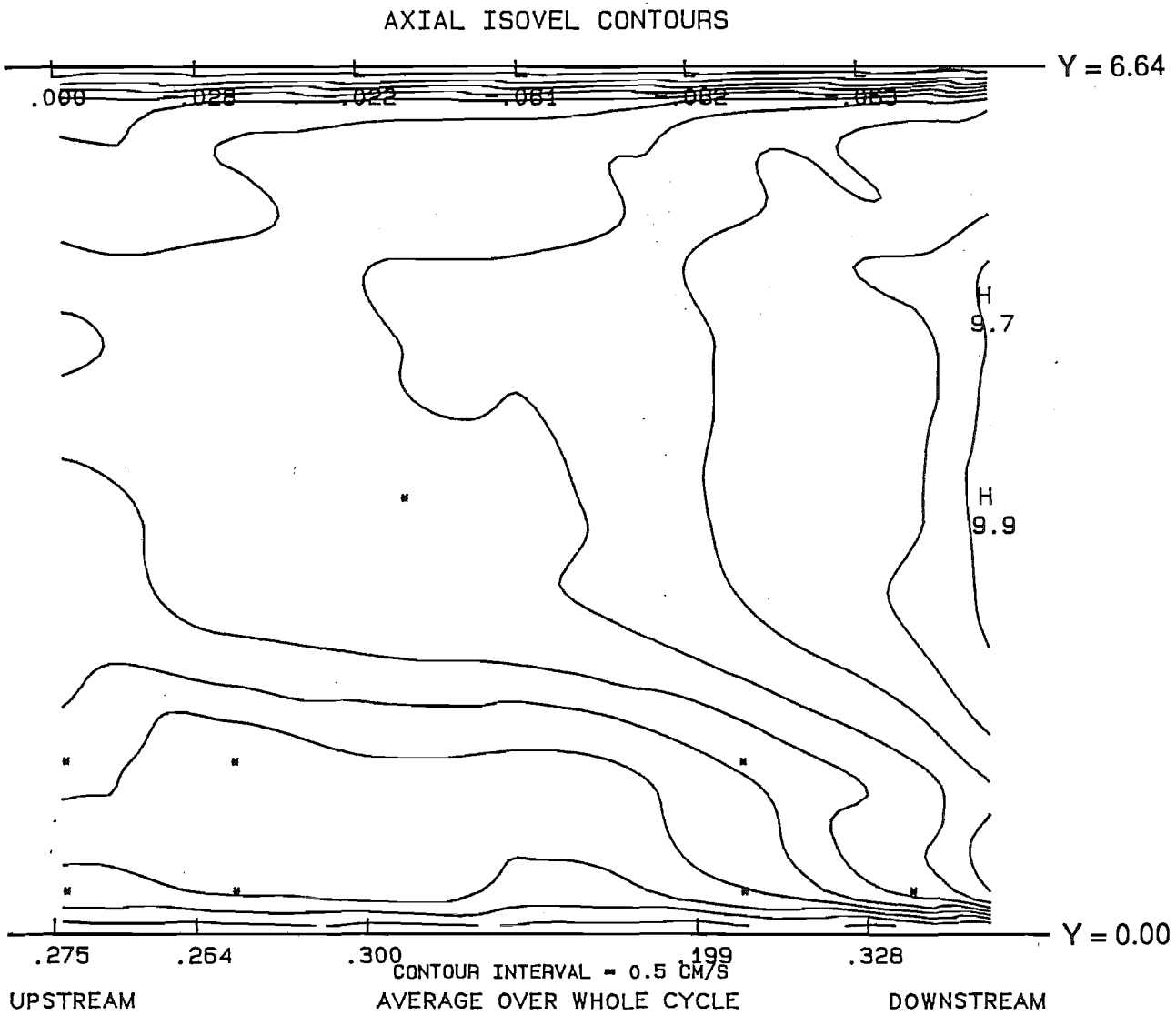

Figure 5.44: Along the $\alpha = 0°$ azimuth of the proximal stem, OA2. $Re_{mean} = 1500$.

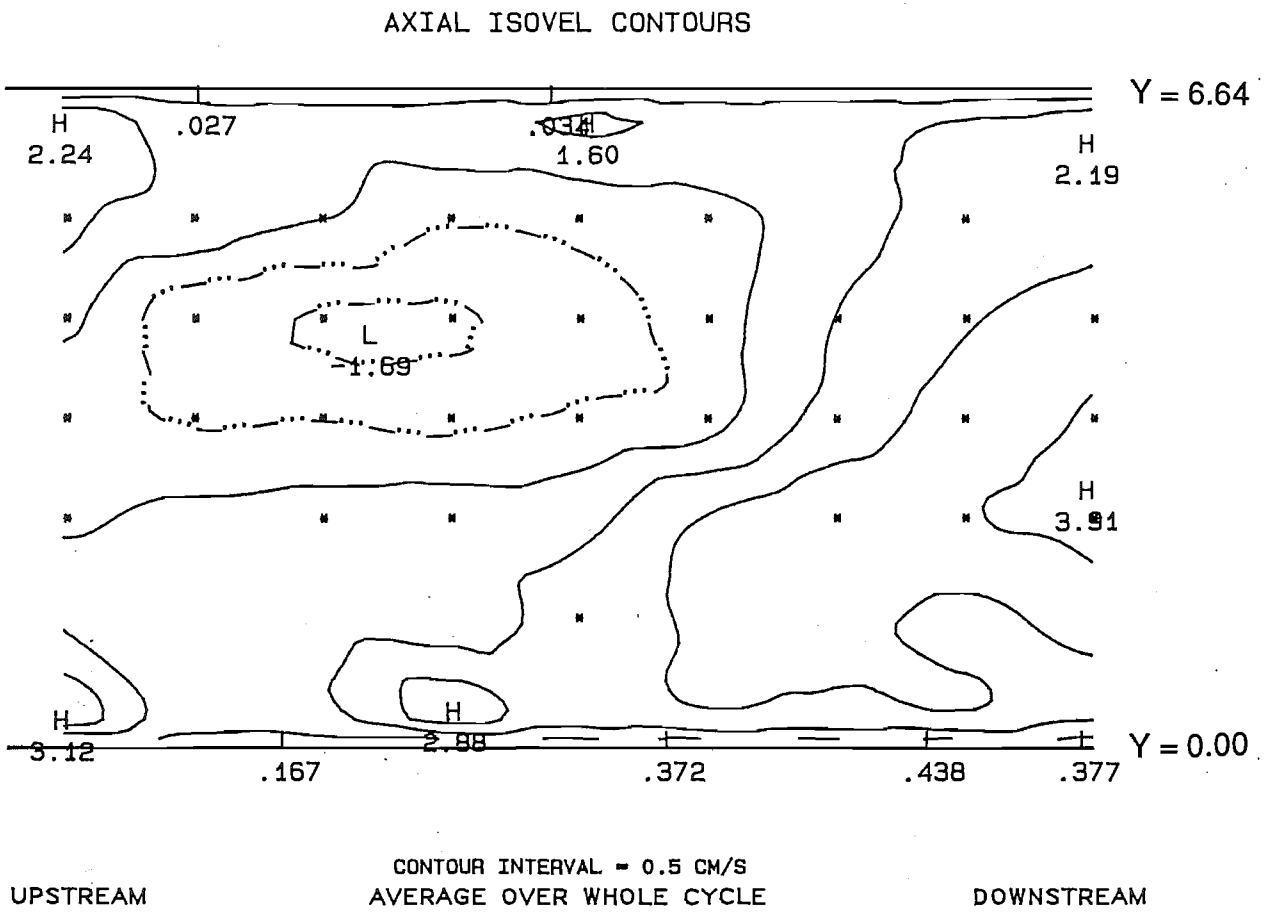

Figure 5.45: Along the $\alpha = 0°$ azimuth of the proximal limb. $Re_{mean} = 1000$.

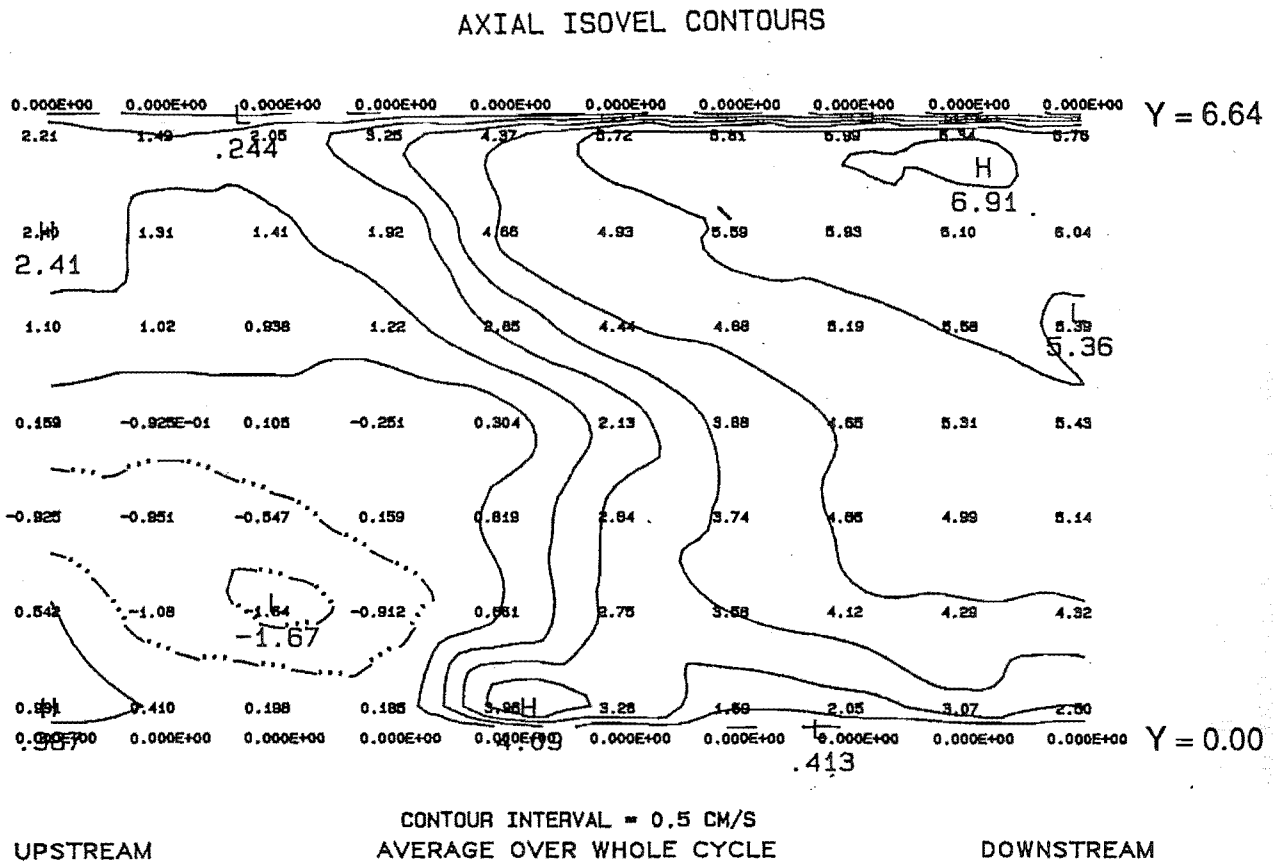

Figure 5.46: Along the $\alpha = 0°$ azimuth of the proximal limb. $Re_{mean} = 1500$.

5.4.2.2 Group 2:

The contours were significantly changed just downstream of the proximal bend, in the slice along the $\alpha = 0°$ azimuth of the proximal limb, BC. Contour plots were generated for $Re_{mean} = 1000$ (figure 5.45) and $Re_{mean} = 1500$ (figure 5.46). At $Re_{mean} = 1000$, the average velocity gradients were low and a large backflow region (A) occurred. The contours were asymmetric, with the backflow region positioned nearest the Y = 6.64 wall of the tube.

At $Re_{mean} = 1500$ the velocity gradients had increased slightly, mainly due to increased positive flow. The backflow velocity at up to 1.69 cm s^{-1} had not changed significantly from that at $Re_{mean} = 1000$. The backflow region (A) was smaller and was positioned towards the Y = 0.00 wall of the slice.

Similar features were seen in the slice along the $\alpha = 0°$ azimuth just downstream of the distal bend (figure 5.47). Backflow here was only up to -0.47 cm s^{-1}, while positive flow was up to 6.6 cm s^{-1}. Velocity gradients were again low. The contours were approximately symmetric, with the backflow region (A) positioned along the centreline of the slice.

The contour features along the $\alpha = 180°$ azimuth, just upstream of the proximal bend (figure 5.48) were similar to those of group 1, except for an area of low velocity gradient (A) at the downstream end of the Y = 6.64 wall.

5.4.2.3 Group 3:

The contours along the $\alpha = 180°$ azimuth just downstream of the proximal bend (figure 5.49) showed high velocity gradients at the walls and a constant positive streamwise velocity gradient along the middle of the contour slice. The maximum velocity was 15.7 cm s^{-1} compared with the maximum upstream centreline value of 18 cm s^{-1}. The contours were almost symmetric. The shear layer near the Y = 0.00 wall (A) appeared to be thicker than that near the opposite wall, but this was due to a lack of measurements close to the wall here. Measurements were not able to be made along this side of the contour slice, because of a poor signal from the LDA photomultiplier arising from optical aberations in the wall of the model - time did not allow for the correction of this problem. One measurement made at the downstream end of the slice on that side forced the contour plotting routine to show a similar velocity gradient there (B) to that near the opposite wall.

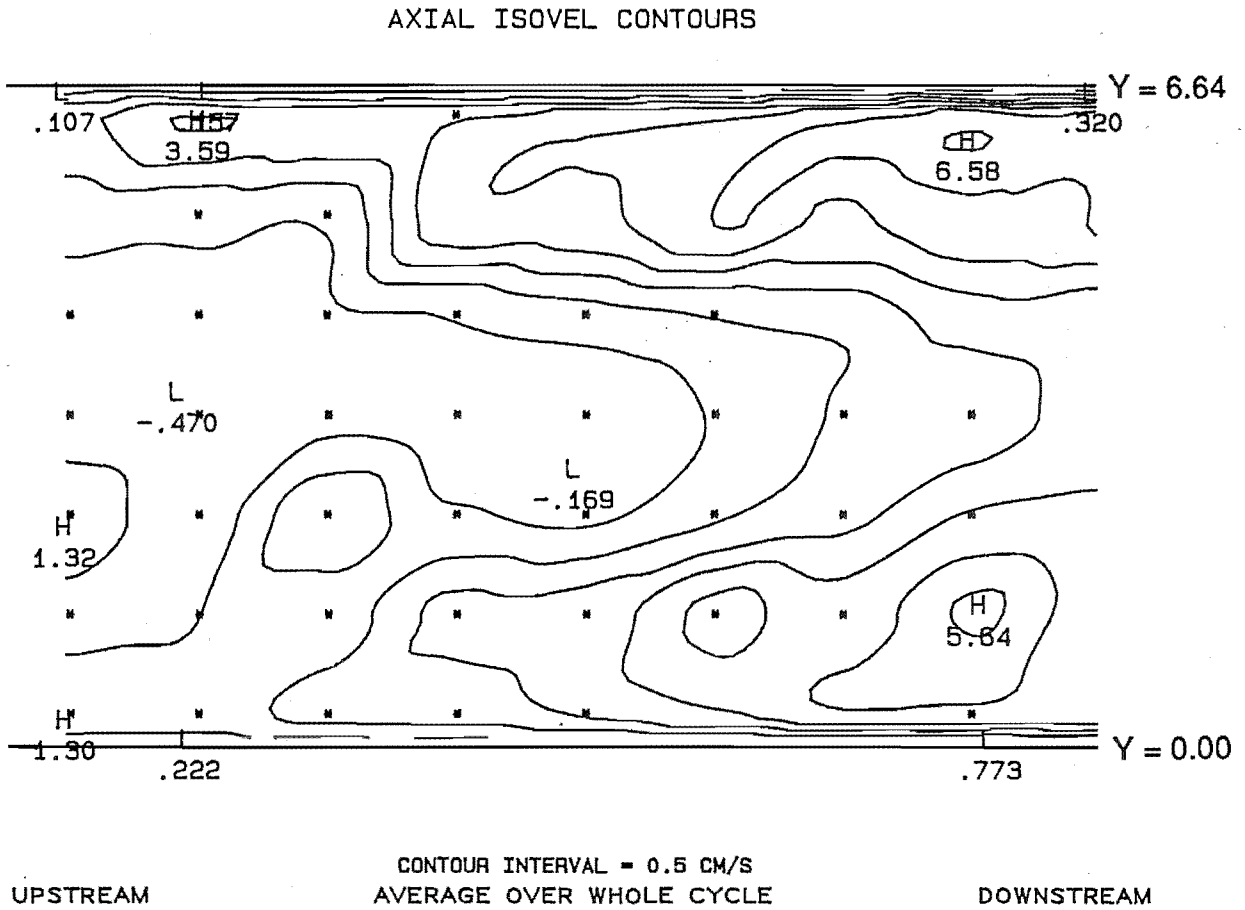

Figure 5.47: Along the $\alpha = 0°$ azimuth of the distal stem. $Re_{mean} = 1500$.

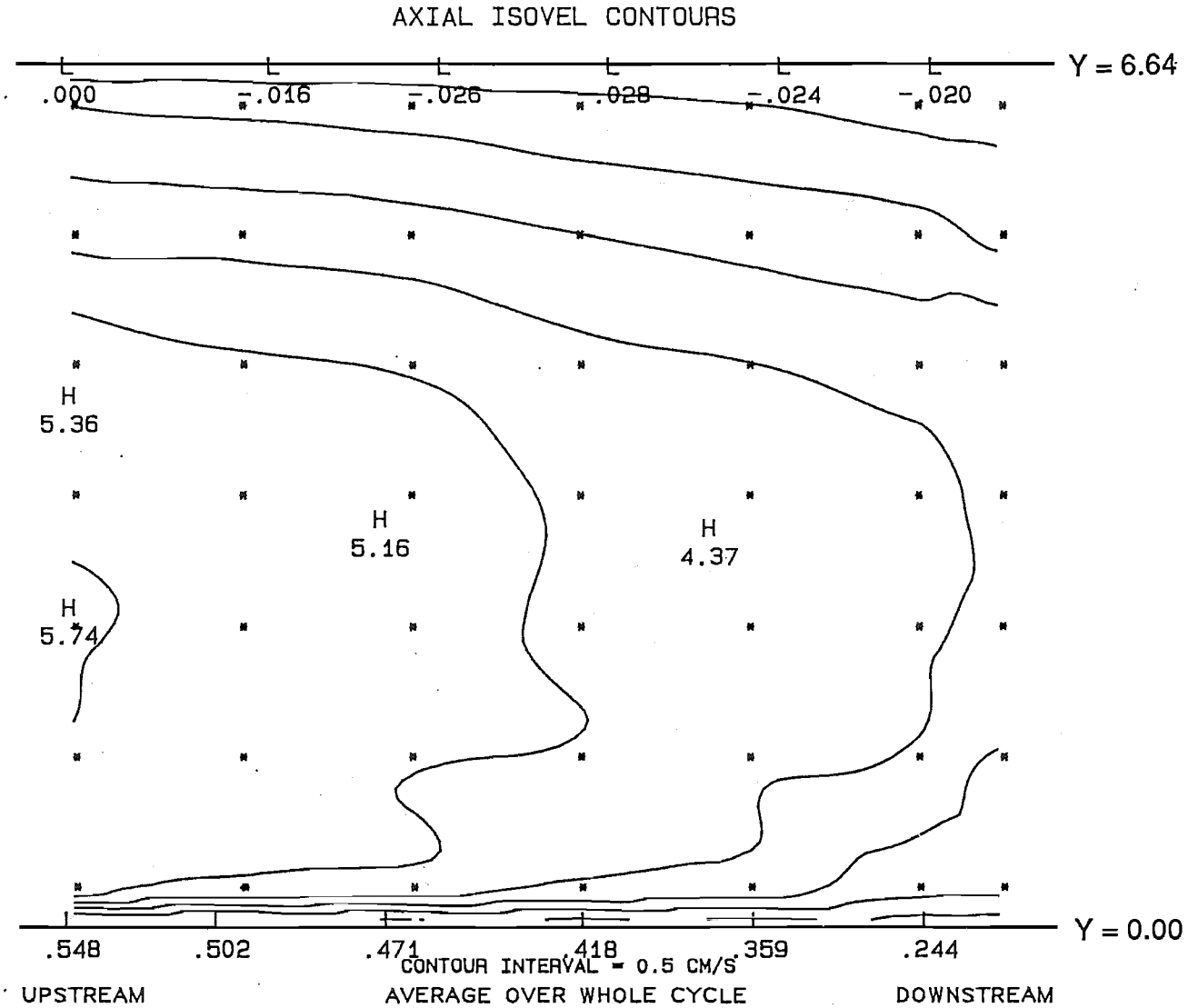

Figure 5.48: Along the $\alpha = 180°$ azimuth of the proximal stem. $Re_{mean} = 1500$.

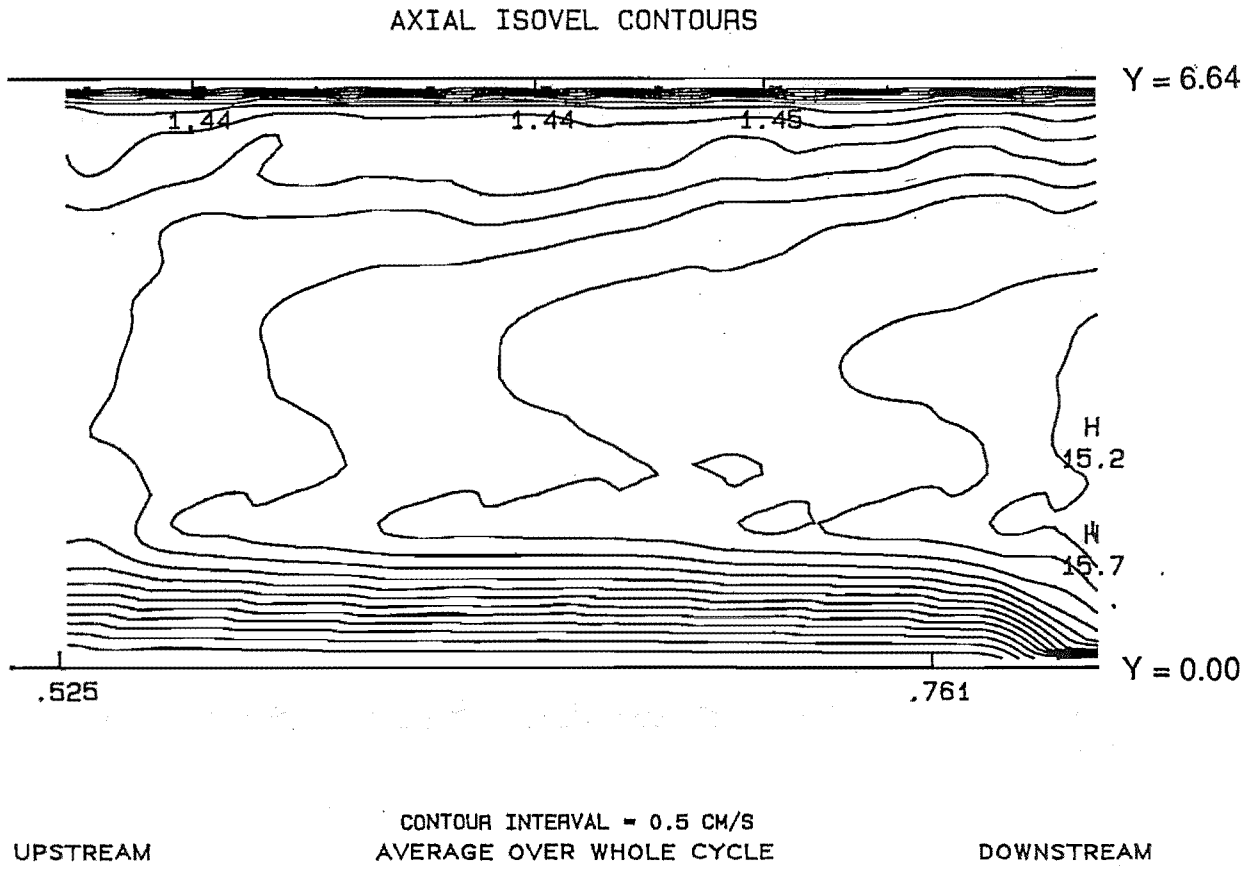

Figure 5.49: Along the $\alpha = 180°$ azimuth of the proximal limb. $Re_{mean} = 1500$.

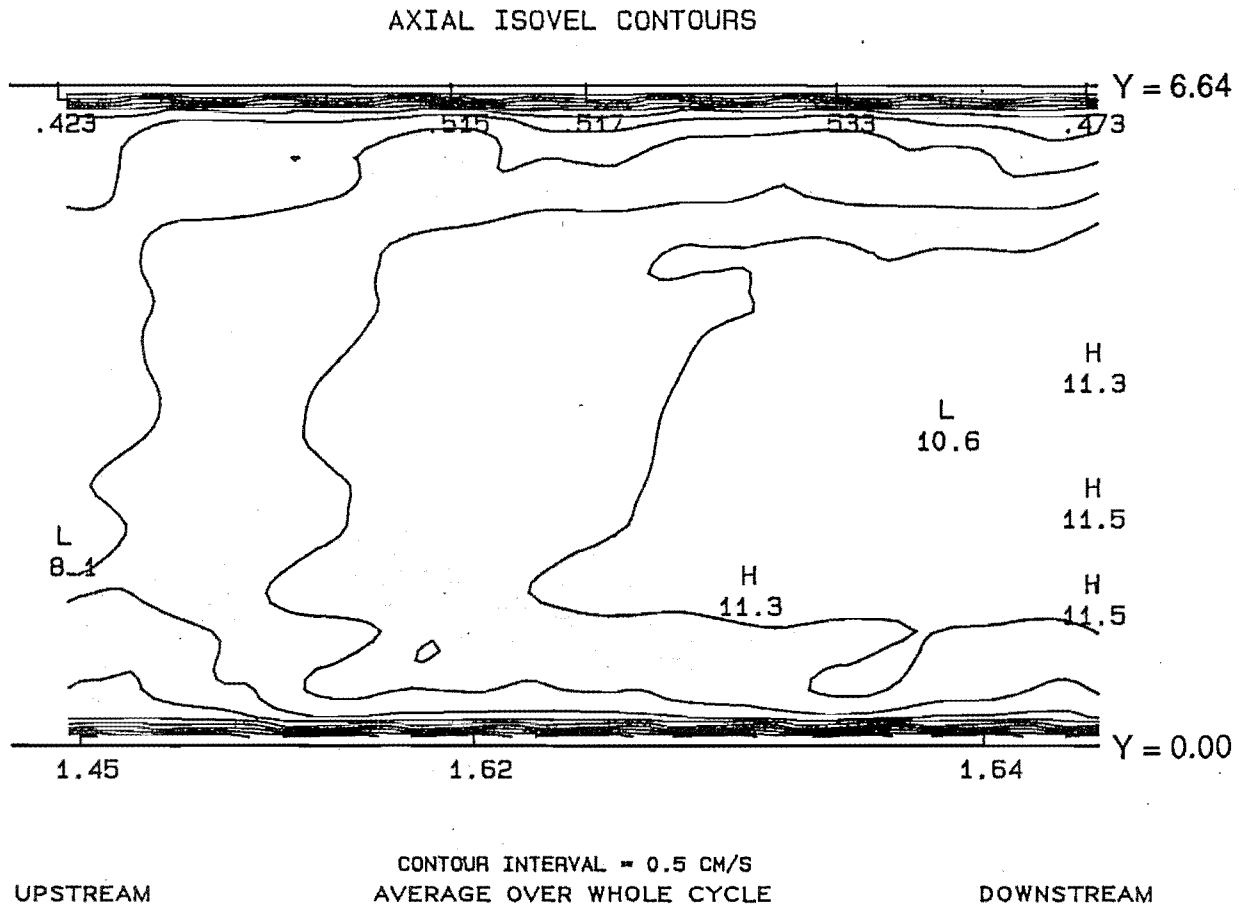

Figure 5.50: Along the $\alpha = 180°$ azimuth of the distal stem. $Re_{mean} = 1500$.

Similar contours were observed along the $\alpha = 0°$ azimuth downstream of the medial bend (Appendix I), though only half of the width of the tube at that position was used for contours, again due to optical problems causing a loss of LDA tracking. The maximum velocity was 14.7 cm s^{-1}.

Similar contours were again observed downstream of the distal bend along the $\alpha = 180°$ azimuth (figure 5.50). The contours were very nearly symmetrical and the maximum velocity was 15.2 cm s^{-1}.

5.4.3 Steady Flow Average Velocities:

Contours were generated for steady flows at Re = 500, 1000, and 1500 along the $\alpha = 0°$ azimuth of the proximal limb, BC, for comparison with pulsatile flow contours at similar instantaneous Reynolds numbers. These are included in this section because the plots are in the same format and the velocity measurements were carried out in the same orientation as the those for pulsatile flow. At Re = 500 (figure 5.51), the velocity gradients were very low and the contours almost symmetric. A large central backflow region (A) existed, with slow, positive flow on each side.

At Re = 1000 (figure 5.52) the flow was less symmetric and the backflow region had progressed to a position further upstream. Velocity gradients had increased, mainly caused by higher positve velocities on each side of the backflow region (A and B).

Higher velocity gradients were observed at Re = 1500 (figure 5.53). The backflow region had shifted from the centreline towards the Y = 6.64 wall of the tube, in agreement with the steady axial flow results of section 5.3. The backflow velocity was relatively large at -3.63 cm s^{-1}.

5.4.4 Centreline Velocities (Pulsatile):

Little of value was gained from plotting the centreline axial or radial velocities. Plots are included in Appendix I for the sake of completeness, but only a few general comments are made here.

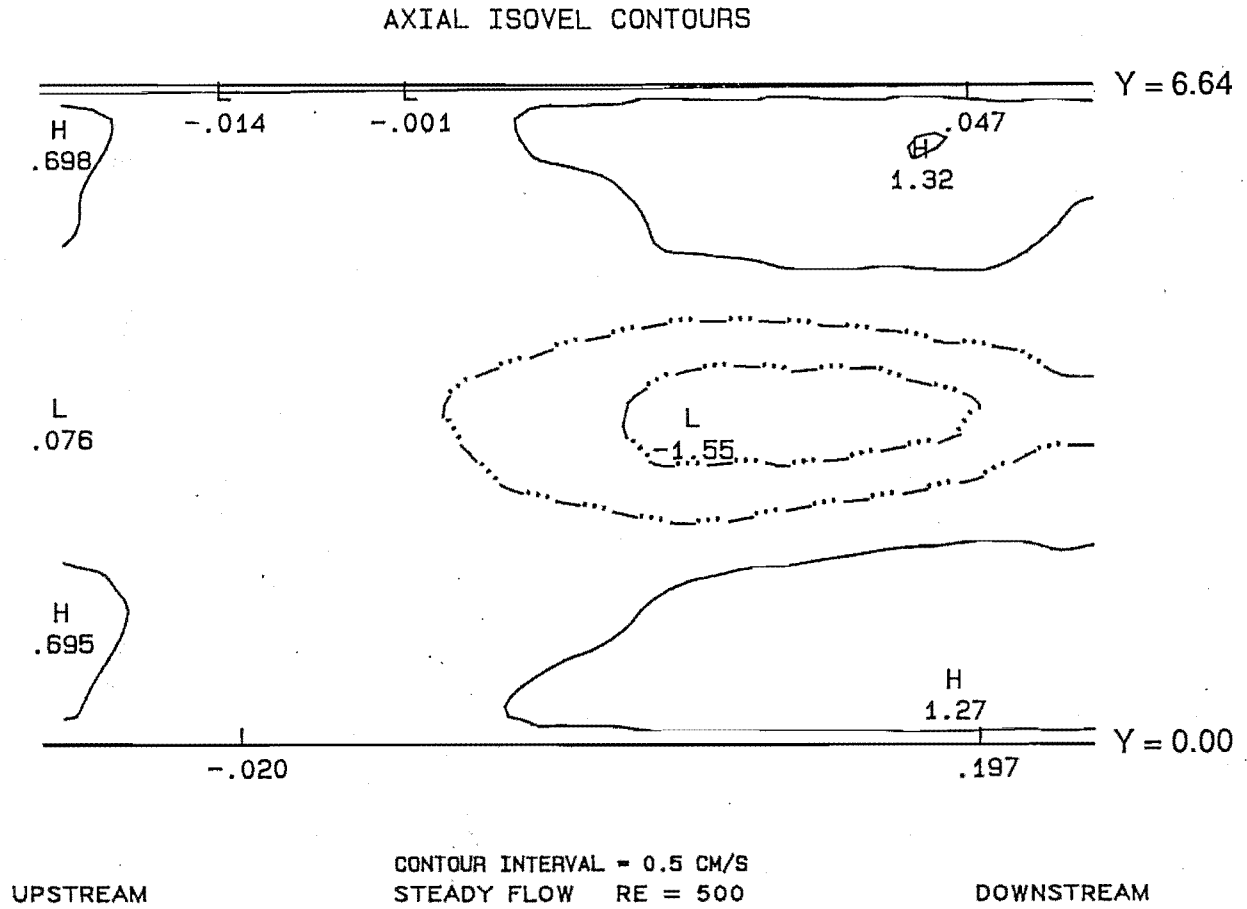

Figure 5.51: Steady Flow Along the $\alpha = 0°$ azimuth of the proximal limb. Re = 500.

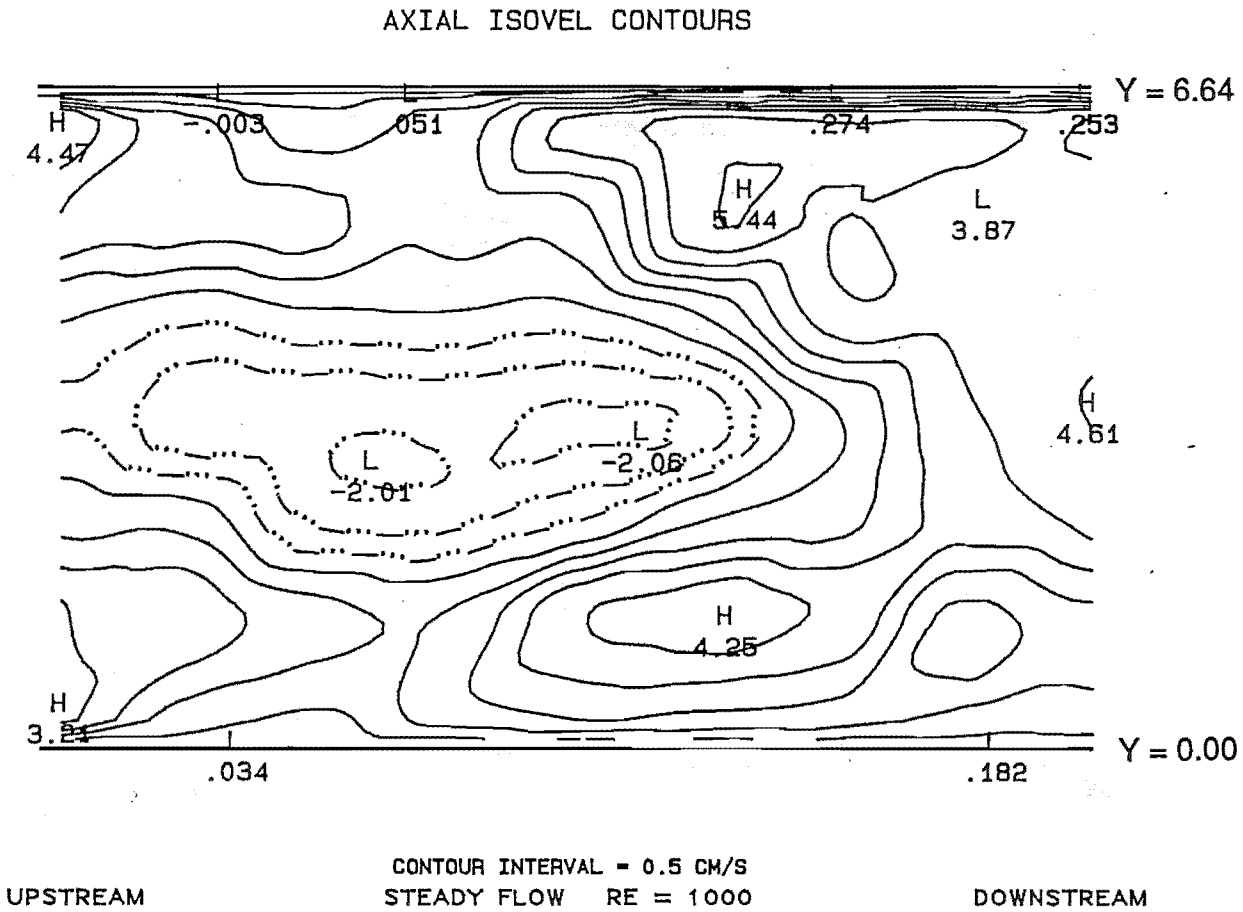

Figure 5.52: Steady Flow Along the $\alpha = 0°$ azimuth of the proximal limb. Re = 1000

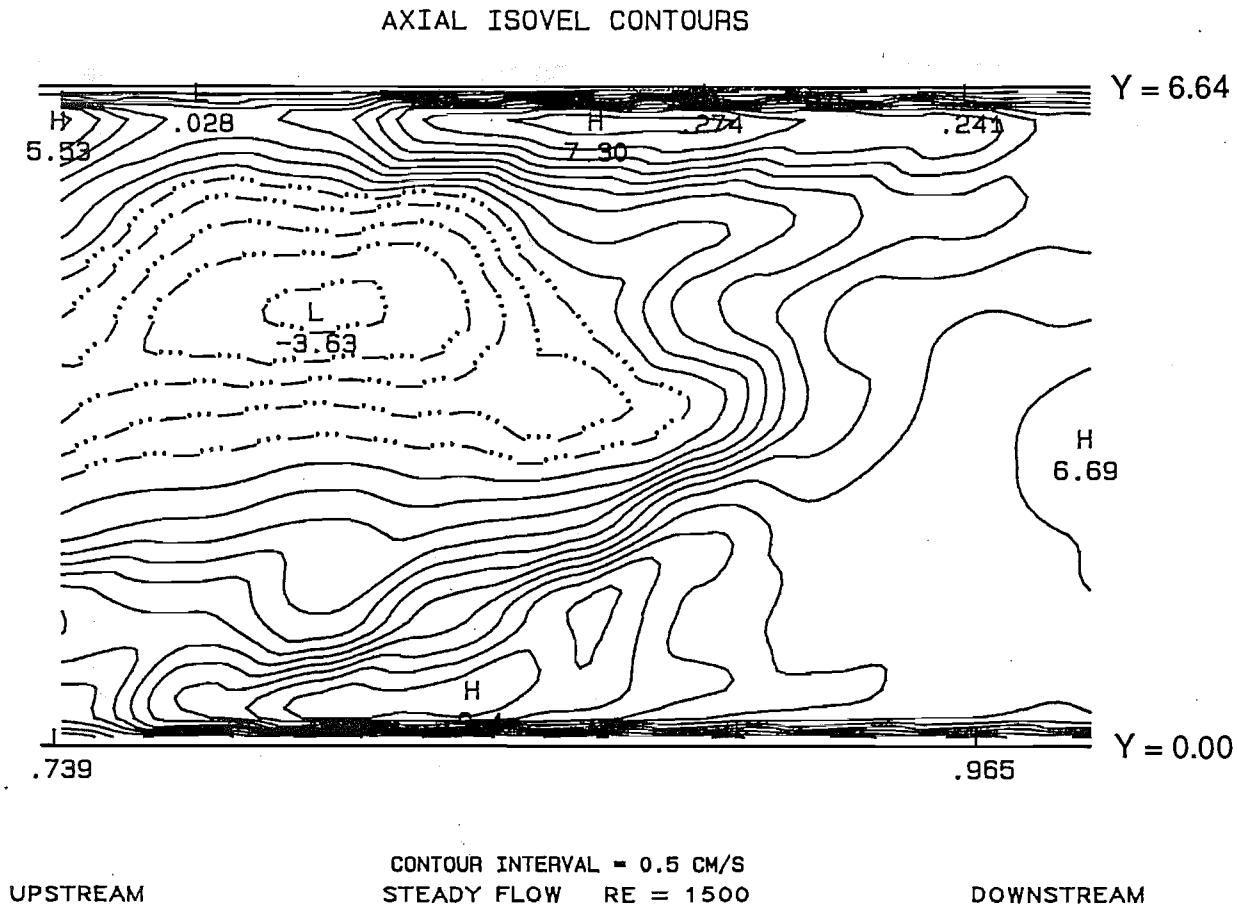

Figure 5.53: Steady Flow Along the $\alpha = 0°$ azimuth of the proximal limb. Re = 1500.

5.4.4.1 Axial Velocities (Pulsatile):

Centreline velocities were almost uniform along the length of the slices in the proximal stem.

In the proximal limb, BC, the axial velocities exhibited a minimum near the mid-length of the slice for both the Re_{mean} = 1000 and Re_{mean} = 1500 cases. The positions of these minima did not correlate with the flow along the $\alpha = 180°$ azimuth of the proximal limb and did not match the positions of the reverse flow along the $\alpha = 0°$ azimuth. Nothing in the centreline flow indicated separation. The centreline axial velocities in pulsatile flow were significantly reduced from the corresponding steady flow cases and the minima more pronounced.

In the distal limb, DE, a maximum occurred near the mid-length of the slice as opposed to the minimum observed in the proximal limb..

Some relationship between wall flows and centreline flows was looked for, but these centreline axial velocities could not be used to indicate even the general features of flow near the walls in the model.

5.4.4.2 Radial Velocities (Pulsatile):

Again, the radial velocities measured along the centreline of the tube parallel to the slices did not appear to correlate with the features of the flow near the walls.

5.4.5 Average Pulsatile Shear Rates:

The shear rates along each wall of the measurement slices were calculated from the average velocity values and plotted in figure 5.54. The vertical dotted lines in figure 5.54 mark the upstream and downstream ends of the slices. The shear rates are plotted for each slice, in columns between the vertical lines, from left to right in order of their axial positions along the slice. The columns are numbered for each slice.

Figure 5.54 shows that the shear rates (averaged over the whole cycle) were lower where separation occurred than those in the upstream proximal stem, OA1 (column 1). Conversely, opposite the separation regions, the shear rates were significantly higher than those in OA1.

The shear rates along the Y = 6.64 wall show several interesting features. Firstly, in the proximal stem near the proximal bend (OA2, the shear rates along the $\alpha = 0°$ azimuth (column 2) are all much higher than those in OA1 and increase towards

the proximal bend entrance to levels as high as those opposite the separation regions.

Secondly, the shear rates in the slice near the opposite wall (along the α = 180° azimuth, (Column 3)) decrease from the level of the OA1 shear rates to almost zero nearest the bend entrance. Recall that this slice was included in Group 2.

Finally, it can be seen that the shear rates can vary markedly from one side of a slice to the other. Average shear rates along the $\alpha = 0°$ azimuth of the proximal limb, BC (column 4), can range from near zero (where separation occurs) to almost as high as those at the opposite azimuth (column 5), where the maximum shear rates in the model occur.

The shear rates at each phase angle are shown in Appendix I. These contain similar features to those mentioned above, except that shear rates became negative (as expected) in those regions where negative flow occurred (following the sign of the velocity). The peak shear rate was observed to be about 250 s^{-1} for the only point measured along the Y = 0.00 wall of the $\alpha = 180°$ azimuth of the proximal limb, BC at a phase angle $\Psi = 210°$. Shear rates near zero and negative shear rates were common at the lowest flowrates ($\Psi = 0°$ and $\Psi = 30°$) of the groups 1 and 2 regions and went as low as -15 s^{-1} in the separation region of the proximal limb at Re_{mean} = 1500. Shear rates did not fall below zero in the group 3 regions.

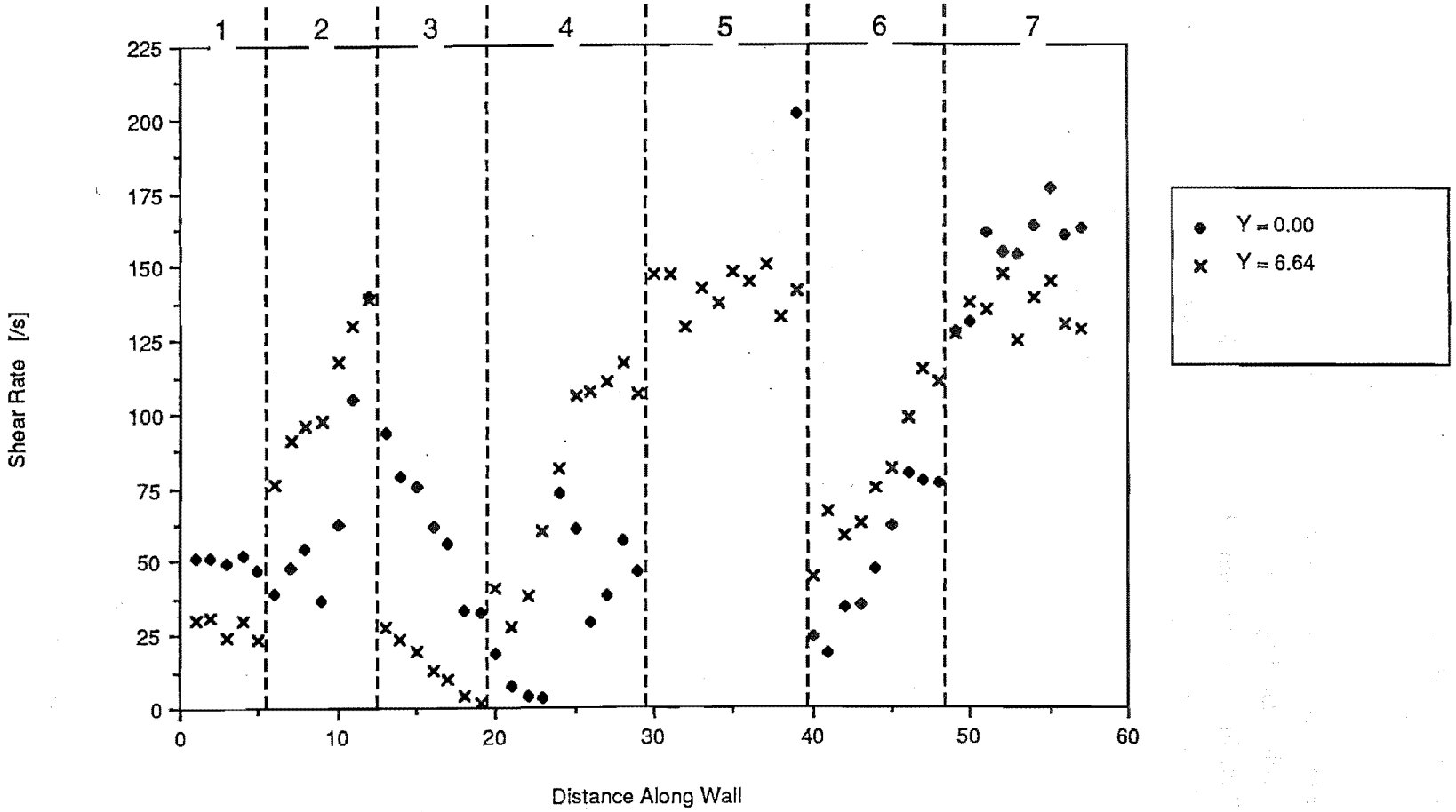

Figure 5.54: Average Shear Rates Along the Walls of the Measurement Slices, Re_{mean} = 1500. 1) OA1 $\alpha = 0°$ azimuth 2) OA2 $\alpha = 0°$ azimuth 3) OA2 $\alpha = 180°$ azimuth 4) BC $\alpha = 0°$ azimuth 5) BC $\alpha = 180°$ azimuth 6) FG $\alpha = 0°$ azimuth 7) FG $\alpha = 180°$ azimuth

5.4.6 Averaged Instantaneous Phase-dependent Velocities:

As in the overall average axial velocity contour plots, the following velocities were averaged at each phase angle over two or three consecutive cycles. The sampling routine is described in the experimental methods section, Chapter 4. Only those contour plots specifically referred to in the text are reproduced in this section, while the complete set of contours at phase angle intervals of 30° are contained in Appendix I.

5.4.6.1 Group 1:

Velocities were fairly uniform during the low velocity parts of the cycle, with very low velocity gradients, as shown at Ψ = 0°, 30°, 60° and 330° (figure 5.56 A,B,C, & D) for the slice along the α = 0° azimuth in the proximal stem, OA1. Velocities were negative, though of low magnitude, over large areas of the slice at the lowest velocity position Ψ = 30° (figure 5.56 B) and the one before it Ψ = 0° (figure 5.56 A).

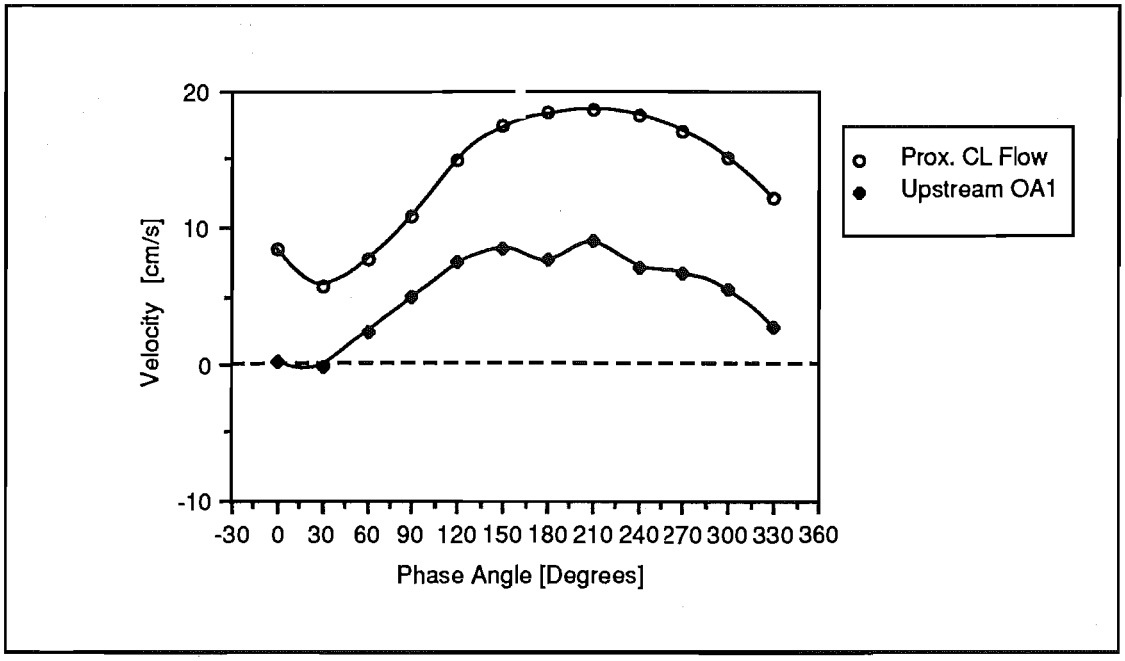

Figure 5.55
Time-dependent velocity at the upstream end of slice OA1 in the proximal stem, Re_{mean} = 1500.

Note that although the instantaneous Re was lower at Ψ = 60° (figure 5.56 C) than at Ψ = 0° (figure 5.56 A), no backflow was observed in the former. The mean flow at Ψ = 60° was accelerating, whilst that at Ψ = 0° was decelerating.

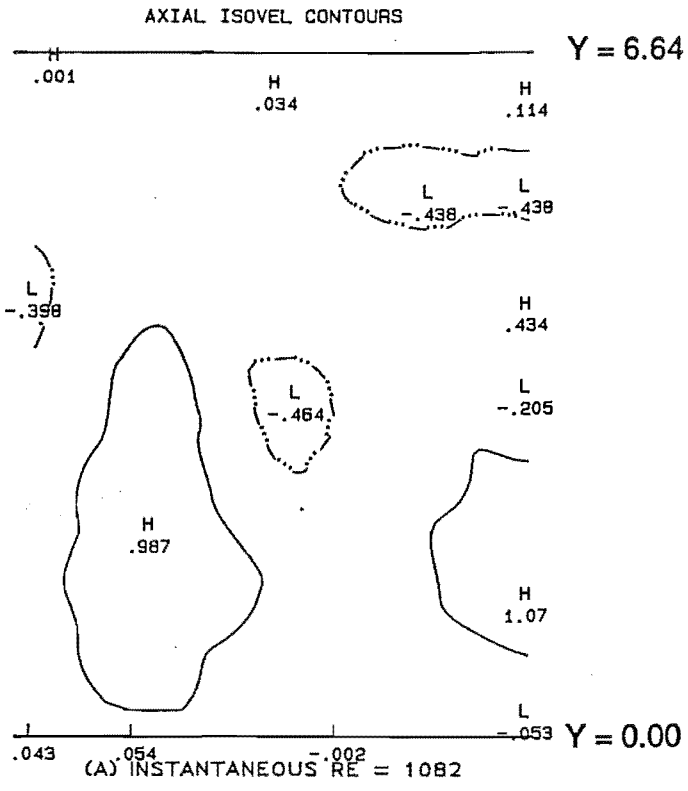

Upstream $\Psi = 0°$ Downstream

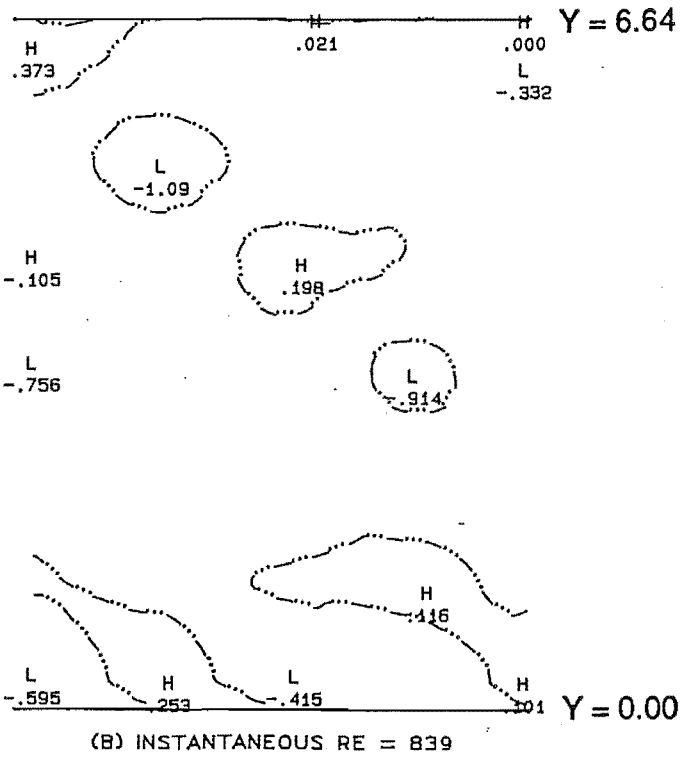

Upstream $\Psi = 30°$ Downstream

Figure 5.56 A-D

Along the $\alpha = 0°$ azimuth of the proximal stem, OA1, $Re_{mean} = 1500$
A)$\Psi = 0°$ B)$\Psi = 30°$ C)$\Psi = 60°$ D)$\Psi = 330°$.(cont. overleaf)

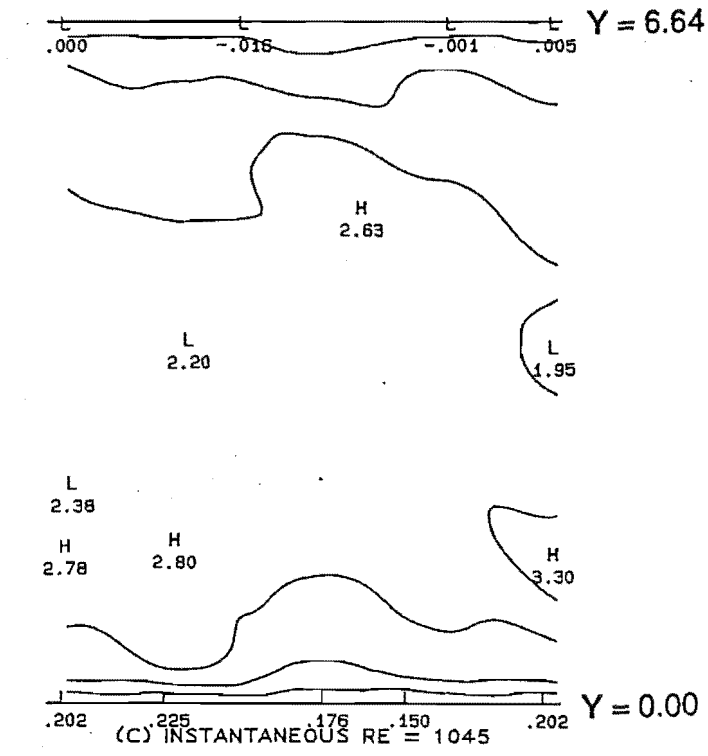

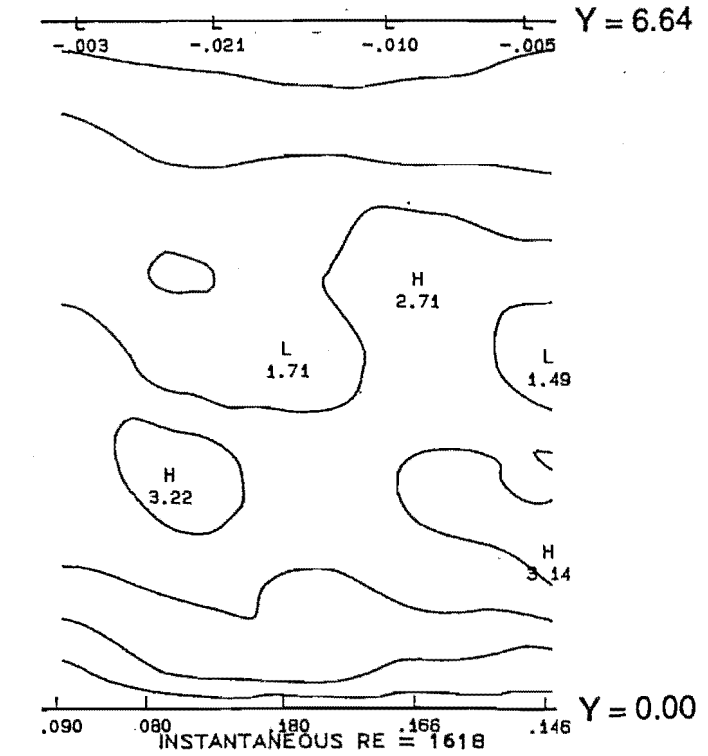

Figure 5.56 A-D (cont...)

Along the $\alpha = 0°$ azimuth of the proximal stem, OA1, $Re_{mean} = 1500$

A)$\Psi = 0°$ B)$\Psi = 30°$ C)$\Psi = 60°$ D)$\Psi = 330°$.

Figure 5.55 shows the time-dependent velocity at a point near the centreline at the upstream end of OA1 in the proximal stem, compared to that along the centreline in the proximal stem.

It can be seen that the velocity remained in phase with the centreline flow and was of smaller magnitude and amplitude. The flow became negative at phase angles of between $\Psi = 0°$ and $\Psi = 30°$.

The velocity gradients were slightly higher in the slice along the $\alpha = 0°$ azimuth of OA nearer the proximal bend, as shown in Appendix I, figure I-2 A-L. The gradient along the Y = 6.64 wall developed evenly throughout the acceleration part of the cycle, whilst that along the Y = 0.00 wall developed unevenly, beginning at the downstream end and developing upstream during the acceleration, and conversely during deceleration (Figure 5.58 A, (i)).

The shear layer was considerably thicker throughout the cycle near the Y = 0.00 wall than at the opposite side. A slight aberation was present near the Y = 0.00 wall (Figure 5.58 B, (ii)). A plot of the time-dependent velocities over the cycle in this position shows (figure 5.57) that more extrema occur at this position than the two in the proximal centreline flow.

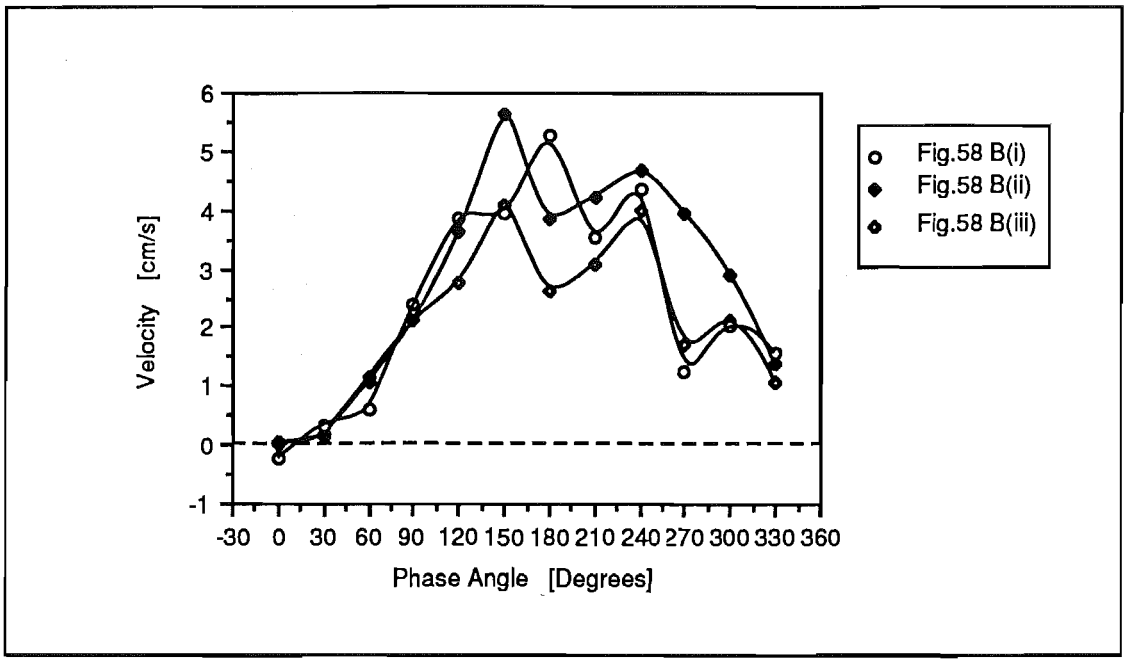

Figure 5.57

Time-dependent velocities near the Y = 0.00 wall of OA2 along the $\alpha = 0°$ azimuth of the proximal stem, $Re_{mean} = 1500$.

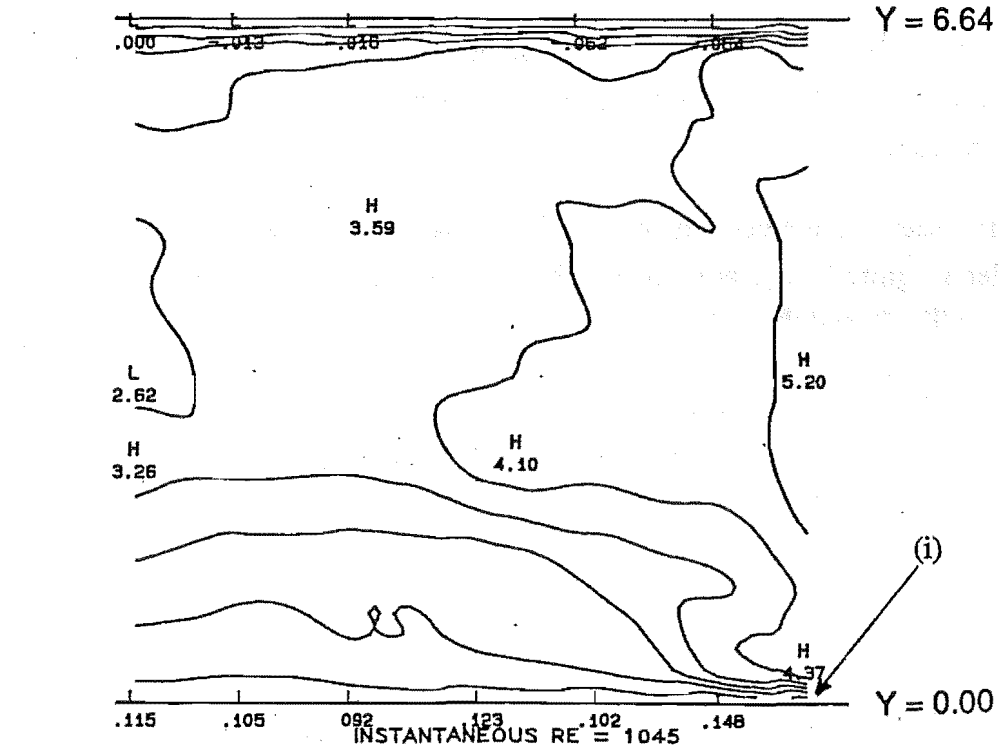

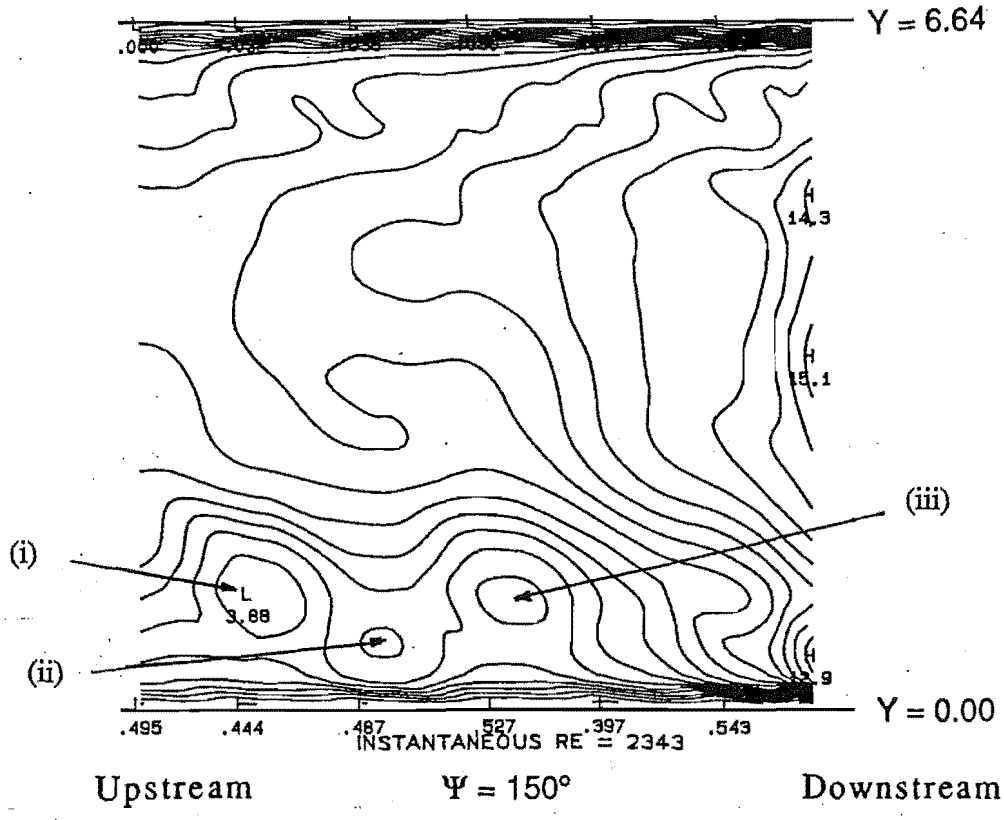

Figure 5.58 A-B

Along the $\alpha = 0°$ azimuth of the proximal stem, OA2, $Re_{mean} = 1500$ A)$\Psi = 60°$ B)$\Psi = 150°$.

5.4.6.2 Group 2:

$\underline{Re_{mean} = 1000:}$

Asymmetric velocity gradients were observed over the whole slice, as illustrated in Appendix I, figure I-3 A-L for the slice along the $\alpha = 0°$ azimuth of the proximal limb, BC.

Negative flow was present at some points at all phase angles of the cycle except at the beginning of the acceleration at $\Psi = 60°$ (Figure 5.60 B). After this phase angle, the backflow reappeared at the downstream end of the slice in $\Psi = 90°$ (figure 5.60 C), moving upstream with increased flowrate until $\Psi = 180°$ at $Re_{inst} = 1862$ (figure 5.60 E). Thereafter, the backflow region maintained it's size and position, decreasing in intensity during deceleration.

The free shear layer between the negative and positive flow (figure 5.60 F) (ii) was dispersed during the deceleration and did not reappear until $\Psi = 120°$ at an instantaneous Reynolds number $Re_{inst} = 1606$ (figure 5.60 D (i)) during acceleration, when the backflow region had moved upstream sufficiently to be bounded at it's downstream end by positive flow.

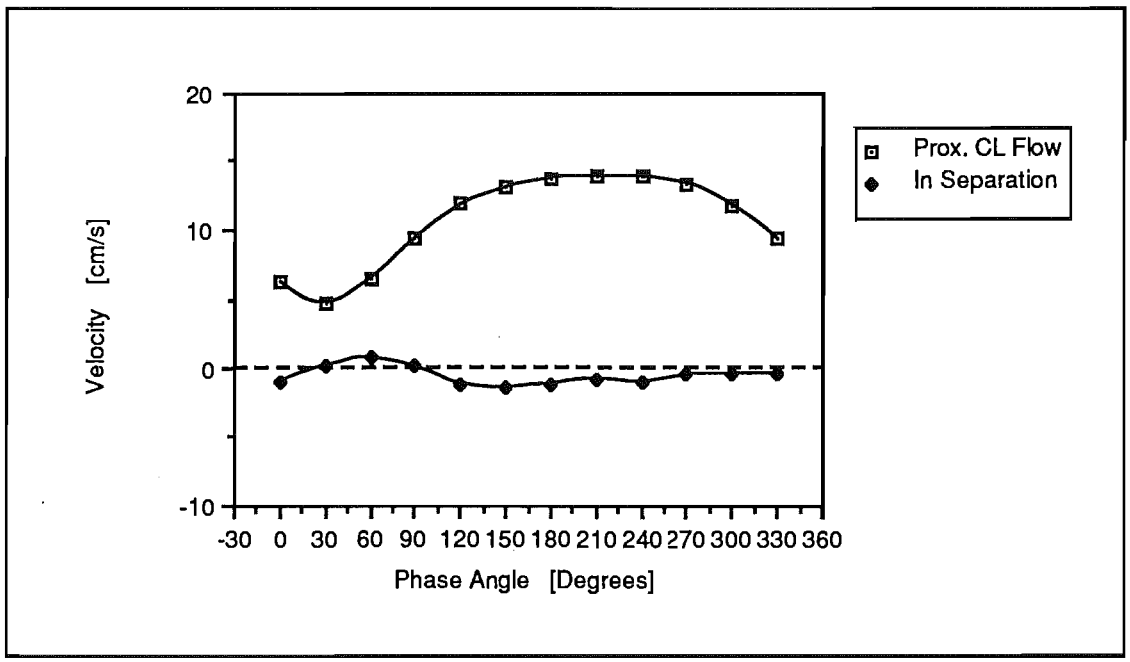

Figure 5.59

Time-dependent velocities in the separation region of the proximal limb, along the $\alpha = 0°$ azimuth, $Re_{mean} = 1000$.

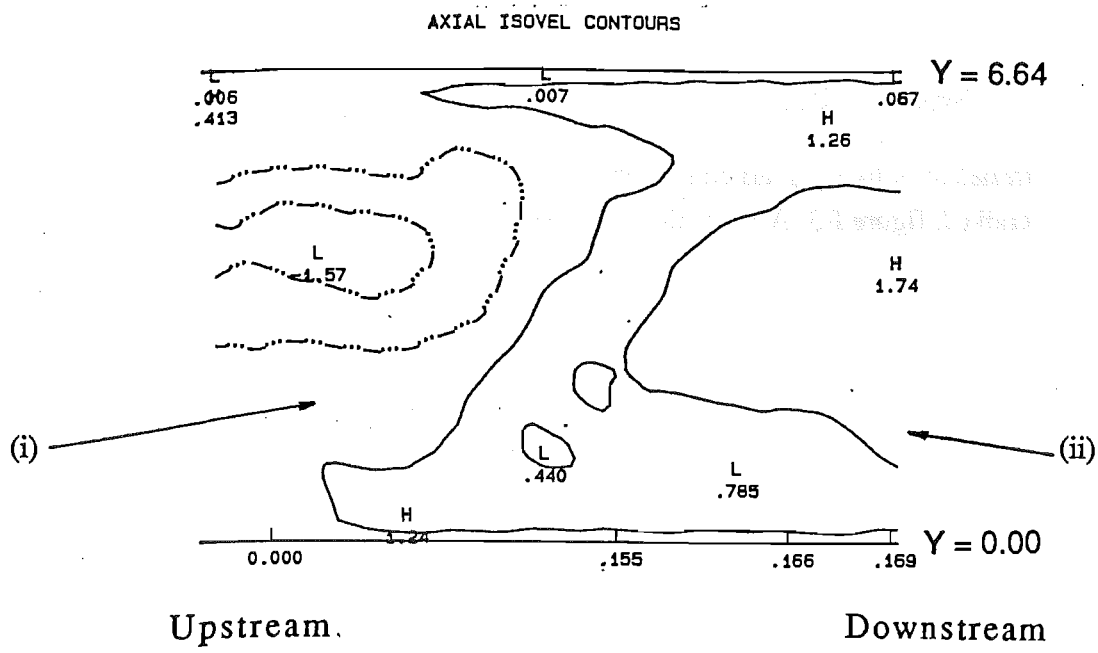

INSTANTANEOUS RE = 851

$\Psi = 0°$

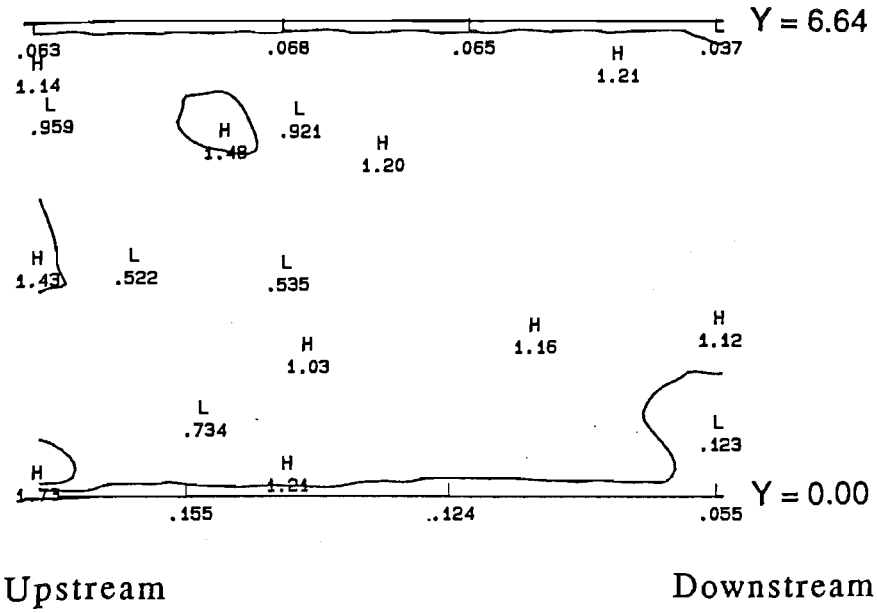

INSTANTANEOUS RE = 864

$\Psi = 60°$

Figure 5.60 A-F

Along the $\alpha = 0°$ azimuth of the proximal limb, $Re_{mean} = 1000$

A)$\Psi = 0°$ B)$\Psi = 60°$ C)$\Psi = 90°$ D)$\Psi = 120°$ E)$\Psi = 180°$

F)$\Psi = 210°$. (cont. overleaf)

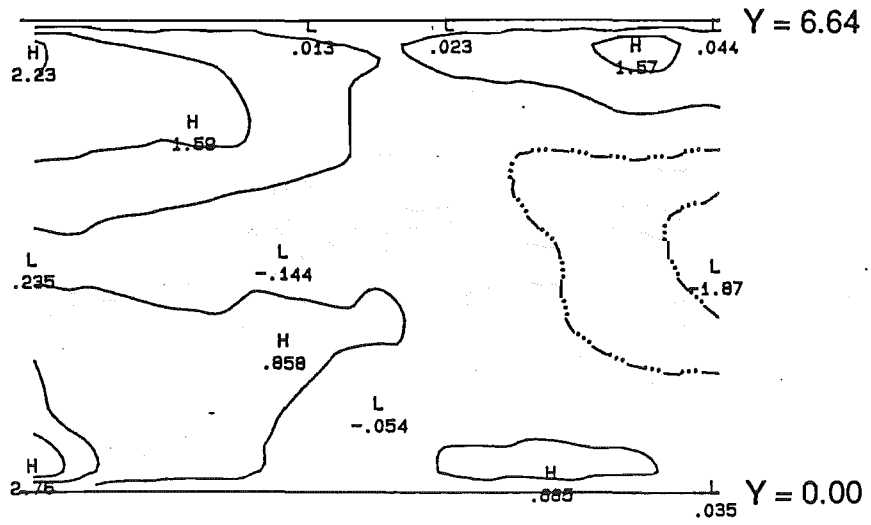

Upstream Downstream

INSTANTANEOUS RE = 1267

$\Psi = 90°$

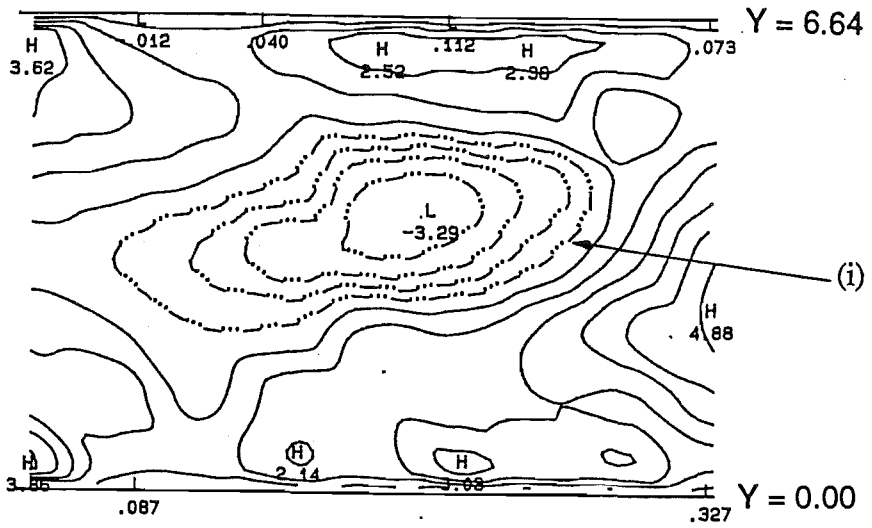

Upstream Downstream

INSTANTANEOUS RE = 1606

$\Psi = 120°$

Figure 5.60 A-F (cont...)

Along the $\alpha = 0°$ azimuth of the proximal limb, $Re_{mean} = 1000$

A)$\Psi = 0°$ B)$\Psi = 60°$ C)$\Psi = 90°$ D)$\Psi = 120°$ E)$\Psi = 180°$

F)$\Psi = 210°$. (cont. overleaf)

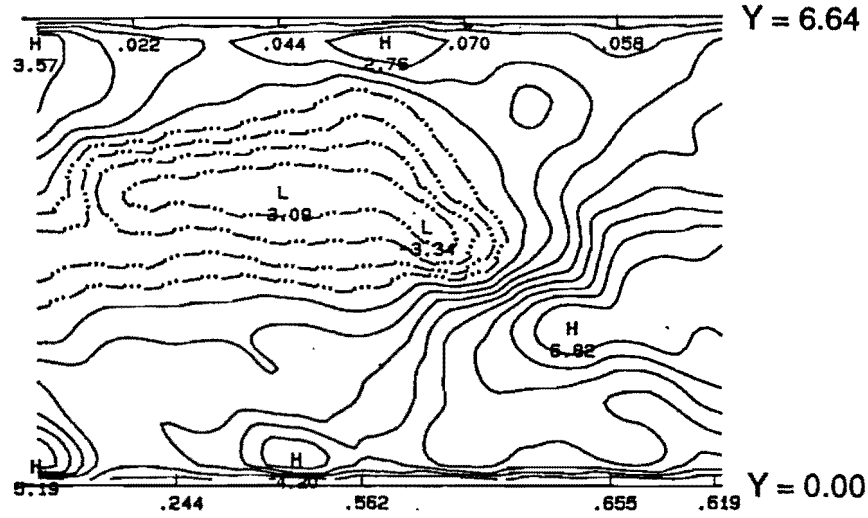

INSTANTANEOUS RE = 1862

$\Psi = 180°$

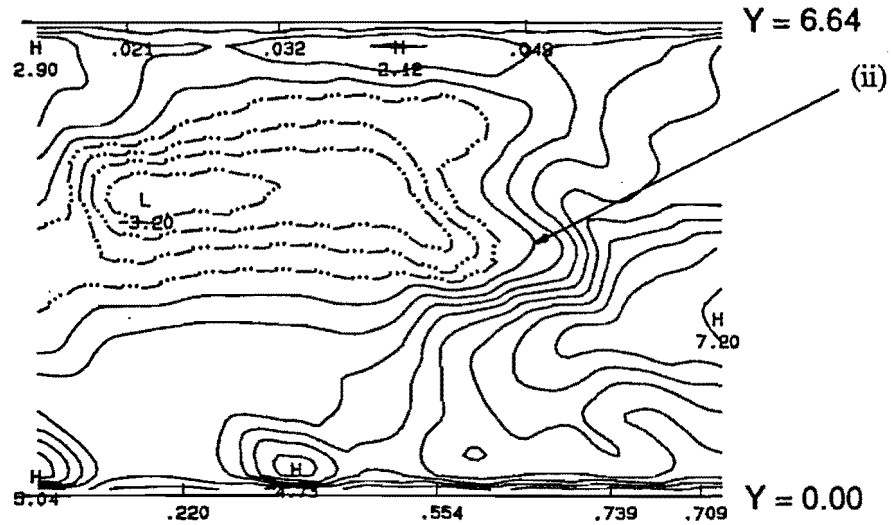

INSTANTANEOUS RE = 1894

$\Psi = 210°$

Figure 5.60 A-F (cont...)

Along the $\alpha = 0°$ azimuth of the proximal limb, $Re_{mean} = 1000$

A)$\Psi = 0°$ B)$\Psi = 60°$ C)$\Psi = 90°$ D)$\Psi = 120°$ E)$\Psi = 180°$

F)$\Psi = 210°$.

The time-dependent velocities at a point in the separation region are shown in figure 5.59. It can be seen that considerable negative flow occured and that the cycle was approximately 180° out of phase with the proximal centreline velocity.

In the free shear region (Figure 5.60 F, (ii)), velocities were fairly constant up until about Ψ = 120°, when the velocities increased suddenly, probably due to movement of the shear layer, as shown by the time-dependent velocities in figure 5.61.

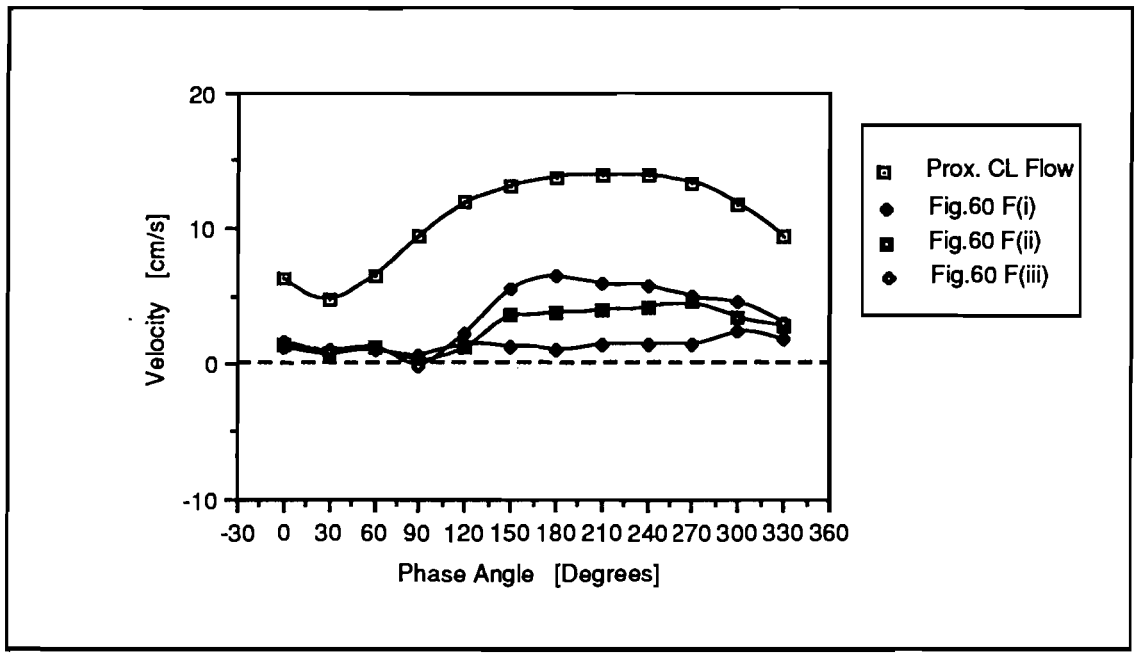

Figure 5.61
Time-dependent velocities in the shear region bounding the separation in the proximal limb, Re_{mean} = 1000.

At a position at the downstream end of the proximal limb, the time-dependent velocities almost matched the phase of the proximal centreline flow, whilst at the upstream end, the phase of the flow was shifted by about 30° (figure 5.62).

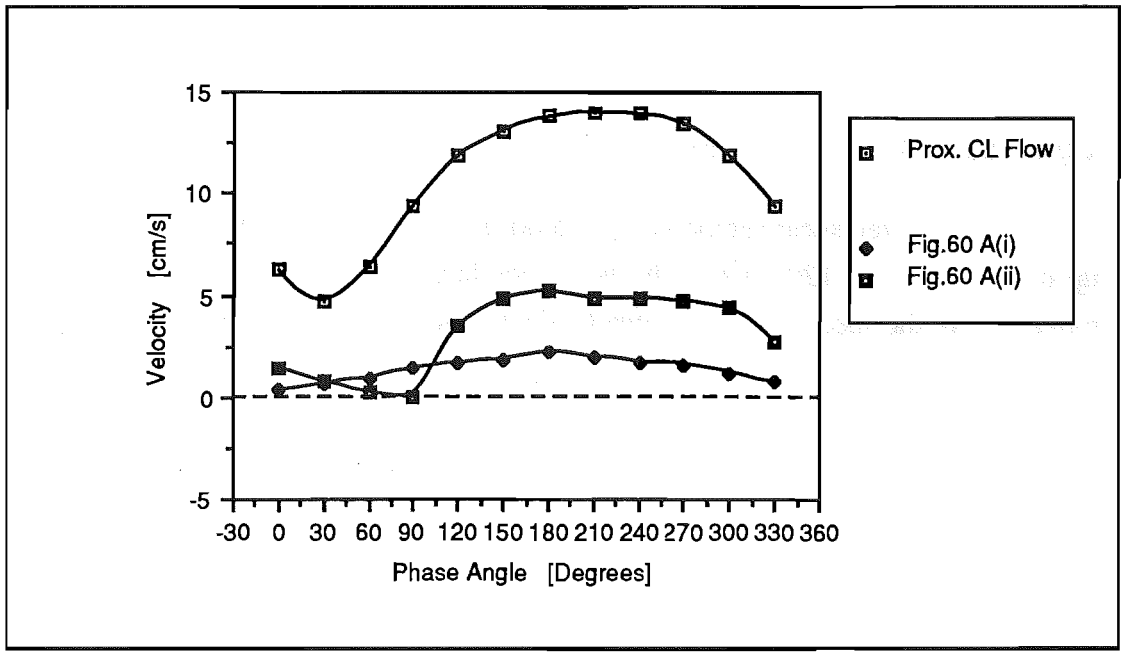

Figure 5.62

Time-dependent velocities at the upstream and downstream ends of the proximal limb, along the $\alpha = 0°$ azimuth, $Re_{mean} = 1000$.

$\underline{Re_{mean} = 1500:}$

At Re_{mean} = 1500, the contours were more disturbed and the velocity gradients were much higher (figure 5.63 A-L). Again the backflow region was not present at the first acceleration phase angle, $\Psi = 60°$ (figure 5.63 C) and reappeared from the downstream end at the subsequent phase angle. The backflow region occupied a constant position during deceleration only (figure 5.63 I-L & A), with velocity gradients decreasing until $\Psi = 30°$ and $\Psi = 60°$ (instantaneous Reynolds numbers of 839 and 1045), at which points the backflow had disappeared altogether. The free shear layer (figure 5.63 F-G, (i)) was most intense during acceleration.

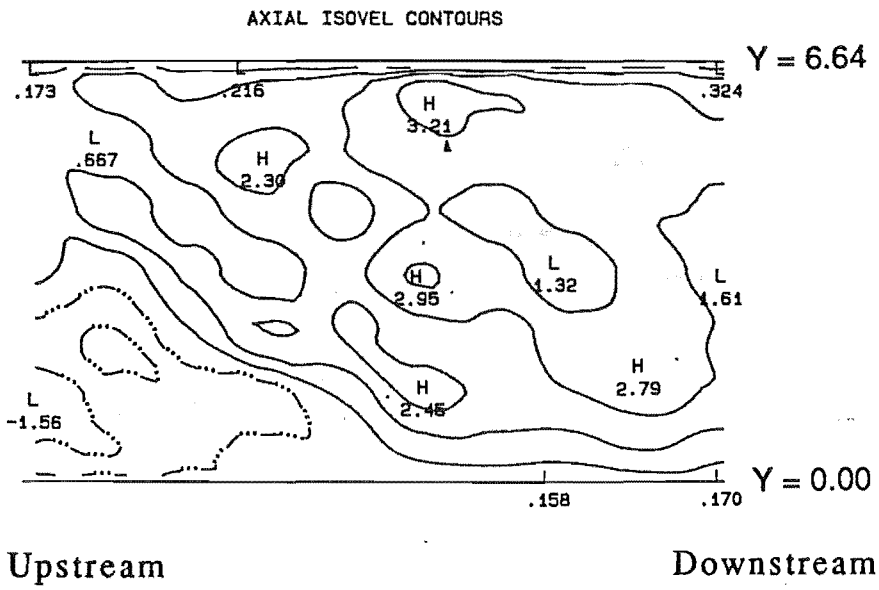

(A) INSTANTANEOUS RE = 1082

$\Psi = 0°$

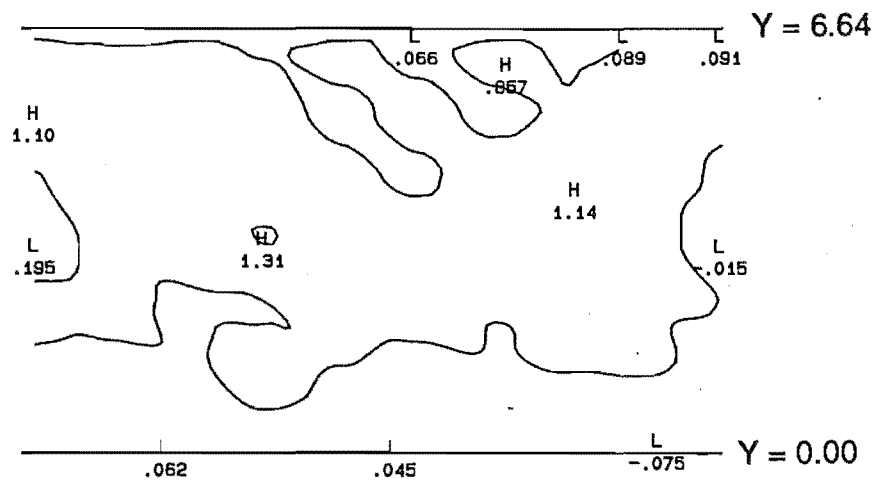

(B) INSTANTANEOUS RE = 839

$\Psi = 30°$

Figure 5.63 A-L

Along the $\alpha = 0°$ azimuth of the proximal limb, $Re_{mean} = 1500$

A)$\Psi = 0°$ B)$\Psi = 30°$ C)$\Psi = 60°$ D)$\Psi = 90°$ E)$\Psi = 120°$

F$\Psi = 150°$ G)$\Psi = 180°$ H)$\Psi = 210°$ I)$\Psi = 240°$ J)$\Psi = 270°$

K)$\Psi = 300°$ L)$\Psi = 330°$. (cont. overleaf)

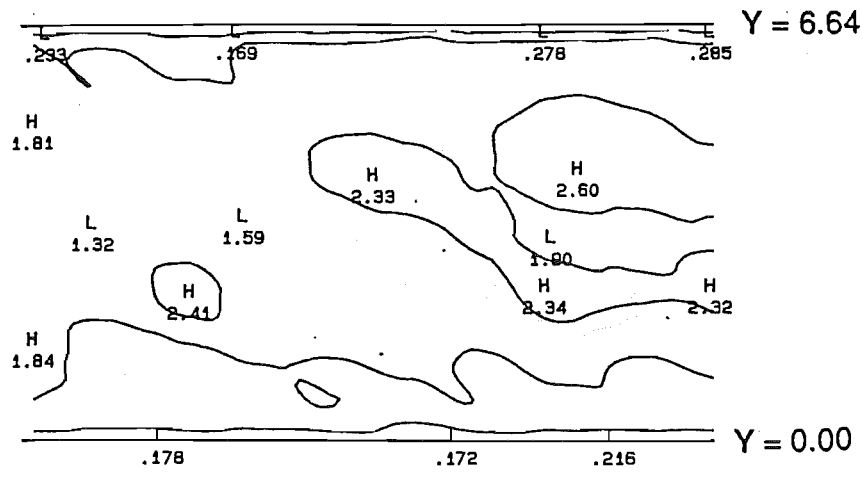

Upstream Downstream

(C) INSTANTANEOUS RE = 1045

$\Psi = 60°$

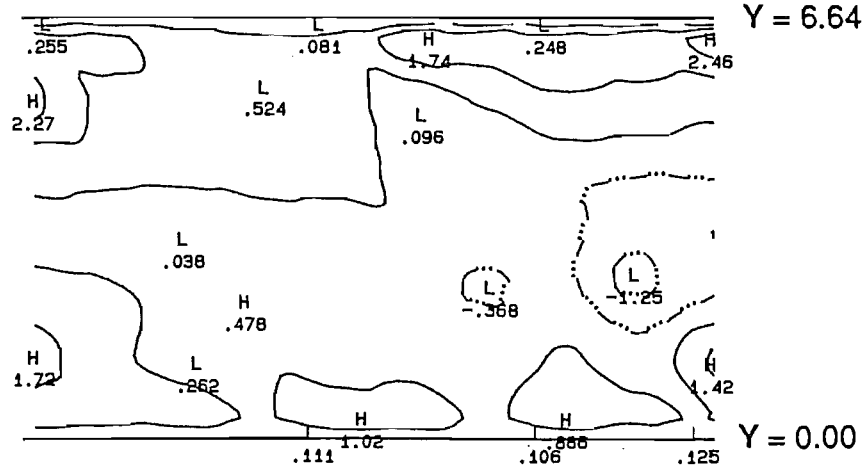

Upstream Downstream

(D) INSTANTANEOUS RE = 1446

$\Psi = 90°$

Figure 5.63 A-L (cont.)

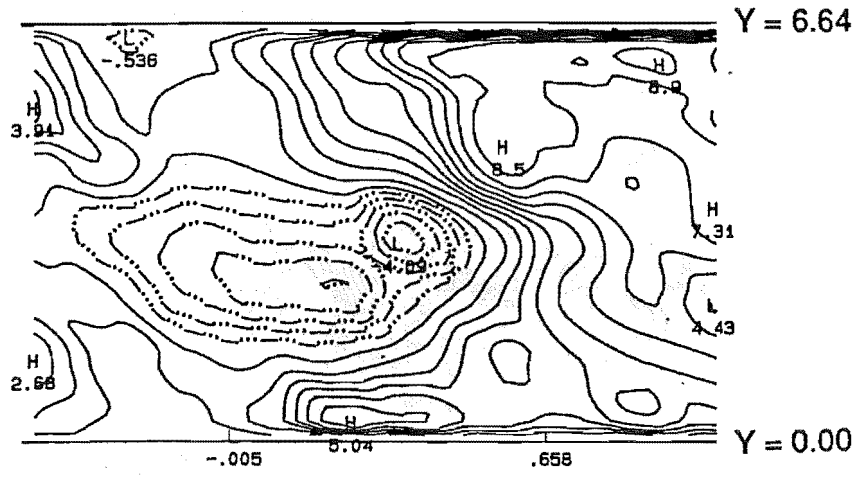

Upstream Downstream

(E) INSTANTANEOUS RE = 2018

$\Psi = 120°$

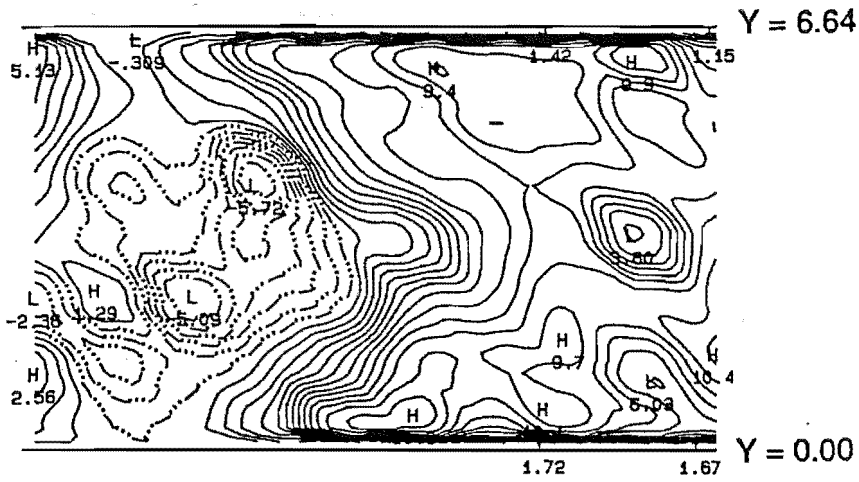

Upstream Downstream

(F) INSTANTANEOUS RE = 2343

$\Psi = 150°$

Figure 5.63 A-L (cont.)

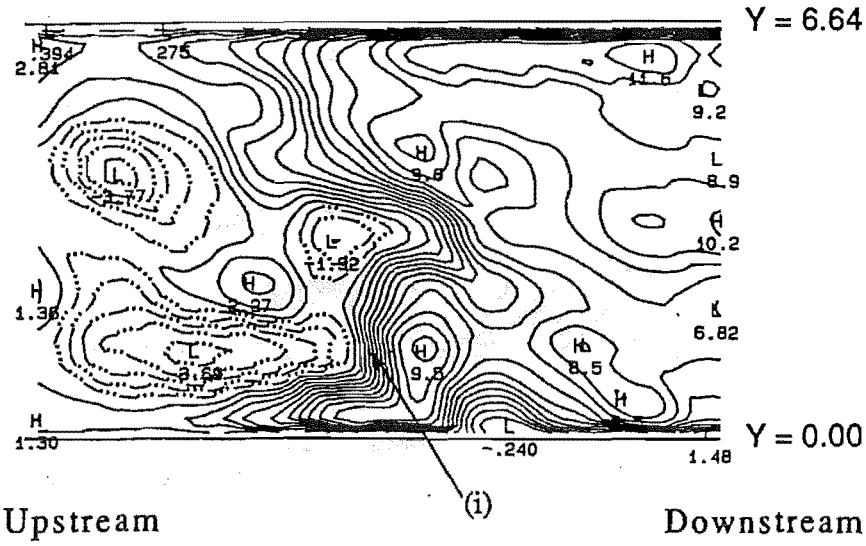

(G) INSTANTANEOUS RE = 2471

$\Psi = 180°$

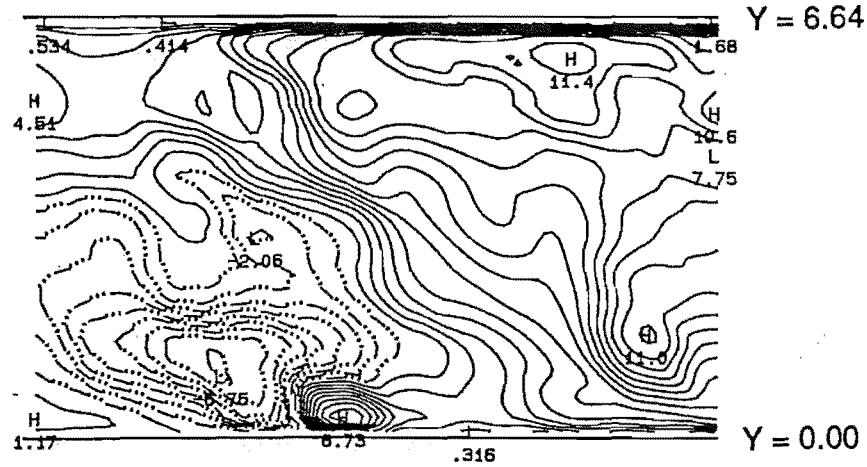

(H) INSTANTANEOUS RE = 2486

$\Psi = 210°$

Figure 5.63 A-L (cont.)

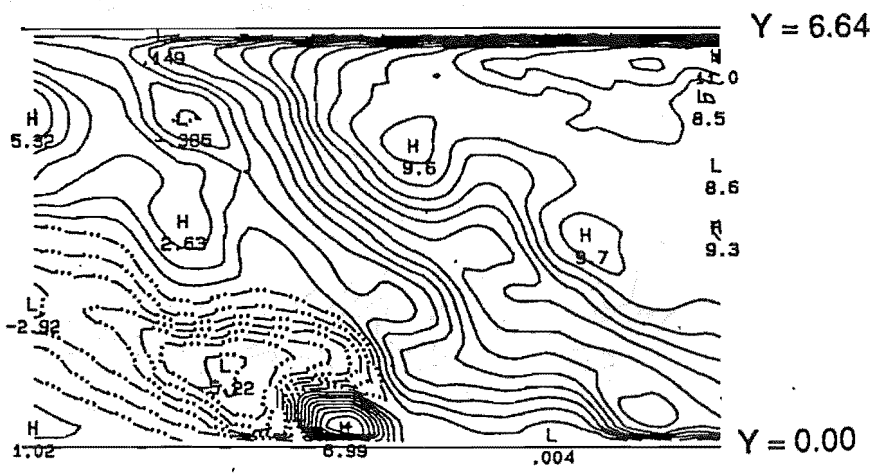

(I) INSTANTANEOUS RE = 2459

$\Psi = 240°$

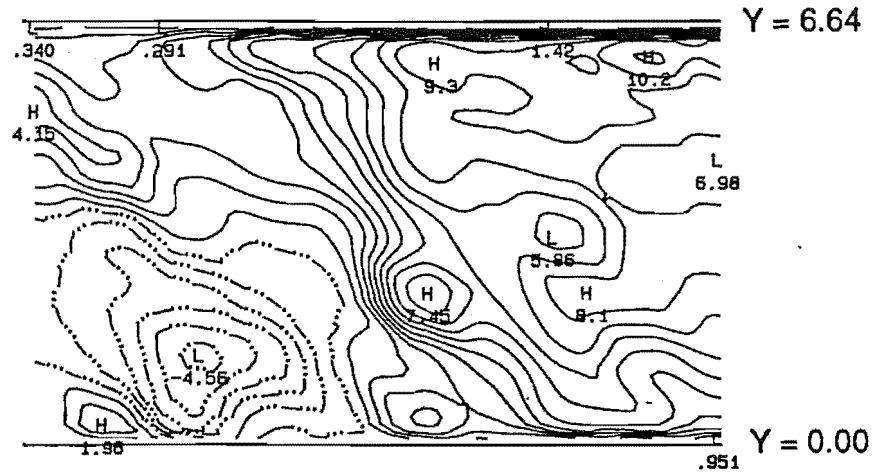

(J) INSTANTANEOUS RE = 2318

$\Psi = 270°$

Figure 5.63 A-L (cont.)

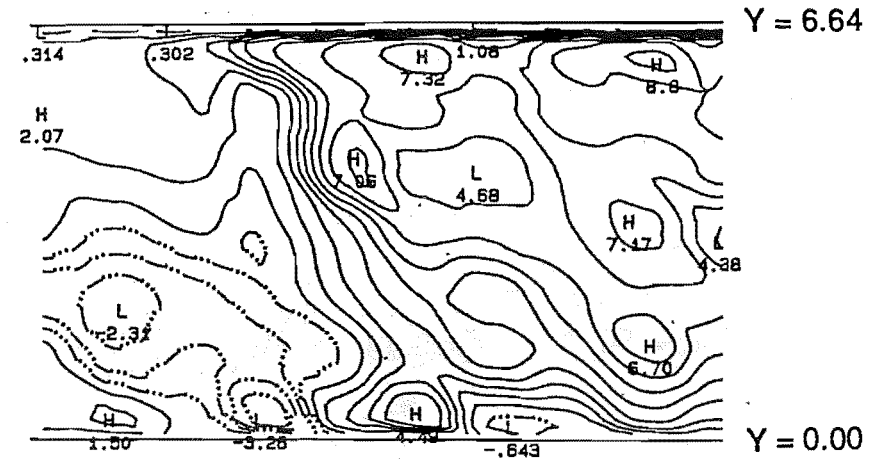

(K) INSTANTANEOUS RE = 2043

$\Psi = 300°$

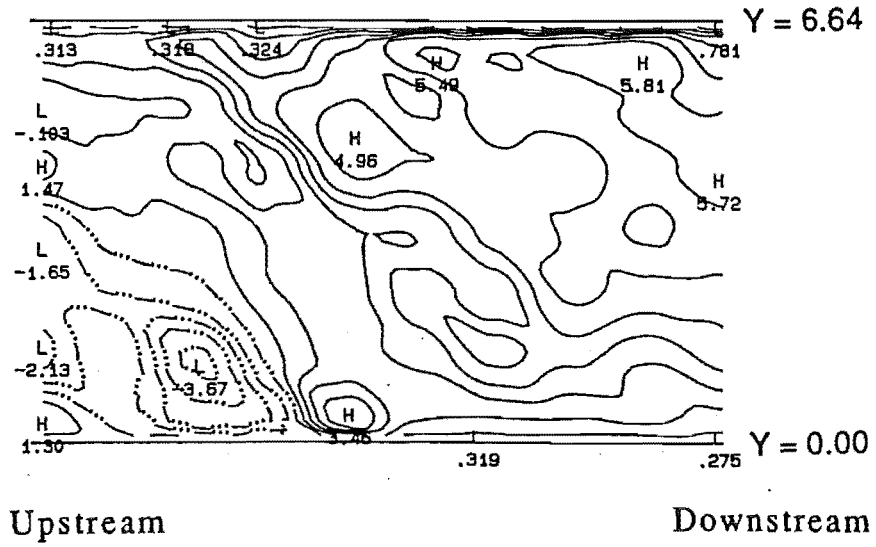

(L) INSTANTANEOUS RE = 1618

$\Psi = 330°$

Figure 5.63 A-L (cont.)

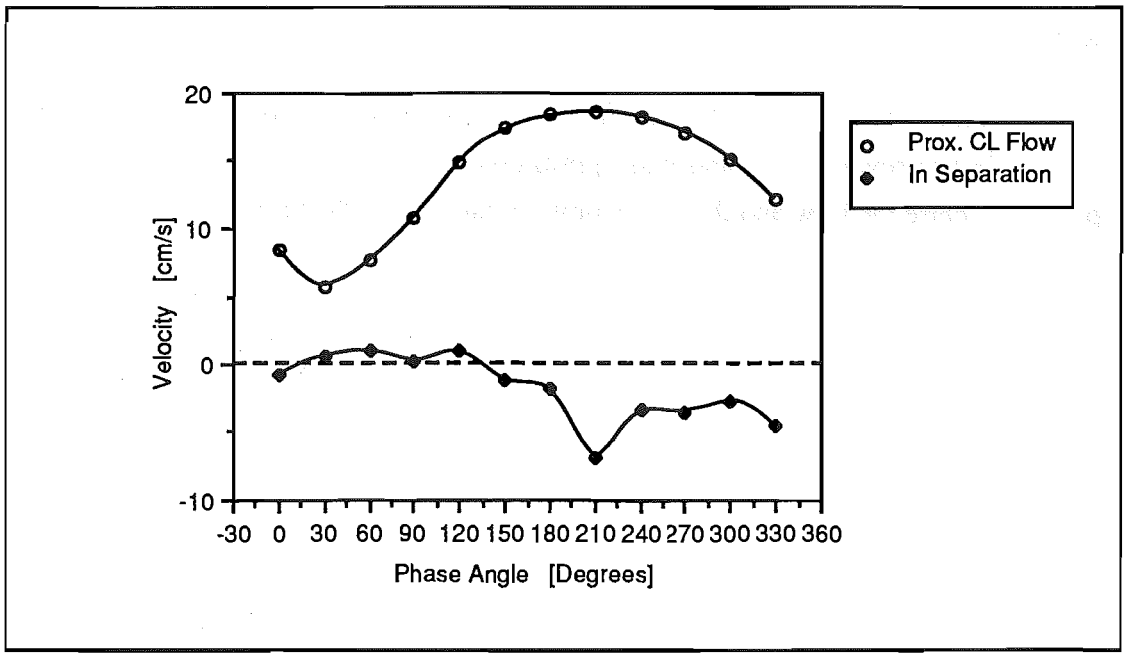

Figure 5.64

Time-dependent velocities in the separation region along the $\alpha = 0°$ azimuth of the proximal limb, $Re_{mean} = 1500$.

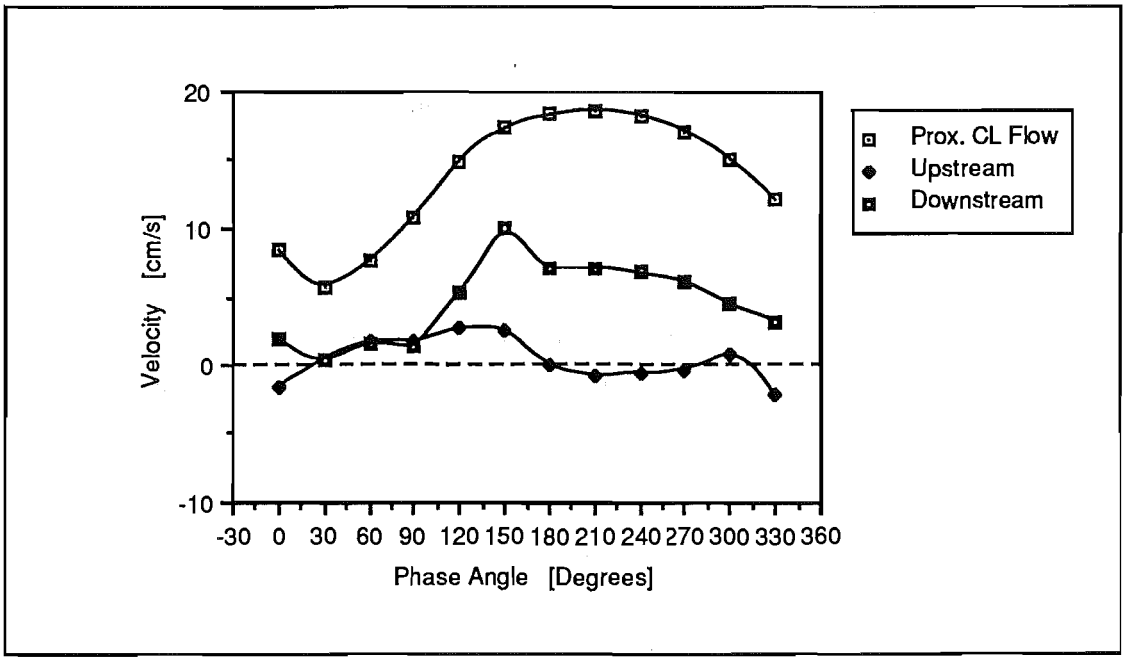

Figure 5.65

Time-dependent velocities at the upstream and downstream ends of the proximal limb along the $\alpha = 0°$ azimuth, $Re_{mean} = 1500$.

Figure 5.64 shows the time-dependent velocity at a point which was subject to backflow over a large part of the cycle. Note that the velocity was 180° out of phase with that of the proximal centreline velocity.

Figure 5.65 shows that the flow at the upstream end of the proximal limb was subject to reverse flow and was approximately 180° out of phase with both the proximal centreline flow and that at the downstream end of the proximal limb.

The time-dependent velocities at two points in the free shear layer are shown in figure 5.66. These show a sudden increase in velocity, probably as the free shear layer swept past and replaced reverse flow with positive flow.

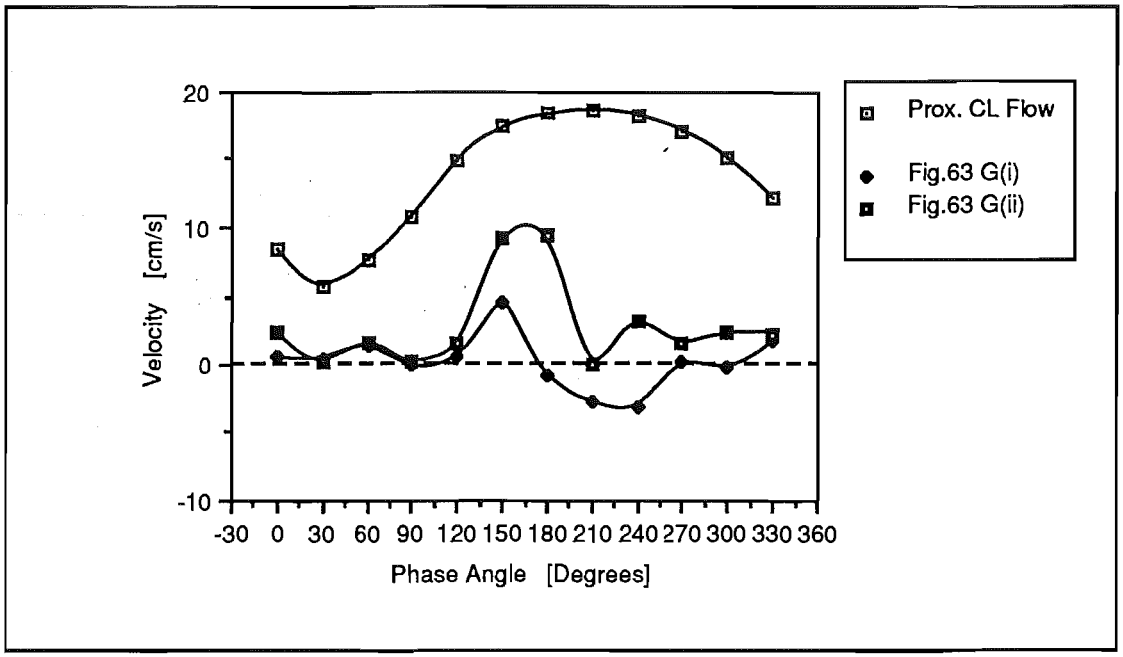

Figure 5.66

Time-dependent velocities in the shear region bounding the separation region in the proximal limb, Re_{mean} = 1500.

Similar characteristics were observed in the slice along the $\alpha = 0°$ azimuth of the distal stem (Appendix I, figure I-7).

Recall that the slice along the $\alpha = 180°$ azimuth of the proximal stem, OA, near the proximal bend was included in group 2 (Appendix I, figure I-5 A-L).

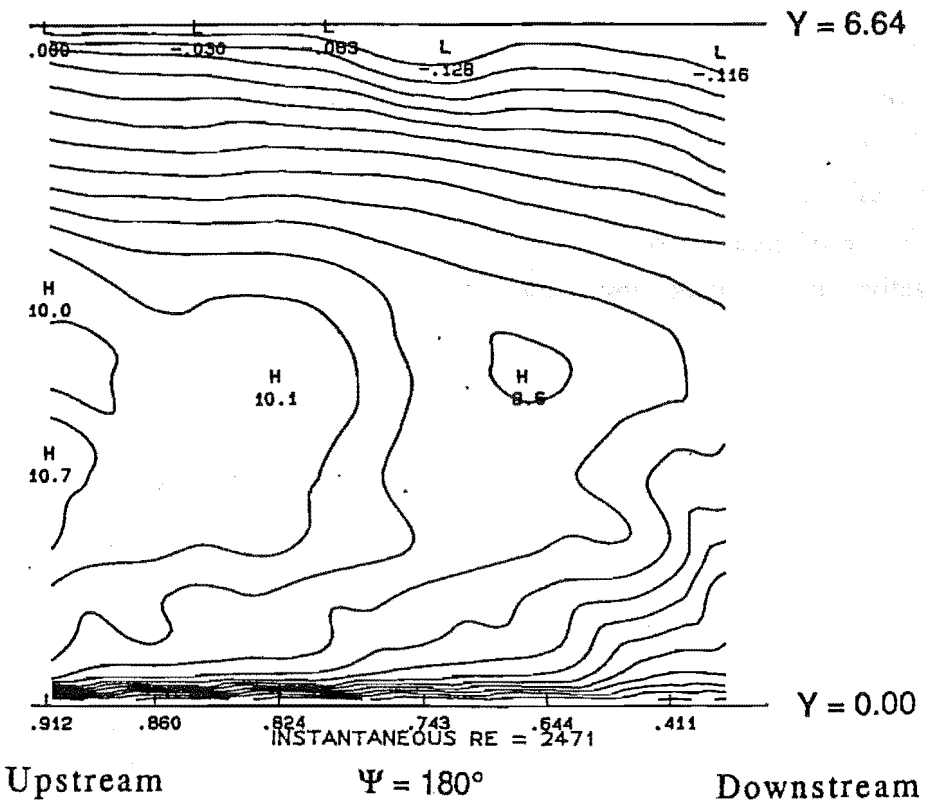

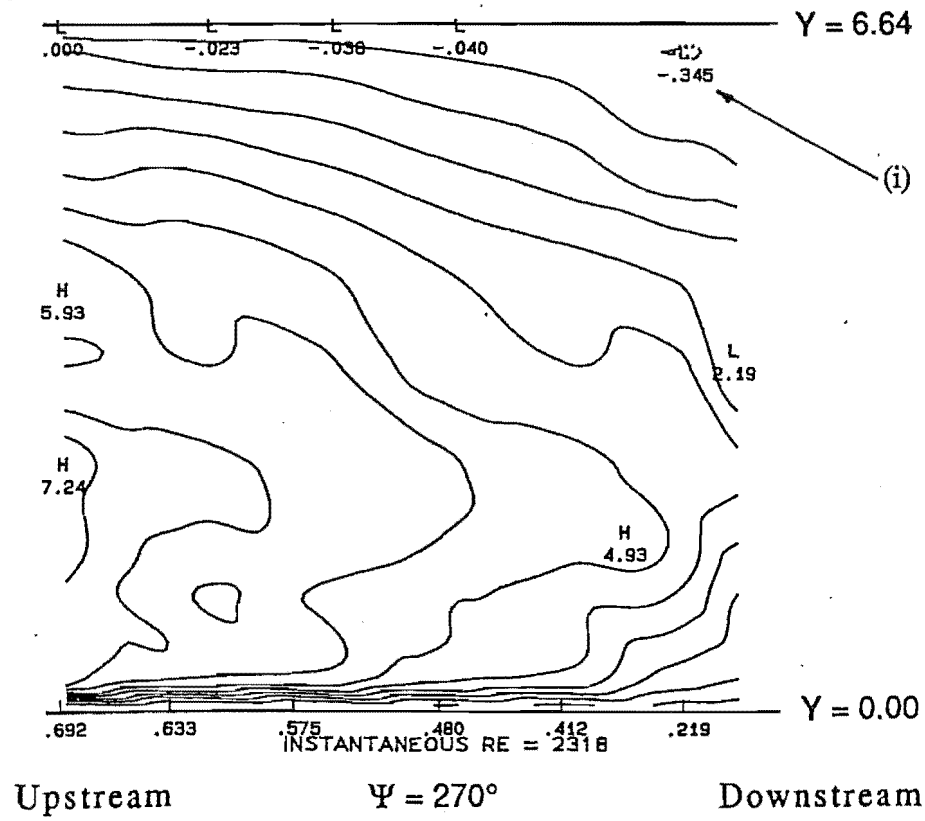

Figure 5.67 A-B

Along the $\alpha = 180°$ azimuth of the proximal stem, $Re_{mean} = 1500$
A)$\Psi = 180°$ B)$\Psi = 270°$.

Here, the characteristics of the contours were similar to those of group 1, except for a region near the downstream end of the Y = 6.64 wall (Figure 5.67 B, (i)). At this position, backflow began to appear at a phase angle of $\Psi = 180°$ ($Re_{inst} = 2471$ (figure 5.67 A)) and continued to enlarge from the wall until $\Psi = 0°$ ($Re_{inst} = 1082$), where (as in the upstream case (Group 1 at $\Psi = 0°$ and $\Psi = 30°$, figures 5.56 A & B)) negative flow occupied most of the slice.

The time-dependent velocities at the point subject to reverse flow in this slice is shown in figure 5.68 .

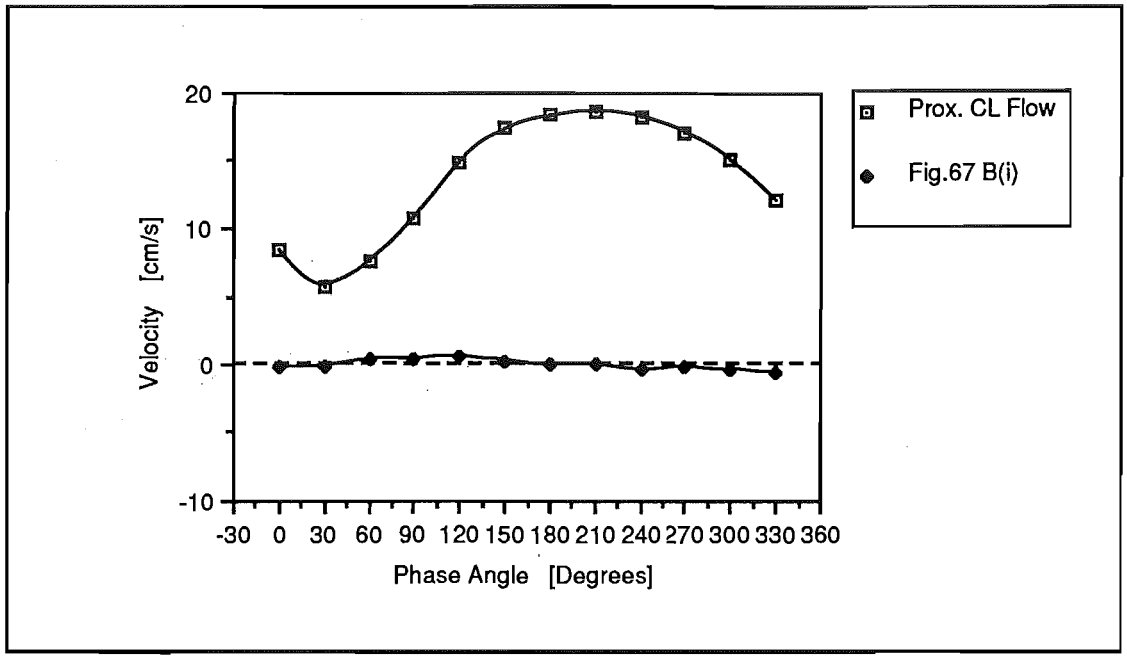

Figure 5.68

Time-dependent velocities in the proximal stem along the $\alpha = 180°$ azimuth, $Re_{mean} = 1500$.

The velocities were very low (almost zero), but it can be seen that the cycle was approximately 180° out of phase with the proximal centreline flow, similar to the velocities at positions in separation regions in other parts of the model.

5.4.6.3 Group 3:

This group was characterised by the presence of high velocity gradients, which were only dispersed at $\Psi = 30°$ (as illustrated in figure 5.69B for the slice along the $\alpha = 180°$ azimuth of the proximal limb, BC). The velocity gradients appeared to be thicker near the Y = 0.00 wall than near the opposite wall, but this was caused by a lack of measurements in all but the downstream end of this wall, as explained in section 5.4.2.3.

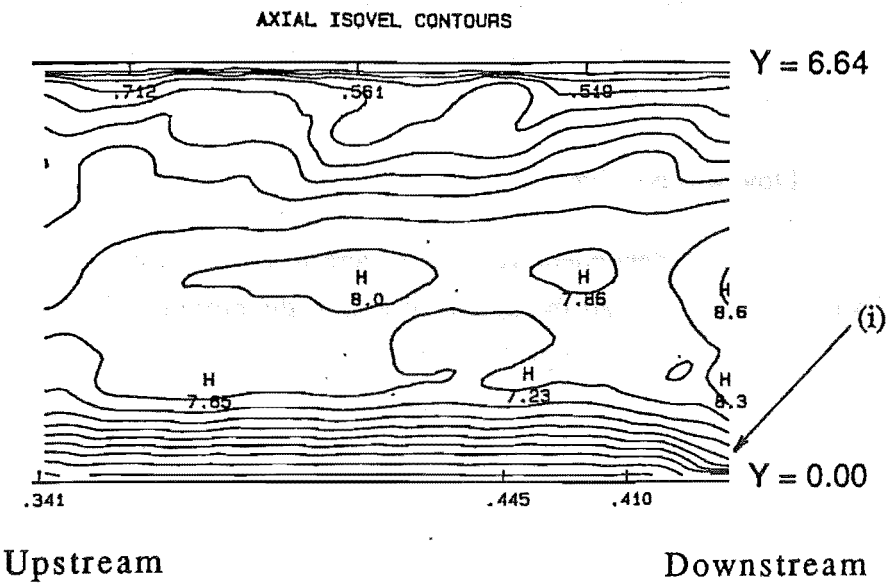

(A) INSTANTANEOUS RE = 1082

$\Psi = 0°$

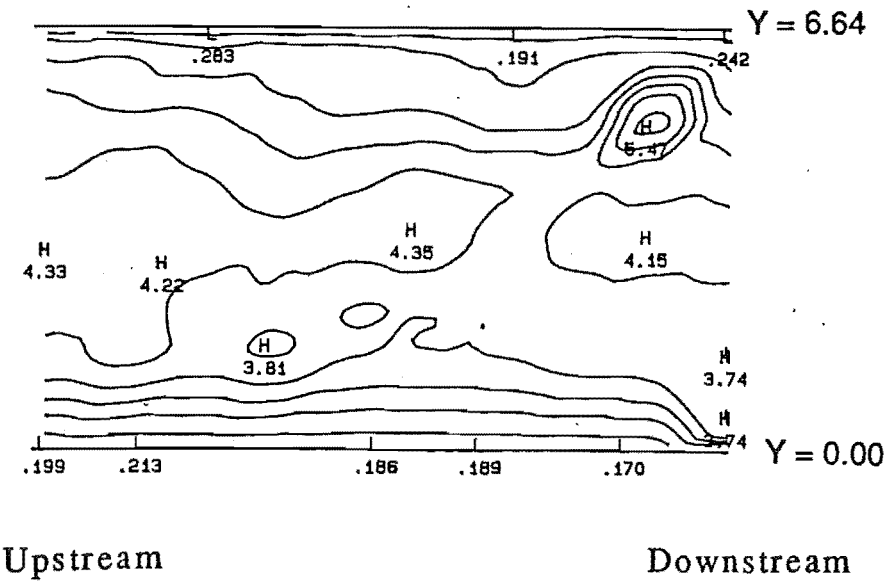

(B) INSTANTANEOUS RE = 839

$\Psi = 30°$

Figure 5.69 A-B

Along the $\alpha = 180°$ azimuth of the proximal limb, $Re_{mean} = 1500$
A)$\Psi = 0°$ B)$\Psi = 30°$.

One measurement point at the downstream end of the slice (figure 5.69A (i)) forced the contour plotting routine to show a velocity gradient at that point similar to that at the opposite side.

Flow was positive throughout the cycle.

The time-dependent velocities were in phase with the proximal centreline velocity (figure 5.70). At the upstream end of the proximal limb the peak flow was lower than the proximal centreline flow. Flow at the downstream end "overshot" the proximal centreline flow, both at the maximum and the minimum of the overall flow cycle.

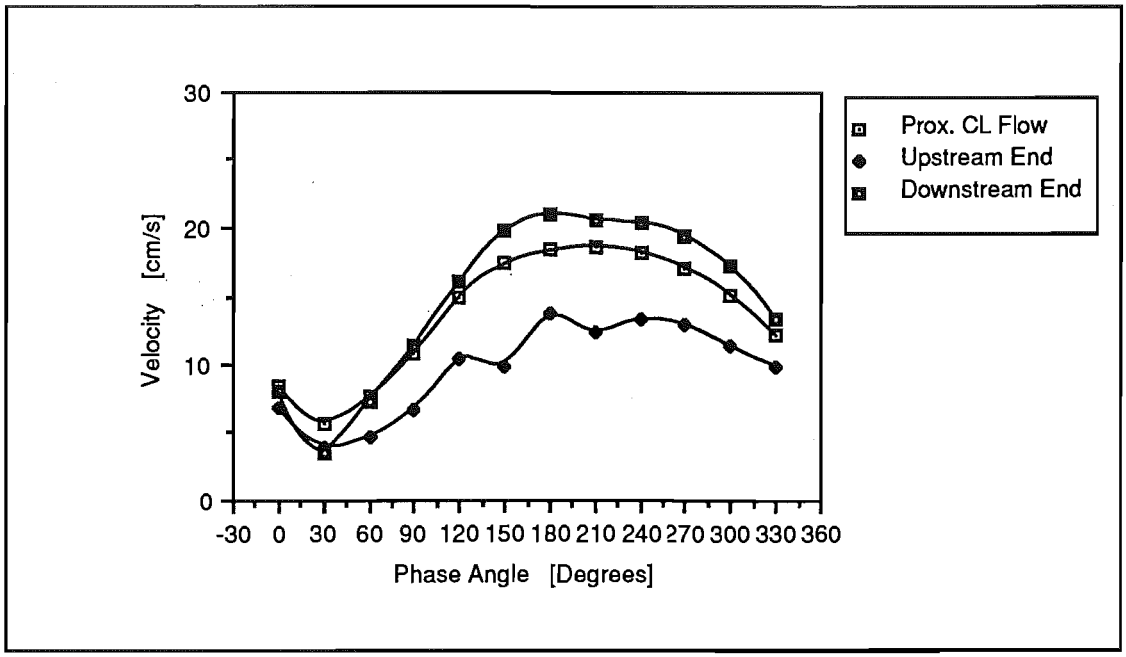

Figure 5.70

Time-dependent velocities at the upstream and downstream ends of the proximal limb along the $\alpha = 180°$ azimuth, $Re_{mean} = 1500$.

Similar characteristics to the above were seen at the two downstream slices of this group (along the $\alpha = 0°$ azimuth of the distal limb (Appendix I, figure I-9) and the $\alpha = 180°$ azimuth of the distal stem (Appendix I, figure I-8), though the contours in the midstream were more disturbed with the downstream location of the slice.

5.5 Hydrophone Results:

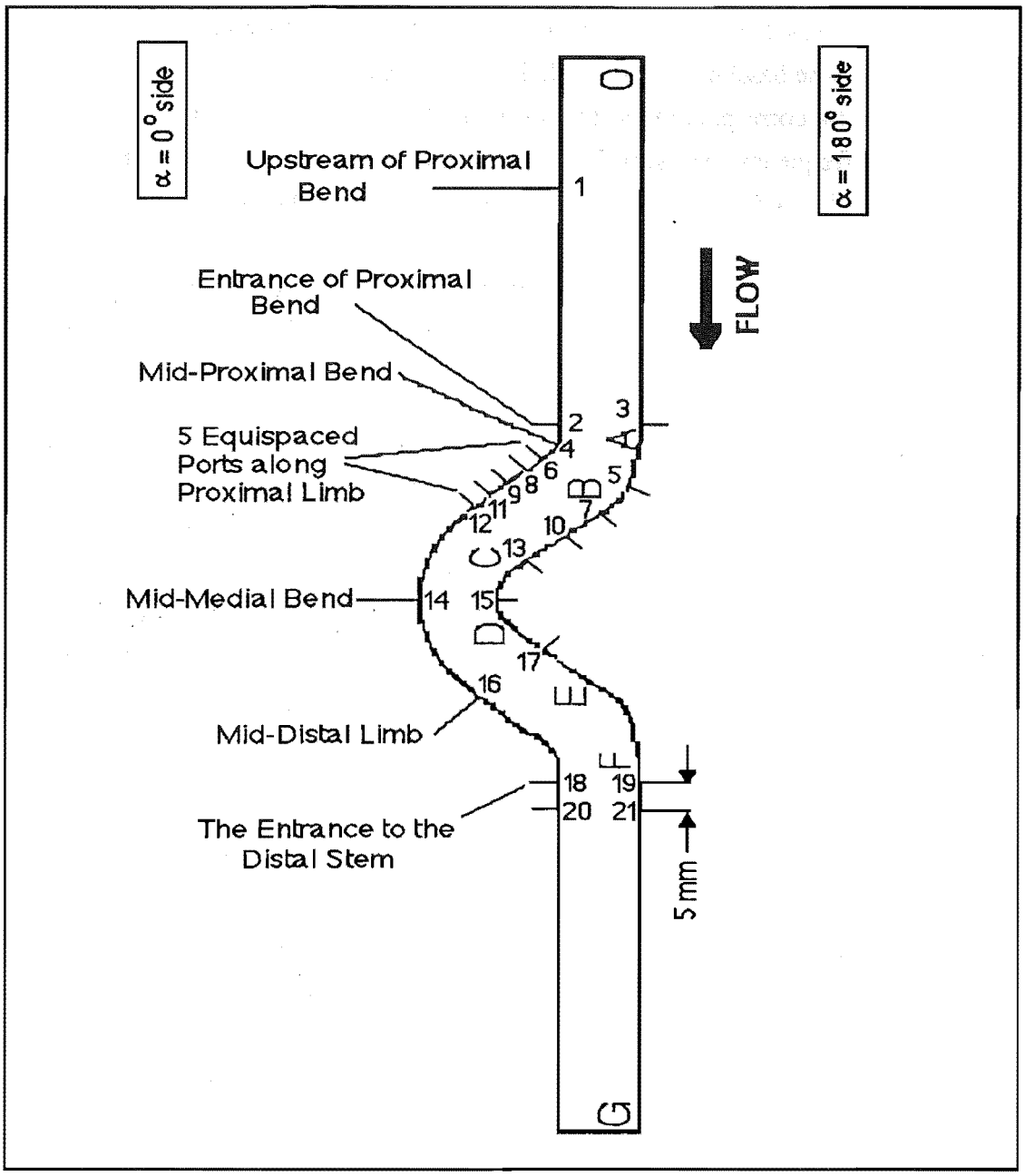

Figure 5.71
Pressure Measurement Port Positions

5.5.1 Baseline Spectra Upstream of Proximal Bend:

The Fast Fourier Transforms (FFT's) of the pressure fluctuations at various sites (figure 5.71) along both the $\alpha = 0°$ and the $\alpha = 180°$ azimuths of the model were examined for four steady flowrates: Re = 520, 800, 1160 and 1640.

Sixty four consecutive FFT's were averaged at each measurement point by a spectrum analyser operating in the summation mode, with AC coupling (see experimental methods section). The resultant spectra at position 1 in the model are shown in figures 5.72 to 5.75 as baseline cases. All subsequent spectra were compared to these baseline spectra by dividing the spectra measured at that point by the baseline spectra corresponding to that flowrate. Note that the gain of the display and the range of frequency may vary from case to case. The frequencies herein are those measured in a hydrodynamic flow through the model, which has a larger diameter than that of the internal carotid artery. The frequencies can be scaled by the Strouhal number (equivalent to scaling by the Wormesley parameter), as shown in Chapter 4, so that an indication of the corresponding in vivo frequencies, may be obtained from those below by multiplying by a factor of 22.

The background noise levels in the spectra for flowrates 1 and 2 was about 200 μV, increasing to about 650 μV at Re = 1160 and 800 μV at Re = 1640.

Comparison of the spectra at the 4 flowrates shows that the peaks broadened and their amplitude increased with increased flowrate. The major peaks situated at 3, 16 and 50 Hz observed at Re = 520 (figure 5.72) were maintained at Re = 800 (figure 5.73) where they were 1.34, 1.37 and 3.18 times larger respectively. A peak at 100 Hz in figure 5.72 (only just shown at the highest frequency on the plot) was also present, with an amplitude about 1.25 times higher, in figure 5.73.

Although any peak at 50 Hz should be viewed with some suspicion whenever electronics are involved in sampling (this being the main electricity supply frequency in New Zealand), the peak is sufficiently broad in figure 5.73 to indicate that not all of the fluctuations around that frequency were caused by mains interference and that there was a genuine flow-related difference between that spectrum and that in figure 5.72. A mains filter was used with both the hydrophone amplifier and the spectrum analyser to minimise mains interference.

The peaks at 150 Hz and 200 Hz in the spectrum at Re = 800 may be harmonics of the 50 Hz fundamental, as may also be the 100 Hz peak in the spectra of all flowrates. Certainly, any caution shown in interpreting the 50Hz peak should also apply to these peaks. Peaks did not occur at 150 Hz and 200 Hz in the highest two flowrates.

The magnitude of a 3 Hz peak increased from 4.24 mV at Re = 520 to 5.70 mV at Re = 800. At Re = 1160, this peak had decreased slightly in magnitude, but remained at that level at Re = 1640.

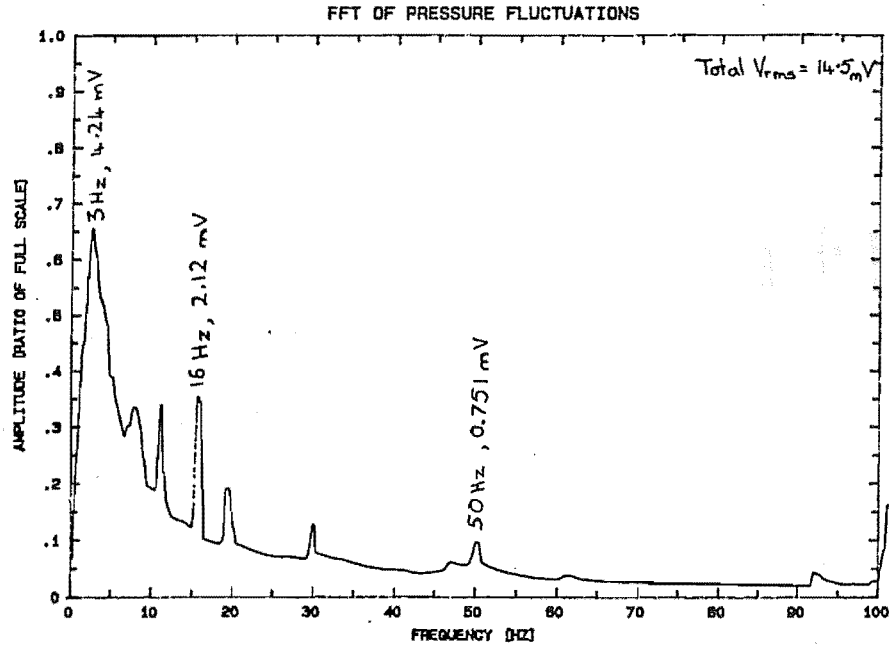

Figure 5.72
Position 1, Re = 520

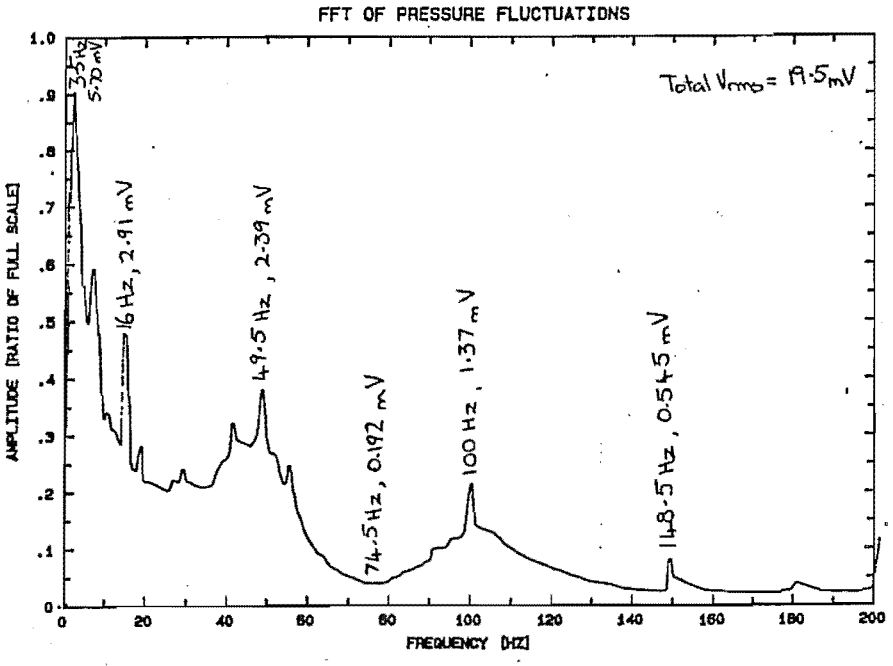

Figure 5.73
Position 1, Re = 800

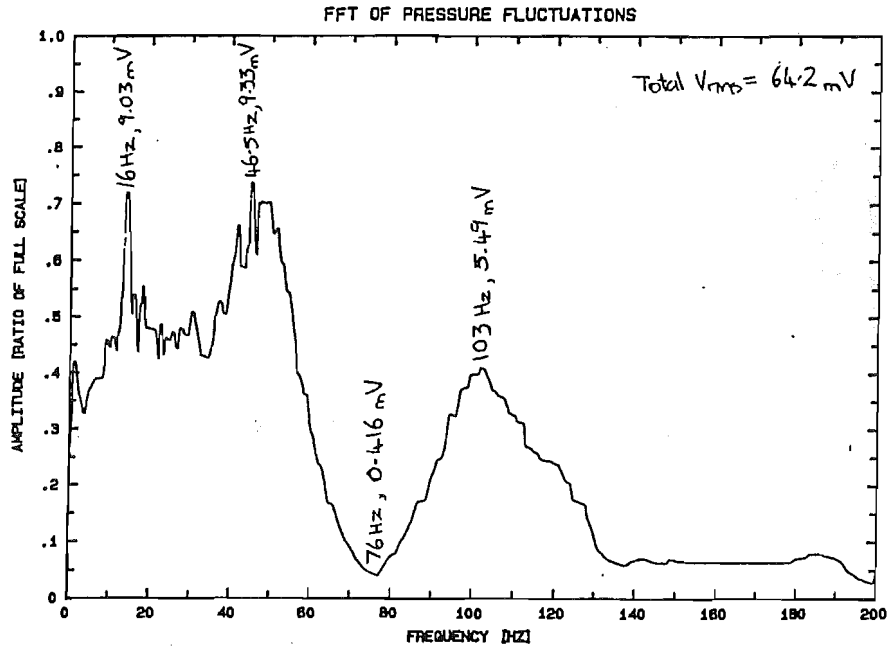

Figure 5.74
Position 1, Re = 1160

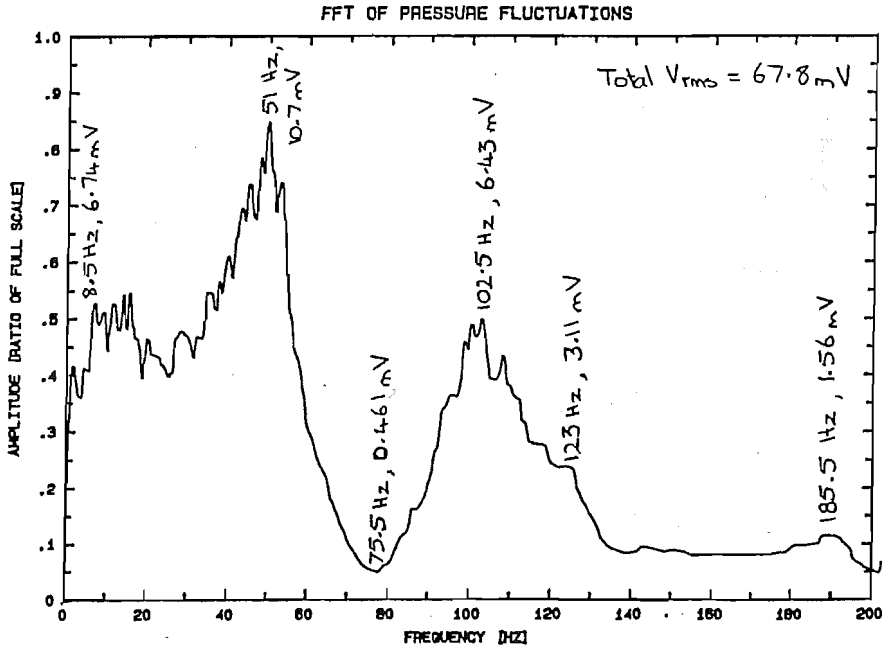

Figure 5.75
Position 1, Re = 1640

The 16 Hz peak observed at Re = 1160 was unexpectedly high and was possibly due to the resonance of a bubble caught in the flow system. These were observed from time to time in the flow system and a check was made for them if unusually high fluctuations were observed in the hydrophone output and measurements repeated if necessary.

A consistent feature in the spectra of the three highest flowrates, was a local minimum situated at about 76 Hz. The magnitude of the spectral power at this point did not increase with flowrate at the same rate as the rest of the spectrum in each case and in the spectra of flowrates 3 and 4 actually lies below the background noise level. This indicates that some sort of damping occurred in the system at about 76 Hz at Re above 800.

The total Vrms values of the spectra at each flowrate were plotted in figure 5.76, indicating a step change somewhere between Re = 800 and Re = 1160, though this is not conclusive with only 4 points measured.

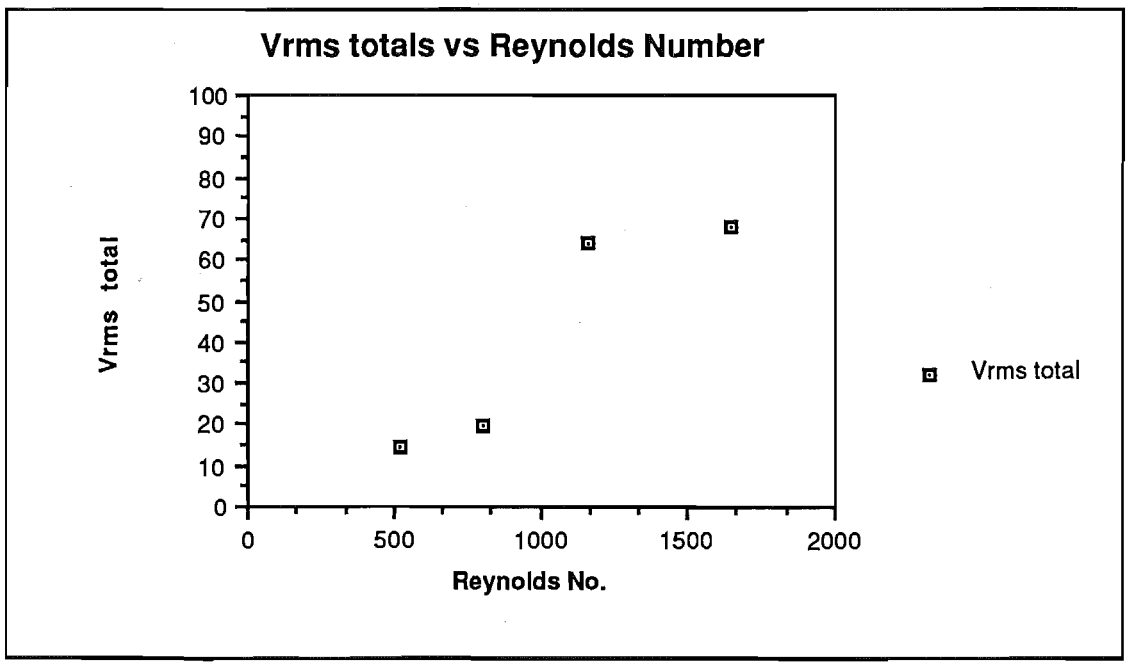

Figure 5.76

5.5.4 Results by Geometry:

5.5.4.1 Overall Trends of Total V_{rms}:

The spectra at all positions were divided by that measured at position 1 and the total V_{rms} values of the resultant spectra are shown in figures 5.77 to 5.80 for flowrates giving Reynolds numbers of 520, 800, 1160 and 1640 respectively.

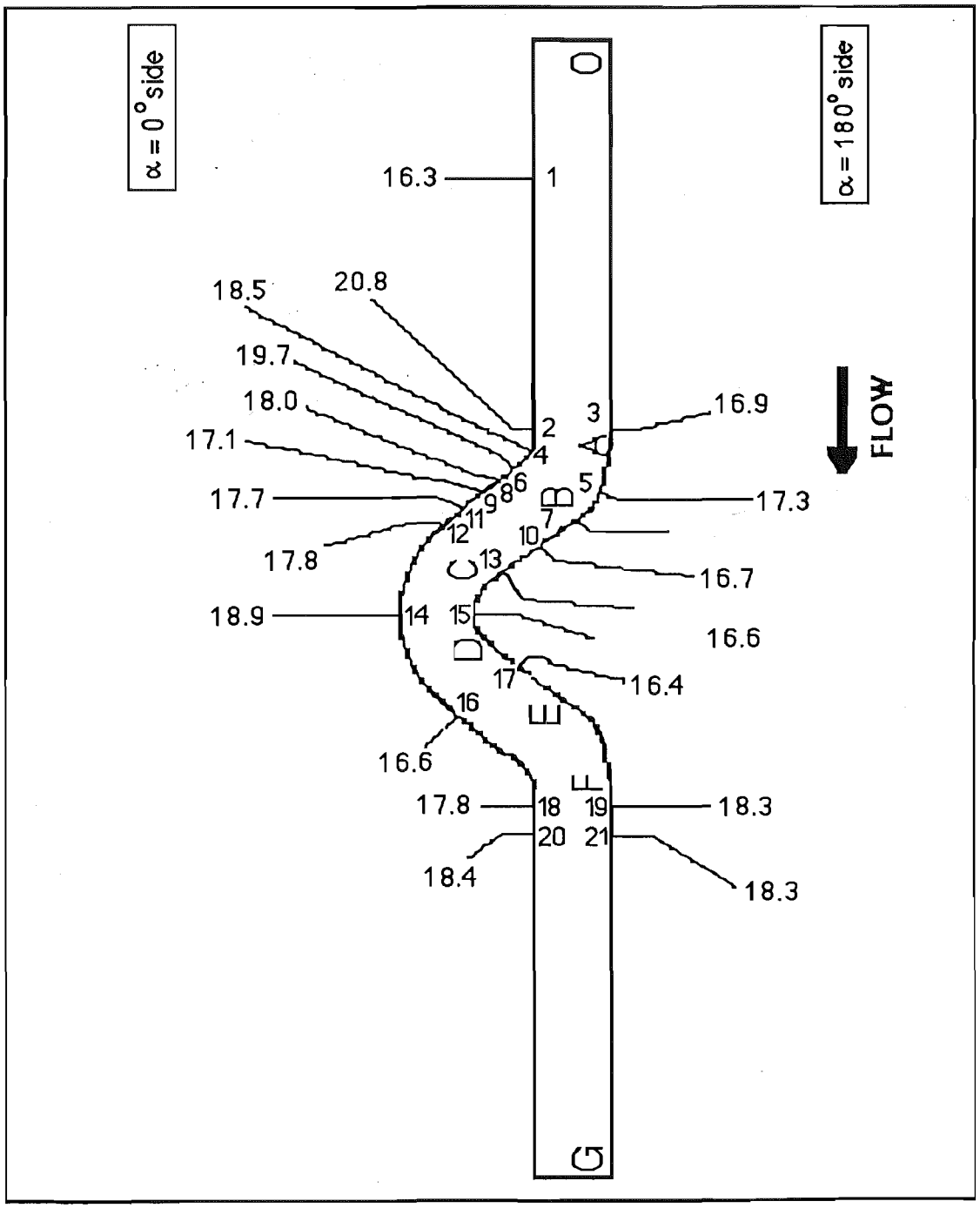

Figure 5.77
Total V_{rms} at Various Positions Re = 520

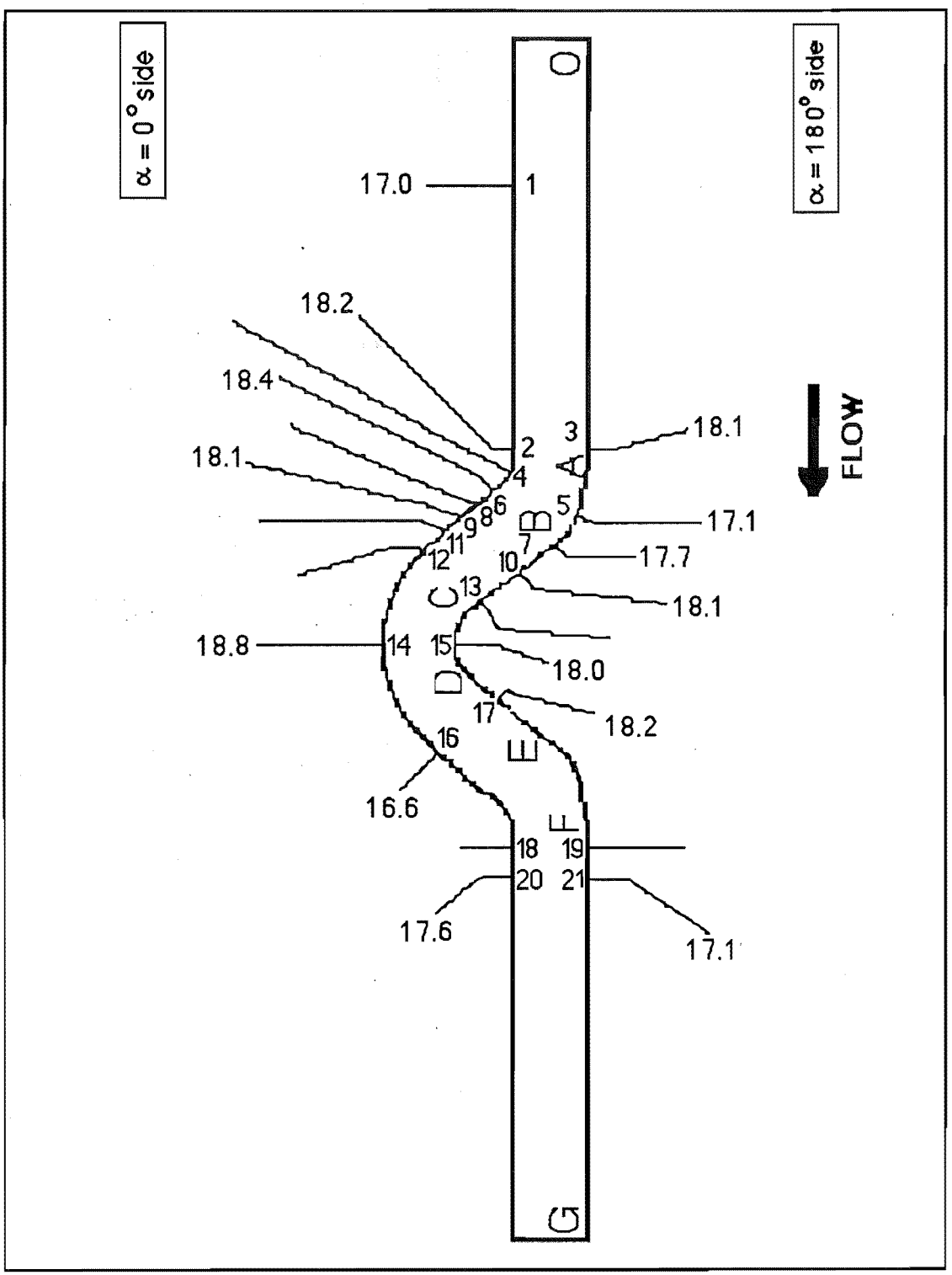

Figure 5.78

Total V_{rms} at Various Positions Re = 800

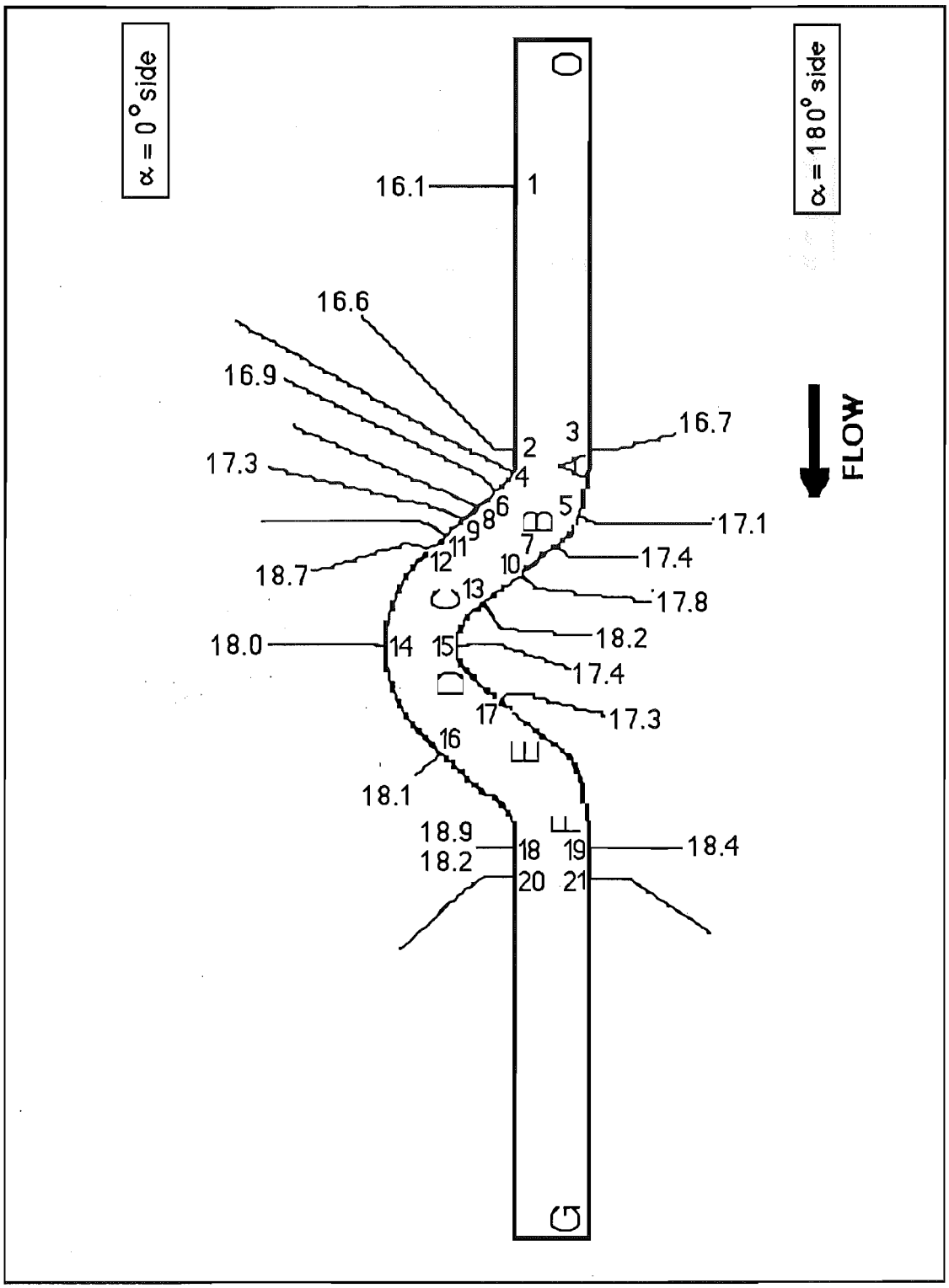

Figure 5.79

Total V_{rms} at Various Positions Re = 1160

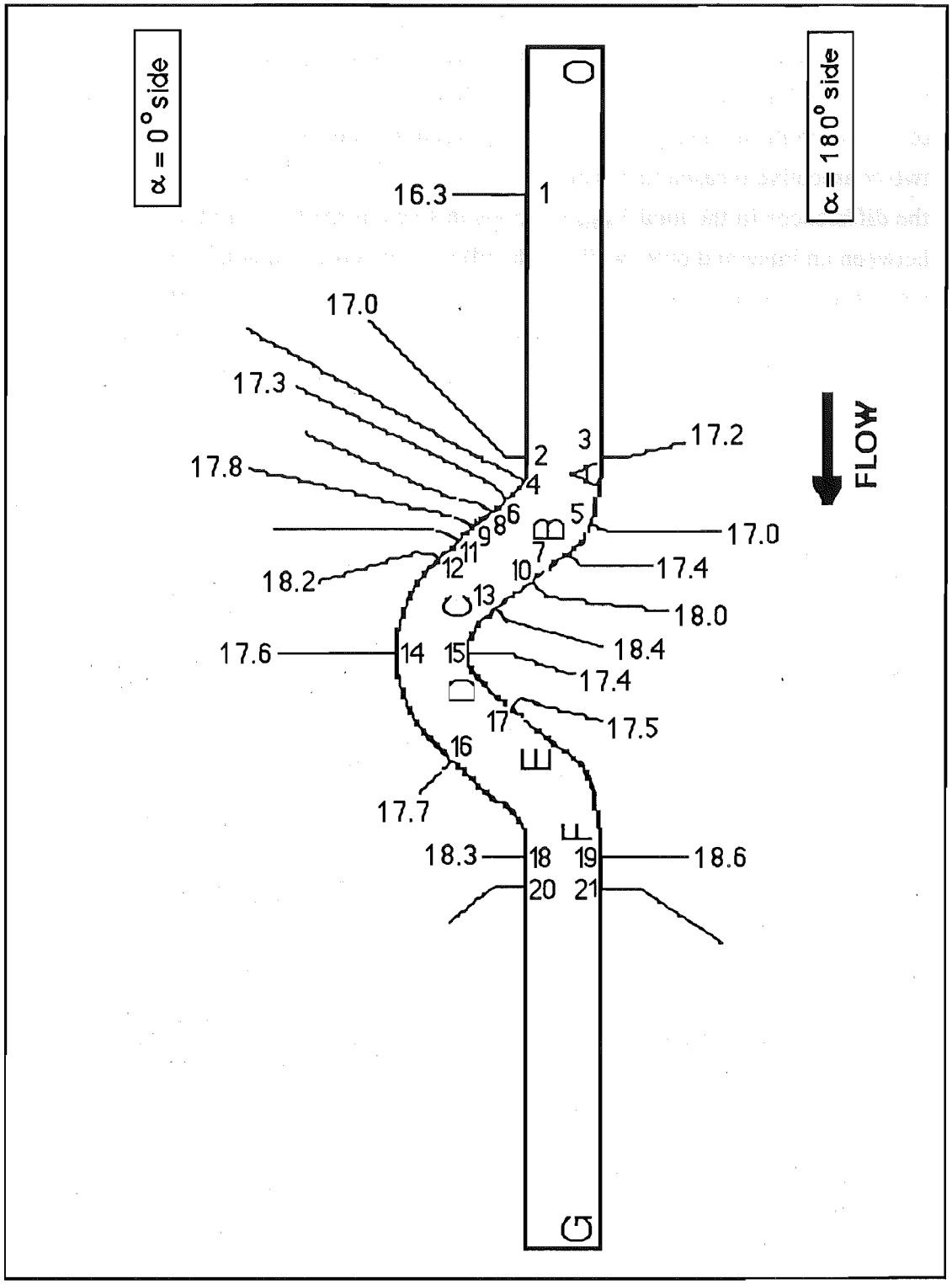

Figure 5.80

Total V_{rms} at Various Positions Re = 1640

The values at position 1 shown in figures 5.77 to 5.80 are ratios of two consecutive FFT's at the same upstream measurement position ie: whereas the spectra at other measurement positions were related to the upstream spectra by dividing the

former by the latter across the entire frequency range, the values at position 1 are equivalent to these, but relating a second measure of the spectrum at the same position to the first. Therefore a value of 16.3 at Re = 520 in any position indicates no more difference in the total v_{rms} to that at the upstream position 1 than the difference between two consecutive measurements at position 1. An inspection of these figures shows that the differences in the total V_{rms} at opposite sides of the tube in various regions (eg: between an inner and outer wall of a bend) were inconsistent at all flow rates. A two-way analysis of variance of the average values in various regions is given in tables 5.2 and 5.3 below. The "inner" side is defined as that side immediately upstream or downstream of the inner (smaller radius of curvature) wall of a bend and conversely for the "outer" side.

POSITION	RE = 520	RE = 800	RE = 1160	RE = 1640	TOTAL	MEAN
INNER BEND	17.55	18.00	17.40	17.40	70.35	17.59
OUTER BEND	18.10	18.80	17.55	17.30	71.75	17.94
INNER LIMB	17.86	18.08	17.88	17.82	71.64	17.91
OUTER LIMB	17.48	17.38	17.98	18.02	70.86	17.72
POSITION 1[1]	16.30	17.10	16.10	16.30	65.80	16.45
POSITION 2	20.80	18.20	16.60	17.00	72.66	18.15
POSITION 3	16.90	18.10	16.70	17.20	68.90	17.23
TOTAL	124.99	125.66	120.21	121.04	491.90	
MEAN	17.86	17.95	17.17	17.29		17.57

Table 5.2
Data for two-way analysis of variance
of Total V_{rms}.

[1] See figure 1

At a 0.05 level of significance, f_1 is required to be greater than 2.46 or f_2 greater than 2.96 if either position or flowrate respectively have a significant affect on the total V_{rms}. It can be seen from table 2 that only flow and not position affects the total V_{rms} in these experiments.

Source of Variation	Sum of Squares	Degrees of Freedom	Mean Square	Computed F
Position Means	3.24	6	0.54	$f_1 = 0.87$
Flow Means	7.93	3	2.64	$f_2 = 4.26$
Error	11.19	18	0.62	
Total	22.35	27		

Table 5.3
Two-way analysis of variance
for Total V_{rms}.

An estimate of the contribution of noise, due to structural vibrations, to the hydrophone output signal shows (Chapter 6) that this was at least as high as the expected signal from the wall pressure fluctuations. In view of the fact that no significant differences in the total V_{rms} signals were found between the various sites in the model, it was decided not to include the spectra measured at individual pressure port positions in the results section. A representative selection of the spectra are instead contained in Appendix M, along with some descriptive comments.

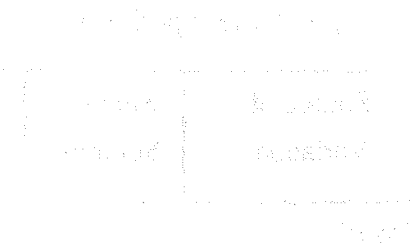

Chapter 6

Discussion

6.1 Experimental Techniques:

6.1.1 The Model:

The method of manufacture provided a tube of constant cross-section, avoiding the problems associated with distortion to the tube, encountered in previous work (Stehbens & Fee 1985). Most importantly, optical distortions were reduced to a minimum, making LDA experiments possible and minimising refractive effects at the water/perspex interface. A further advantage of milling the tube from a block was that there was only one curved surface through which refractive effects could distort flow visualisation and the laser beams, rather than two that would be present in a curved pipe formed by bending a tube. The constant cross-section minimised flow disturbances, but the presence of cracks along the length of the tube at the $\alpha = 0°$ and $\alpha = 180°$ sides was an unavoidable consequence of having access to the model for cleaning, inspection and modification purposes. Both halves of the model were machined to an accuracy of 0.1% so that the surface irregularity was within 0.2% of the tube diameter when the model was assembled. An estimate of the crack mismatch is thus 0.04 mm.

6.1.2 Flow Visualisation and Flowrates:

The hypodermic needle used to introduce dye to the flow would have been a source of flow disturbance. However, the needle diameter was only 6% of the tube diameter and was positioned 350 hypodermic tube diameters upstream of the proximal bend, allowing sufficient distance for disturbances to die out before reaching the bend. Schraub et al (1965) found that the flow disturbances caused by an H_2-bubble wire died out within 70 wire-diameters downstream. No disturbances were evident in the dyestreams moving along the $\alpha = 180°$ wall (the side where the needle was inserted)

prior to the entrance of the model. The laminar nature of the flow upstream of the proximal bend up to a Reynolds number of 2400 indicates that flow disturbances caused by the apparatus were insignificant at the flowrates studied. The transition to turbulence or intermittent turbulence in a straight tube could normally be expected to occur at Re > 2100.

The gravity feeding of the dye provided a steady stream and the use of a controlling clamp on the dye supply line, well upstream of the injection point, allowed a slow injection without a "jetting" effect. The method of providing a sharp dyestream cut-off on closing the dye supply solenoid valve proved an effective way of preventing dye injection disturbances during pulsatile flow.

The flowrates for steady flow conditions were found to remain constant within measurement errors of 4% once set. The flowrate and the flow variation amplitude were measured by LDA under pulsatile conditions and the set points were found to remain constant to within 3% over the period of experimental work.

6.1.3 Laser Doppler Anemometry:

The LDA provided a valuable quantitative measure of axial velocities within the model. A major advantage of the LDA over other velocity measurement tools is that it offers the ability to make quantitative measurements without introducing a probe to the flow. This is particularly important in the case of a fully-elliptic flow as in the present case, because the flow at any point in the tube depends crucially on the flow in all other parts of the tube (Soh & Berger 1984). Conversely, the use of a probe such as a hot wire anemometer would certainly raise questions regarding the effect of the probe on the accuracy of the measurements and even the presence of some of the observed phenomena in the absence of the probe. The limitations of the LDA in this case were a consequence of the desire to study a physiological configuration ie: one with a high curvature ratio.

The small radius of the tube made the measurement of most velocity components, other than axial, difficult, although some transverse velocities could be measured along the diameter normal to the plane of symmetry (as described in Appendix B). The high curvature ratio of the tube restricted velocity measurements within the bends entirely to the measurement of radial velocities on the diameter normal to P. This was because beam focussing, the determination of the measurement volume position within the tube, the measurement of the intersection angle of the beams and even the identification of the velocity component being measured, were all affected by refraction of the beams through the highly curved (in two directions) perspex/water

interface. Even if these quantities could be determined accurately, the velocity component being measured would be a function of the measurement position, making meaningful analysis and presentation of the velocity data extremely difficult. This is unfortunate, since the flow in the curves themselves is of considerable interest, both from the view of understanding the flow in curved pipes in general and of relating such flows to atherogenesis.

Milk was used to seed the flow during LDA experimental work, because a continuous residence of scattering particles within the measurement volume is desirable when using a frequency tracker. The concentration was kept low, but the effect of a high concentration of scattering particles on LDA performance and accuracy is only important if it is high enough to cause aggregation of the particles or a loss of reflected light intensity due to absorption (Durst, Melling & Whitelaw 1976).

Despite the fact that refraction did not alter the beam intersection angle, or the velocity component measured in the straight sections of the tube, problems were encountered in viewing the measurement volume adequately with the photodetector pinhole at times, especially near the tube walls, where reflective and refractive effects were greatest. The determination of the intersection point of the beams was also difficult there, because of the small visible length of the beams on either side of the measurement volume - the exact intersection point could not always be distinguished easily because of the reflections at the nearby perspex/water interface. This meant that (particularly near the walls) the quality of the LDA signal was not always of an optimum quality. Rms fluctuations of the LDA output signal tended to be more a reflection of the quality of the photomultiplier output signal than a measure of actual fluid velocity fluctuations. Fortunately, most of the flows were laminar rather than turbulent, eliminating the need for the measurement of turbulence. Velocity fluctuations in the shear layer of the proximal limb, which were of a larger scale and lower frequency than would be expected in turbulent fluctuations, were able to be measured and the frequency of oscillation quantified.

The traversing table allowed the optical bench to be moved in three directions and the measurement volume to be positioned with an accuracy of within half a laser beam diameter, or 0.33 mm, representing 1.65% of the tube diameter. Beam alignment through the optical unit and Bragg cells of the particular LDA being used was a tedious procedure, requiring "walking" the incident laser beam, back and forth, through the inlet side of the optical head at various angles, until beam splitting and maximum outlet beam intensities were achieved. This process had to be repeated whenever the alignment of the optical unit was altered (to measure velocities in the tube at a different inclination to the vertical plane). The experimental procedure would be speeded up and

much tedium avoided, if the LDA were mounted so that the laser and the optical head could be rotated as one unit. In this way, velocities at any angle could be measured without altering the alignment of the optical unit with respect to the laser. Also, the angle of the unit could be related to a datum, allowing an accurate and fast setting of the velocity component to be measured. Caution would be needed when rotating the unit independently of the photomultiplier, using the forward scattering mode, as damage to the photo-detectors will occur if the intense light from a laser beam is incident directly through the photomultiplier pinhole.

The ability of the LDA to track changing velocities was an important factor, particularly in the case of pulsatile flow. According to the DISA LDA manual, the "slew rate" (the maximum speed at which the Frequency Tracking Unit (FTU) can track a changing Doppler frequency, or velocity) is 1.15 V ms^{-1}, for a tracker range setting of 500 kHz and an input frequency bandwidth of 2%. At the pulsation frequency used in the present study, the voltage change of the driving pulse occurred at only 0.2 mV ms^{-1} so that the LDA could easily track the changing mainstream velocity (provided that the FTU received a good signal from the photomultiplier).

6.1.4 Wall Pressure Fluctuation Measurements:

The sensitivity of the hydrophone used (22.6 mV Pa^{-1}) was adequate for measuring wall pressure fluctuations of the magnitude expected in the model (up to about 3 Pa). Problems were encountered during initial pressure measurement experiments, when the hydrophone output was swamped by noise. This noise was reduced by several modifications to the flow apparatus (see Chapter 4) and the hydrophone output signal was eventually reduced to the correct order of magnitude for the pressure fluctuations expected. Time did not allow further refinement of the apparatus and it was decided that measurements of the wall pressure fluctuations would be made in the hope that flow effects would be evident despite the noisy hydrophone output signal. The source of the noise was not determined at that stage, but it was thought that structural vibrations of the flow apparatus were responsible.

It was discovered after completing experiments that the hydrophone was extremely sensitive to acceleration, with a sensitivity quoted at 110 dB referenced to 1.0 mPa/ms^{-2} (Brüel & Kjær 1978). By assuming that the structural vibrations were simply sinusoidal, with a fixed amplitude about a mean position, an estimate of the acceleration of the apparatus and therefore the acceleration that the hydrophone was subjected to, may be made at a given frequency. This, in turn, gives an estimate of the Sound Pressure Level (SPL) in the hydrophone output signal, due to vibration of the

hydrophone at that frequency. Unfortunately, we have no measure of the amplitude of the structural vibrations. However, the SPL due to a vibration with an amplitude of 10^{-5} m (ie: a maximum displacement of the hydrophone from it's mean position of only 5 μm), at 100 Hz alone, could be as high as 5 Pa. The maximum SPL measured by the hydrophone probe upstream of the proximal bend was only 3 Pa over the entire frequency range at the maximum flowrate studied.

The above estimate is admittedly only approximate, but it does show that the contribution to the hydrophone output from structural vibrations could be at least as high as those expected from the fluid-induced wall pressure fluctuations. This may explain the result that significant differences in the total rms values of the hydrophone output signal were not observed between the various sites in the model, but only between the various flowrates. This method of wall pressure fluctuation measurement has promise, but the type of hydrophone must be chosen with care to avoid any sensitivity to noise induced by structural vibrations.

6.2 Steady-Flow Features:

Flow in the model exhibited several significant differences from the flow in curved pipes described (generally for low curvature ratios) in the literature (Chapter 2).

6.2.1 Flow Asymmetry:

Despite the provision of an entry length sufficient to allow the establishment of fully-developed laminar flow in a straight pipe of the same diameter, the flow in the model was asymmetric, even upstream of the proximal bend. As the pipe was straight and held rigid along it's entire length, the asymmetry in the flow can be attributed to the presence of the tortuosity in the model itself. Considerable upstream adjustment of the flow prior to entering the model was indicated by deviations from Poiseuille flow in the proximal stem. This confirms the view of Soh & Berger (1983), that it is not strictly possible to specify the condition of flow at the entry point of a curved pipe, since it's form depends on the flow development downstream. The location of the maximum axial velocity towards the inner side, upstream of the proximal bend, is consistent with the the results of Ito (1960), who observed large Δp effects upstream of the entrance to a 90° elbow possessing a straight entrance leg.

The asymmetry of the flow far upstream of the proximal bend is of little practical interest in relation to physiological flows. The flow distortion is probably not great enough to account for localised variations in any pathological changes to the arterial walls that might be observed there, and focal atheromic changes to the walls are not normally associated with the straight sections of the internal carotid artery. Given the pulsatile nature of blood flow and the short lengths available within the arterial system for flow development, departures from the Poiseuille flow profile in vivo are likely to be larger than those observed herein, even in the absence of the tortuosity.

The asymmetry of flow in the tortuosities in vivo is likely to be less predictable than that within the idealised model tortuosity, indicating that the positions of observed atheroma will be difficult to match exactly with positions of flow disturbances in vivo. It is important to bear this in mind when considering the mode of action of fluid disturbances on the arterial wall. Any doubt regarding the exact location of a separation zone, for instance, leads to difficulties in assessing the importance, to atherogenesis, of the various flows inherent in separation. It will be unclear in that case, whether it is the recirculating (low shear) flow under the separated shear layer; the reattachment (high shear) of the separated shear layer; a fluctuating shear stress; the flow direction or any pressure fluctuations that are responsible for a particular response of the wall.

Flow asymmetry is also important in theoretical and computational studies of flow in curved pipes, in which entrance flow symmetry with respect to the tube's plane of symmetry is usually either assumed or specified. The present results indicate that these assumptions are not necessarily valid in multiply-curved tubes of high curvature ratio.

6.2.2 The Proximal Bend Flow:

Dean-type flow, with several additional features, was observed in the proximal bend. Firstly, a considerable secondary flow with an inwardly-directed azimuthal velocity was observed in a thin layer about the walls upstream of the proximal bend at all flow rates.

To the author's knowledge, the only analytical model to predict secondary flow prior to entering the bend was that of Smith (1976), in which a novel kind of "upstream response" to Poiseiulle flow entering a bend from a straight pipe was noted (figure 6.1). In his model, Smith described an inwardly-directed azimuthal velocity, generated upstream of the bend and driven by the azimuthal pressure gradient which arose due to the bend. The upstream response of Smith's analysis depended crucially

on the absence of an axial slip velocity upstream. In agreement with this, secondary flow was not observed in the model, upstream of the proximal bend, for a uniform entrance velocity profile (section 5.2.1.3).

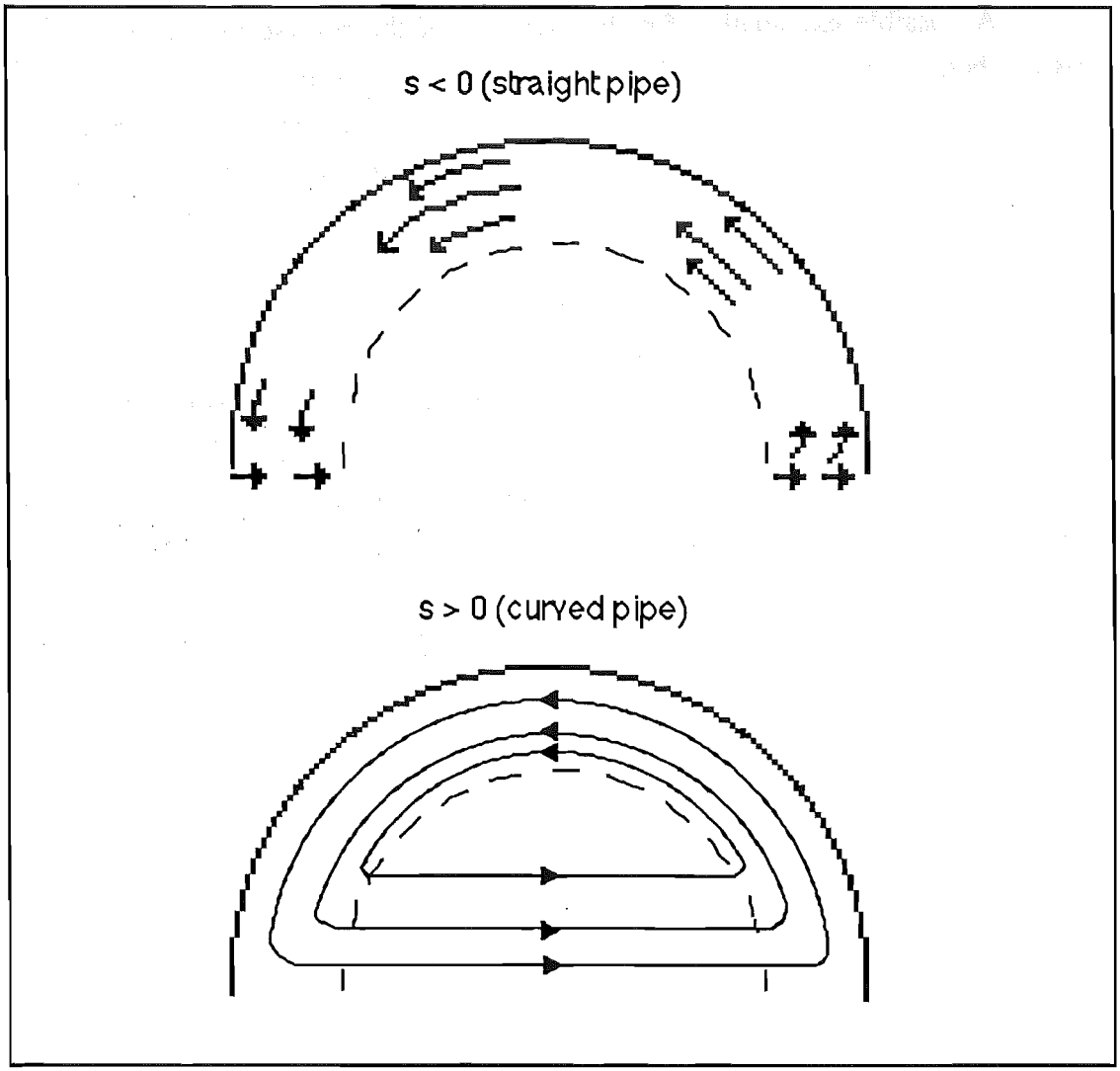

Figure 6.1
The Upstream Response of Curved Pipe Flow
With a Straight Entrance Length (Smith 1976).

The second flow feature, additional to Dean flow, was a reverse flow region observed along the $\alpha = 180°$ wall (the outer side with respect to the bend) of the proximal bend, which indicated the possible presence of an adverse axial pressure gradient there, at all flow rates. The reverse flow extended upstream of the bend entrance at Reynolds numbers above 500 (Deans numbers, $K > 335$).

Smith did not mention reverse flow at the outer bend, but the curvature ratio in his analysis was small (though finite). The reverse flow observed herein was probably a consequence of the high curvature ratio, δ, since the Deans number was not particularly large. Berger, Talbot and Yao (1983) warned against expecting small-Dean number flow with large δ.

A possible explanation for the presence of the reverse flow at the outer proximal bend is offered below and illustrated in figure 6.2: Little interaction between the core flow and the azimuthally-moving secondary flow was observed near the entrance of the bend. Downstream of the entrance, the core flow impinged at the outer wall (at $\alpha = 180°$), giving rise to a stagnation zone there (the "split point" in Plate 5.10), similar to that caused by a jet impinging normally on a planar surface. This impingement may have created a locally high pressure and thickened boundary layer at the outer wall. The fluid initially moving axially along the $\alpha = 180°$ wall far upstream of the bend, was entirely re-directed in the secondary flow about the walls of the tube, so that a position of zero axial velocity occurred at the $\alpha = 180°$ wall. An axial flow reversal then occurred between the core impingement point and the position of zero axial flow, with the thickened boundary layer at the impingement point acting as a source and the azimuthal flow, situated upstream, acting as a sink. The position of zero axial velocity at the $\alpha = 180°$ azimuth was referred to as the "upstream limit of the reversed flow" in Chapter 5 and was shown in figures 5.4 and 5.5.

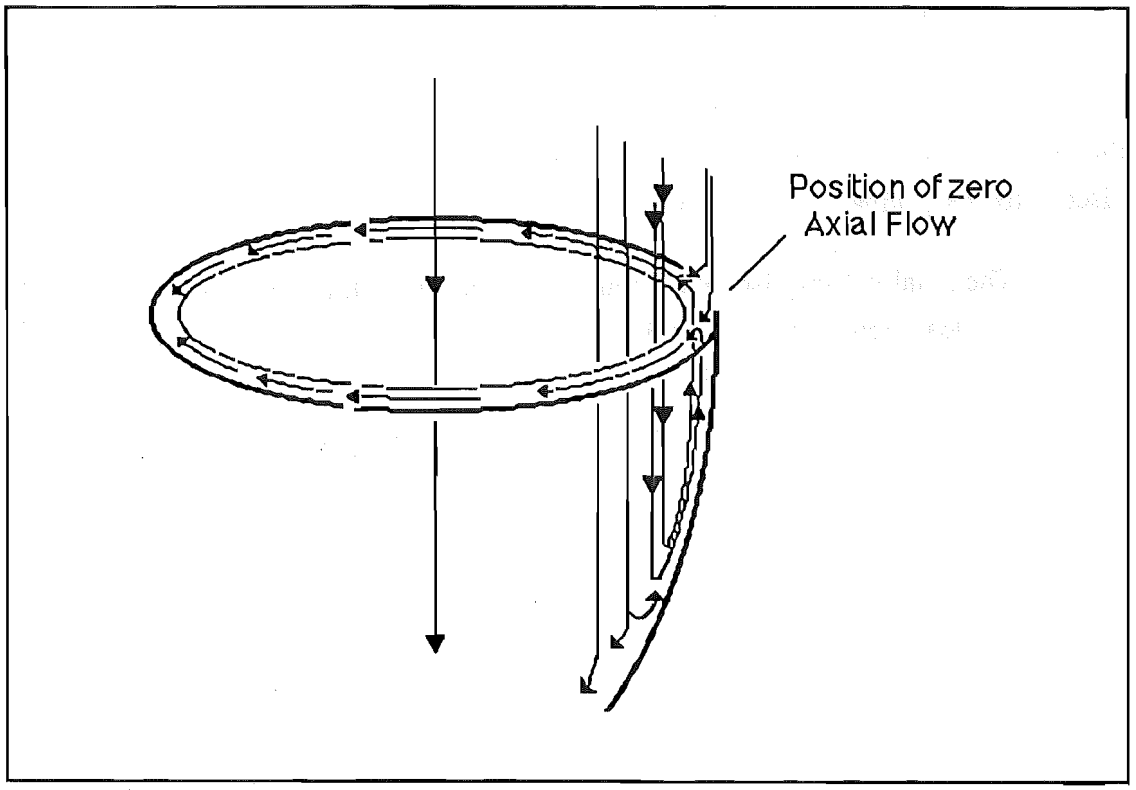

Figure 6.2
The Reverse Flow at the Outer Proximal Bend.

The third additional feature to Dean flow, was an axial flow separation at the inner side of the proximal bend, giving rise to a recirculation region downstream along the $\alpha = 0°$ wall of the proximal limb. This separation is no doubt a consequence of the high δ ratio, since it was observed in the present study by dye visualisation, even at moderately low Deans numbers of less than 200, and has not been reported in the literature for small δ.

The reverse flow region at the outer wall will possesses a low shear rate at the wall, bounded by a shear layer. It is therefore not unlike a separation region, so that the proximal bend is effectively subjected to two separation regions, leading to two areas of low shear at the wall. This is important physiologically, since the identification of low shear regions as a cause of atheroma will be supported by evidence of atheromic plaque at the outer wall at the entrance to the proximal bend. Note that the proximal bend is also subjected to a high shear rate at the outer wall, just downstream of the reverse flow region. The effects of high shear stresses on the wall there may be sufficient to cause the atrophic lesion of atheroma, in an area immediately adjacent to and apparently continuous with, a region of low shear, which may be associated with proliferative atheroma. Hence the discussion above, regarding the importance of accurately locating the flow features in relation to atheroma in vivo assumes even more significance.

6.2.3 The Proximal limb Flow:

Flows in the straight sections downstream of the bends were dominated by the inertial effects set up in the bends, except in the far downstream distal stem where viscous forces gradually began to re-establish normal Poiseuille flow.

The axial velocity isovel contours in the proximal limb were similar to those of classical Dean flow, but they additionally exhibited an axial separation bubble at the inner (with respect to the proximal bend) wall, due to the separation at the inner proximal bend upstream. Also, the contours there exhibited the so-called (Austin and Seader 1973, Soh and Berger 1984) "doubly-peaked" profiles along lines parallel to the tube's plane of symmetry, illustrated in figure 2.9. These doubly-peaked profiles in the proximal limb were associated only with those cross-sections containing an axial separation, indicating that there was a strong interaction between the axial and secondary flows only in the presence of axial separation.

A complicated vortical structure, located in the proximal limb, was probably due to the interaction between the separated axial flow and secondary flow. Under uniform velocity entrance conditions, little secondary flow was observed in the proximal bend and the backflow region, observed by dye visualisation, was comparatively simple at this point.

With Poiseuille entry conditions, the vortical structure appeared to contain two reverse flow regions as one measured along the $\alpha = 0°$ azimuth, with an area of positive flow between them, evident in both the dye visualisation and the LDA results. The positive flow region may have been due to the reattachment of the axial shear layer at that point. At the position of the positive flow, the axial isovels lost their Dean-type form, but regained it immediately downstream. The Dean-type outwardly-centrifuging motion of the central fluid may have been counter-acted in that cross-section, by the reattaching axial shear layer, moving in towards the $\alpha = 0°$ wall. Rather than re-establishing a boundary layer downstream however, the secondary flows may then have swept the shear layer back into the core flow, so that reverse flow along the $\alpha = 0°$ wall again occurred downstream.

This view is supported by loss of outward motion of the central flow, seen in the radial velocity measurements at the position of the positive axial flow within the vortical structure, BC4 (figure 5.34). The outward motion, re-established downstream, was confined to a narrow layer of fluid, rather than the smooth parabolic-shaped region of outwardly-moving fluid seen upstream in the proximal limb and in the bends. A similar narrow layer, later observed moving in the same direction in the

distal limb, could have been the same layer. This shear layer may have been the cause of unsteady wavering which occurred initially in the distal limb and, at progressively higher flowrates, in the medial bend and distal end of the proximal limb. Such wavering was not observed upstream of the vortical structure.

A secondary flow boundary layer separation was predicted at the inner side of a curved pipe by several authors, though this has been in dispute (Berger et al 1983). If secondary flow separation occurred, a re-entrant jet into the core flow would form, leading to a significant axial flow-secondary flow interaction. The present results for flow in the proximal limb support this occurrence.

6.2.4 Flow in the Medial and Distal Sections:

Only small double-peaks were observed downstream of the distal bend and none at all after the medial bend, suggesting that there was little interaction between the secondary flow and axial flow in the distal limb and distal stem, despite axial separation. This view is supported by the planar nature of the free shear layers observed in the axial velocity contour plots of these two sections.

The magnitude of the axial flow-secondary flow interaction in the bends may be explained by the location of the maximum axial flow on entry to the bends. In the proximal bend, the maximum axial flow was located near the centre of the tube, leading to strong Dean-type motions within the bend, possibly with secondary flow separation at the inner wall. The high axial curvature caused separation of the axial flow and strong interactions between the two motions were evident in the doubly-peaked axial flow isovels. In the medial and distal bends however, the maximum flow entering the bends was located close to the inner side of the tube (with respect to the respective downstream bend). Dean-type motions would be weaker in these cases, since the centrifugal effect on the core flow would be minimised. It seems that the flow was therefore dominated by the axial flow separation, with little interaction between this flow and relatively weak Dean-type motions.

Reverse flows were not observed at the outer walls of either the medial or the distal bends. This may also be explained by the fact that the maximum axial velocity was located at the inner side on entry to these bends. The position of the maximum axial flow would minimise any impingement effect of the core flow at the outer walls of the bends, so that the mechanism postulated above to explain the proximal bend reverse flow would not apply.

A thickened boundary layer existed at the $\alpha = 180°$ wall (the outer side with respect to the distal bend) prior to entry to the distal bend, as a result of the separation region in the distal limb. This, in conjunction with the thinner boundary layer at the inner side, would produce a pressure gradient that would tend to reinforce the azimuthal flow from the outer side to the inner side of the distal bend. This may account for similarity of the axial isovels to Dean-type flow in the distal bend, despite large departures from ideal entrance profiles.

Secondary flow was apparent in the distal bend, but not in the far distal stem. Suprisingly, given the shape of the axial isovels in the stem, azimuthal flow was not observed by LDA in the bend and the secondary velocity of the fluid, over the entire cross-section just downstream of the bend, was outwardly-directed. It may have been the case, that an azimuthal flow did occur but that the LDA measurement volume was situated too far from the walls to detect the motion. Dyestreams were too well mixed upon reaching the distal bend to conclusively demonstrate an azimuthal flow. A narrow layer of outwardly-moving core flow persisted downstream and was probably the result of the azimuthal flow colliding and separating at the inner distal bend axial separation point.

The axial velocity contours in the medial bend did not resemble those arising from Dean-type motions, though radial velocity profiles were of the Dean-type. The central region of axial flow upstream of the bend appears to be important in determining the strength of the centrifugal motions within the bend. In this case, the distorted nature of the axial flow upstream of the bend, caused by axial flow-secondary flow interactions, had the effect of decreasing the strength of the Dean motions in the medial bend.

6.2.5 Steady Flow Shear Stresses:

Singh (1974) and Smith (1976) predicted that the maximum axial shear stress occurs initially at the inner wall and shifts to the outer wall (giving rise to the so-called crossover point) at a downstream axial position. The shear rates measured in the present study, at the $\alpha = 0°$ and $\alpha = 180°$ sides just upstream (0.15 diameters) of the entrance of the proximal bend (for an Re of 1500, or a Dean number K = 1060), confirm that the shear rate was higher at the inner side than at the outer. Just downstream (0.15 diameters) of the proximal bend, the maximum shear rate was located at the outer ($\alpha = 180°$) side. The estimation of wall shear stresses from measurements of the fluid velocity near to the wall is not strictly accurate, but should provide a reasonable approximation.

The axial wall shear stress (or skin friction) for a curved tube with an entry condition of uniform pressure across the tube, is found from the boundary layer solution (Berger et al 1983):

$$\tau_{ws} = -\left(\frac{\mu\rho\overline{W_o}^3}{2as}\right)^{1/2}\left[0.4696 + \delta\cos\alpha\,(0.2562\,s^2 - 0.9392)\right] \qquad (6.1)$$

; where τ_{ws} is the axial skin friction, μ is the fluid dynamic viscosity, ρ is the fluid density, $\overline{W}_o$ is the mean axial velocity in the pipe, a is the pipe radius, δ is the curvature ratio, α is zero at the outer wall and s is the axial distance through the bend measured along the central axis, non-dimensionalised by the tube radius (see figure 6.3). The above equation has discontinuity at the entrance of the bend (s = 0), but downstream of the proximal bend entrance at s = 0.35, the axial skin friction for a Reynolds number of 1500 in the model, is calculated from equation 6.1 to be 0.0135 Nm^{-2} at the outside of the bend and 0.7898 N m^{-2} at the inside.

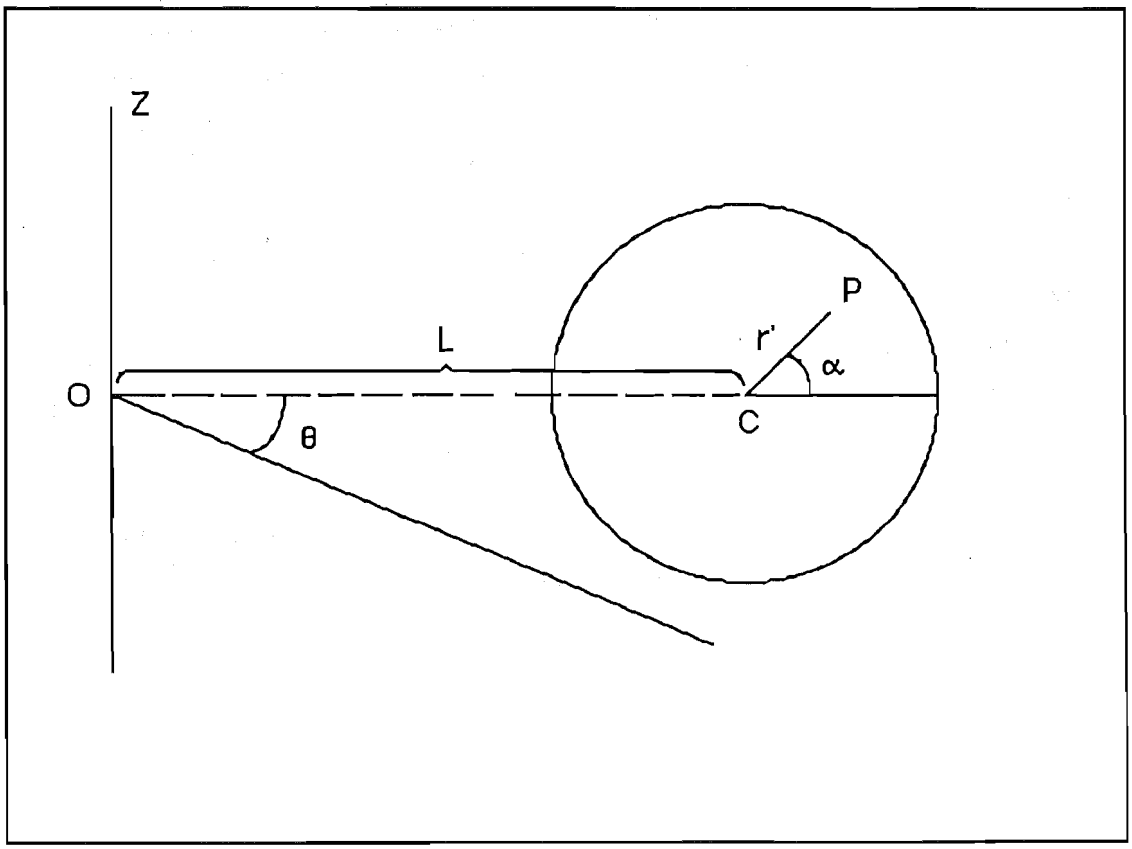

Figure 6.3
Curved Pipe Coordinate System Used by Singh (1974)

The actual shear rates were measured from the LDA velocity measurements, 0.15 diameters upstream of the entrance to the proximal bend, giving wall shear stresses of about 0.023 N m^{-2} and 0.050 N m^{-2} at the outer and inner sides respectively.

At the exit of the proximal bend, s = 1.2217 and the skin friction is calculated from equation 6.1 to be 0.0873 N m^{-2} at the outer side and 0.3416 N m^{-2} at the inner. The shear stresses calculated from the measured shear rates 0.15 diameters downstream of this position were 0.667 N m^{-2} at the outer side and close to zero at the inner side.

The present experimental results are in qualitative agreement with the location of the maximum skin friction predicted from equation 6.1. Near the bend entrance, the calculated shear stress is of the same order of magnitude as that estimated at the outer side, but equation 6.1 overestimates the skin friction at the inner side by more than a factor of 10. The difference in axial position between the measured and the calculated values would not account for an over-estimation of this magnitude.

The lower experimentally-measured value at the inner side may be due to the adjustment of the flow there to the axial separation that occurs within the bend, just downstream of this position. Singh (1974) calculated the cross-over point of the maximum axial skin friction to occur at $s \approx 1.9$, or an axial distance of about 1.9 radii from the bend entrance. Smith found that the crossover was located at a distance s = 1.51 from the onset of curvature. The proximal bend is shorter than these lengths, so that equation 6.1 predicts the maximum skin friction to be located at the inner wall at the exit of the proximal bend. In fact, the separation at the inner bend decreases the axial shear stress markedly, to zero at the separation point, which is located well upstream of the predicted crossover points. The medial bend is long enough to allow the cross-over point for maximum skin friction from the inner to the outer wall but again, separation occurs at the inner wall, upstream of the predicted crossover point locations.

The separation was a consequence of the high δ. The position of the crossover point, was found, by Singh, to be independent of δ, but this is not the case in the presence of separation. Both Smith's and Singh's solutions assume that flow is fully-developed at some downstream location, but this condition is not fulfilled experimentally in this case.

The shear rates measured at the $\alpha = 0°$ and $\alpha = 180°$ azimuths, shown in figure 5.30 are consistent with the finding of Smith, that the axial skin friction continues to increase with downstream distance.

The above findings are important, physiologically, because the solutions to curved pipe flow, at low δ, predict a lower axial wall shear stress at the outer wall than at the inner, throughout the entire lengths of both the proximal and the distal bends. The present results show that this is not the case for a high δ, at least with a multiply-curved tube such as the C-shaped tortuosity. The maximum skin friction in fact occurs at the outer wall just downstream of both these bends and the medial bend and the axial location of the cross-over point is probably just upstream of the separation point. However, the skin friction just upstream of each of the bends, including the proximal bend which is preceded by a straight tube, was found to be higher at the inner wall side than at the outer, in agreement with the theoretical treatments.

The secondary flow (azimuthal) skin friction in the tube near the $\alpha = +90°$ and $\alpha = -90°$ sides can be estimated from velocity gradients measured from the radial velocity measurements nearest walls there, subject to the same reservation noted above, regarding the accuracy of estimation of the skin friction by this method. The skin friction was found to range from 5×10^{-3} to 2×10^{-2} Nm^{-2} throughout the tortuosity. Singh found that the azimuthal skin friction $\tau_{w\alpha}$ is given by the equation:

$$\tau_{w\alpha} = -\left(\frac{\rho\mu\overline{W}_o^3}{2as}\right)^{1/2} \delta \sin(\alpha)\, sg''_{01}(0) \qquad (6.2)$$

; where $g_{01}(0) = 1.535795$.

At the same axial locations as those for which equation 6.1 was used to calculate the axial skin frictions above, equation 6.2 gives the azimuthal skin frictions at $\alpha = \pm 90°$ as 0.23 Nm^{-2} at $s = 0.35$ and 0.43 Nm^{-2} at $s = 1.22$. These values are one to two orders of magnitude larger than those estimated from experiments. The experimentally-obtained values serve as rough guides only, since the measurement points were too far from the wall (0.1 to 0.15 diameters) for the velocity gradients to reliably approximate those at the walls. Velocity measurements closer to the walls would be required to accurately estimate the wall shear rates. Hot film sensors fitted flush with the wall would be one method for achieving this. An alternative method for measuring the wall shear rates is the electrochemical limiting-current technique (eg: Choi et al, 1979).

6.2.6 In Vivo Shear Rates:

Dynamic similarity between the model and the internal carotid artery was ensured by scaling the flows with the Reynolds number. The hydrodynamic mean flow velocity in the model was about 0.11 times that of blood in the artery itself for any given Re and the diameter of the tube was 2.5 times the diameter of the internal carotid artery. From these values, the shear rates in vivo can be scaled from those in the model, by multiplying the velocity in the model by $(1/0.11)$ and the thickness of the shear layer by $(1/2.5)$. Assuming that the shear rates along the walls vary linearly with the mean axial flow velocity, as they do in laminar flow through a straight tube of circular cross-section, the shear rates, v/d, in vivo would therefore be about 22.5 times those observed in the model. The viscosity of blood is about 4 times the viscosity of water, so the shear stresses in vivo would be about 90 (4 x 22.5) times greater than those calculated for flow in the model.

The shear rates in vivo, scaled from those observed in the model, would mostly be in excess of 100 s^{-1}, justifying the assumption that hydrodynamic flow approximates the macroscopic features of blood flow well at the flowrates studied. With the same scaling, the in vivo shear rates within the recirculation regions would mostly be well above the yield shear rate of blood (15 to 20 s^{-1}). The maximum shear rate observed in the model for a pulsatile flow with a mean Reynolds number of 1500 was 300 s^{-1}, corresponding to an in vivo shear rate of 6750 s^{-1}, corresponding to in vivo shear stresses of just over 250 dynes cm^{-2} (25 N m^{-2}).

These shear stresses are below the 400 dynes cm s^{-2} (40 N m^{-2}) determined by Fry (1968, 1969) as sufficient to cause endothelial cell injury. On the other hand, erythrocytes (red blood cells) that are adhered to the vessel wall may be damaged by shear stresses in the range of 10-100 dynes cm^{-2} (Blackshear 1972), while platelets (white blood cells) may be stimulated to release factors such as serotonin when subjected to a shear stress of only 16.5 dynes cm^{-2} (Goldsmith et al, 1976). Aggregation of platelets has been shown to be enhanced in a suspension of platelets subjected to an oscillatory shear stress of 26 dyne cm^{-2} (Yu et al, 1978). The effect of shear stress depends on the duration as well as the magnitude of the applied stress (Blackshear 1972). In the case of an erythrocyte or platelet adhering just upstream of a reattaachment point and within the shear layer, any cell products or contents released by damage to the cell (adenosine triphosphate, platelet-derived growth factors, fibrinogen, etc) would be recirculated within the separation bubble. Because of the longer fluid residence time there, the adjacent wall would be subject to a higher local concentration

of these cell products than other parts of the wall which are subject to the bulk blood concentration.

6.2.7 Separation Effects:

The separated flows observed at various positions in the model were subject to inherent unsteadiness. It has been shown that vortex formation and shedding from the shear layers bounding the separation regions occurred in both the distal limb and distal stem. Also in the proximal limb, the flow downstream of the vortex structure exhibited a periodic wavering.

Local pressure variations should arise from the velocity fluctuations in the shear layers and may be felt at the wall. In the absence of data for calculating the Reynolds stresses, which requires the simultaneous measurement of two orthogonal velocities, an attempt can be made to estimate the likely nature of these pressure fluctuations from the dimensions of the shear layers and the axial velocities.

Driver et al (1987) concluded from their measurements in a reattaching turbulent shear layer behind a backward-facing step that the majority of energy in separated flows resided in the frequencies characteristic of roll-up and pairing of vortical structures seen in free shear layers. These frequencies scale to the shear layer thickness and shear layer average velocity with a Strouhal number, Str = 0.2 (Mabey, 1972) where the Strouhal number is defined as:

$$Str = \frac{f\,b}{U_{sl}}$$

; where f is the frequency, b is the shear layer thickness and U_{sl} is the average velocity in the shear layer.

From the LDA axial isovel plots a measure of b and U_{sl} in the distal limb and stem can be obtained and therefore a likely frequency of oscillation found for the separated shear layers bounding the separation in those regions. For the distal limb, b = 3.3 mm, U_{sl} = 3.5 cm s^{-1} and f is calculated to be 2.11 Hz. In the distal stem, b = 3.9 mm, U_{sl} = 3.5 cm s^{-1} and f is calculated to be 1.81 Hz. The value of f for the distal limb is supported by LDA measurements of the strongest axial velocity fluctuations, found in the shear layer which had a well-defined peak at 2.25 Hz (plus harmonics) shown in Appendix N. Dye visualisation showed the vortex formation to occur at a frequency of about 2.67 Hz.

The Strouhal number may be used to scale the fluctuation frequencies to estimate those that might be expected in vivo, if the shear layer velocity is scaled by the Reynolds number. This gives frequencies of about 44 Hz from the calculated value for the distal limb shear layer and about 40 Hz for the distal stem. The experimentally-measured frequency of oscillation and the vortex formation frequency scale to 50 Hz and 59 Hz in vivo, respectively. These frequencies are close to the 50 Hz used to estimate the magnitude of pressure pulses through the vesicle neck in Chapter 3.

The shear layer in the proximal limb was three-dimensional and therefore neither a characteristic thickness nor velocity could be obtained. However, the frequency of the fluctuations was measured to be O[2 Hz] by both LDA (Appendix N) and dye visualisation (1.25 Hz).

Several authors have attempted to relate the wall pressure fluctuations in a separated flow to the shear layer bounding the flow. Ignoring radiation of pressure from other parts of the flow, the wall pressure fluctuations in the recirculation region are due either to the reverse flow itself or the shear layer. The rms pressure $\langle p^2 \rangle^{0.5}$ of the reverse flow can be estimated from the ordinary boundary layer result (Fricke and Stevenson, 1970) by

$$\frac{\langle p^2 \rangle^{0.5}}{q} = 0.006 \qquad (6\text{-}1)$$

if the pressure gradient is ignored, where q is the kinetic head $0.5\rho u^2$; and where u is the reverse flow velocity. Therefore $\langle p^2 \rangle^{0.5} = 1.9 \times 10^{-3}$ Pa in the hydrodynamic flow through the model. This calculation shows that the contribution to the wall pressure fluctuations from the reverse flow boundary layer is insignificant.

Another source of hydrodynamic pressure fluctuations at the wall in the recirculation zone, is the shear layer. Unfortunately, most estimation techniques require the simultaneous measurement of two orthogonal velocities in the shear layer. An estimate of the spatial variation of a second velocity component normal to the axial flow may often be found from Taylor's hypothesis:

$$\frac{\delta(\varphi)}{\delta x_1} = \left(\frac{-1}{U_1}\right) \frac{\delta(\varphi)}{dt}$$

; where φ is an instantaneous quantity being measured, but this still requires a measurement of the characteristic temporal fluctuation of the second velocity component.

Greshilov (1969) proposed, following Kraichnan (1956), that the rms value of the pressure fluctuations at the wall, in a flow with uniform turbulence in the presence of a velocity shift was:

$$\sqrt{\overline{p^2}} = \frac{1}{3} \text{ to } \frac{1}{4}\left(\rho \frac{\delta U}{\delta y} v_t L_l\right)$$

;where v_t is the transverse component of the velocity fluctuations and L_l is it's longitudinal scale. $v_t = 0.7 v_l$ and $v_l = 0.2 L_l \, \delta U/\delta y$. The axial velocity gradient $\delta U/\delta y$ of the shear layer in the distal limb was estimated from the LDA measurements, and L_l taken to be the shear layer thickness, also taken from the LDA isovels. Then $v_t = 77$ mm s^{-1} and so

$$1.5 \text{ Pa} \leq \sqrt{\overline{p^2}} \leq 2 \text{ Pa}$$

The total kinetic head based on the average flow velocity upstream in the proximal stem was 3.2 Pa and so the estimated rms pressure fluctuation seems to be of the right order of magnitude. Scaling from this, the in vivo pressure fluctuations would be between 120 Pa and 160 Pa. However, v_t appears to be a little on the high side at 7.7 cm s^{-1}, or 50% of the maximum axial flow upstream of the proximal bend. Also, as pointed out by Fricke (1971), $\delta U/\delta y$ should be a minimum at the reattachment point, whilst $\overline{(p^2)}^{0.5}$ should be at a maximum, indicating that Greshilov's expression breaks down near the attachment zone. Fricke pointed out that Revel & Gleason's (1965) empirical relation:

$$\frac{\sqrt{\overline{p^2}}}{q} \propto \left(\frac{\delta}{h}\right)^{3/2}$$

is reasonable, although there is little theoretical foundation for this. In the present case it is difficult to predict an equivalent discontinuity height, h. However, if we use the recirculation zone thickness, then $\overline{(p^2)}^{0.5} \approx 1.28q$, which is slightly higher than that calculated by equation 6-? The corresponding magnitude of the in vivo pressure fluctuations would be about 130 Pa at reattachment, slightly greater than the kinetic head of the shear layer, based on the mean shear layer velocity.

Fricke also states that the empirical relation

$$\frac{\sqrt{\overline{p^{-2}}}}{q_m} = 0.022 \frac{x_1}{y_0}\left(1 - \frac{x_1}{x_r}\right)$$

slightly overestimates the maximum $\overline{(p)}^{0.5}/q_m$ for $0 \leq x_1/x_r < 0.5$ and slightly underestimates $\overline{(p)}^{0.5}/q_m$ for $0.5 < x_1/x_r \leq 1.0$ in the flows he studied, where x_r is the reattachment length. However, this also tends to zero at the reattachment point - exactly the same problem that he criticises Greshilov's relation for. If we use the value 20 mm for x_r and $y_0 = 2.8$ mm ;where y_0 is the thickness of the recirculation zone in the distal limb, then $x_1/x_r = 0.1$ at position DE1 in the LDA plots. This gives $\overline{(p)}^{0.5}/q_m = 0.01$. This value seems rather low, especially if it is supposed to be an overestimate of $\overline{(p)}^{0.5}$.

Roos and Kegelman (1986) measured a fluctuating pressure coefficient $C_p' = p'/q_0$ (; where q_0 is the kinetic head based on the free stream velocity) as a maximum of about 0.04 at reattachment downstream of a backward facing step. In the distal limb, the maximum pressure fluctuation would be about 0.16 Pa, based on a free stream velocity of 9.0 cm s^{-1}, corresponding to in vivo fluctuations of 13 Pa, with the velocity scaled by the Reynolds number.

Driver et al (1987) measured the static pressure fluctuations at the wall, under a separated shear layer behind a rearward-facing step and found that fluctuations in the static pressure coefficient, C_p, could be as high as 0.2, near the reattachment point, where

$$C_p = \frac{P_s - P_{sref}}{1/2\,\rho U_{ref}^2}$$

and P_s is the static pressure at the wall, P_{sref} is a reference pressure, ρ is the density of the fluid and U_{ref} is the velocity, measured at the reference station. Taking U_{ref} to be the maximum velocity upstream of the tortuosity, 13 cm s^{-1}, the static pressure fluctuations at the wall near reattchment are calculate with $C_p = 0.2$, to be 1.7 Pa, or an in vivo value of 140 Pa.

The pressure fluctuations under the flow on the wall opposite the separation regions is likely to be just that calculated from the boundary layer solution and so would be about 0.05 Pa, based on the LDA measurements in the proximal limb at Re = 1500, with $U_0 = 13.0$ cm s^{-1}, or an in vivo magnitude of 4 Pa.

The above estimates of the wall pressure fluctuations likely to be associated with separated flows in the model, are wide-ranging. None of the separated flows used to relate the magnitude of fluctuating pressures to the shear layer properties exactly match the present flow configuration. The backward-facing step, used by Roos & Kegelman (1986), is the closest to the tortuosity, but is effectively only a two-dimensional flow, rather than the three-dimensional flow present in the tube. The separation point for a backward-facing step is constant, due to the sharpness of the step, whilst that at the inner bend of the tortuosity is subject to variation. The reattachment point downstream of a backward-facing step is therefore probably subject to smaller variations in location than is the case for reattachment in the tortuosity and the pressure fluctuations at the mean reattachment point in the tortuosity are therefore likely to be larger.

The best estimate of the static pressure fluctuations at the wall near a reattachment point is that of Driver et al (1987), from which it is estimated that in vivo pressure fluctuations of 140 Pa are likely to occur.

It would be useful if the wall pressure fluctuations in similar models were measured in further work and scaled to the geometry of the model and the Reynolds (or Deans) number, so that in vivo wall pressure fluctuations could be estimated more precisely than is possible at present.

6.3 Pulsatile Flow:

The features under pulsatile conditions were qualitatively similar to those observed during steady flow. Separation and reattachment were associated with the inner walls downstream of the bends; reverse flow occurred in the same regions identified under steady flow conditions; and the high shear rates along the outer walls downstream of bends were consistent with those positions observed in steady flow. The flow features were qualitatively reproducible throughout the pulsatile flow, as shown by flow visualisation.

The emphasis for this section of experimental work was to identify the areas of the tube subjected to the various flow phenomena observed under steady flow conditions. Recall that the types of flow observed at the measurement sites in the model were grouped, in Chapter 5, according to their geometric locations. Group 1 included the contours upstream of the tortuosity, in the straight tube; Group 2, the contours downstream of the inner wall of each bend (but including, also, the contour slice just upstream of the outer ($\alpha = 180°$) proximal bend); and Group 3 included the contour slices downstream of the outer bend walls.

6.3.1 Group 1 Regions:

Flow was characterised in these regions, by forward flow over most of the pulsatile cycle, with negative flow occupying the whole slice during the lowest part of the cycle. This is consistent with the results of other workers, who found a tendency for reverse flow to occur in a layer along the walls of a straight tube, during the deceleration stages of pulsatile flow. Shear rates were moderate, and the contours indicated that flow was homogeneous near the walls in these regions ie: there were no areas of high shear or markedly different velocities between adjacent areas of the contour slices.

Physiologically, this means that in the normal (straight) state, the arterial wall is subjected to relatively gentle oscillations between forward and reverse flow, that are homogeneous between adjacent areas and evenly distributed about the circumference of the vessel.

6.3.2 Group 2 Regions:

It is apparent in all but one of the group 2 regions, that separation of the axial flow occurred upstream of the recirculation zone and reattachent occurred at the downstream end. The exception to this was in the contour slice along the outer (α = 180°) proximal stem near the proximal bend entrance and it is not appropriate to consider this as a separation zone per se. This region showed a tendency towards stagnation rather than recirculation, though it was more susceptable to recirculation during deceleration than the straight parts of the tube in Group 1. No high velocity gradients bounding the region were apparent, and reattachment was not observed, or indicated by the axial isovels there, at any stage during the cycle. However, one of the common features between this region and the others of Group 2 was the existence of a free shear layer bounding the recirculation region was subject to inherent unsteadiness, as discussed in section 6.2.7

A second feature, common to the Group 2 regions, was the heterogeneous nature of the velocities in the contour slices. Unlike the flow in other contour groups, adjacent areas in these regions were exposed to high and low shear rates simultaneously. The movement of the reverse flow regions which occurred during the flow cycle, would cause considerable changes in the wall flow conditions experienced by some positions during each flow cycle. For instance, a sudden velocity increase from close to zero up to about 10 cm s^{-1}, was illustrated in figure 5.66, for a position near the α = 0° wall of the proximal limb at Re_{mean} = 1500. This velocity change represents a change in the kinetic head of the fluid, over a time interval of 1.7 seconds, of approximately 5 Pa in the hydrodynamic flow. The apparent acceleration, found from the slope of the velocity curve at that position, is a conservative estimate of the actual acceleration there and was limited by the length of the sampling interval. The corresponding change in kinetic head in vivo would be more than 400 Pa, over a time interval (scaled by the Strouhal number) of, at most, 76 msec! The reattaching shear layer will therefore have a massaging effect on the arterial wall in vivo, due to changes in the local kinetic head as it moves back and forth during the cycle.

The movement of the reverse flow regions meant that the walls downstream of an inner bend were subjected, during each cycle, to reverse flow over a greater axial length than was the case in steady flow. The location of the flow separation bubble, in the isovels averaged over the flow cycle, differed from that in steady flow at the corresponding Reynolds number. The location of the recirculation region varied considerably at at different instantaneous phase angles. This indicates that the steady flow cannot be relied upon to accurately determine the location of reverse flows in vivo.

The magnitudes of shear rates at the walls of the model, reverse flow velocities and the velocity gradients in free shear layers, were quantitatively different from those observed in steady flow. The velocity gradients in pulsatile flow, averaged over a complete flow cycle, were only 60% of those in steady flow at the corresponding average Re, even though the gradients in the latter were less than the maximum gradients observed during peak pulsatile flow rates. The assumption cannot therefore be made that unsteady components of shear stresses are approximated by those measured in steady flow.

The maximum axial shear rates of the free shear layers in the proximal bend were related to the instantaneous Reynolds number, as shown in figure 6.4 The curve appears to be of exponential form in the laminar flow region, with the maximum axial shear rate being proportional to $\exp(3.24 \times 10^{-2} Re)$. It is interesting to note that the shear rates measured during the deceleration part of the cycle lie above the line of best fit for $Re_{mean} = 1500$, whilst those measured during acceleration lie below it. This suggests that the free shear layers take some time to develop to their final intensity at a given flowrate, which may explain the lower shear rates observed in pulsatile flow than those at the corresponding steady flowrates.

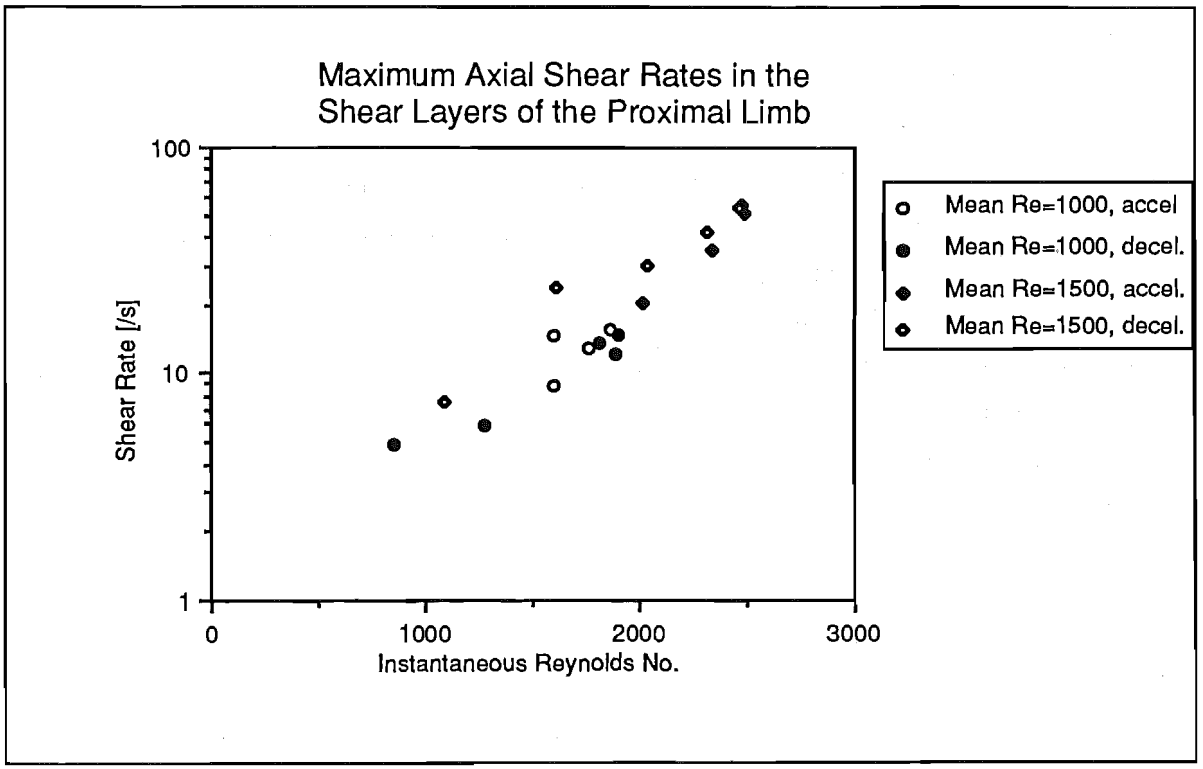

Figure 6.4

Maximum Axial Shear Rates of the Free Shear Layers in the Proximal Limb versus Instantaneous Reynolds numbers.

The average velocity of reverse flows during steady flow in the proximal limb were larger than those under pulsatile conditions, by 120% for $Re_{steady} = Re_{mean} = 1500$, and by 23% for $Re_{steady} = Re_{mean} = 1000$. It appears that the reverse flows, like the velocity gradients in the separated shear layers, take some time to become fully-developed. This has consequences in vivo, where the recirculation velocity may not reach the expected velocity, based on the peak instantaneous Reynolds number. The maximum axial reverse flow velocity measured during pulsatile flow is plotted against the instantaneous Reynolds number in figure 6.5. The relationship is linear, though there is considerable scatter, with the reverse flow in cm s^{-1} equal to approximately $2 \times 10^{-3}(Re)$.

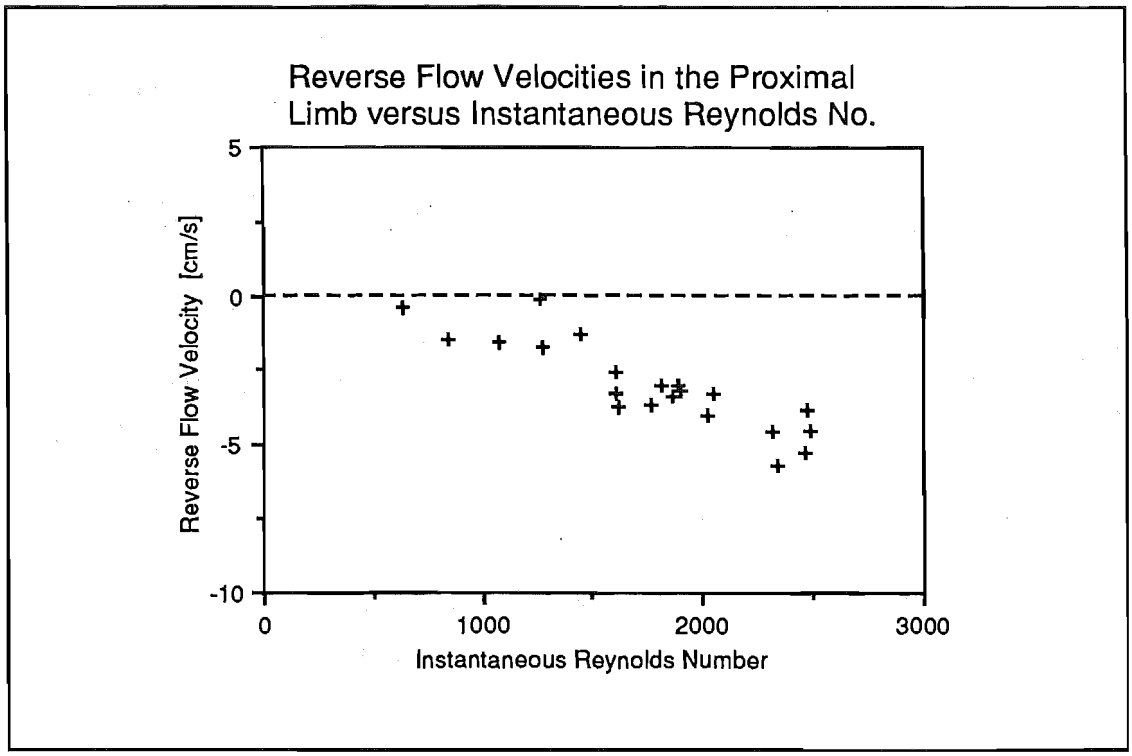

Figure 6.5
Reverse Flow Velocities in Separation Zones of the Proximal Limb versus Instantaneous Reynolds number.

No correlation was found between the reattachment length and the Reynolds number. This is possibly explained by the three-dimensional nature of the separation in the tortuosity, which is unlike the two-dimensional separation downstream of a backward-facing step, for which such a correlation exists. The curved bends in the model provide rounded leading edge effects, which tend to destabilise the separation and the free shear layer. The separation position was not constant during the flow cycle

and randomness in the reattachment length probably resulted from any randomness in the separation position.

The dye visualisation results show that the vortex structure associated with the separation in the proximal limb becomes quite simple at the low velocity part of the pulsatile cycle. This may be due to a weakening of the secondary flows in the proximal limb, decreasing any secondary flow interactions with the axial flow during this part of the cycle. This is not obvious from the steady flow results, where secondary flow-axial flow interactions are indicated even at much lower Reynolds numbers. The secondary flow was confined to a thin layer about the walls of the tube. This layer may have been influenced more strongly by the deceleration in the tube than the fluid in the central region, due to the inertial and viscous forces being out of phase there (similar to the flow reversal near the walls, observed in the straight tube upstream of the tortuosity). The imbalance of the effect of deceleration between the central fluid and that located near the walls would therefore cause the axial flow separation to dominate over the secondary flow and simplify the vortical structure.

6.3.3 Group 3 Regions:

Group 3 regions were associated with high shear rates at the walls and a constant forward velocity throughout the cycle. The contours were similar, both in terms of velocity gradients and peak velocity magnitudes, under the pulsatile conditions of acceleration and deceleration, as a comparison of the isovel contours at similar Re_{inst} under those conditions shows.

The axial velocities were found to be relatively homogeneous over the contour measurement slices, meaning that adjacent areas of the tube in these regions were subjected to similar velocity gradients over the whole of each slice. The velocities varied at a similar rate to the mean flow, so that sudden changes of velocity and therefore variations in the kinetic head near the walls, common in the Group 2 regions, were not experienced by the Group 3 regions.

6.4 Flow Features and Atheromic Sites:

6.4.1 Proliferative Lesion Sites:

Regions of the model in which flow separation occurred, consistently matched reported sites of proliferative atheroma in the tortuous internal carotid artery.

Separation occurred at the inner walls of the bends, leading to a region of recirculating fluid along the walls downstream of the separation point. The flow velocities in the separation zones were low, compared to the maximum velocity in the straight tube upstream of the tortuosity and to the velocities observed near the walls in other parts of the tube. These findings are in agreement with the results of Caro et al (1971), Rodkiewicz (1975), Zarins et al (1981), Ku et al (1985) and other workers, who associated areas of separation and low velocity with the locations of atheromic plaque in other arterial configurations.

A common feature of all the areas subjected to separation (ie: Group 2 regions) was the occurrence of a free shear layer, bounding the separated flow. An unexpected region of reverse flow was found at the outer wall of the proximal bend, though neither separation nor reattachment were indicated there. However, the reverse flow must have been bounded by a free shear layer, separating it from the positive flow observed further from the wall. Although reattachment was not indicated, a feature of it, namely a zone between positive and negative flow located at the wall, with a zero axial shear rate, did exist. Stehbens (1987) illustrated localised intimal thickening downstream of the inner bends in a section of an artery with a similar configuration to that used in this study. In addition to the areas indicated by Stehbens, a region of intimal thickening (not indicated by Stehbens) apparently occurred at the entrance to the outer proximal bend. The thickening there was, however, not as marked as it was in the other regions, and further work is required to conclusively show the existence of a proliferative lesion in that position.

A feature of the flows in areas corresponding to regions of proliferative atheroma, was the heterogeneous nature of the velocities and velocity gradients prevalent in the region. Adjacent parts of the tube wall, within these regions, were subjected, simultaneously, to markedly different velocities and shear rates. Reattachment of the separated shear layer occurred at the downstream end of each recirculation zone, so that in the space of only a few mm, the wall of the tube there was exposed to forward axial flow, at a velocity approaching that of the free shear layer; slow reverse axial flow, in the separation zone and zero axial flow at the reattachment point. These flows, in turn, gave rise to positive, negative and zero axial shear stresses respectively.

Pressure fluctuations, due to the inherent unsteadiness of separated shear layer flows and the impingement of the reattaching shear layers, undoubtedly would have been felt at the walls of the tube in these regions. Unfortunately, attempts to quantify the wall pressure fluctuations were inconclusive, due to unacceptable noise levels in the measuring instrument. This is an important area for future work, in view

of the possibility of increased cholesterol transport by convective loading of LDL into endothelial cell vesicles, as postulated in Chapter 3.

The three-dimensional nature of the flow in the tortuosity meant that the shapes and locations of the recirculation regions and the free shear layers bounding the reverse flows were complex, despite the idealised geometry of the model. Under pulsatile conditions, the shapes of the separation zones were quite variable and the recirculation zones moved extensively along the walls of the tube, for instance over a distance equal to the tube diameter in the proximal limb. The exact matching of particular flow features in these regions with atheromic sites in vivo is therefore not possible.

The movement of the recirculation zones and shear layer reattachment positions during pulsatile flow, exposed some parts of the tube to flow environments that varied considerably throughout the cycle, resulting in uncertainty over which of the flow features are involved in the initiation and progression of atherosclerosis. Fry's (1973) suggestion, that oscillating shear stresses may constitute a causative factor in atherosclerosis, is therefore not refuted by the present findings, even in the regions downstream of separation. The biochemical response of endothelial cells, to unsteady shear stresses may be an important factor in atherogenesis.

The results, under steady flow conditions, do indicate, however, that the regions immediately downstream of the separation points were subjected to the lowest shear rates in the tube. This was also true during pulsatile flow, though these regions were not exposed to recirculating flow throughout the entire flow cycle, as might at first be thought. The shape of the pulse in vivo is different from that used in this study. In this part of the arterial system, the systolic pressure pulse in vivo causes a sharp flow peak at the beginning of each cycle, which is followed by a period of relatively constant forward flow (though with damped oscillations) which lasts until the next systolic pulse. This suggests that the lowest shear rates will be found immediately downstream of the inner bends during most of the flow cycle in vivo. If the intensities of the shear layer velocity gradients take some time to develop, the sharpness of the maximum flow peak in vivo will tend to minimise the gradients, compared to steady flow equal to the instantaneous Re. The period of forward flow, during diastole, will tend to allow the gradients to approach closer to their values during steady flow at the same instantaneous Re.

The flow structures observed in the model, in regions corresponding to sites of proliferative atheroma in vivo, are sufficient to subject areas of the arterial wall, in close proximity to one another, to diverse physical effects, which may vary

dramatically throughout the pulsatile flow cycle. Both the pressure fluctuations and the shear stress fluctuations were a maximum in these regions. Either of these haemodynamic influences could be a candidate for causing increased lipid deposits or intimal thickening. An altered transmural permeability to macromolecules may result from the influence of pressure fluctuations on the walls.

6.4.2 Atrophic Lesion Sites:

Regions of the tube subjected to consistently high shear rates were located at the outer bend walls and matched those regions in vivo, for which Stehbens (1987) reported the occurrence of atrophic lesions and for which Meyer & Lind (1972) noted the occurrence of calcified deposits during the initial stages of atherosclerosis. These regions were subject to unidirectional axial flow over the complete pulsatile flow cycle, in contrast not only to flow at the sites of proliferative lesions, but also that upstream of the proximal bend in the straight tube, where atheroma is generally not accentuated.

The shear rates in these regions varied at approximately the same frequency as the overall flow cycle and little unsteadiness occurred in the boundary layer close to the wall. Pressure fluctuations experienced by the wall under the boundary layer would be small, of the order 6×10^{-3} times the kinetic head of the mainstream flow (about 3 Pa in vivo).

The magnitude of the shear rate does not seem to be as important as the duration or the unidirectional application of the shear. The shear stresses at these walls did not seem to exceed the maximum shear stresses observed bounding the moving recirculation regions of the proliferative sites during pulsatile flow. The shear rates increased in an axial direction along the walls downstream of the outer bends, so that one expects, if the magnitude of the shear rate is important, that the atrophic lesions will increase in severity with downstream distance from the outer bend, in these regions. The sites of the atrophic lesion, indicated by Stehbens (1986), do not correspond exactly with this, being located instead, at the outer walls within the bends and only in the upstream half of the downstream limb.

Stress fluctuation fatigue, suggested by Stehbens (1979) to cause degenerative changes to the arterial wall and a diminished wall strength, is not indicated by the present results in the sites corresponding to the atrophic lesion. The layer of fluid moving along the wall in these regions was, in fact, found to be steadier than that surrounding the proliferative sites. Fluid-induced vibration of the wall is therefore less likely to occur in the atrophic sites than in the proliferative sites of the

tortuosity. Biochemical responses of the endothelial cells exposed to constantly high, unidirectional shear stresses may be the cause of the atrophic lesion observed in vivo.

Stehbens also suggested that stress fluctuation may cause a reparative response in the wall, from which the proliferative lesions may result. This possibility is supported by the present findings of maximum stress fluctuations and pressure fluctuations in the proliferative lesion localities.

Chapter 7

Conclusions and Recommendations for Future Research

The study of haemodynamics remains as an important area of research and in particular, the possible relationship between blood flow and atherosclerosis needs to be explored further. It is now generally accepted that haemodynamic factors are involved in atherogenesis but doubt still remains over which of the flow features are important in the pathogenesis and progression of the disease. The mechanisms by which fluid disturbances may lead to atherosclerosis are still not clear.

7.1 Atherogenesis and Cholesterol Transport:

A modification of the unified hypothesis for the initiation and progression of atherosclerosis described by Steinberg (1983) has been suggested, allowing for the action of haemodynamic influences, especially in the initial stages of the disease. It has been postulated that haemodynamic factors may act in three ways: by inducing endothelial injury; by causing stress fluctuation fatigue of the blood vessel wall material (including the elastic components beneath the endothelium); and/or by altering the transmural permeability to macromolecules, in particular low density lipoproteins.

Transendothelial pinocytotic vesicular transport remains an attractive mechanism for the passage of macromolecules through the arterial endothelium. Ultrastructural studies of the endothelial cell, by ultrathin sectioning, which have raised doubts about the role of pinocytotic vesicles in macromolecular transport have been discussed. It was suggested that the fixation techniques employed in these studies, may have allowed changes from the in vivo vesicular structure of the cells to occur during the static conditions before microscopy. Hence the published conclusions regarding the pinocytotic vesicular arrangement, drawn from the ultrathin sectioning studies, cannot be regarded as clear cut, and the possibility of vesicular transport occurring in vivo should not be ruled out.

The assumption, often made in models of pinocytotic vesicular transport, that the vesicular loading process occurs quickly, compared to the average vesicle attachment time, has been examined. An exponential factor, allowing for hindered diffusion through the vesicle neck, has been added to Arminski et al's (1980) equation, describing the permeability of an endothelial cell. In this, the loading time of an LDL molecule through the vesicle neck was described in terms of an observed diffusion coefficient in the neck, related to the bulk diffusion coefficient by an equilibrium partition coefficient. The time of passage for an LDL molecule through the vesicle neck was found to be a significant fraction of the vesicle attachment time only when the radius of the LDL molecule is very close to the internal radius of the vesicle neck.

The effect of hindered diffusion increases markedly with increased pore length. Diffusion through transendothelial pores, suggested by Frokjær-Jensen (1984) as an alternative mode of macromolecular transport to vesicular transport, would be subject to considerable hindrance, even for molecules with diameters that are a small fraction of the pore diameter.

A fluctuating convective motion through the vesicle neck, caused by nearby blood flow disturbances, has been postulated as a mechanism by which haemodynamics may influence the vesicular transport. The observed diffusion coefficient may be enhanced by convective fluctuations in the neck, even if the average of the fluctuations is zero. The convective effects were found to be negligible when considered solely as perturbations of the observed diffusion coefficient (Malone & Anderson 1978), as is suitable for long pores. This treatment, however, was not suitable for the short vesicle necks.

It was found that a considerable effect on the loading of vesicles with LDL molecules will result from convective flows through the short necks. The analysis depends crucially on the value of the spontaneous curvature of the vesicle lipid bilayer wall material, as buckling of the vesicle is required for this flow, and a bending resistance needs to be overcome. It has been found, assuming a zero spontaneous curvature, that convective flows into and out of the vesicle cavity may be large enough to overide the geometric partitioning effect on the equilibrium LDL concentration within the cavity. The result is to bring the vesicle interior to an LDL concentration equal with that of the plasma. The internal concentration, resulting from diffusional loading only, is limited, by the geometric partitioning effect, to about 32% of the plasma concentration. Convective loading may increase the vesicle's internal LDL concentration by up to three times this, and hence raise the cholesterol transport through the endothelial layer by up to three times.

7.2 Flow Phenomena in the Model Tortuosity:

The expected similarities between the flow in the model tortuosity and the flow reported for curved pipes were observed. The high curvature ratio of the bends in the tortuosity, caused several differences from the flow reported in the literature for low curvature ratios. Flow asymmetry was present both upstream of and within the tortuosity.

Axial flow separation occurred at the inner walls of each bend, leading to recirculation regions downstream of the bends, bounded by free shear layers, followed by shear layer reattachment. Significant secondary flow-axial flow interactions took place in and downstream of the proximal bend, creating a complex vortical structure, which was observed downstream of the bend, along the inner wall.

A significant region of secondary flow was observed upstream of the proximal bend for steady, Poiseuille flow entry conditions. This consisted of an azimuthal flow, directed from the outer side to the inner, with respect to the proximal bend. This was identified as the region of "upstream effect" predicted by Smith (1976) and was not observed under uniform entrance velocity conditions, in accordance with his analysis.

An unexpected region of reverse flow was observed at the outer wall of the proximal bend during steady flow experiments. This extended to a position upstream of the bend entrance at Reynolds numbers above 500.

The predictions of Singh (1974) and Smith (1976) that the maximum axial shear stress would be located at the inner wall of the entrance of a curved pipe were found to be correct, upstream of the proximal bend. The cross-over point, downstream of which the maximum shear stress is located at the outer wall, was located within the bends, due to axial separation occurring at the inner wall, against Singh's and Smith's predictions.

The frequencies of unsteady fluctuations in the separated shear layers were measured, and found to be close to those calculated from a Strouhal number of 0.2, based on the shear layer dimensions, as suggested by Mabey (1972). A large range of estimates for the wall pressure fluctuations, resulting from the proximity and reattachment of a separated shear layer, were found. The best estimate of the likely in vivo wall pressure fluctuations near the reattachment point of a separated shear layer was found from Driver et al (1987) to be 140 Pa.

The positions of the separation regions in pulsatile flow, cannot be accurately determined from steady flow results. The intensities of the separated shear layer velocity gradients and the reverse flow velocities were less that those observed under steady flow conditions at the same instantaneous Reynolds number. This suggests that the separation flows take some time to develop to their steady flow values. The maximum axial shear rates of the separated shear layer and the reverse flow velocity, in cm s^{-1}, in the proximal limb, were related to the instantaneous Reynolds number by $\exp(3.24 \times 10^{-2}Re)$ and $2 \times 10^{-3}(Re)$ respectively.

7.3 Flow Features and Atherosclerotic Lesions:

The steady flow features in the model consistently matched the positions of two types of atherosclerotic plaque. Axial flow separation was observed in regions corresponding to reported sites of proliferative atheroma in vivo. The location of the reverse flow at the outer proximal bend, corresponds with a position in vivo, where intimal thickening has been observed. This single observation of intimal thickening is not conclusive and further investigation of the region is required. Regions of the tube subjected to unidirectional, high shear rates were associated with reported sites of atrophic atheroma.

A free shear layer, bounding the regions of recirculating flow, was a common feature of the reported sites of proliferative lesions. Wall pressure fluctuations, associated with the these layers near reattachment, were estimated to be about 140 Pa in vivo. Shear stress fluctuations, due to the back and forth motion of the shear layer reattachment point, were observed to be maximal in these regions.

It is concluded that the proliferative lesions of atherosclerosis, in the tortuous internal carotid artery, are associated with regions of flow separation, which exhibit low mean wall shear stresses but are subject to the highest shear stress fluctuations in the model. Fluctuating wall pressure fluctuations also occur in these regions, which may lead to increased lipid infiltration of the arterial wall. It is also possible that the proliferative lesions result from reparative changes in the arterial wall, caused by stress fluctuation fatigue, as suggested by Stehbens (1979).

A comparison of the location of the maximum shear stresses in the tortuosity, with reported sites of atrophic atherosclerotic lesions, indicates that the magnitude of the wall shear stresses there, are not as important as their unidirectional nature. Little unsteadiness was observed in the boundary layer close to the wall in the sites of the atrophic lesion, indicating that stress fluctuation fatigue of the arterial wall is unlikely to be the cause of atrophic lesions. The biochemical response of the endothelial cells to

unidirectional shear stresses is a likely candidate for causing atrophic atherosclerotic changes in these regions.

7.4 Recommendations for Future Research:

Several avenues are open for further work on the flow in C-shaped tortuosities and the relationship between atheroma and haemodynamics.

The recent development of new plastics, with refractive indices equal to that of water, has solved the problem of refraction in the application of the LDA to tubes with high curvature ratios. By using these plastics, any velocity component may be studied throughout the tube, and in particular, the axial and secondary velocities within the bends. Velocities very close to the walls of the tube can now be measured, so that the azimuthal flows can be quantified and improved estimates of the wall shear rates made.

The region of upstream effect in the proximal stem and the reverse flow at the outer proximal bend should be studied further, since these comprise significantly different flows to that observed in a straight tube and may provide clues to the relationship between blood flow and atherosclerosis. Further study of the separation regions is required, and this will be simplified, experimentally, by the new plastics mentioned above. Measurements in the positions of separation and reattachment are particularly important.

Turbulent intensities were not measured in this study. Turbulent patches may occur in certain parts of the tortuosity, for instance in the distal bend and at the shear layer reattachment points, especially during pulsatile flow. If found, these could be quantified by the LDA, utilising the Bragg cells.

A relationship between the severity of atheroma and the configuration of the tortuosity may exist and in that case, the ability to scale the flow features with the geometry of the tortuosities would be useful. Geometric features, such as the curvature ratio, the length of the bends and the length of straight tube between the bends, could be varied and the flow features compared at constant flowrates.

The pulsatile flow experiments of this study could be extended to a pulse wave that is closer to the physiological case. The use of a microcomputer-controlled stepping motor to operate a valve, controlling the flow, (as used by Talbot & Gong (1983)) enables great versatility in the shape of the applied flow pulse. The effect of varying the shape of the maximum flow peak, on the separated flow properties (shear

layer velocity gradients and reverse flow velocities) could be examined by this method. An alternative method, employing an artificial aortic valve, was used by Chandran & Yearwood (1981) to produce a near-physiological flow, but this is a less versatile method than that of Talbot & Gong.

New photo-sensitive dyes have been developed recently, which fluoresce for a time after exposure to light with specific properties (eg: intensity and wavelength). This eliminates the need for the introduction of a dye injection needle to the model, and will allow the effective positioning of a dye "injection" point within the tortuosity itself, without affecting the flow. Hence problems associated with dyestream distortions are overcome and a more quantitative investigation of the flow by dye visualisation is now possible.

Wall shear stresses, which were not measured in this study, are an important quantity which may be involved in the relationship between haemodynamics and atherosclerosis. Flush-mounted hot film anemometer probes could be used to measure the wall shear rates, especially along the $\alpha = 0°$ and $\alpha = 180°$ sides of the tube, and from these, the shear stresses could be calculated. Alternatively, the electochemical limiting current method, employed by Choi et al (1979), could be used. In particular, the fluctuating components of the wall shear stresses near the shear layer reattachment points should be measured and compared to values measured elsewhere in the tube.

Gad-el-Hak et al (1984) reported the existence of surface waves in a compliant surface coating, under turbulent patches imbedded in a laminar boundary layer. The compliance of the endothelium offers the possibility of this occurring in vivo, especially near shear layer reattachment points. This possibility could be studied by examining the inner surface of an arterial model, such as the C-shaped tortuosity, coated with a thin, compliant layer of viscoelastic material. As well as the dynamic scaling of the flow, the shear modulus of rigidity, density and the thickness of the coating, would have to be scaled to match those of the endothelial layer.

Pressure fluctuations at the walls of the tortuosity should be measured, particularly in view of the possibility of the convective enhancement of vesicular LDL loading, postulated in Chapter 3. The fluctuating wall pressures in the separation regions and at the mean shear layer reattachment point are particularly important. The measurement of wall pressure fluctuations in the reattachment region, during pulsatile flow, would also be useful. The use of the stepping motor-controlled valve to produce pulsatile flow, as suggested above, would minimise vibrations to the flow.

The ultrastructure of the endothelial cells (in particular the vesicular organisation) may be different in vivo from that present under static conditions. The

effect of the fixation technique on the measured ratios of free to attached vesicles should be investigated, since the cell's environment may have an influence on the vesicular structure.

The vesicular organisation in endothelial cells taken from sites subjected to flow disturbances, may show differences from those taken from quiescent sites. The detachment of vesicles from the plasma membrane, requires the rupture of the quasi-stable vesicle attachment stalk. Shear stress fluctuations and pressure fluctuations are both possible sources of perturbations in the bilayer material of the attachment stalks, and may increase the vesicle detachment rate. An investigation of this possibility could be undertaken, using perfused sections of arteries, subjected to various flow disturbances, followed by rapid fixation.

The analysis of convective LDL loading into vesicles in Chapter 3, shows that the spontaneous curvature of the vesicle's lipid bilayer membrane material is an important quantity. The spontaneous curvature and bending stiffness of the vesicular membrane should be determined, in order to calculate the magnitude of convective flow through the vesicle neck.

References

Adams, C.W.M. & Bayliss, O.B. (1969) Relationship between diffuse intimal thickening, medial enzyme failure and intimal lipid deposition in various human arteries.*J. Athero. Res.* **10,** p 327.

Adler,M. (1934) Strömung in gekrümmten Rohren. *Z Angew. Math. Mech.* **14,** pp 257-75. In Berger, Talbot & Yao, (1983).

Agrawal, Y., Talbot, L. & Gong, K. (1978) Laser Anemometer study of flow development in curved circular pipes. *J. Fluid Mech.* **85,**3, pp 497-578.

Akiyama, M., Hanaoka, Y., Cheng, K.C., Urai, I. & Suzuki, M. (1983) Lecture held in Victoria University Library titled: "Visual Measurements of Laminar Flow in the Entry Region of a Curved Pipe." Proc. of 3rd Int. Symp. on Flow Visualisation. Hemisphere Publ. Corp. In Flow Visualisation III' Edited by Yang, W.J., 1983, pp 526-530.

Amano, R.S. (1984) Laminar heat transfer in a channel with two right-angled bends. *J. Heat Transfer.* **106,** pp 591-96.

Amano, R.S. (1985) Turbulent heat transfer in a channel with two right-angle bends. *Int. J. Heat Mass Transfer* **28,** 11, pp 2177-79.

Arminski, L. & Weinbaum S. (1979) Effect of waveform and duration of impulse on the solution to the Basset-Langevin equation. *Phys. Fluids* **22,** 3, pp 404-11.

Arminski, L., Chien, S., Pfeffer, R. & Weinbaum, S. (1980) Steric hindrance effects on the time dependent diffusion of plasmalemma vesicles across vascular endothelium. *Bioheology* **17,** pp 431-44.

Arminski, L., Weinbaum, S. & Pfeffer, R. (1980) Time dependent theory for vesicular transport across vascular endothelium. *J. Theor. Biol.* **85,** pp 13-43.

Austin, L. (1971) "The development of viscous flow within helical coils." PhD thesis. Univ. Utah, Salt Lake City. In Berger, Talbot & Yao, 1983.

Austin, L.R. & Seader, J.D. (1973) Fully developed viscous flow in coiled circular pipes. *AIChE J.* **19,** 1 pp 85-94.

Barth, J.D. et al (1988) Quantitative ultrasound pulsation study in human carotid artery disease. *Atherosclerosis* **8,** pp 778-81.

Barua, S.N. (1963) On the secondary flow in stationary curved pipes. *Q. J. Mech. & Appl. Math.* **16,** 1, pp 61-77.

Bates, C.J. (1977) Review: Laser Doppler anemometry measurement in water flows. *J. Phys. E: Sci. Instrum.* **10,** pp 669-75.

Beaglehole, R & Jackson, R. (1985) Coronary heart disease mortality, morbidity and risk factor Trends in New Zealand. *Cardiology.* **72,** pp 29-34

Beaglehole, R., Bonita, R, Jackson, R & Stewart, A. (1986) Cardiovascular mortality in New Zealand and Australia 1968-83: How can the diverging trends be explained? *N.Z. Medical Journal.* **99,** 794, pp 1-3

Bell, F.P., Day, A.J., Gent, M. & Schwartz, C.J. (1975) Differing patterns of cholesterol accumulation and ^{3}H-cholesterol influx in areas of the cholesterol-fed pig aorta identified by Evans blue dye. *Exptl. & Molecular Pathology.* **22,** pp 366-75.

Benjamin, T.B. (1960) Effects of a flexible boundary on hydrodynamic stability. *Fluid Mech.* **9,** pp 513-32.

Benjamin, T.B. (1978a) Bifurcation phenomena in steady flows of a viscous fluid. I. Theory. *Proc. R. Soc. London Ser. A.* **359,** pp 1-26.

Benjamin, T.B. (1978b) Bifurcation phenomena in steady flows of a viscous fluid. II. Experiments. *Proc. R. Soc. London Ser. A.* **359,** pp 27-43.

Berger, S.A., Talbot, L. & Yao, L.S. (1983) Flow in curved pipes. *J. Ann. Rev. in FLuid Mech.* **15,** pp 461-512.

Bertelsen, A.F. (1975) An experimental investigation of low Re no. secondary streaming effects associated with an oscillating viscous flow in a curved pipe. *J.Fluid Mech.* **70,** 3, pp 519-27.

Bharadvaj, B.K., Mabon, R.F. & Giddens, D.P. (1982) Steady flow in a model of the human carotid bifurcation. Part 1 - Flow visualisation. *J. Biomechanics.* **15,** 5, pp 349-62

Bhattacharjee, S, Scheelke, B. & Troutt, T.R. (1986) Modification of vortex interactions in a reattaching separated flow. *AIAA J.* **24,** 4, pp 623-29.

Blackshear, P.L., Jr. (1972) Mechanical hemolysis in flowing blood. In: "Biomechanics, It's Foundation and Objectives," by Fung, Y.C., Perrone, N. & Anliker, M. (Eds.) Englewood Cliffs: Prentice-Hall, pp 501-28.

Brown, M.S. & Goldstein, J.L. (1984) "How LDL receptors influence cholesterol and atherosclerosis." *Scientific American* **251,** 5, pp 52-60.

Brüel & Kjear (1978) Hydrophone Type 8103 Handbook.

Bundgaard, M. (1983) Vesicular transport in capillary endothelium - does it occur. *Fed. Proc.* **42,** 8, pp 2425-30.

Bundgaard, M., Frokjaer-Jensen, J. & Crone, C. (1979) *Proc. Nat. Acad. Sci. USA* **76,** pp 6439-42. From Chien et al (1982).

Bundgaard, M et al (1983) The three-dimensional organisation of plasmalemmal vesicular profies in the endothelium of rat heart capillaries. *Microvasc. Res.* **25,** 3, pp 358-68.

Carew, T.E., Pittman, R.C., Marchand, E.R. & Steinberg, D. (1983) Aortic endothelium is an active site of low density lipoprotein degradation in vivo in normal rabbits (abst). *Clin. Res.* **31,** p 382A.

Caro, C.G. (1973) Transport of C^{14} cholesterol between intra-luminal serum and artery wall in isolated dog common carotid artery. *J. Proc. Physiol.Soc.* **June,** p 37.

Caro, C.G. (1974) Transport of ^{14}C-4-cholesterol between perfusing serum and dog common carotid artery: A shear dependent process. *Cardiovasc. Res.* **8,** pp 194-203.

Caro, C.G. (1978) Specialists meeting at the Ohio State University, Columbus, Ohio, August 24-25. From a paper by Arminski et al (1980).

Caro, C.G. & Saffman, P.G. (1966) Extensibility of blood vessels in isolated rabbit lungs. *J. Physiol.* **178,** pp 193-210.

Caro, C.G., Fitzgerald, J.M. & Schroter, R.C. (1971a) Atheroma: a new hypothesis. *British Med. J.* **June,** p 651.

Caro, C.G., Fitzgerald, J.M. & Schroter, R.C. (1971b) Proposal of a shear dependent mass transfer mechanism for atherogenesis. *Med. Res. Soc. Clinical Science.* **40,** p 5.

Caro, C.G. & Nerem, R.M. (1976) Self-consistent analysis of arterial uptake of cholesterol from perfusing serum - reply. *Circul. Res.* **38,** 3, p 216.

Caro, C.G., Lever, M.J., Parker, K.H. & Fish, P.J. (1987) Effect of cigarette smoking on the pattern of arterial blood flow: Possible insight into the

mechanisms underlying the development of atherosclerosis. *Lancet.* **July 4,** pp 11-13

Caro, C.G., Pedley, T.J., Schroter, R. C. & Seed, W.A. (1978) "The Mechanics of the Circulation." Oxford University Press. Oxford.

Casley-Smith, J.R. (1969) The dimensions and numbers of small vesicles in cells, endothelial and mesothelial and the significence of these for endothelial permeability. *J. Microsc.* **90,** 3, pp 251-69.

Casley-Smith, J.R. & Chin, J.C. (1971) The passage of cytoplasmic vesicles across endothelial and mesothelial cells. *J. Microscopy* **93,** 3, pp 167-89.

Casson, N. (1959) Flow equations for pigment oil suspensions of the printing ink type. In "Rheology of Dispense Systems" Ed Mills, C.C. Pergamon: NY, Chpt 5.

Chandran, K.B. & Yearwood, T.L. (1981) Experimental study of physiological pulsatile flow in a curved tube. *J. Fluid Mech.* **111,** pp 59-85.

Cheng, K.C., Inaba, T. & Akiyama, M. (1983) Flow visualisation studies of secondary flow patterns and centrifugal instability in curved circular and semicircular pipes. In Akiyama et al, 1983.

Chien, S. (1982) Effects of pressure variations on macromolecular transport across vessel wall. *Int. J. of Microcirculation: Clinical & Exp.* **3,** p 239.

Chien, S., Usami, S., Jan, K.M., Weinbaum, S. & Caro, C.G. (1978) Effec ts of oscillatory strain on macromolecular uptake by artery wall. *Biorheology.* **15,** p 469.

Chien, S., Laufer, L. & Handley, D.A. (1982) Vesicle distribution in the arterial endothelium determined with ruthenium red as an extracellular marker. *J. of Ultrastructure Res.* **79,** pp 198-206.

Choi, U.S., Talbot, L. & Cornet, I. (1979) Experimental study of wall shear rates in the entry region of a curved tube. *J. Fluid Mech.* **93,** pp 465-89.

Clark, C. (1977) Turbulent wall pfessurfe measurements in a model of aortic stenosis. *J. Biomechanics.* **10,** pp 461-72.

Clementi, F. & Palade, G.E. (1969) Intestinal capillaries I: Permeability to peroxidase and ferritin. *J. Cell Biol.* **41,** pp 33-58.

Clough, G. & Michel, C.C. (1980) The effect of temperature on the labelling of endothelial cell vesicles with ferritin. *Proc. Physiol. Soc.* ***June,*** p 70P.

Collins, W.M. & Dennis, S.C.R. (1975) The steady motion of a viscous fluid in a curved tube. *Q. J. Mech. & Appl. Math.* **28,** 2, pp 133-56.

Colten, C.K., Satterfield, C.N. & Lai, C.J. (1975) Diffusion and partitioning of macromolecules within finely porous glass. *AIChE J.* **21,** pp 289-98.

Conn, E.E. & Stumpf, P.K. (1976) "Outlines of Biochemistry." 4th Ed. NY: John Wiley & Sons Inc.

Dagen, Z., Weinbaum, S. & Pfeffer, R. (1982) An infinite-series solution for the creeping motion through an orifice of finite length. *J. Fluid Mech.* **115,** pp 505-23.

Davies, P.F., Dewey, C.F., Bussolari, S.R., Gordon, E.J. & Gimbrone, M.A. (1984) Influence of hemodynamic forces on vascular endothelial function. *J. Clin. Invest.* **73,** p 1121.

Dean, W.R. (1927) Note on the motion of fluid in a curved pipe. *Phil. Mag. S.* **4,** pp 208-23.

Dean, W.R. (1928) The streamline motion of fluid in a curved pipe. *Phil. Mag. S.* **5,** 30 pp 673-95.

Dennis, S.C.R. & Ng, M. (1982) Dual solutions for steady laminar flow through a curved tube. *Q. J. Mech. & Appl. Math.* **35,** 3, pp 305-24.

Desai, B. & Toole, J.F. (1975) Kinks, coils and carotids - A Review. *STROKE.* **6,** pp 649-53.

Deuling, H.J. & Helfrich, W. (1976) Curvature elasticity of fluid membranes - catalog of vesicle shapes. *J. Physique* **37,** 11, p 1335-45.

Dimotakis, P.E. & Brown, G.L. (1976) The mixing layer at high Reynolds number: large-structure dynamics and entertainment. *J. Fluid Mech.* **78,** pp 535-60.

Dixon, K.C. (1961) *Am. J. Path.* **39,** p 65.

Driver, D.M., Seegmiller, H.L. & Marvin, J.G. (1987) Time-dependent behaviour of a reattaching shear layer. *AIAA J.* **25,** 7, pp 914-19.

Duff, G.L. (1951) The pathogenesis of atherosclerosis. *Can. Med. Assoc. J.* **64,** pp 387-94.

Durst, F., Melling, A. & Whitelaw, J.H. (1976) "Principles and Practice of Laser-Dopler Anemometry." London; Academic Press Inc (London) Ltd.

Eaton, J. K. & Johnson, J.P. (1981) A review of research on subsonic turbulent flow reattachment. *AIAA J.* **19,** 9, pp 1093-1100.

Eustice, J. (1910) Flow of water in curved pipes. *Proc. R. Soc. London Ser. A* **84,** pp 107-18.

Eustice, J. (1911) Experiments of streamline motion in curved pipes. *Proc. R. Soc. London Ser. A* **85,** pp 119-31.

Fischer-Dzoga, K., Fraser, R.A. & Wissler, R.W. (1976) Stimulation of proliferation in stationary primary cultures of monkey and rabbit aortic smooth muscle cells. I. Effects of lipoprotein fractions of hyperlipemic serum and lymph. *Exp Mol Pathol.* **24,** pp 346- 59.

French, J.E. (1966) Atherosclerosis in relation to the structure and function of the arterial intima, with special reference to the endothelium. *Int. Rev. Exp. Pathol.* **5,** pp 253-353.

Fricke, F.R. (1971) Pressure fluctuations in separated flows. *J. of Sound Vibrations.* **17,** pp 113-23.

Fricke, F.R. & Stevenson, D.C. (1970) Estimation of wall pressure fluctuations in a separated flow. *J. of trhe Acoustical Soc. of America.* **50,** 3, pp 985-91.

Friedman, M.H., Deters, O.J., Bargero, C.B., Hutchins, G.M. & Mark, F.F. (1986) Shear-dependent thickening of the human arterial intima. *Atherosclerosis.* **60,** pp 161-71

Frokjær-Jensen, J. (1980) *J. Ultrastruct Research.* **73,** pp 9-20.

Frokjær-Jensen, J. (1984) The plasmalemmal vesicular system in striated-muscle capillaries and in pericytes. Tissue Cell. 16, 1, pp 31-42.

Frokjær-Jensen, J. & Bundgaard, M. (1979) Sessile vesicle clusters in frog mesenteric capillaries - new concept in the endothelial cell. Meeting. Microvasc. Res. 18, 2, p 297.

Fry, D.L. (1968) Acute vascular endothelial changes associated with increased blood velocity gradients. *Circ. Res.* **22,** pp 165-97.

Fry, D.L. (1969) Certain histological and chemical responses of the vascular interface to acutely induced mechanical stress in the aorta of the dog. *Circ. Res.* **24,** p 93.

Fry, D.L. (1972) "Response of the arterial wall to certain physical factors." Ciba Found. Symposium **12,** pp 93-110.

Fry, D.L. (1973) Responses of the arterial wall to certain physical factors. "Atherosclerosis: Initiating Factors. Ciba Found. Symp. **12,** (new series). Elsevier, Amsterdam, pp 93-125.

Gad-el-Hak, M., Blackwelder, R.F. & Riley, J.J. (1984) On the interaction of compliant coatings with boundary-layer flows. *J. Fluid Mech.* **140,** pp 257-80.

Glagov, S. (1965) Hemodynamic factors in localisation of atherosclerosis. *Acta Cardiologica Supplementum.* **11,** pp 331-37

Goldsmith, H.L., Yu, S.S.K. & Ma rlow, J. (1975) Fluid mechanical stress and the platelet. *Thrombos. Diathes. Haemorrh.* **34,** pp 32-41.

Greenhill, N.S. & Stehbens, W.S. (1985) Haemodynamically-induced intimal tears in experimental U-shaped arterial loops as seen by scanning electron microscopy. *Br. J. Exp. Path.* **66,** pp 577-84.

Greenspan, D. (1973) Secondary flow in curved tube. *J. Fluid Mech.* **57,** 1, pp 167-76.

Greshilov, E.M., Evtushenko, A.V. & Lyamshev, L.M. (1969) Spectral characteristics of the wall pressure fluctuations associated with boundary layer separation behind a projection on a smooth wall. *Soviet Physics - Acoustics.* **15,** 1, pp 29-34.

Hagen, G. (1839) *Ann. Phys. Chem.* **46,** pp 423-42.

Hamakiotes, C.C. & Berger, S.A. (1988) Fully developed pulsatile flow in a curved pipe. *J. Fluid Mech.* **195,** pp 23-55.

Hansen, R.J. & Hunstone, D.L. (1974) An experimental study of turbulent flows over compliant surfaces. *J. of Sound & Vibration.* **34,**3, pp 297-308.

Health, D., Smith, P., Harris, P. & Winson, M. (1973) The atherosclerotic human carotid sinus. *J. of Pathology* **110,** pp 49-58.

Helfrich, W. (1986) Size distributions of vesicles: the role of the effective rigidity of membranes. *J. Physique* **47,** pp 321-29.

Hiram, Y. & Nir, A. (1984) On mechanical aspects of vesicular transport. *J. Theor. Biol.* **111,** pp 91-113.

Humphrey, J.A.C., Taylor, A.M.K. & Whitelaw, J.H. (1977) Laminar flow in a square duct of strong curvature. *J. Fluid Mech.* **83,** 3, pp 509-27.

Hussain, A.K.M.F. (1977) In "Cardiovascular Flow, Dynamics and Measurements," (Eds) Hwang, N.H.C. & Norman, N. Baltimore, MD: University Park Press, p 541.

Inaba, T. & Murata, S. (1978) Pulsating laminar flow in a sinusoidally curved pipe. *Bull. JSME* **21,** 155, pp 832-39.

Insel, P.A., Nirenberg, P., Turnbull, J. & Shattil S.J. (1978) Relationship between membrane cholesterol, alpha-adrenergic receptors and platelet functions. *Biochemistry* **17,** pp 5269-74.

Ito, H. (1960) Pressure losses in smooth pipe ;bends. *J. Basic Eng.* **82,** pp 131-43.

Jellinek, H. & Detre, Z. (1986) Role of the altered transmural permeability in the pathomechanism of arteriosclerosis. In 2 parts. Part I: History of arteriosclerosis theories *Path. Res. Pract.* **181,** pp 693-712.

Karnovsky, M.J. (1967) *J. Cell Biol.* **37,** p 213.

Kitoh, O. (1987) Swirling flow through a bend. *J. Fluid Mech.* **175,** pp 429-46.

Kjeldson, K., Wanstrup, J. & Anstrup, P. (1968) Enhancing influence of arterial hypoxia on the development of atheromatosis in cholesterol-fed rabbits. *J. Atheroscler. Res.* **8,** p 835.

Kraichnan, R.H. (1956) Pressure fluctuations in turbulent flow over a flat plate. *J. Acoust. Soc. Am.* **28,** 3, pp 378-90.

Ku, D.N., Giddens, D.P., Zarins, C.K. & Glagov, S. (1985) Pulsatile flow and atherosclerosis in the human carotid bifucation *Arteriosclerosis* **5,** pp 293-301.

Landahl, M.T. (1960) On the stability of a laminar incompressible boundary layer over a flexible surface. *Fluid Mech.* **13,** pp 609-32.

Lebouche, M. & Martin, M. (1976) Lecture given a the 73rd Euromech Colloquim on "Oscillatory Flows in Ducts" held in Aix-en-Provence, France. Reported in Brocher, E., "Oscillatory flows in ducts: A report on Euromech 73." *J. Fluid Mech* **79,** 1, pp 113-26 (1977).

Lightfoot, E.N. Jr. (1974) "Transport Phenomena and Living Systems."NY, John Wiley & Sons.

Lin, J.J. & Tarbell, J.M. (1980) An experimental and numerical study of periodic flow in a curved tube. *J. Fluid Mech.* **100,** pp 623-38.

Lin, T.S. (1972) "Laminar convective transport processes in strongly curved tubes." PhD thesis. Clarkson Coll. Technol, Potsdam., NY. 193pp.In Berger, Talbot & Yao, 1983.

Loudon, M.F., Michel, C.C. & White, F.I. (1979) The labelling of vesicles in Frog Endothelial cells with Ferritin. *J. Physiol.* **296,** pp 97-112.

Luft, J.H. (1965) Capillary permeability. In "The Inflammatory Process" ed. Zweifach, B.W., Grant, L. & McCluskey, R.T. NY: Academic Press.

Luft, J.H. (1966) Fine structure of capillary and endocapillary layer as revealed by ruthenium red. *Fedn. Proc.* **25,** pp 1773-83.

Lyne, W.H. (1971) Unsteady viscous flow in a curved pipe. *J. Fluid Mech.* **45,** pp 13-31.

Mabey, D. (1972) Analysis and correlation of data on pressure fluctuations in separated flow. *J. of Aircraft.* **9,** 9, pp 642-45.

MacDonald, D.A. (1974) "Blood Flow in Arteries." UK., Edward Arnold. 2nd Ed.

Malone, D. M. & Anderson, J.L. (1978) Hindered diffusion of particules through small pores. *Chemical Engineering Science.* **33,** pp 1429-40.

Markovin & Paranjape (1971) *Z Fugwiss* **819,** pp 328-35.

Masliyah, J.H. (1980) On laminar flow in curved semicircular ducts. *J. Fluid Mech.* **99,** 3, pp 469-79.

McMillan, D.E. (1985) Blood flow and the location of atherosclerotic plaques. *Stroke.* **6,** 4, pp 582-87

Merrill, E.W. (1969) Rheology of blood. *Physiol. Reviews.* **49,** 4, pp 863-88.

Metz, H., Murray-Leslie, R.M., Bannister, R.G., Bull, J.W.D. & Marshall, J. (1961) "Kinking of the internal carotid artery in relation to cerebrovascular disease." *The Lancet* **Feb,** pp 424-26.

Meyer, W.W. (1975) "The Inter-relationship of the early arterial calcifications and lipid deposits demonstrated by the dual gross staining method." *Artery* **1,** pp 324-25.

Meyer, W.W. & Lind, J. (1972) Calcifications of th carotid siphon - a common finding in infancy and childhood. *Archives of Dis. in Childhood.* **47,** pp 355-63.

Miasnikov, A.L (1962) "Atherosclerosis: Occurrence, Clinical Forms, Therapy." US National Institutes of Health (trans. from Russian). Bethesda. 444pp.

Michel, C.C. (1980) Filtration coefficients and osmotic reflexion coefficients of the walls of single frog mesenteric capillaries. *J. Physiol.* **309,** pp 341-55.

Mullin, T. & Greated, C.A. (1980a) Oscillatory flow in curved pipes Part 1: The developing flow case. *J. Fluid Mech.* **98,** 2, pp 383-95.

Mullin, T. & Greated, C.A. (1980b) Oscillatory flow in curved pipes. Part 2: The fully developed case. *J. Fluid Mech.* **98,** 2, pp 397-416.

Mullin, T., Greated, C.A. & Grant, I. (1980) Pulsating flow over a step. *Phys. Fluids.* **23,** 4, pp 669-74.

Munson, B.R. (1975) Experimental results for oscillating flow in a curved pipe. *The Physics of Fluids.* **18,** 12, pp 1607-9.

Munson, B.R. (1976) Secondary flows in a slowly oscillating torus. *The Physics of Fluids.* **19,** 11, pp 1823-25.

Murata, S., Miyake, Y. & Inaba, T. (1976) Laminar flow in a curved pipe with varying curvature. *J. FLuid Mech.* **73,** 4, pp 735-52.

Nandakumar, K. & Masliyah, J.H. (1982) Bifurcation in steady laminar flow through curved tubes. *J. Fluid Mech.* **119,** pp 475-90.

Naudascher, E. & Rockwell, D. (1978) in "Engineering for Structures Subjected to Flow-induced Forces and Vibrations." Notes for an intensive course given at VIII Congreso Latho Americano de Hydraulica, Quito, Ecuador. Reported in Rockwell, 1983.

Newman, H.A.I. & Zilversmit, D.B. (1966) *Circ. Res.* **18,** p 293.

Olson, D.E. (1971) "Fluid mechanics relevant to respiration-flow within curved or eliptical tubes and bifurcating systems." PhD thesis. Imperial Coll., London. From a paper by Berger, Talbot & Yao (1983).

Olson, D.E. & Snyder, B. (1983) The growth of swirl in curved circular pipes. *J. Phys. FLuids.* **26,** 2, pp 347-49.

Patankar, S.V., Pratap, V.S. & Spalding, D.B. (1974) Prediction of laminar flow and heat transfer in helically coiled pipes. *J. Fluid Mech.* **62,** pp 539-51.

Pedley, T.J. (1980) "The Fluid Mechanisms of Large Blood Vessels." UK: Cambridge University Press.

Peterson, R.E., Livingston, K.E. & Escobar, A. (1960) Development and distribution of gross atheroslerosis lesions at cervical carotid bifurcation. *Neurology* **10,** 11, pp 955-59.

Poiseiulle, J.L. (1840) *Compte Rendus* **11,** pp 961-1041.

Poiseiulle, J.L. (1841) *Compte Rendus* **12,** p 112.

Rahn, J.D. et al (1967) "Chemical Engineering in Medicine & Biology." Ed. Hershey, D. NY: Plenum, p 45.

Reckless, J.P.D., Weinstein, D.B. & Steinberg, D. (1978) Lipoprotein and cholesterol metabolism in rabbit arterial endothelial cells in culture. *Biophys. Acta* **529,** pp 475-87.

Revel, J.D. & Gleason, R.E. (1965) Turbulent pressure fluctuations under separated supersonic and hypersonic flows. AFFDL-TR-65-77. From a paper by Fricke, F.R. (1971).

Reynolds, O. (1883) An experimental investigation of the circumstances which determine whether the motion of water shall be direct or sinuous,, and of the law of resistance in parallel channels. *Philosophical Transactions of the Royal Society* **174,** pp 935-82.

Rockwell, D. (1983) Oscillations of impinging shear layers. *AIAA J.* **21,** 5, pp 645-64.

Rockwell, D. & Knisely, C. (1979) The organized nature of flow impingement upon corner. *J.F.Mech.* **93,** 3, pp 413-32.

Rockwell, D. & Naudascher, E. (1979) Self-sustained oscillations of impinging free shear layers. *Ann. Rev. Fluid Mech.* **11,** pp 67-94.

Rodkiewitz, C.M. (1975) Localisation of early atherosclerotic lesions in the aortic arch in the light of fluid flow. *J. Biomechanics.* **8,** pp 149-56

Roos, F.W. & Kegelman, J.T. (1986) Control of coherent structures in reattaching laminar and turbulent shear layers. *AIAA J.* **24,** 12, pp 1956-63.

Ross, R. (1981) Atherosclerosis: A problem of the biology of arterial wall cells and their interactions with blood components. *Arteriosclerosis* **1,** pp 293-311.

Ross, R. (1986) The pathogenesis of atherosclerosis - An Update. *New England J. Medicine.* **314,** 8, pp 488-500.

Ross, R. & Glomsett, J. (1973) Atherosclerosis and the arterial smooth muscle cell. *Science* **180,** pp 1332-39.

Ross, R. & Glomsett, J.A. (1976) The pathogenesis of atherosclerosis. *New England J. Medicine* **295,** pp 369-77, 420-25.

Ross, R & Klebanoff, S.J. (1971) The smooth muscle cell. I In vivo synthesis of connective tissue proteins. *J. Cell Biol.* **50,** pp 159-71.

Rowsell, H.C., Mustard, J.F. & Downie, H.G. (1965) Experimental atherosclerosis in swine. *Annals N.Y. Acad. Sciences* **127,** pp743-762.

Rubin, B.T. (1977) A theoretical model of the pinocytotic vesicular transport process in endothelial cells. *J. Theor Biol.* **64,** pp 619-47.

Saffman, P.G. & Baker, G.R. (1979) Vortex interactions. *Ann. Rec. Fluid Mech.* **11,** pp 95-122.

Samuel, K.C. (1956) Aterosclerosis and occlusion of the internal carotid artery. *J. Path. Bact.* **71,** pp 391-401.

Sato, M., Levesque, M.J. & Nerem, R.M. (1987) An application of the micropipette technique to the mesurement of the mechanical properties of cultured bovine aortic endothelial cells. *J. of Biomechanical Eng.* **109,** pp 27-34.

Schraub, F.A., Kline, S.J., Henry, J., Runstadler, P.W. Jr., & Littell, A. (1965) Use of hydrogen bubbles for quantitative determination of time-dependent velocity fields in low-speed water flows. *J. of Basic Eng.* **June,** pp 429-44.

Schweizer, P.M. & Scriven, L.E. (1983) Evidence of Görtler-type vortices in curved film flows. *Phys. Fluids.* **26,** 3, pp 619-23.

Seeto, C.M. (1987) An Experimental study of entrainment at a density interface by mean velocity shear. PhD thesis, University of Canterbury, New Zealand.

Servuss, R.M., Harbich, W. & Helfrich, W. (1976) Measurement of curvature-elastic modulus of egg lecithin bilayers. *Biochim. Biophys. Acta.* **436,** 4, pp 900-3.

Shea, S.M. & Raskova, J. (1983) Vesicular diffusion and thermal forces. *Fed. Proc.* **42,** pp 2431-34.

Siflinger, A., Parker, K. & Caro, C.G. (1974) In vitro study of the kinetics of transport of ^{125}I albumin from serum to arterial wall. *Clinical Sci .& Molecular Med.* **46,** 6, pp31-32.

Siflinger, A., Parker, K. & Caro, C.G. (1975) Uptake of ^{125}I albumin by the endothelial surface of the isolated dog common carotid artery: effect of certain physical factors and metabolic inhibitors. *Cardiovascular Research* **9,** 4, pp 478-89.

Singh, M.P. (1974) Entry flow in a curved pipe. *J. Fluid Mech.* **65,** 3, pp 517-39.

Singh, M.P., Sinha, P.C. & Agarwal, M. (1978) Flow in the entrance of the aorta. *J. FLuid Mech.* **87,** 1, pp 97-120.

Smith, F.T. (1975) Pulsatile flow in curved pipes. *J. FLuid Mech.* **71,** 1, pp 15-42.

Smith, F.T. (1976) Fluid flow into a curved pipe. *Proc. R. Soc. A.* **35,** pp 71-87.

Sobey, I.J. (1985) Observation of waves during oscillatory channel flow. *J. Fluid Mech.* **151,** pp 395-426.

Soh, W.Y. (1988) Developing fluid flow in a curved duct of square cross-section and it's fully developed dual solutions. *J. Fluid Mech.* **188,** pp 337-61.

Soh, W.Y. & Berger, S.A. (1984) Laminar entrance flow in a curved pipe. *J. Fluid Mech.* **148,** pp 109-135.

Stehbens, W.E. (1979)"Haemodynamics and the Blood Vessel Wall." Thomas, C.C., Springfield IL.

Stehbens, W.E., (1986) Experimental arterial loops and arterial atrophy. *Experimental & Molecular Pathology* **44,** pp 177-89.

Stehbens, W.E. (1987) Localization of atherosclorotic lesions in relation to haemodynamics In "Atherosclerosis: Biology & Clinical Science." Ed Olsson, A.G. Edinburgh, Churchill Livingstone.

Stehbens, W.E. & Fee, C.J. (1985) Hydrodynamic flow in U-shaped and coiled glass loops simulating carotid arterial configurations. *Angiology* **36,** 7, pp 442-51.

Stehbens, W.E., Fee, C.J. & Stehbens, G.R. (1987) Flow through s-shaped glass models simulating arterial tortuosities. *Quarterly J. of Experimental Physiology*. **72,** pp 201-13.

Stein, P.D. & Sabbah, H.N. (1980) Overview: Hemorheology of turbulence. *Biorheology*. **17,** pp 301-19.

Stein, Y. & Stein, O. (1973) *Ciba. Found. Symp.* **12,** pp 165-84. From a paper by Chien et al (1982).

Steinberg, D. (1983) Lipoproteins and atherosclerosis. *Arteriosclerosis* **3,** pp 283-301.

Steinberg, D. (1987) Lipoproteins and the pathogenesis of atherosclerosis. *Circulation* **76,** 3, pp 508-14.

Stemerman, M.B., Colton, C. & Morell, E. (1984) Perturbations of the endothelium. *Prog in Hemostasis and Thrombosis*. **7,** pp 289-324.

Stewartson, K., Cebeci, T. & Chang, K.C. (1980) A boundary-layer collision in a curved duct. *Q. J. Mech. Appl. Math.* **33,** pp 59-75.

Talbot, L. & Wong, S.J. (1982) A note on boundary layer collision in a curved pipe. *J. Fluid Mech.* **122,** pp 505-10.

Talbot, L. & Gong, K.O. (1983) Pulsatile entrance flow in a curved pipe. *J. Fluid Mech.* **127,** pp 1-25.

Taylor, G.I. (1929) The criterion for turbulence in curved pipes. *Proc. R. Soc. A.* **124,** pp 243-49.

Texon, M. (1957) A hemodynamic concept of atherosclerosis. *Archives of Internal Medicine*. **99,** pp 418-27.

Texon, M. (1960) The hemodynamic concept of atherosclerosis. *Bull NY Acad. Med.* **36,** pp 263-74.

Thompson, G.R. (1986) Pathogenesis of atherosclerosis.*Pharmacy Int* **7,** 2, pp 276-79.

Tomlin, S.G. (1969) Vesicular transport across endothelial cells. *Biochem. Biophys. Acta.* **183,** pp 559-64.

Troutt, T.R., Scheelke, B.S. & Norman, T.R. (1984) Organised structures in a reattaching separated flow field. *J. Fluid Mech.* **143,** pp 413-27.

Truesdell, L.C. & Adler, R.J. (1970) Numerical treatment of fully developed laminar flow in helically coiled tubes. *AIChE J.* **16,** pp 1010-15.

US Dept. of Health & Human Services. (1981) "Report of the Working Group on Arteriosclerosis of the National Heart, Lung & Blood " Institute of the US Dept. of Health and Human Services. Vol 1. Bethesda.

Virchow, R. (1856) "Phlogose ung Thrombose im Gefassystem, Gesammelte Abhandlungen zur Wissenschaftlichen Medich." Frankfurt-am-Main, Merdinger Sohn & Co. pp 458-63. From a paper by Ross, R. (1981).

Wakeham, W.A., Salpodoru, N.N. & Caro, C.G. (1975) Diffusion coefficients for protein molecules in blood serum. *Ahterosclerosis.* **25,** pp 225-35.

Weibel, J. & Fields, W.S. (1965) "Tortuosity, coiling and kinking of the internal carotid artery I: Etiology and radiographic anatomy." *Neurology* **15,** 1, pp 7-18.

Weinbaum, S. (1979) Theoretical models of vesicular transport and endothelial membrane interaction. *Biorheology* **16,** pp 297-307.

Weinbaum, S. & Caro, C.G. (1976) A macromolecule transport model for the arterial wall and endothelium based on the ultrastructural specialization observed in electron microscopic studies. *J. Fluid Mech.* **74,** 4 pp611-40.

White, C.M. (1929) Steramline flow through curved pipes. *Proc. R. Soc. London Ser.A* **123,** pp 645-63.

Wilens, S.C. (1951) *Am. J. Path.* **27,** p825.

Williams, G.S, Hubbell, C.W. & Fenkell, G.H. (1902) Experiments at Detroit, Mich., on the effect of curvature upon the flow of water in pipes. *Trans. ASCE* **47,** pp 1-196.

Winters, K.H. (1987) A bifurcation study of laminar flow in a curved tube of rectangular cross-section. *J. Fluid Mech.* **180,** pp 343-69.

Womersley, J.R. (1957) The mathematical analysis of the arterial circulation in a state of oscillatory motion. *Tech. Rep. WADC-TR 56-614,* Wright Air Dev. Cent.

Yao, L.S. & Berger, S.A. (1974) Entry flow in a curved pipe. *J. Fluid Mech.* **67,**1, pp 177-96.

Yao, L.S. & Berger, S.A. (1975) Entry flow in a curved pipe. *J. Fluid Mech.* **67,** 1, pp 177-96.

Yao, L.S. & Berger, S.A. (1988) The three dimensional boundary layer in the entry region of curved pipes with finite curvature ratio. *Phys. Fluids.* **31,** 3, pp 486-94.

Yu, S.K., Latour, J.G., Marchandise, B. & Bois, M. (1978) Shear stress-induced changes in platelet reactivity. *Thrombosis. Haemostas.* **40,** pp 551-60.

Zarins, C.K., Giddens, D.P., Balasubramanian, K., Sottiurai, V., Mabon, R.F. & Glagov, S. (1981) Carotid plaques localize in regions of low flow velocity and shear stress. *Circulation.* **64,** Suppl.IV pp 44.

Appendix A

Laser Doppler Anemometry

Velocities were measured by Laser Doppler Anemometer (LDA).

The principles of Laser Doppler Anemometry are well documented (Bates (1977)) and need only a brief description here. A particularly good reference is that of Durst, Melling and Whitelaw (1976).

In differential-mode Laser Doppler Anemometry, two coherent beams of light (obtained by splitting a laser beam) are brought together to form a measurement volume at their intersection at the point in the fluid where the velocity is to be measured (figure 4-8). If the path lengths of each beam from the point of beam splitting do not differ greatly, an interference pattern will be set up at their point of intersection. The light is detected by scattering from small particles moving within the fluid. The velocity of the particles is assumed to match the local fluid velocity. The frequency of the observed interference pattern undergoes a Doppler shift because of the velocity, relative to the observer, of the particles within the measurement volume. This frequency is proportional to the velocity of the particle and, by inference, the fluid velocity within the measurement volume. A photomultiplier observes the light scattered from the measurement volume and emits an alternating current proportional to the velocity of the particle. This frequency is then determined by a frequency tracking unit and the analogue voltage output of the unit is linearly proportional to the input frequency and hence to the particle velocity.

The frequency, f_s, of the light scattered by the particle moving through the measurement volume is related to the frequency, f_i, of the incident light by

$$f_s = f_i + \frac{1}{\lambda} u\,(e_s - e_i) \qquad \text{(A1)}$$

;where λ is the wavelength of the incident light, u is the velocity vector of the particle and e_s and e_i are unit vectors in the scattered and incident directions respectively. The wavelength of the incident light in water is related to that in air by

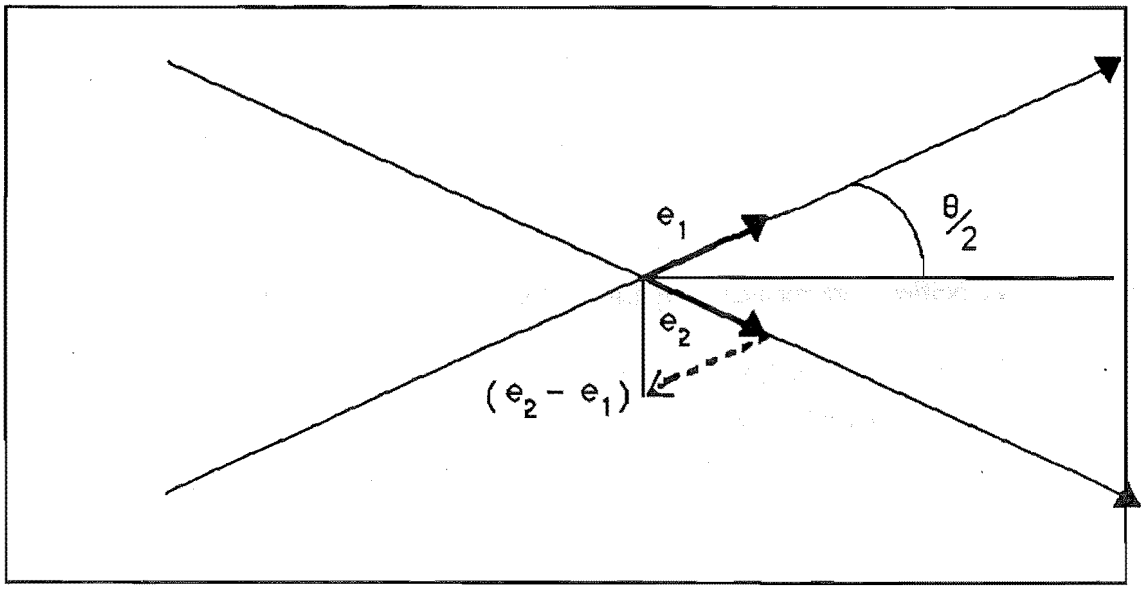

Figure A-1
Incident Light Beams and Unit Vectors

$$n_{air}\lambda_{air} = n_{water}\lambda_{water}$$

; where n is the refractive index. Hence

$$f_{s1} = f_{i1} + \frac{1}{\lambda} u\,(e_{s1} - e_{i1}) \qquad \text{(A2)}$$

and

$$f_{s2} = f_{i2} + \frac{1}{\lambda} u\,(e_{s2} - e_{i2}) \qquad \text{(A3)}$$

; subscripts 1 and 2 stand for the two beams which form the measurement volume. The photo-multiplier emits an alternating current with a Doppler frequency

$$f_D = f_{s2} - f_{s1}$$

and since $f_{i1} = f_{i2}$ and $e_{s1} = e_{s2}$

$$f_D = \frac{1}{\lambda} u\,(e_{i1} - e_{i2}) \qquad \text{(A4)}$$

From the above figure A-1 it can be seen that the direction of u is perpendicular to the bisector of the of the angle between the incident beams and in the same plane. Furthermore, f_D is independent of the angle from which the scattered light is observed. Since $(e_{i1} - e_{i2}) = 2\sin(\theta/2)$, equation (A4) may be written as

$$|u| = \frac{f_D \lambda}{2\sin(\theta/2)} \qquad \text{(A5)}$$

Two problems are apparent from equation (A5). Firstly, the direction of u cannot be ascertained from f_D alone and secondly f_D approaches zero as u approaches zero. The frequency tracker cannot track frequencies close to zero and therefore the LDA unit as it stands above cannot be used to track zero or near-zero velocities. The introduction of an offset frequency Δf overcomes this problem and is achieved by the use of a Bragg cell. With the Bragg cell:

$$f_D + \Delta f = \frac{1}{\lambda} u\,(e_{i1} - e_{i2})$$

The Bragg cell imposes an acoustic wave on the incident light wave at ultrasonic frequencies, resulting in a diffraction pattern that is a maximum when the Bragg condition

$$\sin\theta_b = \frac{1}{2}\left(\frac{\lambda}{\lambda_a}\right)$$

is satisfied, where θ_b is the angle between the incident light beam and the acoustic wave direction, known as the Bragg angle and λ_a is the acoustic wavelength. As θ_b is dependent on λ_a, the frequency of the acoustic wave must be selected before the optic unit is adjusted to optimise the diffraction.

In order to achieve a useful frequency shift, two Bragg cells are used in practice, with one cell shifting the frequency of one light beam downwards and the other cell shifting the frequency of the second beam upwards. Equations (A2) and (A3) then become

$$f_{s1} = f_{i1} + \frac{1}{\lambda} u\,(e_{s1} - e_{i1}) + \frac{\Delta f}{2} \qquad \text{(A2a)}$$

and

$$f_{s2} = f_{i2} + \frac{1}{\lambda} u\,(e_{s2} - e_{i2}) - \frac{\Delta f}{2} \qquad \text{(A3a)}$$

giving

$$f_D + \Delta f = \frac{1}{\lambda} u\,(e_{i1} - e_{i2}) \qquad \text{(A4a)}$$

The velocity calculated from equation (A4a) is no longer directionally ambiguous, since a measured frequency, $f < \Delta f$ indicates a negative velocity and conversely for $f > \Delta f$. Furthermore, the problem with the frequency tracker not being able to track low or zero velocities is removed since Δf corresponds to zero velocity. Δf can be chosen to suit the frequency tracker range.

Appendix B

LDA Radial Velocity Positions

The radial velocities at various points along the diameter normal to the plane of symmetry, P, were measured. Since the beams entered the model symmetrically from the two sides of the tube, intersecting on the diameter, the beams were symmetrically refracted and the velocity component measured was parallel to the plane of symmetery. The beam intersection angle was dependent on the radial position of the velocity measurement, because the angle of beam incidence on the perspex/water interface changed with respect to the normal to the interface for different positions on the diameter.

Both the position and the angle of beam intersection in the model could be calculated from the following geometric analysis and by measuring the distance between the beams at their entry point at the front face of the model.

Figure B-1 shows the geometry of the model and the incident beams from an upstream observation position along the central axis of the tube. The tube is centred at position (20.0, 17.6) in a set of orthogonal coordinates X, Y. The front face of the model lies along Y = 0. Half the measured beam separation at the front face of the model is subtracted from 20.0 to obtain the entry point of the beam relative to the origin. Since the beams enter the model symmetrically with respect to the plane Q, only one beam need be analysed to pinpoint both the position and angle of beam intersection.

The beam enters the front face of the model at a constant angle of incidence, and is refracted so that it passes through the perspex at a constant angle, θ, independent on the position of beam intersection on Q. Since θ remains constant, the angle of beam incidence at the perspex/water interface is always known.

Treating the beam as a line with general equation

$$y = n.x + c \qquad (B1)$$

;where n is the slope of the line and is constant with value y_1/x_1 or $\tan(\theta) = 6.9054$. c is the y-intercept and since y = 0 at position x where the beam enters the front face of the model

$$c = -n.x$$

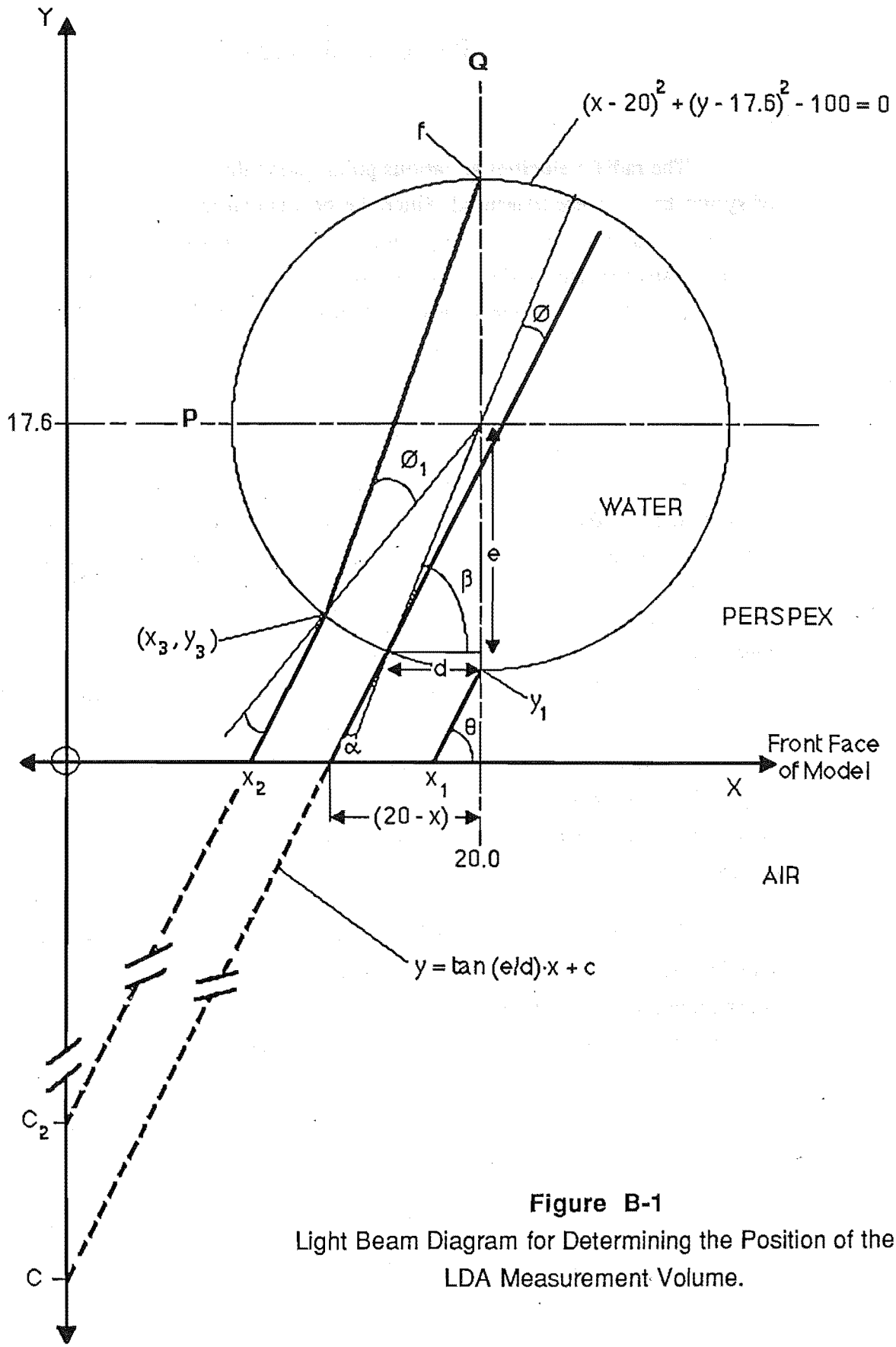

Figure B-1
Light Beam Diagram for Determining the Position of the LDA Measurement Volume.

Hence the equation of the lines corresponding to each radial velocity measurement position is known:

$$y = 6.9054x - c \qquad \text{(B2)}$$

The equation of the circle comprising the perspex/water interface is

$$(x - 20)^2 + (y - 17.6)^2 - 100 = 0 \qquad \text{(B3)}$$

To find the point of beam incidence on the perspex/water interface the equations for the circle and the straight line are solved simultaneously. Equation B2 is subtracted from equation B3 to give the radical axis

$$602.85 + x^2 + y^2 - 39x - 34.2\,y + c = 0 \qquad \text{(B4)}$$

Substitution of B1 into B3 gives the quadratric equation in x:

$$602.85 + c^2 + 48.68x^2 - 13.81cx + 35.2c - 275.16x = 0 \qquad \text{(B5)}$$

The smaller of the two roots of the quadratic (B5) is the point of beam incidence on the perspex/water interface (the other is the point of exit from the tube in the absence of refractive effects). Knowing the point of incidence allows the calculation of the angle of the normal to the interface,

$$\beta = \arctan\left(\frac{e}{d}\right)$$

and then α, the angle between the incident beam and the normal to the interface. The refracted beam then passes through the water at an angle ϕ to the normal, and the ratio

$$R = \frac{\sin\phi}{\sin\alpha}$$

is a constant equal to the ratio of the refractive index of the perspex to that of water. The refracive index of the perspex was not known accurately, but R was found by focusing the beam intersection point on the point f at the back of the tube. Since x_2 is known, the point (x_3, y_3) can be calculated and both α and ϕ found. R was then calculated to be 1.1891.

Thereafter, the positions and angles of beam intersection for any radial velocity measurement point on Q could be calculated by simultaneously solving the

equations B2 and B3 for each measured beam entry position, x, at the front face of the model.

Appendix C

Velocity Measurement Errors

The velocities measured by the LDA were subject to errors from several sources. The velocity was calculated from the equation:

$$u = \frac{(f_D + \Delta f)\,\lambda}{2\sin(\theta/2)}$$

λ was specified by Spectra-physics to an accuracy of 0.4 %.

$\theta/2$ in air was calculated as the arctangent of x/y ; where 2x was the beam separation at a known distance, y from the beam intersection point. y was about 1.0 metres and x was about 190 mm. With the measurement accuracy of $\pm$ 1 mm for each distance, the accuracies of x and y were about 0.5 % and 0.1 % repsectively.

$\theta/2$ in water is related to that in air by Snell's law

$$n_w \sin\left(\frac{\theta_w}{2}\right) = n_a \sin\left(\frac{\theta_a}{2}\right)$$

; where n is the refractive index and the subscripts w and a stand for water and air repectively. n_a is given as 1.000 (760 mmHg, 20 °C) and n_w is 1.334 at 0 °C. No adjustment to n_w was made for the temperature of the water used. DISA gives the dependence of n_w as 0.0001 $°C^{-1}$ so that for water temperatures between 14 and 18 °C as used in these experiments, the maximum error in assuming n_w = 1.334 is 0.13 %.

The air/perspex and perspex/water interfaces were assumed to be parallel for axial flow measurements. The computer-controlled milling machine used to manufacture the model had an acuracy of better than 0.1 %, so errors introduced by the above assumption would be negligable.

The DISA digital voltmeter used to measure the frequency tracker output was able to be read to ± 0.01 V, which, for a minimum voltage of 1.5 V, gives a reading error of ±0.7 %. This voltmeter was used to calibrate the frequency tracking unit, with input frequencies known to within 0.001 %.

In pulsatile flow experiments an A to D convertor was used to measure the frequency tracker output voltage. The DISA digital voltmeter was used to calibrate this. The resolution of the 10-bit A to D convertor was1.023 mV/bit, leading to a reading error of 0.04 % at the minimum frequency traker voltage output of 1.5 V.

The total error in the axial velocity measurements using the LDA was taken as the sum of the above percentage errors, giving a total error of within 3 %.

For radial velocity measurements, the error involved in measuring θ/2 were larger than for axial velocity measurements. The calculation of the beam intersection angle and position within the tube is given in Appendix B The beam separation at the front face of the model was subject to a measurement accuracy equivalent to half the beam diameter, 0.3 mm, yielding an error of about 10 %. The position of the front of the tube is known to 0.1 %, while the positioning of the beam intersection point at this position was subject to an error of (again, half the beam diameter) 0.3 mm, giving an error of 3.9 %. The position at the back of the tube was known to within 0.1 % and again the positioning of the beam intersection point there was accurate to 0.3 mm. The error here was then 1.5 %.

The sum of the errors in calculating θ/2 for the radial velocity measurements was therefore about 16 %. Adding the other errors above, the total radial velocity measurement error was about 18 %.

Appendix D

H_2 - Bubble Flow Visualisation

The H_2-bubble visualisation technique is well documented (Schraub and Kline, et al (1965), Various authors (1967), Clutter and Smith, (1961), Clutter, Smith and Brazier (1959)) but a brief description will be given here.

A 20μm diameter stainless steel wire was held taut across the flow by clamping it between the two halves of the model. This comprised the negative electrode of a d-c circuit, with the downstream brass end-piece (arbitrarily) being the positive electrode. The conductivity of the water was increased by adding a small amount of sodium chloride. Trisodium phosphate and disodium tetraborate were added to inhibit corrosion of the end-pieces and microbial growth in the water (which at that stage was recirculated).

When a potential of about 100 V was applied between the electrodes, hydrogen bubbles were evolved at the negative electrode (the fine wire). The H_2 bubbles were of similar diameter to the wire and were swept downstream with pathlines assumed to follow the streamlines of the flow.

When lit from the side, the H_2 bubbles were clearly visible to the naked eye, providing a visualisation of the flow pattern. By insulating various parts of the wire and pulsing the applied potential, the bubbles could be formed in a grid, a thin sheet, or any number of axial streaklines, providing a versatile flow visualisation technique. These visualisation patterns are well illustrated in the literature cited above.

In practice, several drawbacks were encountered. Firstly, the hydrogen bubbles are not neutrally bouyant, and have a finite, though small rise velocity. Since the model was oriented in the vertical plane with flow moving downwards, bubbles tended to move upwards (particularly in the boundary layer) or remain attached to the wire near the walls at slow flowrates, in the latter case growing in size and causing a flow disturbance downstream. Bubbles collected along the upper walls of the two sections inclined at 70 degrees to the vertical plane. The assumption that the pathlines of the bubbles would coincide with the streamlines of the flow was not justified in the boundary layer or stagnation regions, and was uncertain, at best, in the more complicated features such as recirculation regions or reattachment zones.

Secondly, the wire was extremely fragile, and even with careful handling possessed a very short life span in situ. Examination of the broken wire and

comparison with unused wire under a microscope indicated that failure was due to mechanical fatigue rather than corrosion. Failure tended to occur at the walls of the tube, despite efforts to avoid pinching the wire when clamping it between the two halves of the model. The tensile strength of the wire limited the extent to which it could be held taut across the flow, and consequently the wire flexed when bubbles first formed on its surface. Failure was attributed to stress fluctuation fatigue, a conclusion that was strengthened by the considerable decrease in observed wire life when the circuit was pulsed (thereby flexing the wire with each pulse).

Thirdly, the wire was fouled easily by dirt and hair, despite a 100 micron filter situated at the entrance to the flow system. Fouling disturbed the bubble pattern, bubble formation and caused flow disturbances.

Both wire breakage and fouling caused a 24 hr delay in experiments due to dismantling, reassembly and resealing of the model. This was unacceptable considering the frequency of these occurrences.

Because the bubble life span was short (of the order of a few seconds), the wires had to be located near the features of interest in order to visualise them satisfactorily. The affect of the wire on a particular flow feature is difficult to assess, although disturbances due to the wire should be damped out by 70 - 100 wire diameters downstream (Schraub et al 1965). However, as detailed in Chapter 2, the flow in curved pipes is elliptic, meaning that the flow at any point in the tube depends on the flow at all other locations. The impingement of the wire on a free shear layer (detached boundary layer), a separation point, or a reattachment point may well affect the generation of vortices downstream, even though the point at which these vortices become apparent may be more than 100 diameters downstream of the wire.

The above problems were the main reasons for the abandonment of the H_2-bubble visualisation technique, although some other problems associated with photography, sealing the model about the wire and arranging the wire in other orientations than across the model's plane of symmetry were also encountered.

The H_2-bubble technique would be more appropriate for systems without geometric features in which the bubbles can be trapped and with the wires readily accessible for replacement or cleaning. However, the assumption of neutrally bouyant H_2 bubbles should be viewed with caution to avoid inaccurate visualisation in stagnation regions in particular.

Appendix E

Hydrophone Calibration

A Brüel & Kjær type 4145 microphone was used as a reference for the calibration of the hydrophone probe. The microphone sensitivity was quoted as 46.2 mV Pa^{-1}, with a flat response curve over the frequency range of interest. The sensitivity of the Brüel & Kjær type 8103 hydrophone was quoted as 22.6 $\mu V\ Pa^{-1}$. A Brüel & Kjær type 5140 charge-conditioning preamplifier was set to give an output signal of 100 $\mu V\ Pa^{-1}$ from the hydrophone signal. Therefore the sensitivity of the hydrophone compared to the reference microphone should have been

$$SPL_{\text{hydro ref micro}} = -20 \log\left[\frac{46.2 \times 10^{-3}\ V\ Pa^{-1}}{100 \times 10^{-6}\ V\ Pa^{-1}}\right]$$
$$= -13.3\ dB$$

; where SPL is the Sound Pressure Level.

The actual measured $SPL_{(\text{hydro ref micro})}$ was -13.1 dB.

The dust cover was removed from the microphone and the microphone placed into a perspex block so that the front face of the microphone was flush with the front face of the perspex block (figure E-1). A speaker was mounted in front of the apparatus to act as a pressure source.

The speaker was driven by an amplifier and the microphone used to detect the pressure waves. The frequency and SPL were measured by a Nicolet model 444 mini-ubiquitous spectrum analyser. The microphone was then removed and the hole plugged with a tightly-fitting piece of perspex. The perspex plug contained a pressure measurement port of the same dimensions to those used in the model. The hydrophone was inserted into this and the hydrophone output signal resulting from the same sound source measured by the spectrum analyser.

The calibration procedure was carried out over the range of frequencies from 24.5 Hz up to 323.75 Hz. Several repetitions were made at 175 Hz for different incident SPL's to assess the effect of the incident SPL on the probe's reponse. The calibration curve is shown in figure E-2.

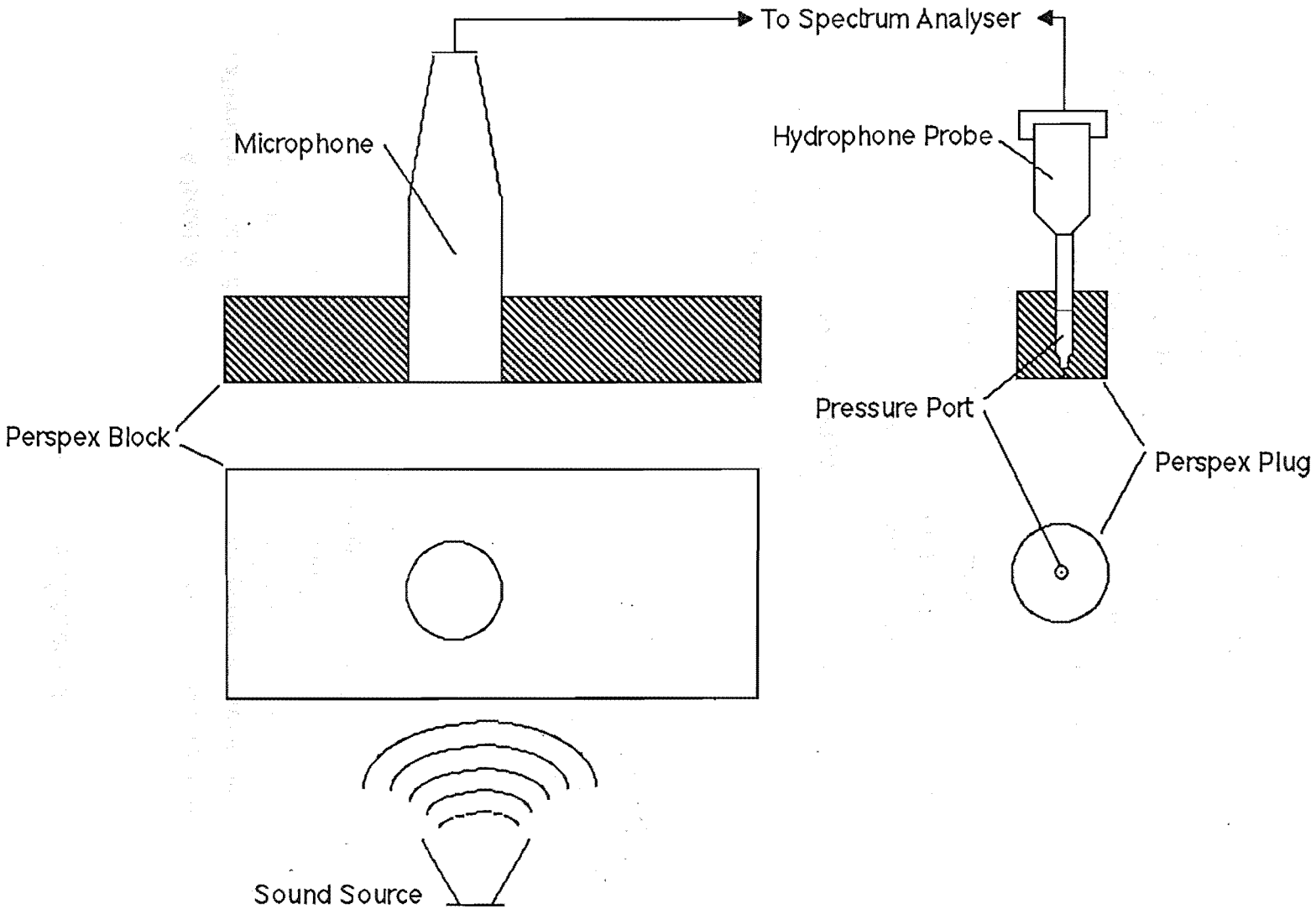

Figure E-1

Arrangement of Hydrophone Probe Calibration Apparatus.

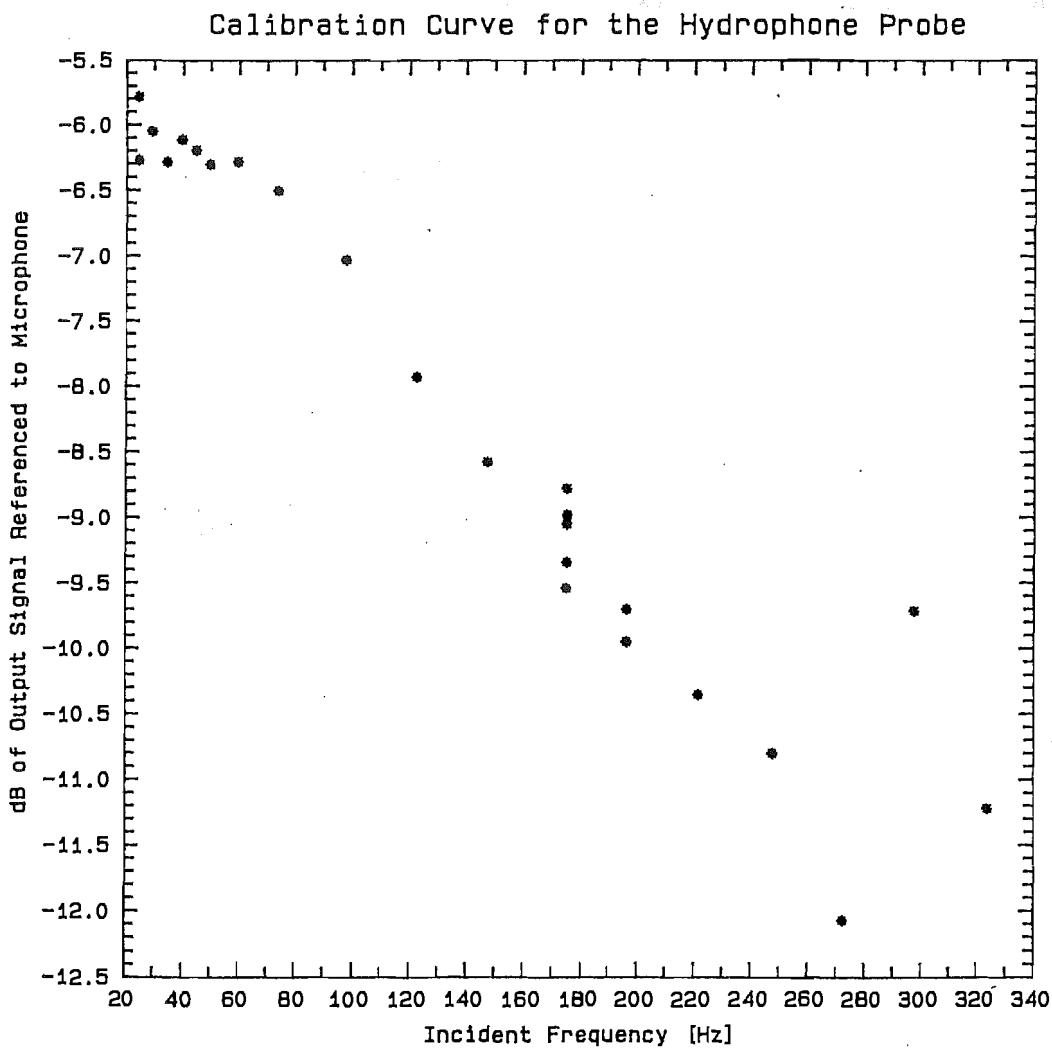

Figure E-2

Hydrophone Calibration Curve (dB ref to microphone).

An additional test was carried out at 250 Hz, using a Brüel & Kjær type 4220 pistonphone. The outputs of the reference microphone and the hydrophone probe (in the same perspex plug with pressure measurement port) were compared. The pistonphone frequency was quoted to be accurate to 1 % and the nominal SPL was 123.9 dB ref 2 x 10^{-4} μbar at 20 °C. These measurements are also shown in figure E-2.

Appendix F

The Helmholtz Resonator

The configuration of the pressure measurement port and hydrophone probe used in the model may be thought of as comprising a Helmholtz resonator, consisting of a rigid enclosed volume V, communicating with an external medium through an opening of radius a and length l (figure F-1).

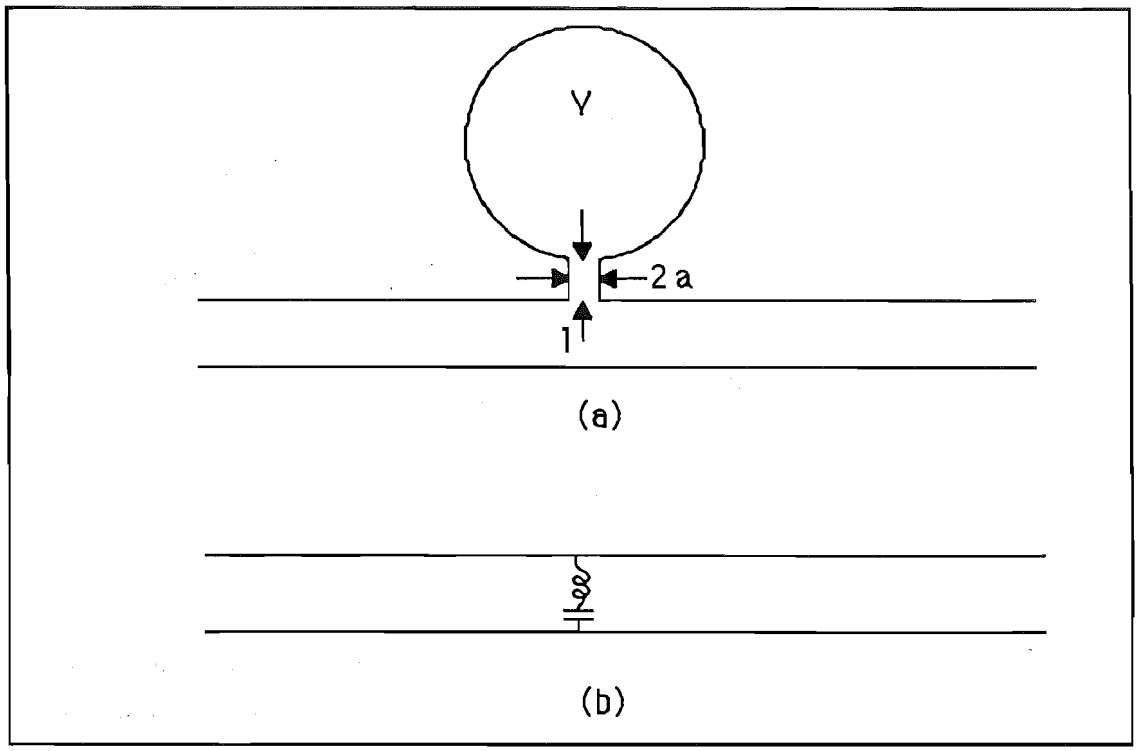

Figure F-1

(a) The Helmholtz Resonator as a side-branch

(b) The electrical analgue of the Helmholtz Resonator as a side-branch

In the following analysis, there are no assumptions which restrict the shape of the resonator to a sphere - rather, it is the volume and not the shape of the cavity that is important for a given opening. The Helmholtz resonator is analogous to a simple mechanical oscillator according to Kinsler and Frey (1962). The fluid in the opening moves as a unit and provides a mass element. The pressure of the gas in the enclosure rises and falls as it is alternately compressed and expanded by the gas moving through the opening, so providing a stiffness element. Finally, the dissipation of acoustic

energy by the radiation of sound into the surrounding medium provides a resistance element.

The elements analagous to the mechanical system are:

$$m = \rho_o S l' \qquad (F1)$$

; where m is the effective mass and l' is the effective length, taking the end effects, Δl, into account. The end effect is caused by the non-negligable mass of fluid near each entrance of the opening neck. $l' = l + 2\,\Delta l$ and $\Delta l = 8a/3\pi$ for an opening terminated in a wide flange (Kinsler & Frey 1962).

$$\text{Stiffness} = \frac{\rho_o c^2 S^2}{V} \qquad (F2)$$

; where c is the speed of sound in the fluid, ρ_o is the density and S is the cross-sectional area of the opening.

$$\text{Resistance} = \frac{\rho_o c k^2 S^2}{2\pi} \qquad (F3)$$

; where k is the wavelength constant in m^{-1}.

An analogy also exists between the Helmholtz resonator and an electrical system. In this case, the acoustic inertance M of the acoustic element is analogous to electrical inductance and is defined as

$$M = \frac{m}{S^2} \qquad (F4)$$

The acoustic compliance, C is analogous to electrical capacitance, and is defined as

Appendix G

Calibration of Analogue to Digital Convertor

Calibration of the Analogue to Digital convertor used to digitise the output of the LDA frequency tracking unit was carried out by supplying a known input DC voltage and measuring the output digital word. The input voltage was measured with the DISA digital voltmeter. The A to D output was read with a QX10 computer via a peripheral parallel interface board. The following calibration chart was obtained:

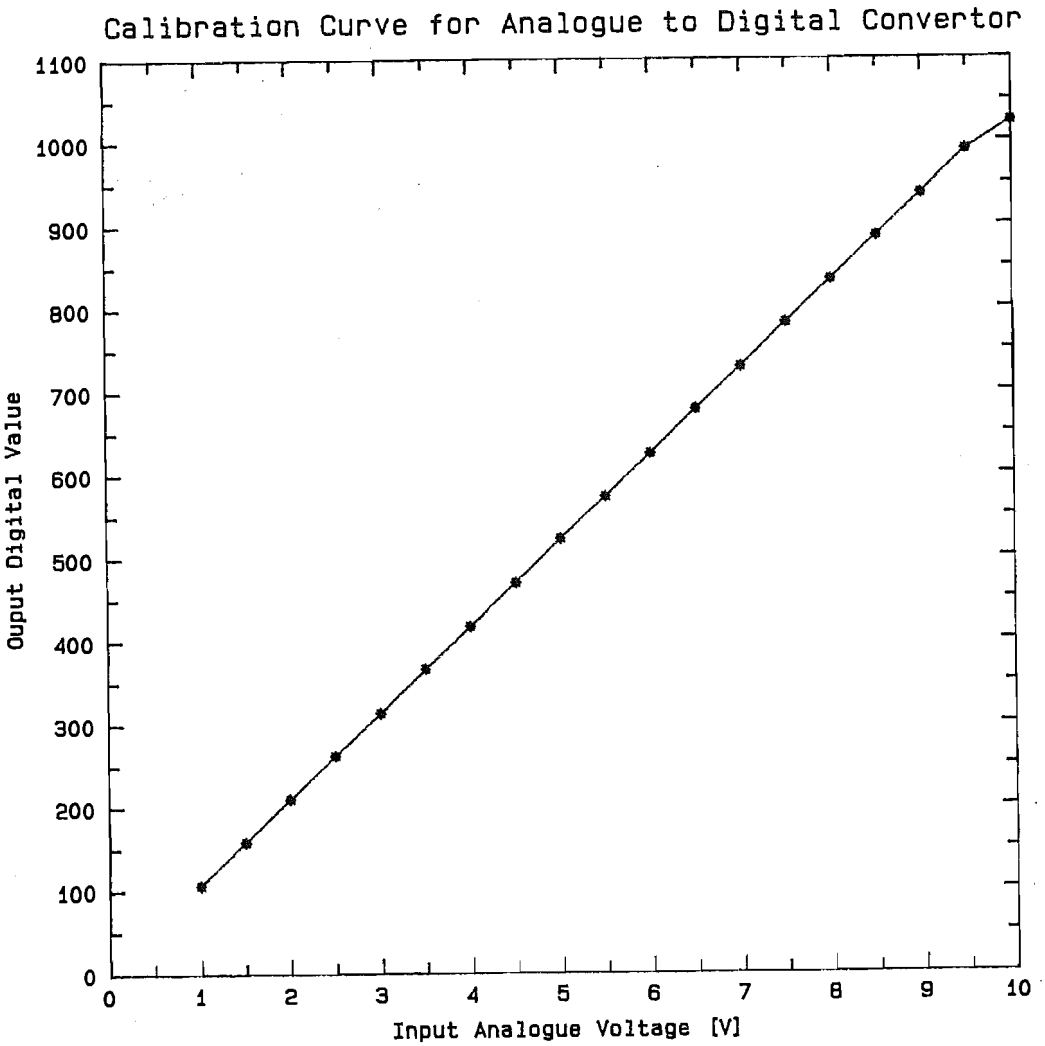

Figure G-1

Calibration Curve for Analogue to Digital Convertor.

Appendix H

Programme Listings

H1.1 Fortran Listings:

```
C
C     CONTOURS.FOR A program to create a contour plot of axial
C     velocities in a cross-section of the tube, from a specified
C     data file of LDA voltage outputs.
C
      CHARACTER FILENAME*12
      DIMENSION XD(130),YD(130),ZD(130),WK(1690),IWK(4030),
      DIMENSION X(130),Y(130),SCRARR(1600)
C
C     Open Metacode file "CONTOUR.MTA" for output of contours.
C
      CALL MCOPEN('CONTOUR.MTA')
C
C     Read in data (voltages) from specified data file "FILENAME"
C
      WRITE (6,50)
50    FORMAT(1X,'FILENAME ?')
      READ(5,100) FILENAME
100   FORMAT(A12)
      OPEN(UNIT=1,FILE=FILENAME,STATUS='OLD')
      NDP=129
      DO J=1,129
      READ(1,*)YD(J),XD(J),ZD(J)
C
C     Calculate velocity from voltage.
C
      ZD(J)=((ZD(J)-0.1354)/0.0212-75.6887)*0.16364
C
C     Set velocity at walls to zero for non-slip condition.
C
      IF(J.LT.29)ZD(J)=0.00
222   END DO
C
C     Section to call CONRAN and to set options (see CONRAN.FOR
C     listing available in NCAR plot package on Uni. of Cant. VAX
C     network)
C
      CALL CONOP1(7HLAB=OFF)
C     CALL CONOP1(6HPDV=ON)
      CALL CONOP1(7HPER=OFF)
      CALL CONOP2(6HTEN=ON,0.5)
      CALL CONOP2(7HDAS=LSS,10H$$$$'''$$$)
      CALL CONOP2(6HDBP=ON,0.2)
      CALL CONOP1(6HPMM=ON)
C     CALL CONOP1(7HMES=OFF)
      CALL CONOP2(6HCIL=ON,0.5)
```

```
      CALL CONRAN(XD,YD,ZD,NDP,WK,IWK,SCRARR)
C
C     Draw circle around contours to represent walls.
C
      CALL GETSET(MXA,MXB,MYA,MYB,XC,XDZ,YC,YDZ,LTYPE)
C
      X_centre = 0.5*(XDZ+XC)
      Y_centre = 0.5*(YDZ+YC)
      RADIUS   = 0.5*(XDZ-XC)
      DO I=1,121
      J= (I-1)*3
      X(I)=X_centre+RADIUS*SIND(FLOAT(J))
      Y(I)=Y_centre+RADIUS*COSD(FLOAT(J))
      END DO
      CALL CURVE(X,Y,121)
      CALL FRAME
      STOP
      END



C     NEWCON.FOR: A program to read in data from a specified data
C     file, corresponding to rows of pulsatile condition velocity
C     data in columns 4 to 15. Columns 1 and 2 contain the x and
C     y coordinates for the contour plotting routine.Column 3
C     contains the average velocity over the complete cycle and
C     column 16 contains mVrms of the totalLDA signal
C     fluctuations.
C     Subroutine NEG searches each plotting position, row by row,
C     fornegative velocities and plots an '*' (super-imposed on
C     the contourplot of the average velocities from column 3) at
C     any position that negative flow is observed at any point in
C     a complete cycle.Contours plots are made of whichever
C     columns are desired,and output in separate frames in
C     'CONT.DAT'.
C
      INTEGER COLUMN
      CHARACTER FILENAME*12
      DIMENSION XD(130),YD(130),ZD(130),WK(1690),IWK(4030)
      DIMENSION X(130),Y(130),ZED(130,16),SCRARR(10000)
C
C     Read in the data from file "FILENAME".
C
      WRITE (6,50)
50    FORMAT(1X,'FILENAME ?')
      READ(5,100) FILENAME
100   FORMAT(A12)
      OPEN(UNIT=1,FILE=FILENAME,STATUS='OLD')

C
C     Open Metacode file "PULSECONT.MTA" for output of contours
C
      CALL MCOPEN('PULSECONT.MTA')
      WRITE(6,60)
C
C     Section to enable reading of differently sized data files
C
60    FORMAT(1X,'INPUT NO OF LINES OF DATA')
```

```
      READ(5,105) ILINES
      WRITE(6,70)ILINES
70    FORMAT(1X,I3,'  INPUT NO OF SLICES')
      READ(5,105) ILEVEL
105   FORMAT(I3)

C
C     Section to re-specify upstream-most slice number to 1 for
C     the purposes of plotting contours.
C
      TYPE *,'INPUT ILOWER - THE LOWER SLICE NUMBER  ',ILEVEL
      READ(5,*) ILOWER
      NDP = ILINES + (ILEVEL*2)
      DO I=1,ILINES
      READ(1,*)(ZED(I,J),J=1,16)
      END DO
      DO I=1,ILINES
      XD(I)=ZED(I,1)-(ILOWER-1)
      YD(I)=ZED(I,2)
      IF (YD(I).GT.10) THEN
      YD(I) = YD(I) - 10.0
      END IF
      END DO
      WRITE(6,106) ILINES,ILEVEL,NDP
106   FORMAT(1X,3I12)
C
C     Set wall velocities to zero for non-slip condition
C
      IBOUND=ILINES+1
      DO I=IBOUND,NDP
      ZD(I)=0.0
      END DO
      JBOUND=ILINES+ILEVEL
      DO I=IBOUND,JBOUND
      YD(I)=1.32
      YD(I+ILEVEL)=8.68
      XD(I)=I-ILINES
      XD(I+ILEVEL)=I-ILINES
      END DO
C
C     Section to change plotting position of data values in two
C     files to match actual measurement positions.
C
      DO I=1,NDP
      IF(FILENAME.EQ.'05050288') THEN
           IF(XD(I).EQ.7.0) THEN
                XD(I)=XD(I)-0.5
                TYPE *,'CHANGED THE LAST SLICE NO. TO MATCH
                ACTUAL POSITION'
           END IF
      END IF
      IF(FILENAME.EQ.'06050188') THEN
           IF(XD(I).EQ.7.0) THEN
                XD(I)=XD(I)-0.5
                TYPE *,'CHANGED THE LAST SLICE NO. TO MATCH
                ACTUAL POSITION'
           END IF
      END IF
C
```

```
C     Scale X coordinate
C
           XD(I)=XD(I)*1.20
      END DO
C
C     Section to select appropriate data column.
C
15    TYPE *,'WHICH COLUMN DO YOU WANT A CONTOUR PLOT OF? [999 TO
      FINISH]'
      READ(5,*) COLUMN
      IF (COLUMN.EQ.999) GO TO 555
      DO I=1,ILINES
C
C     Correct velocity calculation error in NEWAVE.PAS programme
C
      ZD(I)=ZED(I,COLUMN)*1.32128
      END DO
      CALL CONIT(COLUMN,XD,YD,ZD,NDP,WK,IWK,SCRARR)
      TYPE *,'DONE CONTOUR PLOT  ',COLUMN
C
C     Section to allow choice of another column or finish.
C
      TYPE *,' SURELY YOU DONT WANT TO DO ANOTHER ONE?'
      READ(5,143) K
143   FORMAT(I2)
      IF (K.EQ.1) THEN
           TYPE *,'OH ALRIGHT THEN. SOME PEOPLE! PLOTTING
           COLUMN'
           GO TO 15
      END IF
      TYPE *,' PRINT THE EXTENT OF NEGATIVE FLOW TOO?'
      READ(5,143) K
      IF (K.EQ.1) THEN
           TYPE *,'OH ALRIGHT THEN. SOME PEOPLE! PLOTTING
           NEGATIVE'
           CALL NEG(ZED,ILINES,ILOWER)
      END IF
      TYPE *,' WELL AT LAST. IM OFF. BYE'
555   STOP
      END

      SUBROUTINE CONIT(COLUMN,XD,YD,ZD,NDP,WK,IWK,SCRARR)
C
C     Subroutine to call CONRAN.FOR and set options. See
C     CONRAN.FOR listing for description of options.
C
      CALL CONOP1(7HLAB=OFF)
C     CALL CONOP1(6HPDV=ON)
C     CALL CONOP1(7HPER=OFF)
      CALL CONOP2(6HTEN=ON,0.5)
      CALL CONOP2(6HNCP=ON,8)
      CALL CONOP2(7HDAS=LSS,10H$$$$'''$$$)
      CALL CONOP2(6HDBP=ON,0.5)
      CALL CONOP1(6HPMM=ON)
      IF (COLUMN.GT.3) THEN
      CALL CONOP1(7HMES=OFF)
      END IF
C     CALL CONOP2(6HCIL=ON,0.5)
      CALL CONOP2(6HSSZ=ON,100)
```

```
C     IF (J.EQ.3) THEN
C     CALL CONOP1(6HTRI=ON)
C     END IF
      CALL CONRAN(XD,YD,ZD,NDP,WK,IWK,SCRARR)
      CALL FRAME
      RETURN
      END
C
C     Subroutine to plot extent of negative flow over whole cycle
C
      SUBROUTINE NEG(ZED,ILINES,ILOWER)
      DIMENSION ZED(130,16),X(1),Y(1)
      CALL OPTN(5HCSIZE,256)
      DO I=1,ILINES
      ZED(I,1)=ZED(I,1)-(ILOWER-1)
C
C     If negative value encountered in a row, plot an asterisk at
C     that position for super-imposition on another plot.
C
      DO J=3,15
      IF(ZED(I,J).LE.0.0) THEN
      X(1)=ZED(I,1)
      Y(1)=ZED(I,2)
      IF(Y(1).GT.10.0) Y(1)=Y(1)-10.0
      CALL POINTS(X,Y,1,1H*,0)
      GO TO 444
      END IF
      END DO
444   CONTINUE
      END DO
      CALL FRAME
      RETURN
      END
```

H1.2 Turbo-Pascal Listing:

```
PROGRAM NEWAVE;
(*$C+,R+,U+*)
VAR
     A2D,Data                                  :ARRAY[1..8000] of
INTEGER;
     Mark                                      :ARRAY[1..100] of
INTEGER;
     Average,Std_dev,Totav,Tot_std             :ARRAY[1..13] of REAL;
     Clock_freq,Tot,Totsq,Half,Vel,R                :REAL;
     Point,Slice,Avel,Devel,Divider                      :REAL;
     Filename                                  :STRING[15];
     Rawdata                                   :TEXT;
     Sentry,Count,Index,Place,Time,Watchit1    :INTEGER;
     Watchit2,Watchit3,I,J,K,L,M,Q1,Q2,Q3      INTEGER;
BEGIN
{
This program takes in readings from an A/D convertor and a
trigger
```

```
signal from a pump which superimposes a sinusoidal velocity
variation
over the mean flow in the model. The sample rate is 100 Hz.
Cycles are marked by the trigger signal from the pump.
The velocity over about 3 cycles is averaged and standard
deviation
is calculated.
The velocities at 12 positions in a cycle are found and averaged
over
the 3 cycles and stored in FILENAME. Average velocity and
std_dev are
printed out.
}
     Writeln('Program NEWAVE.PAS');Writeln(' ');
     Writeln('Remember to respecify drive and load a data
     disk");Writeln(' ');
     Clock_freq:=498603.0;
     Index:=8000;
     Count:=ROUND(0.01*Clock_freq);
     Port[$DB]:=$36;
     Port[$D8]:=LO(Count);
     Port[$D8]:=HI(Count);
     Port[$D7]:=$9B;
     Port[$D3]:=$9B;
     Writeln('Filname?");
     Readln(Filename);
     Assign(Rawdata,Filename);Rewrite(Rawdata);
     Point:=100.0;
     Repeat
       Writeln('What Slice?');Writeln(' ');
       Readln(Slice);
       Writeln('What Point?');Writeln(' ');
       Readln(Point);
       If (Point <> 0.0) Then Begin
         Writeln('Getting the data');Writeln(' ');
         Inline($21/A2D/       {    LD   HL,A2D    Point at
         array}
  $11/Data/   { LD   DE,Data   Point at array}
  $ED/$4B/Index/     {    LD   BC,(Index)     Get counter}
  $DB/$D6/    {L1:   IN   0D6H      Wait for trigger to go low}
  $E6/$01/    { AND  1         }
  $C2/*-5/    { JP   NZ,L1          }
  $DB/$D6/    { IN   0D6H      Wait for trigger to go high}
  $E6/$01/    { AND  1         }
  $CA/*-5/    { JP   Z,L2      }
  $DB/$D2/    {L3:   IN   0D2H      Wait for EOC to go low}
  $E6/$01/    { AND  1         }
  $C2/*-5/    { JP   NZ,L3          }
  $DB/$D2/    {L4:   IN   0D2H      Wait for EOC to go high}
  $E6/$E1/    { AND  1         }
  $CA*-5/   { JP     Z,L4      }
  $DB/$D6/    { IN   0D6H      Read trigger}
  $E6/$E1/    { AND  1         }
  $12/      { LD     (DE),A    }
  $DB/$D0/    { IN   0D0H      Get least significant byte}
  $77/      { LD     (HL),A    }
  $23/      { INC    HL        }
  $DB/$D1/    { IN   0D1H      Get most sig. 2 bits}
```

```
$E6/$03/    { AND  3          }
$77/       { LD     (HL),A    }
$13/       { INC    DE        }
$E6/00/    { AND    0         }
$12/       { LD     (DE),A    0 in most sig. byte of trigger}
$13/       { INC    DE        }
$ED/$A1/     { CPI             Shift counter and pointer}
$E@/*+5/     { JP   PO,END     }
$C3/*-39/    { JP   L3         }
$ED/$43/I);   {     LD   (I),BC    Save counter}
{
}
      If I > 0 Then Writeln(I,' ','Did not complete the data
      collection');
      If I = 0 Then Begin
      Writeln('Got the data. Thinking...');Writeln(' ');
      Write(Chr(7));
{
Find the positions of the trigger signal. These positions mark
the phase.
Make sure the pump has not slipped up. Can check for this
using Watchit to guard
against unacceptable variations in the period of the cycle ie:
the total number of samples in between the trigger signals.
}
      Mark[1]:=1;J:=13;Sentry:=0;Q1:=0;Q2:=0;Q3:=0;
      For I := 2 to Index Do Begin
      If (Data[I-1] = 0) Then Begin
        If (Data[I] = 1) Then Begin
          Mark[J] = I;
          J := J+12;
          Sentry:=Sentry+1;
      End;
    End;
  End;
  Watchit1:=Mark[25]-Mark[13];
  Watchit2:=Mark[37]-Mark[25];
  Watchit3:=Mark[49]-Mark[37];
  Writeln(Lst,Watchit," ",Watchit2,' ',Watchit3);
  If (Abs(Watchit1-2135)) < 10) Then Q1:=1;
  If (Abs(Watchit2-2135)) < 10) Then Q2:=1;
  If (Abs(Watchit3-2135)) < 10) Then Q3:=1;
{
Divide each cycle into 12 phase positions and mark the spots
in Mark
}
  For K:=2 to 4 Do Begin
    J:=12*K+1;
    L:=12;
    For I:=(J-11) to (J-1) Do Begin
      Place:=Round((Mark[J]-Mark[J-L])/L);
      Mark[I]:=Mark[I-1}+Place;
      L:=L-1;
    End;
  End;
{
Calculate the average velocities and standard deviations from
the data
```

```
in array A2D. Point to each phase position using the data in
array Mark
}
  For I:=1 to 12 Do Begin
    Tot:=0.0;Totsq:=0.0;R=0.0;
    If (Q1 = 1) Then Begin
      M:=2;R:=R+1.0;
      J:=(M-1)*12;
      K:=Mark[I+J+1];
      Vel:=((0.0096*A2D[K]-0.1531)/0.0212-75.6887)*0.12385
      Tot:=Tot+Vel;
      Totsq:=Totsq+Sqr(Vel);
    End;
    If (Q2 = 1) Then Begin
      M:=3;R:=R+1.0;
      J:=(M-1)*12;
      K:=Mark[I+J+1];
      Vel:=((0.0096*A2D[K]-0.1531)/0.0212-75.6887)*0.12385
      Tot:=Tot+Vel;
      Totsq:=Totsq+Sqr(Vel);
    End;
    If (Q3 = 1) Then Begin
      M:=4;R:=R+1.0;
      J:=(M-1)*12;
      K:=Mark[I+J+1];
      Vel:=((0.0096*A2D[K]-0.1531)/0.0212-75.6887)*0.12385;
      Tot:=Tot+Vel;
      Totsq:=Totsq+Sqr(Vel);
    End;
    If (R > 1.0) Then Begin
      Average[I+1]:=Tot/R;
      Std_dev[I+1]:=Sqrt((Totsq-R*Sqr(Average[I+1]))/(R-1.0));
    End;
    Else Begin
      Average[I+1]:=Tot;Std_dev[I+1]:=999.0;
    End;
  End;
  Average[1]:=Average[13];Std_dev[1]:=Std_dev[13];
  End;
  Tot:=0.0;Totsq:=0.0;Divider:=0.0;
  If (Q1 = 1) Then Begin
    Divider:=Divider+Watchit1;
    For K:=Mark[13] to (Mark[25]-1) Do Begin
      Vel:=((0.0096*A2D[K]-0.1531)/0.0212-75.6887)*0.12385;
      Tot:=Tot+Vel;
      Totsq:=Totsq+Sqr(Vel);
    End;
  End;
  If (Q2 = 1) Then Begin
  Divider:=Divider+Watchit2;
  For K:=Mark[25] to (Mark[37]-1) Do Begin
    Vel:=((0.0096*A2D[K]-0.1531)/0.0212-75.6887)*0.12385;
    Tot:=Tot+Vel;
    Totsq:=Totsq+Sqr(Vel);
  End;
End;
  If (Q3 = 1) Then Begin
```

```
      Divider:=Divider+Watchit3;
      For K:=Mark[37] to (Mark[49]-1) Do Begin
        Vel:=((0.0096*A2D[K]-0.1531)/0.0212-75.6887)*0.12385;
        Tot:=Tot+Vel;
        Totsq:=Totsq+Sqr(Vel);
      End;
    End;
    If (Divider > 1.0) Then Begin
      Avel:=Tot/Divider;
      Devel:=Sqrt((Totsq-Divider*Sqr(Avel))/(Divder-1.0));
    End;
    Else Begin
      Writeln('Data absolutely useless. Try again.');
      Writeln(Lst'Data absolutely useless. Try again.');
    End;
  {
  Output the results on the printer
  }
    Writeln(Lst,'At Slice ',Slice:5:2,' and point ',Point:5:2);
    Write(Lst,'Average velocity is ',Avel:5:2,' with std_dev ');
    Writeln(Lst,Devel:5:2,' and the velocities are [cm/s]');
    Writeln(Lst,' ');
    For I:= 1 to 12 Do Begin
      Write(Lst,Average[I]:5:2,' ');
    End;Writeln(Lst,' ');
    Writeln(Lst,'With standard deviation ');Writeln(Lst' ');
    For I:=1 to 12 Do Begin
      Write(Lst,Std_dev[I]:5:2,' ');
    End;Writeln(Lst,' ');Writeln(Lst,' ');Writeln(Lst,' ');
  {
  Output the average velocities to FILENAME.
  }
    Writeln(Rawdata,Slice:5:2,',',Point:5:2,',',Avel:5:2,',');
    For I:=1 to 11 Do Begin
      Write(Rawdata,Average[I]:5:2,',');
    End;
    Writeln(Rawdata,Average[I+1]:5:2,',');
    Writeln(Chr(7));
    End;
  Until (Point = 0.0);
Close (Rawdata);Writeln(Lst,' ');Writeln(Lst,'File in
',Filename);
END.
```

Appendix I

Pulsatile LDA Results

The following pulsatile flow results were obtained using the LDA, in addition to those shown in Chapter 5.

I-1: Pulsatile Flow Instantaneous Re Axial Flow Isovels:

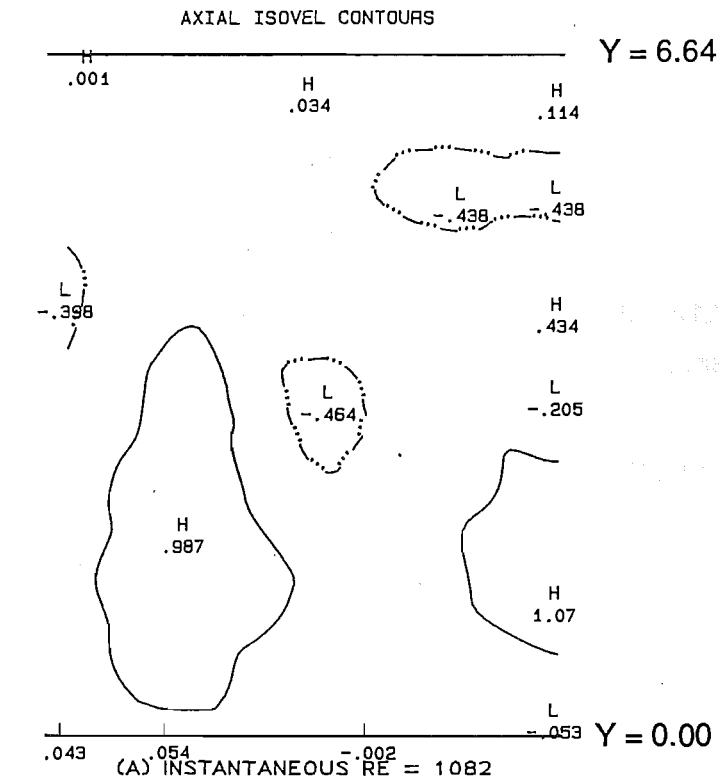

Upstream $\Psi = 0°$ Downstream

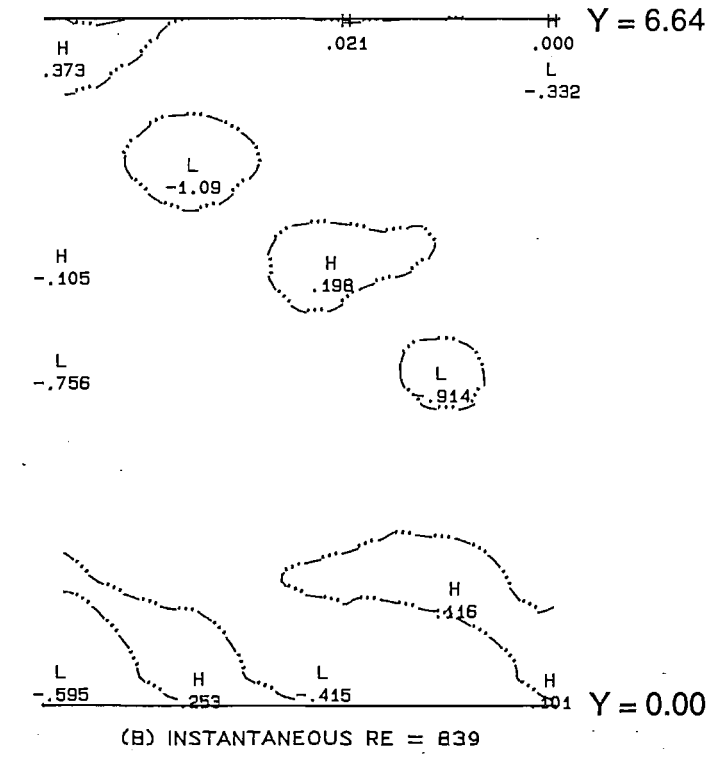

Upstream $\Psi = 30°$ Downstream

Figure I-1 A-L

Along the $\alpha = 0°$ azimuth of the proximal stem, OA1, $Re_{mean} = 1500$

A)$\Psi = 0°$ B)$\Psi = 30°$ C)$\Psi = 60°$ D)$\Psi = 90°$ E)$\Psi = 120°$

F$\Psi = 150°$ G)$\Psi = 180°$ H)$\Psi = 210°$ I)$\Psi = 240°$ J)$\Psi = 270°$

K)$\Psi = 300°$ L)$\Psi = 330°$.

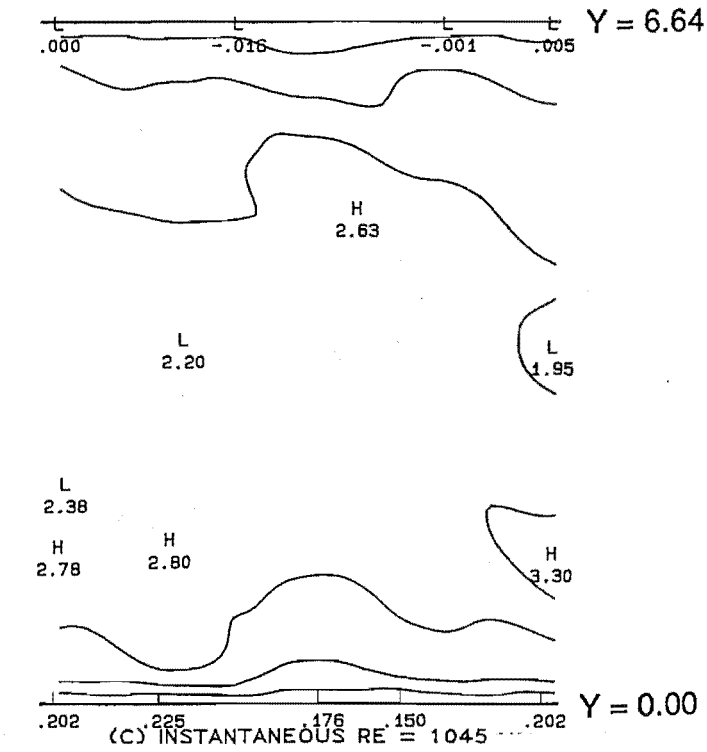

Upstream $\Psi = 60°$ Downstream

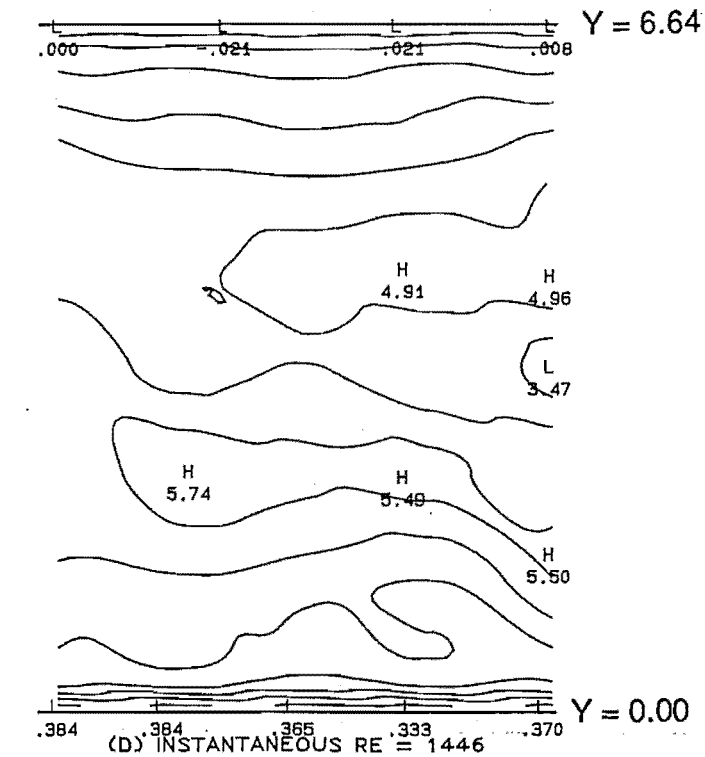

Upstream $\Psi = 90°$ Downstream

Figure I-1 A-L (cont.)

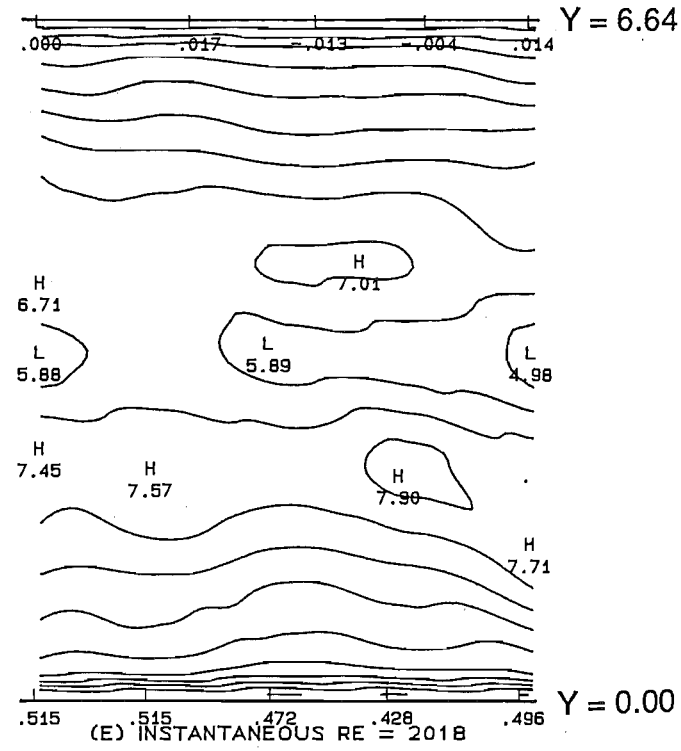

Upstream $\Psi = 120°$ Downstream

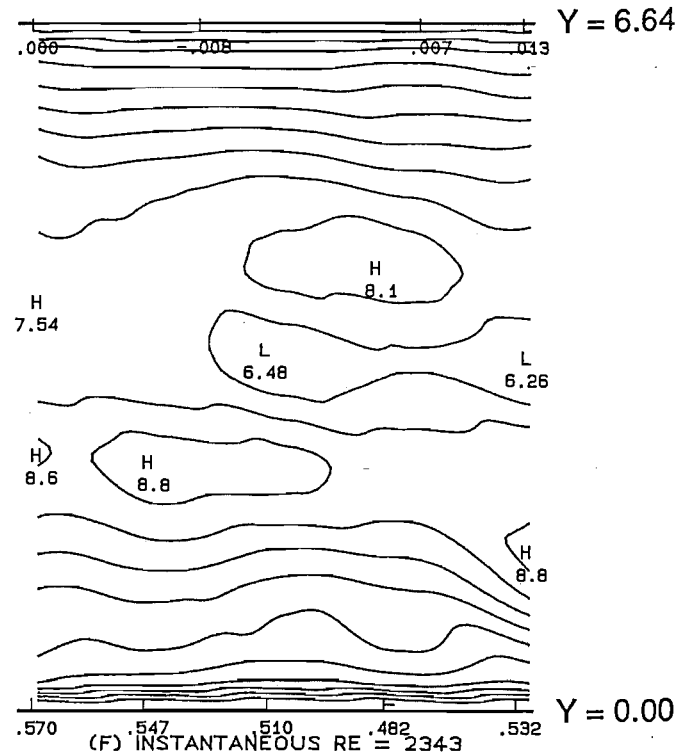

Upstream $\Psi = 150°$ Downstream

Figure I-1 A-L (cont.)

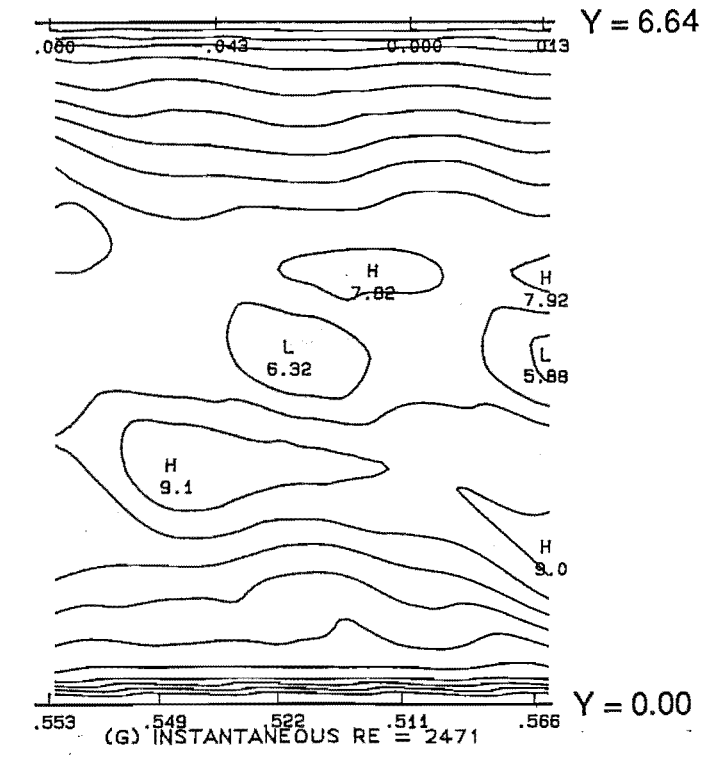

Upstream $\Psi = 180°$ Downstream

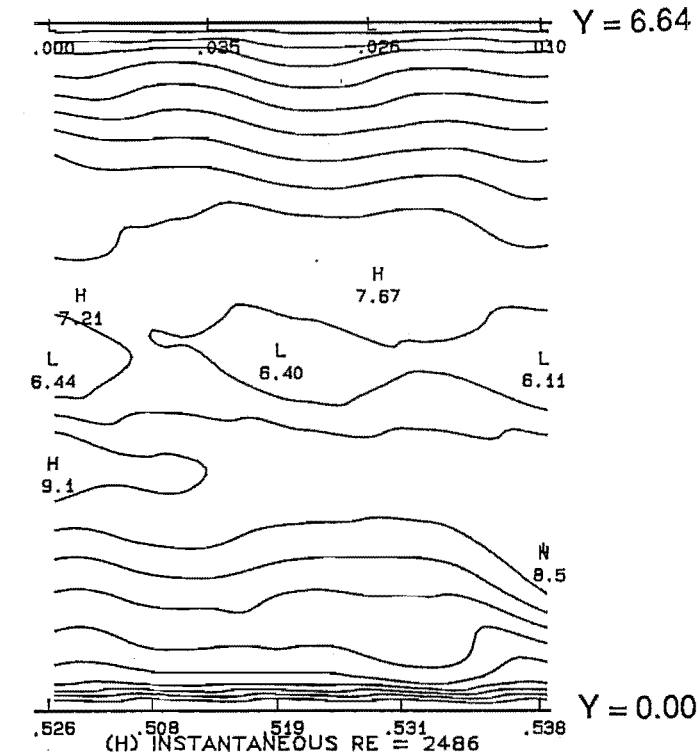

Upstream $\Psi = 210°$ Downstream

Figure I-1 A-L (cont.)

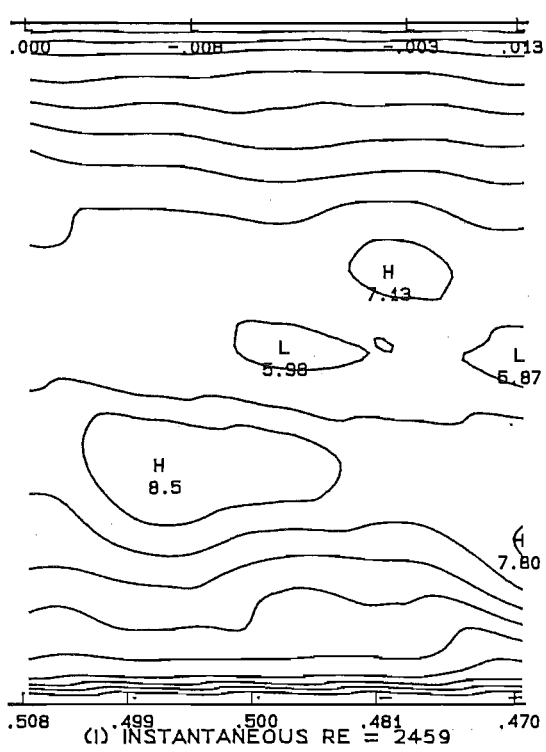

Upstream $\Psi = 240°$ Downstream

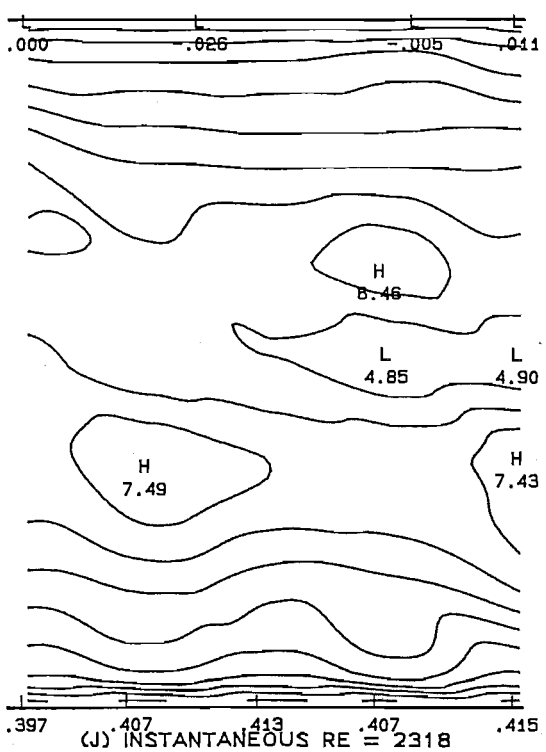

Upstream $\Psi = 270°$ Downstream

Figure I-1 A-L (cont.)

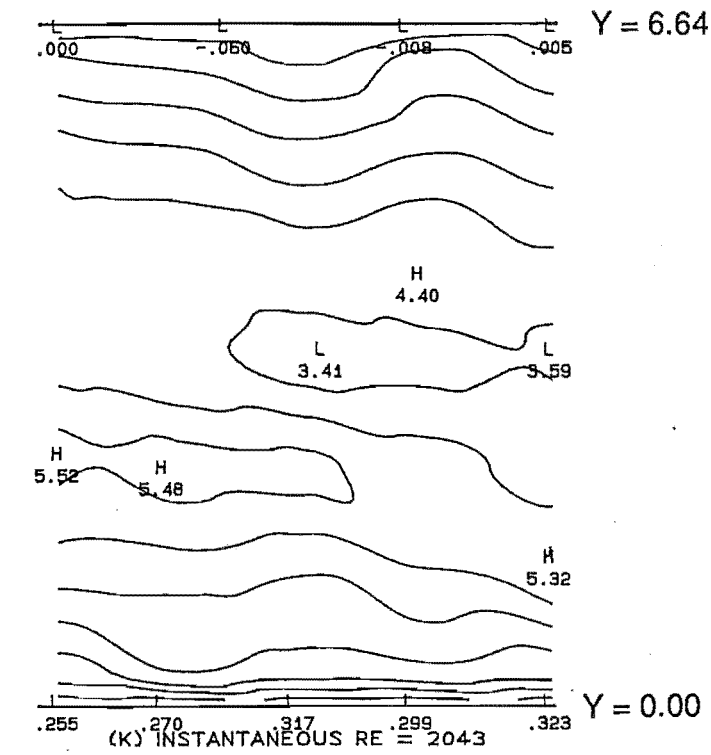

Upstream $\Psi = 300°$ Downstream

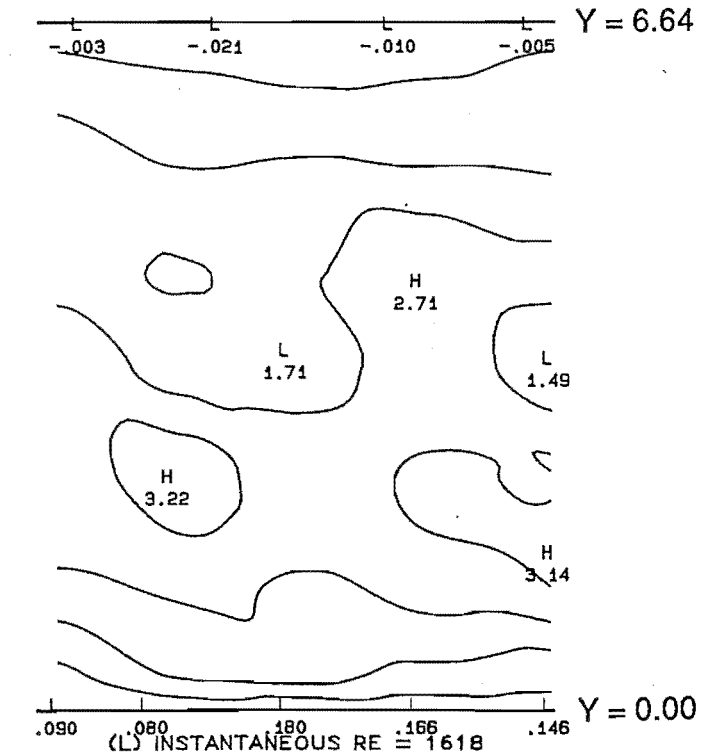

Upstream $\Psi = 330°$ Downstream

Figure I-1 A-L (cont.)

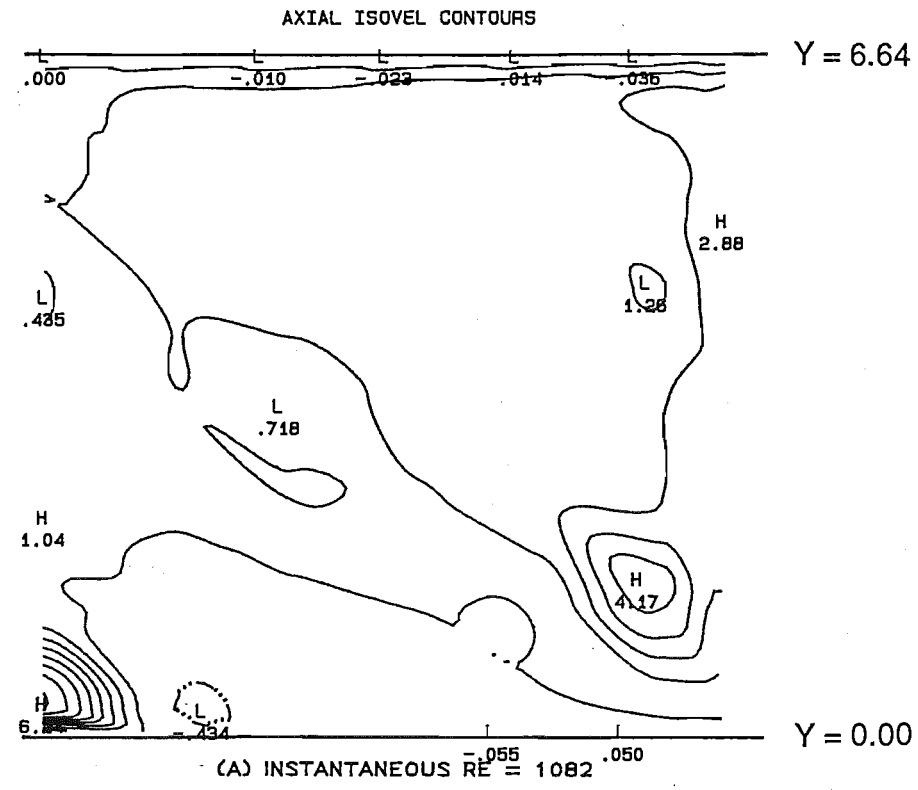

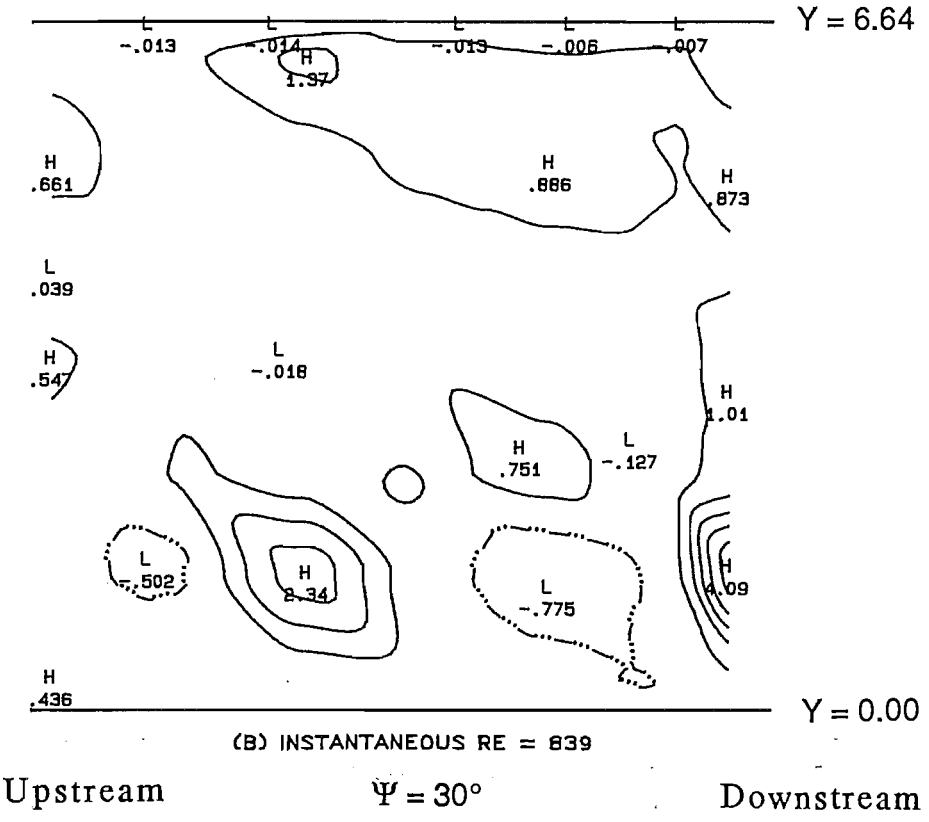

Figure I-2 A-L

Along the $\alpha = 0°$ azimuth of the proximal stem, OA2, $Re_{mean} = 1500$

A)$\Psi = 0°$ B)$\Psi = 30°$ C)$\Psi = 60°$ D)$\Psi = 90°$ E)$\Psi = 120°$

F$\Psi = 150°$ G)$\Psi = 180°$ H)$\Psi = 210°$ I)$\Psi = 240°$ J)$\Psi = 270°$

K)$\Psi = 300°$ L)$\Psi = 330°$.

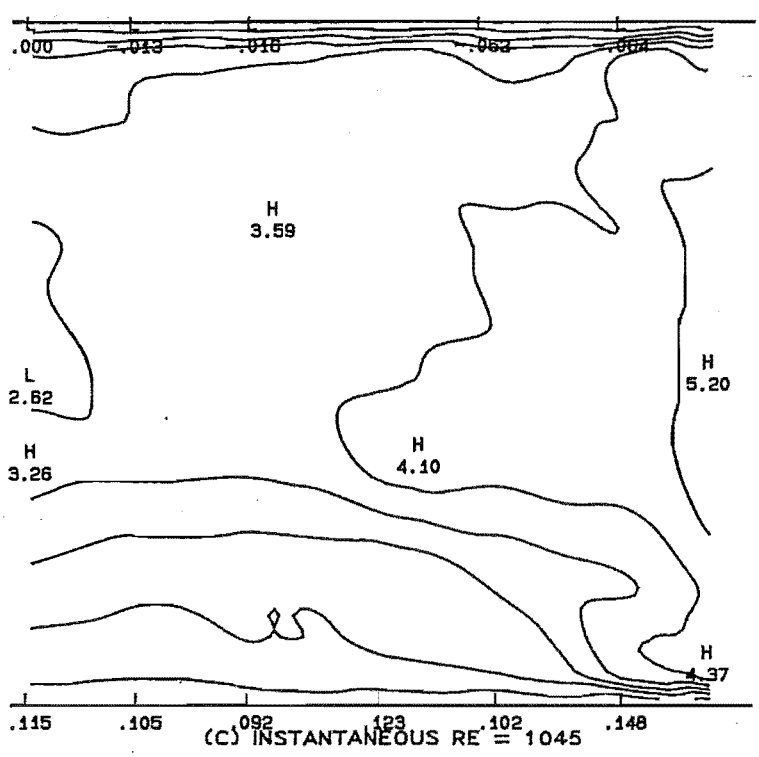

Upstream $\Psi = 60°$ Downstream

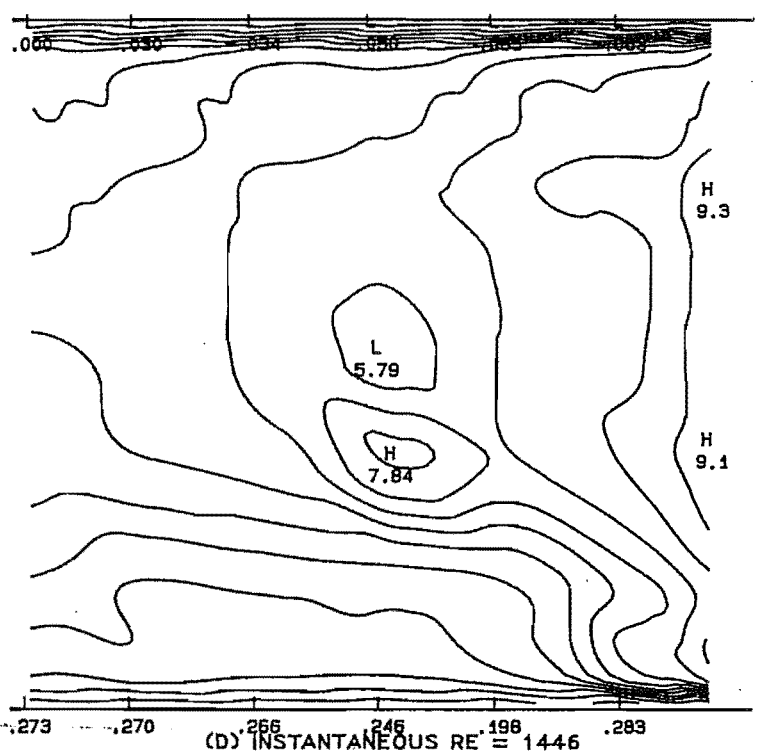

Upstream $\Psi = 90°$ Downstream

Figure I-2 A-L (cont.)

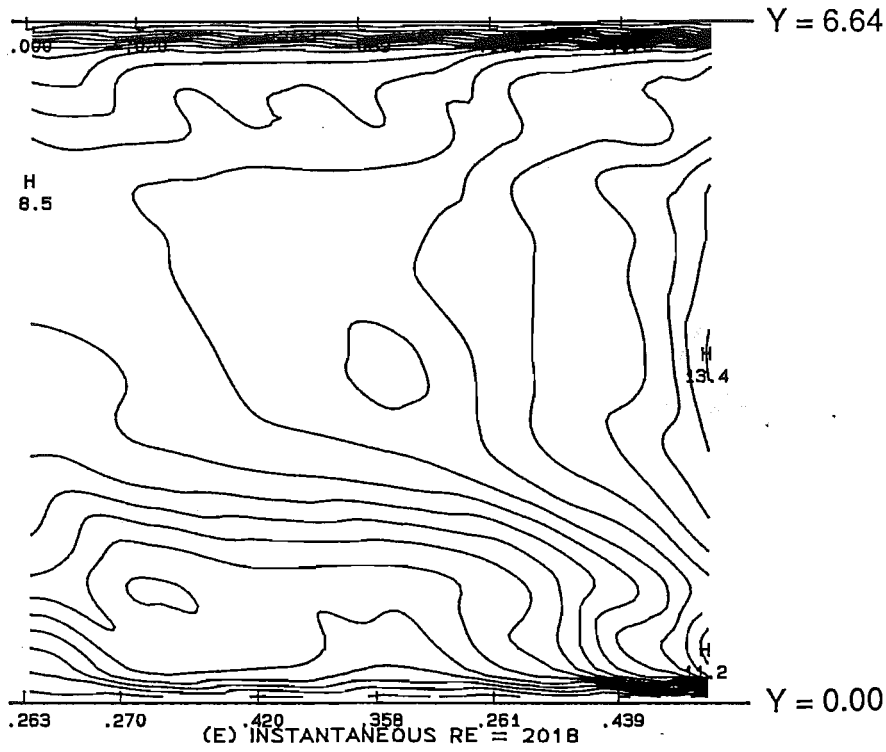

Upstream $\Psi = 120°$ Downstream

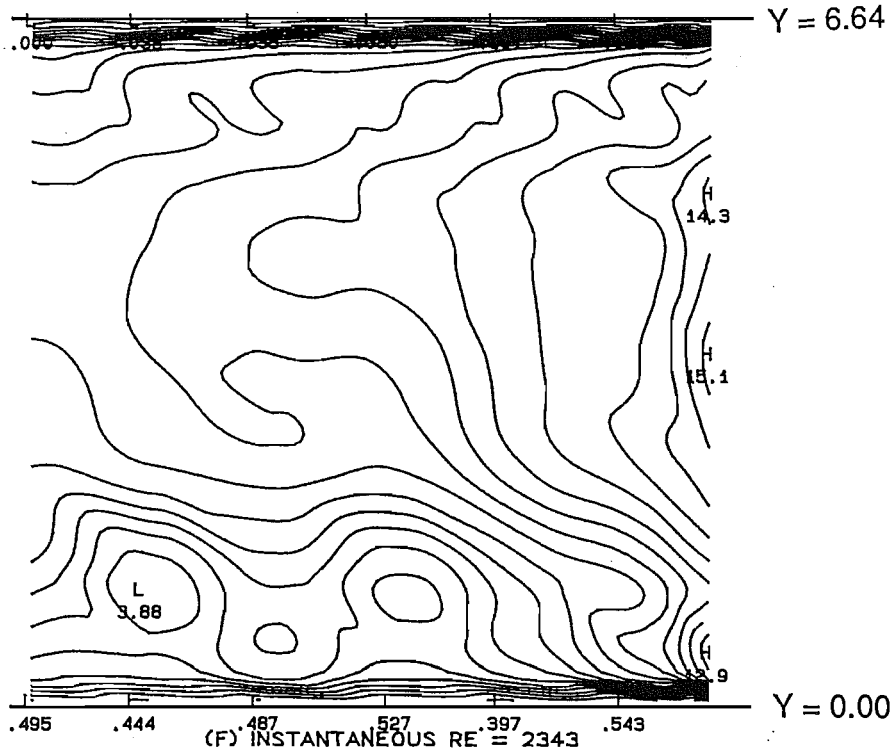

Upstream $\Psi = 150°$ Downstream

Figure I-2 A-L (cont.)

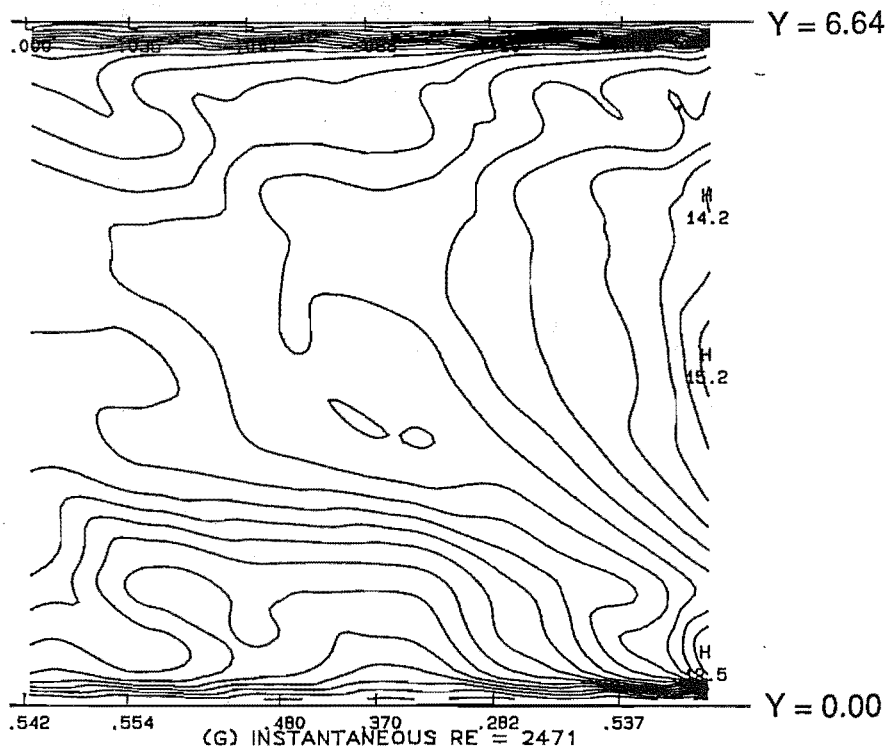

Upstream $\Psi = 180°$ Downstream

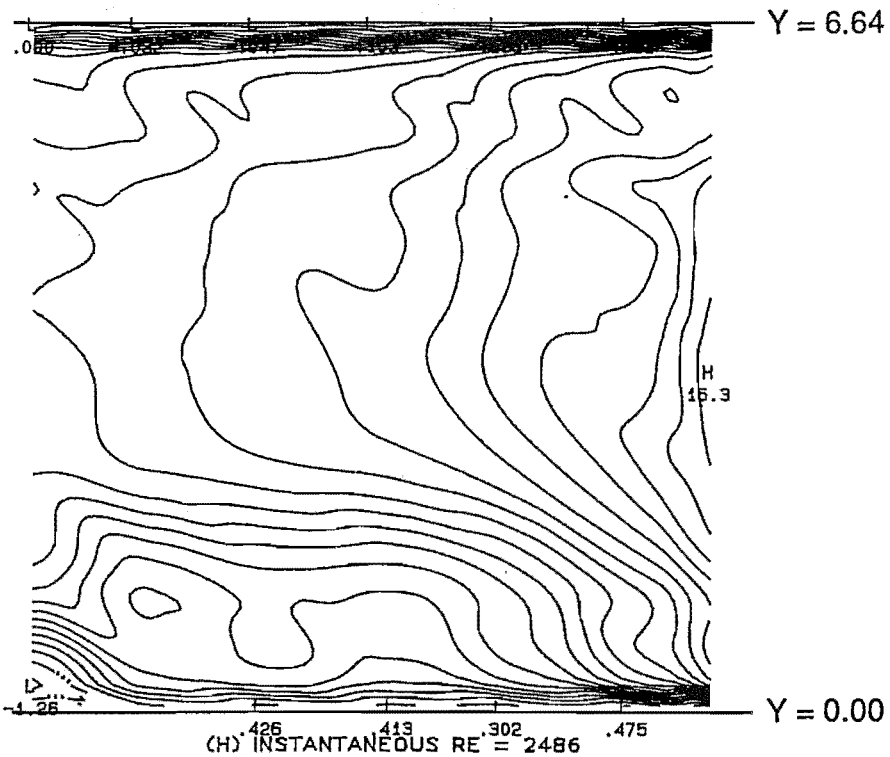

Upstream $\Psi = 210°$ Downstream

Figure I-2 A-L (cont.)

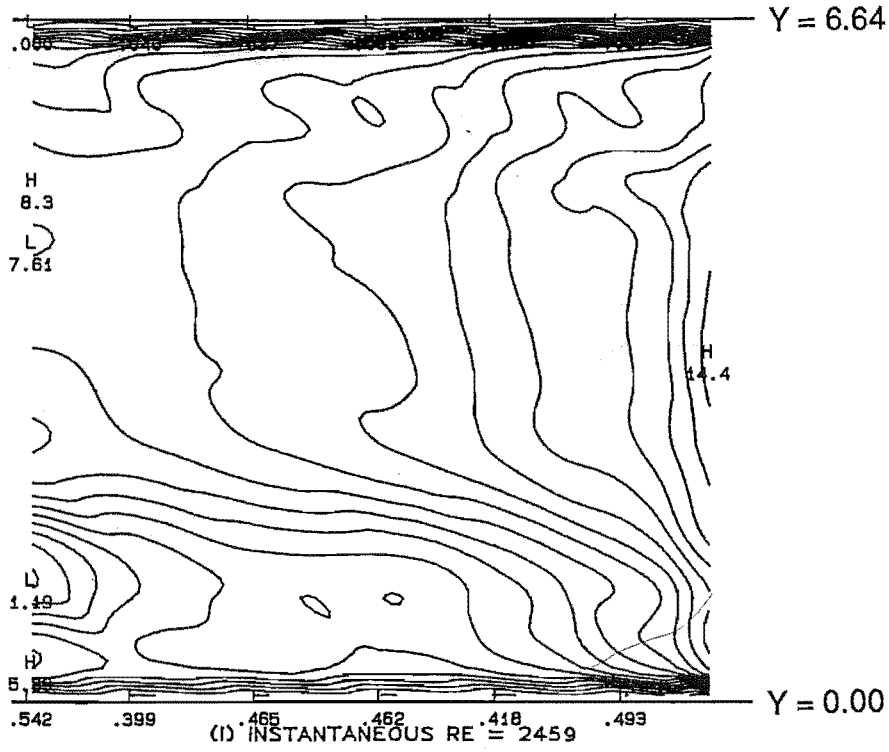

Upstream $\Psi = 240°$ Downstream

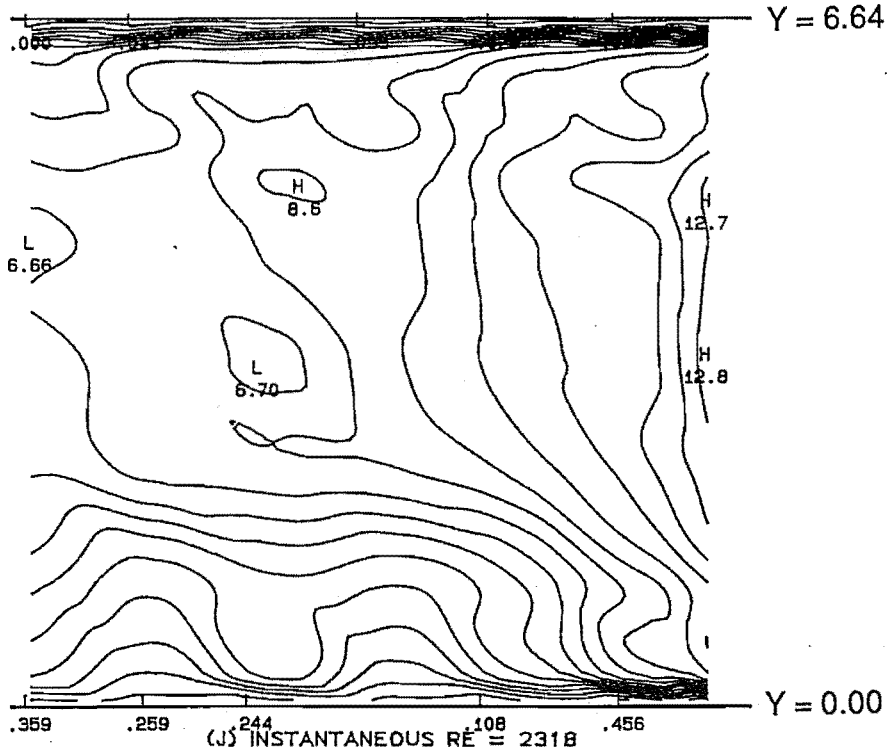

Upstream $\Psi = 270°$ Downstream

Figure I-2 A-L (cont.)

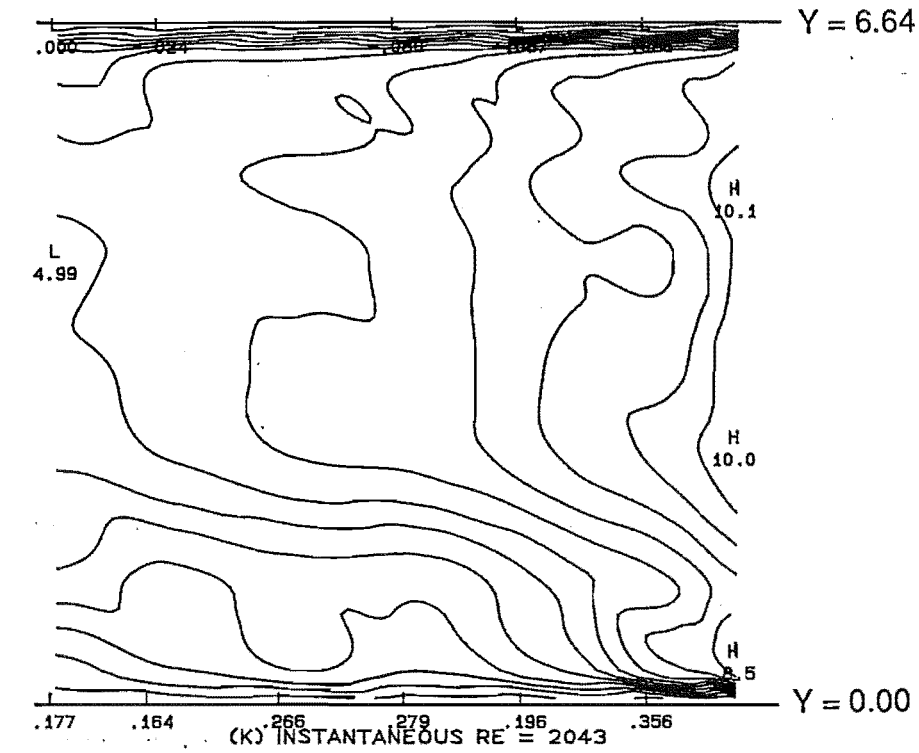

Upstream $\Psi = 300°$ Downstream

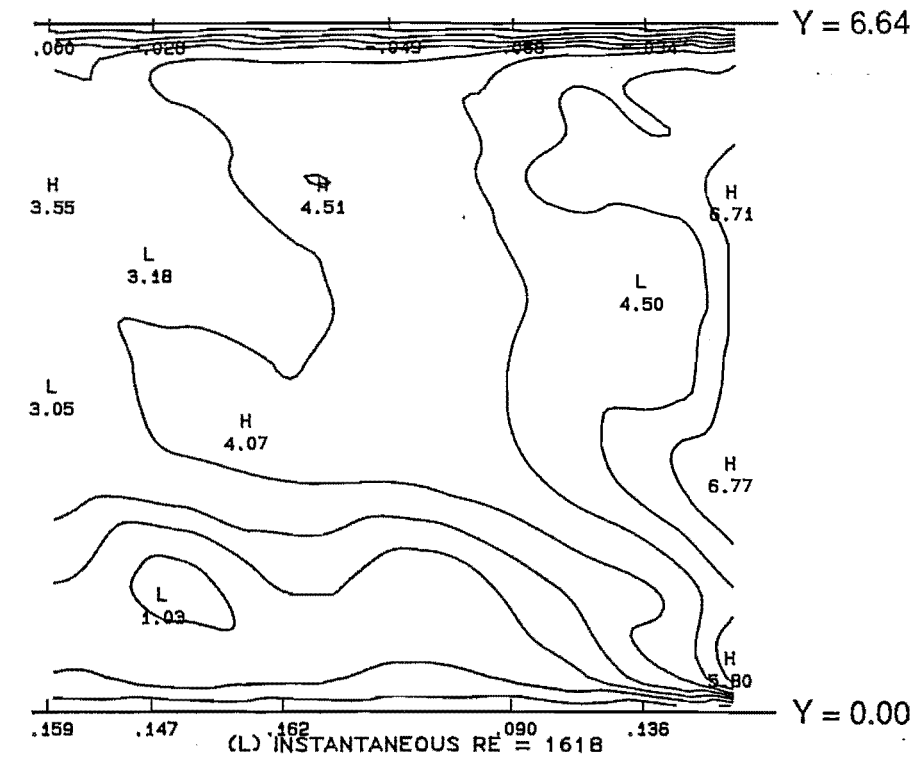

Upstream $\Psi = 330°$ Downstream

Figure I-2 A-L (cont.)

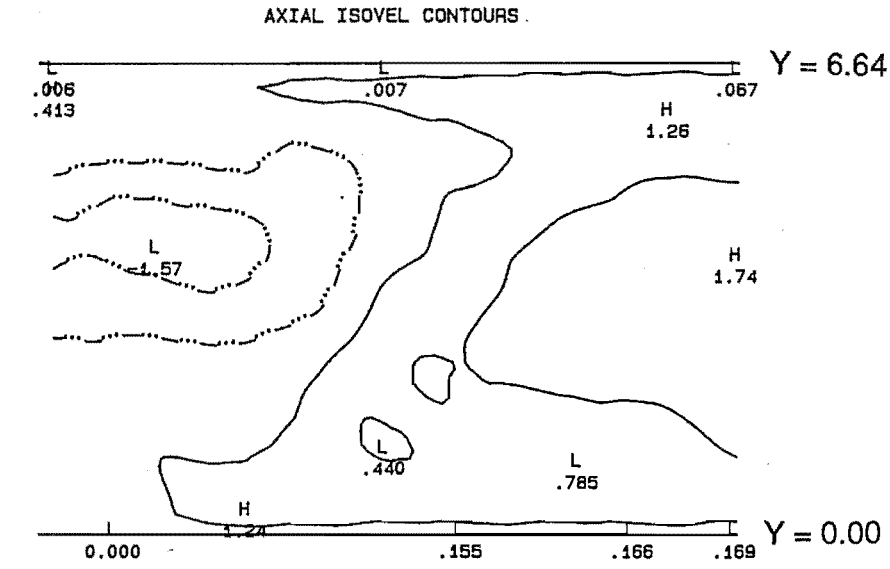

(A) INSTANTANEOUS RE = 851

$\Psi = 0°$

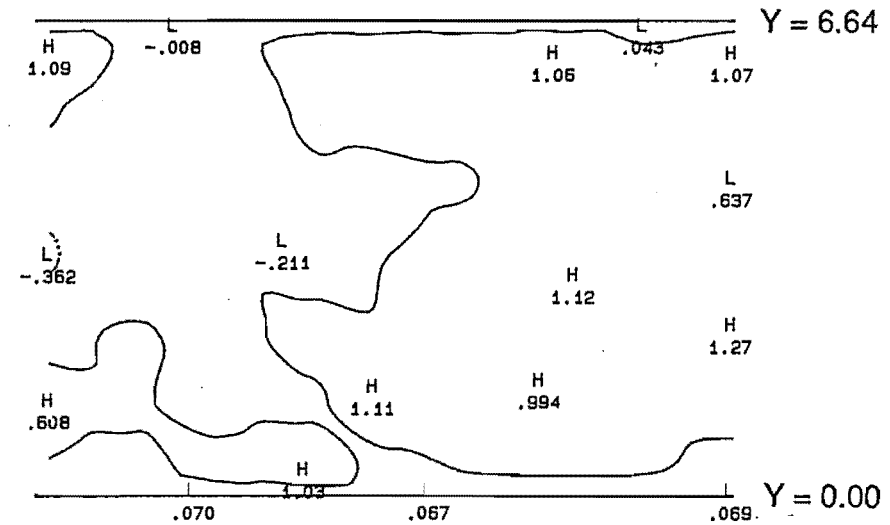

(B) INSTANTANEOUS RE = 632

$\Psi = 30°$

Figure I-3 A-L

Along the $\alpha = 0°$ azimuth of the proximal limb, $Re_{mean} = 1000$

A)$\Psi = 0°$ B)$\Psi = 30°$ C)$\Psi = 60°$ D)$\Psi = 90°$ E)$\Psi = 120°$

F$\Psi = 150°$ G)$\Psi = 180°$ H)$\Psi = 210°$ I)$\Psi = 240°$ J)$\Psi = 270°$

K)$\Psi = 300°$ L)$\Psi = 330°$.

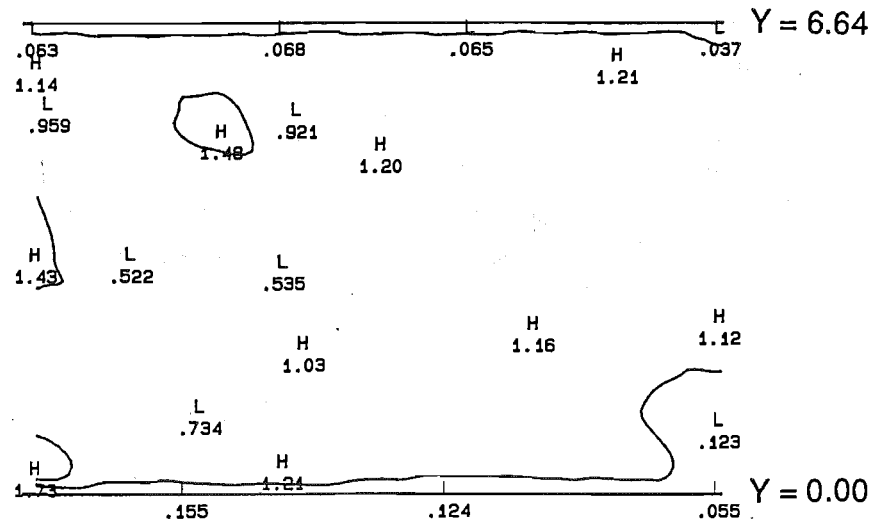

Upstream Downstream

(C) INSTANTANEOUS RE = 864

$\Psi = 60°$

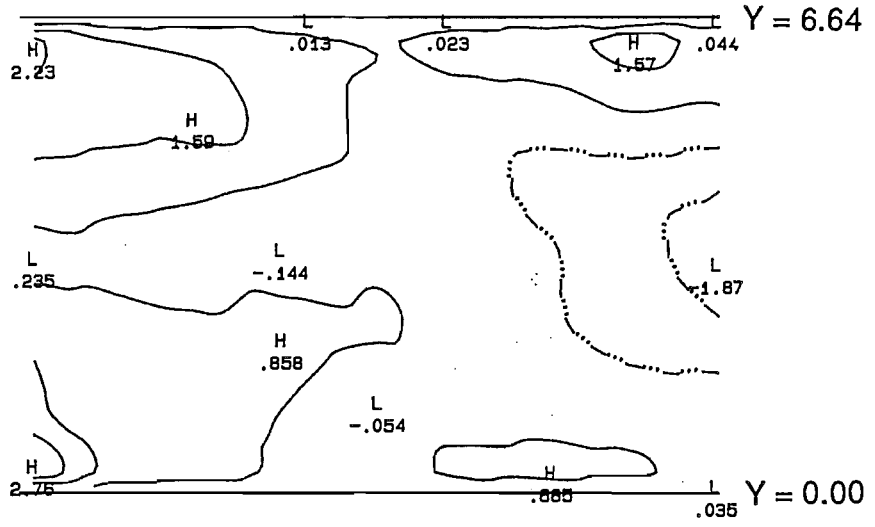

Upstream Downstream

(D) INSTANTANEOUS RE = 1267

$\Psi = 90°$

Figure I-3 A-L (cont.)

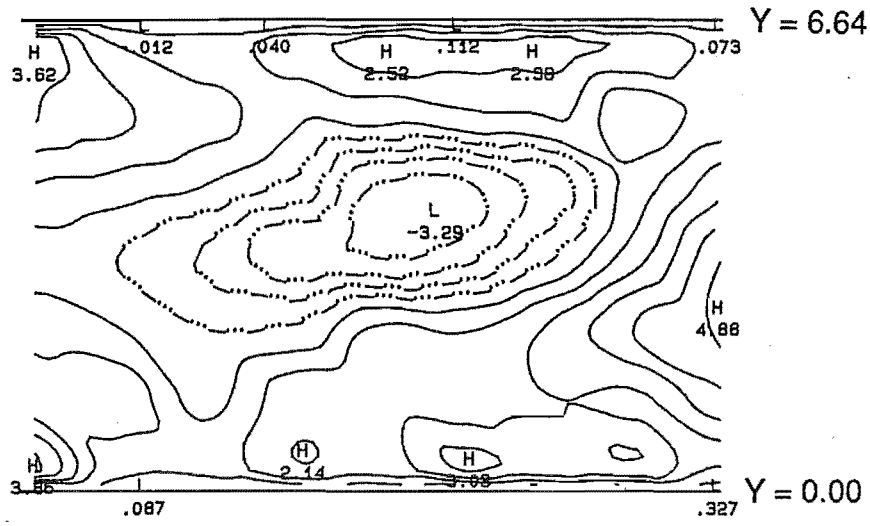

Upstream Downstream

(E) INSTANTANEOUS RE = 1606

$\Psi = 120°$

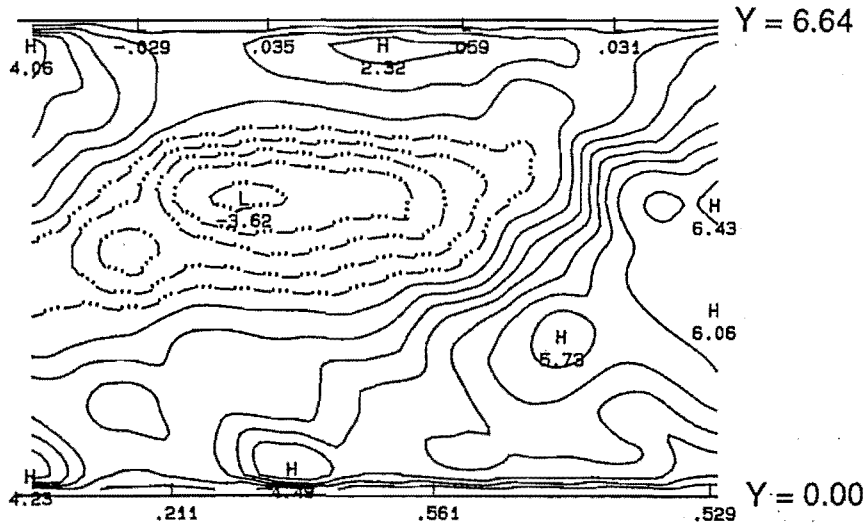

Upstream Downstream

(F) INSTANTANEOUS RE = 1766

$\Psi = 150°$

Figure I-3 A-L (cont.)

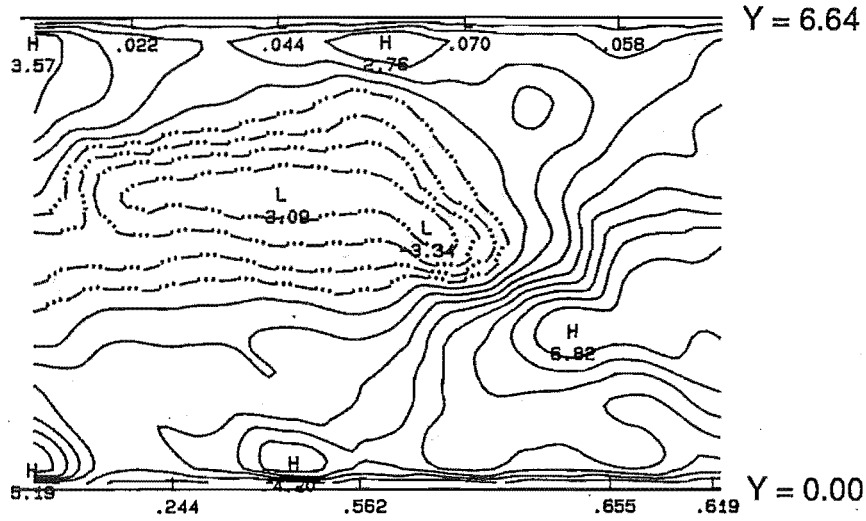

(G) INSTANTANEOUS RE = 1862

$\Psi = 180°$

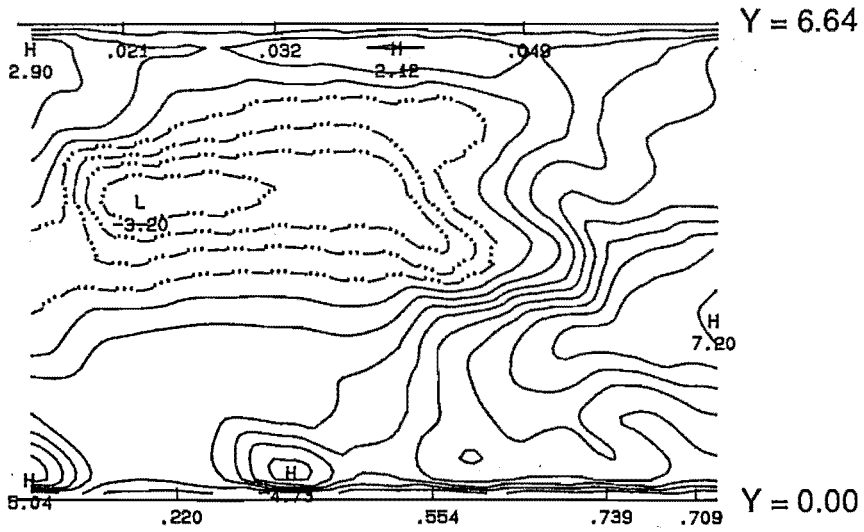

(H) INSTANTANEOUS RE = 1894

$\Psi = 210°$

Figure I-3 A-L (cont.)

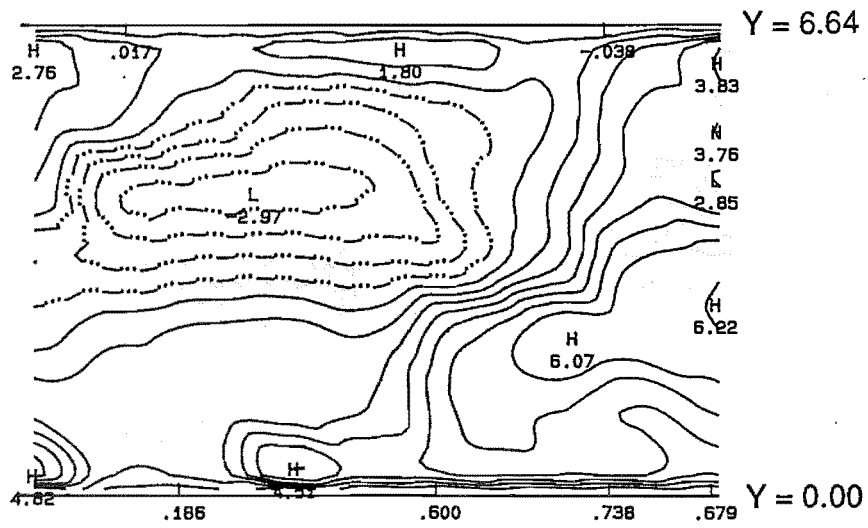

Upstream Downstream

(I) INSTANTANEOUS RE = 1882

$\Psi = 240°$

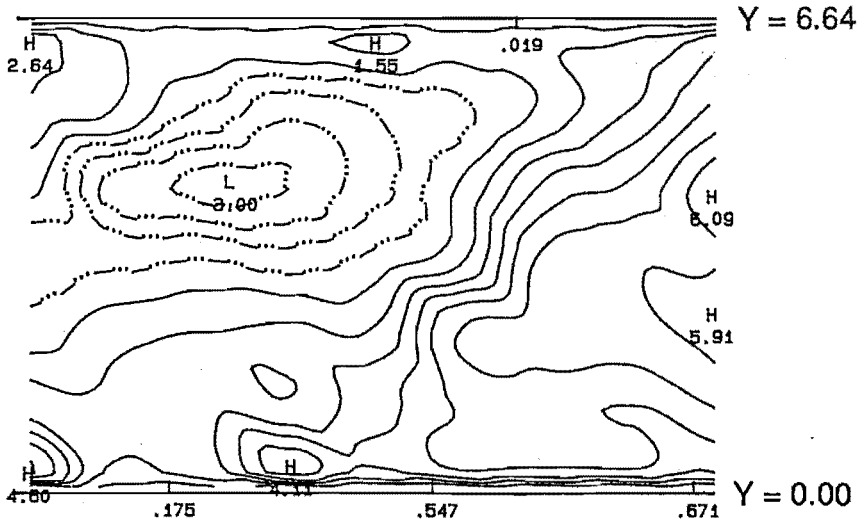

Upstream Downstream

(J) INSTANTANEOUS RE = 1813

$\Psi = 270°$

Figure I-3 A-L (cont.)

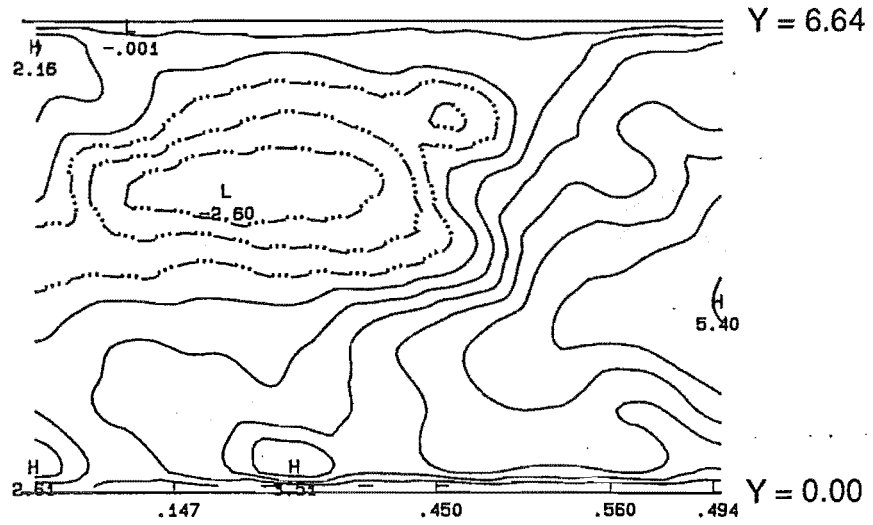

(K) INSTANTANEOUS RE = 1602

$\Psi = 300°$

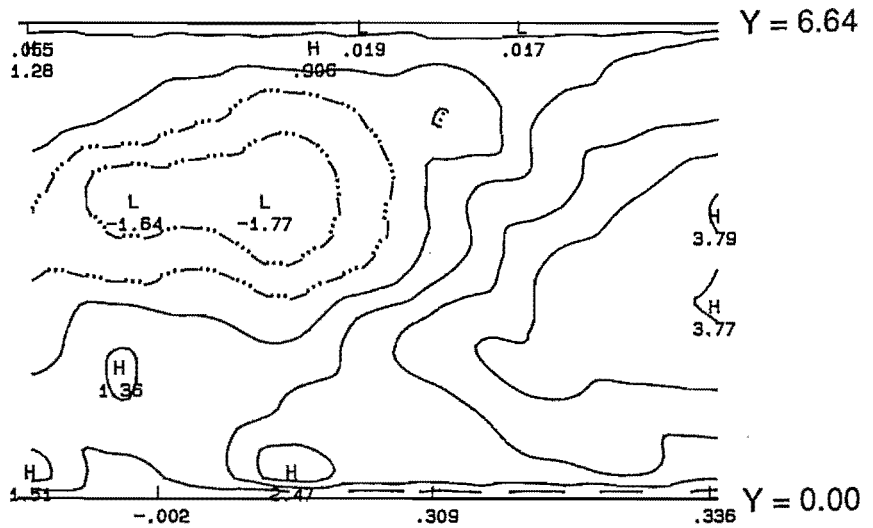

(L) INSTANTANEOUS RE = 1271

$\Psi = 330°$

Figure I-3 A-L (cont.)

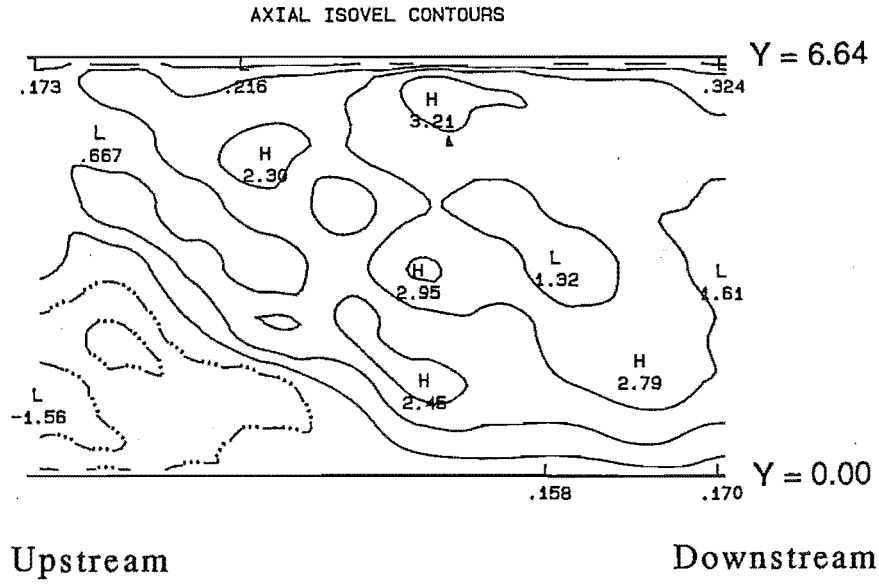

(A) INSTANTANEOUS RE = 1082

$\Psi = 0°$

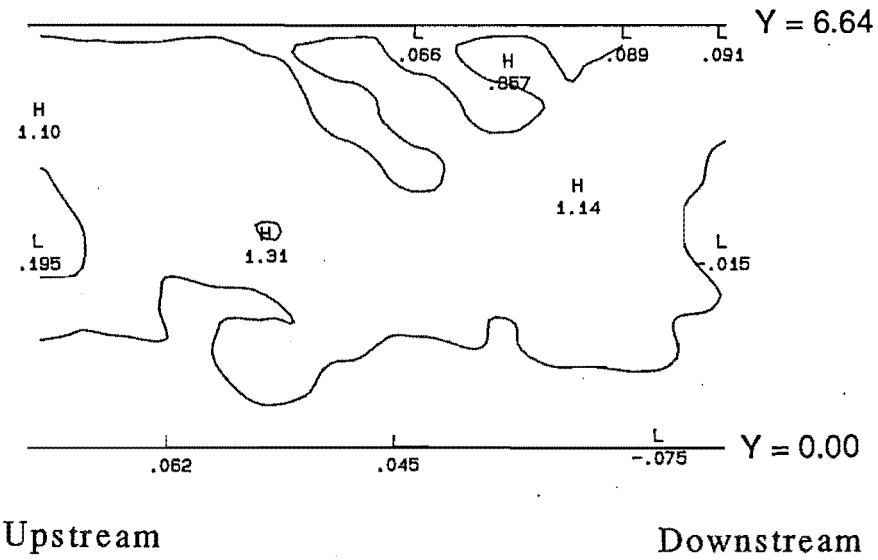

(B) INSTANTANEOUS RE = 839

$\Psi = 30°$

Figure I-4 A-L

Along the $\alpha = 0°$ azimuth of the proximal limb, $Re_{mean} = 1500$

A)$\Psi = 0°$ B)$\Psi = 30°$ C)$\Psi = 60°$ D)$\Psi = 90°$ E)$\Psi = 120°$

F$\Psi = 150°$ G)$\Psi = 180°$ H)$\Psi = 210°$ I)$\Psi = 240°$ J)$\Psi = 270°$

K)$\Psi = 300°$ L)$\Psi = 330°$.

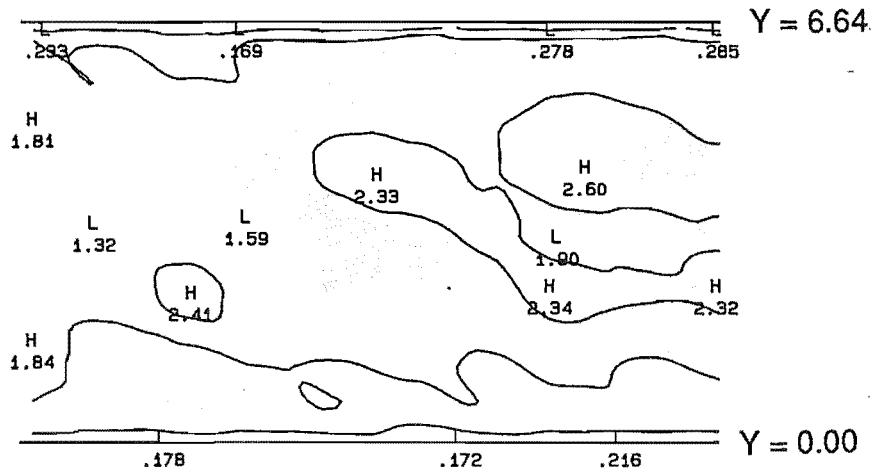

Upstream Downstream

(C) INSTANTANEOUS RE = 1045

$\Psi = 60°$

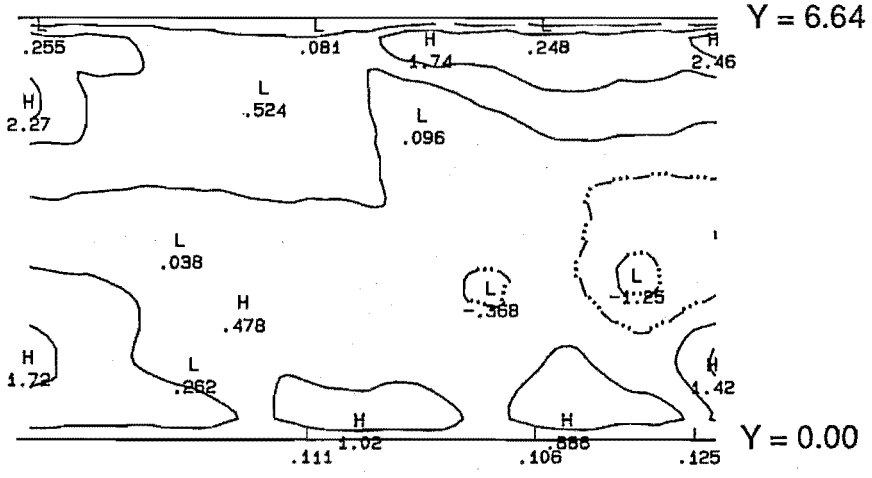

Upstream Downstream

(D) INSTANTANEOUS RE = 1446

$\Psi = 90°$

Figure I-4 A-L (cont.)

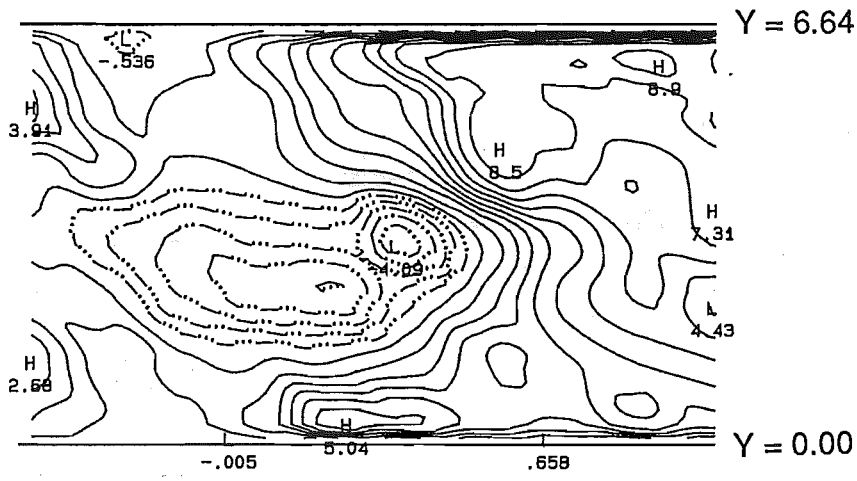

Upstream Downstream

(E) INSTANTANEOUS RE = 2018

$\Psi = 120°$

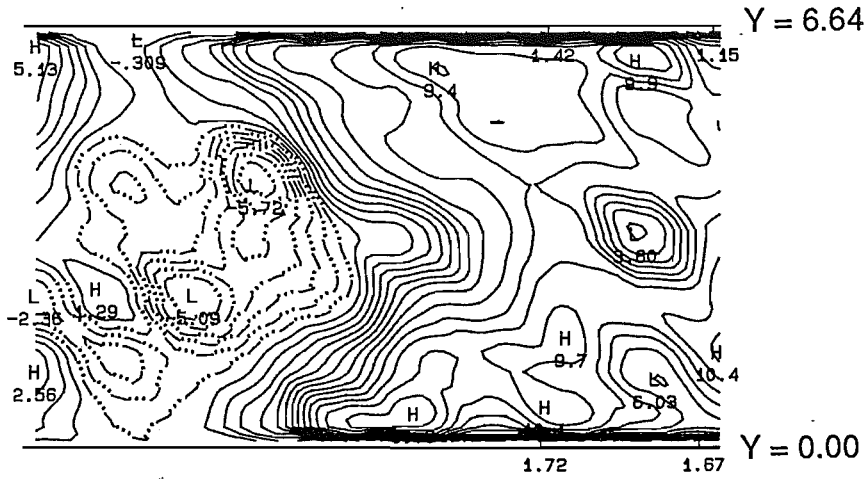

Upstream Downstream

(F) INSTANTANEOUS RE = 2343

$\Psi = 150°$

Figure I-4 A-L (cont.)

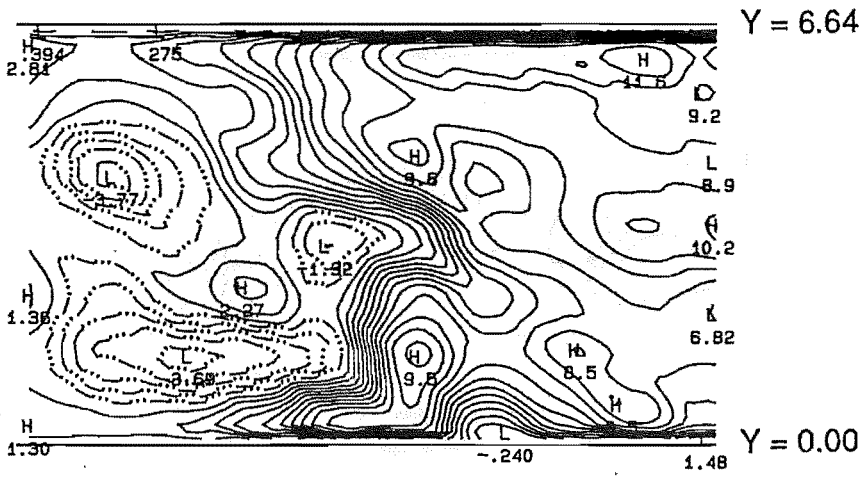

(G) INSTANTANEOUS RE = 2471

$\Psi = 180°$

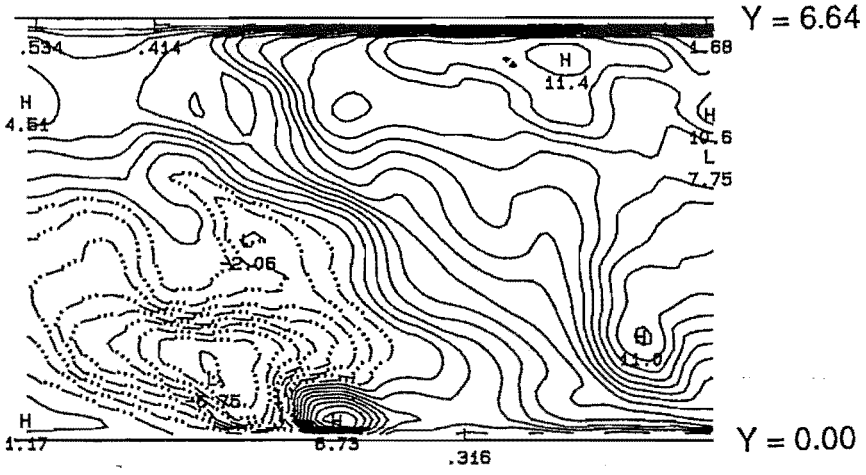

(H) INSTANTANEOUS RE = 2486

$\Psi = 210°$

Figure I-4 A-L (cont.)

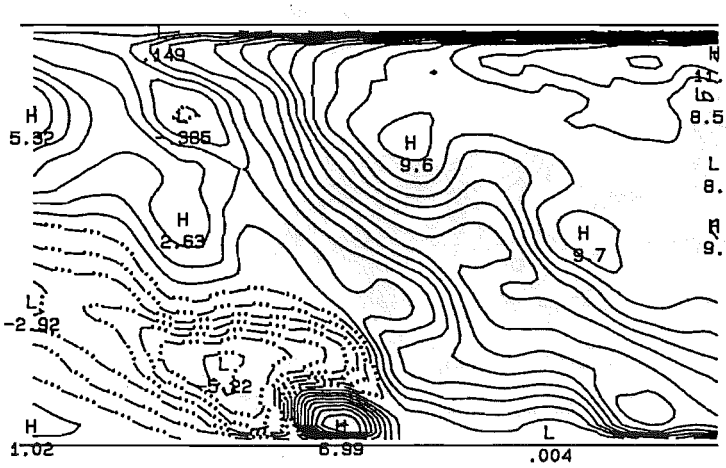

Upstream Downstream

(I) INSTANTANEOUS RE = 2459

$\Psi = 240°$

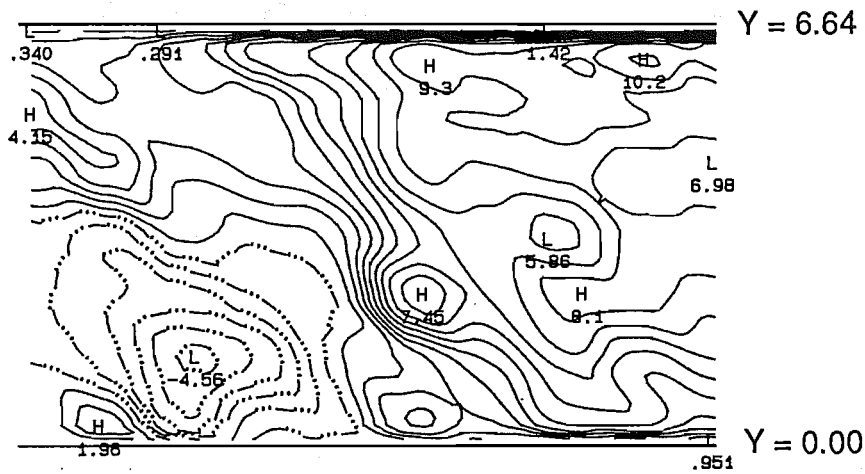

Upstream Downstream

(J) INSTANTANEOUS RE = 2318

$\Psi = 270°$

Figure I-4 A-L (cont.)

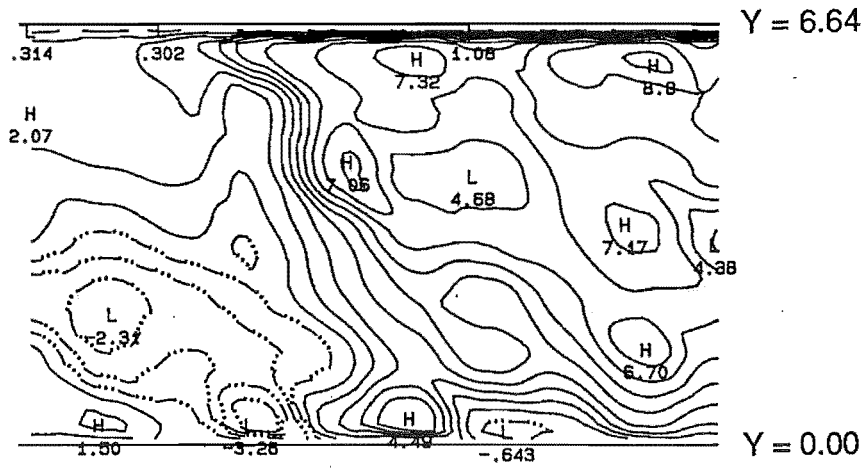

Upstream Downstream

(K) INSTANTANEOUS RE = 2043

$\Psi = 300°$

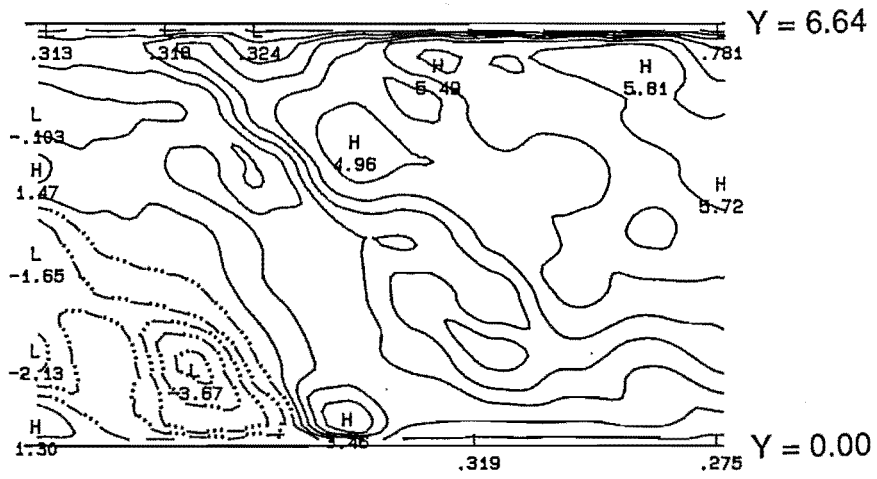

Upstream Downstream

(L) INSTANTANEOUS RE = 1618

$\Psi = 330°$

Figure I-4 A-L (cont.)

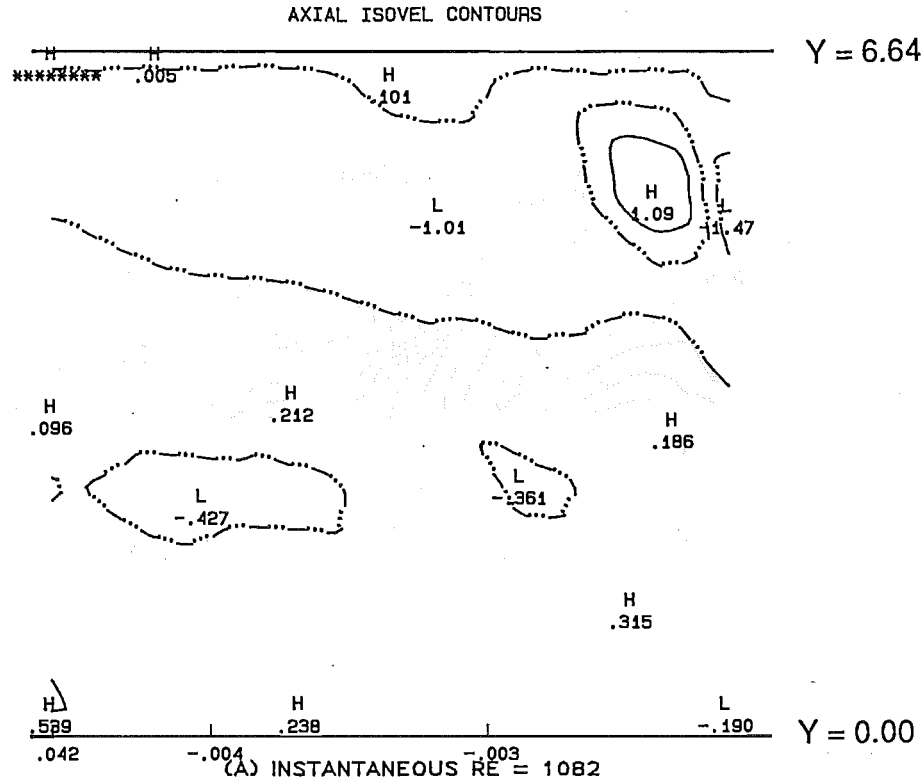

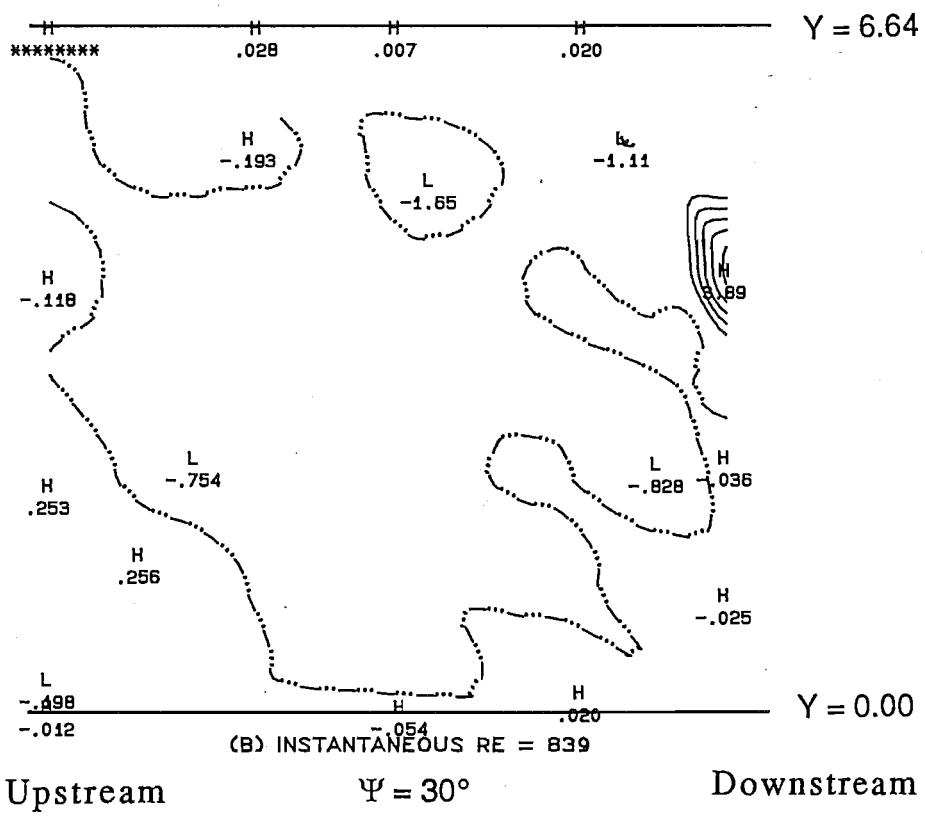

Figure I-5 A-L

Along the $\alpha = 180°$ azimuth of the proximal stem, $Re_{mean} = 1500$

A)$\Psi = 0°$ B)$\Psi = 30°$ C)$\Psi = 60°$ D)$\Psi = 90°$ E)$\Psi = 120°$

F$\Psi = 150°$ G)$\Psi = 180°$ H)$\Psi = 210°$ I)$\Psi = 240°$ J)$\Psi = 270°$

K)$\Psi = 300°$ L)$\Psi = 330°$.

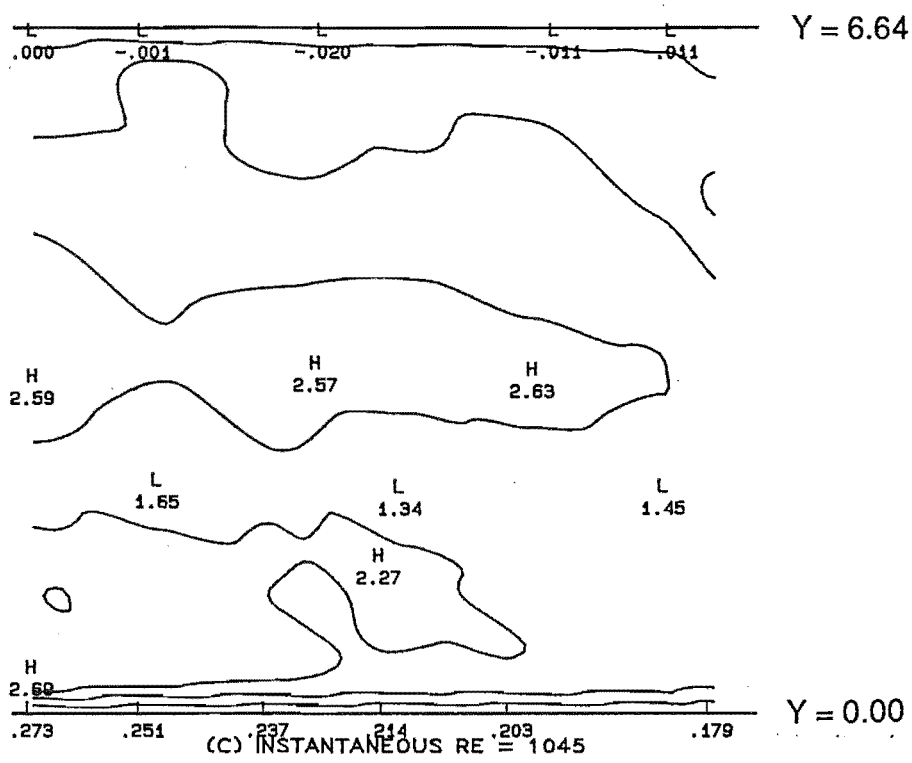

Upstream $\Psi = 60°$ Downstream

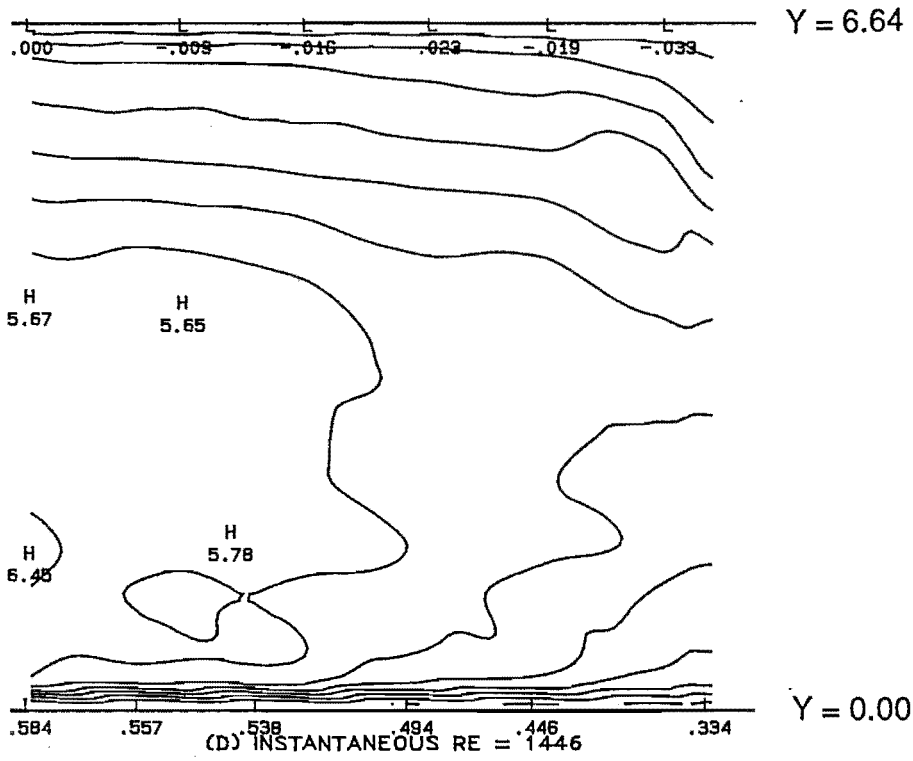

Upstream $\Psi = 90°$ Downstream

Figure I-5 A-L (cont.)

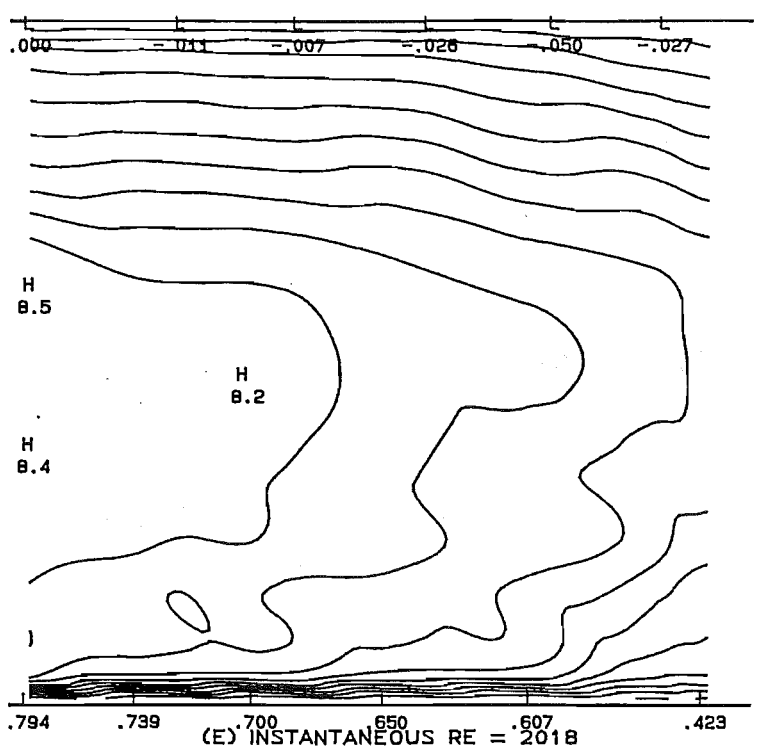

Upstream $\Psi = 120°$ Downstream

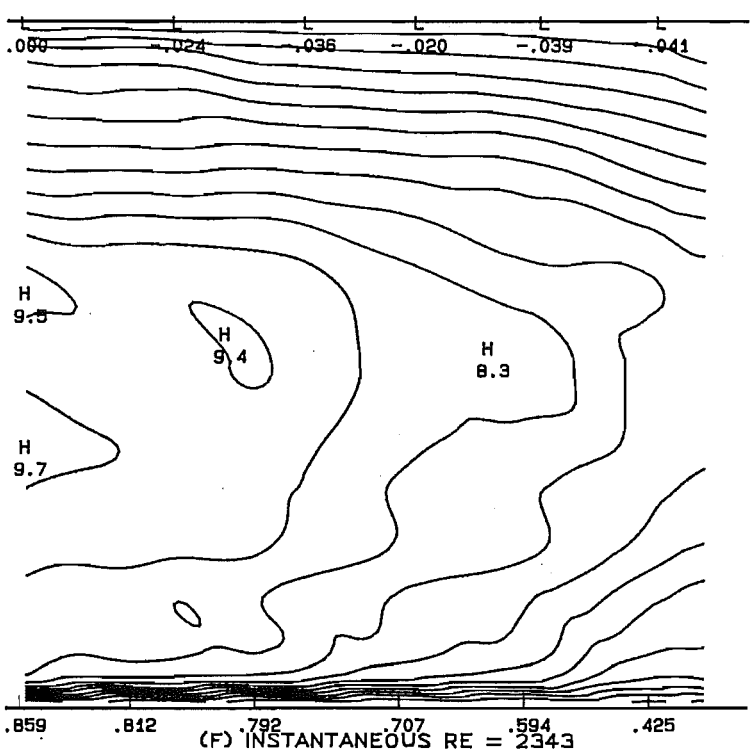

Upstream $\Psi = 150°$ Downstream

Figure I-5 A-L (cont.)

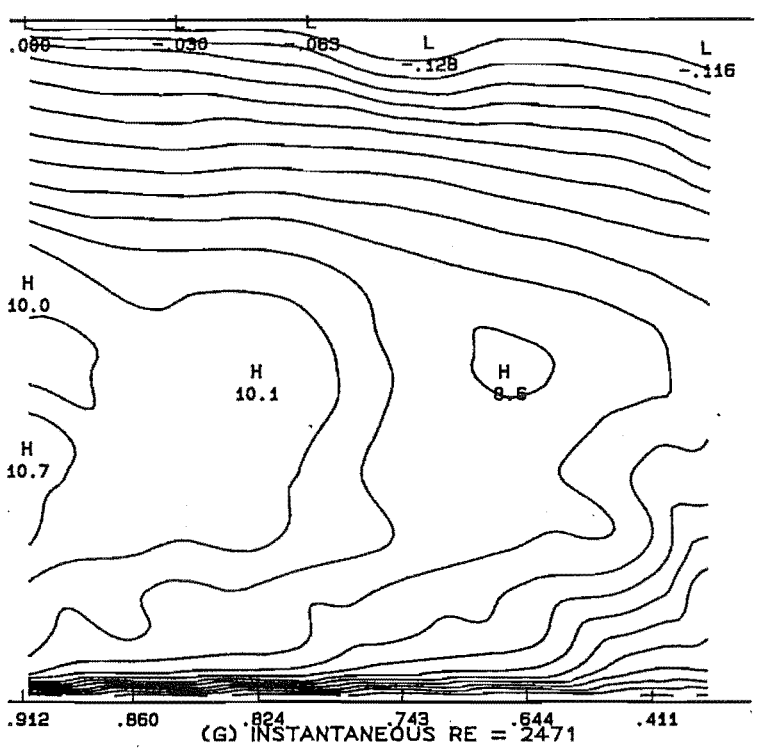

Upstream $\Psi = 180°$ Downstream

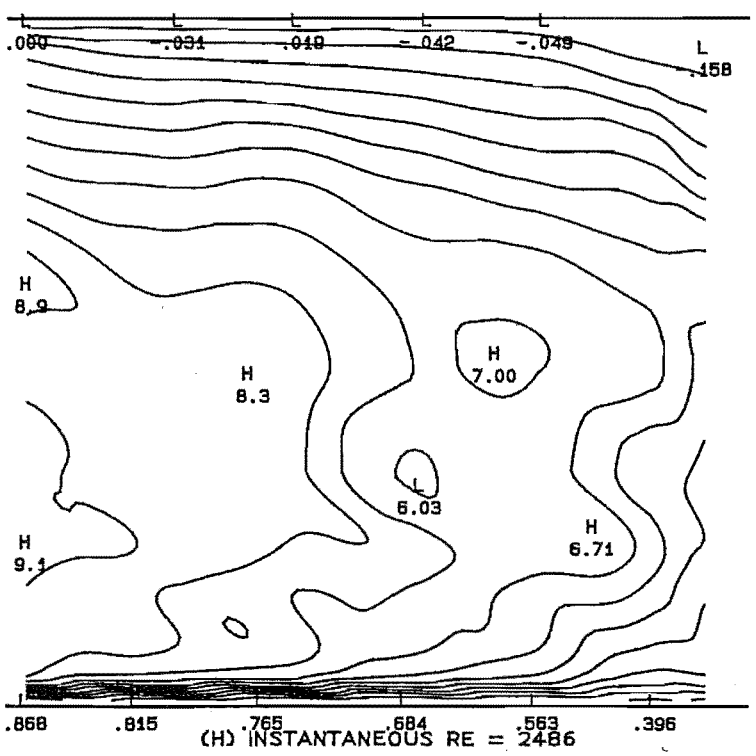

Upstream $\Psi = 210°$ Downstream

Figure I-5 A-L (cont.)

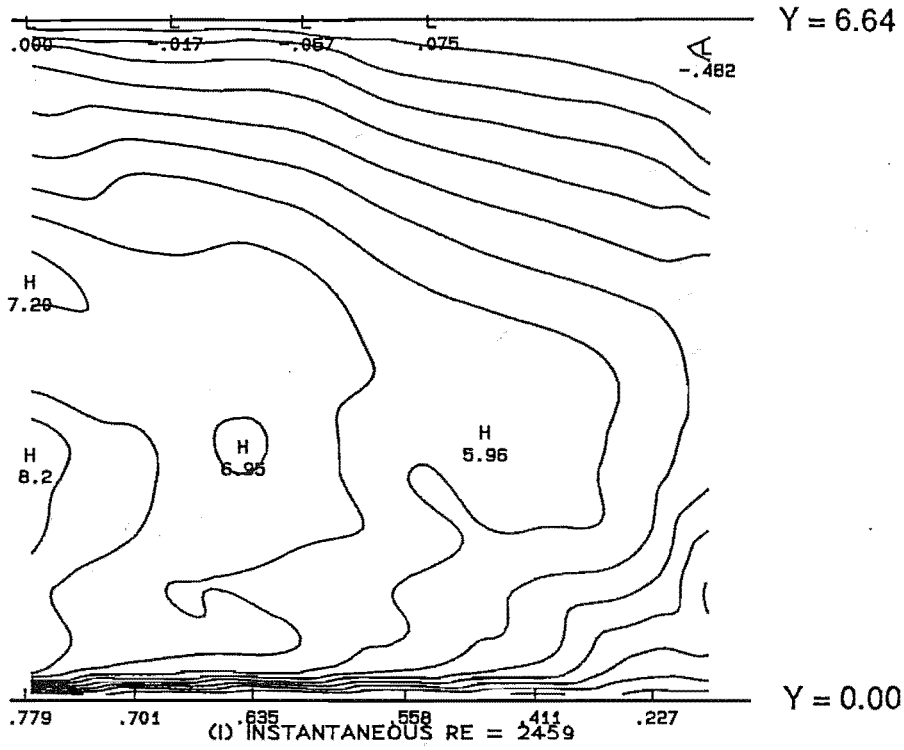

Upstream $\Psi = 240°$ Downstream

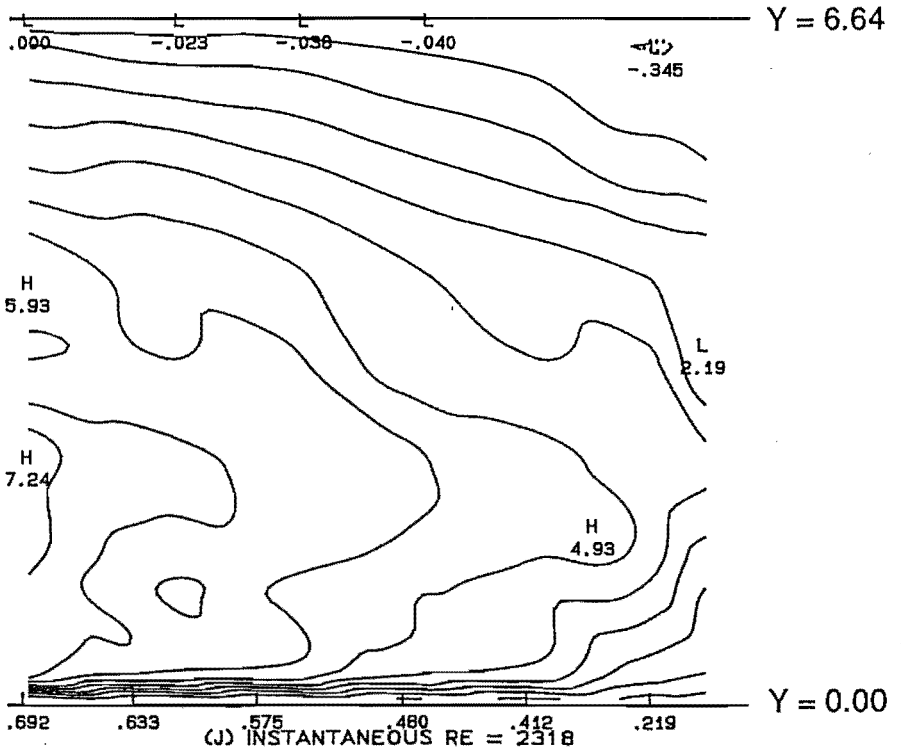

Upstream $\Psi = 270°$ Downstream

Figure I-5 A-L (cont.)

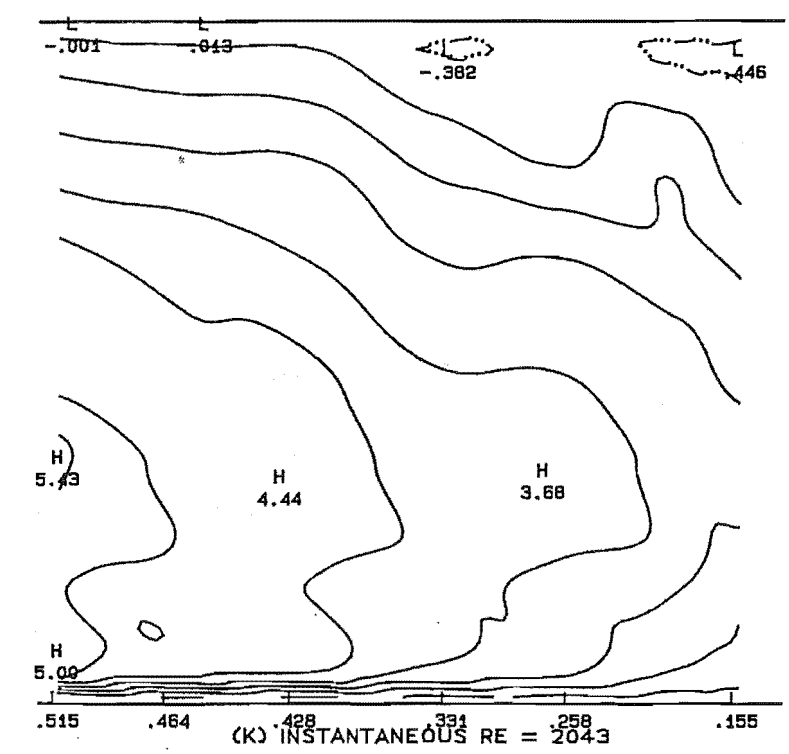

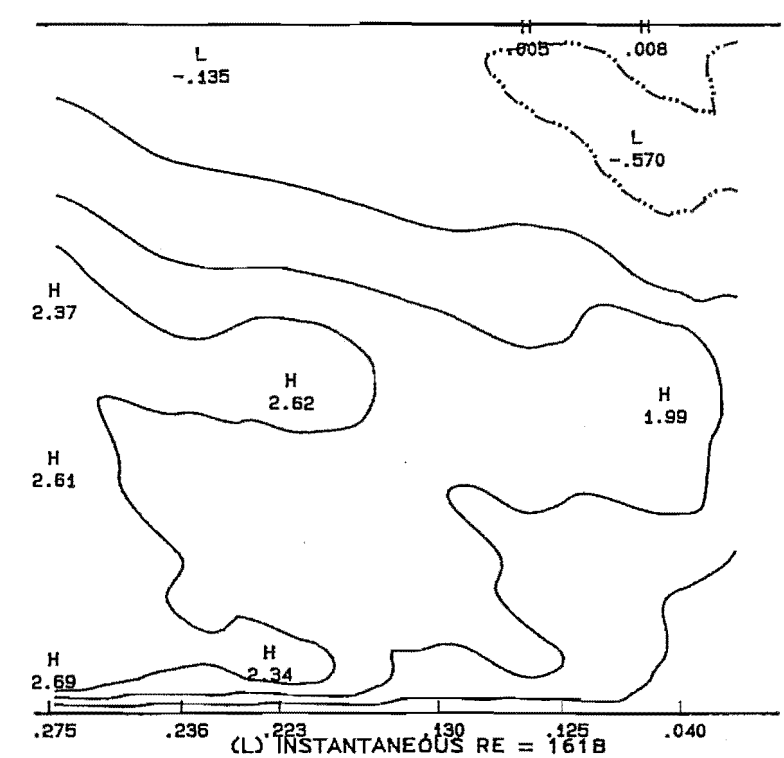

Figure I-5 A-L (cont.)

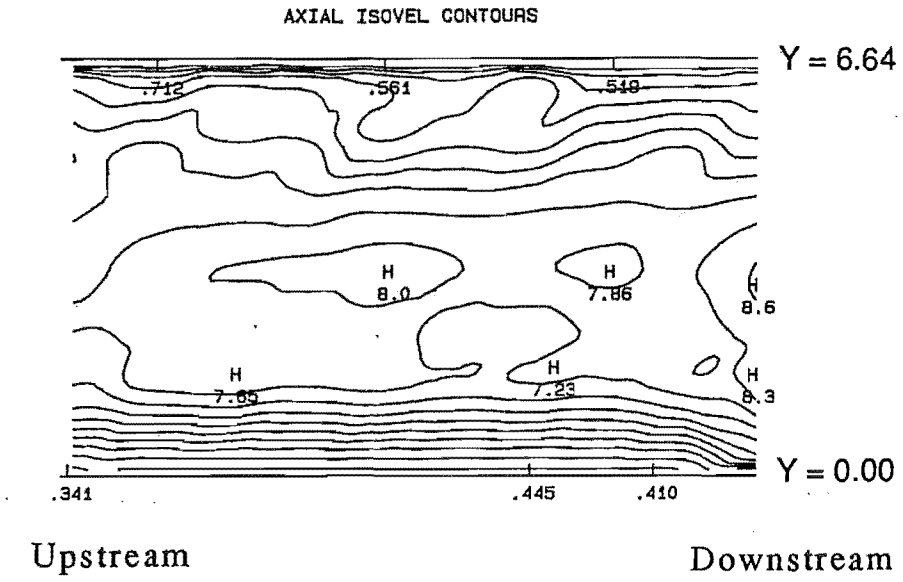

(A) INSTANTANEOUS RE = 1082

$\Psi = 0°$

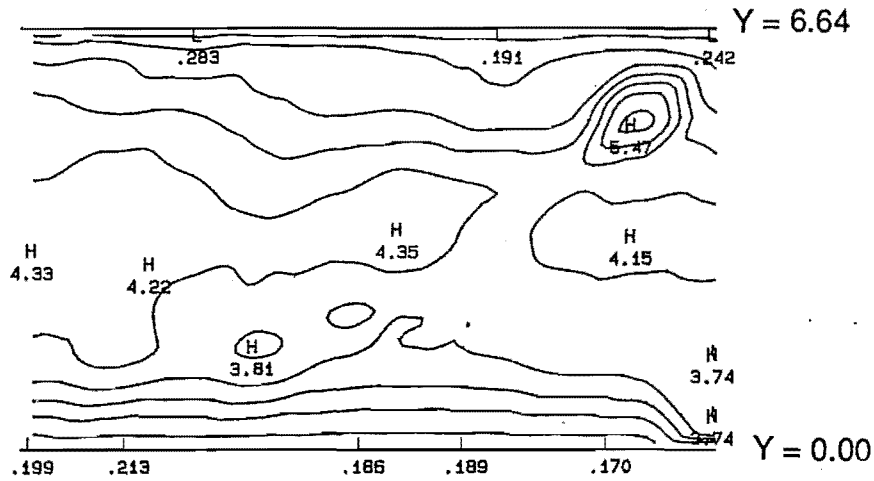

(B) INSTANTANEOUS RE = 839

$\Psi = 30°$

Figure I-6 A-L

Along the $\alpha = 180°$ azimuth of the proximal limb, $Re_{mean} = 1500$

A)$\Psi = 0°$ B)$\Psi = 30°$ C)$\Psi = 60°$ D)$\Psi = 90°$ E)$\Psi = 120°$

F$\Psi = 150°$ G)$\Psi = 180°$ H)$\Psi = 210°$ I)$\Psi = 240°$ J)$\Psi = 270°$

K)$\Psi = 300°$ L)$\Psi = 330°$.

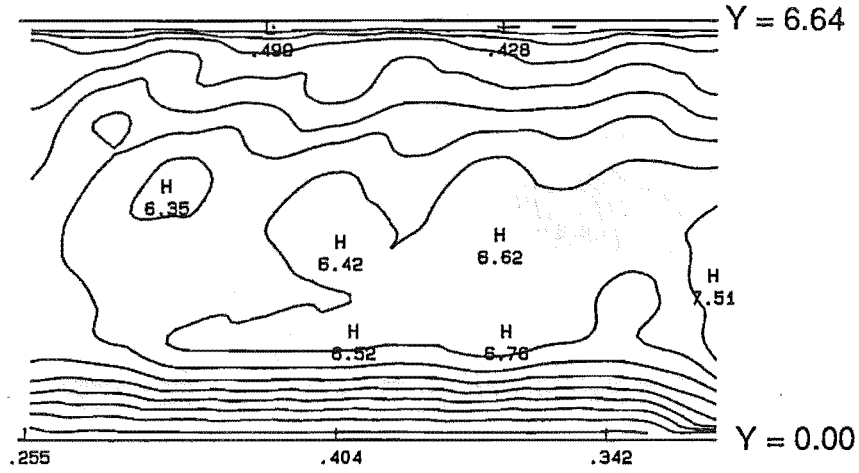

Upstream Downstream

(C) INSTANTANEOUS RE = 1045

$\Psi = 60°$

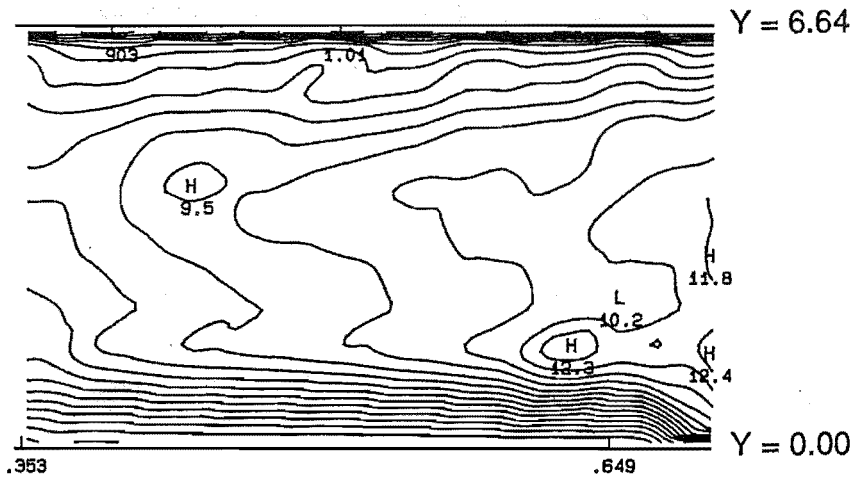

Upstream Downstream

(D) INSTANTANEOUS RE = 1446

$\Psi = 90°$

Figure I-6 A-L (cont.)

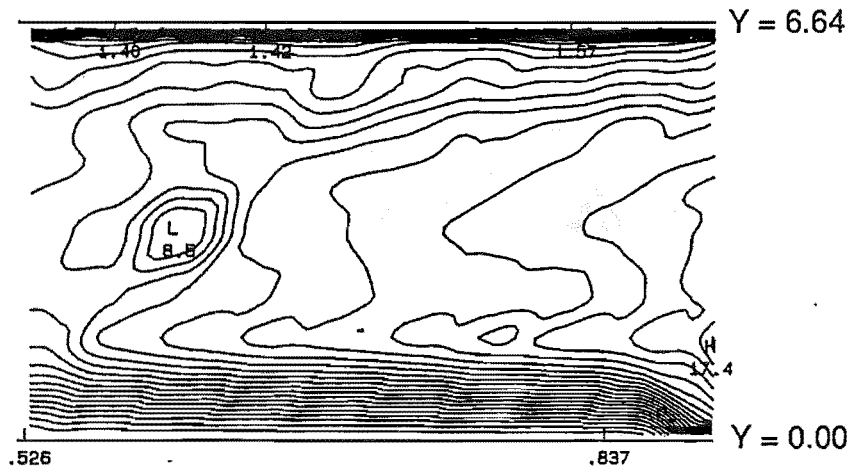

Upstream Downstream

(E) INSTANTANEOUS RE = 2018

$\Psi = 120°$

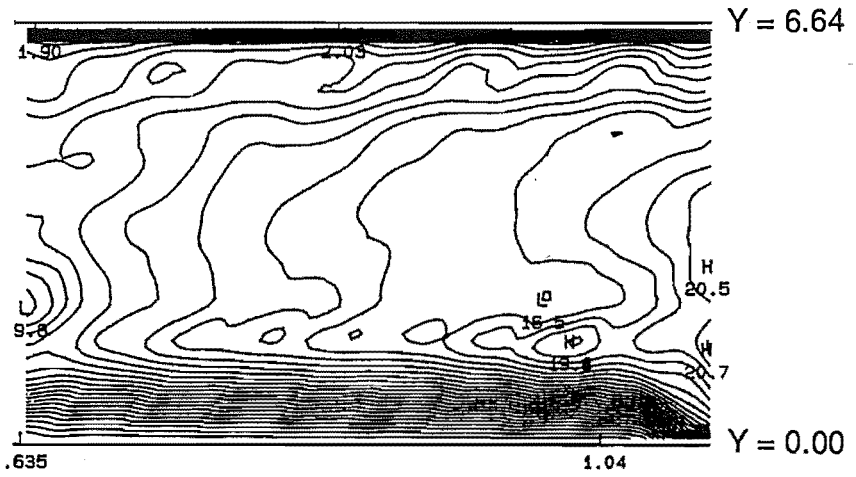

Upstream Downstream

(F) INSTANTANEOUS RE = 2343

$\Psi = 150°$

Figure I-6 A-L (cont.)

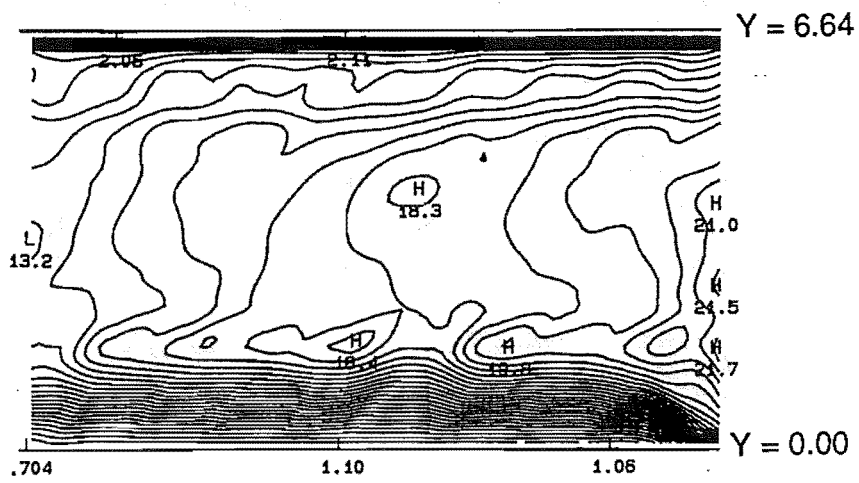

Upstream Downstream

(G) INSTANTANEOUS RE = 2471

$\Psi = 180°$

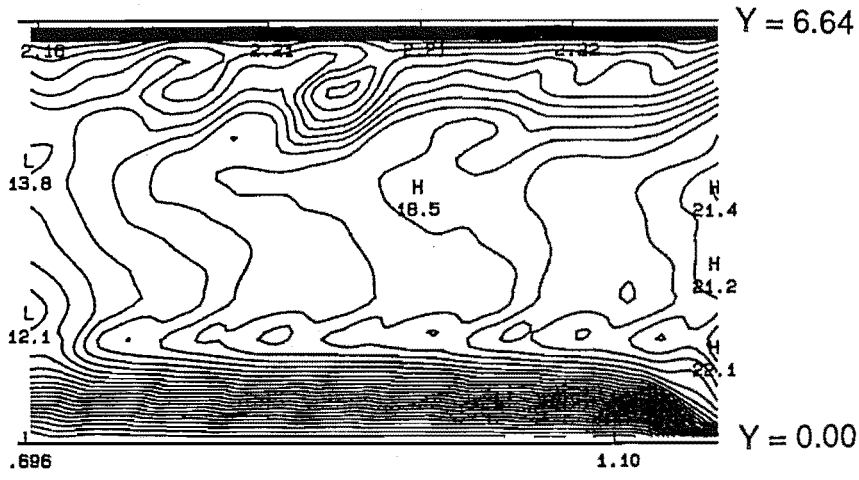

Upstream Downstream

(H) INSTANTANEOUS RE = 2486

$\Psi = 210°$

Figure I-6 A-L (cont.)

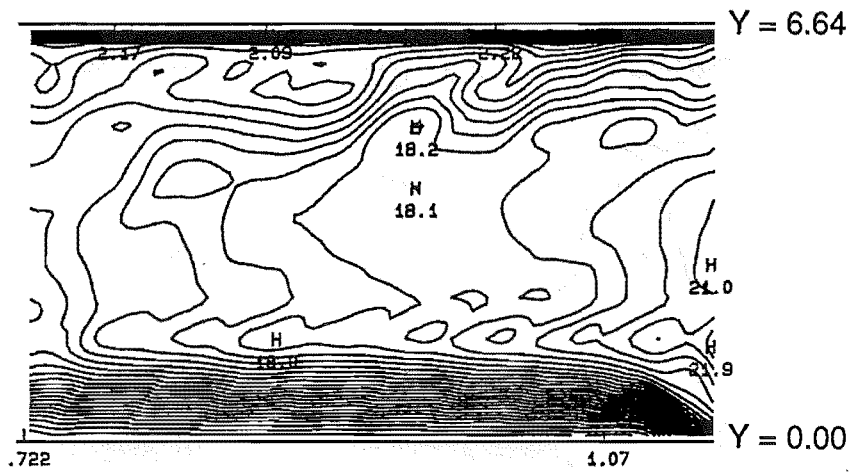

Upstream Downstream

(I) INSTANTANEOUS RE = 2459

$\Psi = 240°$

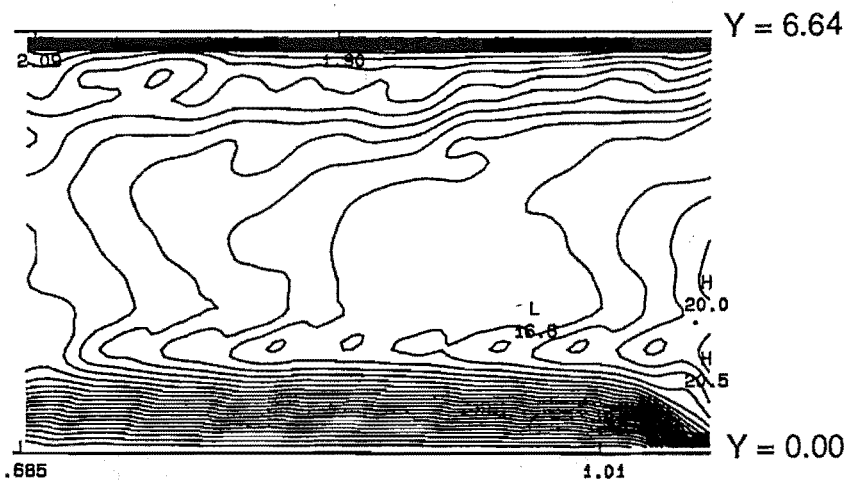

Upstream Downstream

(J) INSTANTANEOUS RE = 2318

$\Psi = 270°$

Figure I-6 A-L (cont.)

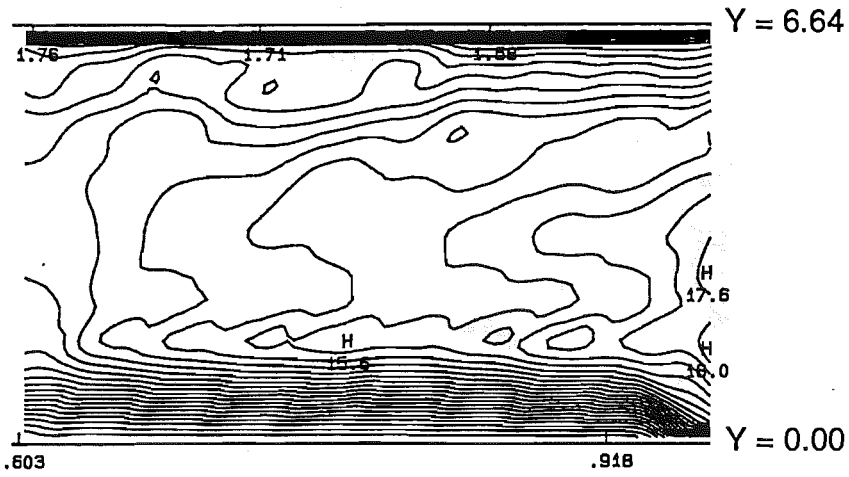

Upstream Downstream

(K) INSTANTANEOUS RE = 2043

$\Psi = 300°$

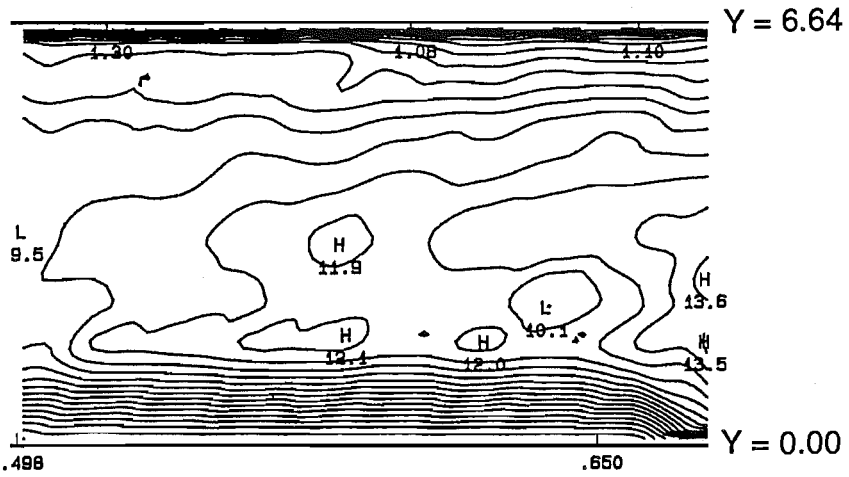

Upstream Downstream

(L) INSTANTANEOUS RE = 1618

$\Psi = 330°$

Figure I-6 A-L (cont.)

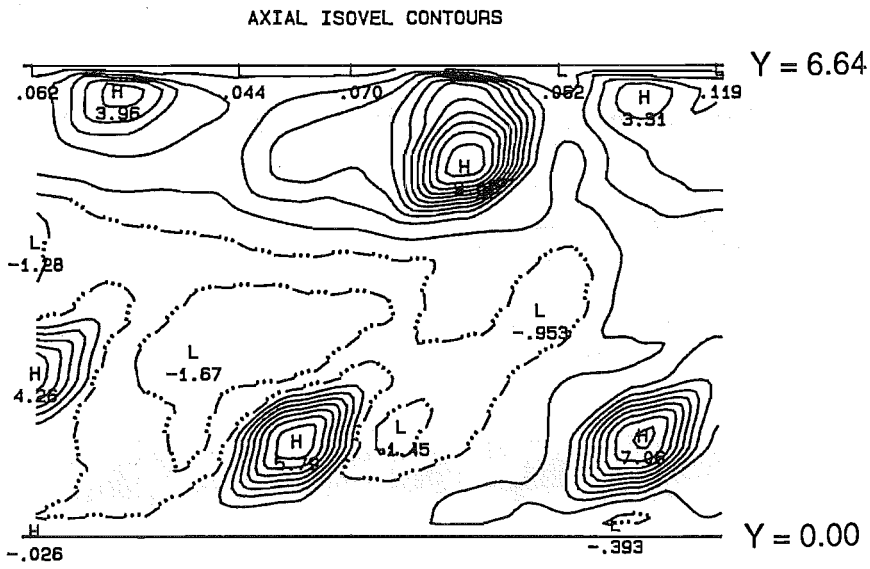

(A) INSTANTANEOUS RE = 1082

$\Psi = 0°$

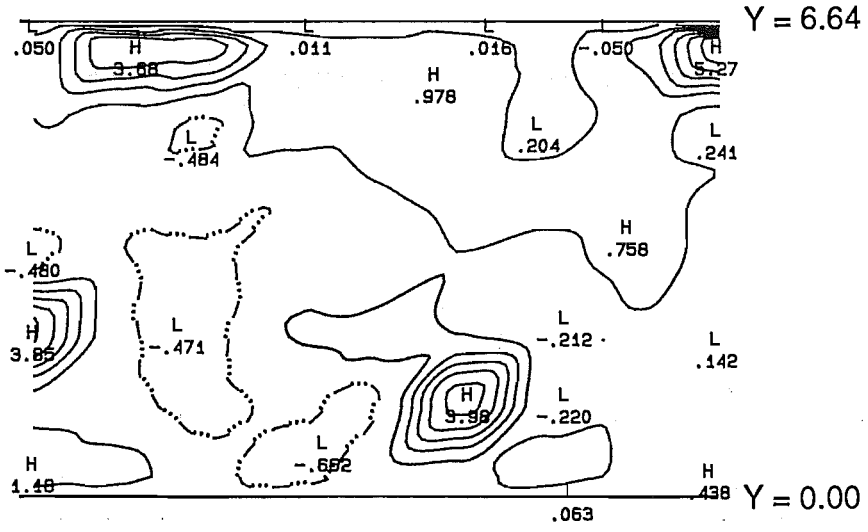

(B) INSTANTANEOUS RE = 839

$\Psi = 30°$

Figure I-7 A-L

Along the $\alpha = 0°$ azimuth of the distal stem, $Re_{mean} = 1500$

A)$\Psi = 0°$ B)$\Psi = 30°$ C)$\Psi = 60°$ D)$\Psi = 90°$ E)$\Psi = 120°$

F$\Psi = 150°$ G)$\Psi = 180°$ H)$\Psi = 210°$ I)$\Psi = 240°$ J)$\Psi = 270°$

K)$\Psi = 300°$ L)$\Psi = 330°$.

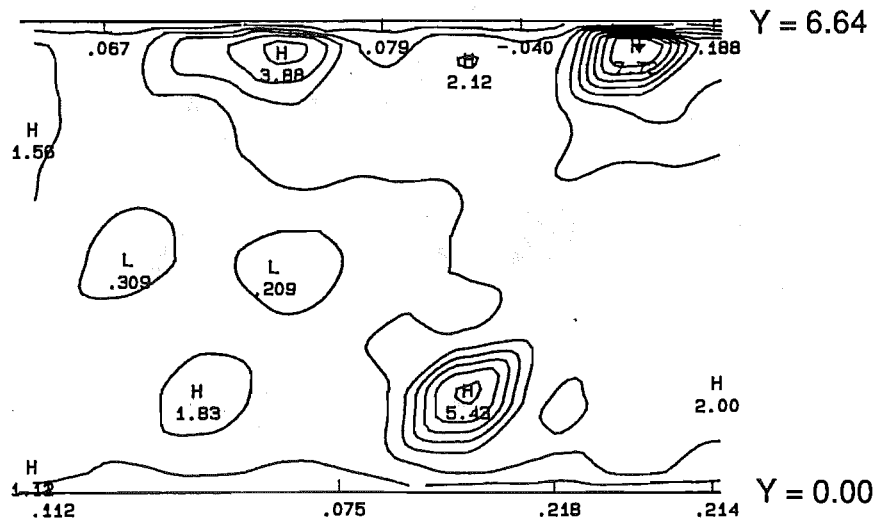

Upstream Downstream

(C) INSTANTANEOUS RE = 1045

$\Psi = 60°$

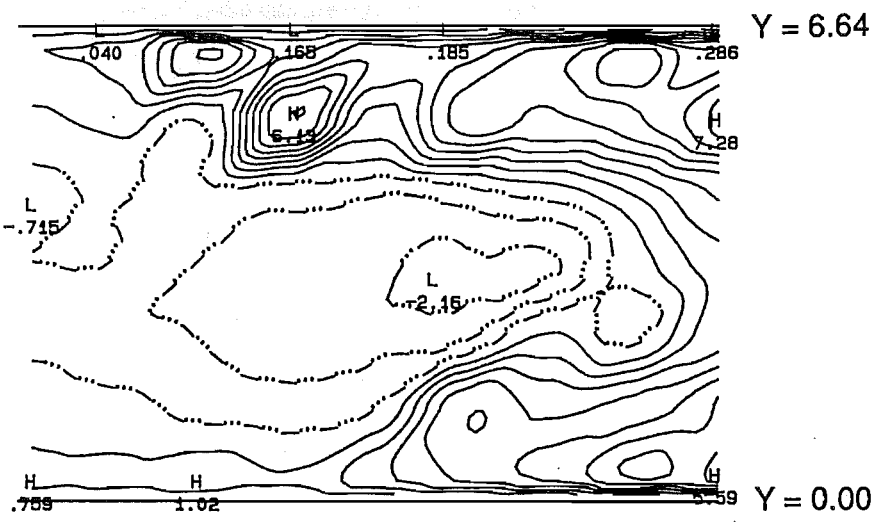

Upstream Downstream

(D) INSTANTANEOUS RE = 1446

$\Psi = 90°$

Figure I-7 A-L (cont.)

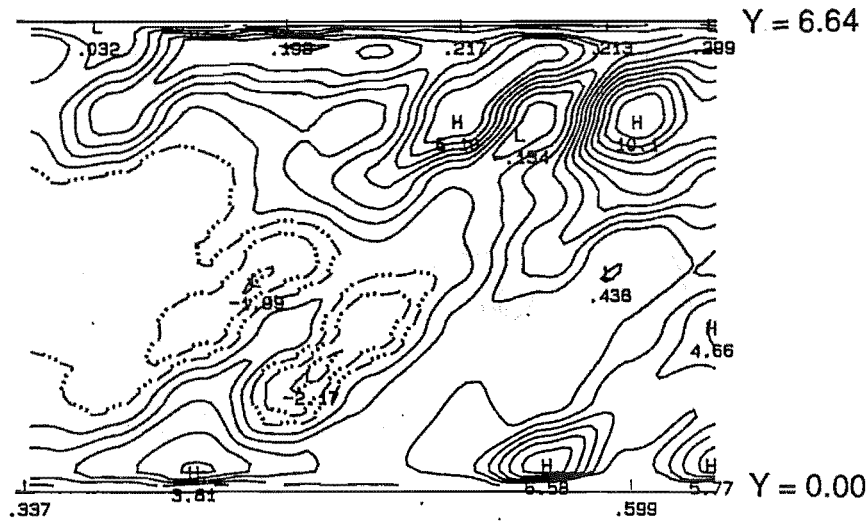

Upstream Downstream

(E) INSTANTANEOUS RE = 2018

$\Psi = 120°$

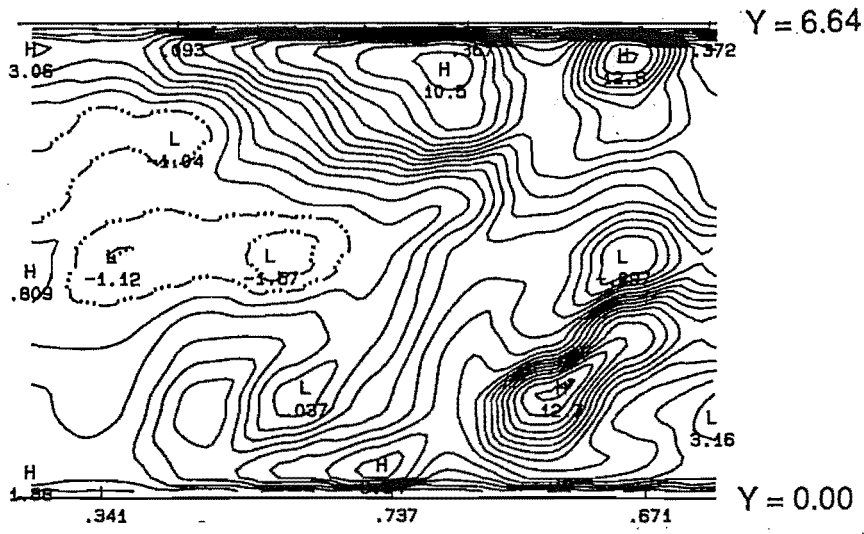

Upstream Downstream

(F) INSTANTANEOUS RE = 2343

$\Psi = 150°$

Figure I-7 A-L (cont.)

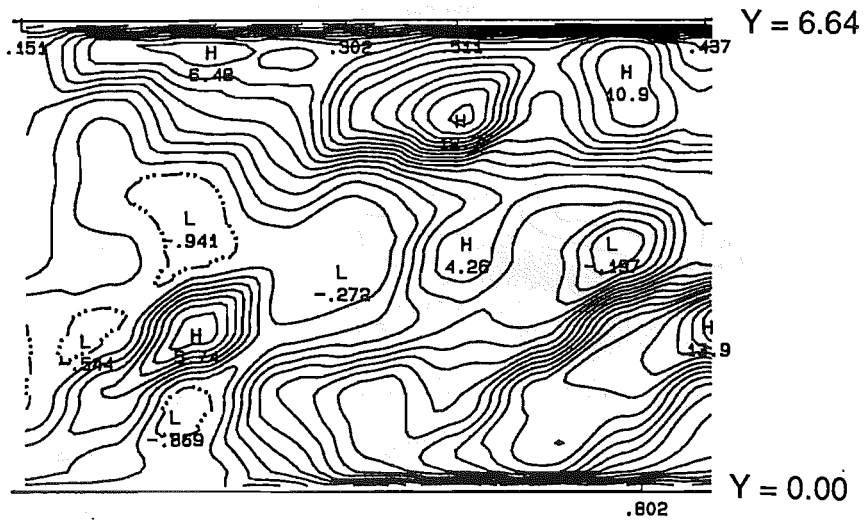

Upstream Downstream

(G) INSTANTANEOUS RE = 2471

$\Psi = 180°$

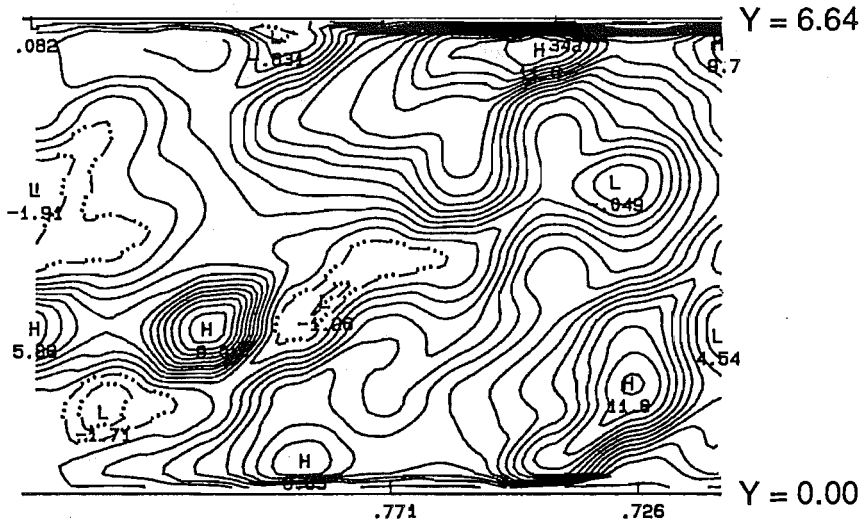

Upstream Downstream

(H) INSTANTANEOUS RE = 2486

$\Psi = 210°$

Figure I-7 A-L (cont.)

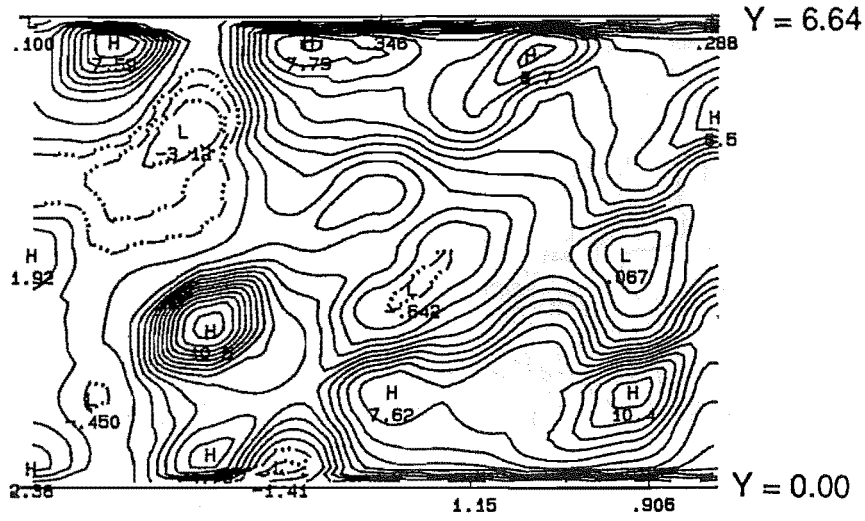

Upstream Downstream

(I) INSTANTANEOUS RE = 2459

$\Psi = 240°$

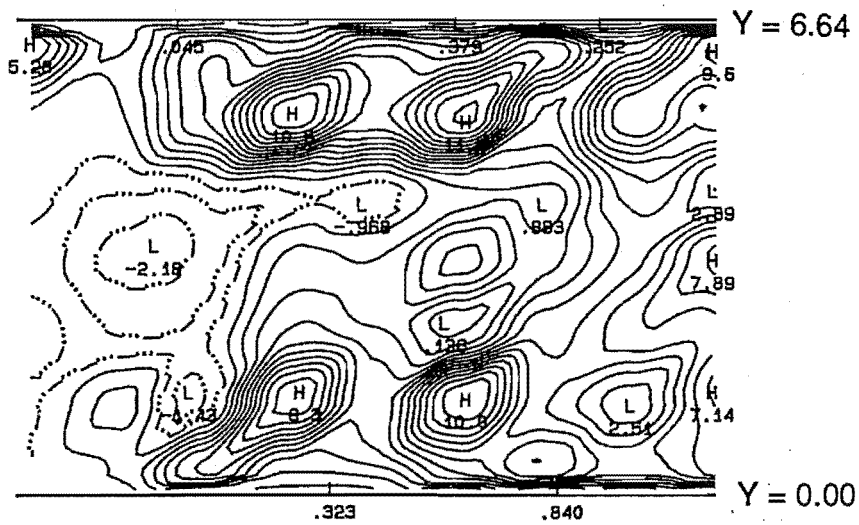

Upstream Downstream

(J) INSTANTANEOUS RE = 2318

$\Psi = 270°$

Figure I-7 A-L (cont.)

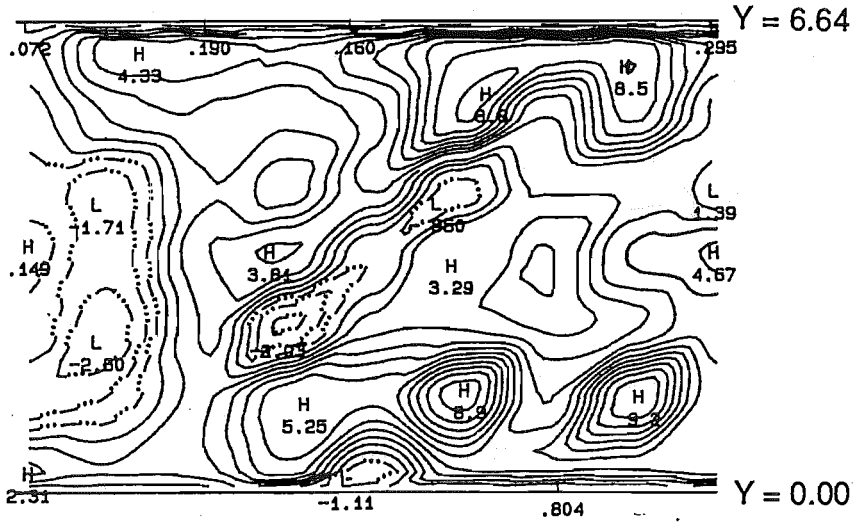

Upstream Downstream

(K) INSTANTANEOUS RE = 2043

$\Psi = 300°$

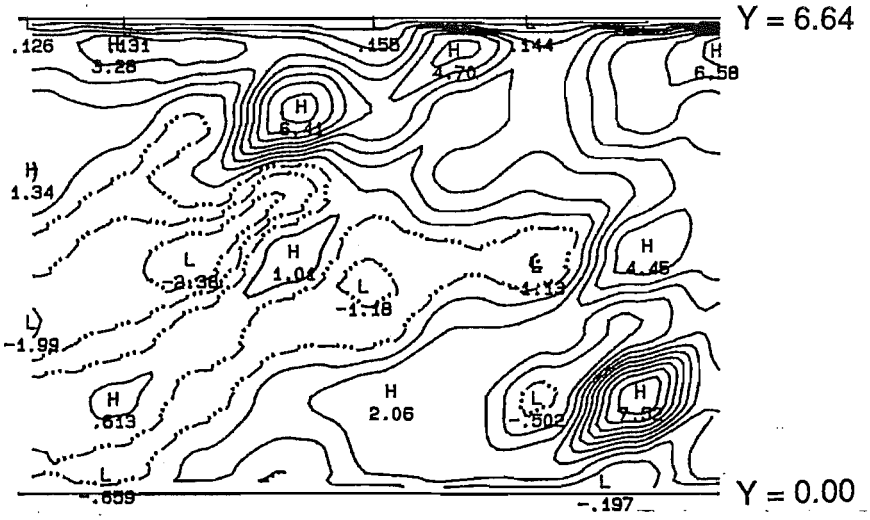

Upstream Downstream

(L) INSTANTANEOUS RE = 1618

$\Psi = 330°$

Figure I-7 A-L (cont.)

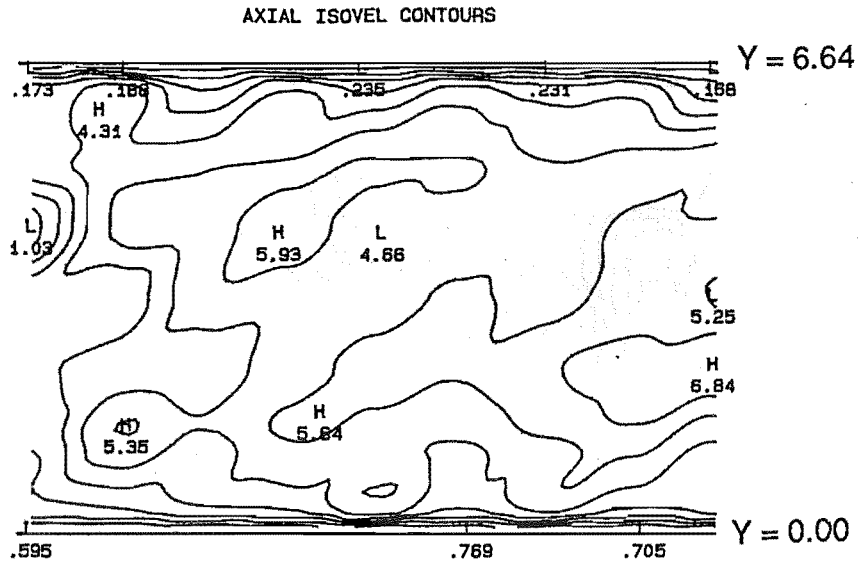

(A) INSTANTANEOUS RE = 1082

$\Psi = 0°$

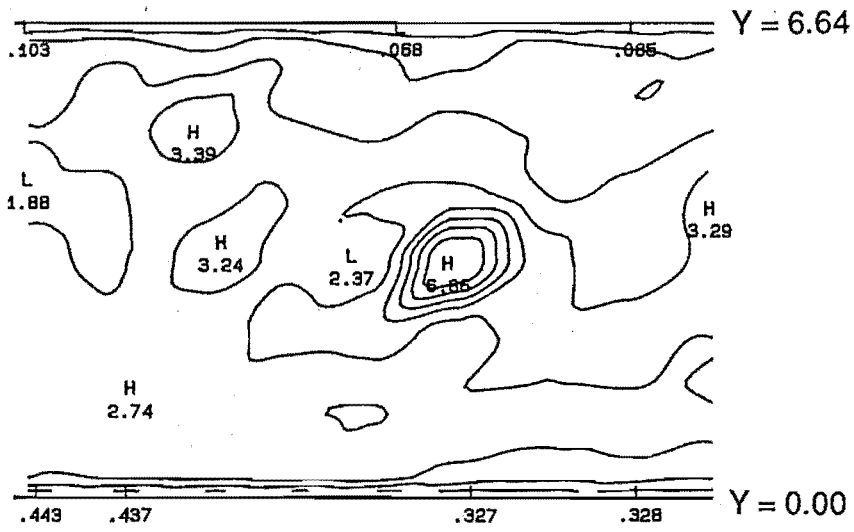

(B) INSTANTANEOUS RE = 839

$\Psi = 30°$

Figure I-8 A-L

Along the $\alpha = 180°$ azimuth of the distal stem, $Re_{mean} = 1500$

A)$\Psi = 0°$ B)$\Psi = 30°$ C)$\Psi = 60°$ D)$\Psi = 90°$ E)$\Psi = 120°$

F$\Psi = 150°$ G)$\Psi = 180°$ H)$\Psi = 210°$ I)$\Psi = 240°$ J)$\Psi = 270°$

K)$\Psi = 300°$ L)$\Psi = 330°$.

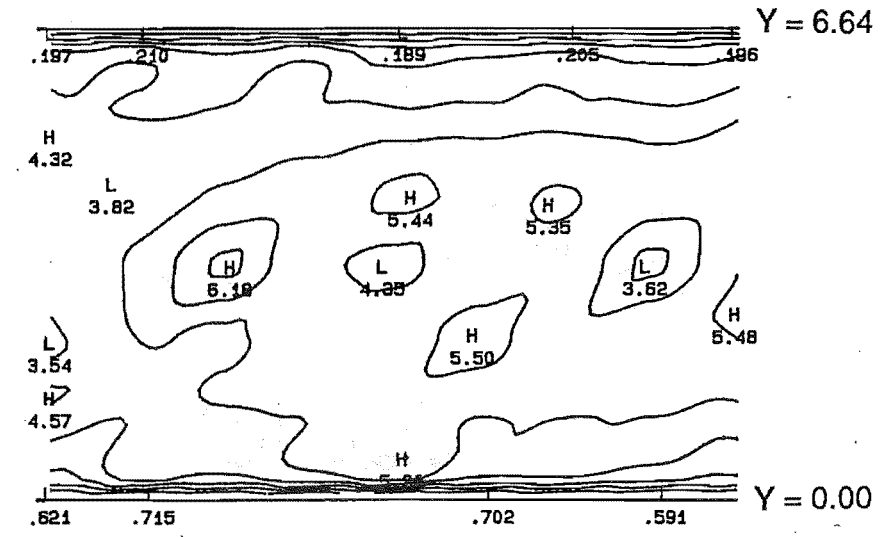

Upstream Downstream

(C) INSTANTANEOUS RE = 1045

$\Psi = 60°$

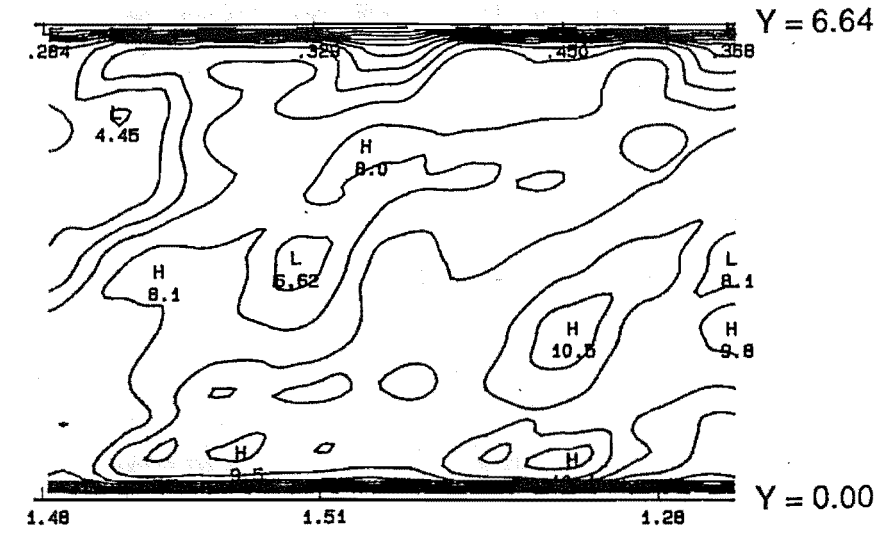

Upstream Downstream

(D) INSTANTANEOUS RE = 1446

$\Psi = 90°$

Figure I-8 A-L (cont.)

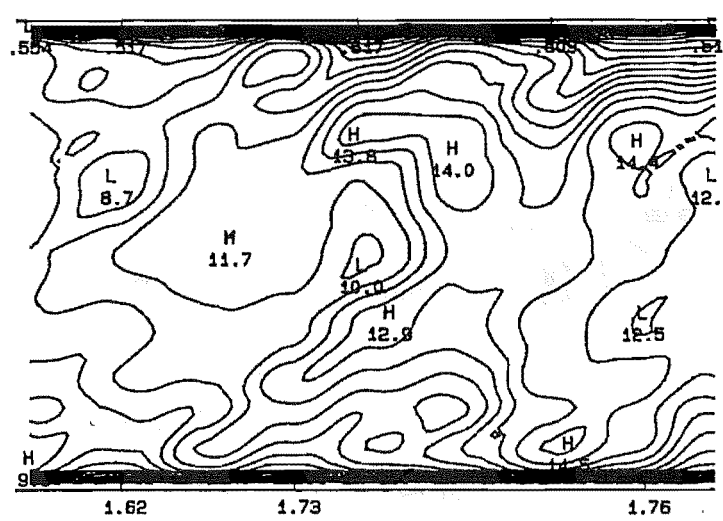

(E) INSTANTANEOUS RE = 2018

$\Psi = 120°$

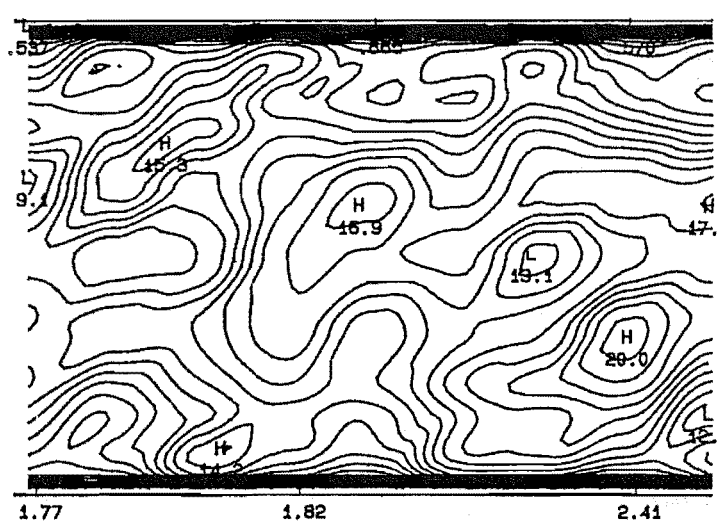

(F) INSTANTANEOUS RE = 2343

$\Psi = 150°$

Figure I-8 A-L (cont.)

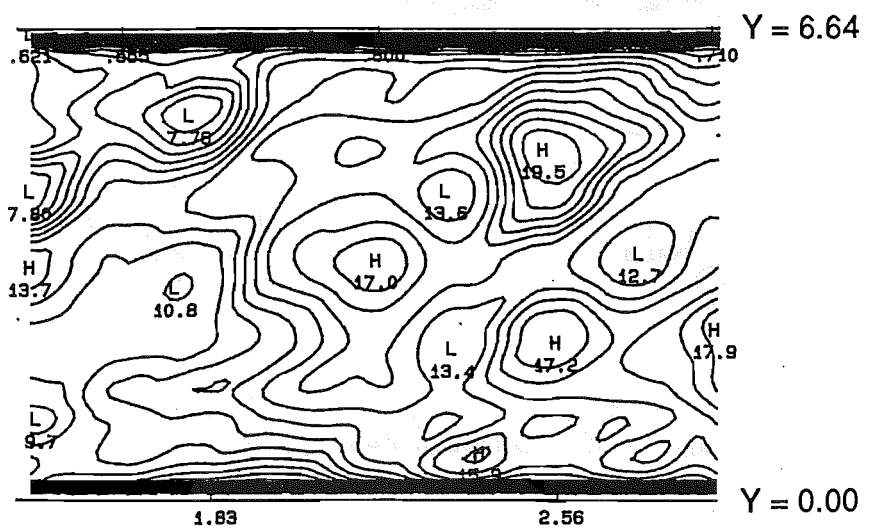

(G) INSTANTANEOUS RE = 2471

$\Psi = 180°$

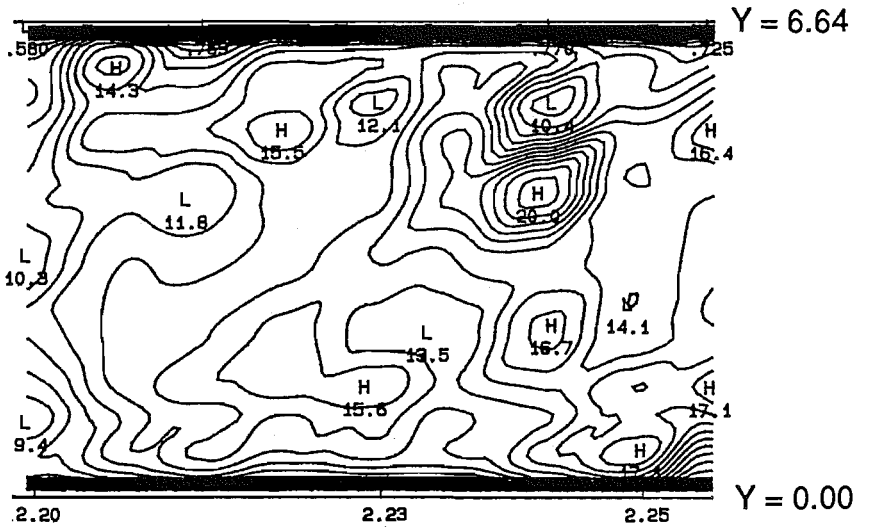

(H) INSTANTANEOUS RE = 2486

$\Psi = 210°$

Figure I-8 A-L (cont.)

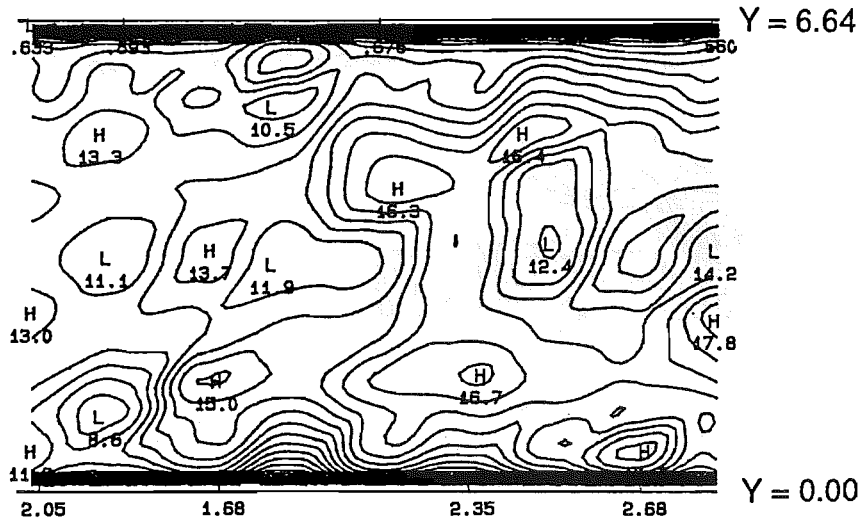

Upstream Downstream

(I) INSTANTANEOUS RE = 2459

$\Psi = 240°$

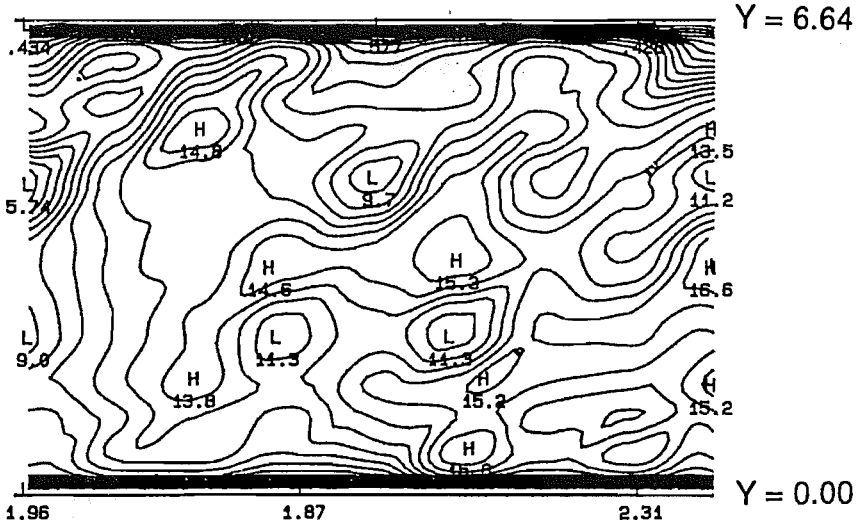

Upstream Downstream

(J) INSTANTANEOUS RE = 2318

$\Psi = 270°$

Figure I-8 A-L (cont.)

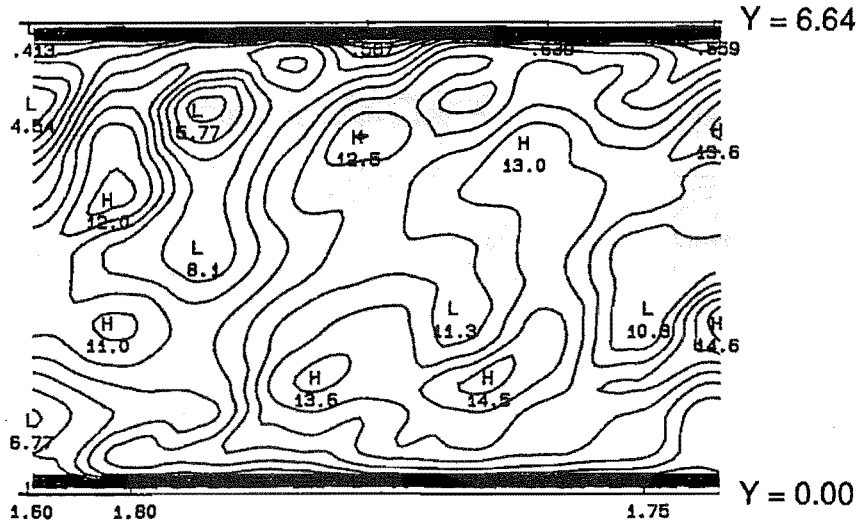

(K) INSTANTANEOUS RE = 2043

$\Psi = 300°$

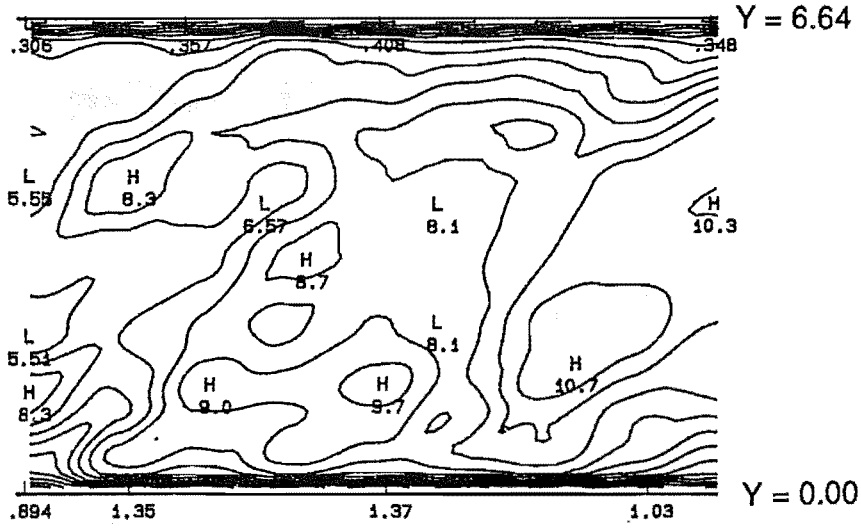

(L) INSTANTANEOUS RE = 1618

$\Psi = 330°$

Figure I-8 A-L (cont.)

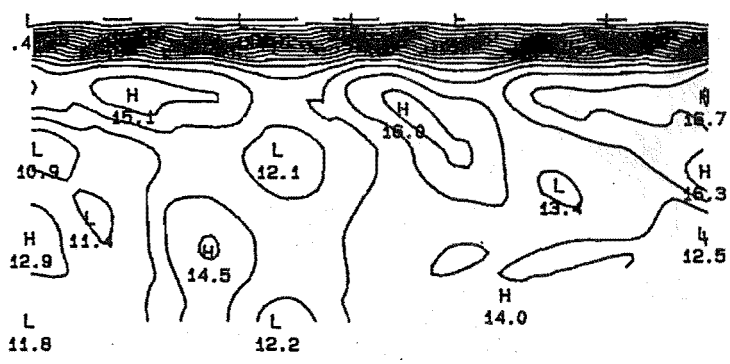

Upstream Downstream

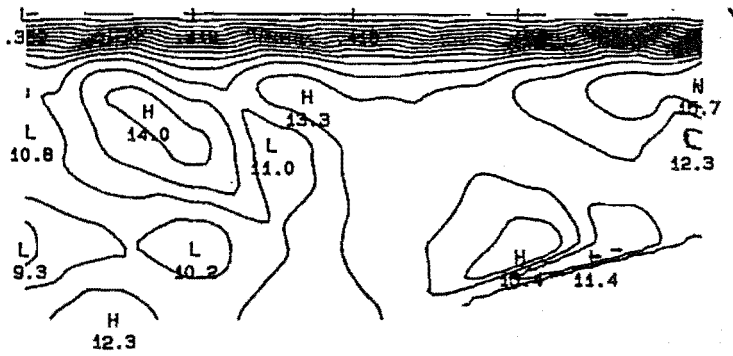

Upstream Downstream

Figure I-9 A-L

Along the $\alpha = 180°$ azimuth of the distal limb, $Re_{mean} = 1500$

A)$\Psi = 0°$ B)$\Psi = 30°$ C)$\Psi = 60°$ D)$\Psi = 90°$ E)$\Psi = 120°$

F$\Psi = 150°$ G)$\Psi = 180°$ H)$\Psi = 210°$ I)$\Psi = 240°$ J)$\Psi = 270°$

K)$\Psi = 300°$ L)$\Psi = 330°$.

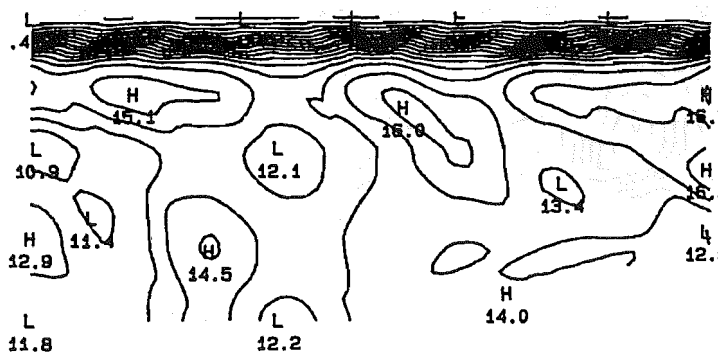

Upstream Downstream

(A) INSTANTANEOUS RE = 1082

$\Psi = 0°$

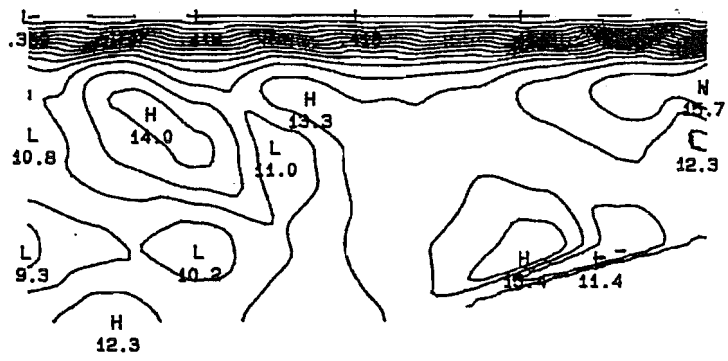

Upstream Downstream

(B) INSTANTANEOUS RE = 839

$\Psi = 30°$

Figure I-9 A-L

Along the $\alpha = 180°$ azimuth of the distal limb, $Re_{mean} = 1500$

A)$\Psi = 0°$ B)$\Psi = 30°$ C)$\Psi = 60°$ D)$\Psi = 90°$ E)$\Psi = 120°$

F$\Psi = 150°$ G)$\Psi = 180°$ H)$\Psi = 210°$ I)$\Psi = 240°$ J)$\Psi = 270°$

K)$\Psi = 300°$ L)$\Psi = 330°$.

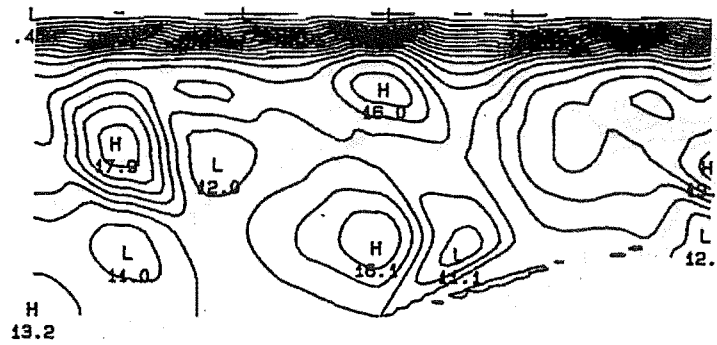

Upstream (C) INSTANTANEOUS RE = 1045 Downstream

$\Psi = 60°$

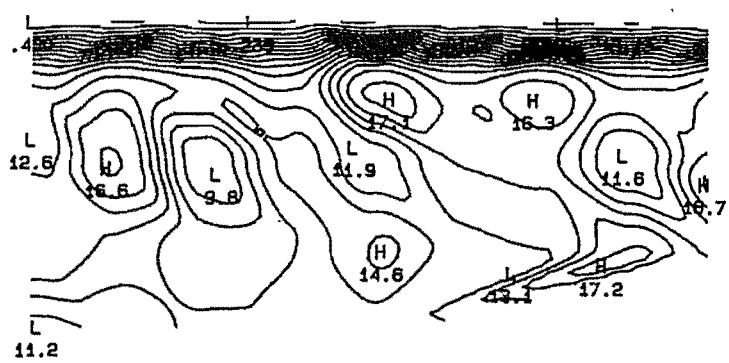

Upstream (D) INSTANTANEOUS RE = 1446 Downstream

$\Psi = 90°$

Figure I-9 A-L (cont.)

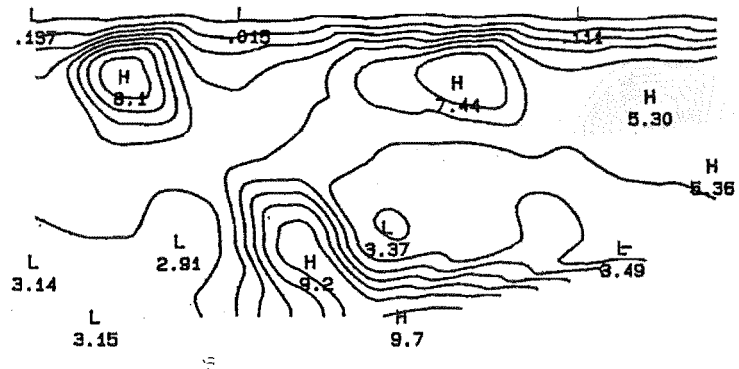

Upstream (I) INSTANTANEOUS RE = 2459 Downstream

$\Psi = 240°$

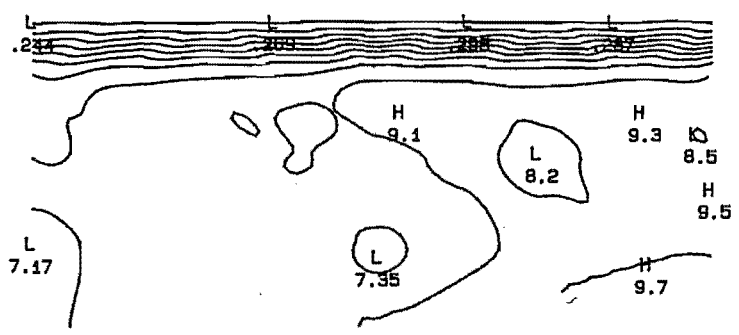

Upstream (J) INSTANTANEOUS RE = 2318 Downstream

$\Psi = 270°$

Figure I-9 A-L (cont.)

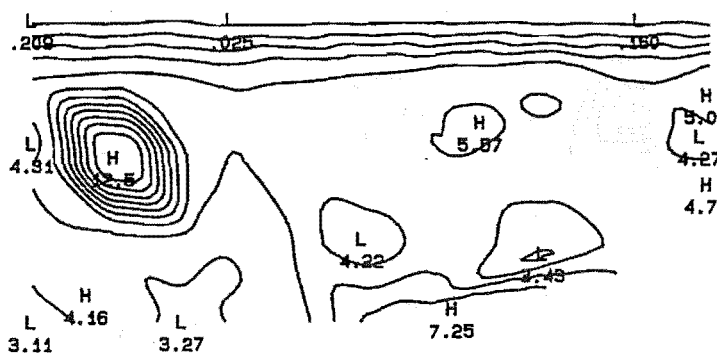

Upstream (K) INSTANTANEOUS RE = 2043 Downstream

$\Psi = 300°$

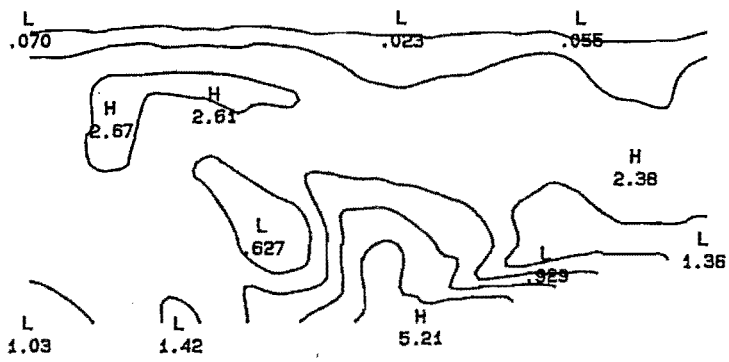

Upstream (L) INSTANTANEOUS RE = 1618 Downstream

$\Psi = 330°$

Figure I-9 A-L (cont.)

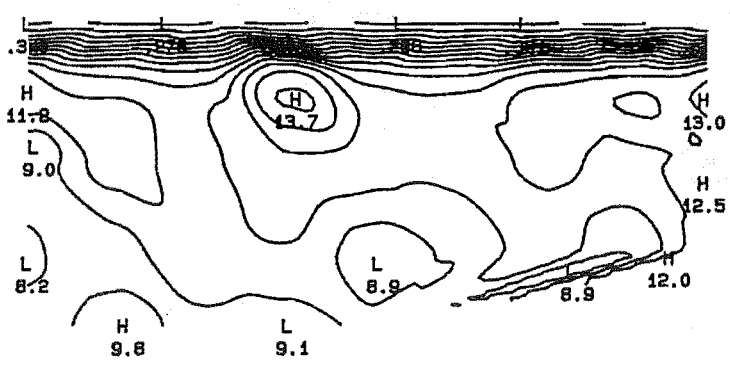

Upstream (E) INSTANTANEOUS RE = 2018 Downstream

$\Psi = 120°$

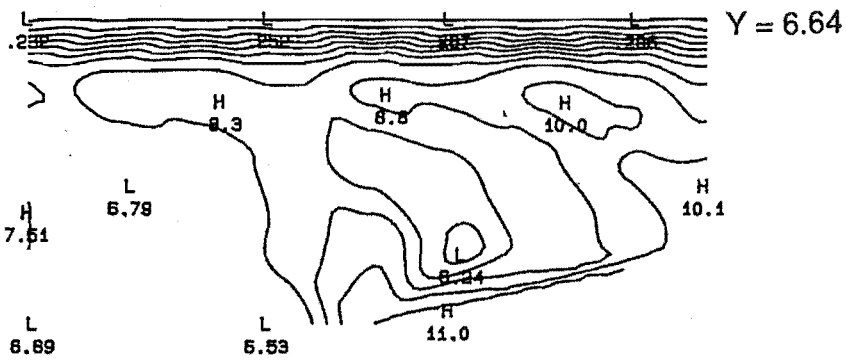

Upstream (F) INSTANTANEOUS RE = 2343 Downstream

$\Psi = 150°$

Figure I-9 A-L (cont.)

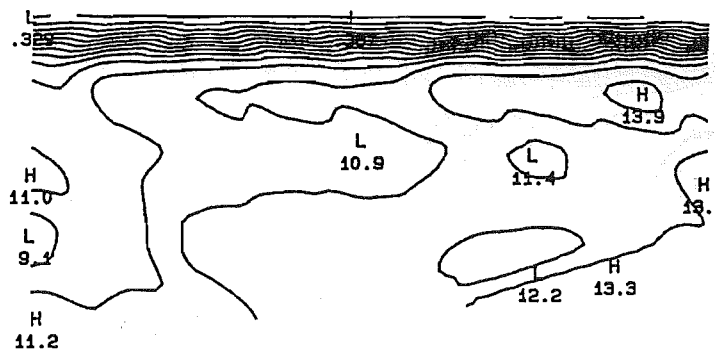

Upstream (G) INSTANTANEOUS RE = 2471 Downstream

$\Psi = 180°$

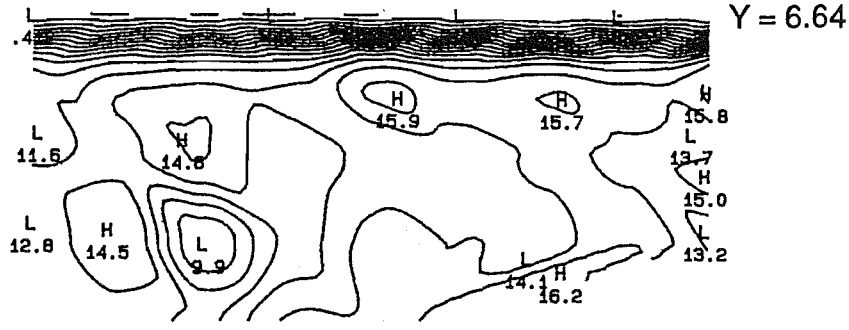

Upstream (H) INSTANTANEOUS RE = 2486 Downstream

$\Psi = 210°$

Figure I-9 A-L (cont.)

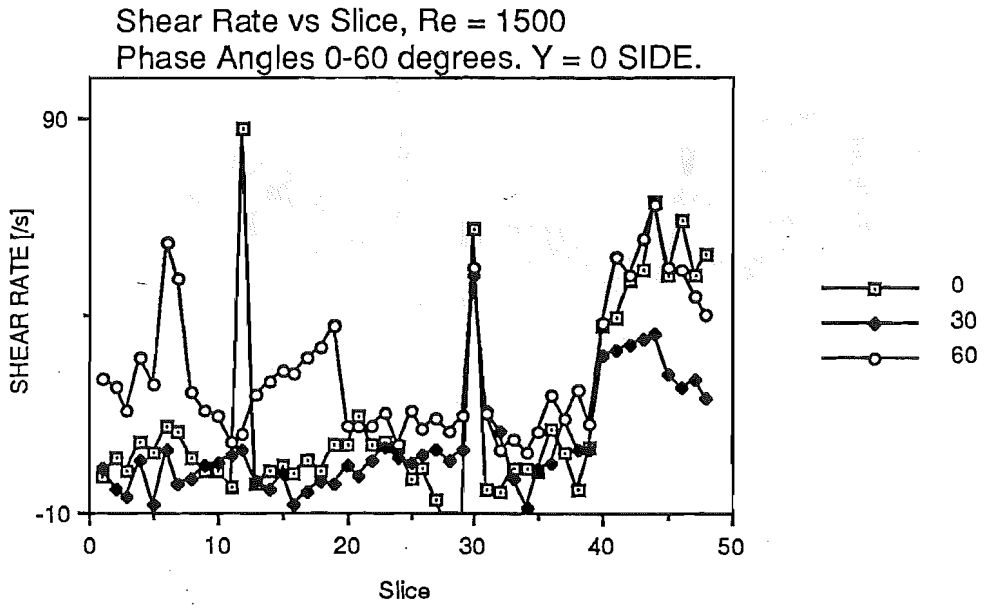

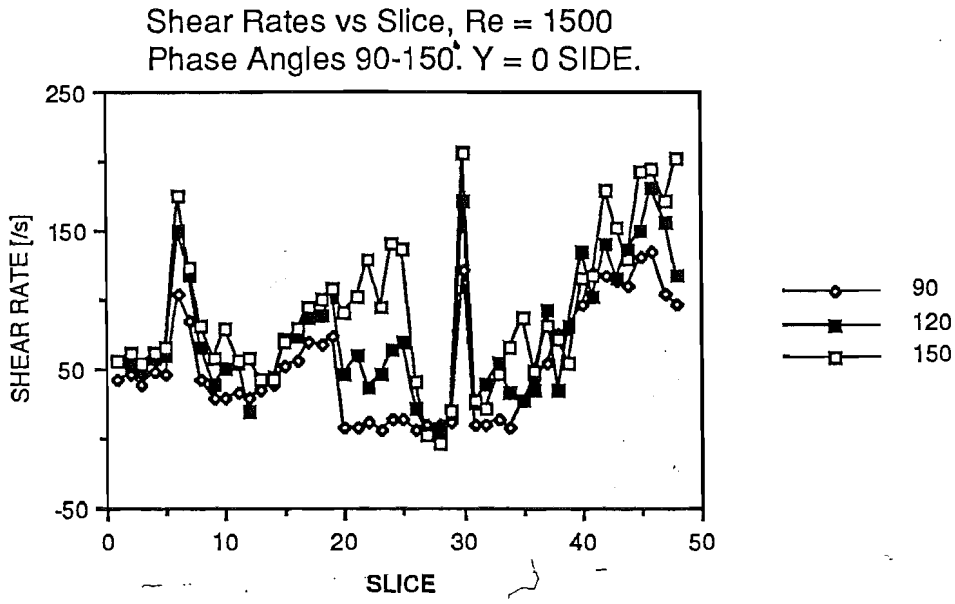

FIGURE I-11: SHEAR RATES IN PULSATILE FLOW
(SLICES AS IN FIG 5.54)

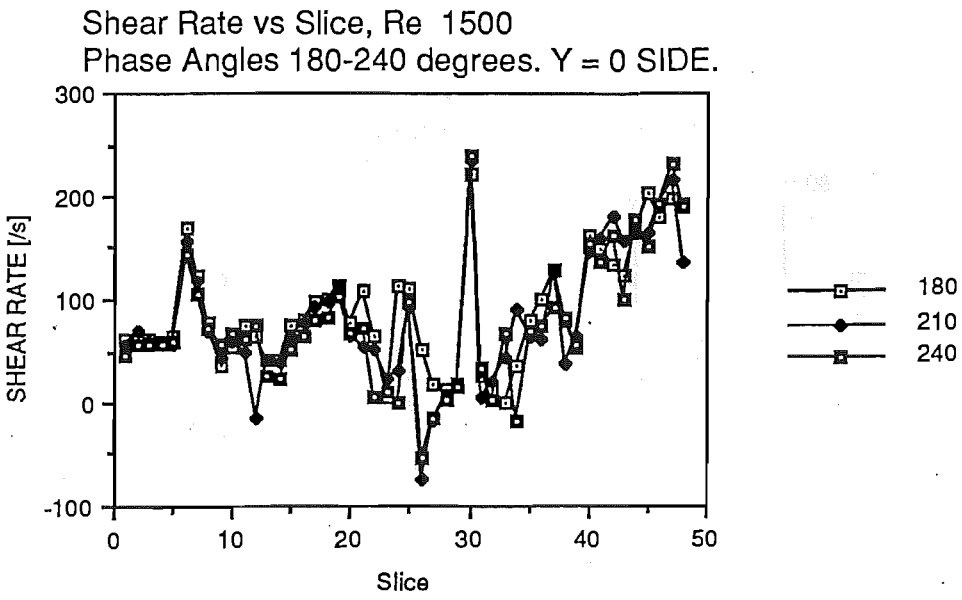

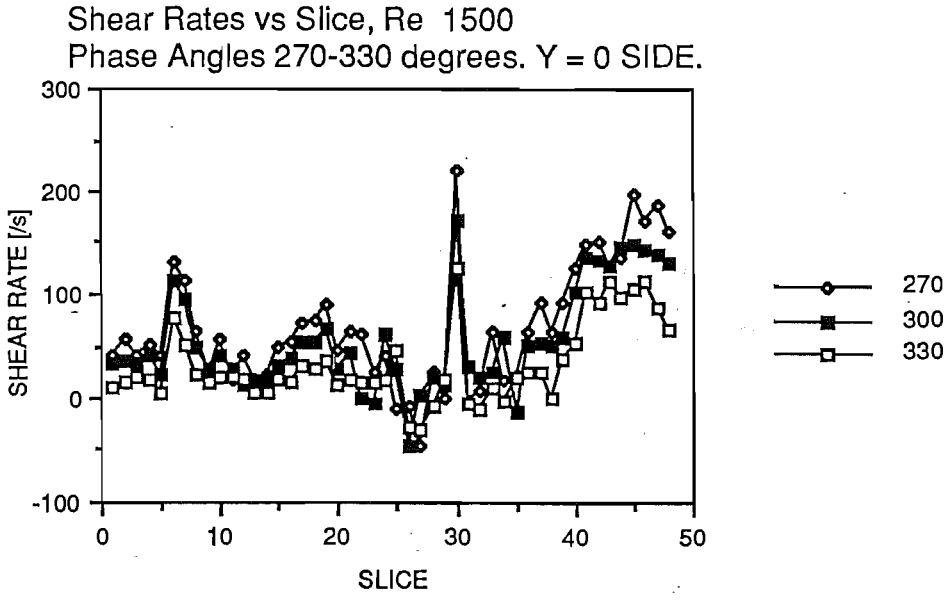

FIGURE I-11 : SHEAR RATES IN PULSATILE FLOW
(SLICES AS IN FIG 5.54)

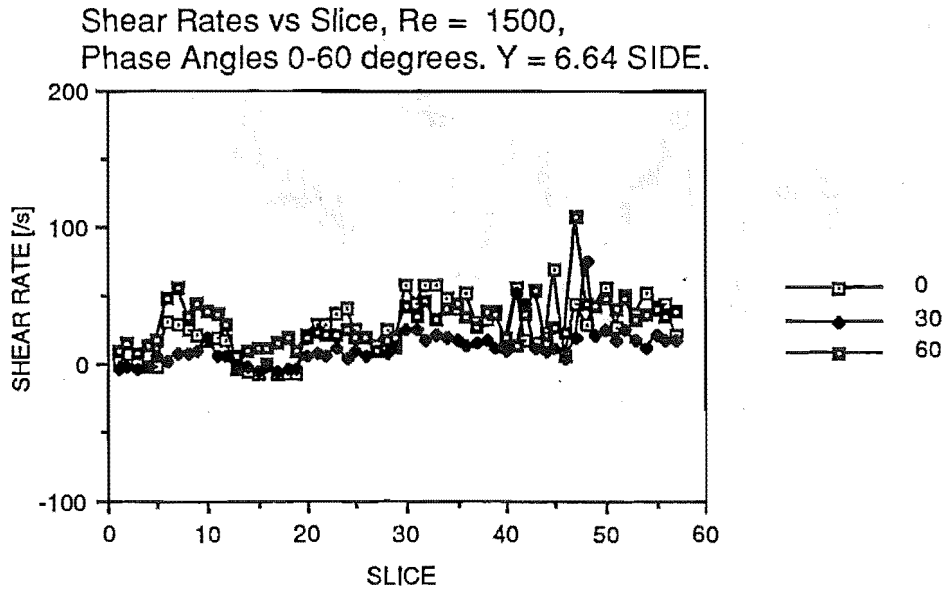

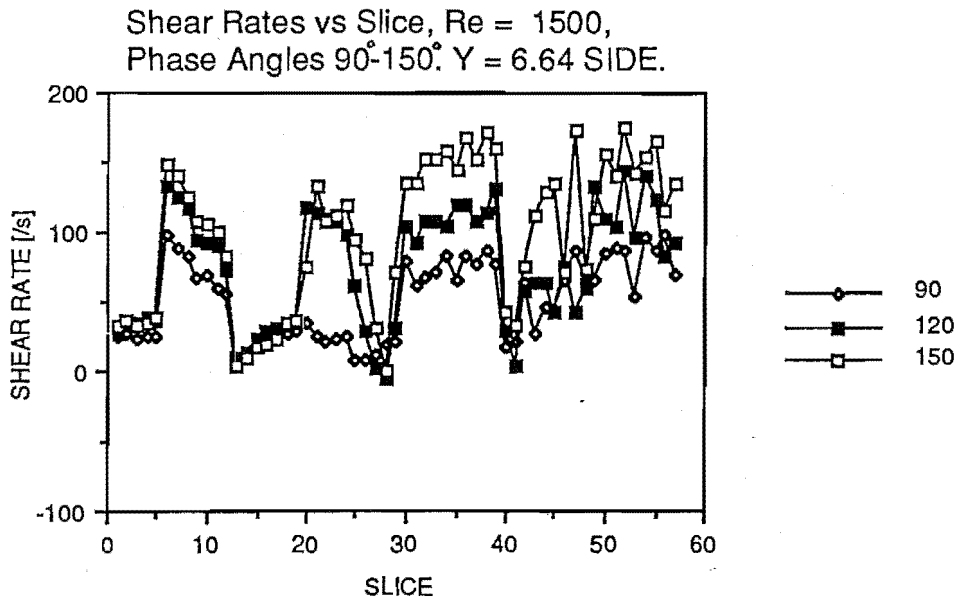

FIGURE I-11 : SHEAR RATES IN PULSATILE FLOW
(SLICES AS IN FIG 5.54)

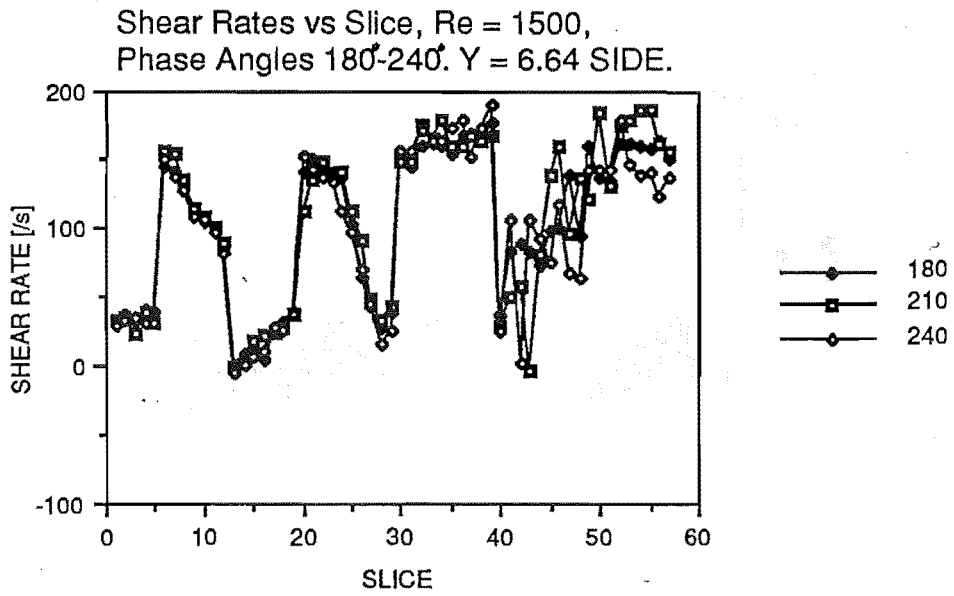

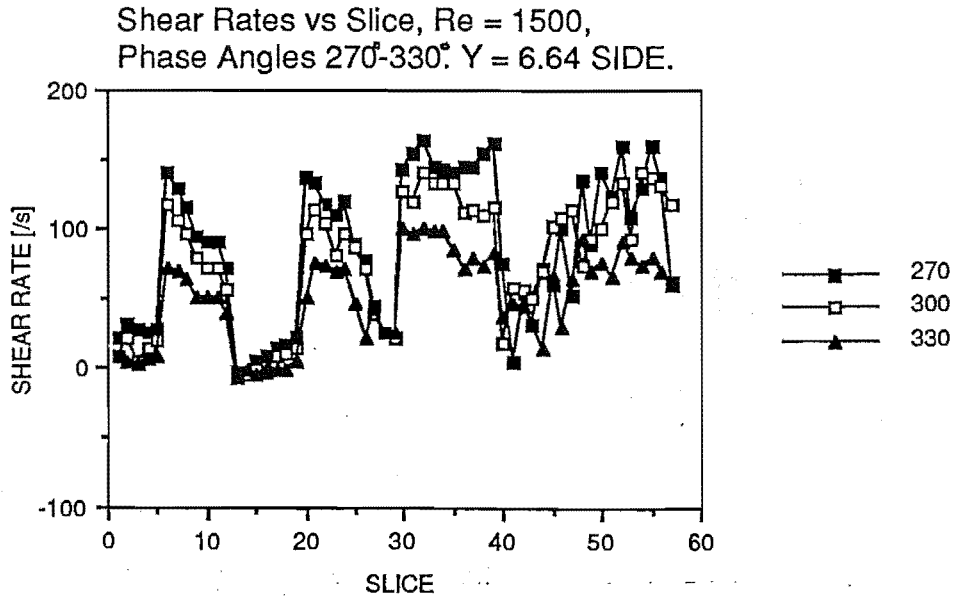

FIGURE I-11 : SHEAR RATES IN PULSATILE FLOW
(SLICES AS IN FIG 5.5a)

Appendix J

Raw Velocity Data from LDA

There follows a listing of the data obtained from the LDA for axial velocity measurements. The steady flow contour velocities are listed first, in the form of the x and y coordinates and LDA output voltages for each measuremet point. The velocity may be obtained from applying the equation given in Chapter 4, for calculating the velocity in cm s^{-1}.

Following the steady flow data, pulsatile data are given as velocities cm s^{-1}. These velocities must be multiplied by the factor 1.32128, to correct for an incorrect velocity calculation in the sampling programme, NEWAVE.PAS. Columns 1 and 2 contain the x and y coordinates; column 3, the average velocity, columns 4-15, the instantaneous phase angle velocities and column 16, the rms output voltage of the LDA. It will be seen that y coordinates of less than 10 correspond to the $\alpha = 0°$ side of the tube, y greater than 10, the $\alpha = 180°$ side, and y equals 10, the centre of the tube.

Data is listed in columns, headed by contour slice name eg:BC1 is the first slice in the region BC, the proximal limb. Columns 1 and 2 contain x and y coordinates; Column 3 contains LDA ouput voltages in Volts.

OA2

5.00,1.34,1.74
5.00,18.66,1.74
15.00,1.34,1.74
15.00,18.66,1.74
1.34,5.00,1.74
1.34,15.00,1.74
18.66,5.00,1.74
18.66,15.00,1.74
0.00,10.00,1.74
0.55,6.66,1.74
0.55,13.33,1.74
2.54,3.33,1.74
2.54,16.66,1.74
3.33,2.54,1.74
3.33,17.46,1.74
6.66,0.55,1.74
6.66,19.45,1.74
10.00,0.00,1.74
10.00,20.00,1.74
13.33,0.55,1.74
13.33,19.45,1.74
16.66,2.54,1.74
16.66,17.46,1.74
17.46,3.33,1.74
17.46,16.66,1.74
19.45,6.66,1.74
19.45,13.33,1.74
20.00,10.00,1.74
1.66,6.66,2.39
1.66,8.33,2.42
1.66,10.00,2.41
1.66,11.66,2.30
1.66,13.33,2.13
3.33,3.33,2.48
3.33,5.00,2.67
3.33,6.66,2.83
3.33,8.33,2.94
3.33,10.00,2.91
3.33,11.66,2.82
3.33,13.33,2.60
3.33,15.00,2.30
3.33,16.66,1.93
5.00,3.33,2.81
5.00,5.00,2.98
5.00,6.66,3.14
5.00,8.33,3.23
5.00,10.00,3.21
5.00,11.66,3.13
5.00,13.33,2.93
5.00,15.00,2.65
5.00,16.66,2.21
6.66,1.66,2.56
6.66,3.33,2.96
6.66,5.00,3.18
6.66,6.66,3.33
6.66,8.33,3.38
6.66,10.00,3.35
6.66,11.66,3.27
6.66,13.33,3.15
6.66,15.00,2.91
6.66,16.66,2.51
6.66,18.33,1.98
8.33,1.66,2.69
8.33,3.33,3.01
8.33,5.00,3.27
8.33,6.66,3.42
8.33,8.33,3.45
8.33,10.00,3.40
8.33,11.66,3.33
8.33,13.33,3.19
8.33,15.00,2.99
8.33,16.66,2.63
8.33,18.33,2.11
10.00,1.66,2.70
10.00,3.33,3.02
10.00,5.00,3.32
10.00,6.66,3.50
10.00,8.33,3.51
10.00,10.00,3.45
10.00,11.66,3.38
10.00,13.33,3.26
10.00,15.00,3.07
10.00,16.66,2.69
10.00,18.33,2.20
11.66,1.66,2.68
11.66,3.33,2.97
11.66,5.00,3.28
11.66,6.66,3.50
11.66,8.33,3.51
11.66,10.00,3.47
11.66,11.66,3.40
11.66,13.33,3.29
11.66,15.00,3.08
11.66,16.66,2.68
11.66,18.33,2.28
13.33,1.66,2.84
13.33,3.33,2.99
13.33,5.00,3.29
13.33,6.66,3.46
13.33,8.33,3.49
13.33,10.00,3.48
13.33,11.66,3.43
13.33,13.33,3.33
13.33,15.00,3.11
13.33,16.66,2.81
13.33,18.33,2.44
15.00,3.33,2.71
15.00,5.00,3.05
15.00,6.66,3.27
15.00,8.33,3.37
15.00,10.00,3.38
15.00,11.66,3.32
15.00,13.33,3.17
15.00,15.00,2.93
15.00,16.66,2.54
16.66,3.33,2.25
16.66,5.00,2.64
16.66,6.66,2.90
16.66,8.33,3.02
16.66,10.00,3.06
16.66,11.66,2.98
16.66,13.33,2.84
16.66,15.00,2.50
16.66,16.66,2.05
18.33,6.66,2.40
18.33,8.33,2.53
18.33,10.00,2.55
18.33,11.66,2.47
18.33,13.33,2.25
2.54,16.66,1.74
3.33,2.54,1.74
3.33,17.46,1.74
6.66,0.55,1.74
6.66,19.45,1.74
10.00,0.00,1.74
10.00,20.00,1.74
13.33,0.55,1.74
13.33,19.45,1.74
16.66,2.54,1.74
16.66,17.46,1.74
17.46,3.33,1.74
17.46,16.66,1.74
19.45,6.66,1.74
19.45,13.33,1.74
20.00,10.00,1.74
1.66,6.66,2.79
1.66,8.33,2.92
1.66,10.00,3.05
1.66,11.66,3.17
1.66,13.33,3.25
3.33,3.33,2.49
3.33,5.00,2.83
3.33,6.66,2.89
3.33,8.33,2.96
3.33,10.00,3.01
3.33,11.66,3.09
3.33,13.33,3.21
3.33,15.00,3.39
3.33,16.66,3.14
5.00,3.33,2.75
5.00,5.00,2.88
5.00,6.66,2.97
5.00,8.33,3.02
5.00,10.00,3.06
5.00,11.66,3.12
5.00,13.33,3.23
5.00,15.00,3.28
5.00,16.66,2.75
6.66,1.66,2.44
6.66,3.33,2.83
6.66,5.00,2.96
6.66,6.66,3.07
6.66,8.33,3.11
6.66,10.00,3.12
6.66,11.66,3.23
6.66,13.33,3.24
6.66,15.00,3.05
6.66,16.66,2.18
6.66,18.33,1.74
8.33,1.66,2.66
8.33,3.33,2.84
8.33,5.00,2.95
8.33,6.66,3.07
8.33,8.33,3.12
8.33,10.00,3.11
8.33,11.66,3.26
8.33,13.33,3.24
8.33,15.00,2.89
8.33,16.66,2.13
8.33,18.33,1.60
10.00,1.66,2.74
10.00,3.33,2.85
10.00,5.00,2.96
10.00,6.66,3.07
10.00,8.33,3.14
10.00,10.00,3.12
10.00,11.66,3.23
10.00,13.33,3.20
10.00,15.00,2.75
10.00,16.66,2.01
10.00,18.33,1.62
11.66,1.66,2.83
11.66,3.33,2.90
11.66,5.00,3.02
11.66,6.66,3.08
11.66,8.33,3.11
11.66,10.00,3.08
11.66,11.66,3.11
11.66,13.33,3.04
11.66,15.00,2.55
11.66,16.66,1.82
11.66,18.33,1.56
13.33,1.66,2.81
13.33,3.33,2.95
13.33,5.00,3.06
13.33,6.66,3.06
13.33,8.33,3.02
13.33,10.00,3.03
13.33,11.66,3.06
13.33,13.33,2.88
13.33,15.00,2.26
13.33,16.66,1.62
13.33,18.33,1.50
15.00,3.33,2.94
15.00,5.00,2.97
15.00,6.66,2.93
15.00,8.33,3.01
15.00,10.00,3.03
15.00,11.66,3.06
15.00,13.33,2.84
15.00,15.00,2.25
15.00,16.66,1.78
16.66,3.33,2.46
16.66,5.00,2.92
16.66,6.66,2.95
16.66,8.33,3.01
16.66,10.00,3.07
16.66,11.66,3.10
16.66,13.33,2.84
16.66,15.00,2.30

DE1

5.00,1.34,1.74
5.00,18.66,1.74
15.00,1.34,1.74
15.00,18.66,1.74
1.34,5.00,1.74
1.34,15.00,1.74
18.66,5.00,1.74
18.66,15.00,1.74
0.00,10.00,1.74
0.55,6.66,1.74
0.55,13.33,1.74
2.54,3.33,1.74

Data is listed in columns, headed by contour slice name eg:BC1 is the first slice in the region BC, the proximal limb. Columns 1 and 2 contain x and y coordinates; Column 3 contains LDA ouput voltages in Volts.

16.66,16.66,1.89
18.33,6.66,2.80
18.33,8.33,3.24
18.33,10.00,3.22
18.33,11.66,3.19
18.33,13.33,3.09

DE3

5.00,1.34,1.74
5.00,18.66,1.74
15.00,1.34,1.74
15.00,18.66,1.74
1.34,5.00,1.74
1.34,15.00,1.74
18.66,5.00,1.74
18.66,15.00,1.74
0.00,10.00,1.74
0.55,6.66,1.74
0.55,13.33,1.74
2.54,3.33,1.74
2.54,16.66,1.74
3.33,2.54,1.74
3.33,17.46,1.74
6.66,0.55,1.74
6.66,19.45,1.74
10.00,0.00,1.74
10.00,20.00,1.74
13.33,0.55,1.74
13.33,19.45,1.74
16.66,2.54,1.74
16.66,17.46,1.74
17.46,3.33,1.74
17.46,16.66,1.74
19.45,6.66,1.74
19.45,13.33,1.74
20.00,10.00,1.74
1.66,6.66,3.08
1.66,8.33,3.14
1.66,10.00,3.12
1.66,11.66,3.07
1.66,13.33,2.72
3.33,3.33,3.12
3.33,5.00,3.31
3.33,6.66,3.25
3.33,8.33,3.20
3.33,10.00,3.16
3.33,11.66,3.12
3.33,13.33,3.00
3.33,15.00,2.84
3.33,16.66,2.35
5.00,3.33,3.31
5.00,5.00,3.31
5.00,6.66,3.24
5.00,8.33,3.19
5.00,10.00,3.10
5.00,11.66,3.05
5.00,13.33,2.92
5.00,15.00,2.73
5.00,16.66,2.47
6.66,1.66,2.67
6.66,3.33,3.33
6.66,5.00,3.29
6.66,6.66,3.22
6.66,8.33,3.16
6.66,10.00,3.12
6.66,11.66,3.02
6.66,13.33,2.89
6.66,15.00,2.67
6.66,16.66,2.53
6.66,18.33,2.21
8.33,1.66,2.98
8.33,3.33,3.30
8.33,5.00,3.29
8.33,6.66,3.21
8.33,8.33,3.15
8.33,10.00,3.13
8.33,11.66,3.03
8.33,13.33,2.72
8.33,15.00,2.45
8.33,16.66,2.29
8.33,18.33,2.12
10.00,1.66,3.12
10.00,3.33,3.29
10.00,5.00,3.26
10.00,6.66,3.19
10.00,8.33,3.12
10.00,10.00,3.05
10.00,11.66,2.88
10.00,13.33,2.53
10.00,15.00,2.26
10.00,16.66,2.09
10.00,18.33,2.08
11.66,1.66,3.14
11.66,3.33,3.33
11.66,5.00,3.29
11.66,6.66,3.19
11.66,8.33,3.06
11.66,10.00,2.95
11.66,11.66,2.75
11.66,13.33,2.30
11.66,15.00,2.05
11.66,16.66,1.96
11.66,18.33,1.87
13.33,1.66,2.84
13.33,3.33,3.38
13.33,5.00,3.31
13.33,6.66,3.15
13.33,8.33,3.02
13.33,10.00,2.85
13.33,11.66,2.58
13.33,13.33,2.20
13.33,15.00,1.98
13.33,16.66,1.84
13.33,18.33,1.81
15.00,3.33,3.26
15.00,5.00,3.16
15.00,6.66,3.08
15.00,8.33,2.88
15.00,10.00,2.73
15.00,11.66,2.49
15.00,13.33,2.21
15.00,15.00,2.01
15.00,16.66,1.91
16.66,3.33,3.28
16.66,5.00,3.18
16.66,6.66,3.06
16.66,8.33,2.89
16.66,10.00,2.73
16.66,11.66,2.54
16.66,13.33,2.34
16.66,15.00,2.19
16.66,16.66,1.93
18.33,6.66,3.17
18.33,8.33,3.04
18.33,10.00,2.90
18.33,11.66,2.76
18.33,13.33,2.56

DE2

5.00,1.34,1.74
5.00,18.66,1.74
15.00,1.34,1.74
15.00,18.66,1.74
1.34,5.00,1.74
1.34,15.00,1.74
18.66,5.00,1.74
18.66,15.00,1.74
0.00,10.00,1.74
0.55,6.66,1.74
0.55,13.33,1.74
2.54,3.33,1.74
2.54,16.66,1.74
3.33,2.54,1.74
3.33,17.46,1.74
6.66,0.55,1.74
6.66,19.45,1.74
10.00,0.00,1.74
10.00,20.00,1.74
13.33,0.55,1.74
13.33,19.45,1.74
16.66,2.54,1.74
16.66,17.46,1.74
17.46,3.33,1.74
17.46,16.66,1.74
19.45,6.66,1.74
19.45,13.33,1.74
20.00,10.00,1.74
1.66,6.66,3.16
1.66,8.33,3.20
1.66,10.00,3.20
1.66,11.66,3.24
1.66,13.33,3.21
3.33,3.33,2.98
3.33,5.00,3.18
3.33,6.66,3.17
3.33,8.33,3.17
3.33,10.00,3.18
3.33,11.66,3.17
3.33,13.33,3.11
3.33,15.00,2.87
3.33,16.66,2.50
5.00,3.33,3.05
5.00,5.00,3.18
5.00,6.66,3.19
5.00,8.33,3.19
5.00,10.00,3.19
5.00,11.66,3.13
5.00,13.33,3.07
5.00,15.00,2.68
5.00,16.66,2.30
6.66,1.66,2.73
6.66,3.33,3.09
6.66,5.00,3.14
6.66,6.66,3.17
6.66,8.33,3.19
6.66,10.00,3.19
6.66,11.66,3.18
6.66,13.33,3.05
6.66,15.00,2.58
6.66,16.66,2.13
6.66,18.33,1.90
8.33,1.66,2.91
8.33,3.33,3.08
8.33,5.00,3.13
8.33,6.66,3.17
8.33,8.33,3.12
8.33,10.00,3.17
8.33,11.66,3.12
8.33,13.33,2.91
8.33,15.00,2.37
8.33,16.66,2.00
8.33,18.33,1.78
10.00,1.66,3.03
10.00,3.33,3.15
10.00,5.00,3.13
10.00,6.66,3.18
10.00,8.33,3.12
10.00,10.00,3.13
10.00,11.66,3.05
10.00,13.33,2.75
10.00,15.00,2.12
10.00,16.66,1.78
10.00,18.33,1.70
11.66,1.66,3.09
11.66,3.33,3.23
11.66,5.00,3.23
11.66,6.66,3.22
11.66,8.33,3.09
11.66,10.00,3.04
11.66,11.66,2.91
11.66,13.33,2.50
11.66,15.00,1.95
11.66,16.66,1.72
11.66,18.33,1.58
13.33,1.66,2.86
13.33,3.33,3.22

Data is listed in columns, headed by contour slice name eg:BC1 is the first slice in the region BC, the proximal limb. Columns 1 and 2 contain x and y coordinates; Column 3 contains LDA ouput voltages in Volts.

13.33,5.00,3.28
13.33,6.66,3.22
13.33,8.33,3.08
13.33,10.00,2.97
13.33,11.66,2.74
13.33,13.33,2.32
13.33,15.00,1.93
13.33,16.66,1.69
13.33,18.33,1.60
15.00,3.33,3.10
15.00,5.00,3.20
15.00,6.66,3.13
15.00,8.33,3.08
15.00,10.00,3.05
15.00,11.66,2.88
15.00,13.33,2.57
15.00,15.00,2.13
15.00,16.66,1.96
16.66,3.33,2.22
16.66,5.00,3.15
16.66,6.66,3.20
16.66,8.33,3.20
16.66,10.00,3.14
16.66,11.66,2.99
16.66,13.33,2.73
16.66,15.00,2.34
16.66,16.66,1.92
18.33,6.66,3.05
18.33,8.33,3.33
18.33,10.00,3.33
18.33,11.66,3.23
18.33,13.33,2.98

OA1

5.00,1.34,1.74
5.00,18.66,1.74
15.00,1.34,1.74
15.00,18.66,1.74
1.34,5.00,1.74
1.34,15.00,1.74
18.66,5.00,1.74
18.66,15.00,1.74
0.00,10.00,1.74
0.55,6.66,1.74
0.55,13.33,1.74
2.54,3.33,1.74
2.54,16.66,1.74
3.33,2.54,1.74
3.33,17.46,1.74
6.66,0.55,1.74
6.66,19.45,1.74
10.00,0.00,1.74
10.00,20.00,1.74
13.33,0.55,1.74
13.33,19.45,1.74
16.66,2.54,1.74
16.66,17.46,1.74
17.46,3.33,1.74
17.46,16.66,1.74
19.45,6.66,1.74
19.45,13.33,1.74
20.00,10.00,1.74
1.66,6.66,2.28
1.66,8.33,2.42
1.66,10.00,2.49
1.66,11.66,2.49
1.66,13.33,2.37
3.33,3.33,2.12
3.33,5.00,2.46
3.33,6.66,2.69
3.33,8.33,2.82
3.33,10.00,2.89
3.33,11.66,2.87
3.33,13.33,2.78
3.33,15.00,2.62
3.33,16.66,2.31
5.00,3.33,2.41
5.00,5.00,2.76
5.00,6.66,2.97
5.00,8.33,3.08
5.00,10.00,3.14
5.00,11.66,3.12
5.00,13.33,3.03
5.00,15.00,2.89
5.00,16.66,2.59
6.66,1.66,2.14
6.66,3.33,2.56
6.66,5.00,2.87
6.66,6.66,3.05
6.66,8.33,3.14
6.66,10.00,3.17
6.66,11.66,3.14
6.66,13.33,3.07
6.66,15.00,2.93
6.66,16.66,2.69
6.66,18.33,2.16
8.33,1.66,2.30
8.33,3.33,2.72
8.33,5.00,3.06
8.33,6.66,3.21
8.33,8.33,3.30
8.33,10.00,3.31
8.33,11.66,3.29
8.33,13.33,3.20
8.33,15.00,3.07
8.33,16.66,2.85
8.33,18.33,2.40
10.00,1.66,2.39
10.00,3.33,2.77
10.00,5.00,3.14
10.00,6.66,3.32
10.00,8.33,3.38
10.00,10.00,3.36
10.00,11.66,3.31
10.00,13.33,3.24
10.00,15.00,3.12
10.00,16.66,2.91
10.00,18.33,2.51
11.66,1.66,2.38
11.66,3.33,2.76
11.66,5.00,3.17
11.66,6.66,3.35
11.66,8.33,3.40
11.66,10.00,3.37
11.66,11.66,3.32
11.66,13.33,3.27
11.66,15.00,3.15
11.66,16.66,2.91
11.66,18.33,2.56
13.33,1.66,2.28
13.33,3.33,2.60
13.33,5.00,3.09
13.33,6.66,3.34
13.33,8.33,3.42
13.33,10.00,3.41
13.33,11.66,3.37
13.33,13.33,3.33
13.33,15.00,3.17
13.33,16.66,2.88
13.33,18.33,2.54
15.00,3.33,2.67
15.00,5.00,3.05
15.00,6.66,3.29
15.00,8.33,3.39
15.00,10.00,3.42
15.00,11.66,3.41
15.00,13.33,3.32
15.00,15.00,3.15
15.00,16.66,2.86
16.66,3.33,2.29
16.66,5.00,2.73
16.66,6.66,3.03
16.66,8.33,3.17
16.66,10.00,3.25
16.66,11.66,3.21
16.66,13.33,3.11
16.66,15.00,2.87
16.66,16.66,2.49
18.33,6.66,2.55
18.33,8.33,2.74
18.33,10.00,2.82
18.33,11.66,2.78
18.33,13.33,2.66

FG1

5.00,1.34,1.74
5.00,18.66,1.74
15.00,1.34,1.74
15.00,18.66,1.74
1.34,5.00,1.74
1.34,15.00,1.74
18.66,5.00,1.74
18.66,15.00,1.74
0.00,10.00,1.74
0.55,6.66,1.74
0.55,13.33,1.74
2.54,3.33,1.74
2.54,16.66,1.74
3.33,2.54,1.74
3.33,17.46,1.74
6.66,0.55,1.74
6.66,19.45,1.74
10.00,0.00,1.74
10.00,20.00,1.74
13.33,0.55,1.74
13.33,19.45,1.74
16.66,2.54,1.74
16.66,17.46,1.74
17.46,3.33,1.74
17.46,16.66,1.74
19.45,6.66,1.74
19.45,13.33,1.74
20.00,10.00,1.74
1.66,6.66,3.00
1.66,8.33,3.17
1.66,10.00,3.13
1.66,11.66,3.02
1.66,13.33,2.87
3.33,3.33,1.98
3.33,5.00,2.87
3.33,6.66,3.25
3.33,8.33,3.36
3.33,10.00,3.22
3.33,11.66,3.12
3.33,13.33,3.03
3.33,15.00,2.98
3.33,16.66,2.70
5.00,3.33,2.02
5.00,5.00,2.66
5.00,6.66,3.08
5.00,8.33,3.22
5.00,10.00,3.16
5.00,11.66,3.05
5.00,13.33,2.98
5.00,15.00,2.96
5.00,16.66,2.90
6.66,1.66,1.66
6.66,3.33,1.93
6.66,5.00,2.54
6.66,6.66,3.00
6.66,8.33,3.16
6.66,10.00,3.06
6.66,11.66,3.00
6.66,13.33,2.90
6.66,15.00,2.89
6.66,16.66,2.91
6.66,18.33,2.85
8.33,1.66,1.61
8.33,3.33,1.90
8.33,5.00,2.60
8.33,6.66,3.00
8.33,8.33,3.13
8.33,10.00,3.01
8.33,11.66,2.92
8.33,13.33,2.89
8.33,15.00,2.83
8.33,16.66,2.79
8.33,18.33,2.86
10.00,1.66,1.68
10.00,3.33,1.88
10.00,5.00,2.63
10.00,6.66,3.06
10.00,8.33,3.10
10.00,10.00,3.01
10.00,11.66,2.92
10.00,13.33,2.85
10.00,15.00,2.81
10.00,16.66,2.77
10.00,18.33,2.84
11.66,1.66,1.71
11.66,3.33,1.88
11.66,5.00,2.71
11.66,6.66,3.09
11.66,8.33,3.12
11.66,10.00,3.03
11.66,11.66,2.89
11.66,13.33,2.83

Data is listed in columns, headed by contour slice name eg:BC1 is the first slice in the region BC, the proximal limb. Columns 1 and 2 contain x and y coordinates; Column 3 contains LDA ouput voltages in Volts.

11.66,15.00,2.77
11.66,16.66,2.78
11.66,18.33,2.81
13.33,1.66,1.85
13.33,3.33,1.97
13.33,5.00,2.80
13.33,6.66,3.16
13.33,8.33,3.16
13.33,10.00,3.01
13.33,11.66,2.89
13.33,13.33,2.79
13.33,15.00,2.78
13.33,16.66,2.70
13.33,18.33,2.76
15.00,3.33,2.96
15.00,5.00,3.20
15.00,6.66,3.26
15.00,8.33,3.14
15.00,10.00,3.00
15.00,11.66,2.93
15.00,13.33,2.84
15.00,15.00,2.84
15.00,16.66,2.81
16.66,3.33,2.77
16.66,5.00,3.22
16.66,6.66,3.24
16.66,8.33,3.11
16.66,10.00,3.03
16.66,11.66,2.92
16.66,13.33,2.86
16.66,15.00,2.80
16.66,16.66,2.68
18.33,6.66,3.20
18.33,8.33,3.12
18.33,10.00,2.99
18.33,11.66,2.88
18.33,13.33,2.76

FG2

5.00,1.34,1.74
5.00,18.66,1.74
15.00,1.34,1.74
15.00,18.66,1.74
1.34,5.00,1.74
1.34,15.00,1.74
18.66,5.00,1.74
18.66,15.00,1.74
0.00,10.00,1.74
0.55,6.66,1.74
0.55,13.33,1.74
2.54,3.33,1.74
2.54,16.66,1.74
3.33,2.54,1.74
3.33,17.46,1.74
6.66,0.55,1.74
6.66,19.45,1.74
10.00,0.00,1.74
10.00,20.00,1.74
13.33,0.55,1.74
13.33,19.45,1.74
16.66,2.54,1.74
16.66,17.46,1.74
17.46,3.33,1.74
17.46,16.66,1.74
19.45,6.66,1.74
19.45,13.33,1.74
20.00,10.00,1.74
1.66,6.66,3.05
1.66,8.33,3.27
1.66,10.00,3.25
1.66,11.66,3.19
1.66,13.33,2.93
3.33,3.33,2.07
3.33,5.00,2.83
3.33,6.66,3.11
3.33,8.33,3.27
3.33,10.00,3.29
3.33,11.66,3.23
3.33,13.33,3.21
3.33,15.00,3.18
3.33,16.66,2.90
5.00,3.33,1.98
5.00,5.00,2.45
5.00,6.66,2.74
5.00,8.33,3.11
5.00,10.00,3.22
5.00,11.66,3.19
5.00,13.33,3.13
5.00,15.00,3.12
5.00,16.66,3.13
6.66,1.66,1.62
6.66,3.33,1.77
6.66,5.00,2.09
6.66,6.66,2.58
6.66,8.33,3.05
6.66,10.00,3.17
6.66,11.66,3.13
6.66,13.33,3.08
6.66,15.00,3.04
6.66,16.66,3.05
6.66,18.33,2.99
8.33,1.66,1.57
8.33,3.33,1.70
8.33,5.00,2.02
8.33,6.66,2.63
8.33,8.33,3.02
8.33,10.00,3.15
8.33,11.66,3.10
8.33,13.33,3.06
8.33,15.00,3.01
8.33,16.66,3.03
8.33,18.33,3.06
10.00,1.66,1.64
10.00,3.33,1.80
10.00,5.00,2.04
10.00,6.66,2.70
10.00,8.33,3.02
10.00,10.00,3.15
10.00,11.66,3.11
10.00,13.33,3.03
10.00,15.00,2.99
10.00,16.66,2.99
10.00,18.33,3.00
11.66,1.66,1.75
11.66,3.33,1.90
11.66,5.00,2.12
11.66,6.66,2.74
11.66,8.33,3.06
11.66,10.00,3.13
11.66,11.66,3.11
11.66,13.33,3.03
11.66,15.00,2.96
11.66,16.66,3.00
11.66,18.33,2.99
13.33,1.66,1.94
13.33,3.33,2.11
13.33,5.00,2.40
13.33,6.66,2.77
13.33,8.33,3.12
13.33,10.00,3.14
13.33,11.66,3.07
13.33,13.33,2.99
13.33,15.00,2.95
13.33,16.66,2.99
13.33,18.33,2.87
15.00,3.33,2.65
15.00,5.00,2.81
15.00,6.66,3.01
15.00,8.33,3.16
15.00,10.00,3.17
15.00,11.66,3.07
15.00,13.33,3.03
15.00,15.00,3.01
15.00,16.66,2.96
16.66,3.33,2.61
16.66,5.00,3.05
16.66,6.66,3.18
16.66,8.33,3.19
16.66,10.00,3.15
16.66,11.66,3.04
16.66,13.33,3.01
16.66,15.00,2.98
16.66,16.66,2.91
18.33,6.66,3.12
18.33,8.33,3.16
18.33,10.00,3.10
18.33,11.66,3.02
18.33,13.33,2.93

FG3

1.66,13.33,2.92
3.33,3.33,2.51
3.33,5.00,2.89
3.33,6.66,3.00
3.33,8.33,3.19
3.33,10.00,3.29
3.33,11.66,3.26
3.33,13.33,3.26
3.33,15.00,3.21
3.33,16.66,2.72
5.00,3.33,2.27
5.00,5.00,2.46
5.00,6.66,2.63
5.00,8.33,3.07
5.00,10.00,3.19
5.00,11.66,3.19
5.00,13.33,3.18
5.00,15.00,3.19
5.00,16.66,3.18
6.66,1.66,1.79
6.66,3.33,1.96
6.66,5.00,2.17
6.66,6.66,2.76
6.66,8.33,2.89
6.66,10.00,3.12
6.66,11.66,3.18
6.66,13.33,3.14
6.66,15.00,3.13
6.66,16.66,3.16
6.66,18.33,2.84
8.33,1.66,1.75
8.33,3.33,1.80
8.33,5.00,2.08
8.33,6.66,2.72
5.00,1.34,1.74
5.00,18.66,1.74
15.00,1.34,1.74
15.00,18.66,1.74
1.34,5.00,1.74
1.34,15.00,1.74
18.66,5.00,1.74
18.66,15.00,1.74
0.00,10.00,1.74
0.55,6.66,1.74
0.55,13.33,1.74
2.54,3.33,1.74
2.54,16.66,1.74
3.33,2.54,1.74
3.33,17.46,1.74
6.66,0.55,1.74
6.66,19.45,1.74
10.00,0.00,1.74
10.00,20.00,1.74
13.33,0.55,1.74
13.33,19.45,1.74
16.66,2.54,1.74
16.66,17.46,1.74
17.46,3.33,1.74
17.46,16.66,1.74
19.45,6.66,1.74
19.45,13.33,1.74
20.00,10.00,1.74
1.66,6.66,3.08
1.66,8.33,3.22
1.66,10.00,3.27
1.66,11.66,3.18

Data is listed in columns, headed by contour slice name eg:BC1 is the first slice in the region BC, the proximal limb. Columns 1 and 2 contain x and y coordinates; Column 3 contains LDA ouput voltages in Volts.

8.33,8.33,2.85
8.33,10.00,3.11
8.33,11.66,3.16
8.33,13.33,3.13
8.33,15.00,3.09
8.33,16.66,3.13
8.33,18.33,3.08
10.00,1.66,1.94
10.00,3.33,1.92
10.00,5.00,2.23
10.00,6.66,2.81
10.00,8.33,2.90
10.00,10.00,3.11
10.00,11.66,3.15
10.00,13.33,3.10
10.00,15.00,3.08
10.00,16.66,3.10
10.00,18.33,3.11
11.66,1.66,2.06
11.66,3.33,2.11
11.66,5.00,2.21
11.66,6.66,2.71
11.66,8.33,2.93
11.66,10.00,3.14
11.66,11.66,3.13
11.66,13.33,3.08
11.66,15.00,3.06
11.66,16.66,3.10
11.66,18.33,3.10
13.33,1.66,2.26
13.33,3.33,2.37
13.33,5.00,2.45
13.33,6.66,2.72
13.33,8.33,3.02
13.33,10.00,3.14
13.33,11.66,3.12
13.33,13.33,3.09
13.33,15.00,3.06
13.33,16.66,3.09
13.33,18.33,3.02
15.00,3.33,2.71
15.00,5.00,2.75
15.00,6.66,2.94
15.00,8.33,3.10
15.00,10.00,3.15
15.00,11.66,3.13
15.00,13.33,3.08
15.00,15.00,3.07
15.00,16.66,3.08
16.66,3.33,2.85
16.66,5.00,3.03
16.66,6.66,3.05
16.66,8.33,3.13
16.66,10.00,3.14
16.66,11.66,3.12
16.66,13.33,3.07
16.66,15.00,3.06
16.66,16.66,2.98
18.33,6.66,3.08
18.33,8.33,3.13
18.33,10.00,3.11
18.33,11.66,3.06
18.33,13.33,3.03

FG4

5.00,1.34,1.74
5.00,18.66,1.74
15.00,1.34,1.74
15.00,18.66,1.74
1.34,5.00,1.74
1.34,15.00,1.74
18.66,5.00,1.74
18.66,15.00,1.74
0.00,10.00,1.74
0.55,6.66,1.74
0.55,13.33,1.74
2.54,3.33,1.74
2.54,16.66,1.74
3.33,2.54,1.74
3.33,17.46,1.74
6.66,0.55,1.74
6.66,19.45,1.74
10.00,0.00,1.74
10.00,20.00,1.74
13.33,0.55,1.74
13.33,19.45,1.74
16.66,2.54,1.74
16.66,17.46,1.74
17.46,3.33,1.74
17.46,16.66,1.74
19.45,6.66,1.74
19.45,13.33,1.74
20.00,10.00,1.74
1.66,6.66,2.54
1.66,8.33,2.81
1.66,10.00,2.91
1.66,11.66,2.88
1.66,13.33,2.60
3.33,3.33,2.37
3.33,5.00,2.72
3.33,6.66,2.90
3.33,8.33,3.02
3.33,10.00,3.05
3.33,11.66,3.12
3.33,13.33,3.15
3.33,15.00,3.02
3.33,16.66,2.46
5.00,3.33,2.53
5.00,5.00,2.74
5.00,6.66,2.83
5.00,8.33,2.89
5.00,10.00,2.94
5.00,11.66,3.01
5.00,13.33,3.13
5.00,15.00,3.18
5.00,16.66,3.01
6.66,1.66,2.44
6.66,3.33,2.61
6.66,5.00,2.67
6.66,6.66,2.75
6.66,8.33,2.79
6.66,10.00,2.82
6.66,11.66,2.90
6.66,13.33,3.01
6.66,15.00,3.12
6.66,16.66,3.15
6.66,18.33,2.61
8.33,1.66,2.50
8.33,3.33,2.62
8.33,5.00,2.61
8.33,6.66,2.70
8.33,8.33,2.73
8.33,10.00,2.77
8.33,11.66,2.86
8.33,13.33,2.98
8.33,15.00,3.08
8.33,16.66,3.14
8.33,18.33,2.89
10.00,1.66,2.63
10.00,3.33,2.68
10.00,5.00,2.68
10.00,6.66,2.72
10.00,8.33,2.74
10.00,10.00,2.83
10.00,11.66,2.86
10.00,13.33,2.98
10.00,15.00,3.07
10.00,16.66,3.15
10.00,18.33,3.04
11.66,1.66,2.60
11.66,3.33,2.79
11.66,5.00,2.78
11.66,6.66,2.83
11.66,8.33,2.82
11.66,10.00,2.91
11.66,11.66,2.93
11.66,13.33,3.00
11.66,15.00,3.08
11.66,16.66,3.15
11.66,18.33,3.02
13.33,1.66,2.57
13.33,3.33,2.81
13.33,5.00,2.87
13.33,6.66,2.97
13.33,8.33,2.93
13.33,10.00,2.99
13.33,11.66,3.00
13.33,13.33,3.08
13.33,15.00,3.11
13.33,16.66,3.13
13.33,18.33,2.77
15.00,3.33,2.73
15.00,5.00,2.89
15.00,6.66,2.93
15.00,8.33,3.00
15.00,10.00,3.01
15.00,11.66,3.09
15.00,13.33,3.07
15.00,15.00,3.12
15.00,16.66,3.12
16.66,3.33,2.42
16.66,5.00,2.81
16.66,6.66,2.95
16.66,8.33,2.98
16.66,10.00,3.04
16.66,11.66,3.09
16.66,13.33,3.07
16.66,15.00,3.02
16.66,16.66,2.56
18.33,6.66,2.68
18.33,8.33,2.83
18.33,10.00,2.87
18.33,11.66,2.93
18.33,13.33,2.72

BC1

5.00,1.34,1.74
5.00,18.66,1.74
15.00,1.34,1.74
15.00,18.66,1.74
1.34,5.00,1.74
1.34,15.00,1.74
18.66,5.00,1.74
18.66,15.00,1.74
0.00,10.00,1.74
0.55,6.66,1.74
0.55,13.33,1.74
2.54,3.33,1.74
2.54,16.66,1.74
3.33,2.54,1.74
3.33,17.46,1.74
6.66,0.55,1.74
6.66,19.45,1.74
10.00,0.00,1.74
10.00,20.00,1.74
13.33,0.55,1.74
13.33,19.45,1.74
16.66,2.54,1.74
16.66,17.46,1.74
17.46,3.33,1.74
17.46,16.66,1.74
19.45,6.66,1.74
19.45,13.33,1.74
20.00,10.00,1.74
1.66,6.66,2.76
1.66,8.33,3.00
1.66,10.00,3.08
1.66,11.66,3.03
1.66,13.33,2.85
3.33,3.33,1.77
3.33,5.00,2.74
3.33,6.66,3.14
3.33,8.33,3.23
3.33,10.00,3.18
3.33,11.66,3.18
3.33,13.33,3.15
3.33,15.00,3.00
3.33,16.66,2.80
5.00,3.33,2.45
5.00,5.00,2.53
5.00,6.66,3.23
5.00,8.33,3.32
5.00,10.00,3.00
5.00,11.66,3.10
5.00,13.33,3.21
5.00,15.00,3.12
5.00,16.66,2.99
6.66,1.66,1.95
6.66,3.33,2.68
6.66,5.00,2.43
6.66,6.66,2.85
6.66,8.33,2.82
6.66,10.00,2.82
6.66,11.66,2.97
6.66,13.33,3.21
6.66,15.00,3.19
6.66,16.66,3.13

Data is listed in columns, headed by contour slice name eg:BC1 is the first slice in the region BC, the proximal limb. Columns 1 and 2 contain x and y coordinates; Column 3 contains LDA ouput voltages in Volts.

6.66,18.33,2.89
8.33,1.66,1.88
8.33,3.33,2.29
8.33,5.00,2.55
8.33,6.66,2.60
8.33,8.33,2.52
8.33,10.00,2.68
8.33,11.66,2.91
8.33,13.33,3.15
8.33,15.00,3.20
8.33,16.66,3.15
8.33,18.33,2.95
10.00,1.66,1.72
10.00,3.33,1.85
10.00,5.00,2.07
10.00,6.66,2.27
10.00,8.33,2.37
10.00,10.00,2.63
10.00,11.66,2.86
10.00,13.33,3.12
10.00,15.00,3.20
10.00,16.66,3.19
10.00,18.33,3.04
11.66,1.66,1.61
11.66,3.33,1.70
11.66,5.00,2.01
11.66,6.66,2.21
11.66,8.33,2.34
11.66,10.00,2.61
11.66,11.66,2.84
11.66,13.33,3.11
11.66,15.00,3.21
11.66,16.66,3.22
11.66,18.33,3.11

13.33,1.66,1.73
13.33,3.33,1.93
13.33,5.00,2.36
13.33,6.66,2.46
13.33,8.33,2.41
13.33,10.00,2.63
13.33,11.66,2.88
13.33,13.33,3.12
13.33,15.00,3.20
13.33,16.66,3.22
13.33,18.33,3.08
15.00,3.33,2.40
15.00,5.00,2.54
15.00,6.66,2.56
15.00,8.33,2.66
15.00,10.00,2.71
15.00,11.66,2.86
15.00,13.33,3.03
15.00,15.00,3.19
15.00,16.66,3.24
16.66,3.33,2.21
16.66,5.00,2.29
16.66,6.66,3.17
16.66,8.33,2.98
16.66,10.00,2.89
16.66,11.66,3.01
16.66,13.33,3.11
16.66,15.00,3.21
16.66,16.66,3.20
18.33,6.66,3.04
18.33,8.33,3.03
18.33,10.00,3.05
18.33,11.66,3.12
18.33,13.33,3.18

BC6

5.00,1.34,1.74
5.00,18.66,1.74
15.00,1.34,1.74
15.00,18.66,1.74
1.34,5.00,1.74
1.34,15.00,1.74
18.66,5.00,1.74
18.66,15.00,1.74
0.00,10.00,1.74
0.55,6.66,1.74
0.55,13.33,1.74
2.54,3.33,1.74
2.54,16.66,1.74
3.33,2.54,1.74
3.33,17.46,1.74
6.66,0.55,1.74
6.66,19.45,1.74
10.00,0.00,1.74
10.00,20.00,1.74
13.33,0.55,1.74
13.33,19.45,1.74
16.66,2.54,1.74
16.66,17.46,1.74
17.46,3.33,1.74
17.46,16.66,1.74
19.45,6.66,1.74
19.45,13.33,1.74
20.00,10.00,1.74
1.66,6.66,2.97
1.66,8.33,3.00
1.66,10.00,3.31

1.66,11.66,3.41
1.66,13.33,3.43
3.33,3.33,2.45
3.33,5.00,2.18
3.33,6.66,2.14
3.33,8.33,2.27
3.33,10.00,2.53
3.33,11.66,2.79
3.33,13.33,3.36
3.33,15.00,3.57
3.33,16.66,3.54
5.00,3.33,2.29
5.00,5.00,2.35
5.00,6.66,2.48
5.00,8.33,2.46
5.00,10.00,2.34
5.00,11.66,2.46
5.00,13.33,2.91
5.00,15.00,3.45
5.00,16.66,3.61
6.66,1.66,2.60
6.66,3.33,2.39
6.66,5.00,2.45
6.66,6.66,2.48
6.66,8.33,2.47
6.66,10.00,2.50
6.66,11.66,2.37
6.66,13.33,2.46
6.66,15.00,2.99
6.66,16.66,3.57
6.66,18.33,3.70
8.33,1.66,2.62
8.33,3.33,2.58
8.33,5.00,2.65

8.33,6.66,2.51
8.33,8.33,2.37
8.33,10.00,2.25
8.33,11.66,2.40
8.33,13.33,2.38
8.33,15.00,2.84
8.33,16.66,3.54
8.33,18.33,2.74
10.00,1.66,2.65
10.00,3.33,2.75
10.00,5.00,2.53
10.00,6.66,2.53
10.00,8.33,2.19
10.00,10.00,2.28
10.00,11.66,2.46
10.00,13.33,2.49
10.00,15.00,2.87
10.00,16.66,3.57
10.00,18.33,3.78
11.66,1.66,2.55
11.66,3.33,2.50
11.66,5.00,2.22
11.66,6.66,2.54
11.66,8.33,2.14
11.66,10.00,2.21
11.66,11.66,2.49
11.66,13.33,2.60
11.66,15.00,3.13
11.66,16.66,3.65
11.66,18.33,3.81
13.33,1.66,2.07
13.33,3.33,2.44
13.33,5.00,2.24
13.33,6.66,2.54

13.33,8.33,2.17
13.33,10.00,2.12
13.33,11.66,2.42
13.33,13.33,2.68
13.33,15.00,3.32
13.33,16.66,3.78
13.33,18.33,3.86
15.00,3.33,2.19
15.00,5.00,2.68
15.00,6.66,2.39
15.00,8.33,2.27
15.00,10.00,2.31
15.00,11.66,2.51
15.00,13.33,2.82
15.00,15.00,3.28
15.00,16.66,3.71
16.66,3.33,1.89
16.66,5.00,2.40
16.66,6.66,2.79
16.66,8.33,2.71
16.66,10.00,2.71
16.66,11.66,2.86
16.66,13.33,3.35
16.66,15.00,3.61
16.66,16.66,3.76
18.33,6.66,2.51
18.33,8.33,3.03
18.33,10.00,3.33
18.33,11.66,3.44
18.33,13.33,3.53

BC4

5.00,1.34,1.74

5.00,18.66,1.74
15.00,1.34,1.74
15.00,18.66,1.74
1.34,5.00,1.74
1.34,15.00,1.74
18.66,5.00,1.74
18.66,15.00,1.74
0.00,10.00,1.74
0.55,6.66,1.74
0.55,13.33,1.74
2.54,3.33,1.74
2.54,16.66,1.74
3.33,2.54,1.74
3.33,17.46,1.74
6.66,0.55,1.74
6.66,19.45,1.74
10.00,0.00,1.74
10.00,20.00,1.74
13.33,0.55,1.74
13.33,19.45,1.74
16.66,2.54,1.74
16.66,17.46,1.74
17.46,3.33,1.74
17.46,16.66,1.74
19.45,6.66,1.74
19.45,13.33,1.74
20.00,10.00,1.74
1.66,6.66,2.96
1.66,8.33,3.06
1.66,10.00,3.22
1.66,11.66,3.32
1.66,13.33,3.30
3.33,3.33,2.74
3.33,5.00,2.48

Data is listed in columns, headed by contour slice name eg:BC1 is the first slice in the region BC, the proximal limb. Columns 1 and 2 contain x and y coordinates; Column 3 contains LDA ouput voltages in Volts.

3.33,6.66,2.50
3.33,8.33,2.51
3.33,10.00,2.52
3.33,11.66,2.89
3.33,13.33,3.39
3.33,15.00,3.46
3.33,16.66,3.30
5.00,3.33,2.55
5.00,5.00,2.53
5.00,6.66,2.61
5.00,8.33,2.33
5.00,10.00,2.27
5.00,11.66,2.51
5.00,13.33,3.14
5.00,15.00,3.42
5.00,16.66,3.50
6.66,1.66,2.54
6.66,3.33,2.44
6.66,5.00,2.59
6.66,6.66,2.74
6.66,8.33,2.30
6.66,10.00,1.98
6.66,11.66,2.39
6.66,13.33,2.60
6.66,15.00,3.26
6.66,16.66,3.55
6.66,18.33,3.50
8.33,1.66,2.45
8.33,3.33,2.48
8.33,5.00,2.50
8.33,6.66,2.62
8.33,8.33,2.31
8.33,10.00,2.03
8.33,11.66,2.18
8.33,13.33,2.48
8.33,15.00,3.16
8.33,16.66,3.57

8.33,18.33,3.60
10.00,1.66,2.36
10.00,3.33,2.53
10.00,5.00,2.46
10.00,6.66,2.55
10.00,8.33,2.14
10.00,10.00,2.14
10.00,11.66,2.13
10.00,13.33,2.49
10.00,15.00,3.13
10.00,16.66,3.57
10.00,18.33,3.65
11.66,1.66,2.20
11.66,3.33,2.62
11.66,5.00,2.40
11.66,6.66,2.73
11.66,8.33,2.35
11.66,10.00,2.17
11.66,11.66,2.23
11.66,13.33,2.57
11.66,15.00,3.20
11.66,16.66,3.61
11.66,18.33,3.66
13.33,1.66,2.05
13.33,3.33,2.53
13.33,5.00,2.35
13.33,6.66,2.75
13.33,8.33,2.44
13.33,10.00,2.31
13.33,11.66,2.40
13.33,13.33,2.78
13.33,15.00,3.34
13.33,16.66,3.65
13.33,18.33,3.61
15.00,3.33,2.65
15.00,5.00,2.45
15.00,6.66,2.72

15.00,8.33,2.66
15.00,10.00,2.51
15.00,11.66,2.62
15.00,13.33,2.91
15.00,15.00,3.37
15.00,16.66,3.63
16.66,3.33,2.07
16.66,5.00,2.80
16.66,6.66,2.60
16.66,8.33,2.59
16.66,10.00,2.64
16.66,11.66,2.94
16.66,13.33,3.34
16.66,15.00,3.56
16.66,16.66,3.50
18.33,6.66,3.07
18.33,8.33,3.15
18.33,10.00,3.27
18.33,11.66,3.43
18.33,13.33,3.48

BC3

5.00,1.34,1.74
5.00,18.66,1.74
15.00,1.34,1.74
15.00,18.66,1.74
1.34,5.00,1.74
1.34,15.00,1.74
18.66,5.00,1.74
18.66,15.00,1.74
0.00,10.00,1.74
0.55,6.66,1.74
0.55,13.33,1.74
2.54,3.33,1.74
2.54,16.66,1.74
3.33,2.54,1.74

3.33,17.46,1.74
6.66,0.55,1.74
6.66,19.45,1.74
10.00,0.00,1.74
10.00,20.00,1.74
13.33,0.55,1.74
13.33,19.45,1.74
16.66,2.54,1.74
16.66,17.46,1.74
17.46,3.33,1.74
17.46,16.66,1.74
19.45,6.66,1.74
19.45,13.33,1.74
20.00,10.00,1.74
1.66,6.66,2.87
1.66,8.33,3.01
1.66,10.00,3.11
1.66,11.66,3.17
1.66,13.33,3.13
3.33,3.33,2.44
3.33,5.00,2.77
3.33,6.66,2.72
3.33,8.33,2.72
3.33,10.00,2.80
3.33,11.66,3.04
3.33,13.33,3.26
3.33,15.00,3.37
3.33,16.66,3.20
5.00,3.33,2.72
5.00,5.00,2.75
5.00,6.66,3.04
5.00,8.33,3.03
5.00,10.00,2.59
5.00,11.66,2.65
5.00,13.33,3.15
5.00,15.00,3.32
5.00,16.66,3.36

6.66,1.66,2.23
6.66,3.33,2.69
6.66,5.00,2.92
6.66,6.66,3.01
6.66,8.33,2.64
6.66,10.00,2.32
6.66,11.66,3.53
6.66,13.33,2.86
6.66,15.00,3.29
6.66,16.66,3.41
6.66,18.33,3.32
8.33,1.66,1.96
8.33,3.33,2.11
8.33,5.00,2.48
8.33,6.66,2.49
8.33,8.33,2.34
8.33,10.00,2.46
8.33,11.66,2.40
8.33,13.33,2.77
8.33,15.00,3.24
8.33,16.66,3.44
8.33,18.33,3.39
10.00,1.66,1.75
10.00,3.33,1.81
10.00,5.00,1.96
10.00,6.66,1.97
10.00,8.33,2.03
10.00,10.00,2.27
10.00,11.66,2.27
10.00,13.33,2.78
10.00,15.00,3.22
10.00,16.66,3.46
10.00,18.33,3.42
11.66,1.66,1.51
11.66,3.33,1.54
11.66,5.00,1.65
11.66,6.66,1.93

11.66,8.33,2.24
11.66,10.00,2.16
11.66,11.66,2.34
11.66,13.33,2.81
11.66,15.00,3.25
11.66,16.66,3.48
11.66,18.33,3.47
13.33,1.66,1.27
13.33,3.33,1.39
13.33,5.00,2.38
13.33,6.66,2.51
13.33,8.33,2.41
13.33,10.00,2.46
13.33,11.66,2.44
13.33,13.33,2.88
13.33,15.00,3.30
13.33,16.66,3.51
13.33,18.33,3.44
15.00,3.33,2.55
15.00,5.00,2.77
15.00,6.66,2.95
15.00,8.33,2.87
15.00,10.00,2.52
15.00,11.66,2.61
15.00,13.33,3.00
15.00,15.00,3.30
15.00,16.66,3.45
16.66,3.33,2.17
16.66,5.00,2.79
16.66,6.66,2.76
16.66,8.33,2.70
16.66,10.00,2.71
16.66,11.66,2.91
16.66,13.33,3.21
16.66,15.00,3.41
16.66,16.66,3.43
18.33,6.66,2.97

18.33,8.33,3.04
18.33,10.00,3.14
18.33,11.66,3.23
18.33,13.33,3.35

BC2

5.00,1.34,1.74
5.00,18.66,1.74
15.00,1.34,1.74
15.00,18.66,1.74
1.34,5.00,1.74
1.34,15.00,1.74
18.66,5.00,1.74
18.66,15.00,1.74
0.00,10.00,1.74
0.55,6.66,1.74
0.55,13.33,1.74
2.54,3.33,1.74
2.54,16.66,1.74
3.33,2.54,1.74
3.33,17.46,1.74
6.66,0.55,1.74
6.66,19.45,1.74
10.00,0.00,1.74
10.00,20.00,1.74
13.33,0.55,1.74
13.33,19.45,1.74
16.66,2.54,1.74
16.66,17.46,1.74
17.46,3.33,1.74
17.46,16.66,1.74
19.45,6.66,1.74
19.45,13.33,1.74
20.00,10.00,1.74
1.66,6.66,2.86
1.66,8.33,3.02

Data is listed in columns, headed by contour slice name eg:BC1 is the first slice in the region BC, the proximal limb. Columns 1 and 2 contain x and y coordinates; Column 3 contains LDA ouput voltages in Volts.

1.66,10.00,3.09
1.66,11.66,3.09
1.66,13.33,3.08
3.33,3.33,2.24
3.33,5.00,2.87
3.33,6.66,2.98
3.33,8.33,2.97
3.33,10.00,3.01
3.33,11.66,3.13
3.33,13.33,3.23
3.33,15.00,3.19
3.33,16.66,3.08
5.00,3.33,2.17
5.00,5.00,2.86
5.00,6.66,3.14
5.00,8.33,3.14
5.00,10.00,2.74
5.00,11.66,2.92
5.00,13.33,3.18
5.00,15.00,3.25
5.00,16.66,3.22
6.66,1.66,1.94
6.66,3.33,2.40
6.66,5.00,2.42
6.66,6.66,2.90
6.66,8.33,2.62
6.66,10.00,2.57
6.66,11.66,2.61
6.66,13.33,3.00
6.66,15.00,3.24
6.66,16.66,3.28
6.66,18.33,3.14
8.33,1.66,1.88
8.33,3.33,2.10
8.33,5.00,2.46
8.33,6.66,2.40
8.33,8.33,2.47
8.33,10.00,2.41
8.33,11.66,2.51
8.33,13.33,2.95
8.33,15.00,3.24
8.33,16.66,3.30
8.33,18.33,3.22
10.00,1.66,1.70
10.00,3.33,1.75
10.00,5.00,1.73
10.00,6.66,1.91
10.00,8.33,2.08
10.00,10.00,2.13
10.00,11.66,2.48
10.00,13.33,2.95
10.00,15.00,3.25
10.00,16.66,3.32
10.00,18.33,3.25
11.66,1.66,1.44
11.66,3.33,1.44
11.66,5.00,1.92
11.66,6.66,2.25
11.66,8.33,2.21
11.66,10.00,2.13
11.66,11.66,2.49
11.66,13.33,2.95
11.66,15.00,3.25
11.66,16.66,3.33
11.66,18.33,3.29
13.33,1.66,1.37
13.33,3.33,1.47
13.33,5.00,2.40
13.33,6.66,2.31
13.33,8.33,2.41
13.33,10.00,2.47
13.33,11.66,2.56
13.33,13.33,2.99
13.33,15.00,3.27
13.33,16.66,3.34
13.33,18.33,3.27
15.00,3.33,2.06
15.00,5.00,2.79
15.00,6.66,3.03
15.00,8.33,2.93
15.00,10.00,2.59
15.00,11.66,2.70
15.00,13.33,3.00
15.00,15.00,3.19
15.00,16.66,3.32
16.66,3.33,2.05
16.66,5.00,2.87
16.66,6.66,3.07
16.66,8.33,2.92
16.66,10.00,2.79
16.66,11.66,2.97
16.66,13.33,3.17
16.66,15.00,3.29
16.66,16.66,3.22
18.33,6.66,2.99
18.33,8.33,3.03
18.33,10.00,3.07
18.33,11.66,3.17
18.33,13.33,3.21

BC5

5.00,1.34,1.74
5.00,18.66,1.74
15.00,1.34,1.74
15.00,18.66,1.74
1.34,5.00,1.74
1.34,15.00,1.74
18.66,5.00,1.74
18.66,15.00,1.74
0.00,10.00,1.74
0.55,6.66,1.74
0.55,13.33,1.74
2.54,3.33,1.74
2.54,16.66,1.74
3.33,2.54,1.74
3.33,17.46,1.74
6.66,0.55,1.74
6.66,19.45,1.74
10.00,0.00,1.74
10.00,20.00,1.74
13.33,0.55,1.74
13.33,19.45,1.74
16.66,2.54,1.74
16.66,17.46,1.74
17.46,3.33,1.74
17.46,16.66,1.74
19.45,6.66,1.74
19.45,13.33,1.74
20.00,10.00,1.74
1.66,6.66,2.84
1.66,8.33,2.95
1.66,10.00,3.09
1.66,11.66,3.17
1.66,13.33,3.15
3.33,3.33,2.56
3.33,5.00,2.65
3.33,6.66,2.52
3.33,8.33,2.49
3.33,10.00,2.50
3.33,11.66,2.87
3.33,13.33,3.24
3.33,15.00,3.31
3.33,16.66,3.21
5.00,3.33,2.61
5.00,5.00,2.55
5.00,6.66,2.72
5.00,8.33,2.68
5.00,10.00,2.34
5.00,11.66,2.49
5.00,13.33,3.00
5.00,15.00,3.33
5.00,16.66,3.34
6.66,1.66,2.24
6.66,3.33,2.60
6.66,5.00,2.73
6.66,6.66,2.85
6.66,8.33,2.54
6.66,10.00,2.07
6.66,11.66,2.39
6.66,13.33,2.58
6.66,15.00,3.16
6.66,16.66,3.40
6.66,18.33,3.38
8.33,1.66,2.10
8.33,3.33,2.48
8.33,5.00,2.67
8.33,6.66,2.51
8.33,8.33,2.08
8.33,10.00,2.04
8.33,11.66,2.33
8.33,13.33,2.46
8.33,15.00,3.09
8.33,16.66,3.41
8.33,18.33,3.42
10.00,1.66,1.82
10.00,3.33,1.70
10.00,5.00,1.86
10.00,6.66,2.00
10.00,8.33,1.88
10.00,10.00,2.12
10.00,11.66,2.17
10.00,13.33,2.45
10.00,15.00,3.08
10.00,16.66,3.41
10.00,18.33,3.45
11.66,1.66,1.67
11.66,3.33,1.88
11.66,5.00,2.58
11.66,6.66,2.19
11.66,8.33,1.95
11.66,10.00,2.25
11.66,11.66,2.17
11.66,13.33,2.51
11.66,15.00,3.12
11.66,16.66,3.45
11.66,18.33,3.46
13.33,1.66,1.48
13.33,3.33,2.07
13.33,5.00,2.65
13.33,6.66,2.82
13.33,8.33,2.52
13.33,10.00,2.30
13.33,11.66,2.37
13.33,13.33,2.60
13.33,15.00,3.22
13.33,16.66,3.45
13.33,18.33,3.42
15.00,3.33,2.73
15.00,5.00,2.63
15.00,6.66,2.87
15.00,8.33,2.81
15.00,10.00,2.43
15.00,11.66,2.48
15.00,13.33,2.81
15.00,15.00,3.27
15.00,16.66,3.49
16.66,3.33,2.19
16.66,5.00,2.80
16.66,6.66,2.61
16.66,8.33,2.58
16.66,10.00,2.54
16.66,11.66,2.78
16.66,13.33,3.18
16.66,15.00,3.41
16.66,16.66,3.20
18.33,6.66,3.02
18.33,8.33,3.11
18.33,10.00,3.11
18.33,11.66,3.23
18.33,13.33,3.30

Columns 1 and 2 contain x and y coordinates, Columns 3-15 contain velocities in cm s^{-1}, Column 17 contains the rms voltage in V. All velocities must be multiplied by a correcting factor of 1.32128.

Centreline Axial Velocities Proximal Stem OA1, Re_{mean} = 1500

1.00	10.00	10.28	6.11	5.80	5.94	7.93	11.35	12.95	13.85	13.71	13.79	13.12	11	.21	9.16	
2.00	10.00	10.32	6.07	4.05	5.66	8.20	11.27	13.23	13.64	14.09	13.77	12.97	11	.62	8.99	
3.00	10.00	10.44	6.35	4.37	5.66	8.37	11.02	13.23	13.88	14.20	13.83	13.32	11	.34	9.23	
4.00	10.00	10.32	6.22	4.18	5.55	8.01	11.12	12.97	14.00	14.33	13.81	13.04	11	.34	9.06	
5.00	10.00	10.37	6.29	4.28	5.57	8.30	11.23	13.14	14.15	14.05	13.87	12.88	11	.53	8.89	
6.00	10.00	10.51	6.92	4.17	5.72	8.55	11.24	13.43	14.18	14.21	14.49	12.89	11	.38	9.42	
7.00	10.00	10.62	6.80	4.52	5.81	8.50	11.72	13.40	14.24	14.50	14.41	13.40	11	.85	9.15	
8.00	10.00	10.59	6.22	4.37	6.16	8.69	11.55	13.68	14.35	14.80	14.02	13.68	11	.83	9.36	
9.00	10.00	10.63	6.42	4.29	5.88	8.60	11.58	13.37	14.46	14.38	13.99	13.29	11	.80	9.36	
10.00	10.00	10.59	6.42	4.37	5.63	8.41	11.41	13.43	14.10	14.24	14.21	13.23	11	.72	9.08	
11.00	10.00	10.67	6.36	4.51	5.86	8.63	11.44	13.48	14.10	14.69	14.35	13.54	11	.66	9.39	

Axial Velocities Proximal Stem OA1, $\alpha = 0\,°$, Re_{mean} = 1500

5.00	2.00	1.93	-0.03	0.08	1.28	2.27	3.02	3.00	3.30	3.00	2.55	2.15	1	.82	0.61	1
4.00	2.00	2.13	0.22	-0.20	1.20	2.46	2.85	3.28	3.30	3.67	3.02	3.00	1	.96	0.78	1
3.00	2.00	2.04	0.05	-0.31	0.86	2.10	2.60	2.91	3.28	3.22	3.05	2.24	1	.76	1.12	1
2.00	2.00	2.11	0.42	0.19	1.57	2.60	3.11	3.28	3.25	3.22	3.08	2.74	2	.15	1.00	1
1.00	2.00	2.10	0.28	-0.45	1.23	2.46	3.19	3.58	3.42	3.08	3.14	2.24	1	.23	0.22	1
1.00	3.00	3.26	0.33	0.02	2.04	3.25	4.76	4.87	5.41	4.93	4.62	4.00	3	.05	1.54	1
2.00	3.00	3.41	0.58	-0.09	2.01	3.39	4.79	5.15	5.18	5.29	4.96	4.43	3	.11	1.85	1
3.00	3.00	3.09	0.33	0.01	1.64	3.14	4.31	4.67	4.71	4.93	4.41	3.90	2	.87	1.57	1
4.00	3.00	3.23	0.28	0.08	1.90	2.85	4.62	4.93	5.27	4.96	4.48	4.12	3	.39	1.96	1
5.00	3.00	4.05	0.82	-0.04	2.48	4.07	5.68	6.44	6.63	6.28	5.70	5.04	3.96	.3	2.31	1
5.00	4.00	3.83	0.54	-0.17	1.86	3.79	5.29	6.24	6.22	6.01	5.62	5.62	3.17	.3	2.20	1
4.00	4.00	3.93	0.26	-0.38	2.07	4.13	5.96	6.15	6.41	6.15	5.60	5.06	3	.60	2.24	1
3.00	4.00	4.04	-0.17	-0.23	1.96	4.09	5.43	6.56	6.50	6.22	6.11	5.21	4	.09	1.90	1
2.00	4.00	4.26	0.72	-0.45	1.93	4.34	5.72	6.64	6.86	6.47	6.42	5.66	4	.14	2.43	1
1.00	4.00	3.88	0.19	-0.17	1.82	3.67	5.58	6.39	5.72	6.81	5.41	5.07	4	.12	2.04	1
1.00	5.00	3.48	-0.14	-0.57	1.83	3.79	4.46	5.58	5.53	4.89	5.14	4.71	3	.32	1.94	1
2.00	5.00	3.30	0.52	-0.06	1.68	3.25	4.74	5.42	5.47	5.30	4.82	4.29	2	.95	1.40	1
3.00	5.00	3.03	-0.34	-0.17	1.73	3.42	4.48	4.93	4.82	4.87	4.59	4.03	2	.63	1.34	1
4.00	5.00	3.19	0.22	-0.68	1.79	3.02	4.43	5.21	5.55	5.21	4.65	3.70	2	.69	1.90	1

Columns 1 and 2 contain x and y coordinates, Columns 3-15 contain velocities in cm s^{-1}, Column 17 contains the rms voltage in V. All velocities must be multiplied by a correcting factor of 1.32128.

5.00	5.00	2.76	-0.15	-0.40	1.48	2.60	3.75	4.73	4.43	4.62	4.45	3.72	2	.74	1.12	1
5.00	6.00	3.41	0.33	-0.47	1.57	3.73	4.69	5.64	5.90	5.43	5.00	4.26	2	.91	1.71	1
4.00	6.00	3.60	0.08	-0.01	1.93	3.70	5.21	6.05	5.83	5.72	5.35	4.85	3	.30	2.01	1
3.00	6.00	3.48	0.11	0.14	1.73	3.58	5.27	5.94	5.85	5.75	4.89	4.54	3	.02	1.53	1
2.00	6.00	3.37	0.33	-0.38	1.68	3.36	4.89	5.47	5.51	5.40	4.99	4.09	3	.14	1.60	1
1.00	6.00	3.22	-0.30	-0.08	1.77	3.17	4.97	5.49	5.12	5.29	4.76	4.09	3	.04	1.34	1
1.00	7.00	2.95	-0.09	-0.48	1.45	3.08	4.34	4.68	5.07	4.71	4.14	3.92	2	.57	1.37	1
2.00	7.00	2.56	-0.04	-0.81	1.27	2.71	4.11	4.65	4.28	4.48	3.88	3.30	2	.35	0.93	1
3.00	7.00	2.46	-0.17	-0.40	1.79	2.60	3.81	4.82	4.06	4.00	3.58	3.19	1	.85	1.00	1
4.00	7.00	2.61	-0.32	-0.14	1.43	2.76	3.92	4.39	4.54	4.26	3.77	3.21	2	.28	0.93	1
5.00	7.00	2.49	-0.34	-0.19	1.40	3.27	3.92	4.31	4.13	4.01	3.64	3.27	1	.88	0.89	1
5.00	8.00	0.98	0.09	-0.25	0.56	1.34	1.49	1.77	1.73	1.73	1.60	1.14	0	.44	0.42	1
4.00	8.00	1.24	-0.01	-0.06	0.84	1.48	1.87	2.01	1.96	1.85	1.79	1.65	1	.14	0.22	1
3.00	8.00	0.99	0.02	-0.17	0.39	1.23	1.82	1.79	1.76	1.28	1.82	1.42	0	.25	0.13	1
2.00	8.00	1.26	-0.10	-0.08	0.76	1.40	2.11	1.85	2.13	2.03	1.68	1.38	0	.76	0.26	1
1.00	8.00	1.23	-0.08	0.28	0.91	1.40	1.96	2.09	2.11	1.71	1.66	1.49	1	.02	0.41	1

Centreline Axial Velocities Proximal Stem OA2, $Re_{mean} = 1500$

12.00	10.00	11.21	6.56	4.45	5.91	9.05	11.72	14.07	15.14	15.59	15.28	14.35	12	.39	9.95	32.00
13.00	10.00	11.24	6.61	4.28	5.96	9.08	11.44	13.90	15.31	15.55	15.38	14.17	12	.80	9.72	35.00
14.00	10.00	10.76	6.28	3.89	5.69	8.69	11.21	13.34	14.69	14.97	14.72	13.96	12	.16	9.33	31.00
15.00	10.00	10.78	6.36	4.09	5.69	8.72	11.24	13.37	14.66	14.97	14.77	13.85	12	.28	9.44	32.00
16.00	10.00	10.81	6.28	3.96	5.83	8.67	11.25	13.47	14.88	15.16	14.74	14.05	12	.18	9.49	32.00
17.00	10.00	10.82	6.24	4.03	5.81	8.54	11.40	13.47	14.88	15.14	14.65	13.88	12	.20	9.51	32.00
18.00	10.00	10.84	6.28	4.00	5.55	8.61	11.21	13.59	14.91	15.04	14.74	14.02	12	.00	9.66	31.00

Axial Velocities Proximal Stem OA2, $\alpha = 0°$, $Re_{mean} = 1500$

18.00	2.00	5.72	0.64	0.33	3.16	5.60	8.13	9.42	9.08	8.38	7.82	7.09	6	.16	4.20	67.00
17.00	2.00	4.29	0.58	-0.15	2.66	4.62	6.30	6.64	6.61	6.33	5.74	6.05	5	.07	2.71	73.00

Columns 1 and 2 contain x and y coordinates, Columns 3-15 contain velocities in cm s^{-1}, Column 17 contains the rms voltage in V. All velocities must be multiplied by a correcting factor of 1.32128.

16.00	2.00	2.55	0.22	-0.06	1.10	2.24	3.58	4.33	4.09	3.70	3.86	3.42	2	.69	1.23	65.00
15.00	2.00	1.50	0.02	0.11	0.86	1.59	2.10	3.08	1.99	2.32	3.02	1.28	1	.59	0.81	97.00
14.00	2.00	2.21	0.03	0.13	0.80	1.60	2.74	4.28	2.91	3.19	3.55	2.99	2	.18	1.04	105.00
13.00	2.00	1.95	-0.17	0.25	0.44	1.79	2.91	3.00	3.98	2.69	3.30	0.95	1	.54	1.17	110.00
12.00	2.00	1.58	4.73	0.33	0.53	1.59	1.03	3.08	3.44	-0.85	4.00	2.24	0	.70	0.92	120.00
12.00	3.00	3.04	0.47	-0.12	1.54	2.85	4.17	5.07	5.32	4.99	1.03	3.75	2	.80	1.65	67.00
13.00	3.00	2.12	0.13	-0.29	1.26	2.27	2.97	3.16	3.36	3.08	3.05	2.60	2	.15	0.86	75.00
14.00	3.00	2.60	0.24	1.75	1.21	2.52	3.42	4.91	3.88	3.88	3.77	3.49	2	.61	1.77	75.00
15.00	3.00	2.51	0.42	0.08	1.34	2.69	3.39	3.50	3.92	3.78	3.81	3.11	2	.60	1.28	76.00
16.00	3.00	3.53	0.52	-0.58	1.94	3.10	4.33	5.58	5.64	5.21	5.10	4.31	3	.73	2.28	75.00
17.00	3.00	4.82	2.88	0.13	2.41	4.73	6.42	7.01	7.12	7.76	6.86	6.61	4	.90	3.19	68.00
18.00	3.00	6.01	1.51	3.14	3.08	5.81	7.88	8.63	8.33	9.66	8.95	8.03	5	.98	4.20	70.00
18.00	4.00	7.31	2.00	0.67	3.88	6.84	9.42	10.58	10.58	11.29	10.31	9.27	7	.57	5.15	55.00
17.00	4.00	6.44	1.59	0.08	3.16	6.11	8.52	9.64	9.44	10.26	8.88	8.21	6	.72	4.62	58.00
16.00	4.00	5.47	1.45	0.54	2.99	5.19	7.30	8.28	7.55	8.37	7.88	6.74	5	.70	3.51	52.00
15.00	4.00	4.71	0.92	0.36	3.00	5.83	6.30	6.53	7.37	7.26	6.92	5.88	4	.76	2.94	58.00
14.00	4.00	4.45	0.99	0.13	2.31	4.29	5.98	6.80	6.86	6.87	6.29	5.68	4	.56	2.89	52.00
13.00	4.00	4.19	0.52	0.39	2.28	3.94	5.64	6.43	6.44	6.44	5.60	5.42	4	.00	2.69	49.00
12.00	4.00	3.75	0.76	0.28	2.41	3.70	5.12	5.83	5.88	5.88	5.68	4.72	3	.45	2.61	49.00
12.00	5.00	4.05	0.69	0.41	2.00	3.90	5.58	6.29	6.24	6.22	5.72	5.04	3	.92	2.33	46.00
13.00	5.00	4.47	0.97	0.33	2.43	4.24	6.00	7.04	6.37	6.91	6.28	5.58	4	.31	3.00	47.00
14.00	5.00	4.69	0.56	-0.01	2.52	4.82	6.72	7.01	7.57	7.40	6.61	5.10	4	.82	2.80	49.00
15.00	5.00	4.89	1.23	0.33	2.77	4.45	6.33	7.20	7.31	8.07	6.98	6.42	4	.90	3.00	55.00
16.00	5.00	5.84	1.38	0.09	2.91	5.38	7.60	8.71	8.69	9.34	8.18	7.40	5	.88	3.60	49.00
17.00	5.00	6.32	1.57	0.09	3.12	5.88	8.30	9.58	9.66	10.00	9.08	8.09	6	.33	3.75	53.00
18.00	5.00	7.54	2.01	0.74	3.96	6.89	10.18	11.51	11.55	11.66	10.95	9.75	7	.53	4.78	50.00
18.00	6.00	7.29	2.07	0.33	3.86	6.74	9.66	10.74	10.63	11.14	10.67	9.55	7	.15	4.71	50.00
17.00	6.00	6.13	0.98	0.30	2.94	5.83	8.44	9.25	9.87	9.44	9.02	8.10	5	.86	3.50	38.00
16.00	6.00	5.78	1.45	0.24	3.04	5.43	7.60	8.82	8.82	8.97	8.41	7.55	5	.70	3.53	34.00
15.00	6.00	5.03	1.10	0.11	2.50	4.72	6.99	7.90	8.01	7.68	7.27	6.26	4	.95	3.02	40.00
14.00	6.00	4.92	1.26	0.28	2.71	4.79	6.78	7.76	7.62	7.54	6.92	5.88	4	.37	2.77	40.00
13.00	6.00	4.54	1.02	0.09	2.59	4.31	6.39	7.10	7.32	6.74	6.33	5.51	4	.29	2.43	39.00
12.00	6.00	4.14	0.33	0.03	2.11	4.05	5.92	6.65	6.59	6.28	5.85	5.12	3	.81	2.56	40.00
12.00	7.00	4.13	0.98	0.50	2.41	3.72	6.16	6.08	6.39	6.16	6.02	5.15	4	.26	2.60	41.00
13.00	7.00	4.16	1.17	0.28	2.49	3.92	6.08	6.47	5.86	6.19	5.94	5.27	4	.40	2.43	41.00
14.00	7.00	4.75	1.06	0.16	2.55	4.54	6.25	6.81	7.31	6.98	6.67	6.25	4	.65	3.33	39.00
15.00	7.00	4.86	1.34	0.48	2.54	4.87	6.31	7.57	7.17	7.34	6.89	5.96	4	.91	3.06	42.00

Columns 1 and 2 contain x and y coordinates, Columns 3-15 contain velocities in cm s^{-1}, Column 17 contains the rms voltage in V. All velocities must be multiplied by a correcting factor of 1.32128.

16.00	7.00	5.82	1.37	0.67	2.46	5.58	7.45	8.44	8.55	8.83	8.27	7.71	5	.83	4.09	42.00
17.00	7.00	6.17	1.36	0.37	3.19	5.81	8.00	9.12	9.10	9.53	8.99	8.05	6	.46	4.26	43.00
18.00	7.00	6.87	2.11	0.65	3.30	6.65	8.84	10.13	10.01	10.22	9.85	8.99	7	.34	4.87	44.00
18.00	8.00	5.67	1.64	0.07	2.61	5.25	7.21	8.01	7.75	8.46	8.11	7.60	6	.33	3.85	52.00
17.00	8.00	5.32	1.60	0.44	3.00	4.74	6.71	7.58	7.53	8.26	7.36	6.93	5	.66	3.71	54.00
16.00	8.00	4.82	1.36	0.39	1.86	4.46	6.31	6.78	7.10	7.32	6.86	6.28	5	.15	3.45	47.00
15.00	8.00	3.99	1.15	0.57	2.35	3.60	5.08	5.86	5.85	6.11	5.81	5.08	4	.28	2.72	43.00
14.00	8.00	3.93	0.98	1.03	2.07	3.75	4.96	5.72	5.60	5.80	5.72	4.87	3	.89	2.71	47.00
13.00	8.00	3.71	1.00	0.30	1.93	3.19	4.87	5.38	5.29	5.43	5.24	4.90	3	.86	2.74	46.00
12.00	8.00	3.11	0.89	0.33	1.58	3.04	3.98	4.50	4.61	4.78	4.39	3.83	3.02	2.09	42.00	

Axial Velocities Proximal Stem OA2 $\alpha = 180°$, $Re_{mean} = 1500$

18.00	18.00	0.07	-0.17	-0.17	0.28	0.36	0.50	0.19	-0.01	-0.06	-0.34	-0.17	-0	.34	-0.43	39.00
17.00	18.00	0.15	-0.32	-0.12	0.48	0.67	0.69	0.57	0.37	0.20	-0.04	-0.23	-0	.29	-0.08	35.00
16.00	18.00	0.40	-0.40	-0.27	0.65	1.04	1.21	0.89	0.71	0.89	0.33	0.18	-0	.12	-0.36	36.00
15.00	18.00	0.54	0.05	-0.12	0.67	1.23	1.57	1.06	0.16	1.12	0.56	0.39	-0	.23	-0.12	36.00
14.00	18.00	0.80	-0.43	-0.31	0.78	1.45	1.62	1.28	1.26	1.28	1.42	0.72	0	.44	-0.06	35.00
13.00	18.00	0.96	-0.40	-0.17	1.00	1.49	1.73	1.90	1.71	1.43	1.38	0.78	0	.52	-0.08	36.00
12.00	18.00	1.13	-0.42	-0.23	0.57	1.58	1.85	2.00	2.09	2.01	1.96	1.15	0	.74	0.16	35.00
12.00	17.00	2.47	-0.27	-0.27	1.14	2.91	3.86	4.35	4.54	4.39	3.40	2.61	1	.83	0.71	36.00
13.00	17.00	2.38	-0.49	-0.17	1.15	2.80	3.92	4.28	4.20	4.00	3.68	2.67	1	.66	0.37	39.00
14.00	17.00	2.22	-0.57	-0.23	0.93	2.65	3.75	4.33	4.29	4.16	3.27	2.18	1	.57	0.24	41.00
15.00	17.00	1.91	-0.75	-1.22	1.04	2.48	3.79	4.13	4.09	3.53	2.46	1.64	0	.80	-0.06	41.00
16.00	17.00	1.63	-0.60	-0.64	1.17	2.33	3.14	3.96	3.60	2.93	1.96	1.21	0	.31	-0.12	42.00
17.00	17.00	1.39	0.72	-0.54	0.78	2.38	3.02	3.05	3.14	2.66	1.54	0.53	0	.84	-0.40	44.00
18.00	17.00	0.99	-1.11	-0.47	0.95	1.34	2.57	2.67	2.50	1.71	0.85	0.33	-0	.01	-0.29	43.00
18.00	16.00	2.52	-0.73	3.04	0.95	2.99	4.26	4.67	4.87	4.09	2.82	1.83	0	.87	0.18	41.00
17.00	16.00	2.32	-0.30	-0.40	1.17	2.91	4.56	5.12	5.02	4.13	2.80	2.03	1	.15	0.11	41.00
16.00	16.00	2.67	-0.40	-0.19	1.10	3.47	4.86	5.25	5.53	4.76	3.30	2.41	1	.60	0.69	40.00
15.00	16.00	2.86	-0.31	-0.73	1.54	3.50	5.21	5.86	5.94	4.90	3.84	2.80	1	.59	0.67	38.00
14.00	16.00	3.34	-0.21	-0.44	1.51	3.96	5.58	6.54	6.52	5.57	4.65	3.43	2	.18	0.93	39.00
13.00	16.00	3.49	-0.17	-0.40	1.45	4.14	5.63	6.70	6.56	5.55	4.65	3.75	2	.57	1.00	39.00

Columns 1 and 2 contain x and y coordinates, Columns 3-15 contain velocities in cm s^{-1}, Column 17 contains the rms voltage in V. All velocities must be multiplied by a correcting factor of 1.32128.

12.00	16.00	3.91	-0.03	-0.09	1.76	4.12	6.19	6.95	7.29	6.53	5.29	4.34	3	.00	1.71	38.00
12.00	15.00	3.81	0.07	-0.23	1.96	4.24	5.94	6.89	6.80	6.16	4.89	4.03	3	.10	1.68	42.00
13.00	15.00	3.76	-0.01	-0.44	1.60	4.20	6.11	6.80	7.23	6.09	5.02	4.05	2	.99	1.71	42.00
14.00	15.00	3.86	0.16	-0.34	1.93	4.14	6.14	7.03	7.57	6.22	5.04	4.17	2	.85	1.96	40.00
15.00	15.00	3.30	-0.17	-0.36	1.88	3.96	5.49	6.22	6.37	5.27	4.48	3.14	2	.18	1.28	43.00
16.00	15.00	3.26	0.02	-0.31	1.99	3.78	5.43	6.22	6.50	5.27	4.26	2.85	2	.15	1.06	40.00
17.00	15.00	2.91	0.11	-0.17	1.62	3.70	4.93	5.10	6.00	4.82	3.81	2.91	1	.85	1.45	44.00
18.00	15.00	2.44	-0.21	-0.34	1.25	3.62	4.46	4.84	5.27	3.86	3.12	1.68	1	.27	0.82	50.00
18.00	14.00	2.46	-0.04	-0.06	1.23	2.97	4.28	4.61	5.08	3.25	2.97	2.87	2	.03	0.65	44.00
17.00	14.00	2.78	0.05	-0.62	1.12	3.08	4.37	4.93	5.15	3.70	3.64	3.14	1	.90	1.28	48.00
16.00	14.00	3.17	-0.26	-0.20	1.28	3.50	4.82	5.41	6.00	4.99	4.43	3.61	2	.77	1.06	39.00
15.00	14.00	3.27	-0.06	-0.29	1.02	3.79	5.30	5.85	6.20	4.61	4.05	4.16	2	.43	1.04	43.00
14.00	14.00	3.75	-0.30	-0.45	1.55	4.11	5.85	6.59	7.15	6.05	5.17	4.48	3	.30	1.36	42.00
13.00	14.00	3.77	-0.32	-0.53	1.25	4.29	6.01	6.97	7.10	5.86	5.23	4.80	3	.25	1.28	39.00
12.00	14.00	4.30	-0.23	0.19	1.48	4.54	6.22	7.20	8.01	6.67	6.14	5.46	4	.09	1.96	42.00
12.00	13.00	3.97	0.28	-0.01	1.65	4.73	6.02	6.50	7.31	6.64	5.69	5.27	3	.58	1.85	59.00
13.00	13.00	3.67	-0.04	0.16	1.81	4.01	5.57	6.29	6.76	6.13	4.87	4.16	3	.25	1.58	40.00
14.00	13.00	3.53	0.11	-0.45	1.59	4.09	5.43	6.08	6.64	5.60	4.54	4.14	2	.88	1.12	59.00
15.00	13.00	3.29	0.03	-0.30	1.68	3.88	5.21	5.51	6.07	5.47	4.16	3.73	2	.54	1.21	41.00
16.00	13.00	2.88	0.14	-0.34	1.49	3.36	4.72	5.08	5.51	4.74	3.62	3.34	2	.14	0.84	46.00
17.00	13.00	2.51	0.19	-0.03	1.34	2.97	4.00	4.03	4.87	4.23	3.08	3.00	1	.76	0.42	65.00
18.00	13.00	1.82	-0.04	-0.02	1.30	2.69	3.32	3.55	3.43	3.14	1.71	1.77	1	.19	0.28	44.00
18.00	12.00	1.32	-0.15	-0.12	1.09	1.87	2.29	2.32	2.24	2.24	1.42	0.98	0	.72	0.30	47.00
17.00	12.00	1.37	0.03	-0.21	1.27	2.05	2.41	2.31	2.22	2.13	1.27	1.30	0	.95	0.29	41.00
16.00	12.00	2.28	0.11	-0.01	1.42	2.78	3.86	3.75	4.01	3.53	2.74	2.65	1	.70	0.95	39.00
15.00	12.00	2.52	0.01	-0.42	1.38	2.97	3.94	4.24	4.35	4.14	3.51	2.91	2	.09	0.80	40.00
14.00	12.00	3.10	0.18	-0.25	1.58	3.73	4.65	5.14	5.25	4.99	4.29	3.86	2	.84	1.64	38.00
13.00	12.00	3.21	0.03	-0.12	1.71	3.68	4.74	5.36	5.45	5.23	4.37	4.01	2	.97	1.49	39.00
12.00	12.00	3.82	0.41	-0.15	2.00	3.98	5.47	5.83	6.11	5.98	5.47	4.84	3	.62	1.98	41.00

Axial Velocities Distal Stem $\alpha = 180°$, $Re_{mean} = 1500$

19.00	12.00	5.22	2.00	1.62	2.07	5.15	7.27	6.24	8.71	7.83	8.33	6.78	5	.49	2.84	86.62
20.00	12.00	5.36	2.11	1.68	2.95	6.41	5.53	6.37	7.98	8.65	7.32	8.05	7	.40	5.60	120.80
21.00	12.00	6.57	2.63	1.77	2.69	6.37	7.62	9.70	7.14	9.66	8.78	8.15	7	.21	4.93	115.87

Columns 1 and 2 contain x and y coordinates, Columns 3-15 contain velocities in cm s^{-1}, Column 17 contains the rms voltage in V. All velocities must be multiplied by a correcting factor of 1.32128.

22.00	12.00	6.33	2.76	1.85	3.21	6.16	6.20	8.24	6.67	8.43	5.36	6.95	6	.95	6.05	131.10
23.00	12.00	6.28	3.70	1.92	3.66	5.94	7.42	6.97	8.87	8.86	9.60	7.36	7	.88	5.29	125.11
24.00	12.00	6.69	2.71	1.38	2.80	7.01	8.05	10.43	10.91	8.80	8.13	10.67	8	.09	5.73	123.85
25.00	12.00	7.21	3.45	1.17	2.78	7.25	9.81	10.48	9.73	10.41	10.41	9.27	7	.75	6.11	115.75
26.00	12.00	6.53	2.69	1.28	2.43	5.63	8.46	9.22	10.73	11.63	12.42	10.09	7	.45	4.73	118.87
27.00	12.00	6.65	2.97	1.04	2.16	5.21	6.29	10.89	10.37	7.36	10.18	8.78	7	.12	3.57	113.75
27.00	13.00	8.34	3.44	2.18	3.33	6.02	8.91	9.58	12.56	12.47	11.30	11.07	7	.59	6.44	117.77
26.00	13.00	8.16	4.35	2.05	3.57	6.56	10.31	13.38	11.08	12.22	10.93	9.70	9	.23	6.35	117.77
25.00	13.00	8.02	3.96	2.01	3.57	6.97	10.09	12.84	10.99	10.86	11.44	10.18	9	.44	7.60	116.25
24.00	13.00	7.97	3.42	2.09	3.55	6.78	7.72	11.85	10.31	10.26	11.98	10.97	10	.43	6.11	109.74
23.00	13.00	7.89	3.66	1.60	3.68	6.89	8.09	9.57	10.84	11.44	11.60	10.56	9	.44	7.17	118.78
22.00	13.00	7.55	4.01	1.66	3.55	6.99	9.06	10.13	10.71	11.10	10.09	9.06	9	.72	6.50	109.75
21.00	13.00	7.20	3.30	1.86	3.40	6.93	7.34	8.87	9.72	10.69	10.91	9.92	6	.99	6.65	110.73
20.00	13.00	6.57	3.94	2.03	2.95	5.72	7.40	6.89	9.30	9.72	7.08	8.95	6	.71	4.50	117.73
19.00	13.00	6.24	2.31	1.73	3.38	5.47	6.48	9.06	7.62	7.44	8.59	7.88	5	.47	6.13	106.71
19.00	14.00	6.25	2.63	1.98	2.71	5.43	7.42	9.45	8.65	8.97	9.66	6.86	7	.77	4.20	113.67
20.00	14.00	6.74	3.12	1.66	3.42	5.70	7.36	9.87	8.58	10.24	9.25	8.91	8	.33	5.19	109.69
21.00	14.00	7.11	3.02	1.85	3.30	6.00	8.07	10.20	8.69	10.59	9.42	10.16	7	.51	5.94	112.74
22.00	14.00	7.54	3.71	2.35	3.79	5.92	8.01	11.68	9.94	11.45	10.15	8.61	9	.08	5.72	114.78
23.00	14.00	7.81	4.22	2.54	3.79	6.76	9.70	9.73	11.45	10.48	10.44	9.88	9	.79	6.46	115.78
24.00	14.00	8.14	4.05	1.96	4.16	6.76	9.15	11.16	10.24	10.33	11.70	8.63	8	.69	6.20	120.78
25.00	14.00	8.34	4.54	2.35	3.58	7.90	10.37	11.83	13.01	12.61	11.21	11.32	10	.26	7.85	117.78
26.00	14.00	8.46	4.79	2.43	4.00	6.67	9.47	15.08	11.83	10.76	11.16	11.41	7	.90	8.01	115.79
27.00	14.00	8.55	5.12	2.22	4.05	7.34	9.81	13.40	13.44	11.75	13.34	10.71	10	.95	6.95	122.80
27.00	15.00	8.37	3.98	2.35	4.00	6.11	9.50	12.00	11.24	11.72	10.73	12.53	8	.07	7.12	113.84
26.00	15.00	8.05	4.29	1.79	2.74	7.31	10.31	11.72	9.67	10.82	12.64	9.42	7	.96	7.43	119.89
25.00	15.00	8.12	3.75	2.52	3.86	6.86	9.62	9.94	10.82	11.64	9.45	10.58	9	.60	7.01	119.85
24.00	15.00	8.05	4.13	5.17	3.77	6.33	9.62	12.07	11.47	11.29	11.85	11.55	8	.76	6.26	114.80
23.00	15.00	7.73	3.72	1.87	3.30	6.70	7.59	11.80	12.84	11.27	9.39	10.87	8	.72	6.39	113.81
22.00	15.00	7.48	3.62	2.13	3.51	5.06	8.61	11.87	11.77	10.37	9.04	11.02	7	.75	6.54	108.78
21.00	15.00	7.26	3.79	2.41	4.67	5.98	8.76	8.31	8.46	9.85	10.33	9.70	6	.15	5.06	120.92
20.00	15.00	6.58	2.35	1.54	3.50	5.91	8.27	7.82	8.83	9.98	8.38	9.08	6	.89	4.76	104.70
19.00	15.00	6.10	2.63	1.73	2.97	4.14	7.62	8.74	10.37	7.79	9.08	7.45	8	.18	5.04	106.75
19.00	16.00	5.99	0.78	1.45	2.97	3.64	7.96	6.95	5.94	8.52	9.53	4.37	6	.56	4.26	97.73

Columns 1 and 2 contain x and y coordinates, Columns 3-15 contain velocities in cm s^{-1}, Column 17 contains the rms voltage in V. All velocities must be multiplied by a correcting factor of 1.32128.

20.00	16.00	6.66	3.50	1.54	2.97	3.78	6.64	10.99	9.67	9.28	9.25	9.36	9	.00	6.22	108.74
21.00	16.00	7.04	3.68	2.01	3.47	5.21	8.41	9.25	10.20	8.97	9.49	9.64	6	.31	5.53	108.72
22.00	16.00	7.41	4.48	2.18	3.60	5.83	8.78	11.12	10.69	10.26	9.83	9.29	8	.20	5.06	112.76
23.00	16.00	7.75	3.53	2.13	4.09	5.77	8.30	12.56	11.27	10.37	12.05	7.51	8	.52	6.39	109.76
24.00	16.00	7.92	3.68	2.28	3.88	5.85	10.37	10.86	10.43	12.59	11.83	10.91	9	.47	6.16	112.81
25.00	16.00	8.04	3.70	1.57	4.03	5.88	9.36	12.61	14.13	15.14	9.64	8.74	9	.64	6.56	120.67
26.00	16.00	8.28	4.09	1.70	3.68	6.46	10.65	12.84	10.82	10.71	11.62	10.16	9	.32	7.40	118.87
27.00	16.00	8.29	4.12	2.41	3.86	6.75	9.61	12.87	10.26	11.13	11.86	8.72	8	.69	7.59	114.74
27.00	17.00	7.77	3.73	1.45	3.43	6.20	10.48	8.24	10.89	12.02	10.11	9.79	10	.01	6.93	118.76
26.00	17.00	7.40	3.53	1.08	3.08	6.31	10.26	9.23	12.48	10.43	10.91	8.52	7	.88	5.53	116.76
25.00	17.00	7.50	3.34	1.43	3.21	5.85	7.73	10.54	13.87	8.33	11.75	10.18	9	.19	6.74	121.80
24.00	17.00	7.50	4.00	1.66	3.12	5.62	9.94	8.63	11.19	12.02	9.64	8.54	7	.75	6.71	110.75
23.00	17.00	7.32	3.98	1.34	3.06	5.68	10.05	8.67	10.76	9.49	10.50	8.50	9	.01	6.11	104.73
22.00	17.00	7.01	3.36	1.58	3.06	5.23	7.70	9.36	10.56	11.45	8.20	8.46	7	.01	5.81	110.74
21.00	17.00	6.68	3.16	2.49	3.00	5.29	7.90	11.16	6.30	10.34	8.44	10.87	4	.51	5.55	112.73
20.00	17.00	6.37	3.04	1.92	2.84	3.47	7.25	8.95	7.57	10.18	9.55	7.12	8	.01	4.43	108.74
19.00	17.00	5.82	2.50	1.55	3.17	4.18	7.66	9.34	9.27	7.36	8.78	8.41	3	.71	4.43	102.72
19.00	18.00	5.17	2.32	1.17	2.32	3.50	7.20	5.94	8.58	6.58	7.71	4.79	4	.99	3.78	92.64
20.00	18.00	5.61	2.97	1.34	2.57	4.57	5.91	8.41	7.34	9.98	7.71	7.62	5	.35	4.00	104.64
21.00	18.00	5.50	1.47	0.89	2.13	4.78	5.58	7.60	7.29	7.10	7.70	6.65	6	.41	3.58	93.66
22.00	18.00	6.02	2.67	1.36	2.57	4.67	7.81	9.42	8.72	9.49	9.68	8.59	7	.12	4.84	103.66
23.00	18.00	5.07	1.94	0.91	1.79	2.95	5.21	7.73	8.74	9.68	7.92	5.77	5	.02	4.29	106.76
24.00	18.00	5.67	2.85	0.61	2.01	5.15	7.62	8.35	8.63	10.09	7.51	6.95	7	.57	3.98	109.76
25.00	18.00	5.90	2.31	1.17	2.16	4.65	6.65	8.97	8.52	10.11	7.60	8.65	7	.34	4.29	105.71
26.00	18.00	5.32	2.43	0.95	1.85	5.30	4.48	6.24	8.84	8.71	6.69	7.36	7	.04	3.71	109.71
27.00	18.00	5.24	1.12	0.95	2.09	3.70	4.95	7.25	8.13	8.41	7.42	3.32	6	.31	3.27	101.75

Centreline Axial Velocities Distal Stem, $Re_{mean} = 1500$

27.00	10.00	6.60	1.68	2.24	3.47	7.59	7.82	7.57	8.44	11.66	9.25	8.32	9	.33	4.71	173.116
26.00	10.00	6.71	3.19	1.42	4.46	7.55	10.56	7.45	8.87	8.41	10.61	9.08	5	.92	3.64	163.109
25.00	10.00	7.54	2.28	1.23	4.57	8.15	8.95	9.42	9.40	11.10	6.50	13.38	7	.27	5.06	160.110
24.00	10.00	8.15	4.11	1.21	4.13	8.56	8.80	12.73	14.26	11.27	9.29	11.16	9	.83	6.20	168.108
23.00	10.00	8.33	2.63	1.28	4.16	7.98	12.00	12.67	12.39	12.93	13.94	10.80	6	.78	7.42	160.103
22.00	10.00	8.85	2.46	0.53	4.17	7.93	8.97	15.28	13.01	14.58	9.25	13.43	9	.36	4.96	145.950

Columns 1 and 2 contain x and y coordinates, Columns 3-15 contain velocities in cm s^{-1}, Column 17 contains the rms voltage in V. All velocities must be multiplied by a correcting factor of 1.32128.

21.00	10.00	8.80	4.00	0.87	4.29	8.26	10.22	13.04	13.23	11.70	14.30	10.84	9	.04	6.97	132.860
20.00	10.00	8.67	3.92	1.25	4.26	7.27	10.56	12.91	13.81	11.81	11.59	11.06	9	.38	6.69	134.920
19.00	10.00	8.24	3.81	1.53	4.13	6.99	8.76	12.39	12.07	12.84	11.87	11.19	9	.66	6.61	126.870

Axial Velocities Distal Stem $\alpha = 0°$, $Re_{mean} = 1500$

19.00	8.00	1.83	0.93	0.57	1.02	0.95	1.58	2.33	2.01	1.51	1.30	4.01	0	.91	2.01	125.115
20.00	8.00	2.71	3.00	2.76	0.72	1.19	0.16	1.81	4.43	2.69	5.75	0.24	3	.14	2.48	125.118
21.00	8.00	2.39	0.95	2.44	1.98	3.43	3.14	4.07	4.82	3.10	0.11	2.91	3	.04	2.37	125.110
22.00	8.00	2.57	0.84	0.67	2.91	1.42	3.42	6.02	4.45	-0.20	5.66	1.65	2	.74	1.79	140.116
23.00	8.00	3.05	1.28	0.48	0.78	2.48	3.40	6.99	3.96	4.39	5.00	3.81	3	.75	0.74	130.107
24.00	8.00	3.31	3.70	0.67	1.49	2.43	2.33	7.32	5.32	7.51	4.01	3.21	5	.51	3.49	125.115
25.00	8.00	4.03	0.28	0.25	1.20	3.53	4.00	3.81	5.43	8.66	6.30	5.41	5	.80	1.51	126.109
26.00	8.00	4.68	2.43	1.06	5.83	4.71	2.27	9.30	7.43	5.21	3.61	2.80	6	.11	3.44	135.111
27.00	8.00	4.53	1.55	4.00	2.43	3.49	3.25	3.94	5.14	7.34	3.45	7.25	3	.94	4.97	122.115
27.00	7.00	4.23	2.11	0.24	1.98	5.51	5.58	4.86	6.97	5.62	6.44	5.40	2	.67	3.19	136.115
26.00	7.00	4.02	1.48	0.50	2.21	3.86	7.45	6.33	7.87	3.22	4.17	6.92	5	.97	3.64	140.110
25.00	7.00	3.33	0.41	0.16	1.40	3.30	0.16	4.82	5.70	1.73	3.32	2.74	2	.85	2.01	140.116
24.00	7.00	4.16	6.78	0.65	1.45	3.64	4.61	7.32	9.51	5.66	5.21	8.33	6	.48	1.15	132.110
23.00	7.00	3.17	1.96	0.67	1.10	1.36	0.82	5.57	6.99	5.62	3.66	5.10	2	.59	2.78	132.112
22.00	7.00	3.13	1.85	0.85	1.51	4.59	1.06	2.82	3.23	4.50	3.25	8.01	1	.71	4.76	136.125
21.00	7.00	0.53	0.72	-0.20	0.78	-0.12	0.25	-0.09	2.74	1.79	-1.72	3.39	2	.15	-0.15	69.500
20.00	7.00	0.66	0.95	0.18	0.69	0.57	2.56	-0.34	0.46	0.01	1.10	0.29	1	.73	0.91	69.500
19.00	7.00	0.78	0.56	0.39	1.17	0.30	0.50	0.19	1.62	1.28	0.95	0.30	0	.11	0.70	65.480
19.00	6.00	-0.31	-0.96	0.08	1.00	-0.51	-0.43	-0.71	1.48	-1.44	-0.73	0.19	-0	.51	0.95	63.480
20.00	6.00	-0.15	-0.29	0.14	0.48	-0.17	-0.45	0.26	-0.10	0.26	-1.13	-0.68	-1	.09	-0.30	63.510
21.00	6.00	0.22	-0.15	0.09	0.63	-0.38	-0.62	0.14	-0.40	1.15	-0.66	-0.32	1	.47	0.37	68.530
22.00	6.00	0.43	0.29	-0.12	1.00	-0.47	0.91	0.57	1.77	2.39	1.43	-0.02	0	.72	-1.20	82.600
23.00	6.00	0.82	0.53	0.36	0.95	-0.68	2.18	1.26	0.95	2.74	0.22	-0.37	2	.94	0.50	81.600
24.00	6.00	1.16	0.48	0.54	1.02	-0.42	0.41	1.08	2.57	5.02	1.90	1.00	-0	.44	1.75	82.610
25.00	6.00	1.41	0.11	0.50	1.54	0.05	1.90	4.26	3.08	1.42	2.13	0.92	1	.79	1.17	83.610
26.00	6.00	2.30	0.67	0.56	1.40	1.06	4.20	3.28	3.05	0.13	4.31	3.78	1	.82	1.62	81.620
27.00	6.00	2.30	0.76	0.33	1.32	2.28	3.06	5.00	3.90	4.07	1.85	2.20	1	.06	2.50	81.600

Columns 1 and 2 contain x and y coordinates, Columns 3-15 contain velocities in cm s^{-1}, Column 17 contains the rms voltage in V. All velocities must be multiplied by a correcting factor of 1.32128.

27.00	5.00	2.04	0.67	0.25	1.28	1.28	1.51	1.99	3.19	6.02	2.07	5.97	3	.53	2.55	76.550
26.00	5.00	1.40	0.67	0.53	1.12	0.05	0.47	-0.17	0.13	3.02	0.05	3.11	2	.85	3.19	78.570
25.00	5.00	1.20	-0.70	0.26	1.32	-1.54	2.56	2.56	1.86	4.20	1.77	1.36	0	.33	-0.81	79.580
24.00	5.00	0.41	0.28	0.37	1.04	-1.54	0.22	2.41	3.12	0.07	-0.10	2.93	2	.48	-0.34	78.570
23.00	5.00	-0.07	-0.87	0.01	0.50	-1.35	0.16	0.16	-0.06	-0.58	1.21	0.97	-0	.19	-0.81	76.550
22.00	5.00	-0.02	-0.94	-0.01	0.18	-1.05	-1.30	-1.13	0.11	0.87	1.10	1.08	2	.80	0.76	76.560
21.00	5.00	0.22	-0.93	-0.29	0.44	-0.87	-0.20	-0.45	-0.45	1.42	0.42	-1.30	2	.07	-1.77	82.620
20.00	5.00	-0.27	-0.14	-0.17	0.24	-0.25	-0.57	-0.83	0.61	-0.19	-0.21	-1.58	-1	.15	-1.30	76.580
19.00	5.00	-0.03	-0.75	-0.34	0.74	-0.23	-0.55	0.59	1.32	-0.66	1.45	-0.51	0	.07	-0.62	66.540
19.00	4.00	1.00	3.22	2.91	0.53	-0.37	-0.31	0.30	-0.23	4.45	0.56	0.08	-0	.37	-1.49	64.520
20.00	4.00	-0.01	-0.68	-0.08	0.52	-0.72	-0.47	0.24	-0.32	2.31	0.61	-0.90	-1	.80	-0.83	69.560
21.00	4.00	1.70	-1.11	-0.34	0.76	-0.87	-1.20	1.47	4.31	6.78	7.85	-0.49	1	.64	0.16	79.580
22.00	4.00	0.47	-0.96	0.39	0.44	-1.21	0.72	1.45	0.44	-0.59	2.94	2.21	-1	.52	-0.59	78.560
23.00	4.00	0.22	-0.17	0.57	0.95	-1.16	-1.33	0.84	1.06	2.54	0.18	1.64	1	.38	-0.64	79.580
24.00	4.00	1.02	-0.55	0.35	0.95	-1.01	1.19	3.45	2.28	2.05	1.86	0.28	1	.53	0.99	80.580
25.00	4.00	1.65	0.13	-0.08	1.25	0.44	0.82	2.69	2.31	4.57	4.56	3.17	0	.85	1.25	84.600
26.00	4.00	2.70	0.50	0.33	1.34	-0.45	1.68	7.45	7.34	7.68	1.23	4.43	1	.51	0.33	82.610
27.00	4.00	2.78	1.40	0.11	1.28	1.34	3.53	5.46	10.54	3.44	5.10	4.45	2	.35	1.34	82.610
27.00	3.00	3.20	0.80	0.18	1.47	3.49	2.33	2.56	4.52	4.57	4.11	5.29	3	.04	1.64	82.600
26.00	3.00	4.23	5.24	0.25	1.34	2.43	2.71	3.98	7.62	8.74	7.85	1.93	6	.89	5.60	85.630
25.00	3.00	2.87	0.44	-0.08	0.99	2.07	1.21	9.36	7.34	5.60	5.77	3.47	2	.18	-0.30	84.620
24.00	3.00	3.58	-0.27	2.99	4.05	2.63	1.64	4.05	3.98	4.24	5.40	7.49	6	.71	1.25	84.620
23.00	3.00	2.17	-0.90	-0.25	0.85	-0.25	0.97	2.00	5.00	2.69	5.60	2.41	3	.53	1.51	84.600
22.00	3.00	2.03	4.35	-0.12	0.61	-0.58	-1.31	0.18	3.47	3.73	2.50	6.16	3	.86	0.89	82.620
21.00	3.00	0.68	-0.82	-0.34	1.37	-0.43	1.57	3.11	-0.45	0.30	2.52	-0.85	1	.40	-0.45	75.580
20.00	3.00	0.36	-0.38	-0.08	0.54	-0.06	-0.47	0.89	2.18	-1.05	-0.01	1.14	-0	.66	0.46	71.580
19.00	3.00	0.13	-0.15	0.24	0.59	0.13	-0.04	1.10	-0.27	0.20	0.67	-0.30	-1	.33	0.14	65.550
19.00	2.00	0.99	-0.23	0.87	0.84	0.57	1.32	1.43	1.42	0.24	1.81	-0.19	1	.73	-0.27	70.580
20.00	2.00	0.78	-0.25	0.59	0.31	0.52	2.03	1.19	0.63	1.12	0.13	0.44	1	.06	-0.49	69.580
21.00	2.00	1.39	0.07	-0.06	0.46	0.76	2.87	2.48	-0.01	2.41	3.55	3.45	1	.34	0.54	75.610
22.00	2.00	1.43	0.08	-0.48	0.30	0.44	1.79	3.50	1.87	4.90	-0.96	0.98	3	.16	-0.20	81.620
23.00	2.00	1.92	0.05	0.07	0.56	1.42	1.42	4.72	4.28	3.53	3.73	1.25	-0	.70	1.06	82.620
24.00	2.00	2.51	0.61	0.14	1.08	2.28	1.92	2.57	5.43	3.30	3.96	3.43	2	.80	1.36	85.640
25.00	2.00	3.26	0.29	0.74	0.74	2.87	4.95	4.35	6.87	6.93	4.97	4.93	2	.91	1.38	84.640
26.00	2.00	3.16	-0.23	0.31	1.14	4.01	1.85	3.87	4.26	2.10	4.40	3.53	2.	80	0.03	84.620
27.00	2.00	3.14	0.37	0.33	0.67	4.24	4.35	2.93	2.93	3.47	3.04	4.93	3	.17	2.07	82.620

Columns 1 and 2 contain x and y coordinates, Columns 3-15 contain velocities in cm s^{-1}, Column 17 contains the rms voltage in V. All velocities must be multiplied by a correcting factor of 1.32128.

Axial Velocities Proximal Limb $\alpha = 0°$, $Re_{mean} = 1500$

28.00	4.00	-0.70	-0.38	0.46	1.36	0.56	0.61	-1.78	1.02	-1.41	-2.21	-0.66	-1	.26	-1.07	38.04
29.00	4.00	-0.72	-0.92	0.50	1.12	0.44	0.48	0.87	-1.09	-2.01	-1.93	-1.37	-1	.69	-0.83	44.04
30.00	4.00	-0.49	0.29	0.32	1.81	0.27	-1.44	-3.80	0.38	-0.27	-0.15	-1.78	-1	.05	-0.46	58.04
31.00	4.00	0.12	1.55	0.37	1.28	0.35	-2.29	-1.73	1.58	-0.90	-0.57	-0.85	-0	.23	0.84	64.05
32.00	4.00	0.62	1.62	0.71	1.34	0.22	-2.57	-0.38	0.14	-0.47	0.54	-0.23	1	.38	1.23	73.05
33.00	4.00	2.15	1.36	0.71	1.33	-0.07	-0.44	4.56	5.09	2.51	1.08	5.40	2	.82	2.57	76.05
34.00	4.00	2.83	1.45	0.42	1.47	-0.27	1.30	5.36	3.70	3.51	4.33	4.61	2	.35	1.79	79.05
35.00	4.00	3.53	1.81	0.63	1.75	-0.07	3.55	6.97	5.06	4.36	4.84	6.04	3	.83	3.49	78.05
36.00	4.00	3.78	2.07	0.46	1.62	-0.88	4.67	6.84	5.92	7.85	6.61	6.03	4	.56	3.08	74.05
37.00	4.00	3.89	1.51	0.37	1.71	-0.25	3.45	7.30	5.34	7.68	6.52	5.51	4	.33	3.12	79.05
28.00	3.00	0.41	-1.18	0.33	1.34	1.30	2.03	1.92	0.03	-0.55	-0.45	-0.23	0	.65	-1.56	50.04
29.00	3.00	-0.82	-0.68	0.28	0.67	0.48	0.03	-1.63	-1.99	-3.07	-1.54	-1.15	-1	.30	-0.38	54.04
30.00	3.00	-1.24	-.72	.33	.83	.21	.49	-.66	-2.79	-4.92	-3.69	-3.31	-.72	-2.77	6	0.05
31.00	3.00	-0.69	-0.53	0.56	1.04	0.31	0.33	0.61	-2.25	-4.53	-3.67	-2.53	-1	.00	0.01	49.04
32.00	3.00	0.50	0.41	0.37	0.99	-0.06	0.39	3.42	-0.60	-2.14	-2.36	0.09	-0	.12	1.28	68.06
33.00	3.00	2.08	1.71	0.18	1.21	0.14	1.15	6.97	7.06	-0.06	2.39	1.21	1	.75	1.70	45.04
34.00	3.00	2.71	1.43	0.33	0.93	0.07	2.80	7.02	4.71	1.45	3.10	2.78	3	.15	2.95	60.04
35.00	3.00	3.12	1.49	0.39	1.23	0.41	2.69	7.01	6.00	3.36	3.27	4.89	2	.67	2.33	68.04
36.00	3.00	3.25	1.86	0.41	0.97	0.04	3.46	4.81	5.54	7.72	4.05	3.71	4	.70	1.67	72.05
37.00	3.00	3.27	1.47	0.27	1.14	1.05	4.00	7.58	5.31	5.31	5.15	4.56	3	.35	2.43	67.04
37.00	2.00	1.89	0.39	0.11	0.65	0.39	2.46	4.87	4.11	3.53	3.66	2.54	1	.57	0.65	62.04
36.00	2.00	2.32	0.78	-0.04	0.65	0.44	3.19	5.49	5.77	2.89	3.94	3.47	2	.31	1.02	60.04
35.00	2.00	1.55	0.39	0.18	0.63	0.67	2.00	6.91	3.47	2.74	0.22	3.36	-0	.04	0.87	89.06
34.00	2.00	1.20	0.44	0.35	0.84	0.31	2.52	5.04	0.29	1.25	0.57	1.40	-0	.27	0.85	91.07
33.00	2.00	2.48	0.35	0.22	0.41	0.74	3.42	7.57	6.03	1.66	0.05	2.20	3	.36	0.95	77.06
32.00	2.00	3.00	-0.08	0.14	0.87	0.76	3.75	7.38	5.98	4.99	5.23	-0.49	1	.51	2.56	71.06
31.00	2.00	0.14	0.07	0.27	0.60	0.35	1.14	2.23	2.73	-3.97	-2.90	-0.41	-2	.45	-1.47	41.04
30.00	2.00	0.15	-0.35	0.32	0.74	0.57	0.18	0.10	1.02	-1.00	-0.86	-2.45	0	.07	-1.73	38.03
29.00	2.00	0.31	-0.79	0.18	0.56	0.48	0.29	-0.21	0.67	0.35	0.16	1.43	1	.12	-0.40	38.04
28.00	2.00	0.75	-0.70	0.31	0.80	0.61	0.95	1.08	0.99	0.89	0.78	-0.06	0	.63	0.99	42.04
28.00	5.00	0.12	0.49	0.15	1.08	0.07	0.32	0.41	0.29	-0.66	-0.58	-0.55	0	.46	-1.16	36.03

Columns 1 and 2 contain x and y coordinates, Columns 3-15 contain velocities in cm s^{-1}, Column 17 contains the rms voltage in V. All velocities must be multiplied by a correcting factor of 1.32128.

29.00	5.00	-0.07	-0.04	0.48	1.02	0.07	-0.81	-0.70	-0.06	-1.28	-0.17	-1.16	-0	.29	0.16	37.03
30.00	5.00	0.08	1.11	0.55	1.30	0.04	-1.56	-1.16	-0.49	0.55	1.81	0.52	0	.41	0.18	40.03
31.00	5.00	-0.19	0.57	0.99	1.22	0.13	-1.19	-2.71	0.49	-1.36	0.27	0.01	-0	.01	1.11	46.04
32.00	5.00	0.23	1.38	0.67	1.27	0.13	-1.01	-0.19	-1.31	0.16	1.79	0.74	2	.03	1.47	68.05
33.00	5.00	1.61	2.23	0.66	1.53	0.21	-2.73	1.11	0.71	3.46	3.91	3.91	4	.28	1.67	79.05
34.00	5.00	2.94	1.86	0.77	1.64	-0.01	0.77	4.81	5.82	5.12	3.86	5.00	4	.16	3.01	72.05
35.00	5.00	3.52	1.02	0.69	1.44	-0.01	3.24	6.21	6.35	4.78	7.14	4.47	4	.56	3.49	70.05
36.00	5.00	4.02	1.83	0.61	1.45	-0.73	4.78	2.80	7.62	6.82	6.97	6.01	5	.35	3.74	68.05
37.00	6.00	4.08	1.47	0.28	1.70	-0.10	5.49	5.49	6.78	5.90	6.54	5.30	5	.42	4.28	55.04
36.00	6.00	4.22	1.66	0.65	1.90	-0.10	4.74	5.77	6.86	6.31	6.48	5.42	4	.69	3.83	54.04
35.00	6.00	3.93	1.88	0.85	1.96	0.03	5.45	5.75	6.44	5.60	6.41	6.01	4	.76	2.99	56.04
34.00	6.00	3.69	1.30	0.71	1.57	0.20	5.66	5.58	5.17	5.85	5.38	5.72	3	.58	3.23	53.04
33.00	6.00	3.36	1.56	.3	1.75	.21	2.01	5.06	6.75	4.81	6.77	5.82	3.78	.5	3.35	55.04
32.00	6.00	2.16	0.69	0.55	1.70	0.66	1.36	3.07	4.00	5.03	4.39	2.76	5	.03	3.46	59.04
31.00	6.00	0.92	1.51	0.71	1.27	0.69	0.46	-4.01	2.46	2.46	1.21	1.77	0	.63	0.48	48.04
30.00	6.00	.71	.66	.52	1.25	.55	.18	-.35	-.75	-.05	1.67	1.11	1.11	1.19	39.34	
29.00	6.00	0.77	1.36	0.46	1.14	0.63	1.34	-1.37	-2.81	1.38	1.40	2.71	0	.95	0.52	39.36
28.00	6.00	0.83	0.56	0.37	1.27	0.72	0.59	1.53	-0.01	1.28	2.24	1.34	0	.71	1.10	38.35
28.00	7.00	1.82	0.71	0.83	1.33	1.72	2.96	3.35	1.30	3.41	4.02	3.13	1	.56	-0.07	56.46
29.00	7.00	0.99	0.54	0.46	1.04	0.85	0.44	0.56	0.22	2.57	1.88	1.64	1	.38	0.33	41.37
30.00	7.00	1.07	1.43	0.54	1.21	0.71	0.56	0.54	0.87	3.32	-0.25	2.09	1	.60	0.42	45.35
31.00	7.00	1.45	1.70	0.59	1.19	0.42	0.78	1.36	1.73	2.89	2.18	1.92	0	.74	2.67	48.39
32.00	7.00	3.53	1.58	0.24	1.38	0.52	2.74	4.57	5.55	7.01	6.07	3.88	4	.37	3.45	51.39
33.00	7.00	3.73	2.14	0.61	1.21	0.11	3.60	5.32	6.48	6.78	6.95	6.05	4	.78	2.67	44.35
34.00	7.00	4.23	2.09	0.24	1.45	0.42	6.00	6.93	6.72	6.82	6.71	6.35	4	.39	3.68	44.35
35.00	7.00	4.49	2.09	0.44	1.68	0.93	5.77	6.74	6.74	8.01	6.97	6.63	5	.70	3.64	40.34
36.00	7.00	4.62	2.00	0.69	1.57	0.82	5.49	4.72	7.45	6.67	7.38	6.43	5	.45	4.13	44.34
37.00	7.00	4.57	1.85	0.46	1.36	0.56	6.43	5.62	7.29	7.94	6.61	6.15	6	.22	3.90	49.35
37.00	8.00	4.36	1.11	0.32	0.99	1.86	6.29	4.02	7.56	6.07	8.20	7.33	5	.23	2.68	37.30
36.00	8.00	4.80	1.53	0.41	1.23	1.30	6.16	7.17	8.15	7.23	7.73	7.19	6	.09	4.00	37.30
35.00	8.00	4.53	1.56	0.29	1.14	1.14	5.90	5.82	7.58	7.95	7.42	6.38	5	.57	3.91	31.28
34.00	8.00	4.40	2.00	0.63	1.10	1.27	5.81	6.05	7.62	7.40	7.14	5.96	4	.37	3.73	34.31
33.00	8.00	4.33	2.20	0.18	1.30	1.30	5.34	6.41	7.39	7.53	6.07	6.41	5	.17	3.83	37.33
32.00	8.00	3.31	1.32	0.56	1.00	0.44	3.32	5.08	5.51	6.01	5.17	4.74	4	.67	2.52	40.34
31.00	8.00	2.46	1.00	0.33	1.04	0.42	1.55	4.41	3.47	4.91	3.73	4.14	3	.88	1.10	36.33
30.00	8.00	1.55	0.74	0.54	0.56	0.59	0.07	1.66	2.24	2.63	2.41	2.44	2	.07	2.28	32.30
29.00	8.00	1.13	1.36	0.43	0.94	1.08	-0.27	-0.01	1.47	1.75	0.83	1.30	1	.33	1.30	34.32

Columns 1 and 2 contain x and y coordinates, Columns 3-15 contain velocities in cm s^{-1}, Column 17 contains the rms voltage in V. All velocities must be multiplied by a correcting factor of 1.32128.

28.00	8.00	1.67	0.63	0.69	0.99	1.16	1.70	3.88	2.12	2.28	1.33	1.16	1	.14	1.30	47.36

Axial Velocities Proximal Limb $\alpha = 180°$, Re_{mean} 1500

28.00	18.00	5.78	3.10	1.33	2.26	4.30	5.65	7.22	8.20	8.03	8.40	7.67	6	.86	5.45	56.50
29.00	18.00	5.41	2.40	1.36	1.86	3.32	5.00	7.25	7.81	8.03	8.37	8.26	6	.49	5.20	65.54
30.00	18.00	6.16	3.13	0.97	2.48	3.66	5.82	8.20	8.62	9.49	9.24	8.87	7	.53	5.37	73.62
31.00	18.00	5.90	3.07	1.14	1.81	3.80	5.82	8.20	8.73	8.96	8.87	7.81	7	.19	5.26	68.56
32.00	18.00	6.04	2.59	1.08	2.14	4.44	5.57	8.48	8.65	9.66	8.82	7.64	7	.14	5.34	60.57
33.00	18.00	5.60	2.14	0.91	2.37	3.55	6.41	7.78	8.34	8.59	9.30	7.56	7	.16	4.58	81.66
34.00	18.00	5.81	2.82	0.69	1.86	4.44	6.46	8.99	9.04	8.65	9.66	7.75	6	.01	3.83	81.67
35.00	18.00	5.28	1.71	0.78	1.47	4.16	5.77	8.18	9.12	9.01	8.18	7.83	6	.15	4.22	91.78
36.00	18.00	6.01	1.81	0.94	2.12	4.70	6.13	9.27	9.13	8.87	9.38	8.34	5	.90	3.91	78.62
37.00	18.00	6.00	2.03	0.66	1.95	4.19	7.08	8.57	9.55	9.07	10.33	8.76	6	.27	4.42	94.77
37.00	17.00	9.2	3.49	1.59	3.02	7.61	9.94	12.43	13.67	13.67	13.2	12.92	10.48		6.83	75.63
36.00	17.00	9.45	4.43	4.03	3.71	7.38	10.09	12.82	13.53	11.79	13.64	12.11	10	.16	7.42	60.54
35.00	17.00	8.76	3.96	1.42	3.30	6.71	9.42	12.09	12.76	11.73	13.01	12.03	9	.72	7.21	56.52
34.00	17.00	8.50	3.12	1.25	3.27	6.48	9.14	11.57	12.13	12.84	11.04	11.59	9	.87	6.78	62.57
33.00	17.00	7.85	3.25	1.60	3.43	5.81	8.44	11.21	11.34	12.46	12.93	10.15	8	.97	6.65	87.76
32.00	17.00	7.24	2.82	1.53	2.82	5.45	7.36	10.05	10.95	9.21	9.83	10.39	8	.37	6.29	76.66
31.00	17.00	7.59	4.05	1.81	3.42	5.81	8.35	10.30	11.49	12.07	9.92	10.41	8	.18	6.78	91.79
30.00	17.00	7.46	4.01	2.20	3.23	5.75	8.33	9.90	11.02	10.28	10.43	9.90	9	.34	6.56	91.79
29.00	17.00	7.52	4.61	2.18	3.83	5.29	7.62	9.29	9.98	11.12	10.69	9.94	8	.74	6.72	61.55
28.00	17.00	6.99	4.41	2.54	2.72	5.36	7.08	8.56	9.36	10.80	9.51	9.62	8	.16	6.74	56.52
28.00	16.00	7.49	4.43	2.76	3.30	5.90	7.30	9.53	10.28	10.61	10.78	10.15	9	.01	7.47	55.51
29.00	16.00	8.12	4.89	3.06	4.05	6.24	7.75	9.60	10.82	11.81	10.99	10.99	9	.51	7.23	50.45
30.00	16.00	8.65	4.95	2.82	4.72	7.08	8.65	10.56	11.90	12.86	12.63	11.62	9	.94	7.30	59.52
31.00	16.00	8.91	4.81	2.40	4.14	6.91	9.32	11.59	12.02	13.08	12.30	11.34	10	.00	7.89	45.41
32.00	16.00	9.22	5.06	2.61	4.56	7.14	9.87	11.81	12.76	13.29	12.88	12.11	10	.86	7.77	40.40
33.00	16.00	9.53	4.98	2.87	4.14	7.56	10.14	12.58	13.70	13.84	13.53	12.46	10	.56	8.23	41.39
34.00	16.00	9.63	5.08	2.69	4.74	7.66	10.33	12.76	13.27	13.66	13.45	12.59	10	.43	8.05	43.41
35.00	16.00	9.89	5.23	2.63	4.39	7.51	10.80	13.32	14.22	14.56	13.92	13.14	11	.02	8.44	51.48
36.00	16.00	10.11	5.15	2.59	4.71	8.15	11.06	13.66	14.58	14.67	14.22	13.49	10	.93	8.61	43.40

Columns 1 and 2 contain x and y coordinates, Columns 3-15 contain velocities in cm s^{-1}, Column 17 contains the rms voltage in V. All velocities must be multiplied by a correcting factor of 1.32128.

37.00	16.00	10.50	5.42	2.43	4.61	8.54	11.64	14.48	15.36	15.72	14.86	13.75	11	.77	8.69	49.42
28.00	15.00	7.63	4.98	3.27	3.71	5.40	7.84	9.38	9.97	10.47	10.50	10.00	9	.01	7.22	41.039
29.00	15.00	8.42	5.51	3.10	4.46	6.11	8.50	10.43	11.23	11.53	11.70	10.74	9	.49	8.07	39.039
30.00	15.00	8.80	5.83	3.15	4.59	6.61	6.50	11.06	11.90	12.11	11.90	11.44	10	.41	8.11	41.039
31.00	15.00	9.29	5.90	2.87	4.61	7.04	9.75	11.81	12.45	12.63	12.97	12.09	10	.69	8.44	40.037
32.00	15.00	9.53	6.01	3.00	4.84	7.15	9.98	12.33	13.02	13.02	13.21	12.48	10	.78	8.93	38.037
33.00	15.00	9.79	5.86	3.25	4.61	7.47	10.58	12.61	13.38	13.66	13.53	12.67	11	.12	8.76	39.037
34.00	15.00	9.96	5.75	2.57	4.99	7.81	10.80	12.86	13.60	13.77	13.60	12.91	11	.47	9.17	40.039
35.00	15.00	10.30	5.94	3.00	4.82	8.13	11.19	13.51	14.18	14.46	14.11	13.04	12	.03	9.36	40.038
36.00	15.00	10.60	5.75	3.14	5.02	8.48	11.49	14.13	14.39	14.86	14.67	13.88	12	.24	9.44	42.041
37.00	15.00	11.25	6.46	3.13	5.45	8.90	12.07	15.35	15.77	15.94	15.72	14.93	13	.05	9.77	45.043
37.00	14.00	11.25	6.05	2.63	5.53	8.59	12.20	15.01	15.92	15.60	15.45	14.73	13	.01	10.11	57.055
36.00	14.00	10.19	5.40	2.48	4.46	7.75	11.19	13.23	14.03	14.37	14.48	13.53	11	.66	8.71	53.051
35.00	14.00	9.69	5.34	2.54	4.84	7.87	10.44	12.52	13.64	14.65	13.19	12.63	11	.17	7.70	48.046
34.00	14.00	9.46	4.93	2.28	4.71	7.15	10.37	12.74	13.17	13.42	13.10	12.59	11	.04	8.54	50.048
33.00	14.00	9.46	4.93	2.28	4.71	7.15	10.37	12.74	13.17	13.42	13.10	12.59	11	.04	8.54	50.048
32.00	14.00	9.23	5.65	2.23	4.61	6.55	9.74	11.82	12.63	12.77	12.83	12.44	10	.56	8.68	46.045
31.00	14.00	8.97	5.45	2.73	4.47	6.46	9.35	11.65	12.58	12.77	12.18	11.45	10	.22	8.17	47.046
30.00	14.00	8.50	5.30	2.61	4.24	6.01	8.89	10.89	11.44	11.64	11.73	11.08	9	.92	7.92	49.047
29.00	14.00	8.21	5.40	3.15	4.11	5.66	8.16	9.96	10.82	10.89	11.42	10.35	9	.55	7.57	49.046
28.00	14.00	7.72	5.23	3.04	3.60	5.09	7.87	7.50	10.36	9.32	10.14	9.80	8	.57	7.44	62.056
28.00	13.00	6.99	4.44	2.48	3.49	4.50	6.74	9.38	9.49	9.32	9.88	9.49	7	.98	6.69	52.050
29.00	13.00	8.06	5.12	2.82	3.66	5.40	8.29	10.00	11.17	11.26	11.09	10.42	9	.18	7.72	43.040
30.00	13.00	8.49	5.27	2.46	4.41	5.88	8.91	11.04	11.85	11.87	11.53	11.21	9	.98	7.87	45.043
31.00	13.00	8.91	4.98	2.65	4.44	6.07	9.41	11.37	12.07	12.58	12.38	11.96	10	.47	8.26	44.042
32.00	13.00	8.91	5.15	2.07	4.43	6.33	9.53	11.77	12.67	12.69	12.09	11.79	10	.74	8.26	54.051
33.00	13.00	8.97	4.80	1.98	4.28	6.78	9.90	11.83	11.14	12.91	12.50	12.02	10	.43	7.90	60.058
34.00	13.00	9.49	4.93	2.05	4.61	7.27	10.44	12.71	13.60	13.51	13.16	12.50	10	.86	8.30	53.050
35.00	13.00	9.66	4.78	2.37	4.22	8.59	10.73	13.87	13.36	14.03	13.64	13.08	11	.73	8.03	70.065
36.00	13.00	10.21	5.31	2.43	4.28	8.23	11.29	13.47	14.54	14.88	14.85	13.81	11			
37.00	13.00	11.47	6.00	2.74	5.29	9.08	12.78	15.17	15.83	16.24	16.05	15.02	13	.19	9.79	53.051
37.00	12.00	8.23	3.34	2.69	2.80	6.59	9.21	11.16	11.94	12.59	12.84	11.85	9	.34	6.72	94.080

Centreline Axial Velocities Proximal Limb, $Re_{mean} = 1500$

Columns 1 and 2 contain x and y coordinates, Columns 3-15 contain velocities in cm s^{-1}, Column 17 contains the rms voltage in V. All velocities must be multiplied by a correcting factor of 1.32128.

28.00	10.00	4.64	0.24	0.18	2.59	5.90	7.81	8.26	7.64	6.58	6.58	5.23	4	.22	1.58	25.25
28.00	10.00	4.86	0.91	0.01	2.71	5.45	7.58	8.43	7.53	7.19	5.73	4.78	3	.88	4.05	25.25
29.00	10.00	3.91	1.02	0.57	2.54	5.79	7.25	7.25	6.07	5.23	3.94	2.71	2.76	3.43	25.25	
29.00	10.00	4.03	0.20	0.41	2.57	5.43	7.17	7.38	6.13	5.02	4.28	2.99	2	.91	2.61	25.25
30.00	10.00	3.21	0.91	0.27	2.73	4.98	5.90	5.71	5.06	2.26	2.90	3.13	3	.66	2.00	33.28
31.00	10.00	2.95	1.19	0.74	2.48	4.22	4.28	4.33	3.55	4.11	4.11	5.34	2	.03	3.38	36.29
31.00	10.00	2.97	0.91	0.18	2.48	4.56	5.06	3.94	3.43	3.55	4.56	4.05	3	.27	2.31	36.29
32.00	10.00	2.74	0.46	0.07	2.14	4.28	3.21	3.94	3.43	2.76	4.39	2.99	2	.65	0.69	40.30
32.00	10.00	2.72	0.80	0.57	2.48	4.35	3.32	4.14	3.42	3.70	3.62	3.25	2	.18	0.82	40.30
33.00	10.00	2.49	1.49	0.67	2.35	2.76	3.28	4.13	4.89	5.00	3.06	2.44	1	.90	1.19	55.35
34.00	10.00	2.47	1.32	0.56	2.35	2.41	2.69	3.94	3.02	1.88	2.80	2.97	2	.11	3.32	34.10
35.00	10.00	2.76	0.80	0.54	2.41	2.00	2.37	4.31	2.43	4.20	5.12	4.37	3	.08	2.31	76.48
36.00	10.00	3.10	1.56	0.74	2.45	2.31	3.57	3.24	3.04	4.86	4.11	4.22	3	.13	2.85	77.48
37.00	10.00	3.21	0.94	0.41	2.26	2.37	2.65	5.03	3.66	5.82	6.52	5.09	2	.28	3.60	75.50

Axial Velocities Proximal Limb $\alpha = 0°$, $Re_{mean} = 1000$

9.00	8.00	1.56	0.80	0.80	0.38	0.88	0.91	1.70	1.64	2.20	2.79	1.98	1	.67	1.30	31.027
8.00	8.00	1.16	0.88	0.38	0.88	1.19	1.50	0.80	0.80	1.25	1.53	1.02	1	.42	0.88	28.026
7.00	8.00	0.91	0.77	0.77	0.83	0.77	1.78	1.08	1.19	0.97	0.49	0.88	0	.52	0.63	28.025
6.00	8.00	1.06	0.74	0.69	0.77	0.63	1.70	1.61	1.56	1.58	1.30	0.60	0	.97	0.49	35.029
5.00	8.00	1.21	0.52	0.63	0.77	0.35	1.89	1.75	2.09	1.61	1.36	1.19	0	.94	0.69	28.024
4.00	8.00	0.89	0.46	0.55	0.88	0.46	1.33	1.42	1.36	1.30	1.14	0.83	0	.46	0.69	25.024
3.00	8.00	0.66	0.35	0.24	0.69	0.83	0.55	0.71	0.97	0.99	0.83	0.77	0	.63	0.66	23.023
2.00	8.00	0.87	0.29	0.29	0.74	0.97	0.91	1.14	1.36	1.11	1.16	0.99	0	.69	0.71	25.023
1.00	8.00	1.70	0.32	0.83	0.83	1.67	2.73	3.07	2.71	2.20	2.09	2.00	1	.64	0.97	25.024
1.00	7.00	1.36	-0.07	0.41	0.77	1.47	2.23	2.40	2.20	1.67	1.67	1.44	1	.02	0.80	32.030
2.00	7.00	0.82	-0.18	0.10	0.80	1.14	1.67	1.50	1.19	0.94	0.94	0.88	0	.63	0.32	30.027
3.00	7.00	0.39	-0.10	0.07	1.08	1.19	1.14	0.35	0.29	-0.21	-0.15	-0.32	-0	.49	-0.15	40.032
4.00	7.00	-0.30	-0.30	0.43	0.71	0.66	0.52	0.15	-0.18	-0.63	-1.19	-1.30	-0	.86	-0.66	40.030
5.00	7.00	-0.14	-0.01	0.52	0.88	0.29	0.66	0.43	-0.66	-0.60	-1.00	-0.83	-0	.49	-0.13	38.029
6.00	7.00	0.14	0.29	0.55	0.80	0.10	0.91	0.41	0.55	-0.49	-0.35	-0.38	-0	.83	-0.18	36.032

Columns 1 and 2 contain x and y coordinates, Columns 3-15 contain velocities in cm s^{-1}, Column 17 contains the rms voltage in V. All velocities must be multiplied by a correcting factor of 1.32128.

7.00	7.00	0.75	0.56	0.54	0.78	0.11	1.04	0.01	0.37	0.61	0.37	0.56	1	.14	1.08	35.029
8.00	7.00	1.44	0.88	0.52	0.46	0.38	-0.01	1.16	1.56	1.98	2.28	1.64	2	.28	1.39	31.026
9.00	7.00	1.60	0.82	0.59	0.56	0.33	0.50	2.63	2.28	2.39	2.76	3.02	1	.96	1.57	34.027
9.00	6.00	2.20	1.28	0.49	0.55	-0.77	1.98	4.72	2.48	2.45	2.23	4.50	3	.29	2.76	34.027
8.00	6.00	1.81	1.23	0.57	0.74	-0.49	0.65	4.24	2.48	2.11	2.50	2.87	2	.11	2.11	39.027
7.00	6.00	1.13	1.05	0.57	0.74	-0.46	-1.16	0.10	1.22	1.89	0.94	2.28	2	.00	1.30	39.032
6.00	6.00	0.07	0.74	0.38	0.69	0.13	-2.12	-1.16	-0.27	0.07	-0.35	0.41	0	.71	0.85	38.031
5.00	6.00	-0.83	0.07	0.27	0.85	0.27	-2.03	-2.29	-2.12	-1.89	-2.03	-1.11	-1	.47	-0.41	33.028
4.00	6.00	-1.20	-0.60	0.29	0.74	0.35	-0.32	-2.57	-2.29	-2.01	-2.23	-2.06	-1	.78	-1.28	30.026
3.00	6.00	-1.19	-0.94	-0.10	0.71	0.49	0.38	-2.51	-2.15	-2.26	-2.15	-2.20	-1	.92	-1.16	30.027
2.00	6.00	-0.81	-1.16	0.07	0.69	0.63	0.74	-0.38	-1.89	-2.23	-1.95	-1.67	-1	.39	-1.16	33.028
1.00	6.00	0.51	-0.88	0.01	0.97	0.80	0.97	1.30	0.57	0.57	0.91	0.52	0	.52	-0.15	36.032
1.00	5.00	-0.32	-0.72	-0.27	1.08	0.18	0.07	-0.44	-1.11	-0.66	-0.83	-0.72	-0	.60	-0.27	30.028
2.00	5.00	-0.44	-0.58	0.01	0.41	0.21	-0.24	-1.61	-1.11	-0.88	-1.00	-0.44	-0	.55	-0.55	31.029
3.00	5.00	-0.41	-0.77	0.15	0.60	0.13	-0.91	-1.00	-0.88	-0.55	-0.80	-0.32	-0	.32	-0.35	31.028
4.00	5.00	-0.57	-0.38	-0.10	0.41	-0.10	-1.89	-1.39	-1.28	-0.49	-0.77	-0.66	-0	.66	-0.88	30.028
5.00	5.00	-0.26	0.56	0.39	0.57	0.31	-2.10	-0.90	-1.20	-0.66	-0.94	-0.12	-0	.68	-0.19	31.028
6.00	5.00	0.12	0.94	0.66	0.71	0.15	-1.70	-0.41	-1.75	-1.02	-0.66	0.80	0	.21	0.97	36.030
7.00	5.00	1.38	1.22	0.83	0.71	-0.18	-0.35	2.17	1.19	0.80	1.30	3.52	2	.87	2.20	40.031
8.00	5.00	2.20	1.11	0.63	0.60	-0.58	1.33	4.02	4.36	4.08	3.97	3.86	3	.35	2.59	36.028
9.00	5.00	2.73	1.28	0.69	0.71	-1.41	3.34	4.33	4.69	4.87	4.44	3.94	3	.90	2.78	34.027
9.00	4.00	2.88	1.02	0.95	0.82	-0.77	3.60	4.41	4.76	5.34	4.59	4.37	3	.94	2.72	27.025
8.00	4.00	2.60	1.14	0.69	0.63	-0.60	2.82	3.83	4.95	4.95	4.44	3.83	3	.60	2.71	28.026
7.00	4.00	2.44	1.14	0.71	0.87	-0.14	1.64	4.16	4.84	4.41	4.37	3.68	3	.38	2.28	31.026
6.00	4.00	1.91	1.00	0.65	0.82	0.13	0.87	2.67	2.76	2.91	3.08	3.36	2	.56	2.05	33.028
5.00	4.00	0.90	0.91	0.49	0.74	0.43	1.02	0.94	0.74	1.05	0.99	0.99	1	.75	1.33	34.030
4.00	4.00	0.74	0.32	0.66	0.77	0.63	-0.21	0.83	0.94	1.08	1.19	1.05	0	.74	0.29	32.029
3.00	4.00	0.67	-0.01	0.10	0.66	0.43	-0.27	0.99	0.74	1.14	1.11	0.94	0	.77	0.55	34.030
2.00	4.00	0.56	0.07	0.41	0.94	0.57	0.35	0.27	0.71	0.94	0.77	0.71	0	.85	0.88	30.028
1.00	4.00	0.27	0.13	0.29	0.80	0.91	0.80	-0.10	-0.04	0.01	0.13	0.01	0	.29	0.07	33.031
1.00	3.00	1.08	0.24	0.46	0.71	1.05	1.28	1.39	1.70	1.50	1.28	1.19	0	.91	0.52	36.032
2.00	3.00	1.10	0.29	0.41	0.80	0.74	1.36	1.75	1.47	1.53	1.42	1.08	1	.08	0.97	31.029
3.00	3.00	0.95	0.22	0.20	0.56	0.54	0.22	1.38	1.17	1.36	1.08	1.43	1	.12	0.56	34.032
4.00	3.00	0.91	0.46	0.29	0.63	0.38	1.30	1.33	1.08	1.30	1.14	0.99	1	.08	1.02	33.031
5.00	3.00	1.30	0.35	0.80	0.66	-0.04	1.44	2.26	1.72	1.86	1.64	1.95	1	.75	1.19	37.033
6.00	3.00	2.06	0.88	0.69	0.66	0.07	1.30	2.68	3.10	3.10	3.57	2.90	2	.62	1.56	38.034
7.00	3.00	2.14	0.63	0.69	0.74	0.07	1.58	3.43	3.32	3.77	3.60	3.04	2	.93	2.14	40.034

Columns 1 and 2 contain x and y coordinates, Columns 3-15 contain velocities in cm s^{-1}, Column 17 contains the rms voltage in V. All velocities must be multiplied by a correcting factor of 1.32128.

8.00	3.00	1.70	0.77	0.60	0.41	0.04	1.53	2.65	2.79	2.90	2.87	2.87	2	.23	1.95	41.033
9.00	3.00	2.27	1.08	0.57	0.13	0.01	2.65	3.60	3.94	3.60	3.66	3.55	3	.32	2.03	34.029
9.00	2.00	1.20	0.55	0.18	0.15	0.15	0.94	1.64	1.98	2.34	2.23	2.23	1	.56	1.05	48.036
8.00	2.00	1.82	0.80	0.38	0.52	0.43	2.09	2.54	2.87	2.99	2.90	2.76	2	.26	1.58	41.032
7.00	2.00	1.63	0.63	0.41	0.49	0.52	1.98	2.45	2.37	2.79	2.87	2.71	2	.09	1.33	42.033
6.00	2.00	1.80	0.74	0.38	0.43	0.49	2.23	2.71	3.04	3.13	2.90	2.79	2	.31	1.30	39.031
5.00	2.00	1.46	0.63	0.18	0.52	0.01	1.25	2.20	2.14	2.14	2.48	2.14	1	.70	1.30	37.032
4.00	2.00	2.15	0.85	0.77	0.88	0.27	1.53	3.35	3.15	3.55	3.38	3.07	2	.62	1.84	60.040
3.00	2.00	1.03	0.91	0.52	0.80	0.60	0.52	1.33	1.67	1.39	1.25	1.33	1	.39	0.71	42.038
2.00	2.00	0.75	0.10	0.27	0.60	0.80	0.57	0.97	1.11	1.11	0.97	0.88	0	.66	0.15	37.032
1.00	2.00	2.37	0.01	0.35	1.30	2.09	2.93	3.21	3.94	3.83	3.66	3.49	1	.98	1.14	37.031

Centreline Axial Velocities Proximal Limb, $Re_{mean} = 1000$

1.00	10.00	3.93	0.74	0.71	3.07	4.95	5.99	5.68	5.79	5.45	5.03	4.70	3	.49	2.00	21.019
2.00	10.00	3.26	0.57	0.67	2.85	4.33	5.15	4.57	4.67	4.41	3.83	3.53	2	.69	1.66	22.021
3.00	10.00	2.52	0.35	0.97	2.65	3.83	3.77	3.27	3.21	3.15	3.15	2.93	2	.09	1.47	21.020
4.00	10.00	1.92	0.29	0.97	2.45	2.87	2.65	1.95	2.14	1.89	2.73	2.09	1	.50	1.19	22.020
5.00	10.00	1.73	0.49	0.85	2.43	2.23	2.48	1.86	1.81	1.81	2.06	2.06	1	.75	1.14	22.020
6.00	10.00	1.87	0.99	1.11	2.09	1.92	2.59	2.00	2.06	2.37	1.86	1.58	0	.91	0.57	23.020
7.00	10.00	1.79	1.44	1.39	2.09	2.57	2.43	2.17	1.72	2.54	1.53	1.61	1	.50	1.22	29.024
8.00	10.00	2.00	1.51	1.25	2.16	2.87	1.66	1.86	2.28	1.73	1.64	1.66	1	.85	2.35	30.024
9.00	10.00	2.71	1.36	1.16	2.09	2.73	2.87	3.71	4.02	3.60	4.19	3.77	3.49	2.79	31.023	

Axial Velocities Proximal Limb $\alpha = 0°$ Steady Flow, Re = 500

LDA Voltages [V]

5.57	5.59	5.54	5.51	5.54	5.57	5.59
5.51	5.55	5.52	5.51	5.53	5.54	5.53

Columns 1 and 2 contain x and y coordinates, Columns 3-15 contain velocities in cm s^{-1}, Column 17 contains the rms voltage in V. All velocities must be multiplied by a correcting factor of 1.32128.

5.50	5.52	5.52	5.48	5.51	5.51	5.51
5.55	5.50	5.49	5.46	5.49	5.50	5.54
5.59	5.54	5.47	5.39	5.49	5.53	5.59
5.64	5.60	5.45	5.30	5.47	5.60	5.64
5.63	5.64	5.48	5.30	5.48	5.64	5.65
5.65	5.65	5.52	5.35	5.51	5.61	5.66
5.63	5.64	5.54	5.44	5.55	5.56	5.62

Axial Velocities Proximal Limb $\alpha = 0°$ Steady Flow, Re = 1000

LDA Voltages [V]

5.91	5.89	5.64	5.45	5.57	5.87	6.08
5.62	5.84	5.62	5.28	5.48	5.82	5.79
5.55	5.70	5.33	5.27	5.54	5.80	5.59
5.72	5.68	5.32	5.28	5.55	5.70	5.71
5.78	5.97	5.45	5.24	5.52	5.74	6.00
5.75	6.04	5.66	5.30	5.67	6.17	6.11
5.72	5.96	5.74	5.66	6.03	6.08	6.07
5.65	5.64	5.92	5.96	6.01	6.01	6.09
5.63	5.74	6.02	6.09	6.02	6.04	6.09

Axial Velocities Proximal Limb $\alpha = 0°$ Steady Flow, Re = 1500

LDA Voltages [V]

5.92	6.19	5.57	5.24	5.36	5.73	6.22
6.39	6.09	5.66	5.35	5.10	5.33	5.85
6.63	5.88	5.76	5.39	5.03	5.33	5.91
6.61	6.25	5.72	5.36	5.11	5.31	6.33
6.47	6.61	5.81	5.30	5.46	5.73	6.44
6.31	6.37	6.33	5.51	5.84	5.68	6.41
6.25	6.22	6.22	6.04	6.09	5.83	6.28
6.20	6.22	6.25	6.24	6.18	5.96	6.23
6.18	6.25	6.32	6.36	6.18	6.02	6.02

Appendix K

LDA Frequency Tracking Unit Calibration

The DISA Frequency Tracking Unit was calibrated by supplying an input signal with a known frequency and measuring the output voltage. The input signal frequency was supplied by a signal generator working the sine wave mode and the frequency of the signal was measured with a Hewlett-Packard frequency counter. The output voltage of the frequency tracking unit was measured with the DISA digital voltmeter supplied with the LDA. The following calibration curves were found for specified frequency tracking ranges of 0 -150 kHz and 0 - 500 kHz.

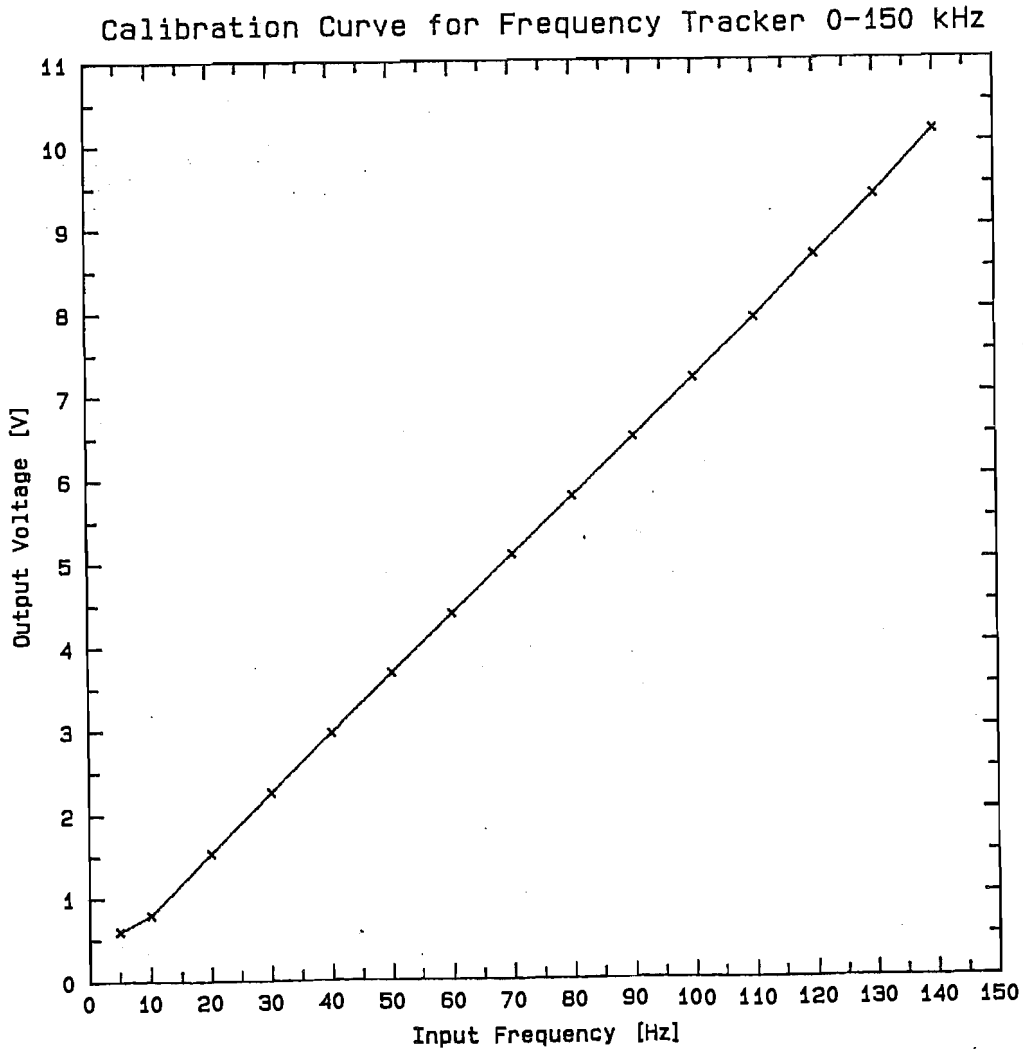

Figure K-1

Calibration Curve for LDA Frequency Tracking Unit
0 - 150 kHz Range.

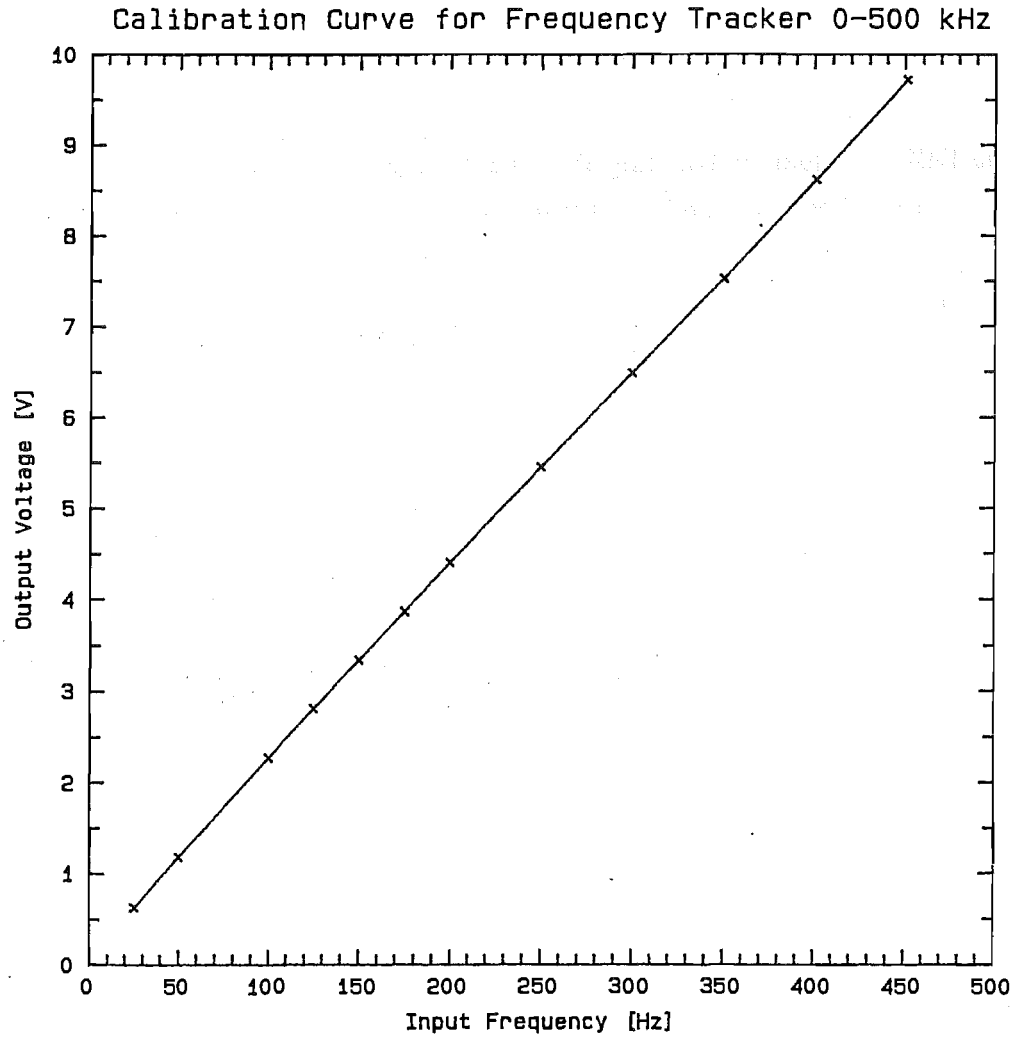

Figure K-2

Calibration Curve for LDA Frequency Tracking Unit

0 - 500 kHz Range.

APPENDIX L

Rotameter Calibration Curve

The Metric Series 10 rotameter with stainless steel float was calibrated using a measuring cylinder and stop-watch. The following calibration curve was obtained for water at 16 ± 2 °C.

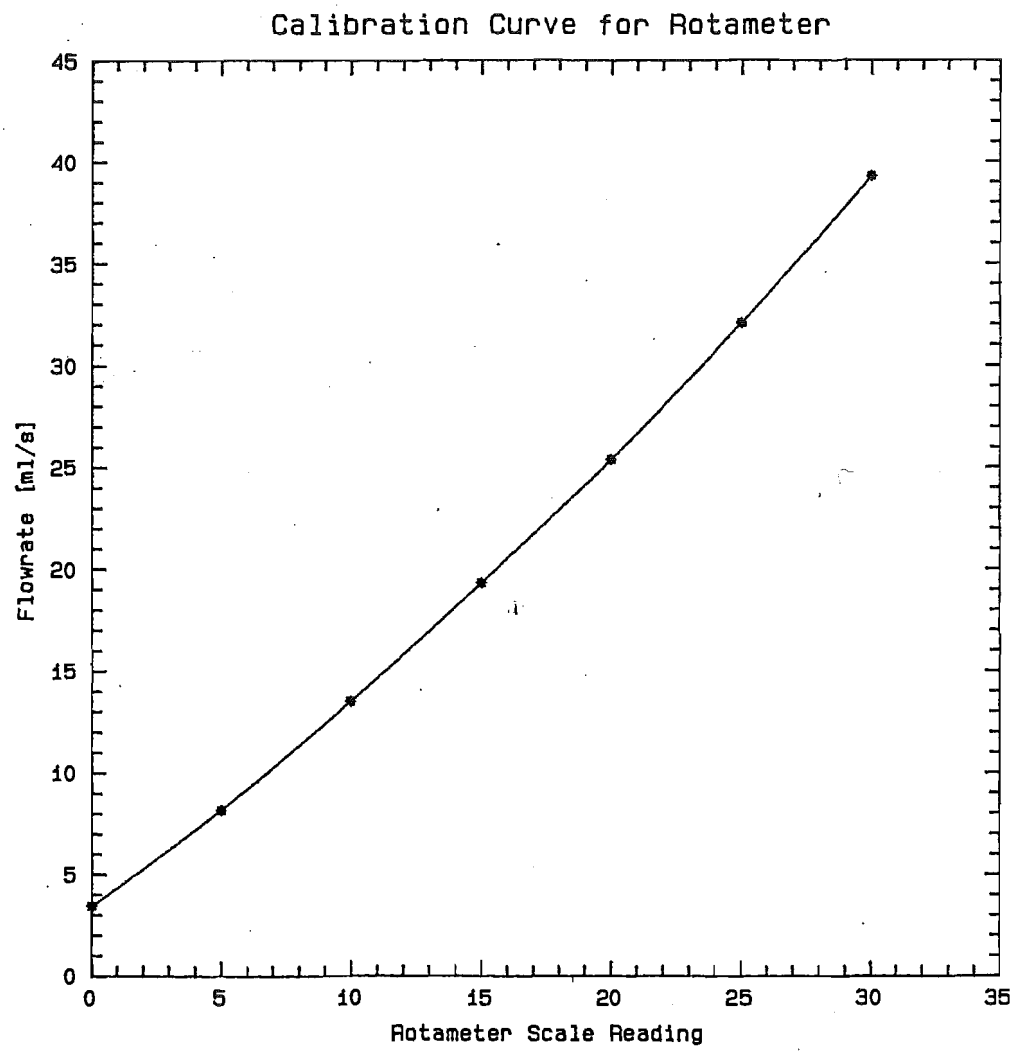

Figure L-1
Calibration Curve for Metric Series 10 Rotameter.

Appendix M

Wall Pressure Spectra at Individual Port Positions

In the following, all spectra have been divided at each frequency by a reference spectrum upstream of the model at position 1. In figures M-10, M-11 and M-14, the spectra referred to are the top ones of the two in each figure, with a baseline at a y-axis value of 0.5

At Re = 520, at a position at the entrance to the proximal bend (positions 2 and 3 in figure 5.71), notable differences between the spectra at the $\alpha = 0°$ (figure M-1) and the $\alpha = 180°$ (figure M-2) sides of the model were observed. At $\alpha = 0°$, many large peaks occurred, as well as several frequencies where damping occurred, whilst the spectra at $\alpha = 180°$ contained virtually no changes from the reference spectrum.

Similar differences were observed at Re = 520 between the two sides of the mid-proximal bend (figures M-3 and M-4).

The spectra at Re = 520 along the $\alpha = 0°$ wall of the proximal limb, BC, showed both peaks and damping in all positions. The peaks became smaller with downstream position along the limb (figures M-5 and M-6). The spectra on the opposite side ($\alpha = 180°$) was much smoother, with few differences from the reference spectrum (figure M-7).

More peaks were observed at the $\alpha = 0°$ (outer bend) than at $\alpha = 180°$ in the spectra of the medial bend at Re = 520 (figures M-8 and M-9).

The spectra on both sides of the distal limb, DE, were smooth at Re = 520 (figures M-10 and M-11) with a magnitude of close to 1.0 throughout and therefore were very similar to the reference spectrum.

In the distal stem, more peaks were observed at Re = 520 across a wide range of frequencies at the $\alpha = 0°$ side than at the $\alpha = 180°$ side (figures M-12 and M-13).

At the three highest flowrates, no differences in the spectral characteristics between the two sides of the model were apparent at any position and often the comparitive spectra were quite smooth, as shown in figure M14 for position 5 at the outer proximal bend, Re = 800.

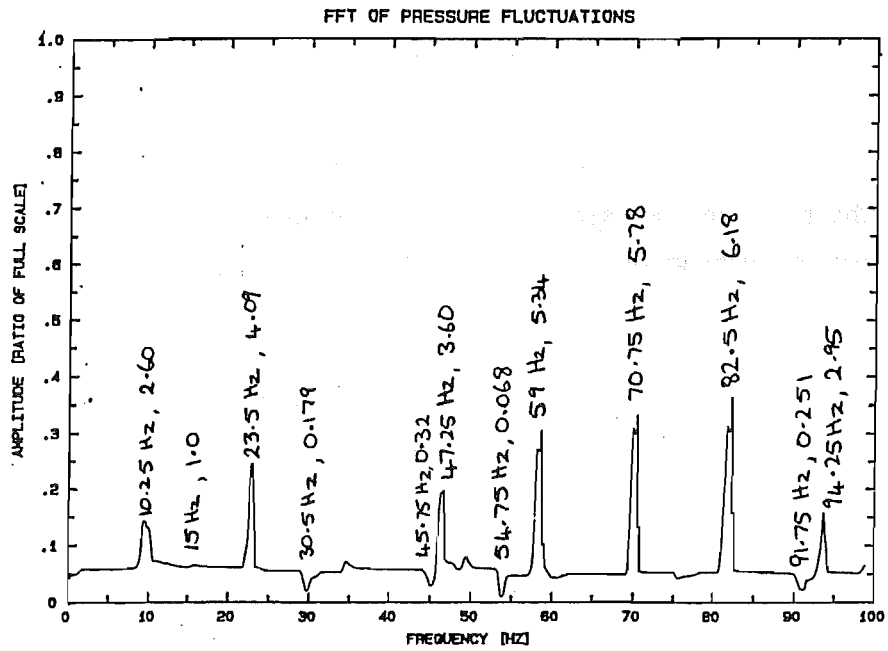

Figure M-1

Position 1, Re = 520.

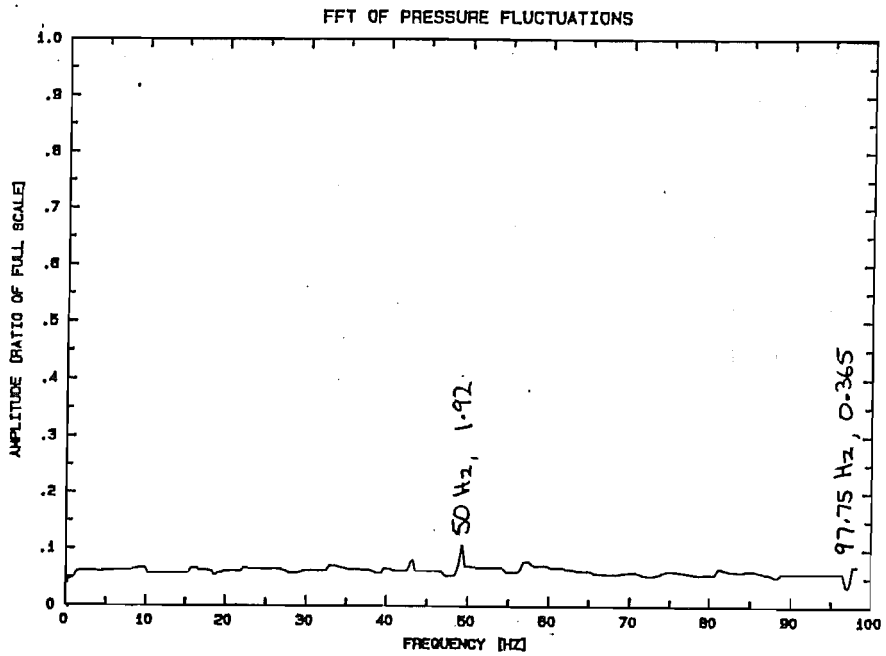

Figure M-2

Position 3, Re = 520.

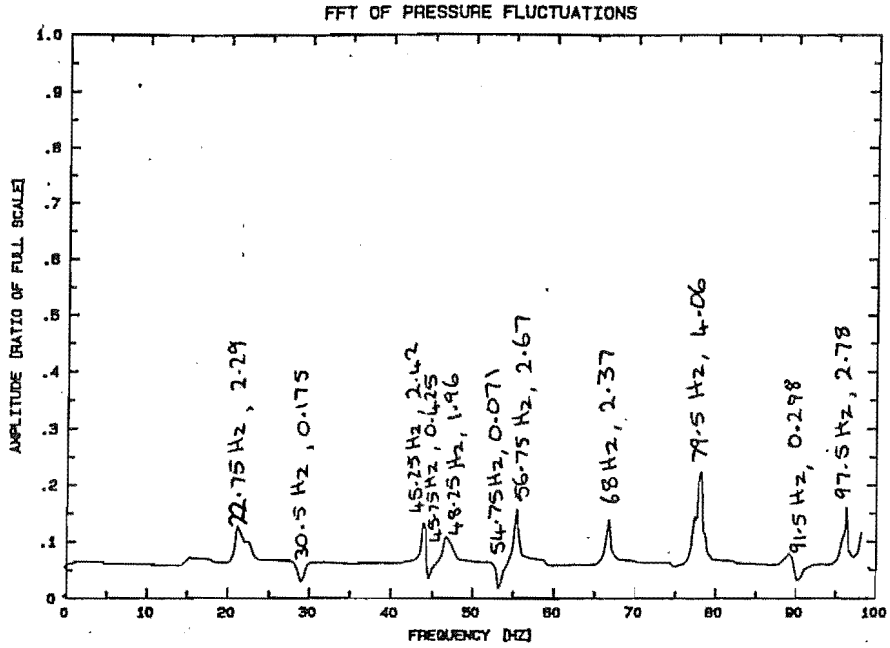

Figure M-3

Position 4, Re = 520.

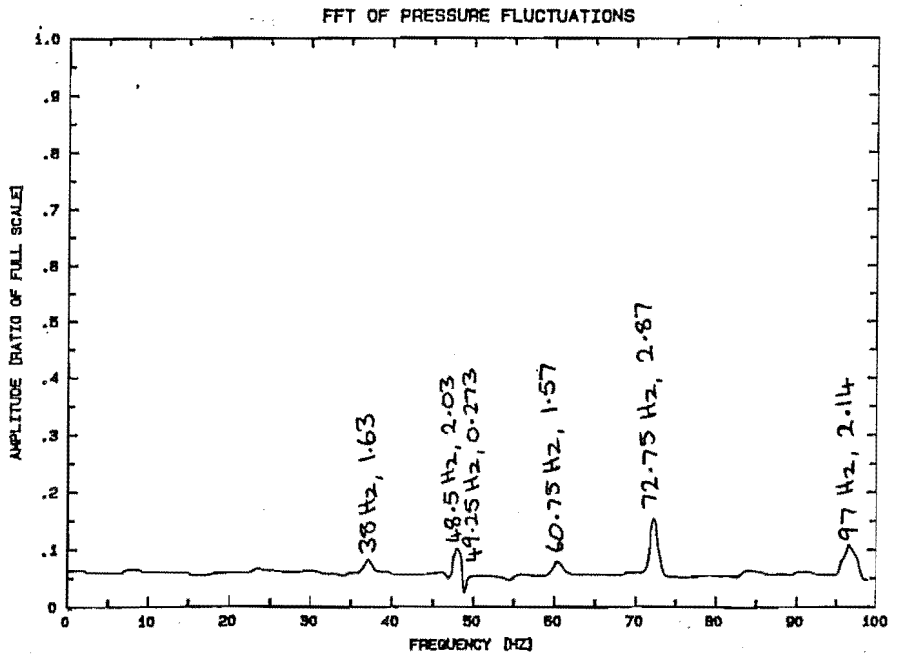

Figure M-4

Position 5, Re = 520.

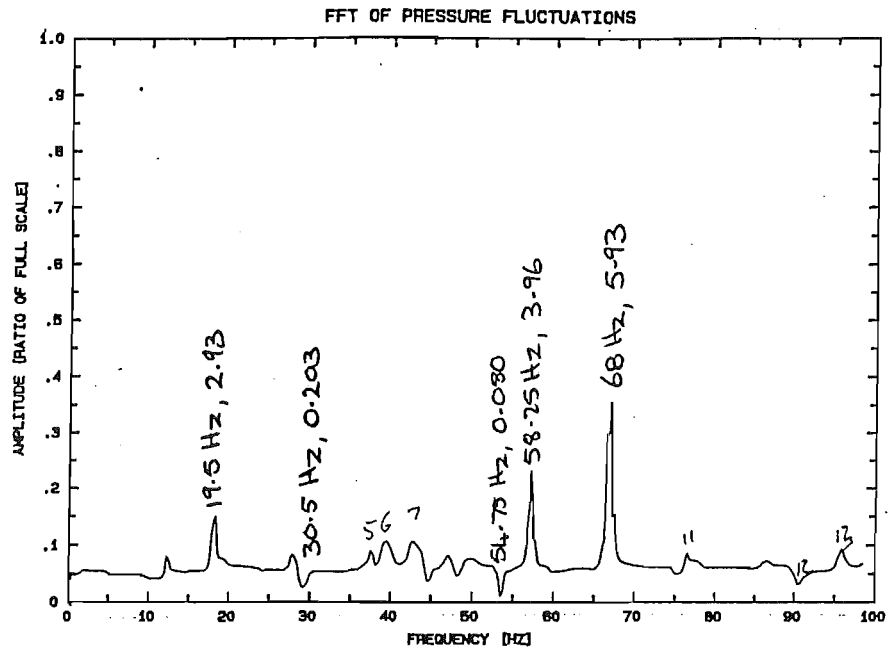

Figure M-5

Position 6, Re = 520.

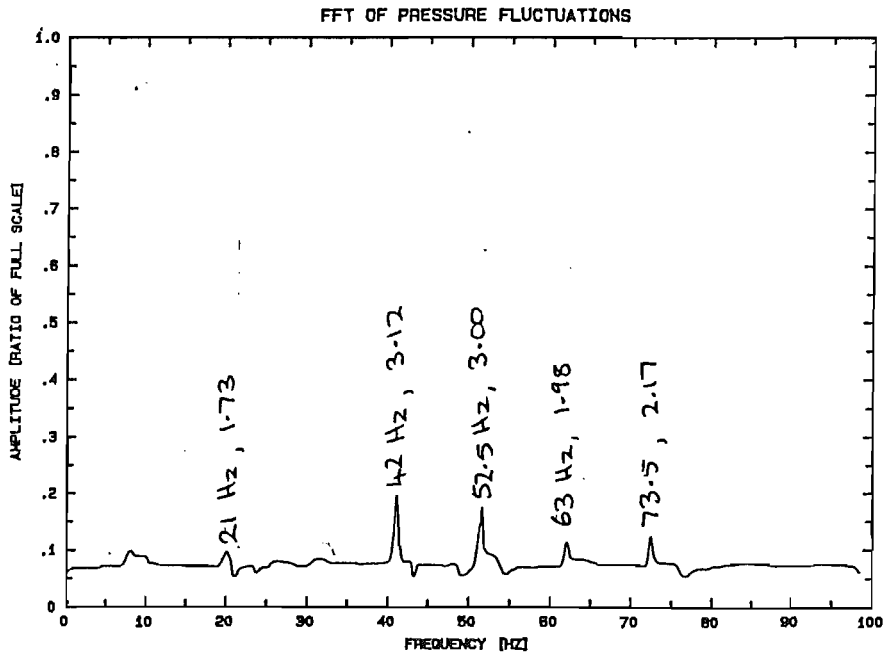

Figure M-6

Position 12, Re = 520.

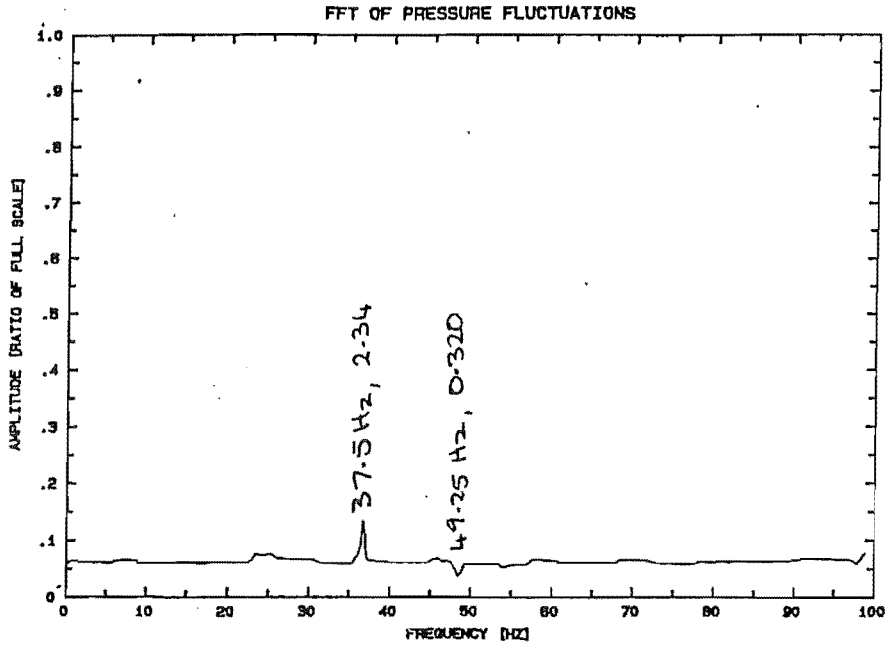

Figure M-7

Position 10, Re = 520.

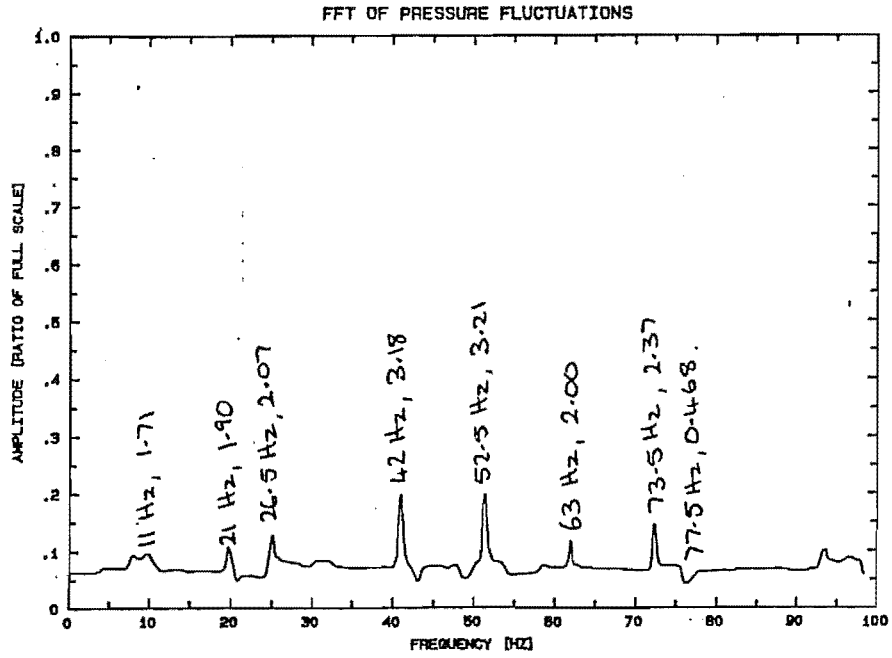

Figure M-8

Position 14, Re = 520.

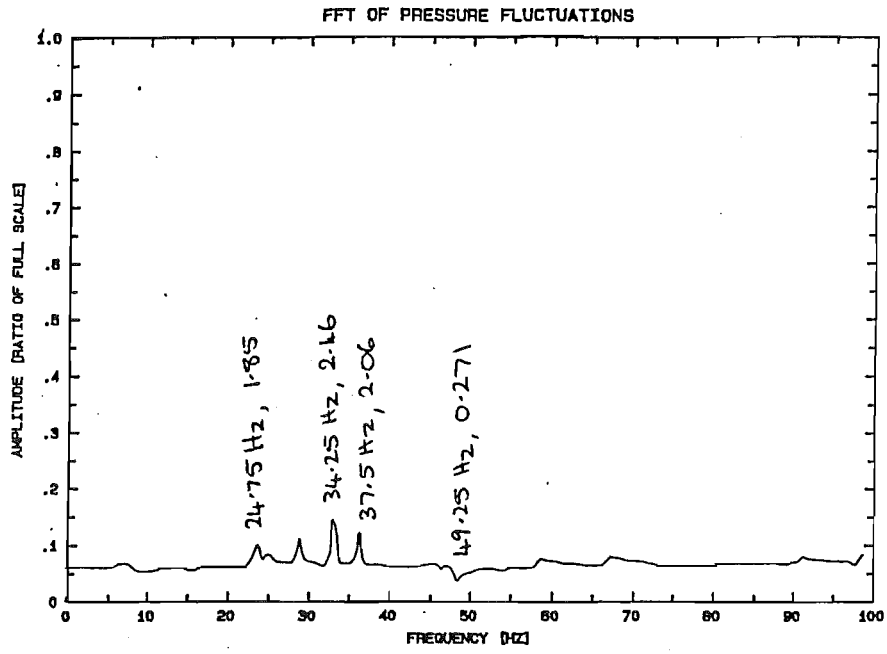

Figure M-9

Position 15, Re = 520.

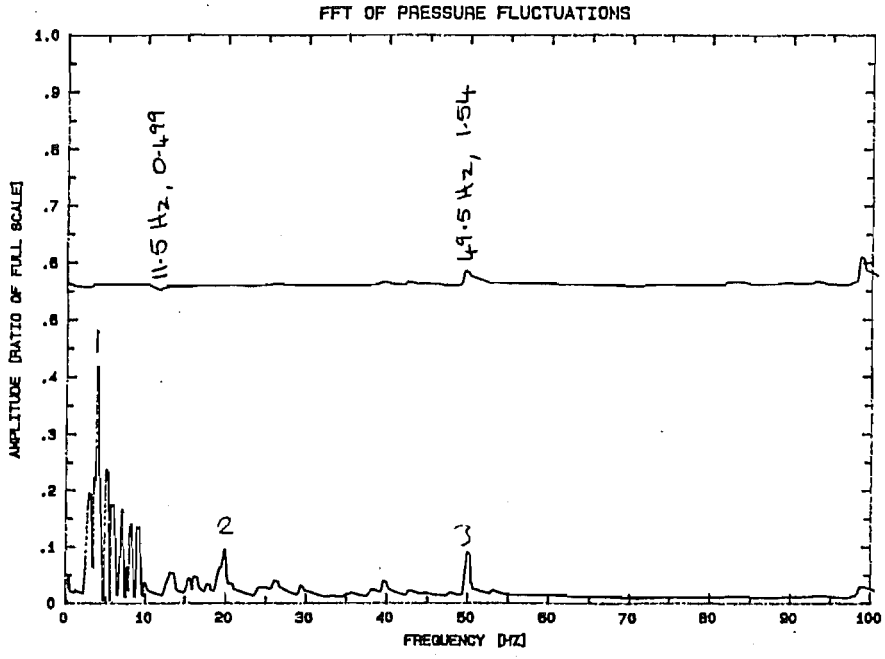

Figure M-10

Position 16, Re = 520.

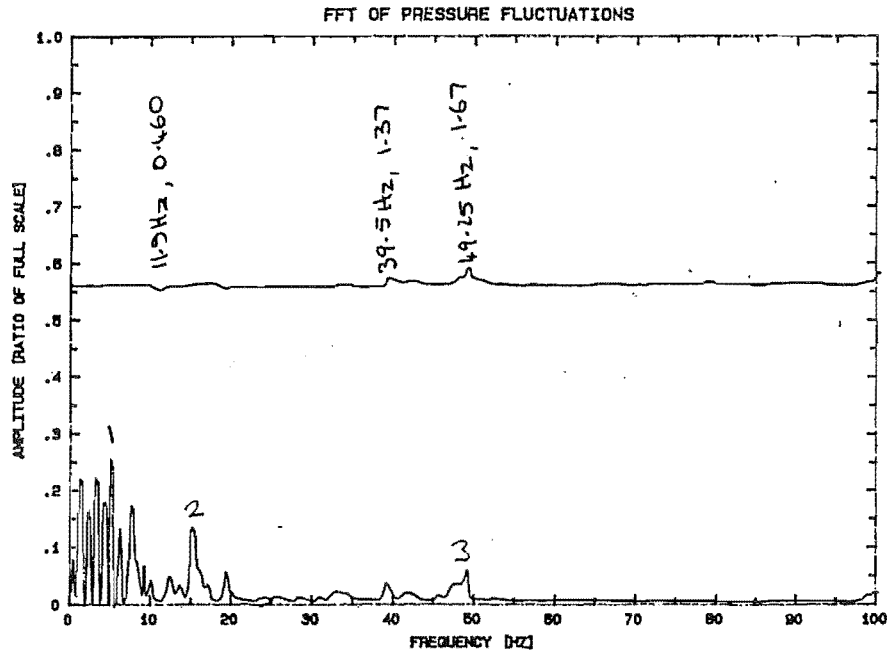

Figure M-11

Position 17, Re = 520.

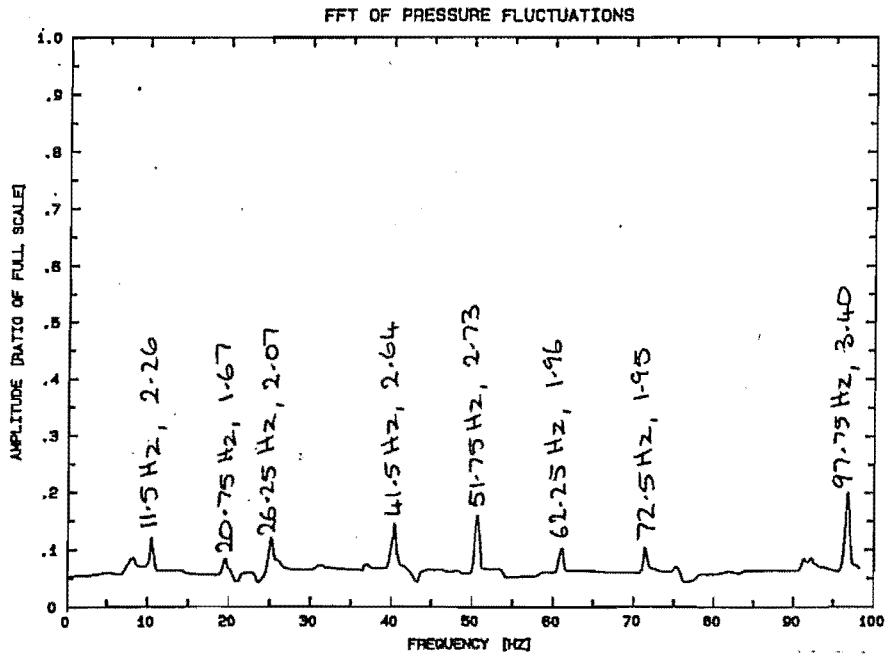

Figure M-12

Position 18, Re = 520.

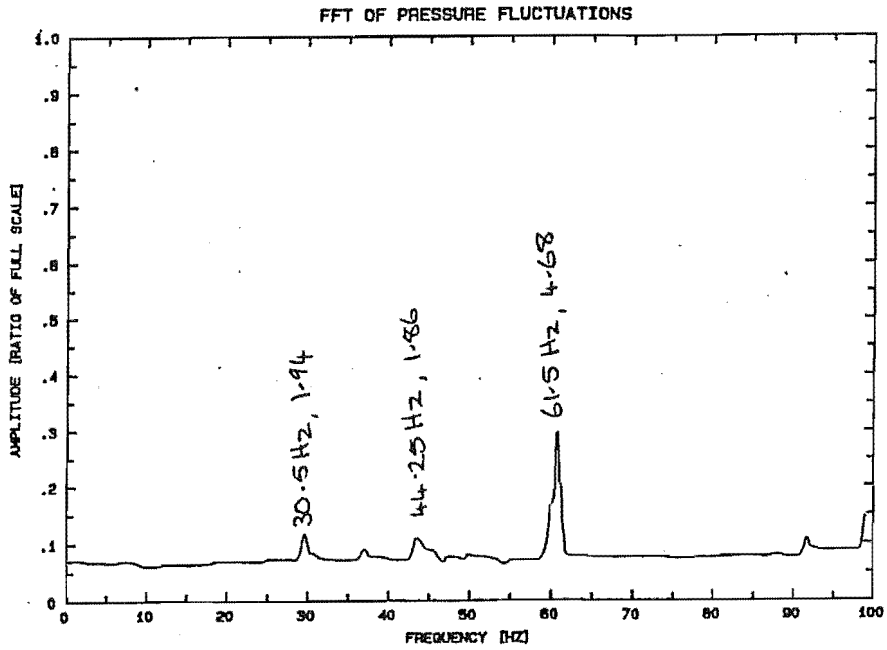

Figure M-13

Position 19, Re = 520.

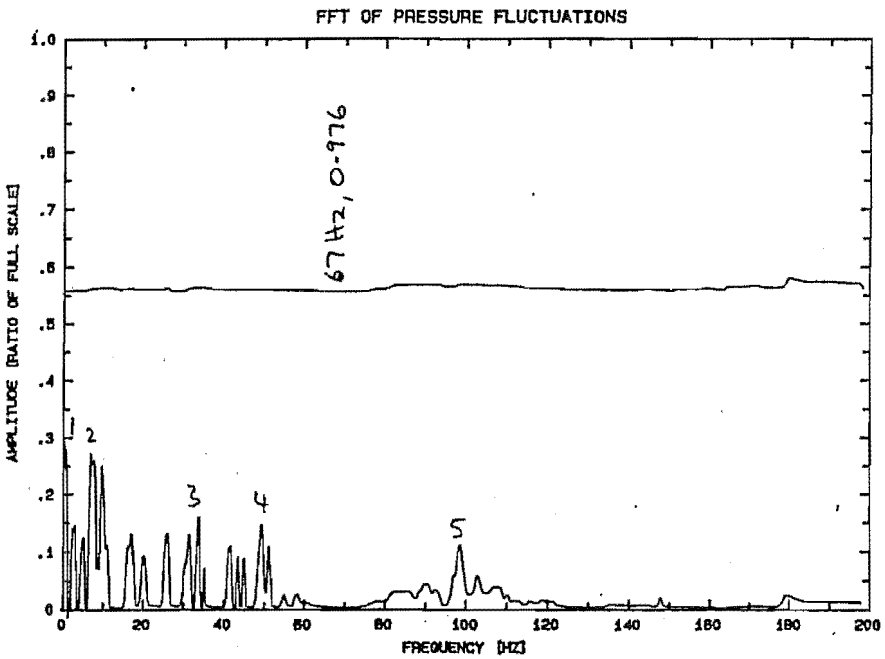

Figure M-14

Position 5, Re = 800.

Appendix N

Shear Layer Velocity Fluctuations

The following Fast Fourier Transforms (FFT's) of the shear layer velocity fluctuations in the proximal and distal limbs were calculated from axial velocities, measured by laser Doppler anemometry. FFT's were computed on the Nicolet Mini-Ubiquitous spectrum analyser, averaged from 8 consecutive sets of 1024 velocity samples.

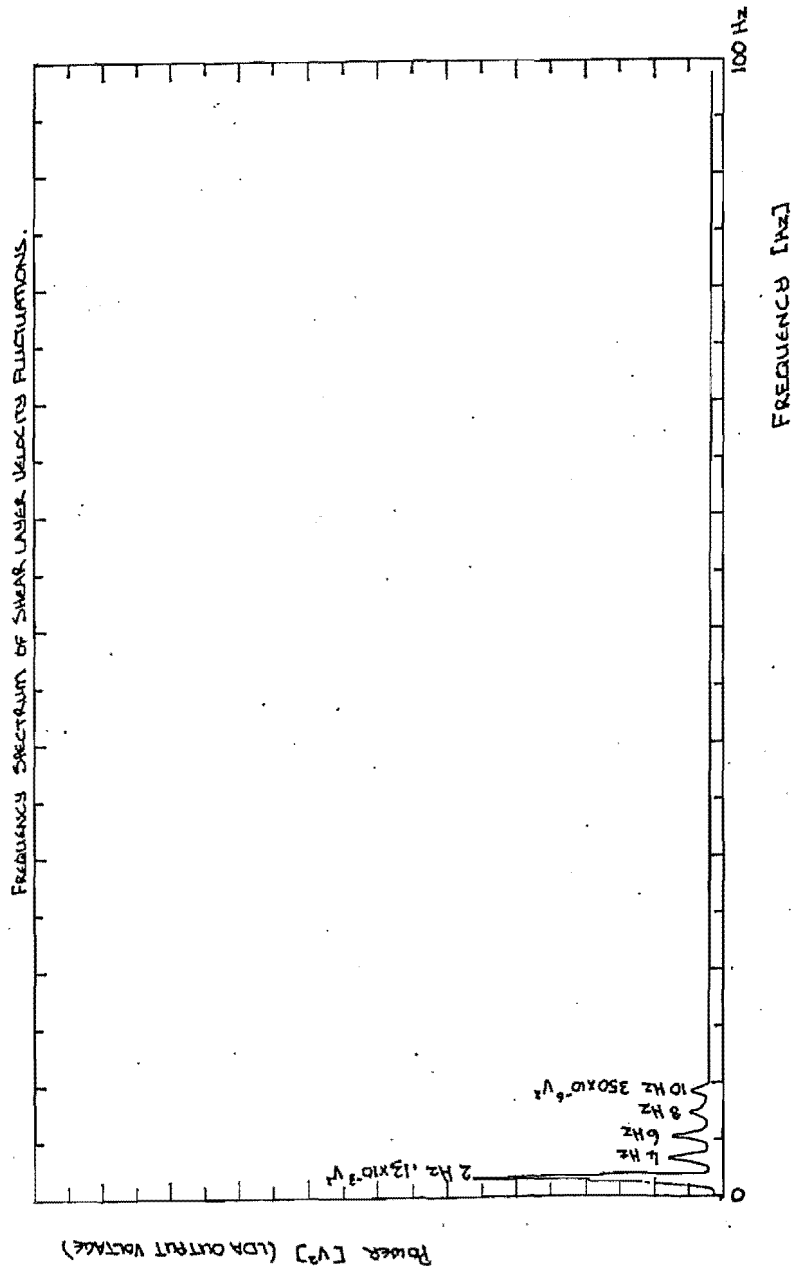

Figure N-1
FFT of Shear Layer Velocity Fluctuations in the Proximal Limb

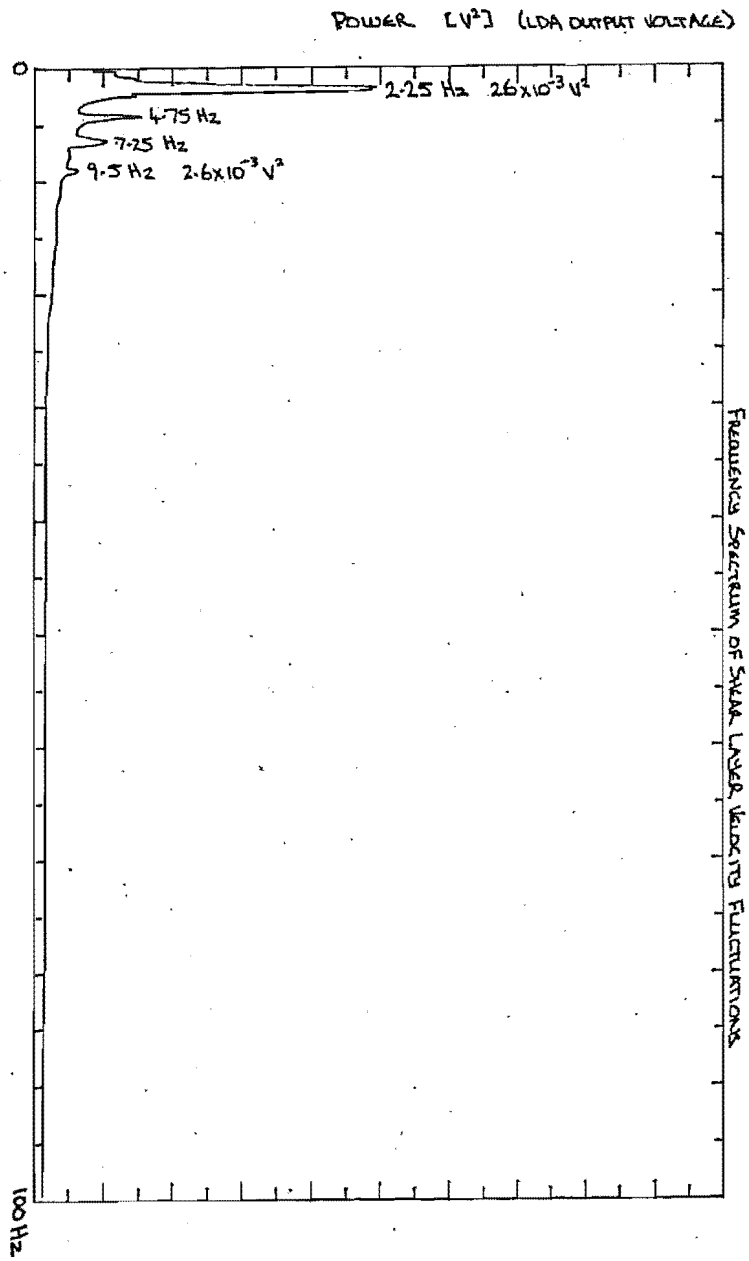

Figure N-2

FFT of Shear Layer Velocity Fluctuations in the Distal Limb